LA-11139-C
Conference

UC-20
Issued: November 1987

LA--11139-C

DE88 001915

Proceedings of the International Workshop on Engineering Design of Next Step Reversed Field Pinch Devices

Held at Los Alamos National Laboratory July 13–17, 1987

Compiled by
David B. Thomson

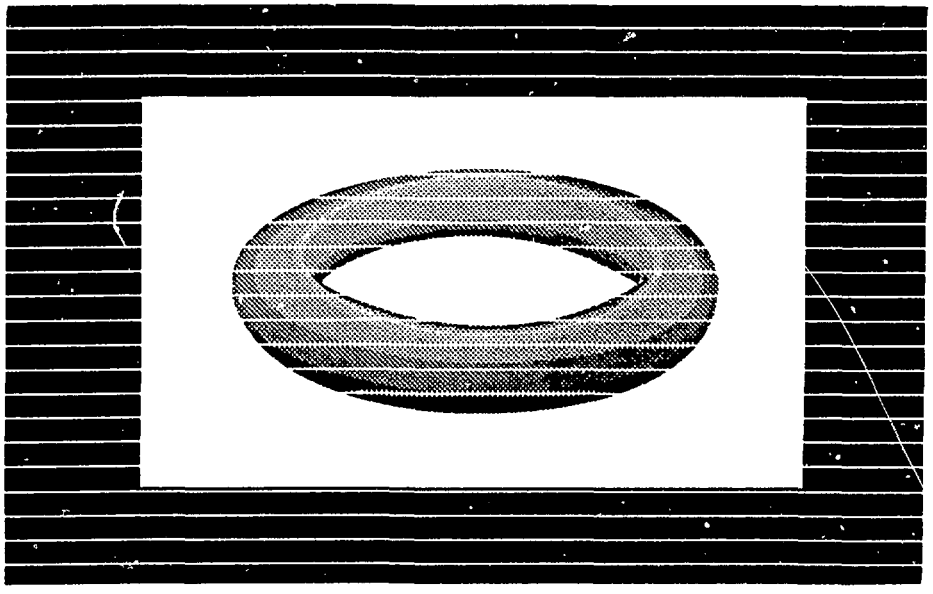

Los Alamos Los Alamos National Laboratory
Los Alamos, New Mexico 87545

Preface

Discussions held by the U.S. and Japanese representatives of the Joint US/Japan Fusion Cooperation Program resulted in the "International Workshop on Engineering Design of Next Step RFP Devices," hosted at Los Alamos, NM, July 13-17, 1987. Participants from the RFP programs in Europe were invited to join their colleagues from the U.S. and Japan in submitting papers and/or participate in the workshop. The workshop concentrated on the engineering solutions to RFP physics design criteria. The workshop was timely in that several large new RFP devices are presently being designed and constructed [the RFX device at Padua in Italy and the ZTH device at Los Alamos].

Participants submitted copy-ready papers for both the formal sessions, and the less formal topical discussion sessions, as listed in the abstract. The Chairman of each topical workshop session gave an oral summary on the last day of the meeting, and submitted a written version for these Proceedings shortly after the workshop. These Proceedings include the papers as submitted by the authors without further editing.

The Los Alamos organizing committee for the workshop included J.N. DiMarco, J.N. Downing, E.O. Ballard, W.E. Fox, P.P. Prince, D.M. Weldon, R.F. Gribble, K.F. Schoenberg, P. Thullen, W.E. Quinn, and D.B. Thomson.

The Committee would like to acknowledge the valuable work of Leeroy Herrera and members of the Protocol staff for coordinating logistics to assure that the overall workshop, including the reception and banquet, went smoothly. Annettee Gonzales was most helpful at the registration and information desk. Grace Vanduyn assisted ably with telex information. Mabel Marquez was most helpful with advance correspondence and with the preparation of these Proceedings. Members of IS Division were very helpful during final preparations of this manuscript.

PROCEEDINGS OF THE
INTERNATIONAL WORKSHOP ON ENGINEERING DESIGN
OF NEXT STEP REVERSED FIELD PINCH DEVICES

Held at Los Alamos National Laboratory

July 13-17, 1987

Compiled by
David B. Thomson

Abstract

These Proceedings contain the formal contributed papers, the workshop papers and workshop summaries presented at the International Workshop on Engineering Design of Next Step RFP Devices held at Los Alamos, July 13-17, 1987.

Contributed papers were presented at formal sessions on the topics: (1) Physics Overview (3 papers), (2) General Overview (3 papers), (3) Front-End (9 papers), (4) Computer Control and Data Acquisition (1 paper), (5) Magnetics (5 papers), and (6) Electrical Design (9 papers).

Informal topical workshop sessions were held on the topics: (1) RFP Physics (9 papers), (2) Front-End (7 papers), (3) Magnetics (3 papers), and (4) Electrical Design (1 paper).

Summaries written by the Chairmen of each of the informal topical workshop sessions are included.

The papers in these Proceedings represent a significant review of the status of the technical base for the engineering design of the next step RFP devices being developed in the U.S., Europe, and Japan, as of this date.

CONTENTS

ATTENDEES

Name	Institution
Paul Anderson	GA Technologies Inc.
Don A. Baker	Los Alamos National Laboratory
Heinrich J. Boenig	Los Alamos National Laboratory
Evan O. Ballard	Los Alamos National Laboratory
Curtis Baker	Los Alamos National Laboratory
Joel G. Bennett	Los Alamos National Laboratory
Stephen O. Dean	LANL Consultant
Richard N. Dexter	University of Wisconsin-Madison
Joseph N. DiMarco	Los Alamos National Laboratory
James N. Downing	Los Alamos National Laboratory
Harry Dreicer	Los Alamos National Laboratory
Lorenzo Fellin	Istituto Gas Ionizzati (Padua)
Will E. Fox	Los Alamos National Laboratory
Michael T. Gamble	Los Alamos National Laboratory
Richard A. Gerwin	Los Alamos National Laboratory
Andrew J. Giger	Los Alamos National Laboratory
Steven P. Girrens	Los Alamos National Laboratory
Francesco Gnesotto	Istituto Gas Ionizzati (Padua)
James W. Gray	Culham Laboratory
Robert F. Gribble	Los Alamos National Laboratory
Albert Haberstich	Los Alamos National Laboratory
Charles F. Hammer	Los Alamos National Laboratory
Jeffery O. Hill	Los Alamos National Laboratory
Steve Huddlestone	Los Alamos National Laboratory
Nobuyuki Inoue	University of Tokyo
Yukio Ishigaki	Hitachi Works, Hitachi Ltd.
Yutaka Itou	Hitachi Works, Hitachi Ltd.
Yutaka Kamada	University of Tokyo
Ralph W. Kewish	Los Alamos National Laboratory
Herb E. Konkel	Los Alamos National Laboratory
Robert A. Krakowski	Los Alamos National Laboratory
Rulon K. Linford	Los Alamos National Laboratory
Lawry W. Mann	Los Alamos National Laboratory
George J. Marklin	Los Alamos National Laboratory
Warren Marton	Department of Energy/OFE
Alvise Maschio	Istituto Gas Ionizzati (Padua)
Jimmy G. Melton	Los Alamos National Laboratory
Francis D. Michaud	Los Alamos National Laboratory
Kenyo Miyamoto	University of Tokyo
Ronald W. Moses, Jr.	Los Alamos National Laboratory
Carter P. Munson	Los Alamos National Laboratory
Richard A. Nebel	Los Alamos National Laboratory
Alan A. Newton	Culham Laboratory
Sergio Ortolani	C.N.R. (Padua)
Hiroshi Oshiyama	Kyoto Institute of Technology

Name	Institution
Isao Oyabu	Mitsubishi
James A. Phillips	Los Alamos National Laboratory
Mark M. Pickrell	Los Alamos National Laboratory
Peter P. Prince	Los Alamos National Laboratory
Warren E. Quinn	Los Alamos National Laboratory
William A. Reass	Los Alamos National Laboratory
Scott Robertson	University of Colorado
John D. Rogers	Los Alamos National Laboratory
Boris Rosev	Los Alamos National Laboratory
Kurt F. Schoenberg	Los Alamos National Laboratory
Aldred E. Schofield	Los Alamos National Laboratory
Arthur R. Sherwood	Los Alamos National Laboratory
Kenneth Sidikman	Los Alamos National Laboratory
Andrea Stella	Istituto Gas Ionizzati (Padua)
Vernon J. Stephens	Los Alamos National Laboratory
Nobuhara Suzuki	Heavy Industries Co., Ltd.
Teruo Tamano	GA Technologies Inc.
David B. Thomson	Los Alamos National Laboratory
Philip Thullen	Los Alamos National Laboratory
Richard K. Traeger	Sandia National Laboratory
Paul G. Weber	Los Alamos National Laboratory
David M. Weldon	Los Alamos National Laboratory
Ronald W. Wilkins	Los Alamos National Laboratory
Glen A. Wurden	Los Alamos National Laboratory
Ed Yavornik	Los Alamos National Laboratory
Zensho Yoshida	University of Tokyo

RFP PHYSICS AND RFX

CHARACTERISTICS AND OBJECTIVES

S. ORTOLANI

ISTITUTO GAS IONIZZATI DEL C.N.R.

EURATOM-ENEA-CNR ASSOCIATION

PADOVA (ITALY)

1987 INTERNATIONAL WORKSHOP ON ENGINEERING DESIGN OF NEXT STEP RFP DEVICES

LOS ALAMOS NATIONAL LABORATORY, U.S.A. - JULY 13-17, 1987

A B S T R A C T

Some main physics aspects of the present RFP research are briefly summarized in relation to the RFX parameters and performance.

Relaxation phenomena are of fundamental importance for the RFP dynamics and their experimental evidence has become firmer in recent years | 1,2,3,4 |. The experimental distributions, although not fully relaxed, are dominated by relaxation phenomena which also impose constraints and difficulties on the achievable global plasma confinement | 5,6 |. The outer region plays a fundamental role in determining the global confinement and accurate plasma position and purity control | 7 | is essential. These aspects largely favour the operation with an active toroidal equilibrium control and a relatively thin shell | 8 |.

Resistive MHD instabilities underly the relaxation process and their role and characteristics are related to the experimental magnetic boundary conditions | 9,10 |.

Transport is stochastic magnetic fields is a good candidate to explain the observed plasma confinement | 11 |. However

the quality of the magnetic geometry remains critical to produce conditions in which the system is not dominated by externally induced field errors. The main parameters of RFX are reviewed and the critical aspects are underlined followed by a discussion of the expected plasma performance.

REFERENCES

| 1 | Antoni V., Ortolani S., Phys. of Fluids, to be published.

| 2 | Antoni V., Buffa A., Carraro L. et al, in Proc. 11th Int. Conf. on Plasma Physics and Controlled Nuclear Fusion Research, Kyoto, IAEA Vienna, (1986).

| 3 | Antoni V., Martin P., Ortolani S., Plasma Phys., Vol. 29 No 2, p. 279 (1987)

| 4 | Antoni V., Martin P., Ortolani S., International Conference on Plasma Physics, Kiev, Vol. 3 p.12 (1987)

| 5 | Ortolani S., Plasma Magnetic Confinement Physics in the Reversed Field Pinch, International Conference on Plasma Physics, Kiev (1987)

|6 | Ortolani S., Magnetic Confinement in Reversed Field Pinch Plasmas, International School of Plasma Physics, Varenna, (1987), to be published

|7 | Gabellieri L., Giubbilei B., Martini S. et al. , Enhanced Dynamo Contribution to the Resistivity of a RFP due to Non-Uniform Effective Charge Profiles, I.G.I. Report 86/03 (July 1986), to be published in Nuclear Fusion.

|8| Ortolani S., Antoni V., Martini S., T. Tamano et al., XIV European Conference on Controlled Fusion and Plasma Physics, Madrid, Vol. 11 D, part II, pag.477 (1987)

|9| Antoni V., Merlin D., Ortolani S., Paccagnella R., Nuclear Fusion, Vol. 26, No 12, p. 1711 (1986)

|10| Merlin D., Ortolani S., Paccagnella R., XIV European Conference on Controlled Fusion and Plasma Physics, Madrid, Vol.11 D, part II, p. 442 (1987)

|11| Antoni V., Giubbilei M., Martin P. et al., in Proc. XIII Europ. Conf. on Controlled Fusion and Plasma Heating, EPS, Sclersee, Vol. 10, part I, p.337 (1986)

RFP PHYSICS AND RFX CHARACTERISTICS AND OBJECTIVES

PRESENT MAIN PHYSICS ASPECTS:

- RELAXATION PHENOMENA
- MAGNETIC DISTRIBUTION ($B(r)$)
- GLOBAL CONFINEMENT (V_{LOOP})
- MHD ACTIVITY (RELAXATION MECHANISM)
- TRANSPORT MECHANISM (SCALING)

MAIN RFX PARAMETERS

CRITICAL ISSUES

EXPECTED PERFORMANCE

RELAXATION PHENOMENA

INCREASING EXPERIMENTAL EVIDENCE AND THEORETICAL STUDIES

THEORETICAL : (3D-MHD)

EXPERIMENTAL :

- FLUCTUATIONS
- *LARGE AMPLITUDE OSCILLATIONS*
- CURRENT DENSITY PROFILE REDISTRIBUTIONS

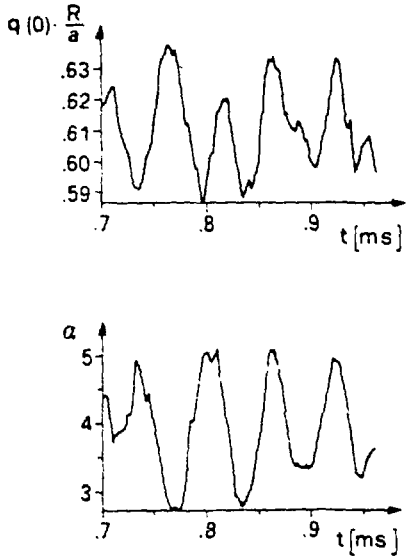

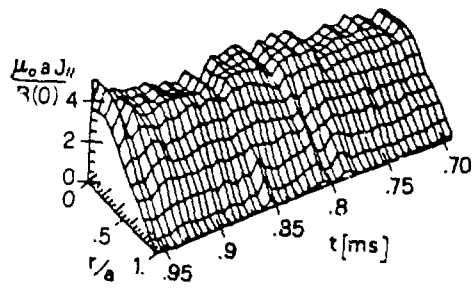

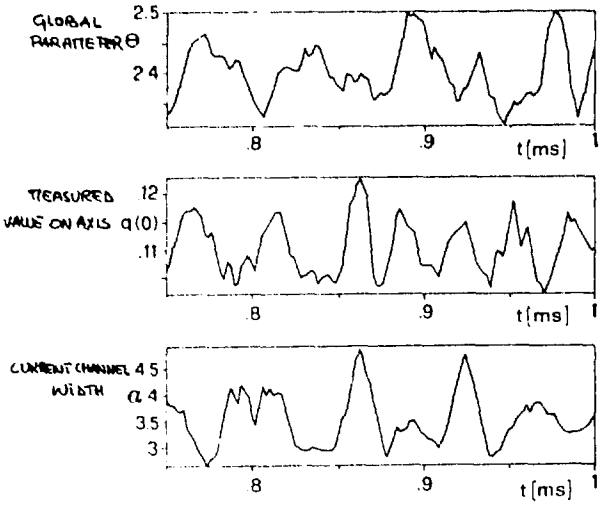

THESE PHENOMENA ARE OF FUNDAMENTAL IMPORTANCE FOR THE RFP DYNAMIC AND IT IS NECESSARY TO GUARANTEE THAT EXPERIMENTAL CONDITIONS CAN BE PRODUCED IN WHICH RELAXATION IS FULLY AT WORK (E.G. SMALL RADIATION, SMALL STREAMING , APPROPRIATE BOUNDARY CONDITIONS, ETC.).

MAGNETIC DISTRIBUTION

IS NOT THE FULLY RELAXED STATE

$$\nabla \times B = \mu B = \mu_0 J_{//}$$

∇p EFFECTS

DIRECT $\quad J_\perp = -\dfrac{\nabla p \times B}{B^2}$

INDIRECT $\quad \nabla T \rightarrow \nabla \eta$

$\Rightarrow$ LESS $J_{//}$ THAN THAT OF THE FULLY RELAXED STATE IN THE OUTER HIGHER RESISTIVITY REGION

IT IS EXTREMELY IMPORTANT TO HAVE DETAILED MEASUREMENTS IN THE PLASMA OUTER REGION WHERE SMALL DIFFERENCES IN TEMPERATURE AND CURRENT PROFILES MAKE SIGNIFICANT DIFFERENCES IN THE GLOBAL CONFINEMENT PROPERTIES OF THE RFP CONFIGURATION.

GLOBAL CONFINEMENT:

OHMIC HEATING

$$\tau_E = \frac{3}{8}\mu_o R \beta_\theta \frac{I}{V} \simeq \frac{\beta_\theta}{2} \frac{R(m)\ I(MA)}{V(volts)}$$

$$\tau_E^{RFX} \simeq \beta_\theta \frac{I(MA)}{V(volts)}$$

$\beta_\theta \simeq 0.1$

$\tau_E \sim 2 - 20$ ms

$V \sim 10 - 100$ volts

IN PARTICULAR:

ROLE OF THE OUTER REGION

- HIGH DISSIPATION REGION IN GENERAL
- DETAILED KNOWLEDGE OF RESISTIVITY AND CURRENT DENSITY PROFILES IS ESSENTIAL
- IMPURITY CONTROL

IMPURITIES THROUGH THE Z_{EFF} PROFILE CAN SIGNIFICANTLY INCREASE THE DISSIPATION IN THE OUTER REGION AND THEREFORE THE POWER/HELICITY INPUT REQUIREMENT, THOUGH NOT SIGNIFICANTLY CONTRIBUTING TO THE GLOBAL PLASMA POWER BALANCE AS A RADIATION SOURCE.

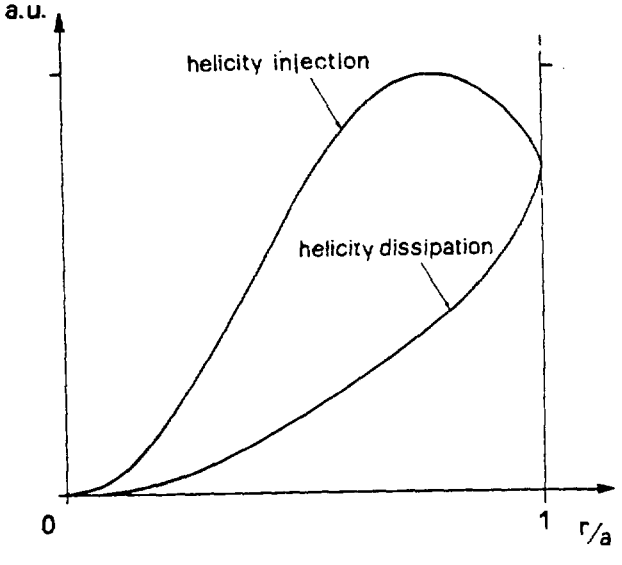

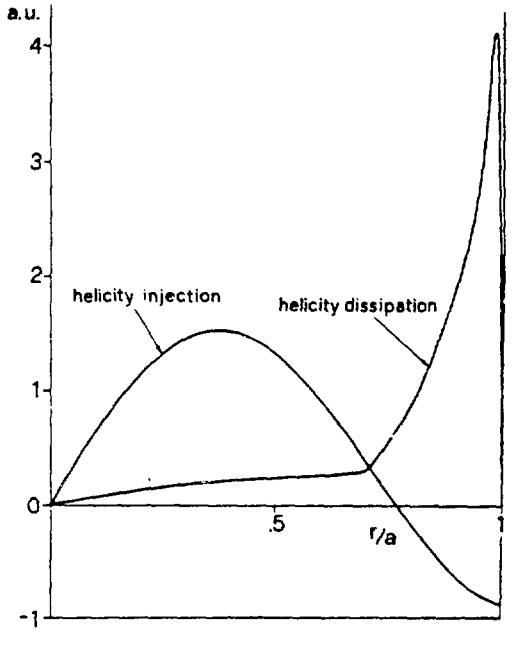

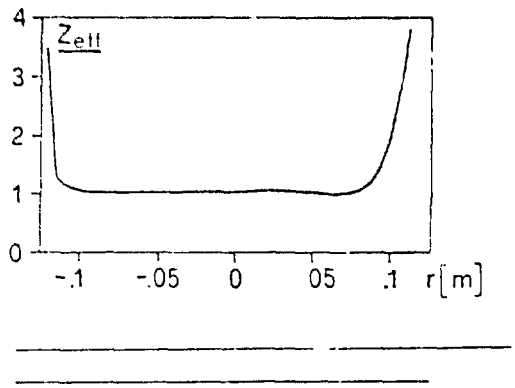

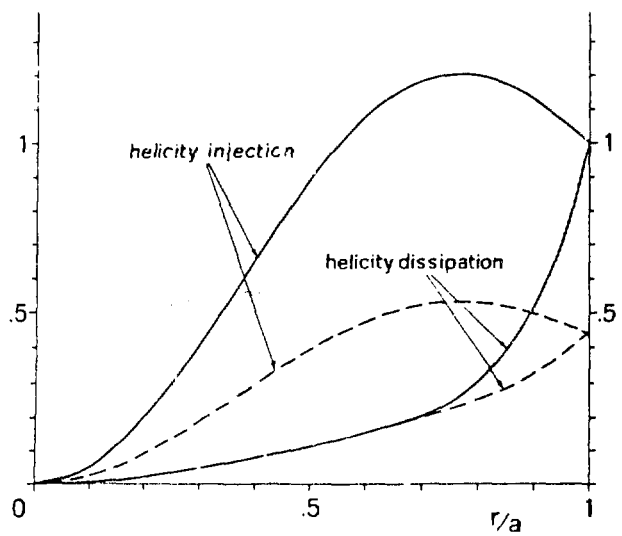

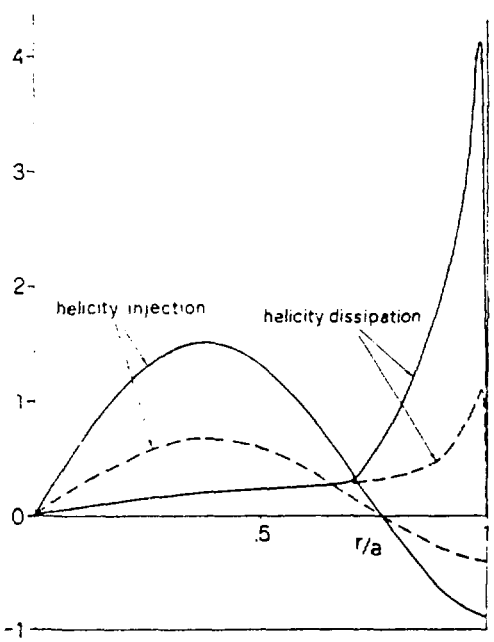

THE ENHANCED DISSIPATION IN THE OUTER REGION DUE TO THE HOLLOW Z_{EFF} PROFILE MUST BE COMPENSATED BY A HIGH LOOP VOLTAGE TO SUSTAIN THE CURRENT DENSITY PROFILE.

THIS RESULTS IN AN INCREASE OF THE APPARENT RESISTIVITY AND THEREFORE IN DEGRADED CONFINEMENT.

THIS EFFECT IS PARTICULARLY IMPORTANT AT LOW DENSITY SINCE

$$Z_{EFF} \propto \frac{1}{n_e} \sum n_z z^2$$

IF THIS INTERPRETATION MAY SOLVE SOME DOUBTS ABOUT THE PECULIARITIES OF THE HIGH I/N REGIME, IT ALSO STRESSES THE IMPORTANCE OF OPERATING AT HIGH DENSITY.

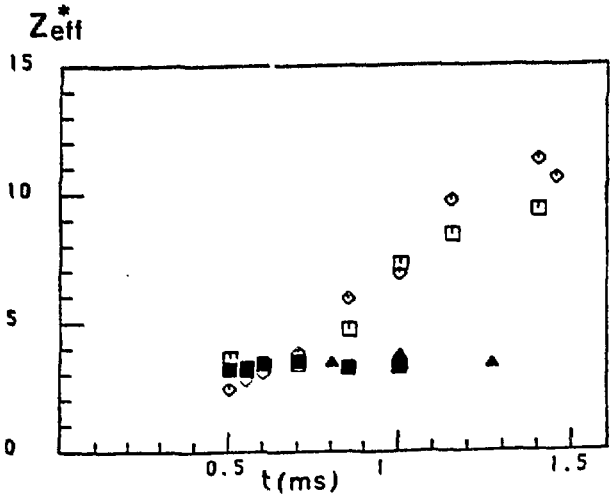

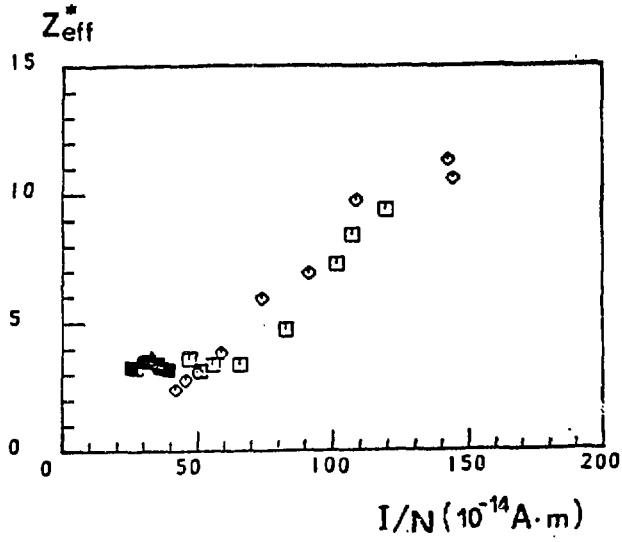

- MINIMIZE PLASMA - WALL INTERACTIONS
- ACCURATE PLASMA POSITION CONTROL
- ACCURATE MAGNETIC GEOMETRY

$$V_{loop} = \frac{1}{\phi}\int_V \eta \underline{J}\cdot\underline{B}\,dv$$

⇑

OUTER REGION DOMINATED

MHD INSTABILITIES (RELAXATION MECHANISM ?)

THE EXPERIMENTAL PROFILES ARE NEARLY FORCE FREE ($\beta < 10\ \%$)

BUT THE PARALLEL CURRENT DISTRIBUTION IS NOT DESCRIBED BY

$$\mu \propto \frac{J_{//}}{B} = \text{CONST}$$

$$\mu(r) = \mu(0)\,f(r)$$

$$\mu(0) = \frac{?}{Rq(0)} = \frac{2\Theta_0}{a}$$

$$f(r) = 1 - (r/a)^{\alpha}$$

⇒ PARAMETRIC MHD STABILITY ANALYSIS

$$\mu(r) = \frac{2\Theta_0}{a}\left(1-\left(\frac{r}{a}\right)^{\alpha}\right)$$

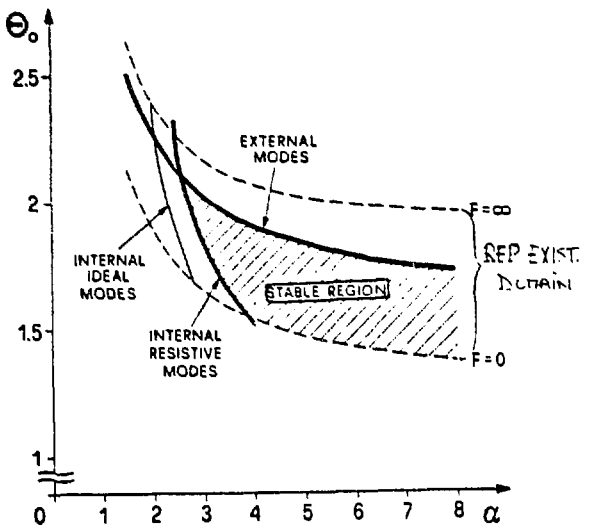

FIG. 7

ALTHOUGH ON AVERAGE THE EXPERIMENTAL PROFILES ARE STABLE TO CURRENT DRIVEN MODES, RESISTIVE DIFFUSION TENDS TO DESTABILIZE THE CONFIGURATION LEADING TO LOWER $q(0)$ BY PEAKING THE CURRENT DISTRIBUTION ON AXIS.

WHEN $q(0)$ DROPS BELOW A CRITICAL VALUE $q \simeq \frac{2}{3}\frac{a}{R}$, THE INTERNAL MODES ARE EXCITED AND THESE MODES ARE RESPONSIBLE FOR THE CURRENT REDISTRIBUTION WHICH RESTORES THE INITIAL TEARING MODE STABLE CONFIGURATION AND SO FORTH IN A CYCLIC FASHION.

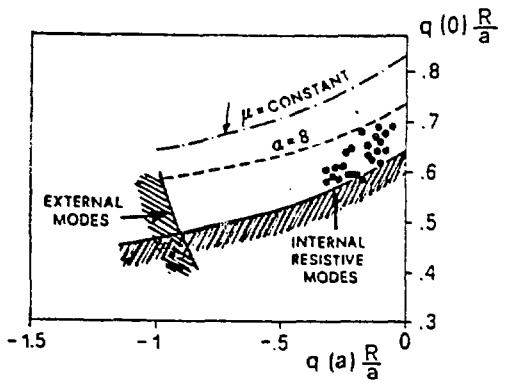

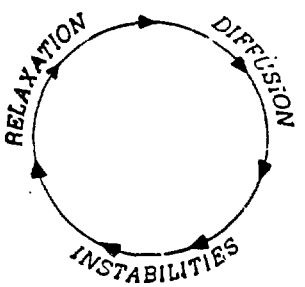

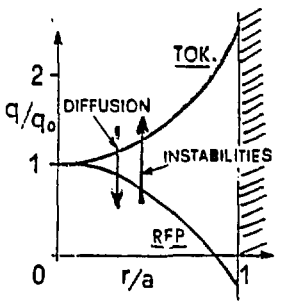

THIS PICTURE CAN SATISFACTORLY DESCRIBE, AT LEAST QUALITATIVELY THE DYNAMICS OF THE PLASMA CORE.

THE OUTER REGION IS PROBABLY DOMINATED BY A WIDER, MORE COMPLICATED SPECTRUM OF SIMULTANEOUSLY OCCURRING MODES RELATED TO .

- THE CLOSER SPACING OF RATIONAL SURFACES
- ROLE OF $M=0$ MODES RESONANT AT B_θ REVERSAL SURFACE
- PRESSURE GRADIENT EFFECTS

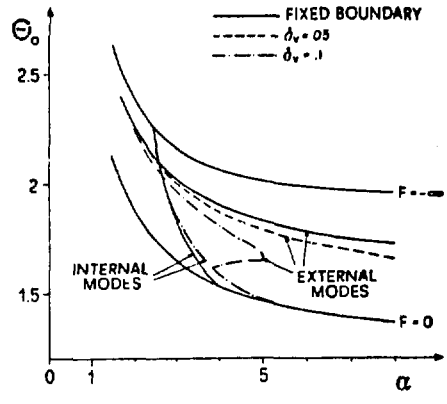

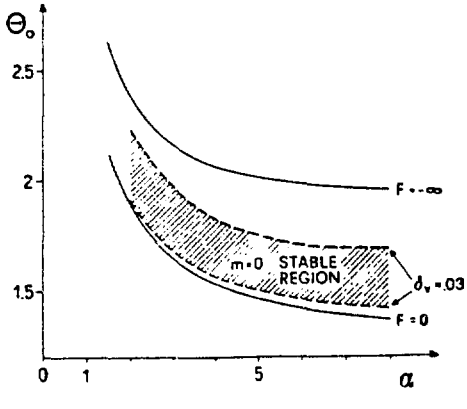

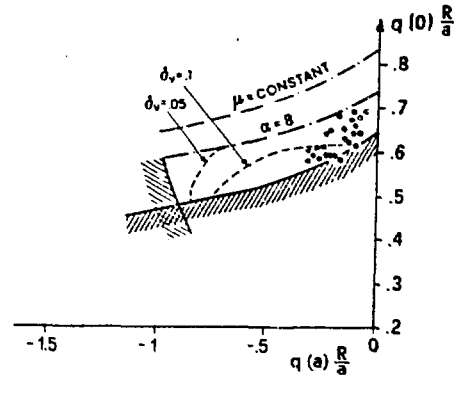

- RELAXATION WITH DIFFERENT B.C.

- WHICH ARE THE APPROPRIATE B.C. ?

- CONSTRAINTS ON THE VACUUM VESSEL AND SHELL DESIGN IN TERMS OF THICKNESS (I.E. CHARACTERISTIC TIMES) AND IN TERMS OF PLASMA - SHELL INTERSPACE

GRAPHITE INNER RADIUS = 457 MM.

VACUUM VESSEL INNER RADIUS = 475 MM.

VACUUM VESSEL OUTER RADIUS = 505 MM.

SHELL INNER RADIUS = 535 MM.

SHELL OUTER RADIUS = 600 MM.

$$\frac{\Delta_{vac}}{a} \simeq 15 - 30\ \%$$

TRANSPORT MECHANISM

STOCHASTIC MAGNETIC FIELDS

DIFFUSION IN STOCHASTIC MAGNETIC FIELDS DEPENDS ON $\delta B/B$

THE PERTURBATIONS INDUCED BY THE MAGNETIC SYSTEM MUST NOT BECOME DOMINANT

FOR THE RFP TO HAVE SOME PROSPECTS FOR FUSION IT IS NECESSARY THAT $\delta B/B$ DECREASES AT HIGHER CURRENTS AND TEMPERATURES => IN A PLASMA REGIME OF REDUCED FLUCTUATION AMPLITUDES THE PERTURBATIONS DUE TO THE EXTERNAL MAGNETIC SYSTEM MUST NOT BECOME DOMINANT.

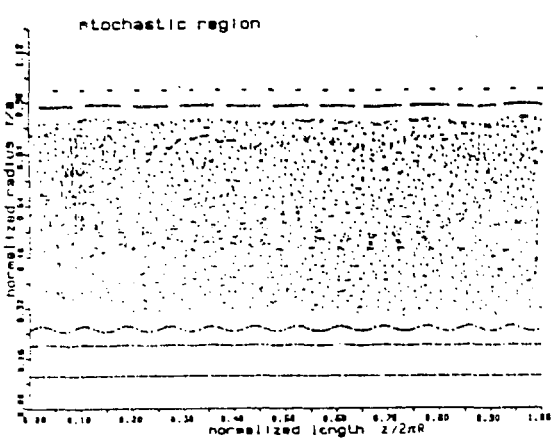

D_{MAGN}

$\chi^e_{stoch.} = D_{MAGN}\, v^e_{th} \simeq 5(-10)\ m^2/s$

$\chi^e_{stoch.} \simeq \chi^e_{exp}$ in the plasma intermediate region

$0 < q \leq \frac{q(0)}{2}$

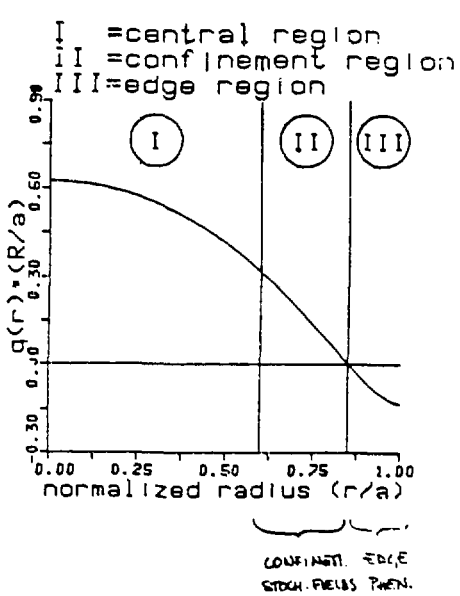

RFX . MAIN MACHINE PARAMETERS

major radius	2 m
minor radius	0.5 m
maximum current	2 MA
rise time	15-50 ms
flat-top time	0.25 s
flux swing	15 V.s
maximum applied toroidal field	0.7 T
inductive stored energy	72 Mj
DC converters	400 MVA
capacitive stored energy	5 Mj
vacuum system volume/speed	2 s

GEOMETRICAL FACTORS

	R/a^2	a^2
RFX	1	1
HBT-Y	1.5	0.26
ZT-H	1.7	0.64
WISCONSIN	2.0	0.41
REPUTE	2.56	0.16
ZT-40	3.5	0.16
OHTE	4.6	0.13
TPE-1RM (15)	4.8	0.07
ETA-BETA II	5.2	0.06
STP-3 (M)	6.25	0.04

MAXIMUM INITIAL VOLTAGE 0.7 KV

TRANSFER RESISTANCE .175 - 2.8 Ω

=> $\hat{V}$ BETWEEN $\hat{I}$ & $\hat{I}/4$

$\hat{I}$ BETWEEN $\hat{V}$ & $\hat{V}/4$

FLAT TOP VOLTAGE $\leq$ 80 V ($\leq$ 40 V)

MAXIMUM TOROIDAL FIELD $\leq$ 0.7 T

$$\langle B_\theta \rangle = \frac{1}{5} \frac{I\,(MA)}{a\,(m)\,\Theta}$$

2MA <=> ~ 0.7 T

=> NO FLUX LOSS

TOKAMAK $\leq$ 200 KA

CRITICAL ISSUES

- DENSITY CONTROL
- OUTER REGION & HELICITY DISSIPATION
- MHD ACTIVITY & VACUUM INTERSPACE
- ACTIVE PLASMA POSITION CONTROL
- THIN CONDUCTING SHELL

TABLE 1 - RFX PARAMETERS

a	(m)			0.5			
R	(m)			2			
I/N	(10^{-14} A·m)			4			
Z_{eff}				4			
I	(MA)		1			2	
<n>	(10^{20} m^{-3})		0.3			0.6	
β_θ	(%)	10	5.8	4.6	10	4.6	3.7
<T>†	(KeV)	0.6	0.4	0.3	1.2	0.6	0.5
T(o)	(KeV)	0.9	0.55	0.4	1.8	0.9	0.7
V_{Loop}	(V)	6	12.5	18	4	12.5	18
τ_E	(ms)	16	4.5	2.5	47	7	4
<n> τ_E	(10^{18} m^{-3} s)	0.5	0.15	0.1	3	0.5	0.25
$\beta_\theta \tau_E$	(ms)	1.6	0.25	0.12	4.7	0.3	0.15
ξ	(%)	2.4	3.1	3.5	1.7	2.5	2.8
B	(10^5)	3.5	1.1	0.8	10	4.6	1.5
		a)	b)	c)	a)	b)	c)

a) β = const scaling

b) $\beta = I^{-1/3}$ scaling

c) $\beta = I^{-1/3}\, a^{-1/6}$ scaling

† Temperature averaged over density profile

RFX PLASMA PARAMETERS

I (MA)	2	1
V (volts)	20	30
β_θ	0.1	0.1
τ_E (ms)	10	3
I/N (A·m)	$2 \cdot 10^{-14}$	$2 \cdot 10^{-14}$
$\langle T \rangle$ (eV)	600	300
Z_{eff}^*	9	10
$\langle n \rangle$ (m^{-3})	$1.2 \cdot 10^{20}$	$0.6\ 10^{20}$
ξ (%)	1.2	1.7
$\langle n \rangle \tau_E$ (m^{-3} s)	$1.2 \cdot 10^{18}$	$0.2 \cdot 10^{18}$
$\langle n \rangle \tau_E \langle T \rangle$ (keV m^{-3} s)	$0.7 \cdot 10^{18}$	$0.06 \cdot 10^{18}$

Fig 1

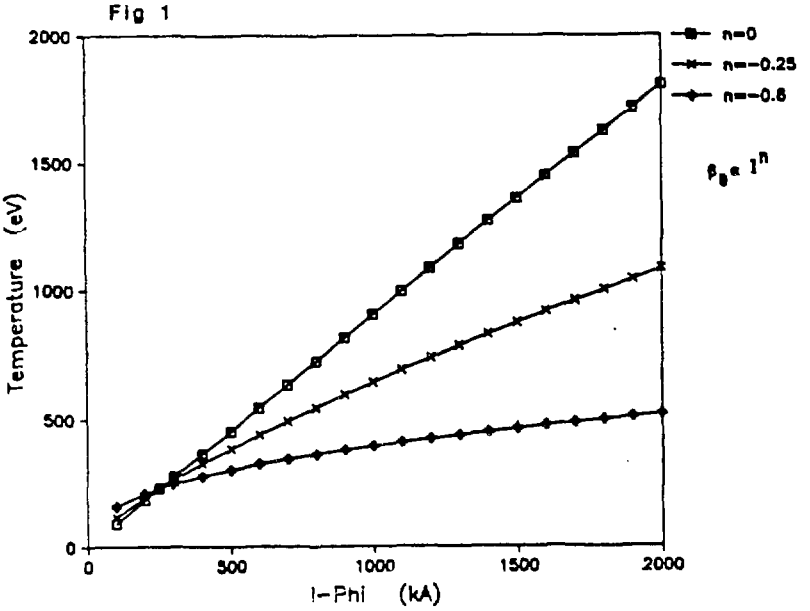

Fig 2

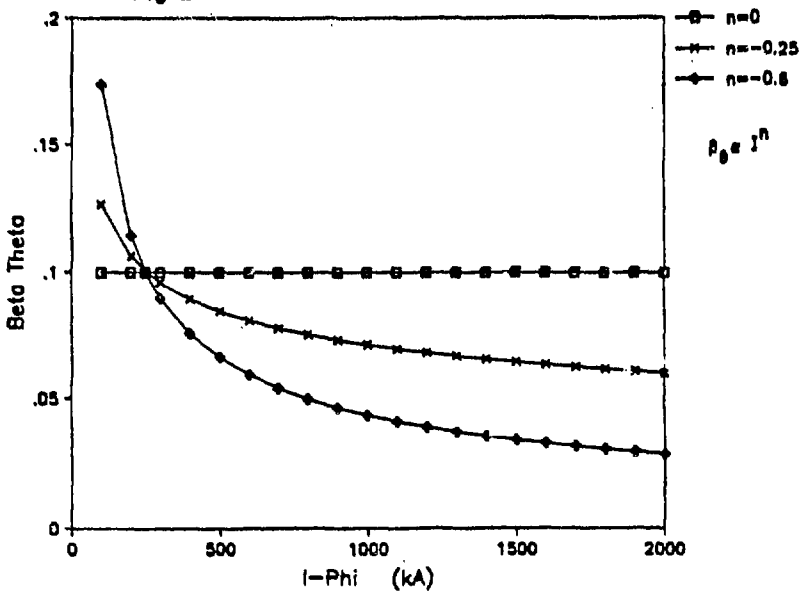

Fig. 3

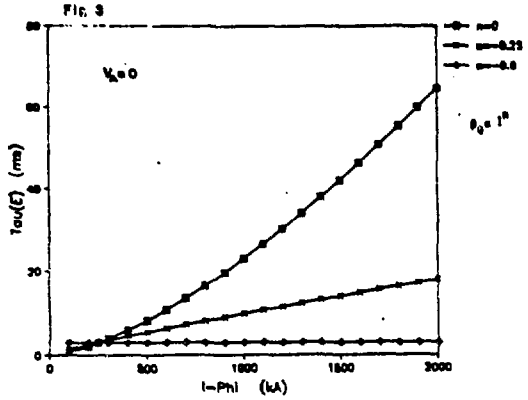

Fig 4

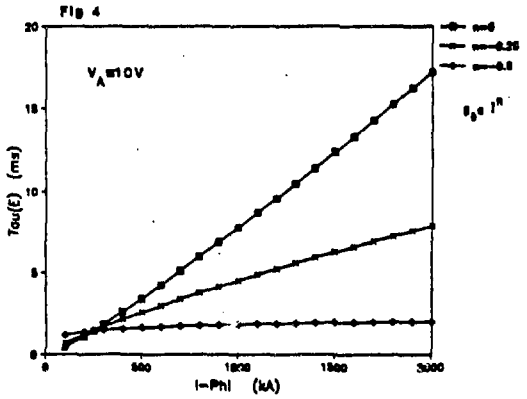

Fig 5

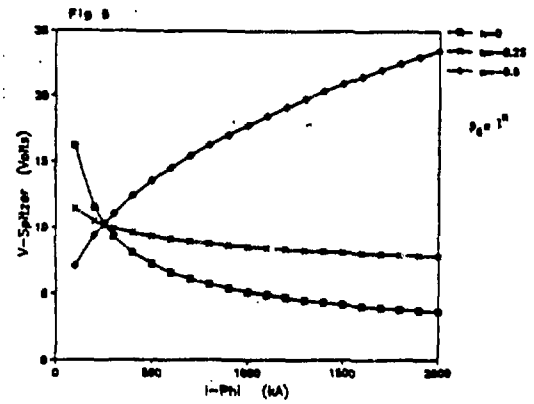

STP-4 PROJECT

K.I.Sato, S.Masamune,* S.Yamada, H.Arimoto,
A.Nagata,+ and T.Tamaru+

(Presented by H.Oshiyama)

Institute of Plasma Physics, Nagoya University,
Chikusa-ku, Nagoya 464, Japan.
* Department of Electrical Engineering, Kyoto Institute of Technology,
Sakyo-ku, Kyoto 606, Japan.
+ Faculty of Engineering, Hiroshima University,
Higashi-Hiroshima 724, Japan.

1. Introduction

The STP-4 (Symmetric Toroidal Pinch #4) has been designed as a successor of the STP-3(H) Reversed Field Pinch (RFP)[1] at the Institute of Plasma Physics in Nagoya University. One of the two major objectives of the STP-4 project is to provide experimental data in a RFP for the total understandings of the behavior of the plasma in current-carrying torcidal systems from the standard tokamak through the ultra-low q (ULQ) to the RFP regime. The other is to establish the confinement scalings

of RFP's in high-current density regime, which plays a key role in designing the Compact RFP Reactor (CRFPR). Moreover, the STP-4 is expected to play the role of the host machine in Japan for US-Japan and EC-Japan collabotations in the field of RFP.

2. Brief Summary of STP-3(M) Results

The STP-4 is a succesor of the STP-3(M). For convenience, we will give a brief summary of the STP-3(M) results.

(i) A stable high-current density ($j>8$ MA/m^2) RFP plasma has been attained with the use of semi-cylindrical limiters.(Fig.1)[1]

(ii) A favorable scaling (dependence of the temperature and effective ion charge Zeff on the plasma current) has been obtained in the current density regime lower than 4 MA/m^2.(Fig.2)[1]

(iii) The enhancement of the plasma-wall interaction is caused by the enhanced dynamo activity which is observed as a series of pulsive increase of the toroidal flux in high-current density regime ($j>4$ MA/m^2). This results in the increase of the resistive anomaly or Zeff with the plasma current in this regime.(Fig.2) [1,2,3]

(iv) It is found that the metal impurity release is caused by the sputtering which accompanies with the toroidal flux enhancement. [2,3]

(v) Other results relevant to the RFP physics have been reported in references 4-7.

3. Physics Issues in STP-4

It is expected that we will obtain the RFP plasma with the magnetic Reynolds number S of 10^6 in the STP-4 device. The plasma physics relevant to RFP, such as the dynamics of the relaxation phenomena, dynamo action, magnetic and density fluctuations, mechanism of the self-organization, etc. should be intensively studied in this parameter regime in the STP-4.

4. Design of STP-4

The principle of the design is rather conservative because it is given the first priority to attain a high-current density RFP discharge which will result in the production of the RFP plasma with S of 10^6. According to the present data base (scaling) of RFP's, the following parameters are required to produce the plasma with S of 10^6.
The profile-oriented diagnostics such as the temperature and density measurements will require the minor radius of 0.2 m at least.
The aspect ratio should be 5-6 for the purpose of making the phenomena clear without toroidal effects.

R (major radius)	1.2 m
a (minor radius)	0.2-0.25 m
Ip (plasma current)	$\gtrsim$ 1 MA
τ_d (discharge duration)	$\gtrsim$ 0.1 sec
Te ~ Ti	$\gtrsim$ 1 keV
τ_E (energy confinement time)	~ 1 msec

The iron core will be used for the Ohmic heating, because it is estimated that the air core system will require 30-40 MJ energy, which

is intolerably high for this project. The use of the flywheel generator is under consideration.

A thick conducting shell is used for maintaining the equilibrium. The poloidal coil system for the equilibrium control will be almost the same as that for the TPE-1R(M)15.

An example of the STP-4 design is given in Fig.3.

REFERENCES

1) K.I.Sato, T.Amano, Z.X.Chen, H.Arimoto, S.Yamada et al., Proc. 11th Int. Conf. on Plasma Physics and Controlled Nuclear Fusion Research (1986), IAEA-CN-47/D-II-2.
2) A.Matsuoka, K.I.Sato, H.Arimoto, S.Yamada, A.Nagata, S.Masamune and H.Murata, J. Phys. Soc. Jpn. 55 (1986) 4186.
3) Y.Kamada, H.Arimoto, S.Yamada, K.Nagashima, A.Matsuoka, K.I.Sato and N.Inoue, J. Phys. Soc. Jpn. 56 (1987) 859.
4) H.Arimoto, S.Masamune, A.Nagata, K.Ogawa, A.Matsuoka, H.Shindo, H.Oshiyama, T Tamaru and K.I.Sato, J. Phys. Soc. Jpn. 54 (1985) 1232.
5) S.Masamune, H.Oshiyama, A.Nagata, H.Arimoto, S.Yamada and K.I.Sato, J. Phys. Soc. Jpn. 56 (1987) 1278.
6) S.Shiina, K.Saito, H.Arimoto, A Matsuoka, S.Yamada, S.Masamune, A.Nagata and K.I.Sato, J. Phys. Soc. Jpn. 56 (1987) 1282.
7) H.Arimoto, A.Nagata, K.I.Sato, S.Masamune, Y.Aso, K.Ogawa, S.Yamada, A.Matsuoka, H.Oshiyama and T.Tamaru, to be published in Nucl. Fusion (1987).

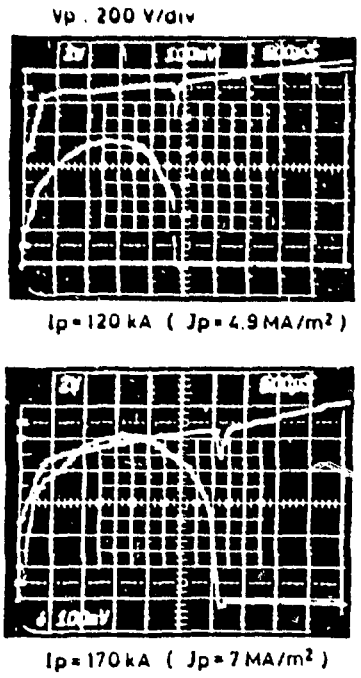

Fig.1. Examples of high-current Density Discharge.

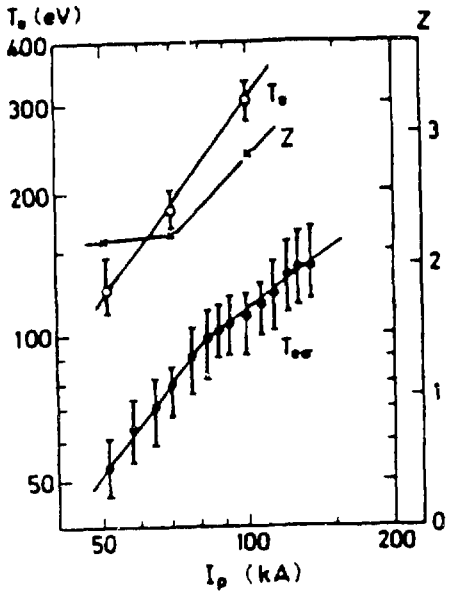

Fig.2. Depandence of the temperature and Zeff on the plasma current.

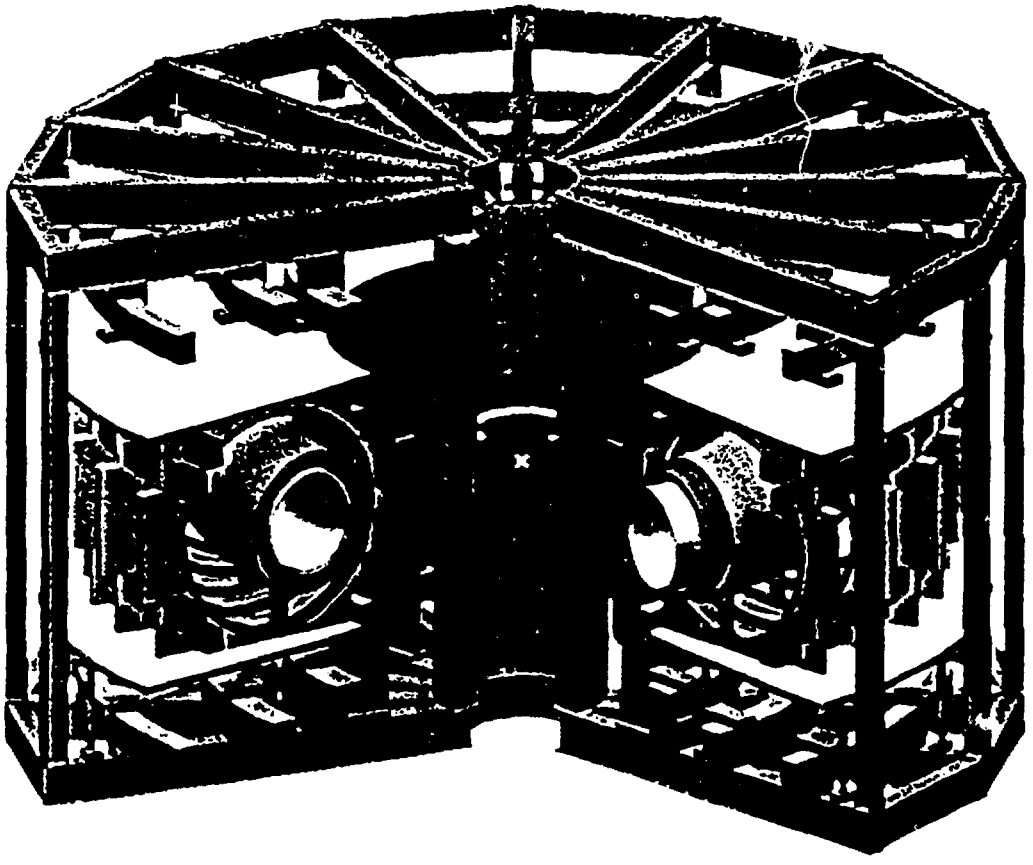

Fig.3. Example of the design of the STP-4.

PHYSICS RATIONALE FOR THE ENGINEERING SPECIFICATIONS FOR ZTH*

by

J.N. DiMARCO

UNIVERSITY OF CALIFORNIA
LOS ALAMOS NATIONAL LABORATORY
LOS ALAMOS, NEW MEXICO 87545

INTRODUCTION

This report presents the physics rationale that established the engineering design of ZTH. The physics criteria are given and the implications regarding the engineering design are presented. Experimental and theoretical background evidence is given in support of the criteria but the justification is left to other reports and peer reviews. In the interests of controlling the length of this report the physics criteria to be discussed here are limited to the ones deemed to be of highest engineering priority

The issues and physics criteria are not presented in a mathematically closed fashion. The process of developing the physics criteria is a complicated procedure; constraints related to available resources are involved in the process, but are not discussed here. The final engineering specifications are the result of an intricate interplay of physics requirements coupled with engineering constraints. The values presented here represent an intense effort on the part of the ZTH Technical Steering Committee to determine priorities and resolve the issues.

The ZTH design issues are listed in alphabetical order in the first section of this report, along with the design specifications for each issue. The physics criteria that generated the values for the design specifications are addressed in the same order in the following section. This method of presenting the information will cause some repetition and requires premature presentation of some new criteria. These criteria will be justified later in this report. The author asks the reader to accept the procedure in the interests of simplifying this presentation.

* Work performed under the auspices of the USDOE.

ZTH DESIGN ISSUES

ZTH ISSUE	VALUE
ASPECT RATIO A=R/a	6
BETA THETA β_θ	DESIGN VALUE =0.1; RANGE 0 TO 0.2
CURRENT I_θ (MA)	DESIGN VALUE =4; RANGE 0.5 TO 4
CURRENT RISE TIME τ_r (ms)	50
FIELD ERRORS	FIELD LINE DEVIATION ±5mm WRT LINER AND/OR MAX. ISLAND WIDTH AT REVERSAL SURFACE ±.0875a WRT REVERSAL SURFACE(MBFM)
INTERNAL INDUCTANCE[1] l_i	DESIGN VALUE =1.4; RANGE 0.5 TO 2.0
LINER RESISTANCE(mΩ)	8.5
MAJOR RADIUS of LINER R(m)	2.400
MINOR RADIUS of LINER a(m)	0.4
SHELL TIME CONSTANT τ_s (ms)	≈ 50
TERMINATION VOLTAGE(kV)	20
TOROIDAL VOLTAGE V_θ (V)	4MA DESIGN VALUE = 7; RANGE 15 to -9 2MA DESIGN VALUE =10; RANGE 30 to-18 1MA DESIGN VALUE =14; RANGE 60 to-30 .5MA DESIGN VALUE =20; RANGE 60 to-36
VOLT-SECONDS (Wb)	28.8*
WALL-LOAD LIMITS ($MW/m^2/\sqrt{s}$)	$10\sqrt{t}$

*For 60kA in the Ohmic Heating coil

PHYSICS RATIONALE FOR SPECIFICATIONS

ASPECT RATIO

The aspect ratic is selected by using criteria based on equilibrium and thermal wall loading specifications. Because of the possibility of highly localized thermal flux either damaging the first wall or increasing the impurity level of the plasma, a criterion is established (see Wall Load, this report) to keep the outer flux surface tangent with the liner surface by ±5mm. However, the presence of a highly conducting shell surrounding the liner limits control of the equilibrium position by windings outside the shell. Attempts at equilibrium control will generate an m=1 toroidal current in the shell. This current will generate field errors in the area of the ports and the poloidal field gap in the shell. Limits on the magnitude of the field errors then constrain the degree of achievable equilibrium control. Reducing the time constant for the vertical field to penetrate into the shell allows an increased degree of equilibrium control for times greater than the shell time constant. However, there are bounds to the smallest

allowed value for the shell time constant (see Shell Time Constant, this report). Since it is difficult to gain equilibrium control on time scales less than the shell time constant, it becomes necessary to design the system so that the ± 5mm limit to equilibrium shift is passively obtained. This is accomplished by selecting the most likely value for expected plasma parameters that is, design values, and, in addition, a range of possible values for the relevant plasma parameters. The equilibrium position[1] depends on geometry (aspect ratio) and the plasma parameters, β_θ, and l_i. For the expected range of these plasma parameters the aspect ratio is selected so that the maximum shift of the outer flux surface is within ± 5mm of the equilibrium shift for the design values of the plasma parameters. The liner is then shifted outward in major radius by an amount equal to the design value. Figure 1 illustrates the concept and shows that an aspect ratio of six satisfies the condition. Increasing the aspect ratio beyond six will increase the cost.

BETA THETA (β_θ)

The design value for β_θ is selected from the ZT-40M data base and from an evaluation of the international RFP data base. The range is selected on the basis of the lowest possible beta that could be considered, for example at times early in the discharge, to the highest value, which derives from experimental experience and consideration of resistive MHD stability theory.

CURRENT

The selection of the current is based on the requirement for ZTH to achieve specific goals. It is expected that ZTH will achieve parameters that address confinement issues at the Proof of Principle (POP) level. One of the significant issues is the potential for ohmic heating to ignition level temperatures. This goal has to be considered in the light of available resources. The achievement of 4keV temperatures by ohmic heating alone, without auxiliary heating, is deemed to be at the POP level and is a major factor in the determination of the current for ZTH.

Scaling data from the ZT-40M experiment is used to predict the current necessary to achieve a 4keV electron temperature. Temperature data from ZT-40M are shown in Figures 2a, and 2b. Figure 2a shows the electron temperature measured by Thomson scattering vs. the toroidal plasma current and illustrate that the temperature for a specific current can vary over a relatively wide range. Figure 2b presents the same data but the ordinate is now the

product of density and temperature. The improved fit to the data illustrates the interdependence of the density and temperature for this scaling run. From these data the temperature is taken to scale as T(keV)=I(MA) with I/N= $3x10^{-14}$A-m; This scaling is referred to the "Design Point Scaling" in the ZTH Technical Specifications. Depending on experimental conditions various scalings for the temperature have been measured and documented in other publications[2,3,4,5,6,7]. The reported scaling has varied from $I_p^{1.2}$ to $I_p^{0.6}$. The significance of the various scalings on the performance of ZTH is discussed later in this report in the section "Toroidal Voltage."

The above justification for the current simplifies the procedure of generating the global parameters for ZTH. An overall set of design values for plasma parameters is established consistent with the goals of ZTH[2]. Variations around the design values are then determined to allow for experimental exploration.

CURRENT RISE TIME

The selection of the current rise time is dictated by a balance between technological limits and physics requirements. In principle, there are no direct plasma physics criteria that specify the current rise time. The specification is initially constrained by the recognition that a longer risetime will require a larger ohmic heating coil. The initial magnetic flux in the ohmic heating coil must be sufficient to establish the magnetic flux associated with the inductance of the plasma discharge as well as the resistive voltage drop of the plasma. The flux associated with the plasma inductance is independent of time, being equal to LI. However, with a long risetime for the current, the discharge remains in a relatively low-current high resistance state for a longer period of time and more volt-seconds are required.

Some of the constraints that are put on the system to establish a risetime involve deciding on the maximum voltage that can be applied to the ohmic heating coil, total current that can be switched with an inductive energy storage system, aspect ratio, minor diameter of the plasma, and the diameter of the ohmic heating coil. These constraints, together with mechanical stress limits for the ohmic coil, determine the available volt-seconds as a function of the diameter of the coil. The results are then compared to the volt-second predictions based on scaling results[8] from the present data base. The selected constraints are: Maximum voltage at a coil terminal, 50kV; Aspect ratio six or greater; Mechanical stress limits in the OH coils at accepted fusion engineering levels;

Maximum current in the OH circuit 200kA (The specific ZTH design[9] uses four 50kA inductive energy storage opening switches);Minor radius ≈ 0.4m. The result of these iterations is the specification of 50ms for the current risetime with the additional constraint of a specific form[8] for the evolution of the current.

FIELD ERRORS

Magnetic field errors can arise from the construction and installation of the coils, the discrete nature of the coils, skin effect of the conductor, currents induced in structures, and magnetic field fluctuations induced by the plasma. Whatever the source, specific conditions can be established with the goal of maintaining good flux surface geometry. The consequences of some of the field errors, and the criteria applied to limit their effect on the ultimate performance of ZTH will be considered next.

MAGNETIC ISLANDS

Magnetic field errors can change the topology of the flux surfaces producing a structure termed magnetic islands[10,11,12]. The criterion established here for the allowable size of the magnetic island deals specifically with the m=0 perturbations. These perturbations can resonate for all values of toroidal mode number n at the position where the toroidal magnetic field in the plasma goes through zero. Since this position is near the liner (≈70mm for ZTH), relatively small holes or other perturbations in the liner and shell can produce large magnetic islands. The width of the magnetic island, in vacuum, can be calculated from the following equation[10],

$$W = 4\left[\frac{bB_r}{nB_\theta q'(b)}\right]^{1/2} \qquad (1)$$

Where, b is the radial position, in this case the position at which the toroidal magnetic field reverses in direction, $B_r(b)$ is the magnitude of the error field, n is the toroidal mode number, $B_\theta(b)$ is the magnitude of the poloidal field, and $q'(b)$ is the derivative of q ($q=bB_\theta/RB_\theta$) at the reversal position.

The criterion established for the maximum size of the magnetic island limits its width to be equal to the distance between the reversal position and the wall. Since the island is centered on the reversal position, this criterion limits the breakup of the magnetic flux surfaces by the magnetic islands to one-half of the above distance. Figure 3 displays the results of the error field calculation as a function of the toroidal mode number n. The MBFM[13]

is used to calculate the derivative of q at the reversal position ($q'=6x10^{-3}cm^{-1}$), assuming that the cut-off value for the MBFM is 0.7a.

Detailed numerical calculations of the size of the magnetic field islands for the actual arrangement of ports in the ZTH shell are reported at this workshop[14].

The engineering implications regarding the tolerances for the coil manufacture and mounting can be noted by referring to Figure 3. Specific calculations have to be done for each coil set to translate the allowed field error into a manufacturing tolerance. A general observation can be made regarding the toroidal field coils. The specification on the location of one toroidal field coil with respect to its neighbor is not severe because of the high toroidal mode number (n) of the toroidal coil set(n=48). However, the global position of the entire coil set must be aligned with the axis of the shell, liner, and other coil sets with a high degree of accuracy to assure that the low n resonances are of small amplitude. This would imply that provision for in-place measurement of the magnetic field be provided in the design along with the ability to use shims to locate the coils.

The allowed field errors for higher m modes are taken to have the same n dependence as the m=0 modes. Note that the resonance condition m/n = q means that for m =1 the resonance modes are $n \geq 10$ for the RFP q profile. In general, imposing the same allowed error is found[14] to be a conservative procedure for the ZTH design.

GLOBAL DISTORTION OF FLUX SURFACE

A toroidally symmetric field error induces a global distortion of the magnetic flux surfaces.These distortions can result in magnetic field lines that are close to the liner or first wall intersecting the surface of the liner or first wall. Also, a localized field error from a port in the liner or shell can produce a local distortion of the magnetic flux surface without inducing a large magnetic island because of high m and n mode numbers associated with the perturbation and the rapid decrease of the amplitude of the field error with distance from the port. It is possible that the field error from a pump port can satisfy the island criterion but induce a local deviation of the magnetic field line that is unacceptable. The criterion that defines the limits on the distortion of the flux surface is presented in the section on thermal wall loading. The deviation of the magnetic field line at the surface of the liner is specified to be less than or equal to 5mm. The 5mm limit derives from the requirement to limit the

localized wall loading to be no more that twice than average. This limit then constrains the size of ports in the liner and shell and the magnitude of liner and shell currents.

INTERNAL INDUCTANCE

The value of internal inductance is essential to establishing the basic equilibrium characteristics of the plasma. Its value has been calculated[15] for the RFP as a function of the parameter Θ ($\Theta=B_\theta(a)/B_\bullet$ average). The design value for Θ is taken to be 1.5, from operational experience with ZT-40M. Theta can range from 0 at t=0 to as high as 1.9 or 2. The zero value is by definition at t=0, and the high value again comes from operational experience with ZT-40M. The range for l_i is obtained from ref. 17 for the range of Θ from zero to 2.

LINER RESISTANCE

If the liner resistance is too small, toroidal and poloidal voltages will drive currents in the liner that can give rise to magnetic field errors in the form of localized field errors of relatively high toroidal mode number near diagnostic ports and gaps in the shell, and a global (n=0) addition to the vertical magnetic field required for equilibrium. The voltage that drives the liner current is induced by the time variation of the flux in the ohmic heating coil (toroidal current drive), time variation of the flux associated with the toroidal magnetic field, and time variation of the vertical magnetic field used for equilibrium control.

Constraints that bound the high values of liner resistance are limits on the allowed termination voltage, liner material, and mechanical stress. The termination voltage is discussed later in this report. Liner material is specified as stainless steel or Inconel, based on present experimental experience. Limits on the resistivity of the liner material have not been established in a controlled way; however, highly insulating materials such as ceramic are not materials of choice.

To develop the value for the specification for the liner resistance first consider the relative magnitude of the field errors.

GLOBAL DISTORTION OF EQUILIBRIUM

A poloidally uniform current flowing in the toroidal direction on the surface of a torus gives rise to a vertical magnetic field. The magnitude of the vertical field, in the absence of a conducting shell surrounding the liner, can be calculated[1] using the equation,

$$B_v = \frac{\mu_0 I_l}{4\pi R} [\ln(8R/a) - \tfrac{1}{2}]. \qquad (2)$$

Where, I_l is the liner current, R is the major radius, and a is the liner radius.

This value of the vertical field is to be compared to the vertical field required to keep the plasma in equilibrium as given by Shafranov[1],

$$B_v = \frac{\mu_0 I_\phi}{4\pi R} [\ln(8R/a) + \text{lambda} - \tfrac{1}{2}]. \qquad (3)$$

Where, I_ϕ is the toroidal plasma current, and

$$\text{lambda} = \beta_\theta + l_i/2 - 1. \qquad (4)$$

For the design values of ZTH the last two terms in equation 3 (lambda - ½) are relatively small compared to the natural log term (≈20%). Therefore, a substantial vertical field can be generated by the current in the liner, depending on applied toroidal voltage and liner resistance. For example, the initial voltage in ZTH will be ≈700 volts, if the liner resistance were one milliohm, then the initial liner current would be ≈700kA. Since the plasma current would be starting from zero, the equilibrium would be severely distorted for a substantial fraction of the current rise to the 2MA level. The situation is somewhat more complicated by the fact that the liner has a time constant for penetration of the vertical field. Therefore, at time t=0 the vertical field inside the liner will be zero. It will build up on a time scale for vertical field to penetrate the liner (≈ 1ms) to the value determined by the toroidal loop voltage and liner resistance.

The presence of shell surrounding the liner modifies the amplitude of the vertical field. In addition to the functional dependence on the toroidal liner current and aspect ratio, the vertical field now depends on other factors like, the position of the liner in shell and the time constant of shell.

Assuming an infinitely conducting shell, the vertical field in the liner is reduced by image currents in the shell that are generated by the time dependent liner current. In fact, the

vertical field can be cancelled[1] by selecting the position of the liner with respect to the shell. However, for the particular geometric and plasma parameters of ZTH, the horizontal position of the liner with respect to the shell that would zero the vertical field is neither the geometric axis nor the plasma equilibrium position defined in the section on aspect ratio.

The time evolution of the vertical field inside the liner can now be examined. At $t=0^+$, the vertical field inside the liner is zero. Then on the time scale for field to penetrate the liner ($\approx$ 1ms), the field builds up to the maximum determined by the cancelling effect of the image currents in the shell. The resulting vertical field is still relatively small, being on the order of 10% of the vertical field if there were no shell (for the parameters of ZTH). Then on the time scale for the image currents in the shell to resistively decay (50ms for ZTH), the vertical field builds up to the no-shell value determined in part, by the toroidal voltage. Of course, the toroidal voltage is decreasing in time as steady state conditions are achieved. The approach taken here to resolve the question is to establish the liner resistance, initial and steady state(flat top) toroidal voltage, size of the diagnostic ports, time constant of the shell, and aspect ratio based on satisfying other design constraints, and then verifying that the global distortion of the equilibrium flux surface, resulting from the vertical field produced by the liner current, is within the criteria. The effect is illustrated in Figure 4. A liner resistance of 10mΩ is assumed and the shell time constant is assumed to be 50ms. The resulting normalized shift of the equilibrium is less than the specification of .0125(5mm/400mm) for the assumed liner resistance. Note that the shift is directly proportional to the current in the liner.

A 10mΩ liner satisfies the specification for the global equilibrium shift for the test case examined above. The assumption of a toroidal voltage that linearly decreases with time is within the expected variance for ZTH. Specific details will not be the same for other experiments, however.

Other constraints on the liner resistance are considered next.

LOCALIZED DISTORTION OF EQUILIBRIUM

Pump ports, diagnostic ports, poloidal field gaps cause a localized distortion of the magnetic flux surface. Two conditions are established to control this distortion. One condition is based on the size of the magnetic islands generated by the field error (see Magnetic Islands, this report), and the other on the magnitude

of the distortion of the flux surface from a circular geometry and the resulting localized heating(see Wall Loading, this report). The limitation on the liner resistance imposed by the size of the magnetic island criteria will be considered first.

Magnetic Islands. The liner planned for ZTH has a sixteen-fold toroidal symmetry(imposed for structural strength). Each of the sixteen toroidal positions has some magnetic field perturbing element such as, diagnostic ports and pump ports. (There is a single poloidal field gap in the shell). A detailed analysis of the final design is underway[14]. For the purpose of establishing an initial design, simplifications are required. A conservative approach assumes that the mode number n=16 dominates the field error spectrum and the poloidal mode number is m=0 even though the ports are localized in the poloidal direction. The radial field error (B_r) is calculated[16] assuming a circular hole in the liner with a uniform parallel magnetic field (B_{EXT}) on one side of the hole.

The maximum value of the ratio B_r/B_{EXT} is found to be equal to $\approx$ 0.02 using 50.2mm as the radius of the pump port, and 101.1mm for the distance from the port to the reversal surface. The latter distance is the sum of 67.4mm, calculated from the MBFM[13], and 33.7mm the distance from the port to the plasma surface. The value of 50.2mm for the radius of the pump port is determined by compromise between field errors and vacuum system requirements. Referring to the section on magnetic islands, it is noted on figure 3 that for n=16 the maximum allowed field error is $\approx .008B_\theta(a)$, where $B_\theta(a)$ is the value of B_θ at the liner. Therefore, the field error exceeds the allowed value by a factor of two and one-half if the liner current were equal to the plasma current. This situation then limits the liner current to be ≤ 0.4 of the plasma current. Using the ZTH voltage specifications for the 0.5MA flat-top current phase, a liner resistance of greater than or equal to 0.3mΩ (60v/(0.5MAx0.4)) would satisfy the island width criteria. However, the start-up voltage ($\approx$700V) can be ten times the flat top voltage ($\leq$60v) and the plasma current is initially zero. It is impossible therefore, to satisfy the island criteria for all time. A cut-off value for the plasma current must be chosen below which the criterion does not apply. Since the plasma experiences large fluctuations and low confinement until the reversed field is established, a plasma current cut-off could logically be established at $\approx$0.2MA or about 5ms after current initiation. All these conditions would require the liner resistance to be $\approx$ 9mΩ (700v)/(0.2MAx0.4).

Localized Perturbations. The selection of 5mm as the limit for the localized deviation of a magnetic field line near the liner is presented later in this report. The basic premise is that a localized perturbation will result in an increase in the wall loading of the first wall, driving the local wall temperature above specified limits. The limit that this criterion places on the liner resistance is essentially the same as presented earlier. The new feature is that the deviation of a magnetic field line in the presence of the field error is now calculated by integrating the equation for a magnetic field line in the vicinity of the port. The geometric parameters of the problem are essentially the same as defined earlier. The field error is generated by the same liner current flowing around the 50.2mm radius port. The field line deviation is calculated with respect to the first wall rather than the toroidal magnetic field reversal surface, as was done earlier. All the other aspects of the problem, such as a cut-off current concept, still apply to the calculation.

The definition of the problem is further complicated by the need to define the location and material of the first wall. Two cases can be considered: the first wall is the liner, completely exposed to the plasma; the first wall is the surface of a graphite armor that entirely covers the liner. In the first case, the first wall will be located 18.7mm radially inward from the port; in the second, the first wall is designed to be 33.7mm from the port(The Technical Specification for ZTH allows as much as 20mm for the armor). This difference in radial position for the metal and graphite first wall results in a factor of two in the calculated magnitude of the field line deviation. For the same case as treated earlier, namely the liner current being equal to the plasma current, the field line deviation is ≈ 20mm and ≈ 10mm for the metal and graphite wall, respectively. The specification of 5mm deviation can be exceeded by a factor of four or two, depending on the location of the first wall, which is to be compared to the factor of two and one-half based on the magnetic island criterion. A factor of two and one-half required that the liner resistance be ≈ 10mΩ. For this armored wall case, the magnetic island criterion controls the liner resistance. It should be noted that if ZTH is operated without armor to protect the metallic liner, the temperature of the liner in the vicinity of the pump ports should be monitored.

The specification that the liner resistance be ≈ 10mΩ satisfies the physics criteria established for the ZTH project within the restrictions discussed above. The reader may wonder why the

resistance is not made as high as possible, subject only to material constraints. There is a definite upper bound on the resistance as discussed in the section on Termination Voltage.

MAJOR RADIUS

The major radius is defined by the aspect ratio once the minor radius has been specified.

MINOR RADIUS

The primary constraint bounding the lower value of the minor radius is the projected power loading on the first wall. Upper bounds are established by the requirements to keep relatively high values of the current density to maintain power densities in the range of the present experimental experience, and to operate in the region of current density where DT ignition by ohmic heating is possible in a compact reactor[17].

The current-density constraint is in fact met by present RFP experiments. Compact reactor current densities range from ≈6MA/m² to 10MA/m², and present experiments are in the range from ≈2MA/m² to 10MA/m². Using the current density range noted above for the present experiments, the radius for ZTH would range from ≈.36m to ≈.7m, at 4MA. A selection is made by considering the thermal loading of the first wall.

The thermal loading of the first wall is determined by assuming that all of the resistive input power is deposited on the surface of the first wall with some local peaking taken into account. The functional dependence for the first-wall thermal load can then be determined through a scaling law for the resistive energy loss. The scaling[2,18] of plasma resistance is taken to be,

$$R = 0.85 T_e^{-3/2}(eV) \left[\frac{0.2}{a(m)}\right]^2 \frac{R(m)}{1.14} . \quad (ohms) \quad (5)$$

Average wall loading is calculated by multiplying the resistance by the square of the current and dividing by the wall area. The local wall load is assumed to be greater than the average by a peaking factor of ten (see Wall Loading). The local wall loading is shown in Figure 8. The maximum local wall loading is limited by specifying the maximum temperature, of an assumed graphite first wall, of 1500 degrees centigrade[19]. This temperature constraint combined with other fusion experience[20] related to maximum transient wall loading of ≈ 10MW/m²√t, determines the lower bound on the radius of the first wall. Referring to equation 8, the lower bound is ≈.37m. Making an allowance of 1.5 or 2 cm for the

material of the first wall would place the radius of the metal liner at ≈0.4m. Moving to even larger values for the radius increases cost at the expense of reduced current density and decreased wall loading. The selection of 0.4m for the minor radius is considered to be within the operational experience of the fusion community.

SHELL TIME CONSTANT

Physics criteria that are used to determine the shell time constant are:

1) The time constant of the shell must be sufficient to sustain passive control of the global equilibrium within the limits imposed by the bandwidth of equilibrium feedback control system. This condition would impose a lower limit on the shell time constant of ≈ 20ms.

2) The time constant should be small enough to allow external control of the plasma global equilibrium position within the limits imposed by the field errors that result from shell currents induced by a time dependent vertical field.

3) A time constant that is large enough to assure passive control of the equilibrium against slowly growing kink modes, for the entire duration of the current pulse.

The above criteria impose conflicting demands, but experimental evidence indicates that a solution can be found. The importance of good equilibrium conditions to obtain optimum performance has been illustrated experimentally[21,22,23]. Most present RFP experiments use thick shells that have a time constant greater than the duration of the discharge. The equilibrium position in these experiments is modified by applying a dc vertical field before the plasma discharge. Limits exist however, on the magnitude of a dc vertical magnetic field that can be applied and still achieve electrical breakdown of the neutral gas in the discharge chamber. Equilibrium control can be obtained with these "thick" shells by overdriving the external vertical field. The resulting large m=1 shell currents then cause field errors at holes and gaps in the shell that can degrade[23] the performance of the device.

The decision on the time constant must reflect a balance between the need to control the equilibrium and the risk that slowly growing kink modes will destroy the equilibrium. Based on experimental[22,24] and theoretical[25] work that indicates that the shell time constant can be as small as one-tenth of the duration of the discharge, 50ms is chosen for the shell time constant. A shell time constant of 50ms will satisfy all three conditions, but the

degree of equilibrium control on a comparable time scale will be limited by the allowable field errors.

It is this mandate to obtain the the maximum degree of equilibrium control within the limits imposed by the field error constraints that established the ZTH design for the poloidal field gap in the shell. The poloidal field gap is an overlapping tapered structure specifically designed[26] to reduce field errors arising from vertical magnetic fields penetrating the shell.

TERMINATION VOLTAGE

The physics understanding of the current termination in RFP's is not yet fully developed. The maintenance of sufficient density has a major role in controlling the termination[27] and discharges have been extended a significant amount by controlling[28] the density. In fact the current can be decreased to approximately zero without the occurrence of a termination[29,30]. Since the guaranteed absence of terminations is not possible, it is necessary to plan accordingly. The approach taken is to consider the worst case termination on ZT-40M (time scale for the termination is ≈ 100us) and scale the termination time as predicted for the resistive tearing mode . The time scale for the growth of the tearing mode is predicted to scale as the square root of the product of the Alfven and resistive diffusion times giving,

$$t \approx (\tau_a \tau_r)^{1/2} \quad \alpha \quad \frac{a^2 T^{3/4} n^{1/4}}{I^{1/2} (\ln(\text{lambda}))^{1/2}} \qquad (6)$$

This scaling predicts a termination time of ≈1ms in ZTH. Computer simulations, shown in Figure 5, of a ZTH termination on a millisecond time scale with a resistive liner predict the termination voltage to be 24 kV. This is to be compared to a predicted 40kV resulting from an instantaneous termination at 4MA with a 10mΩ liner resistance. To a first approximation, the termination voltage can be scaled by the ratio of the final design liner resistance to the
10mΩ value used for these calculations.

It is recognized that the present experiments do not experience a rapid current termination when operating at higher current. In ZT-40M the current will slowly decrease from ≈300kA to ≈100kA before a current termination occurs. The design voltage specified above is considered to be very conservative. A primary reason for

the conservative approach is the serious nature of the fault that would occur if the poloidal field gap in the shell arced over. Breaching the voltage insulation in the gap at a time when the ohmic heating coil is fully charged could result in substantial damage to the front end.

Termination voltage specifications tend to force the liner resistance to the lowest value possible. In view of the constraints imposed by the magnetic field errors from liner currents, and the fact that the technology is available to design for voltages ≈25kV, a liner resistance of ≈ 10mΩ appears an acceptable compromise value.

TOROIDAL VOLTAGE

The flat-top toroidal voltage ($V_\phi = I_\phi R$) is obtained using equation 5. Therefore, the functional dependence of the voltage on current will depend on the scaling of temperature with current. Depending on experimental conditions, the scaling of the electron temperature with the current can have various functional forms.

The voltage for ZTH will be specified by first establishing a "design voltage" and then a "voltage range" that allows for variation of experimental parameters. The design voltage is specified by scaling the temperature with the current as

$$T_e\,(\mathrm{keV}) = I_\phi\,(\mathrm{MA}), \qquad (7)$$

and substituting into equation 5.

A range of electron temperature for various scalings of temperature with current is shown in Figure 6a. Figure 6b shows the predicted voltage for the various temperature scalings. As noted earlier, the experimental temperature scaling has varied from $I_\phi^{1.2}$ to $I_\phi^{0.6}$.

The range for the toroidal voltage must be sufficient to allow exploration of the scaling predictions together with a reasonable variation of experimental parameters that effect the voltage, such as the value of Θ and the electron temperature. This programmatic need has to be balanced against the resources available because the power system is a major cost in the project.

At this time, a variation of the toroidal voltage by a factor of two greater than the design voltage at the highest operating current is requested by the ZTH Technical Steering Committee.

It can be seen that the factor of two in the toroidal voltage specification allows operation over slightly less than a factor of two variation in the temperature at 4MA. At lower current the

voltage can be larger. The magnitude of the voltage depends on the modularity of the power supplies. The ZTH Technical Steering Committee has requested 60 volts at 0.5MA.

VOLT SECONDS

The primary externally controlled factor determining the volt-seconds derives from the specification of the time scale for the duration of the discharge. This can be explained by noting that the volt-seconds can be divided into two parts. One of the parts is the flux that must be supplied to establish the magnetic field of the discharge. Since the flux can be expressed as LI_ϕ where, L is the inductance of the discharge, calculated in an appropriate manner, and I_ϕ is the toroidal plasma current, this part of the volt-seconds is proportional to the current. The second part is the volt-seconds required to maintain the resistive voltage drop, integrated over the time scale for the discharge.

The first part of the volt-seconds is easily specified for the designer once the design current is established. Evaluation of the second part of the volt-seconds (resistive) is achieved by detailed experimental[8] investigation of various RFP formation and current programing techniques. The details will not be covered here. Rather the rational behind the specification of the time scale for the duration of the discharge will be presented.

Since there is an obvious penalty for long duration discharges in terms of the resistive volt-seconds that must be supplied by the OH coil, the tendency is to make the duration as short as possible. Factors that constrain this tendency are limits to the maximum toroidal voltage at the terminals of the OH coil, the amount of power available to ramp the current in time, and the time to reach an equilibrium by ohmic heating. The first two constraints are limited by technology and available resources, and are discussed in other papers in this workshop. The last can be investigated using numerical modeling. Figure 7 shows the results from a O-D model[31] used to predict the temperature as a function of time for an assumed current waveform. The assumptions used in this model are; $T_i = T_e$, $n = 2.5 \times 10^{17}$, ohmically heated electrons with $Z_{eff} = 2$, and the energy containment time scales as $(I_\phi/N) I_\phi^{3/2}$.

By definition, the ohmic heating time will be the same as the energy confinement time, expected[2] to be $\leq$ 85ms. Having a total current duration of $\approx$0.6s is considered to be compatible with the technological constraints and the physics requirement to reach an equilibrium.

WALL LOAD

The specifications and assumptions for the first wall thermal load strongly influence the design by placing a lower limit on the minor radius of the liner. It is taken as a given that the metal wall of the liner will have to be protected from the plasma discharge. ZT-40M has experienced impurity influx and physical damage to the liner caused by locally high thermal flux. Driven by the requirement to protect the liner under any condition results in the specification that the liner will be completely covered by a protective cover. The material selected for this protective cover is graphite because of its low Z and the extensive experience with this material in tokamaks.

Experience regarding the use of graphite in tokamaks is used to establish limits to the maximum wall loading. Figure 8 presents operational results reported[22] for tokamaks operating at various thermal wall loading and pulse durations. Also shown on the graph is a calculation of the highest wall loading based on limiting the maximum temperature of the graphite to 2300°K. The curve marked "Los Alamos design spec." is obtained by reviewing the comments[20] regarding operational experience and excluding wall loads that have resulted in substantial impurity influx or graphite tile damage. The resulting curve is plotted as $Q \approx 10/\sqrt{t}$ ($MW/m^2\sqrt{s}$) which implies a maximum temperature for the front surface of the graphite. The references on the figure are given in appendix A.

Having established a limit for the maximum thermal wall loading, it is now necessary to establish a relation between the maximum wall loading and the average wall loading. Average is defined by dividing the resistive power input by the surface of the first wall. The ratio between the maximum and average wall load is termed the "peaking factor." Contributors to the peaking factor are listed below.

CONTRIBUTOR	FACTOR
a) Unidirectional energy flow[32]	2
b) Displacement of flux surface with respect to the first wall[32].	2
c) Enhancement to allow for a factor of two increase in the toroidal voltage and experimental flexibility.	2.5

Considering the catastrophic effect on the performance of the device if the wall impurities restrict its operation, a conservative value of ten is assumed for the peaking factor.

An analytic expression for the first wall radius as a function

of the plasma current can be obtained using equation 5 for the resistance.The dependence of the ohmic input power on the current is obtained by assuming $T_e \propto I_e$. The average wall load is then obtained by dividing by the area of the first wall. Including a peaking factor of ten the following equation is obtained,

$$a \geq 0.3(I(MA)t(s))^{1/6} \quad \text{(meters)} \qquad (8)$$

For a 4MA plasma current and a total pulse duration of one second (the current run-down time is included), the value for a is ≥ 0.37m. This is the position of the graphite first wall so allowance must be made for the thickness of the material when specifying the liner radius.

ACKNOWLEDGEMENTS

The background material,ideas,and data presented above are the work of a large number of people. The Author especially thanks the other members of the ZTH Technical Steering Committee: D.A. Baker, R.A. Gerwin, R.A. Krakowski, M.M. Pickrell, W.E. Quinn, K.F. Schoenberg, D.B. Thomson, P.N. Thullen, and G.A. Wurden. In addition, intensive discussions among many professional scientists and engineers helped clarify the understanding of the physics and design criteria that were finally established for ZTH. The list is long and includes recognition of not only the Los Alamos RFP Staff but also Staff from General Atomics Technologies, Phillips Petroleum and National and International RFP programs.

REFERENCES

1. V.S. Mukhovatov and V.D. Shafranov, "Plasma Equilibrium in a Tokamak," Nuclear Fusion 11, (1971) p. 605.

2. P.N. Thullen and K.F. Schoenberg, Editors., "Reversed Field Pinch Experiment," Technical Proposal, LA-UR-84-2602.

3. K. Ogawa, et al., "Experimental and Computational Studies of Reversed- Field Pinch on TPE-1R(M)," Plasma Physics and Controlled Nuclear Fusion Research., Proc. 9th International Conference Baltimore, 1982. Vol. 1, IAEA, Vienna (1983) p. 575.

4. B. Alper and S. Martini, "Electron Temperature Studies on ETA-BETA II RFP," Istituto Gas Ionizzati, I.G.I. 85/04.

5. B. Alper, et al., "The Influence of Density on Plasma Behavior in the HBTX1A Reversed Field Pinch," Bulletin of the American Physical Society 30, (1985) p. 1406, San Diego, Nov. 1985, DPP Meeting.

6. G.A. Wurden, et al.' "Scaling Results from ZT-40M," Bulletin of the American Physical Society 30, (1985) p. 1402, San Diego, Nov. 1985, DPP Meeting.

7. G.A. Wurden, et al., "Hot Ion Plasmas in ZT-40M," Bulletin of the American Physical Society 31, (1986) p. 1547, Baltimore, Nov. 1986, DPP Meeting.

8. J.A. Phillips, et al., to be published.

9. Ohmic coil design originally suggested by G. Rostagni at the 1979 RFX US/Euratom Joint Engineering Workshop, Culham Laboratory.

10. R.L. Spencer, "Magnetic Islands and Stochastic Field Lines in the RFP" Proceedings of the Reversed-Field Pinch Theory Workshop, at Los Alamos National Laboratory, April 29-May 2, 1980., LA-8944-C. p. 129.

11. S. Ortolani, "Equilibrium and Stability Properties of Reversed Field Pinch Configurations," International School of Plasma Physics, Course on Mirror-Based and Field-Reversed Approaches to Magnetic Fusion, Varenna, Italy, Sept. 7-17, 1983. p. 513.

12. A.H. Boozer, "Classical Transport in the Reversed Field Pinch," Proceedings of the Reversed-Field Pinch Theory Workshop, at Los Alamos National Laboratory, April 29-May 2, 1980., LA-8944-C. p. 201.

13. J.W. Johnston, "A Plasma Model for Reversed Field Pinch Circuit Design," Plasma Physics, 23 187 (1981).

14. K. Sidickman and R. Nebel, this workshop.

15. D.A. Baker, L.W. Mann, and K.F. Schoenberg, "Equilibrium Poloidal Field Distributions in Reversed Field Pinch Toroidal Discharges," LA-9162-MS.

16. J.D. Jackson, "Classical Electrodynamics," John Wiley & Sons

17. R.A. Krakowski, et al., "Compact Reversed-Field Pinch Reactors (CRFPR)," Nuclear Engineering and Design/Fusion 4 (1986) p. 75.

18. Technical Meeting on First Wall Thermal Loading, at Los Alamos, May 8-10, 1985., to be published.

19. R. Behrisch, "Evaporation for Heat Pulses on Ni, Mo, W, and AJT Graphite as First Wall Materials," Journal of Nuclear Materials 93 & 94 (1980) p. 498.

20. "Technical Assessment of the Critical Issues and Problem Areas in High Heat Flux Materials & Component Development," Vol II., DOE, Office of Fusion Energy, Joint publication PPG-815 and UCLA-ENG-84-25.

21. T. Shimada, et al., "Results From the Reversed Field Pinch Experiment TPE-1RM15 with Programmed Vertical Field," 11th International Conference on Plasma Physics and Controlled Nuclear Fusion Research, Kyoto, Japan., Nov. 13-20, 1986., IAEA-CN-47/K-I.

22. S. Ortolani, et al., "Reversed Field Pinch Operation with a Thin Shell," 14th European Conference on Controlled Fusion and Plasma Physics, Madrid., June 22-26, 1987.

23. R.S. Massey, et al., "Equilibrium and Field Error Studies on ZT-40M," LA-9567-MS.

24. S. Robertson, this workshop, S. Robertson and P. Schmid, "Operation of a Reversed Field Pinch Without a Conducting Shell," Bull. Am. Phys. Soc. 31 (1986) p.1549.

25. G. Marklin, this workshop.

26. R. Moses, this workshop.

27. A.R. Jacobsen and M.G. Rusbridge, "Observed Mechanism of Termination in the ZT-40M Reversed Field Pinch," LA-9589-MS.

28. K.S. Schoenberg, et al., "Reversed Field Pinch Experiments in ZT-40 and ZT-P," 11th International Conference on Plasma Physics and Controlled Nuclear Fusion Research, Kyoto, Japan., November 13-20, 1986., IAEA-CN-47/DII-3.

29. A.A. Newton and P.G. Noonan, "Controlled Termination of Reversed Field Pinch Discharges," Nuclear Instruments and Methods in Physics Research, A245 (1986) p. 167.

30. C.P. Munson, private communication.

31. D.A. Baker, private communication.

32. J. Downing, this work shop.

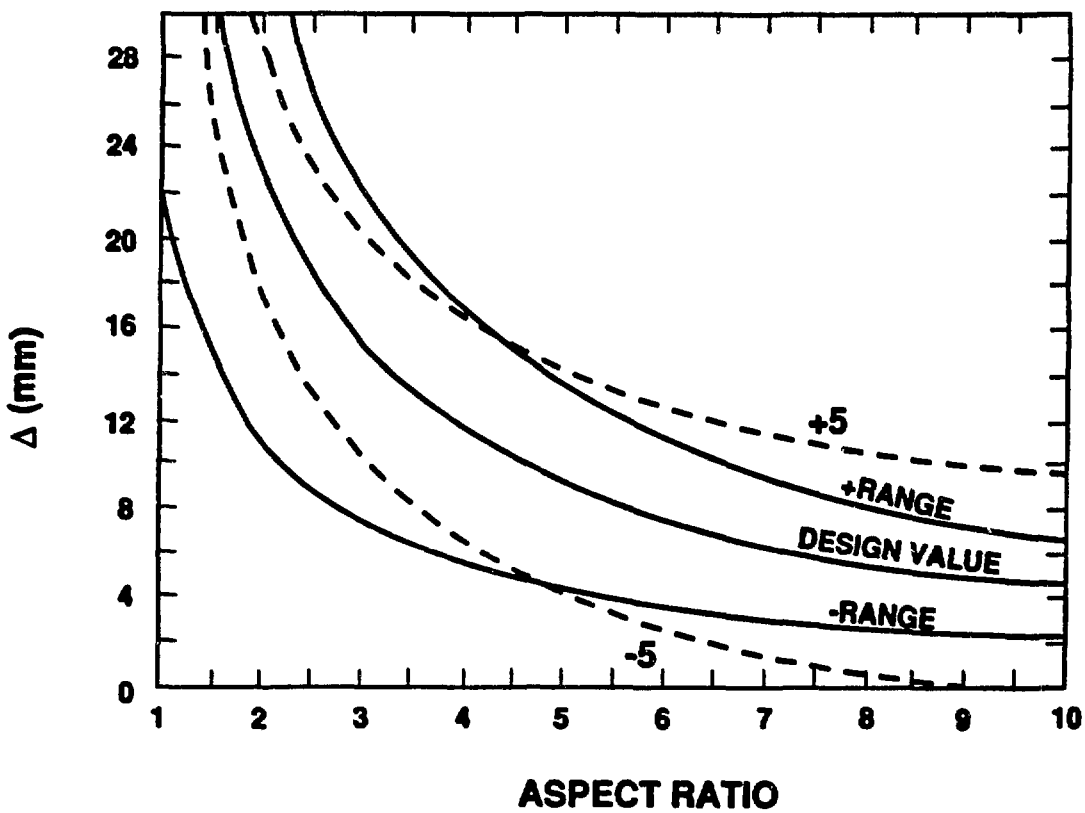

FIGURE 1

Shafranov shift for the design value, and the maximum and minimum values, of beta theta(β_θ) and internal inductance(l_i), plotted against aspect ratio. Also shown is the specification of ±5mm shift of the flux surface with respect to the design value.

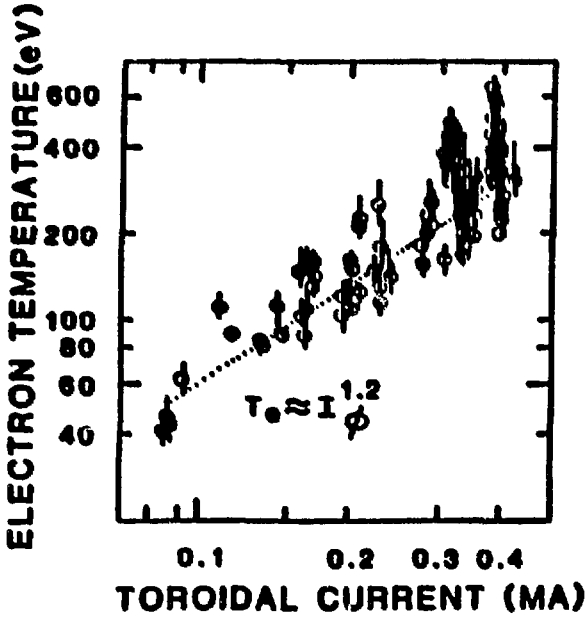

FIGURE 2a
Temperature as a function of plasma current for various plasma densities.

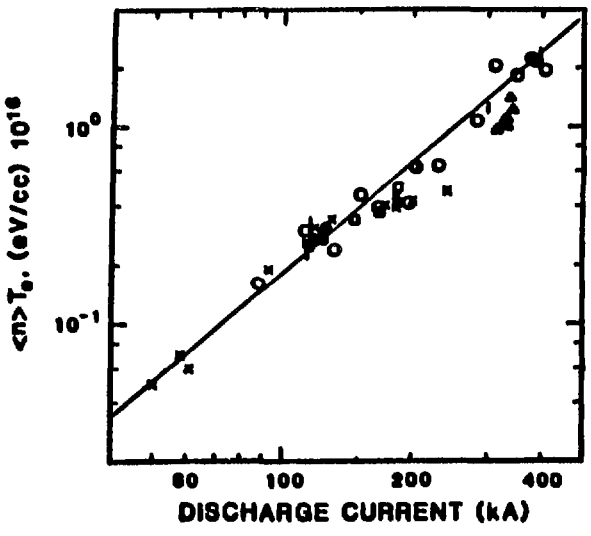

FIGURE 2b
The product of density and temperature as a function of plasma curent.

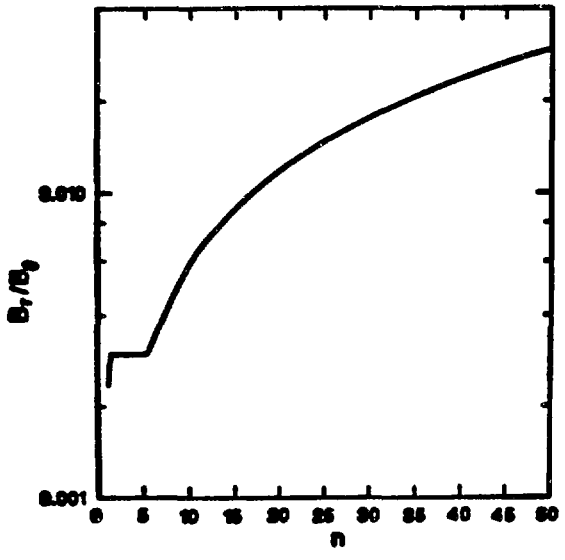

FIGURE 3
Magnitude of the m=0 field errors normalized to B_ϕ at the wall. The solid line defines the maximum allowed error for a specific toroidal mode number.

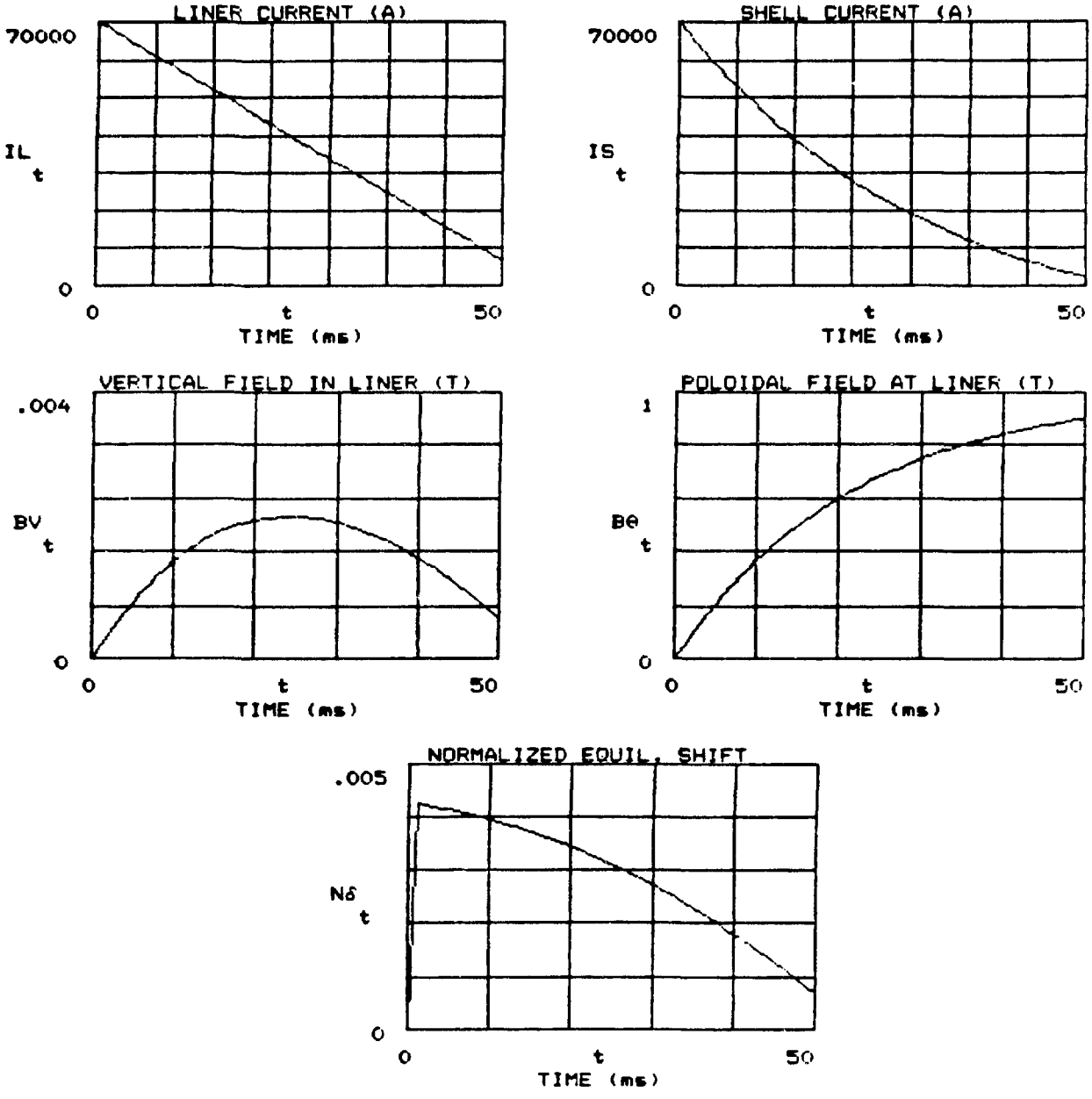

FIGURE 4

An illustrative calculation of the outward shift of the plasma equilibrium due to toroidal liner current. The liner current is shown for a linearly decreasing toroidal voltage. The shell time constant is assumed to be 50ms, and the toroidal shift (Nδ) is normalized to the minor radius of the liner.

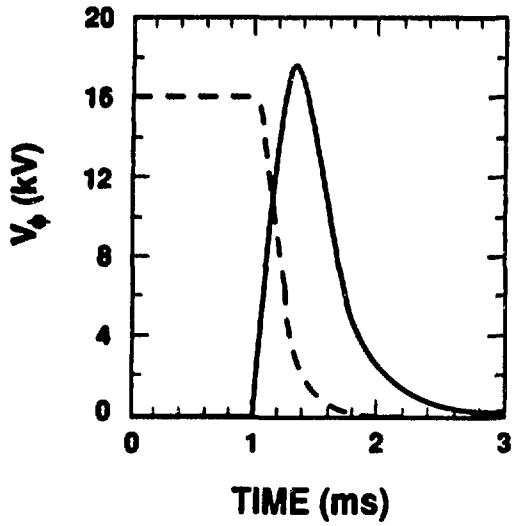

FIGURE 5
Computer simulation of a termination from 4MA on a millisecond time scale. The liner resistance is taken to be 10mΩ.

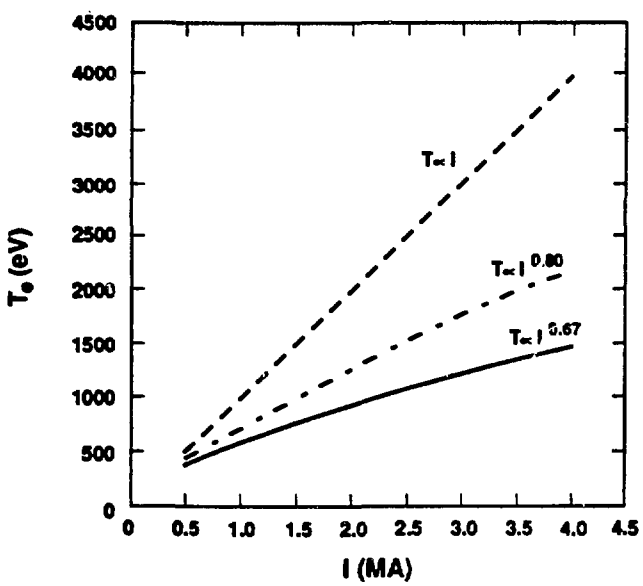

Figure 6a
Electron temperature dependence on current for various scalings of temperature with current.

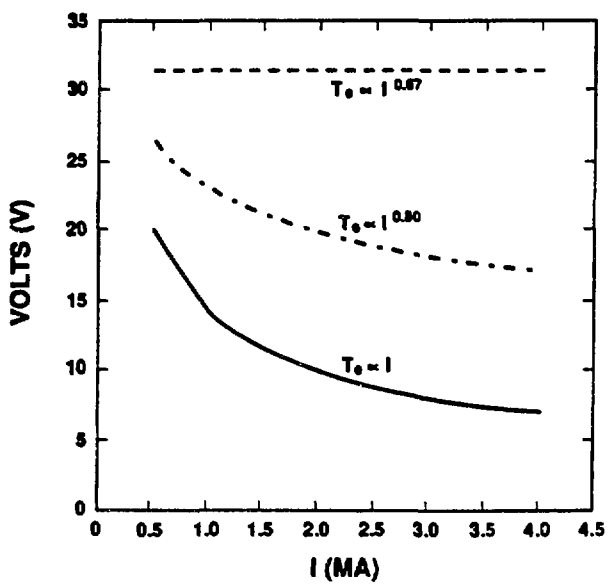

Figure 6b
Toroidal voltage dependence on current for the various scalings of temperature with current.

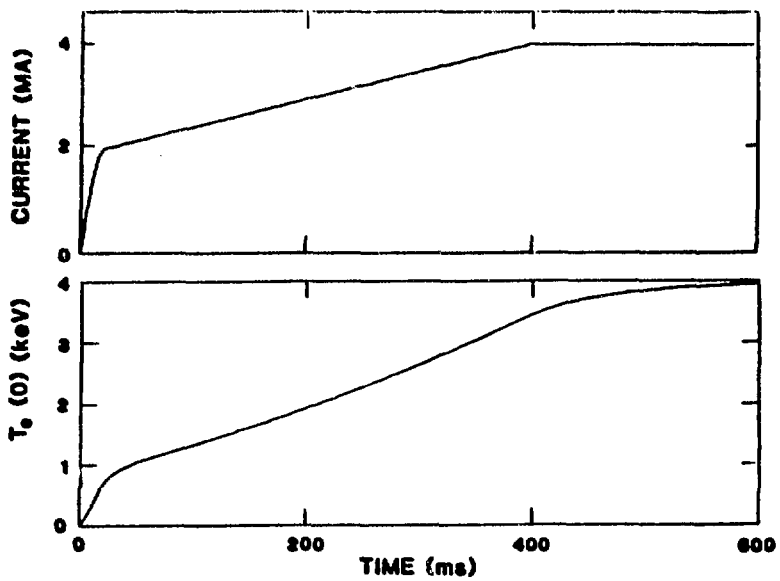

Figure 7

O-D Computer simulation of the plasma temperature as a function of time. The plasma is ohmically heated with a Z_{eff} of two.

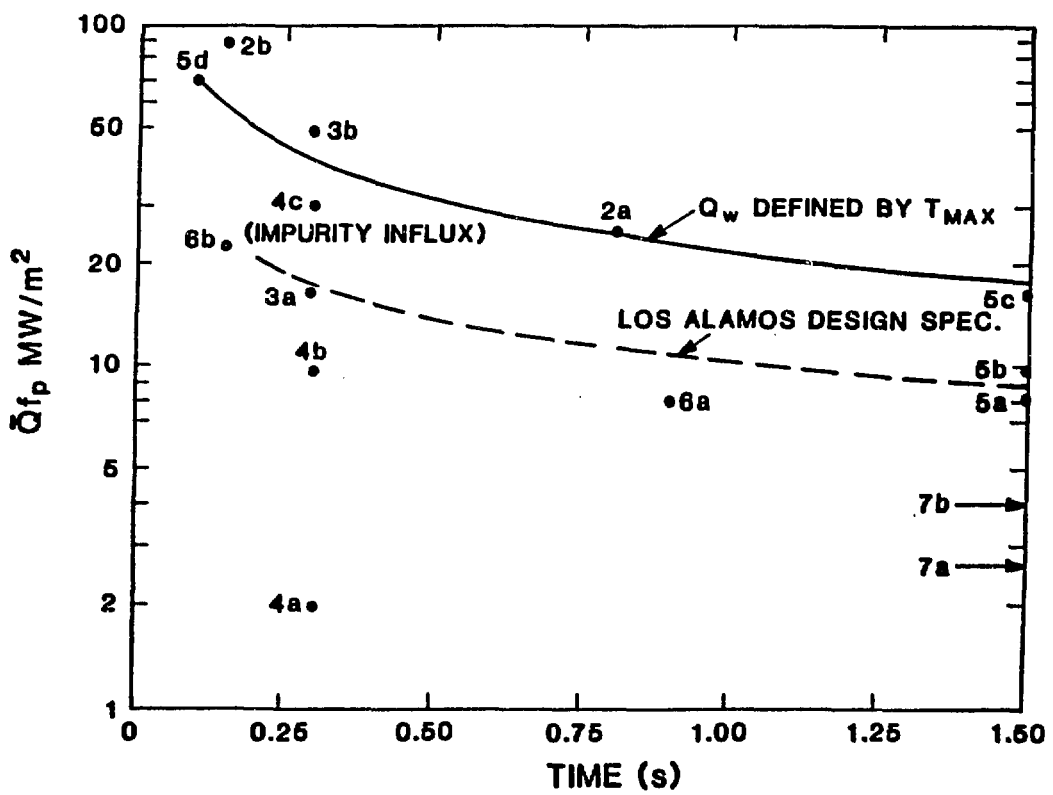

FIGURE 8

Wall loading as a function of time. The solid curves are defined by specifying the temperature of the first wall. T_{MAX} is taken to be 2300° K, and the Los Alamos Design Spec. is 1500° K.

APPENDIX 1 -- TABLE 1

Symbol	Machine	Component	Peak Heat Flux	Pulse Length	Remarks
1.	ISX-B				
		Mushroom Limiter	100 MW/m^2	< 0.20	Z_{eff} < 3, dominated by Oxygen ~ 3000°C.
2.	PLT				
		a. Rail Limiter	25 MW/m^2	0.8 s	Inferred from melt-layer
		b. Rail Limiter	90 MW/m^2	0.15 s	Z_{eff} 3-4.
3.	Alcator-C				
		a. Poloidal Limiter (two)	16 MW/m^2	< 0.30	Z_{eff} 1.2-1.5 peaking factor
		b. Poloidal Limiter (one)	50 MW/m^2	< 0.30	of 4 in calculation.
4.	PDX				
		a. Bumper Limiter	2 MW/m^2	< 0.30	Z_{eff} 1.8-2.9.
		b. Divertor Plates	10 MW/m^2	< 0.30	Z_{eff} 1.3-1.7.
		c. Rail Limiter	30 MW/m^2	< 0.30	Impurity influx and frequent disruption if beam pulse length > 0.150 s, Z_{eff} 2-4.
5.	TFTR				
		a. Movable Limiter Design	8.5 MW/m^2	1.5 s	
		b. Bumper Limiter Design	10 MW/m^2	1.5 s	
		c. Movable Limiter Oper.	17 MW/m^2 (NBI)	0.5 s	~ 5.5 MW/m^2 ON for 30 s with NBI at 2.5-3.0 s, Z_{eff} ~ 2.0.
		d. Movable Limiter Design	70 MW/m^2	~ 0.1 s	
		e. Movable Limiter Oper.	29 MW/m^2 (NBI)	0.5 s	~ 5.5 MW/m^2 ON for 3.0 s with NBI at 2.5-3.0 s, Z_{eff} ~ 3.4 (1.7-3.8).
					One cracked tile and general surface cracking carbon increases by 2.
6.	Doublett III				
		a. Primary Limiter	8 MW/m^2	0.9 s	Cracked
		b. Plus NBI	23 MW/m^2	0.15 s	Tiles
		c. NBI Armor	5 MW/m^2	0.20 s	
		d. NBI Armor	40 MW/m^2	0.50 s	No plasma, no damage
7.	JET				
		a. Limiter Operation	2.6 MW/m^2	10 s	
		b. Limiter Design	4.0 MW/m^2	20 s	~ 1000°C, Z_{eff} 3-6

TABLE 1. Operational experience with graphite in tokamak experiments. For information regarding "remarks" see reference 32.

JULY 10, 1987

CPRF

Overview of CPRF/ZTH and the CPRF Construction Program

Los Alamos National Laboratory
Los Alamos, New Mexico 87545

OVERVIEW OF CPRF/ZTH
and the
CPRF CONSTRUCTION PROGRAM

Philip Thullen
Los Alamos National Laboratory

1.0 Introduction

The Confinement Physics Research Facility (CPRF) and the ZTH reversed field pinch (RFP) experiment are being constructed at the Los Alamos National Laboratory. The characteristics of the facility and experiment will be similar to those presented in the ZT-H Reversed Field Pinch Experiment proposal of January 1985 (LA-UR-84-2601, 2, 3) with the toroidal plasma current increased from 2 to 4 MA.

The CPRF construction program includes the base facility and the initial experiment, ZTH. In ZTH the confinement properties of the RFP magnetic field configuration will be studied in support of the establishment of the scientific base for fusion energy. ZTH consists of a vacuum liner, limiters and/or wall armor, equilibrium shell, toroidal field coils, poloidal field coils, support structure, and other components required to establish desired plasma conditions in a 4-MA RFP fusion experiment. The remainder of CPRF includes control and data acquisition systems, vacuum and fueling systems, diagnostics, buildings, and electrical energy storage and power systems to drive the toroidal and poloidal coils.

2.0 Objective and Scope

2.1 CPRF Research Program Objective

The objective of the CPRF research program is: to extend and enhance the physics base of the RFP toroidal confinement configuration by demonstrating the principle of self-sustainment and high-beta operation in a compact configuration. Achievement of this objective is important for the development of an economical fusion reactor. The CPRF is an element of this research program, and CPRF research results will contribute in a major way to the physics of RFP toroidal confinement in the following areas:

a. Study of high beta (10 to 20%), toroidal plasma parameter (β,n,T,τ_E), and ohmic heating dependences on toroidal current;

b. Study of transport in the collisionless regime and the effect of field errors on confinement;

c. Study of RFP formation, current ramping, F-Θ control, and equilibrium control;

d. Study of density control and termination control techniques;

e. Study of edge plasma physics, impurity control, and wall protection techniques;

f. Exploration of steady-state current drive using F-θ pumping or other helicity injection techniques;

g. Study of technological issues and confinement physics at high-current, ignition-like temperatures, fusion relevant thermal wall loads, and significant d-d neutron flux.

The CPRF will be designed to allow, after system modification, the installation of: pellet injectors, divertors, and helicity injection systems including F-θ pumping. These components and related system modifications are not included in the scope or cost of the CPRF construction program.

2.2 CPRF Construction Program Objective

The objective of the CPRF construction program is to design and construct a research facility with capabilities that satisfy the engineering requirements and performance expectations listed below for the ZTH experiment.

2.3 CPRF Engineering requirements

The principal engineering requirements for the CPRF are:

a. The CPRF shall have a 4-MA toroidal current capability with a 0.6 second experimental pulse (ramp and flattop);

b. The vacuum liner minor radius is 0.40 m with an aspect ratio of about 6;

c. The ohmic heating coils, which drive the plasma discharge, must maximize electromagnetic energy transfer to the plasma consistent with minimizing field errors in the plasma volume and allowing good diagnostic and maintenance access to the torus;

d. The equilibrium field coils, which provide a time-varying vertical field and field index to maintain plasma equilibrium, must minimize the required control power and asymmetric field errors in the discharge chamber and allow good diagnostic and maintenance access to the torus, and;

e. The facility operating criteria are:

   (1) 10,000 4-MA discharges;
   (2) 20,000 2-MA discharges;
   (3) 50,000 1-MA discharges;
   (4) One 4 MA discharge per 10 minute period at the plasma design point conditions specified in the technical design criteria.

2.4 CPRF Performance Expectations

The performance expectations of the CPRF at the 4 MA current level are:

a. Ion and electron temperature: $T_i \sim T_e \sim 4$ keV

b. Plasma density: $n_e \sim 10^{14}$ cm^{-3}

c. Average plasma poloidal beta: β = 10 to 20%

d. $n\tau_E \sim 10^{13}$ cm^{-3} s

2.5 Schedule Objectives

The design and construction of the CPRF started in FY86, and project completion is scheduled for the last quarter of FY92 (July-September, 1992) at which time a 4 MA current capability will exist. An interim milestone occurs in the first quarter FY91 (October-December, 1990) at which time plasma operation will begin with 2 MA current capability.

3.0 Program Description

3.1 Overview

The CPRF will provide a modern facility for research into the plasma confinement properties of various magnetic field configurations in support of the establishment of the scientific base for fusion energy. The first configuration studied will be the RFP. The initial RFP front end, called ZTH, will include a vacuum liner with limiters and/or armor, equilibrium shell, toroidal field coils, poloidal field coils, structure and other components needed to produce a 4 MA RFP. The remainder of the CPRF includes the poloidal and toroidal energy systems, equilibrium control systems, computer control and data acquisition systems, large electrical power generator, capacitor banks, power conversion and conditioning systems, vacuum system, diagnostics, and buildings.

The CPRF is located at Los Alamos National Laboratory technical area TA-35 as shown in Fig. 3.1-1. In this figure, existing buildings are shown in outline and new construction is shaded. Building 124 has adequate floor space (10,640 ft^2) to house the 4 MA ZTH experiment and has sufficient neutron shielding to allow experiments at reactor relevant plasma conditions. The CPRF Construction Program will construct in addition: a 13,000 ft^2 power supply building, an 11,000 ft^2 generator building, and add a users area to the former Antares control room located in TSL-125 (the former Antares Laser Hall). In addition, 5,600 ft^2 of space in TSL-125 has been secured for assembling and testing CPRF components. A power line extension from the ETA substation to the area of the generator building will be installed to provide power to spin-up the generator.

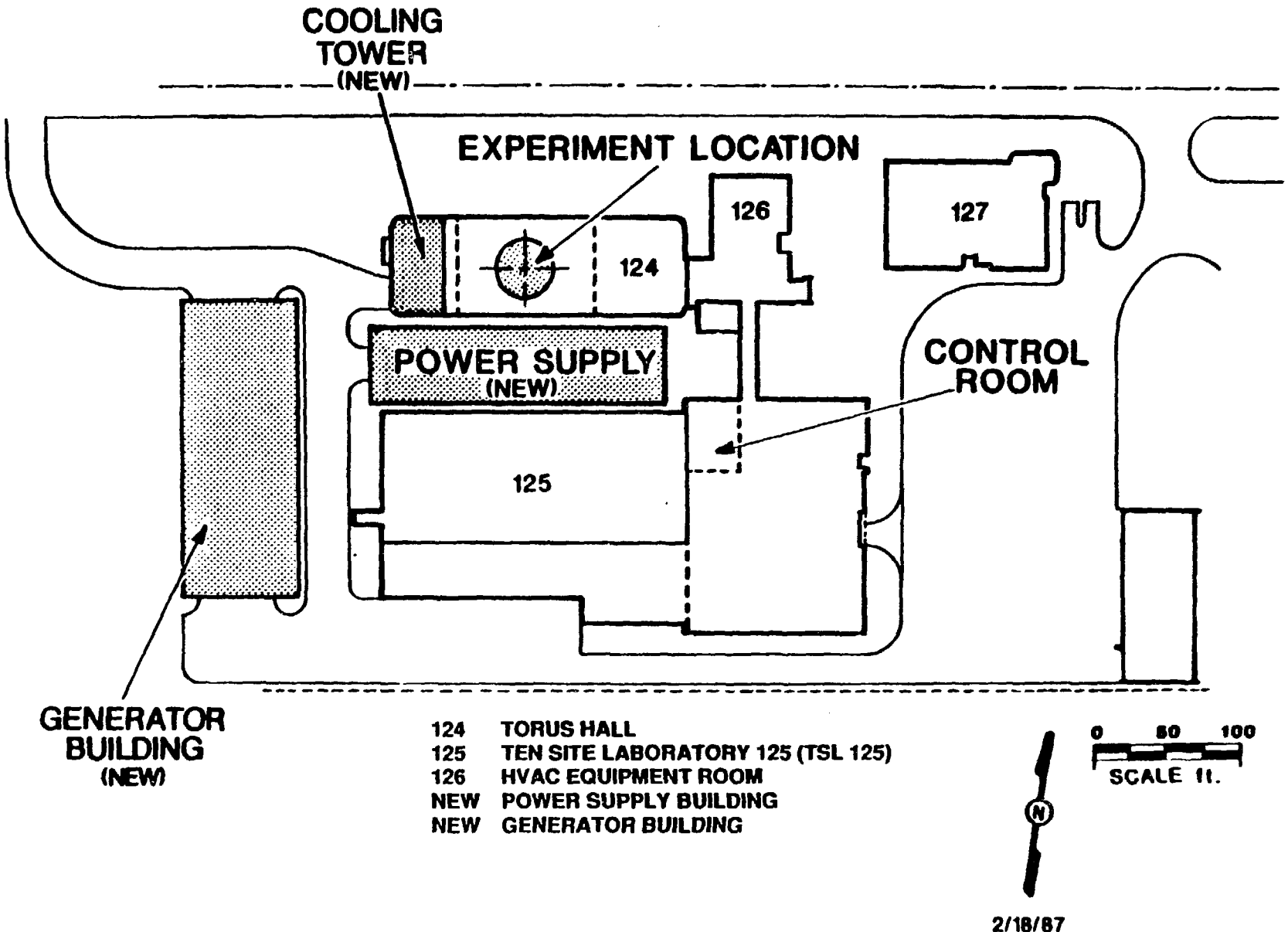

Fig. 3.1-1, CPRF Site Plan at TA-35

The CPRF will be powered by a generator with a rated output of 1,430 MVA, 600 MJ over a frequency range of 60 to 42 Hz. Power conversion equipment will be sufficient to supply the 4-MA RFP experiment. The generator facility design allows retrofit of a flywheel to provide an additional 1,400 MJ of usable energy.

3.2 System Description

The components of the CPRF and their functions are briefly described in this section. Figure 3.2-1 shows a cross section of ZTH, in the Torus Hall, which may be used for reference.

Facilities. The CPRF Torus Hall (TA-35, Bldg. TSL-124) has a floor area of 56 ft. x 190 ft. with a height of 33 ft to the 30 ton crane. The walls are of six foot and roof of five foot thick concrete which is sufficient to shield d-d neutrons (2-5 MeV) and even the few 14 MeV neutrons that would result from a trace of tritium. The 13,000 ft^2 power supply building will house the a.c. power distribution system, transformers, d.c. converters, controllers, capacitor banks, bus ducts, and other associated equipment. A pre-engineered metal building, with an area of approximately 11,000 ft^2 will provide a weather tight enclosure for the generator. The former Antares control room and computer area will house the CPRF control room and the control computer. An upgrade of space adjacent to the former Antares control room will provide a users-area housing data analysis terminals. Building TSL-125 will also house staff shops, assembly areas and the vacuum equipment cleaning facility. A 10 MVA power line extension (~ 1.5 miles) will provide a.c. power for the generator drive system. A 10-MW cooling tower will provide cooling for the generator and other CPRF equipment.

Liner and Shell. The liner, which forms the torus vacuum boundary, will have minor and major diameters of approximately 0.8 and 4.8 m respectively, and will include vacuum and diagnostic ports and tabulations. The liner wall will be protected by limiters and/or graphite armor. The continuous liner must be designed to allow magnetic field penetration into the torus volume while limiting currents and minimizing resistive losses in the liner.

The shell, located between the liner and the toroidal field coils, helps to maintain plasma equilibrium in conjunction with the equilibrium coils. The shell will have special design features to minimize field errors at the electrically insulated gaps that allow changes of the toroidal and poloidal field during short time periods.

Coil Systems. The magnet coil systems will produce the magnetic fields required to establish and confine the plasma, while minimizing field errors. The poloidal field (PF) coil system consists of the ohmic heating (OH) coils, which provide the flux linkage to establish and maintain the

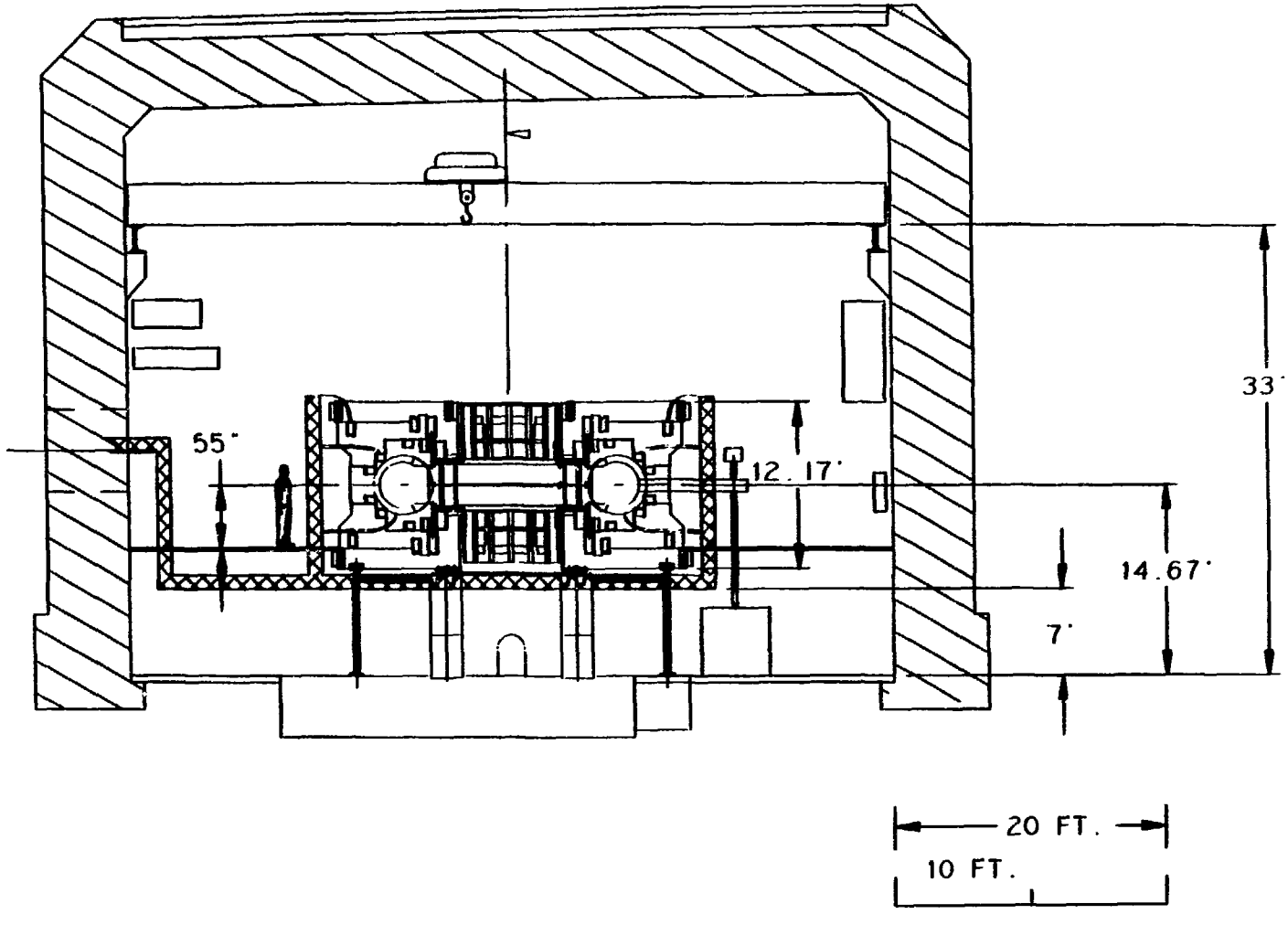

Fig. 3.2-1, Cross Section View of TSL 124 and ZTH

plasma current, the equilibrium field (EF) coils which provide the vertical fields to maintain plasma equilibrium, and the horizontal and vertical field trim coils (HT and VT) which can produce up to 150 g of trim field.

The toroidal field (TF) coils, located between the shell and equilibrium coils, provide the initial toroidal magnetic field and assist in maintaining the desired toroidal field at the vacuum wall during the discharge. These coils must be designed to allow ease of assembly and rapid access to the shell and liner for maintenance.

The coil systems must be designed to minimize magnetic field errors, to allow good torus access for diagnostics and maintenance, and to minimize overall costs including power supply cost.

Vacuum and Gas Fueling Systems. The CPRF vacuum and gas fueling systems will consist of three or four high vacuum pumping stations, a roughing system, a gas-fill system, and a control system. The pumping stations will use turbomolecular pumps. Metal sealed joints will be used wherever possible throughout the high vacuum pumping system and liner. The systems will be bakable in the 150 to 300°C range. Initially a gas puff system will be used to fuel the discharge; provision will be made for subsequent addition of pellet injectors. The base pressure in the liner will be $\leq 10^{-7}$ Torr and the characteristic pumping time ≤ 15 s.

Energy Systems. The CPRF power supplies will be fed from a variable frequency, 1,430 MVA, free running generator, which can supply 600 MJ. The generator output bus will feed transformers which will drive various solid state power supplies required by the CPRF.

The ohmic heating power supply in a high current configuration will first be used to charge the OH coils. Magnetic energy transfer from the OH coils will then be used to raise the plasma current to 2 MA in approximately 50 ms. Following this, the plasma current will be ramped from 2 to 4 MA and sustained by the ohmic heating power supply in a low voltage configuration powering the OH coils.

The EF coils wild be driven by a fast response power supply system, which also provides corrections to the vertical field by a plasma position feedback system that fine tunes the plasma equilibrium.

Separate 1 MW power supplies will be provided for the HT and VT coil sets. These coils will be capable of providing steady 150 G trim fields and 300 G fields for short times, limited by coil temperature. Proper operation of these trim coils may reduce the control required on other PF power supplies.

An initial toroidal field of up to 10 kG will be supplied by a 5 MJ, 10 kV capacitor bank. After toroidal field reversal at the vacuum liner, a thyristor convertor will be connected to the TF coils to maintain a reversed toroidal field of up to 5 kG. The supply will be feedback controlled to provide the desired reversal value during the ramp and flat-top times.

The CPRF power supplies will consist of a number of three phase, twelve pulse, full wave, thyristor controlled convertor units. Opening switches are critical components in the ohmic heating system, and vacuum circuit breakers appear to be the best choice.

Control and Data Acquisition Systems. A computer system will be used for machine control and data handling of all experimental devices in the CPRF. A distributed computer system will use three main computers, one each for the control, data acquisition, and data analysis function.

The machine control computer provides overall control of all devices associated with the operation of the machine. This computer will oversee and coordinate a number of lower-level processors that will operate the various subsystems.

The data acquisition computer, with CAMAC interfaces to the various diagnostics, will record all relevant parameters and data and ship them to the data analysis computer in a time that is short compared to the shot-to-shot time. The system will support multiple diagnostic processors which read out process data for several diagnostic channels.

Data analysis support for the CPRF will rely on existing equipment. Program development will be done on the Los Alamos National Laboratory CTR-Division User Service Center (USC) VAX 8600. An upgrade to a VAX 8650 is planned before the beginning of operations in FY91. During operation CPRF tasks will be run at the highest priority so that data will be available between shots. The link to the USC and through it to the National Magnetic Fusion Energy Computer Center (NMFECC) will provide computational capability for sophisticated data analyses.

Diagnostics. Optical, particle, and electrical diagnostics will be used to determine plasma parameters and characteristics. The major diagnostics are listed in Table 3.2-1. The main tasks of the diagnostics will be to obtain data that can be used to determine the energy confinement properties, the transport mechanism, the configuration sustainment mechanisms, and parameter dependence on plasma current, plasma density control techniques, plasma edge control techniques, etc. Provision of the diagnostic neutral beam is contingent on acquisition at no cost of the source and accelerator.

TABLE 3.2-1

MAJOR DIAGNOSTICS

Measurement	Diagnostic
Magnetic Field Distribution	Electrical diagnostics Internal probe
Electron Density	Multichord interferometer Multipoint Thomson scattering
Electron Temperature	Multipoint Thomson scattering Si(Li) detector
Ion Temperature	Doppler spectroscopy Neutral particle analyzer Diagnostic neutral beam Neutron diagnostics
Hard X-Rays and Neutrons	Scintillators Neutron counter array, activation analysis, fluctuation diagnostic Neutron spectroscopy
Radiation and Particle Losses	Bolometer array Spectroscopy*
Impurity Concentration	Spectroscopy* Surface-barrier diode arrays Si(Li) detector
Fluctuations	Electrical diagnostics Multichord interferometer Surface-barrier diode array Neutron fluctuation diagnostic Spectroscopy*
Edge Plasma	Internal probe Neutral particle analyzer Charge-exchange Doppler broadening Spectroscopy*
Plasma-Wall Interacting	Armor/liner thermocouple arrays IR and visible cameras Bolometer array Spectroscopy*
*Spectroscopy Diagnostics	Visible spectrometer Normal incidence VUV spectrometer Grazing incidence VUV spectrometer Bent-crystal spectrometer D-alpha filter monochromators Z-effective filter monochromators

4.0 Schedule

Schedule Baseline and Milestones

The CPRF initial schedule baseline calls for a project schedule of 80 months duration, beginning in February 1986 and concluding with the completion of the 4-MA capability in September 1992, with 2-MA capability in October 1990. First plasma experiments will begin in FY 91 and continue during the addition of power supplies to complete the 4-MA capability. Final closeout of construction activities should be complete by September 1992. Table 4.3-1 lists significant CPRF Construction Program milestones.

TABLE 4.3-1

CPRF Construction Program Milestones

Milestone		Level	Date
1.	Conduct integrated review of CPRF and ZTH design	1	July 1987
2.	Deliver last toroidal coil to LANL	1	May 1989
3.	Complete startup testing of generator	1	Oct 1989
4.	Deliver last poloidal coil to LANL	1	Dec 1989
5.	Deliver shell to LANL	1	Feb 1990
6.	Complete facility capability for 2 MA	1	Sept 1990
7.	Complete facility capability for 4 MA	1	Sept 1992
8.	Remove last equipment from TSL-124	2	Nov 1986
9.	Complete modifications of TSL-124	2	Feb 1987
10.	Complete design of generator foundation	2	July 1987
11.	Complete design power line extension	2	Oct 1987
12.	Place contract for poloidal coils	2	June 1988
13.	Mount generator stator on foundation at site	2	Feb 1988
14.	Place contract for toroidal coils	2	June 1988
15.	Place contract for shell	2	Nov 1988
16.	Place contract for first order of power supplies	2	Aug 1989

5.0 Construction Program Organization

The CPRF/ZTH Construction Program is organized at Los Alamos as shown in Fig. 5.0-1. The CPRF and ZTH have been divided into a number of relatively self contained tasks and a Task leader assigned to each.

Integration-type tasks have been created to assure that interrelationships between the tasks and components are properly considered. The Task leaders are responsible for the technical and administrative performance of the work required to complete their tasks and generally have a number of people who report to them. The Task Leaders report to the Program Manager for CPRF Construction. Personnel for this effort are drawn from many divisions within the Laboratory with the majority from CTR-Division.

The relationship of the CPRF Construction Program to the CTR-Division and the Laboratory Administration is illustrated in Fig. 5.0-2. There are two major administrative organizations working together to direct the CPRF: the MFE Program Office with Rulon Linford as the MFE Program Director and the CTR-Division with Harry Dreicer as Division Leader. The MFE Program Office has program responsibility (program direction) and the CTR-Division provides the resources (expert personnel, space, etc.). Joe DiMarco, Chairman of the Technical Steering Committee, provides the scientific direction necessary to assure the proper design and construction of the CPRF/ZTH. Philip Thullen, Program Manager for CPRF Construction, oversees the day-to-day design and construction activities.

The CPRF Construction Program is funded by the United States Department of Energy (DOE). The Office of Fusion Energy (OFE), which is within DOE Headquarters is the lead organization for the CPRF Construction Program. Warren A. Marton is the OFE Program Manager for the CPRF Construction Program. Within DOE, the Albuquerque Operations Office (AL) has the responsibility and authority for the successful execution of programs and construction projects assigned to AL including among others the CPRF. Ethan Walker is the AL Program Coordinator. Within the DOE, the Los Alamos Area Office (LAAO) has the day-to-day responsibility for the successful construction of CPRF by virtue of their on-site presence at LANL. A LAAO Project Manager for the CPRF activities will be assigned.

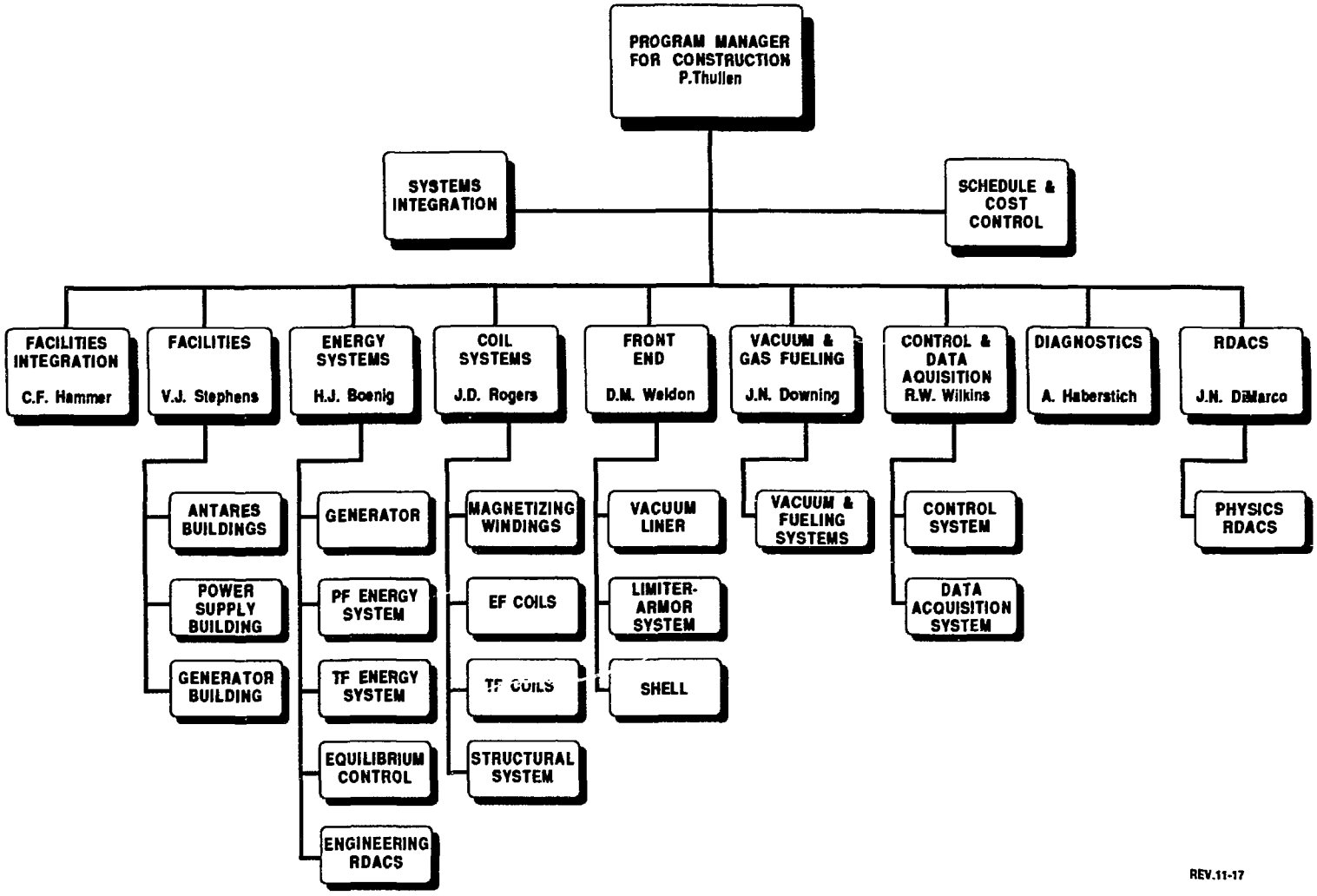

Fig. 5.0-1, CPRF Task Responsibilities

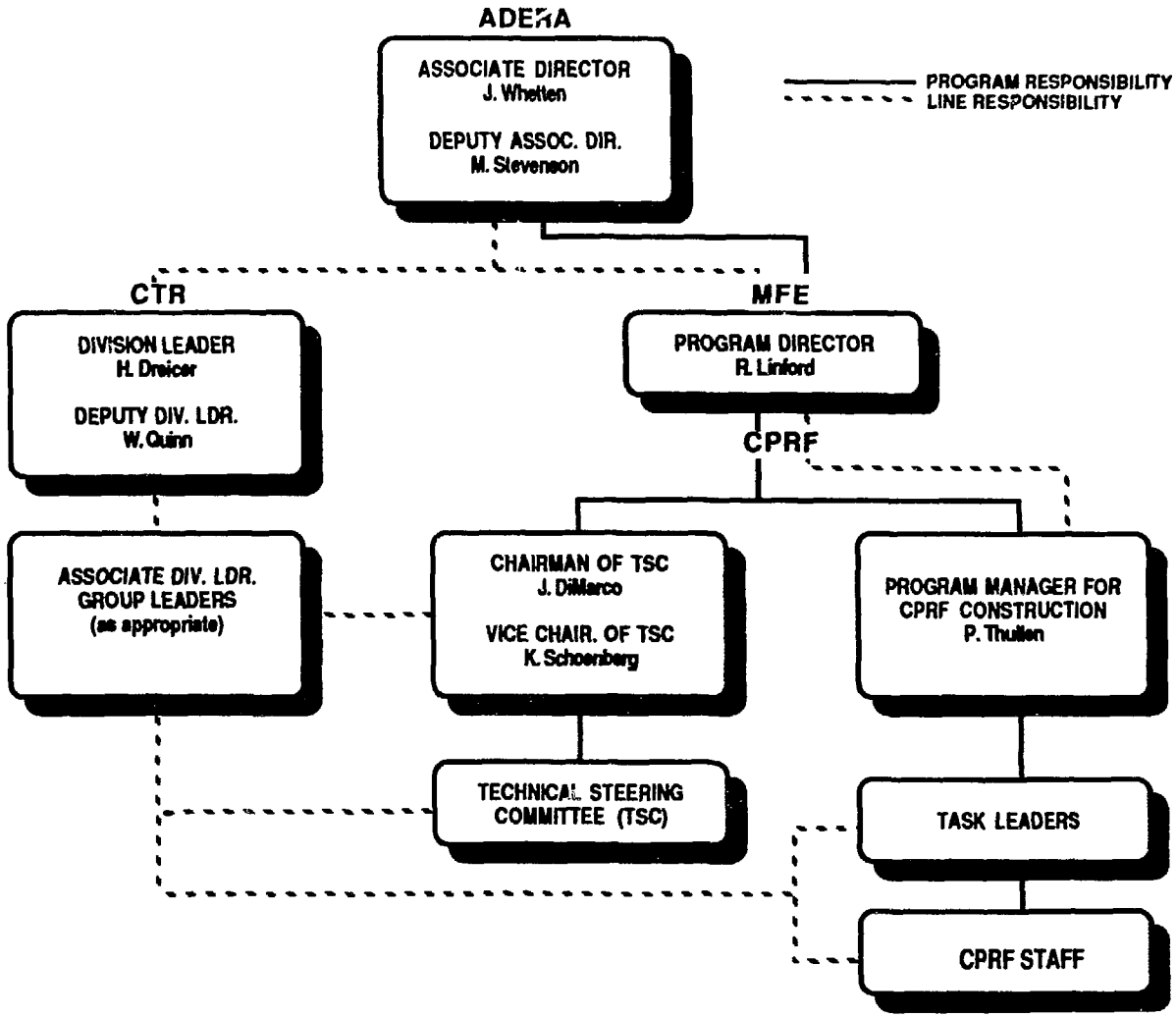

Fig. 5.0-2, CPRF Operational Matrix Structure

RFX EXPERIMENT LAYOUT

L. Fellin
Università di Padova - Italy

ABSTRACT

The layout of the buildings forming the site of the RFX experiment is described. The main features concerning the grounding system (both for the safety and for the operation of the machine) are discussed together with those of the screening system for the diagnostics and control areas.

1. GENERAL OVERVIEW

The RFX experiments is located over an area of 20.000 m^2 which is part occupied by 400 kV transformer substation (8.000 m^2) and part occupied by the buildings (4.500 m^2).

The schematic drawings of Fig. 1 and 2 show how the various functional areas are split. The total volume of the buildings is 48.000 m^3 and the useful surface is 7000 m^2.

The buildings are modular (1.20 m module) pre-fabricated structures with large conditioning system able to control the temperature in the 20-26°C range and the relative umidity between 40% and 50%.

The general facilities in site include an emergency system (up to 350 kVA) and a rotating no-break system (up to 100 kVA).

The electrical distribution system is divided in six separate networks:

- lighting
- general services
- climate services
- dedicated services
- no-break network
- auxiliary networks and feeding for safety and security networks.

All local distribution panels are available with or without insulating transformers up to 20 kVA each.

To avoid the effect of the sudden voltage drop which takes place during the pulse on the 21.6 kV network fed through the step-down transformers by the 400 kV grid, all the previous networks are derived from the 20 kV commercial network, which is completely independent of the first one.

2. TORUS HALL

The torus hall is split in two parts: the first one is the torus site, surrounded by a thick wall; the second, separate from the first one by a big gliding door, is dedicated to the pre-assembly operations of the machine. The walls and the roof are designed to act as neutron shielding (70 cm thickness and overlapping - Fig. 3).

Because of the air core design of the machine it is necessary to reduce the interactions between the steel in the concrete and the magnetic field produced by the machine. To limit the stray field to 1 mT an open loop stainless steel reinforcement has been adopted for the foundations of the machine.

Moreover, some electric "cuts" were provided along the reinforcement of the walls, parallel with the machine axis.

Many protected windows are made in the wall for power supply and diagnostics connections. In order to prevent induced dangerous voltages or electromagnetic interference all the signal cable coming out from the torus to the diagnostic building (except, of course, fiber optic links) must be arranged as in Fig. 4, employing only one window located parallel with the major axis of the torus. The torus hall is also equipped with a 50 tonn crane with very accurate controls of the movements.

3. POWER SUPPLY AREA

In the center of the power supply area a two floor volume is located dedicated respectively to the 21.6 kV metal clad switchgear (1^{st}floor) and to the local control area (2^{nd}floor). The last one is completely screened by a metal cage: the in-and-out connections are made only via fiber optics or through galvanic insulations of the circuits.

4. VACUUM SYSTEM AND DIAGNOSTICS AREA

This building is partially dedicated to the vacuum system (1^{st}floor) and to the diagnostics (2^{nd} and 3^{th} floors). This very compact solution allows to have all vacuum equipment under the equatorial level of the Torus without interference with the diagnostic system.

All these areas are completely screened by individual modular iron cages at each floor (Fig. 4 and 5).

5. MAIN CONTROL AREA

It is located at the 2^{nd} floor of the R1-R3 building, sufficiently far away from

the torus, in order to avoid electromagnetic interference in the computer and PLC system. As the local control area in the power supply building the main control area is completely enclosed in an iron cage.

6. GROUNDING SYSTEM

The grounding system is a relevant part of the layout because of the air core machine, of the fast varying magnetic fields and of the very high level of the fault-to-ground currents. Since the detailed problems connected to the grounding system are not completely defined up to now, a very flexible arrangement has been provided in order to make possible modifications during the construction of the different subsystems.

The main structure of the grounding system consists of:

a) a large main earthing electrode, made up with a 10x10 m grid and 50 mm^2 of copper conductor, directly buried under the 400 kV substation and building (Fig. 6). This assures personal safety and gives a reliable potential reference. Because the fault to ground current in the 400 kV substation may reach 29 kA, the total voltage may reach 1500 V;

b) an external iron cage working as Faraday protection in case of direct or indirect lightning to the building (Fig. 5); the cage is directly welded to the main earthing electrode, as well as the reinforcement in the concrete structure of the buildings;

c) two 1000 mm^2 closed copper rings, simmetrically placed with respect to the equatorial plane of the torus; they are large enough to include the torus hall, the diagnostics and the power supply areas. The aims of the rings is to reduce the induced voltage outside and to create a good earthing reference for the experiment. In particular, calculations show that the rings may reduce the induced voltage of about 10 times in the control area. On the other hand maximum vertical field error produced by the rings is very negligible;

d) a group of iron cages, insulated each others and from conducting element like concrete reinforcement, cable ducts, copper rings and Faraday's cage, located in the main and local control areas and in the diagnostics area.

The final earthing phylosophy is still under discussion but the principles should be the following:

- the buried net and the Faraday's cage have negligible interactions with the machine: they are essentially a compact electrode which assures to be a "potential reference": the interactions with it are only "external problems",

i.e. safety on the boundaries of the area and capability to disperse the maximum fault current in the earth;

- neutral points of step down and distribution transformers are directly connected to the net;
- safety ground distribution is made with a "tree" structure, insulated wires, directly connected in only one point of the net;
- taking care of what is mentioned in par. 2 all the reinforcements inside the concrete are directly connected to the net;
- the two main copper rings are connected to the net in only one points; the lower ring may be the only reference voltage for the experiment;
- incoming from the lower ring there are a number of separate "tree type" grounding structures dedicated to the experiment;
- the iron cage located in the diagnostics and control areas prevent electromagnetic interferences from outside, from the transfer energy system in the power supply area and from the magnetizing winding. They are connected to the lower ring and to the central point of the torus via a copper collector; all the earthing connections inside each cage (also those related to the safety) are referred to the same grounding point as A in Fig. 5;
- finally, all the signal cables must be routed as in Fig. 4.

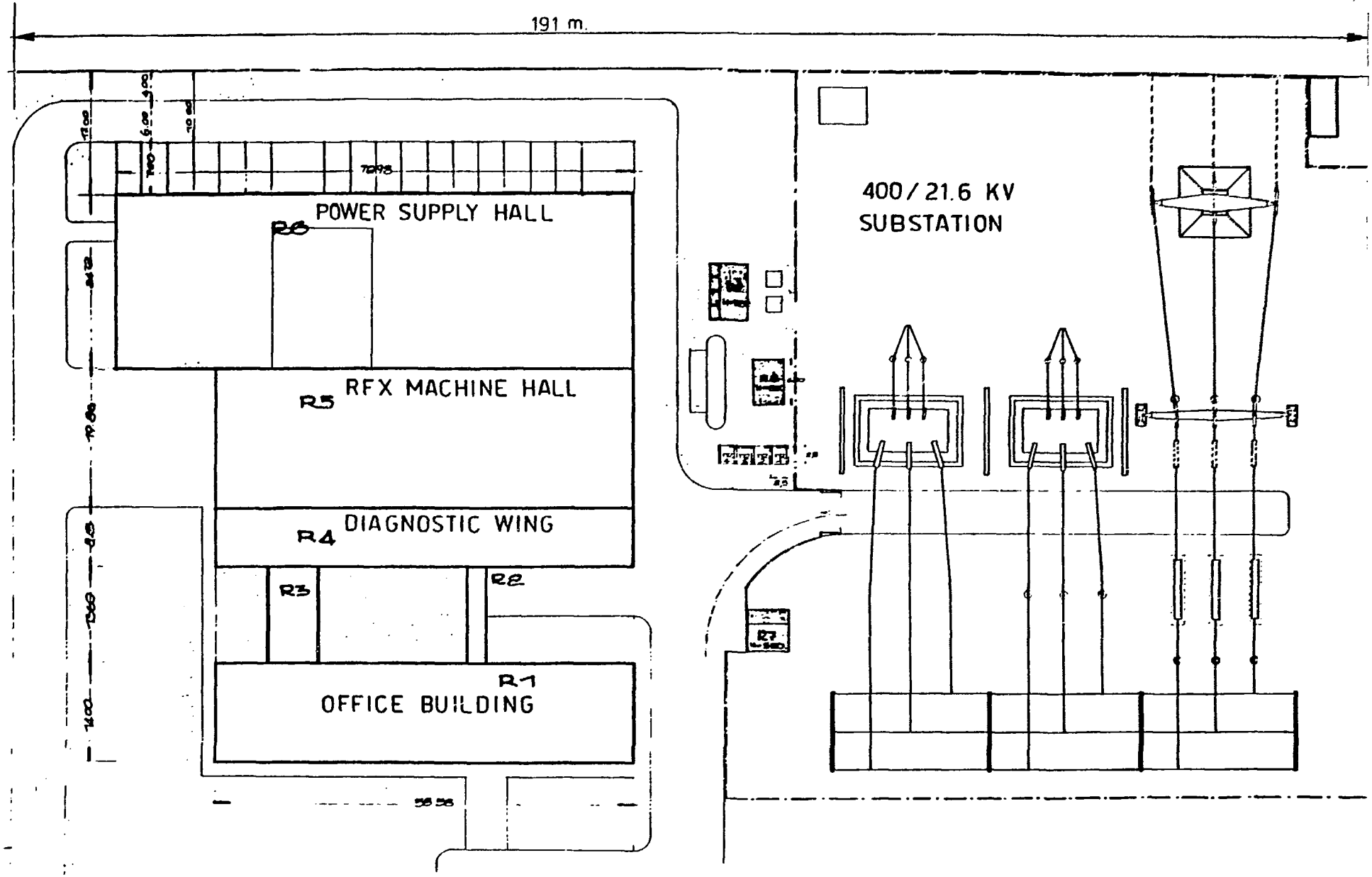

Fig. 1 - RFX AREA GENERAL LAYOUT

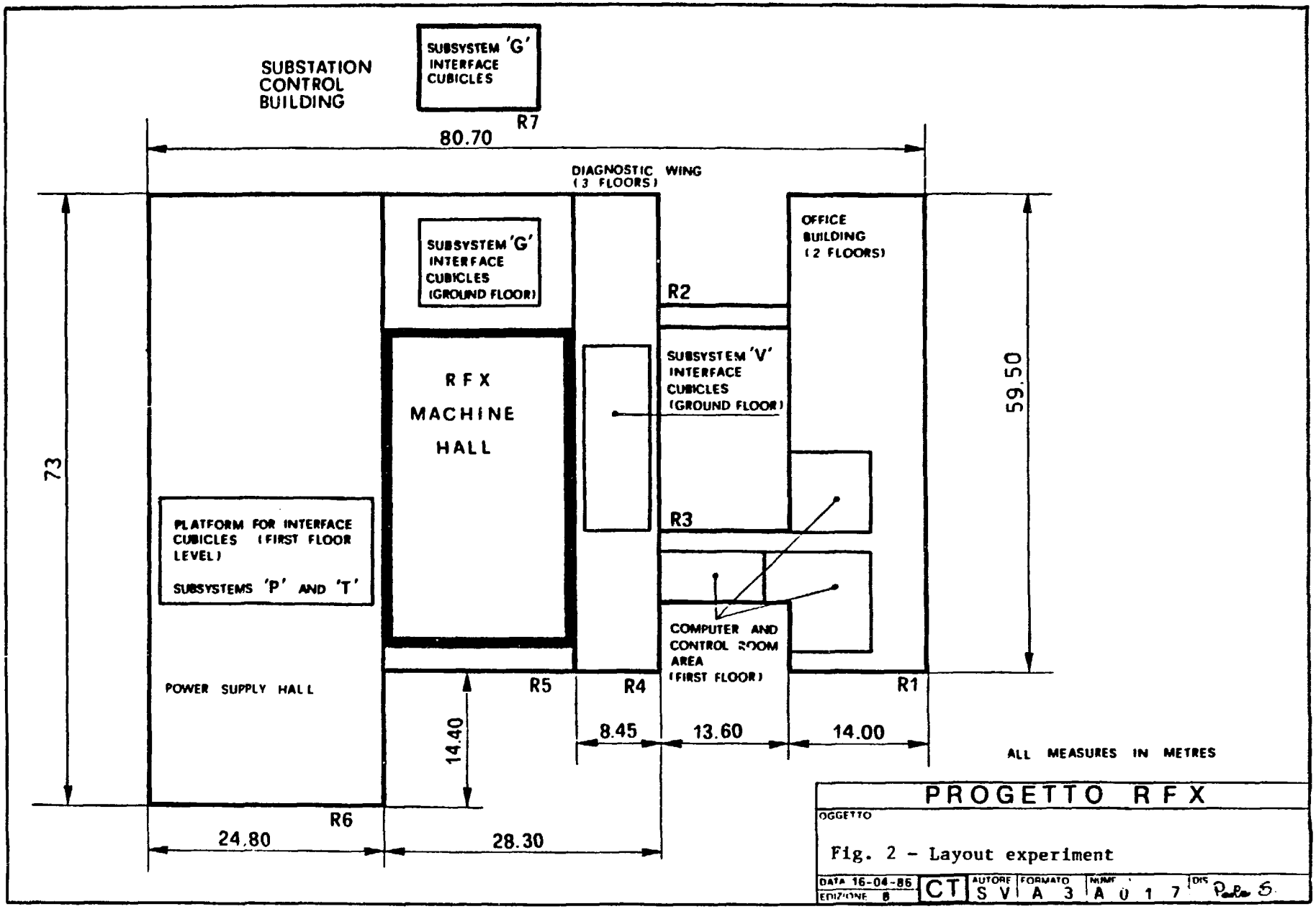

PROGETTO RFX

OGGETTO

Fig. 2 - Layout experiment

DATA 16-04-86 | EDIZIONE B | CT | AUTORE SV | FORMATO A3 | NUM A017 | DIS Paola S.

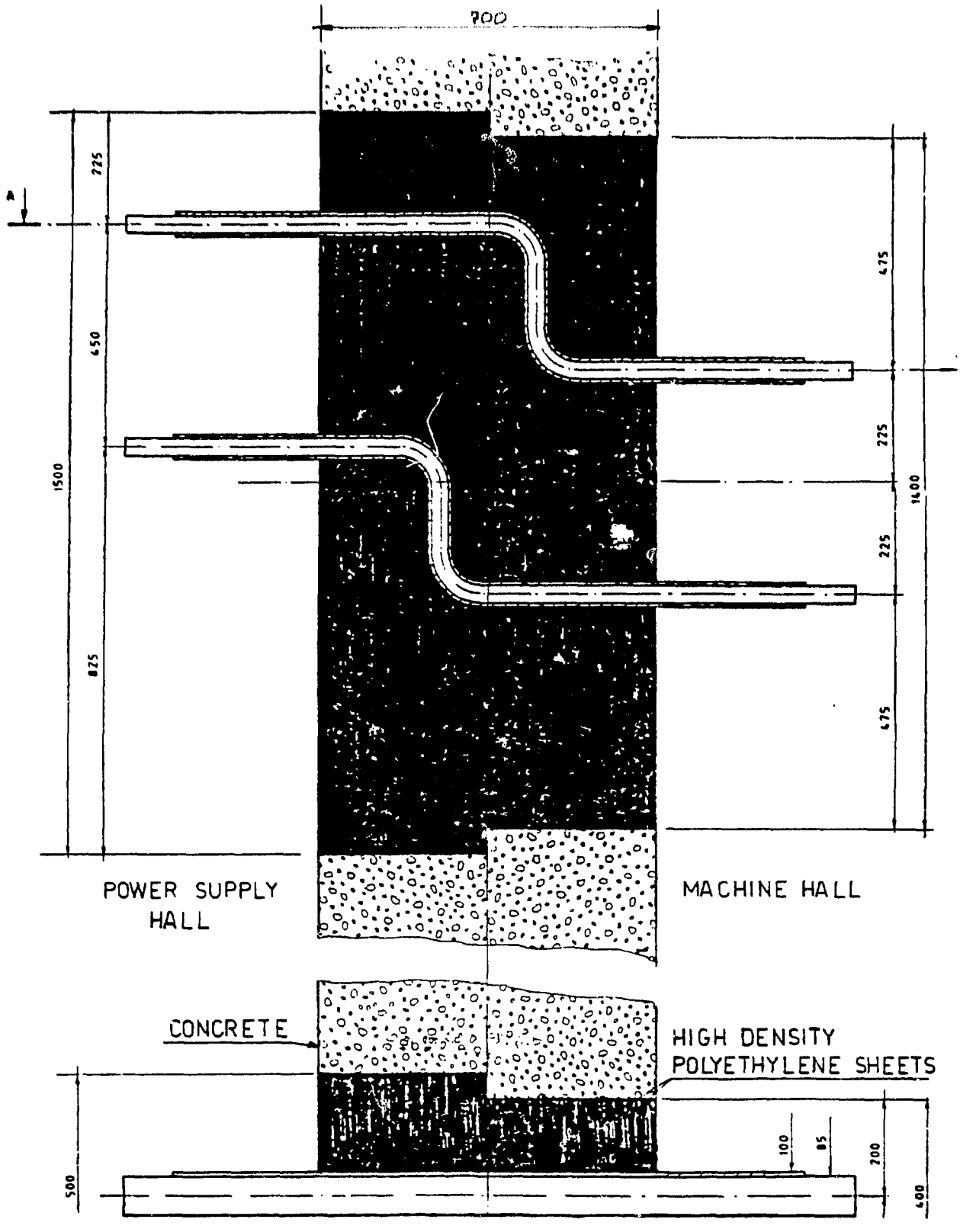

Fig. 3 - SHIELDING WALL WITH PENETRATIONS

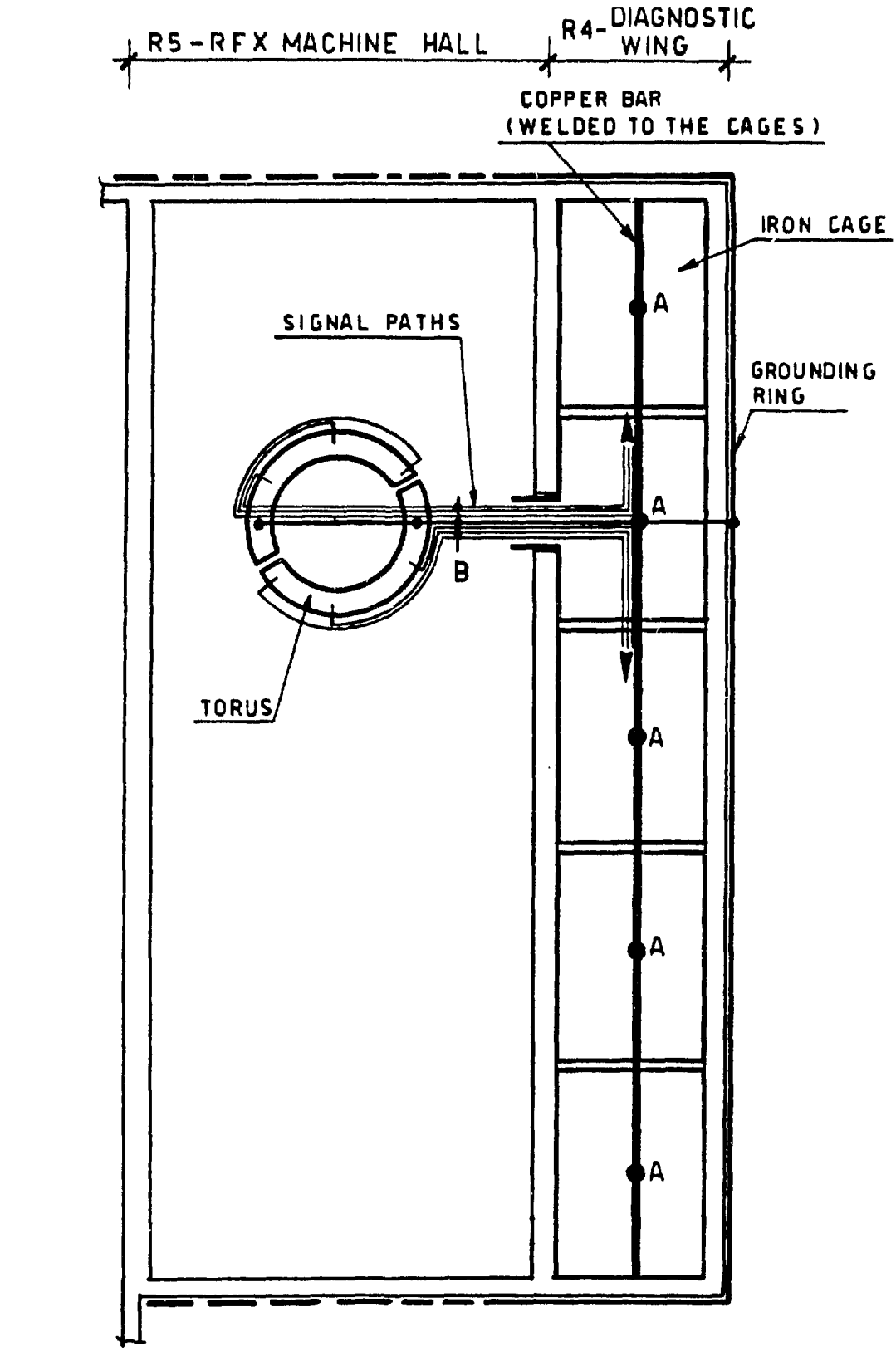

A=REFERENCE EARTHING POINT FOR EACH CAGE

B=REFERENCE EARTHING POINT FOR SIGNAL CABLE SHIELDING

Fig. 4- EARTHING SYSTEM LAYOUT (Plant)

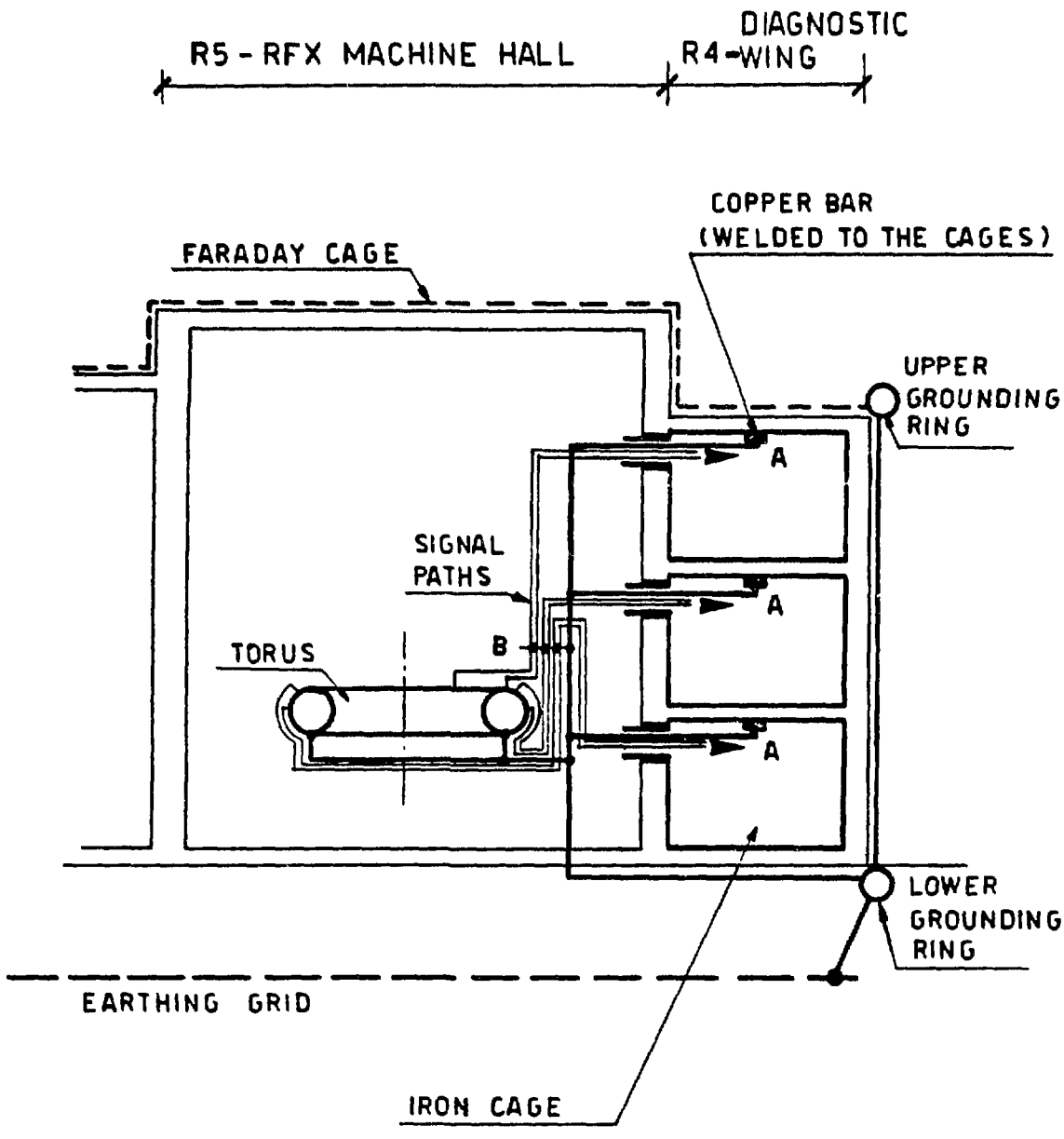

A = REFERENCE EARTHING POINT FOR EACH CAGE

B = REFERENCE EARTHING POINT FOR SIGNAL CABLE SHIELDING

Fig. 5 - EARTHING SYSTEM LAYOUT (Elevation)

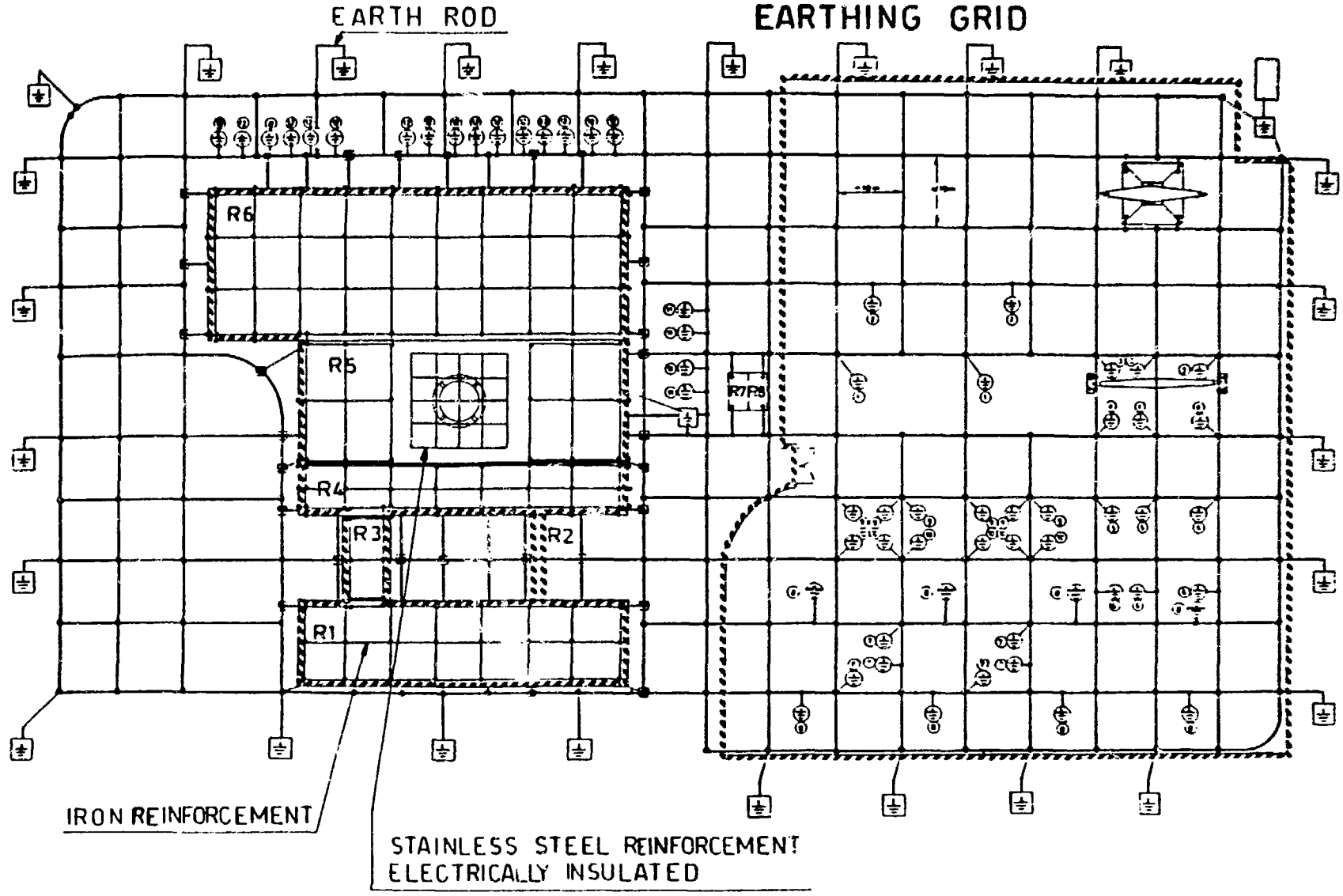

Fig. 6 - RFX AREA EARTHING GRID

Workshop on Engineering Design of Next Step RFP Devices
July 13 - 17, 1987 at Los Alamos

Overview of REPUTE-2 Project

K. Miyamoto* and N. Inoue+

* Department of Physics, Faculty of Science

+ Department of Nuclear Engineering, Faculty of Engineering

University of Tokyo

Objectives of REPUTE-2 Project are followings:

1) equilibrium control of plasma position, current ramp up, density control during ~ 0.3 sec discharge with 2 MA plasma current
2) MHD stability (ideal as well as resistive) and relaxation phenomena of RFP plasma
3) transport scaling of RFP plasma with high tempeature $T_e(0) \approx$ 1-2 keV
4) MHD stability and transport of ultra-low-q tokamak
5) impurity control

and so on.

Major parameters of REPUTE-2 device are followings : the major radius R = 1.5 m, the plasma radius a_p = 0.3 m and the expect plasma current I_p=2 MA. When the pinch parameter is Θ = 1.6 and the field reversal ratio is F = -0.4, the average toroidal field for I_p = 2 MA is $\langle B_t \rangle$ = 0.83 T and the toroidal field at r = a_p is $B_t(a_p)$ = 0.33 T. Plasma inductance is L_p =

4.3 μH. The vertical equilibrium field is B_v = 0.39 T for I_p = 2 MA. The shell thichness of aluminium is 5 cm with skin time of 0.46 sec for vertical field penetration. The magnetic flux of ohmic heating coil is Φ = 14.2 V-s. In the case of ultra-low-q (ULQ) tokamak experiment, the toroidal field coils is aimed to provide 1.4 ~ 2 T.

Expected plasma parameters of RFP plasma are followings. The poloidal beta value β_p is expected to be 0.1, that is ,

$$\beta_p = \frac{\langle p \rangle}{B_p^2/2\mu_0} = 0.64 \frac{N_{20}}{I_p(MA)} \frac{\bar{T}(keV)}{I_p(MA)} \sim 0.1$$

where $2\bar{T} = \langle n(T_e+T_i)\rangle/\langle n\rangle$ and $N_{20} = \langle n\rangle \pi a_p^2$ is the line density in 10^{20} m^{-3} unit. $\langle\ \rangle$ is the volume average. When n and T are parabolic profile, the average temperature $\bar{T}$ is $\bar{T} = (2/3)T_0$, where T_0 is the value at the center. When the following scaling is assumed

$$\frac{\bar{T}_e(keV)}{I_p(MA)} \sim 0.5 \qquad \frac{N_{20}}{I_p(MA)} \sim 0.3 \qquad (\beta_p \sim 0.1)$$

then we have $T_{e0} \approx T_{i0} \approx 1.5$ keV, $\langle n\rangle \approx 2.3\times10^{20}$ m^{-3} in the case of I_p = 2 MA. The average current density is $\langle j_p\rangle = I_p/(\pi a_p^2)$ = 7 MA/m^2. The drift parameter is $\xi = \langle j_p\rangle/[e\langle N\rangle v_{Te}(\bar{T})] \sim 0.013$, where $v_{Te}(\bar{T})$ is the thermal velocity $(\bar{T}/m_e)^{1/2}$.

The plasma resistance R_p is estimated by

$$R_p I_p^2 = \int \eta\,(J_z^2+J_\theta^2)dV$$

Then we have

$$R_p(\Omega) = 3 \times 10^{-3} T_{e0}^{-3/2}(keV) \frac{2R}{a^2} Z_{eff}\,\zeta$$

where

$$\zeta = \frac{\int \eta (J_z^2 + J_\theta^2) 2\pi r\, dr}{\eta(0)\, J_z(0)\, I_p} \frac{J_z(0)}{\langle J_z \rangle} \approx 2 \sim 4 \sim 8$$

for standard modified Bessel function model and parabolic profile of the electron temperature. Then the energy confinement time is

$$\tau_E = \frac{0.8}{Z_{eff}\, \zeta} a^2 T_{e0}^{3/2} (keV) \quad (s)$$

and $\tau_E \sim 8.3$ ms for $T_{e0} = 1.5$ keV, $Z_{eff} = 2$, $\zeta = 8$ ($I_p = 2$ MA).

Coil system of REPUTE-2 is designed taking account of following items. The vertical field coils are arranged to decouple with the plasma current and ohmic heating coils inductively. The toroidal field coils are strong enough to provide B_t = 1.5-2 T for ULQ experiment. The ripple of the toroidal field coil is less than 0.1%, therefore the toroidal field coils are shifted radially and the number of the coils is 48. The inductance of ohmic heating coil for 1 turn equivalent is $L_{OH} = 0.81\,\mu$H, so that coupling constant with the plasma current is $k_{OH}^2 = L_{OH}/L_p = 0.188$. The inductance of vertical field coil for 1 turn equivalent is $L_{BV} = 4.88\,\mu$H and $B_V = 0.19$ T when the 1 turn equivalent current of the vertical field coil is $I_V = 1$ MA.

The schematic diagram of the coil systems of REPUTE-2 is shown in fig. 1.

An operating scenario of REPUTE-2 discharge is schematically given in fig. 2. The plasma current is ramped up fastly in the formation phase (for example 0.1 MA/ms) and then the plasma

current is slowly ramped up to 2 MA and is sustained for a while. In this operating scenario the most severe issue of the power supplies is the requirement for the capacity of the circuit braker of ohmic heating coils (the required volt-ampere is 0.4 x 8.75 = 3.5 GVA for 0.1 MA/ms current rise). Therefore if RFP plasma is formed by slower current ramp up in the initial phase, the required capicity of the circuit braker is much reduced.

The other issue is the large amount of heat wall loading. The ohmic heating power in the previously mentioned case of 2 MA is about 26.4 MW, therefore even the uniform wall loading is already 1.6 MW/m^2 for the duration of around 0.3 sec. An carbon protector such as isographoite or C-C composites in necessary for such high heat flux.

Physics of ULQ (ultra-low-q) experiment, more detailed design of REPUTE-2 device and its power supplies are also presented in this workshop.

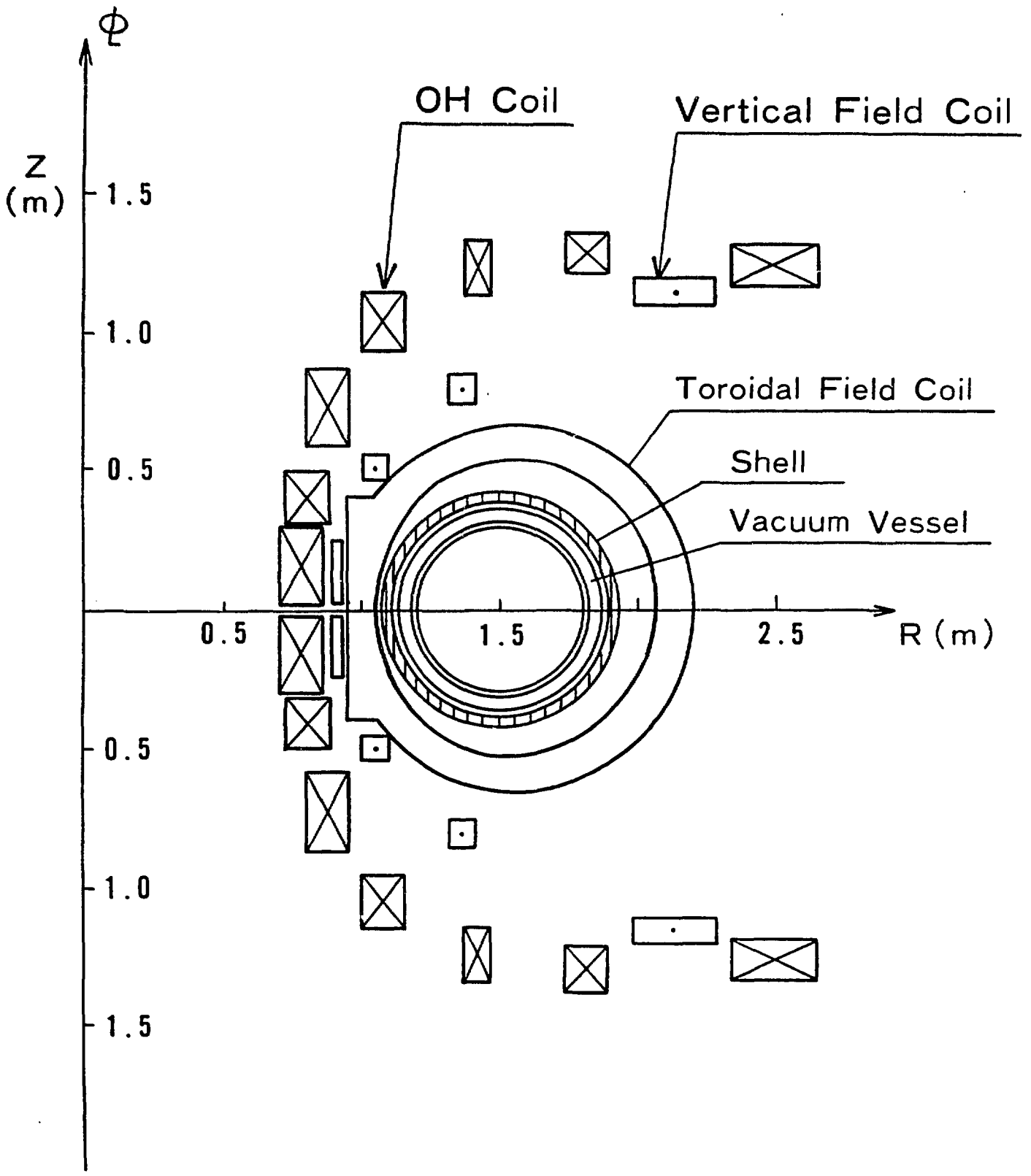

Fig. 1 Coil Systems of REPUTE-2

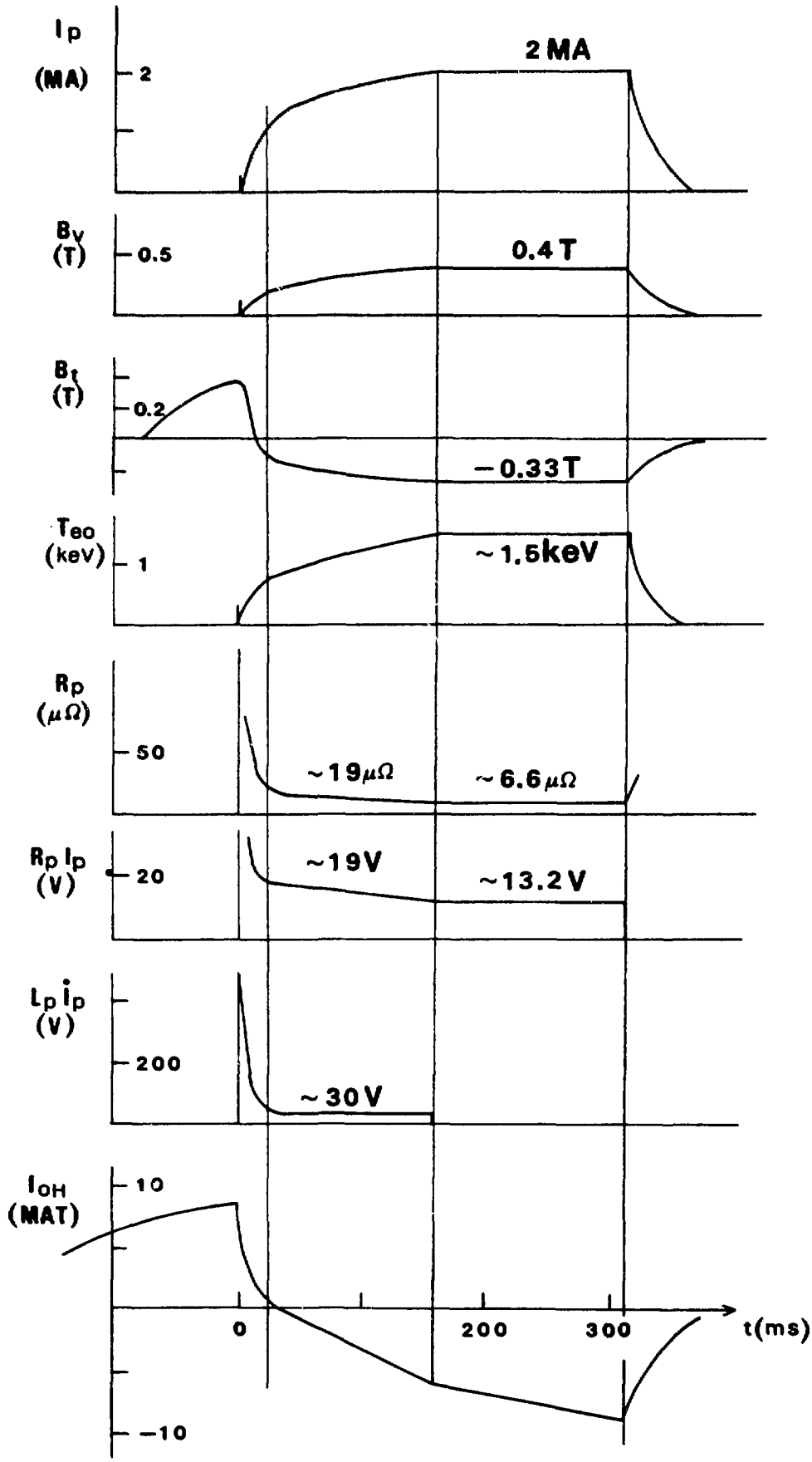

Fig. 2 An Operating Scenario of REPUTE-2

OVERVIEW OF THE ZTH FRONT-END DESIGN

David M. Weldon
Los Alamos National Laboratory, Los Alamos, New Mexico

INTRODUCTION.

The front-end of ZTH is defined as the vacuum liner, graphite armor, and conducting shell. This paper will give a brief overview of the present ZTH front-end design and the reasons for selecting various features of the design. Details of the design will be discussed in other papers presented at this workshop.

VACUUM LINER.

The liner is mostly constructed of inconel bellows sections separated by ring shaped ribs. At 16 places around the torus, the bellows is replaced by a cylindrical section to accommodate diagnostic ports. Ribs are welded to the diagnostic sections to provide additional bracing. Figure 1 is a cross sectional view of the liner wall near a diagnostic port. The inconel bellows are 1.5 mm thick, and have a convolution depth of 2.7 cm and a pitch length of 2.8 cm. The inconel ribs increase the strength of the liner, but mainly provide a precise structure indexed to the shell for positioning the graphite armor. The liner is designed to withstand crushing forces along the minor radius but must be blocked against the shell to maintain the shape of the major circumference. There will be 4 support blocks between the liner and the shell at each rib. Diagnostic tubulations exist at 15 locations around the torus; the 16th cylindrical section is at the poloidal gap and contains no tubulations.

It is desirable to operate the liner and graphite armor at 200 C and to bake out the armor at 300 C after the machine has been opened to the atmosphere. These operating and bakeout temperatures are chosen on the basis of Tokamak experience and the rate of water evolution from graphite. Maximum continuous operating temperature of most organic electrical insulation is about 240 C. Consequently protective thermal insulation is necessary between the electrical insulation and liner. Heating of the armor will be accomplished by low power 60 Hz discharges between shots.

In addition to the vacuum forces there are potentially large electromagnetic forces produced by induced currents in the liner and shell at termination of the discharge. The magnitude of the forces depends upon the rate of plasma current decay, which can not be predicted with complete accuracy. The main forces on the liner are a crushing force caused by self field and an interactive force between liner and shell. During rapid termination of the plasma current, saddle currents are induced in the shell to maintain the vertical field. Interaction of the liner current with the shell currents produces an inboard directed force on the liner and an outboard reaction on the shell.

The toroidal resistance of the liner is about 8.5 mohms. During startup, induced currents in the liner can produce an undesired vertical field in which the field lines pass through the plasma and close around in the space between the liner and shell. There are several solutions to this problem. The ZTH design maintains the liner toroidal resistance high so the undesired vertical field will die out as soon as possible. In contrast, the RFX design maintains an inboard and outboard resistance of the liner in the correct ratio to produce no vertical field. The poloidal rings used to support the armor cause a small perturbation to the toroidal field during startup, but the magnitude is never larger than 30 gauss 1 cm below the plasma surface.

ARMOR.

The inside of the liner is protected by 4200 graphite tiles which cover 90 % of the inside surface. Only the diagnostic ports and a 0.5 cm gap between tiles remain uncovered. The tiles are flat plates held in inconel clips which are in turn screwed into tapped holes in the liner ribs. A single hole through the center of the tile allows a screw to pass through the tile to fasten the clip to the rib. An alternate to the clip design was considered in which the graphite tile was brazed to an inconel backing plate. This option was finally rejected because the residual stress trapped in the graphite after cool down from the brazing process appeared to be too large. Figure 2 shows the earlier version of the liner using a brazed backing plate. A more complex arrangement for hanging the tiles was also considered. Instead of a screw, a spring locking device which could be released by pushing a recessed button in the center of each tile was considered. This would allow single tiles to be replaced by a tile manipulator inserted through one of the larger diagnostic ports. The idea was shelved because of the cost of the tile manipulator and tile fasteners. Installation and repair of the armor will require that the liner be cut open for personnel access.

Calculations of the erosion rate of the tiles using a scrape-off length model suggest that the tiles should be positioned to an accuracy of 5 mm with respect to the flux surfaces. Problems arise at the diagnostic ports because the energy which would have been deposited in the missing graphite area is deposited on the edge of the first tile downstream in the direction of electron flow. A combination of tile shaping at the diagnostic port and erosion should finally machine the tile into a shape in which the energy deposition is evenly distributed.

Forces on the armor depend upon the loop voltage during termination and several other assumptions about the likelihood of breakdown between the tile gaps rather than through the volume of the chamber. Each tile will be designed to withstand an inward force of 900 N, although present feeling is that the maximum force experienced will be much smaller. Eddy current forces in the armor tiles are neglible.

SHELL.

The shell is made of 32 clam-shell sections bolted together with flanges. Each section consists of a double wall stainless steel water jacket bolted to a structural cage. The flanges are part of the strctural cage. The inner sheet of the water jacket is clad with 3 mm thick copper explosively bonded to the stainless steel. The copper cladding is brought around the face of the flanges so all current joints are copper-to-copper. The purpose of the water jacket is to remove heat generated by the heating of the graphite tiles and more particularly to protect the electrical insulation from high temperatures. The electrical insulation might even be glued to the inside surface of the shell for better thermal contact. The structural cage increases the strength of the shell section and also serves as part of the support for the toroidal field coils. Cross bracing between the toroidal field coils will be required because of topling forces induced by the vertical field. Figure 3 shows one of the shell sections.

The shell time constant for soak in of vertical field is 50 ms, which is considerably shorter than the 0.6 s discharge anticipated. The decision to design to a short time constant shell recognizes the need to eventually abandon passive shell stabilization and pursue active feedback methods to maintain plasma equilibrium. The short time constant causes many design problems. The original plan was to use a cast aluminum shell similar to the ZT-40 shell.

This is acceptable if the time constant is 150 ms or larger, but for short time constants only very resistive aluminum can be used, and the thickness of 1.5 cm or less makes casting difficult. The shell serves as the principal structural element for the entire front end, and a thin shell complicates the problem of supporting the forces bearing on the liner and shell. A stainless steel shell would be about 12 cm thick to obtain the proper time constant. A copper shell would be only 3 mm thick, clearly too thin to give much structural support.

The side diagnostic ports are flared to give a larger viewing angle. The shell slips down over these side ports and consequently a section of the shell has to be removable to provide a slot for sliding the shell over the tubulation. These insert pieces are installed after the shell is in place. The size of the shell holes has been severly limited to reduce field errors from currents flowing around the holes. The currents considered here are those induced in the shell during the discharge by the equilibrium control system. The largest shell hole permitted is 11.4 cm in diameter at the pumping stations.

Assembly of the front-end is done on a separate stand with the liner cut in half at two poloidal cuts. The insulation package and shell are installed over each half of the liner at the same time the armor is installed on the inside. The toroidal field coils are also slipped on and installed. The two halves are then pushed together so the two liner parts can be joined. After the final insulation and shell sections are installed, the front end is ready to be lifted in place. Total weight of the front end is about 20 tons.

The toroidal gap is on the inboard side and made by inserting insulation between the flanges. Insulated bolts will be used to fasten the flanges together. Resistive shunts can be bolted across the toroidal gap to simulate gapless operation with various time constants.

The poloidal gap is made of three interleaved copper-clad sheets as shown in Fig. 4. The length of each sheet is about 80 cm. The copper is tapered on the three sheets to be thickest at the stem and of negligible thickness at the end. The insulation will be an epoxy-fiberglass layup around the center sheet. Because of the complicated design, the gap will be forced air cooled along the inside wall rather than water cooled. The tapered overlapped gap was selected after calculations were made of field errors for butt joint gaps, overlapped gaps, and nested double shells.

CONCLUSION.

Designs exist for the ZTh liner, armor, and shell which satisfy the technical design criteria established for the machine. Details of the manufacturing plan have yet to be worked out.

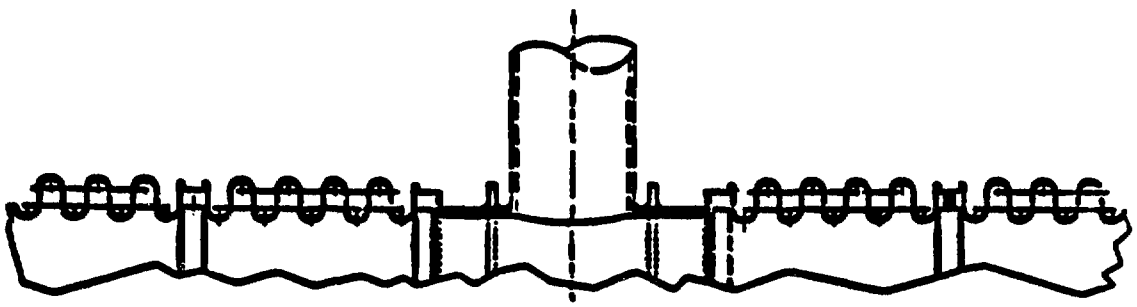

Fig. 1. Cross sectional view of the liner wall near a diagnostic port.

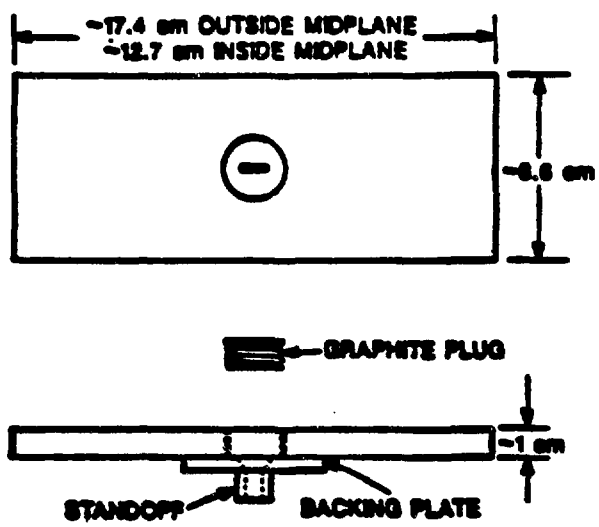

Fig. 2. Two views of an early version of a graphite tile.

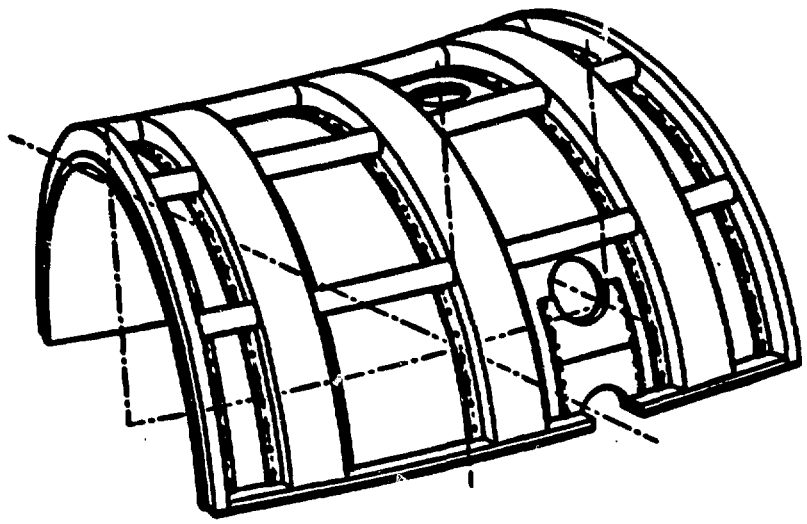

Fig. 3. One section of the shell, showing the water jacket, structural cage, and insert pieces.

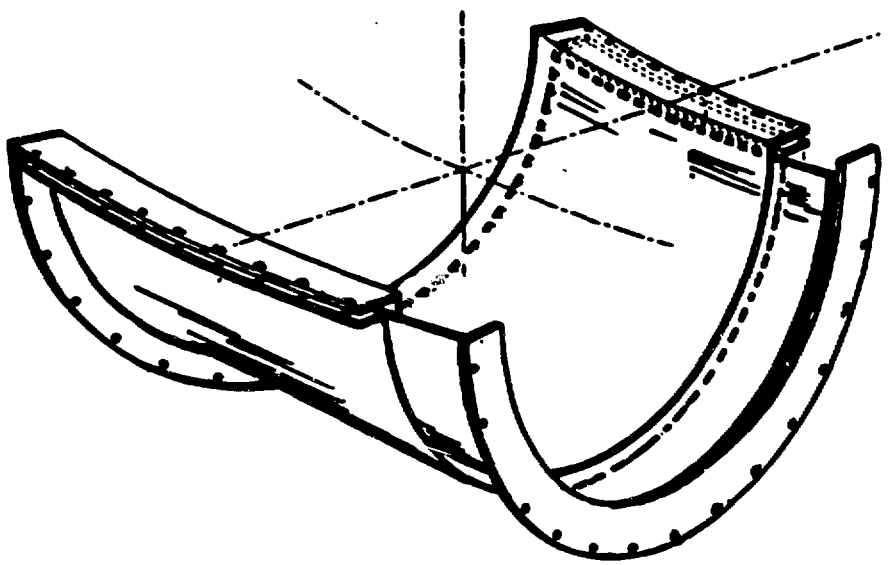

Fig. 4. Physical arrangement of the three conducting sheets forming the poloidal gap.

Work shop on Engineering Design
of Next Step RFP Device
July 13-17, 1987 at Los Alamos

Design Study of REPUTE-2 Machine

Yutaka Itou

Hitachi Works, Hitachi Ltd.

REPUTE-2 project is the next RFP fusion research program which has been planned by the University of Tokyo. Very early phase design of REPUTE-2 machine has been performed.

Design valve of plasma current is 2 MA in RFP mode operation. And it is aimed to use ultra low-q tokamak mode operation too. So REPUTE-2 is required to generate rather high troidal field than usual RFP machine.

Major machine parameters are listed in Table 1, and cross sectional view of the machine is shown in Fig.1.

Magnet system consists of three kind of coils which are toroidal field coils (TFC), ohmic heating coils (OHC) and vertical field coils (VFC). Number of TFC is 48. Each coil, shown in Fig.2, has only 1 turn, and is divided into two parts demountably.

Vacuum vessel (VV) consists of 24 thin ring sectors and 24 bellows. Inconel-625 is adoped because of its high electric resistibity. Inner wall of the vaccum vessel is covered by graphite armor tiles in order to protect the high heat load from plasma.

Table 1.

Major Design Parameters of REPUTE-2

Major radius	1.5 m
Plasma minor radius	0.3 m
Plasma current	2 MA at RFP operation
Magnet system	
• Toroidal field coil	0.4 T at plasma axis
• OH coil	14.2 V•s
• Vertical field coil	0.4 T
Core components	
• Vacuum vessel	Bellows type, Inconel 625
• Armor	Graphite tile
• Shell	Alminum
Operation (RFP operation)	
• Pulse length	400 ms
• Reverse time	100kA/ms

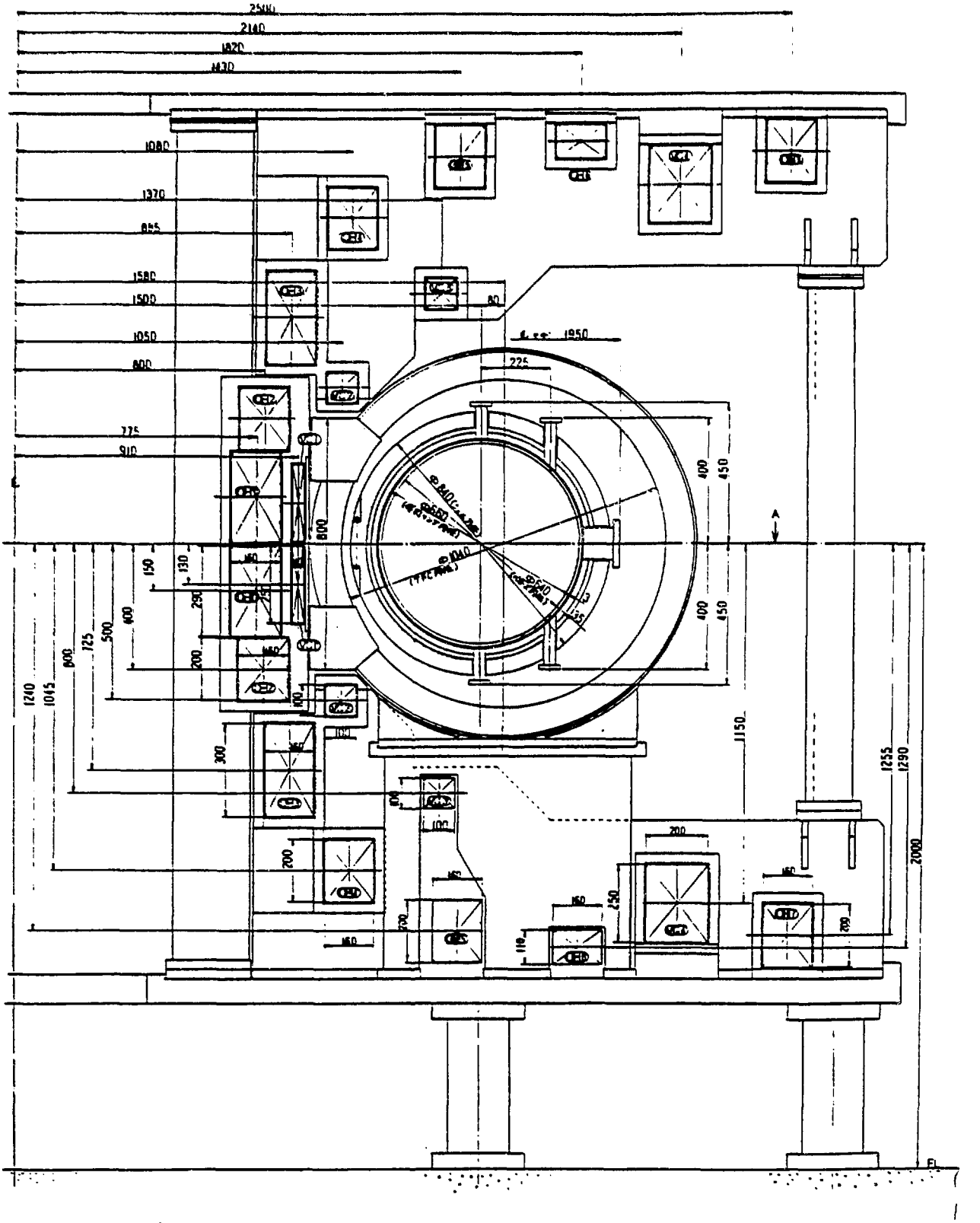

Fig. 1. Cross Sectional View of REPUTE-2

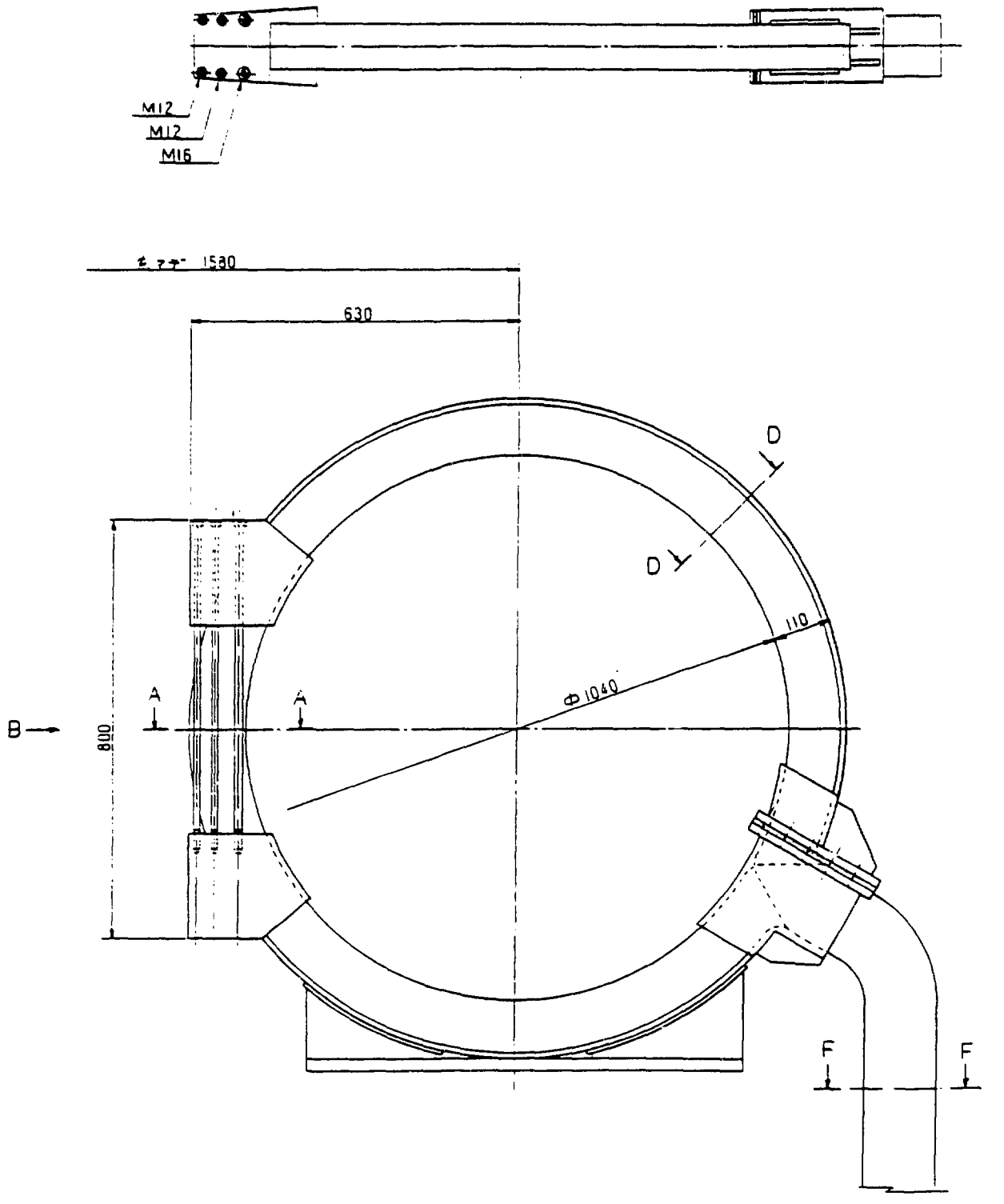

Fig. 2. Toroidal Field Coil

Construction of TPE - 1RM15

Reversed Field Pinch

in

ETL

(Video Tape Presentation)

Oct. to Dec. 1985

Electrotechnical Lab.

Mitsubishi Electric Corp.

1. Introduction

This video tape has been taken in ETL from Oct. to Dec. 1985, and shows the transportation, the setting, the assembling of the TPE-1RM15 & its power supply system, the electric & structual test until the first plasma.

2. Summary

1) Floor Construction
   - 1st Floor for Power Supply System
   - 2nd Floor, Insulated Steel Reinforced Concrete Floor to avoid the eddy current.

2) The setting of Power Supply
   - Capacitor Bank
   - Switching Bank
   - High Power Closing Switch

3) Machine Centering
   - Machine Base
   - Centering Measument

4) Baking & Leak Test of Vacuum Vessel
   - V/V Size Gage
   - Vacuum and Leakage Test
   - Baking

5) The Construction of TPE-1RM15
   - Lower Part Setting
   - TF/Coil Setting
   - Insulation of Vacuum Vessel
   - Assembly of Shell and Vacuume Vessel
   - Assembly of TF/Coil Setting
   - Final Construction

6) The first Plasma

CPRF/ZTH TOROIDAL CONDUCTING SHELL DESIGN AND FABRICATION CONSIDERATIONS

E.O. Ballard, R.L. Smith, D.M. Weldon, Los Alamos National Laboratory.

Introduction

Design is in progress of a new generation RFP machine to be assembled at Los Alamos National Laboratory during FY 86-92. The confinement Physics Research Facility (CPRF), houses the front-end ZTH experiment. Figure 1 shows the ZTH in its present configuration without the diagnostic platform surrounding the outer periphery.

Discussion

The ZTH torus, shown by Figure 2, consists of an internal Inconel 625 vacuum liner which contains the high temperature plasma. The liner is protected by a graphite armor system consisting of 4224 tiles attached to ribs in the liner with Inconel 625 spring clips. The liner is supported by the shell through spacer blocks attached to the outside of the liner ribs. The present design consists of four spacer blocks attached to each of the 80 liner ribs at 90^{0} increments. The spacer blocks encompass 120^{0} around each liner rib, 30^{0} per segment. The magnetic and vacuum loads from the liner are transmitted to the shell through these spacer blocks. The loading is non-uniform around the minor diameter and varies from approximately 175 to 195 psi for a worst case plasma termination during which current flow is transferred from the plasma to the liner.

The shell consists of a stainless steel external structural support cage with a stainless steel double-walled water cooling jacket attached to the structure with bolt-on clips. Figure 3 shows a 22.5^{0} segment of the shell cage and cooling jacket.

On the inside of the cooling jacket is a 0.125-in. thick copper liner to provide the required resistivity for the shell electrical time constant. The copper liner will either be explosively bonded or plated to the inner stainless steel plate of the cooling jacket. The cooling jacket will then be die-formed to the proper toroidal configuration.

The present requirements for the overall tolerances for the shell are + 0.170-in. on the 188.0-in. major diameter and + 0.040-in. on the 36.0-in. minor diameter of the copper surface. These tolerances make it very difficult to fabricate the shell without considering elaborate fabrication techniques. Two fabrication processes are emerging as the design progresses. The first process, which may be the most costly, is as follows: a) The shell structural cage will be assembled on a welding fixture, stress-relieved, and final machined. The machining of the toroidal shape inside can be done on individual segments with a CNC 4-axis machine or with 16 segments bolted together to form half of the torus. Each half would then be turned on a large vertical boring machine to achieve the true toroidal configuration within tolerance. The stiff structural cage would then act as the rigid member for accurately supporting the more flexible cooling jacket, b) The cooling jacket would

consist of a 0.375-in. thick stainless steel inner plate and a 125-in. thick stainless steel outer plate, die-formed to the correct torodial shape. The plates would then be welded in a fixture with spacer blocks between them to provide the water cooling passages. After stress-relieving and machining, the jacket segments would be bolted into the structural cage which is positioned in a machining fixture. Final machining would be performed on the inside surface to meet the required tolerances. The jacket segments would then be copper plated on the inside surface to 0.125-in. thick plus some cleanup allowance, reassembled into the structural cage and re-machined to remove the uneveness in the copper-plated surface. This overall fabrication method would probably achieve the required tolerances, assuming the thick copper-plating were successful, however, this would be a very expensive process and still leaves some uncertainty in achieving the desired results. The second process is as follows: a) proceed as described above for the structural cage, b) the cooling jacket would consist of a 0.375-in. thick stainless steel inner plate with 0.125-in. thick copper explosively bonded to this plate. Cooling channels, 0.25- in. deep would be machined into the plate in the flat condition. A top cover plate, 0.125-in. thick would be welded to the bottom plate to form the cooling channels. This assembly would then be die-formed to the final configuration. If the tolerances could not be achieved at this point, a second, explosive coining or final sizing operation may be required. The cooling jacket would then be bolted into the structural cage to form the final shell structure. This overall process has merit in that it may be cheaper to produce the final parts without final machining, however, there exists a large uncertainty in achieving the required tolerances in the as-fabricated condition.

Summary

Because of the difficult fabrication aspects of the shell design associated with the rigorous tolerances, a prototype shell segment is planned to help evaluate certain fabrication considerations. These results will hopefully establish the appropriate process for the remaining segments to achieve the desired fabricated hardware in a cost effective manner.

FIGURE 1

MEE-12

MECHANICAL ENGINEERING

ITH FRONT END

- PLASMA CURRENT - 4MA
- PLASMA VOLTAGE - 8\
- PLASMA RESISTIVITY - 8mΩ
- PLASMA TEMPERATURE - 4Kel
- FLATTOP PULSE LENGTH - .4sec

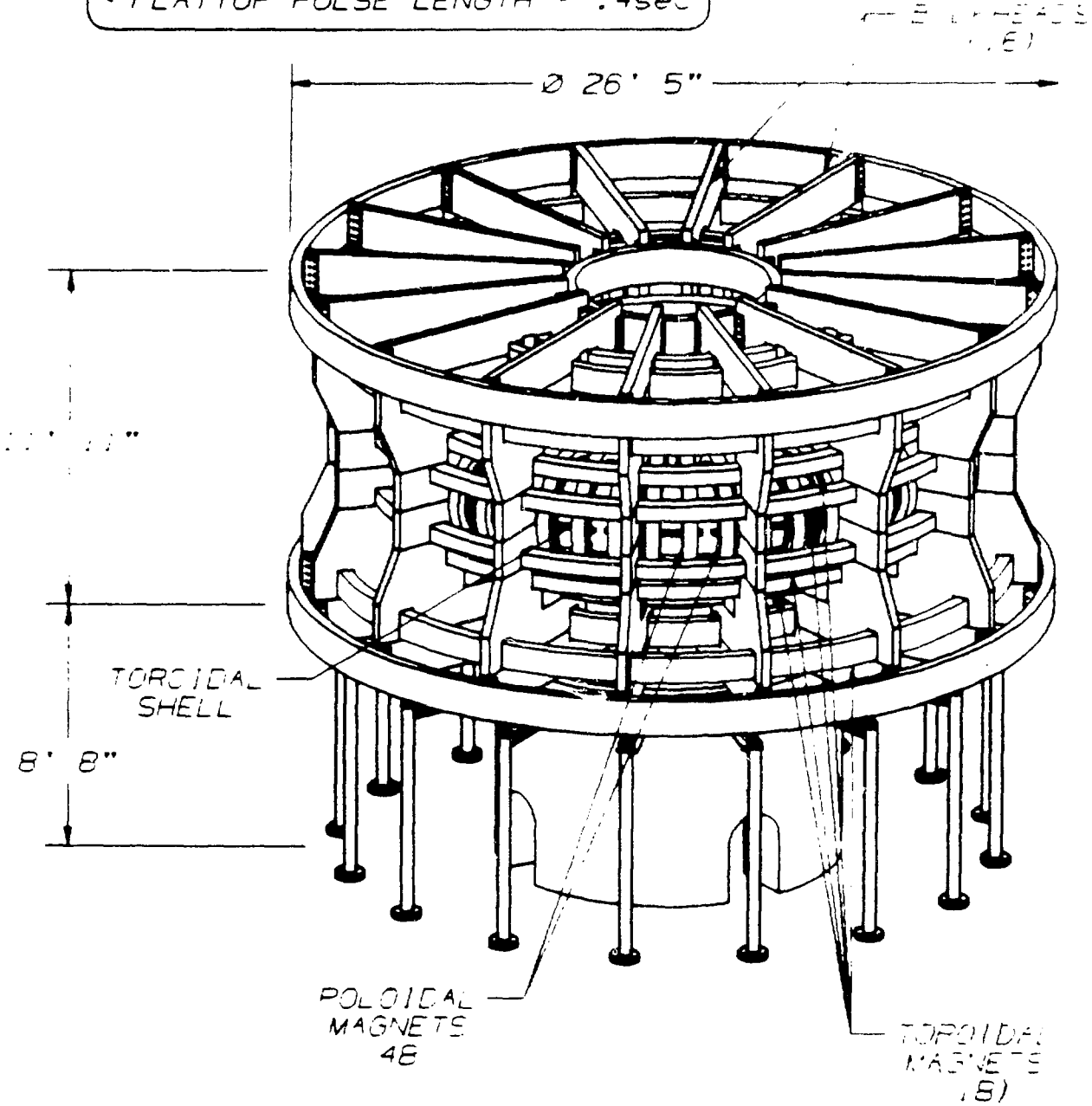

FIGURE 2

MEE-12
MECHANICAL ENGINEERING
ZTH SHELL

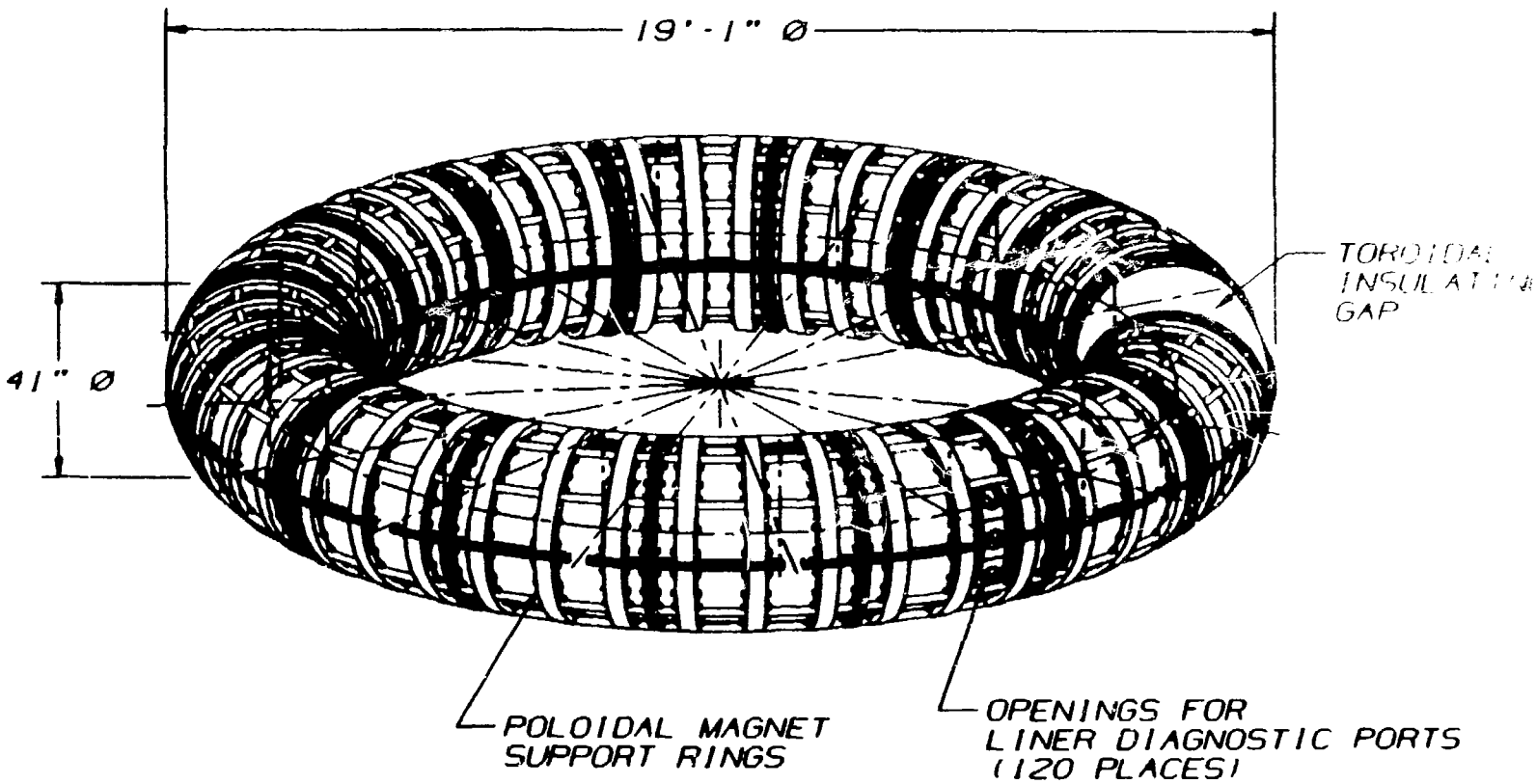

FIGURE 3

MEE-12

MECHANICAL ENGINEERING

ZTH SHELL SEGMENT

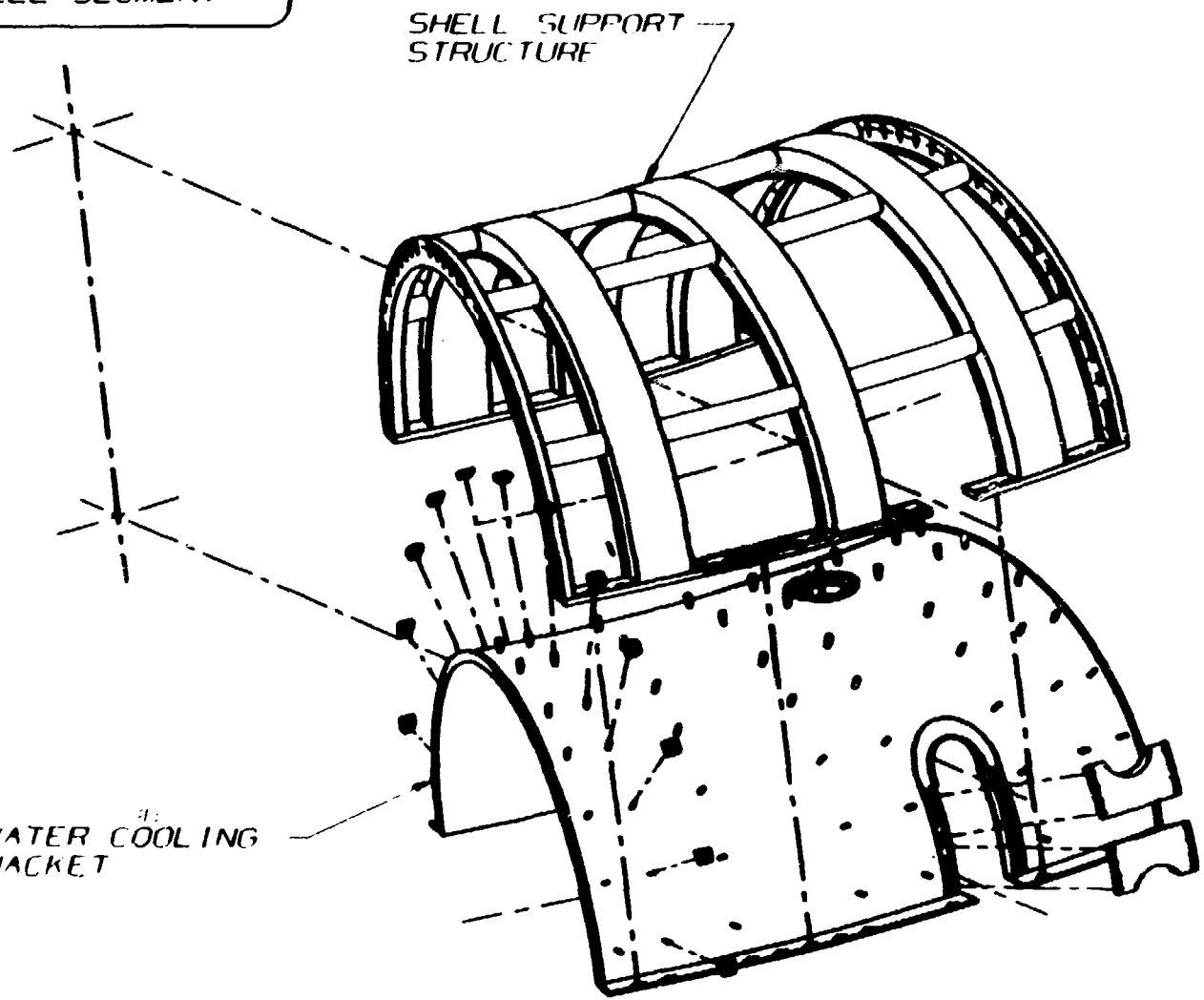

8/5/16

DESIGN OF THE ZTH VACUUM LINER*

PETER P. PRINCE

INTERNATIONAL WORKSHOP ON
ENGINEERING DESIGN OF NEXT STEP RFP DEVICES
JULY 13-17, 1987
LOS ALAMOS NATIONAL LABORATORY
LOS ALAMOS, NM USA

The current status of the ZTH vacuum liner design is covered by this report. ZTH will be the first experiment to be installed in the CPRF (Confinement Physics Research Facility) at the Los Alamos National Laboratory and is scheduled to be operational at 2 MA in 1990 and at the rated current of 4 MA in 1992. The vacuum vessel has a 2.4m major radius and a 40 cm minor radius. Operating parameters which drive the vacuum vessel mechanical design include a 300 C bakeout temperature, an armour support system capable of withstanding 25 kV, a high toroidal resistance, 130 psi magnetic loading, a 10 minute cycle time, and high positional accuracy with respect to the conducting shell. The vacuum vessel design features which satisfy the operating parameters are defined. The liner is constructed of inconel 625 and has a geometry which alternates sections of thin walled bellows with rigid ribs. These composite sections span between pairs of the 16 diagnostic stations to complete the torus. The thin bellows sections maximize the liner toroidal resistance and the ribs provide support and positional accuracy for the armour in relation to the conducting shell. Heat transfer from the vessel is controlled by a blanket wrap of ceramic fiber insulation and the heat flux is dissipated to a water cooling jacket in the conducting shell.

---

* Work done under contract with The Office of Magnetic Fusion Energy for the US Department of Energy.

Design Requirements

From an engineering design viewpoint the design requirements for ZTH can be separated into two groups. Table 1. The most important group, the primary requirements, determines the nature of the liner geometry. If one of these parameters were to change it is possible that the geometry which satisfied the new parameter would be quite different than that of the original design. For instance, if the required toroidal resistance were to decrease by a factor of two, the liner solution would not be restricted to thin walled bellows configurations but could include double walled or thick walled options. This impact on design is not as strong with the secondary requirements. With the exception of the liner aspect ratio, the ratio of the minor to major radius, the secondary requirements are satisfied by the characteristics of the innerspace between liner and shell. A change in one of these parameters, say an increase in bakeout temperature, would not result in a new liner geometry but could be satisfied by altering the thermal properties, decreasing the thermal concuctivity, of the innerspace.

Table 1

DESIGN REQUIREMENTS FOR THE ZTH VACUUM LINER

PRIMARY REQUIREMENTS	SECONDARY REQUIREMENTS
LARGE TOROIDAL ELECTRICAL RESISTANCE	300 °C BAKEOUT
25 KV ISOLATION IN ARMOR SUPPORT	10 MIN REP RATE @ 4 MA
900 KPa MAGNETIC LOADING	PLASMA OFFSET FROM SHELL
HIGH POSITIONAL ACCURACY	2.4 M MAJOR RADIUS
16 AXIS SYMMETRY	40 cm MINOR DIAMETER

The solutions which satisfy the design requirements becomes more apparent when each parameter is justified by its impact on the overall mechanical design:

A high liner toroidal resistance is desirable as it limits the amount of current which will flow in the liner and disturb plasma equilibrium. This affects the mechanical design because a smaller liner current results in reduced magnetic loading on the liner. Without the benefit of this relationship the light structure required for the high resistance would not be sufficient to resist the imposed loading. Analysis of the physics of ZTH predicts a mag-

netic loading of 900 kPa and this in addition to the vacuum loading of 1 ATM is assumed to be the design loading.

It is also desirable to limit the current carried in the armour. If large currents are present in the armour the armour supports must resist large magnitudes of magnetic loading. In an effort to reduce this loading to acceptable levels, steps must be taken to limit the current which flows in the armour. In ZTH the armour current is driven by voltage developed across the toroidal resistance of the liner. To prevent toroidal armour currents the armour must be at least as resistive as the liner and this is done by designing the armour to include a series of 96 poloidal gaps. If toroidal currents can be eliminated the liner support must only resist the forces generated by eddy currents flowing in each armour section.

The positional accuracy of the liner with respect to the conductive shell is important because of field error considerations. With some experiment designs this requirement does not merit special attention as the solution is inherant in the designs. However, in ZTH, since the liner geometry is a bellows configuration and since the bellows are nonuniform in shape, special features must be provided to align the liner within the shell. This is done by alternating solid ribs with the bellows sections. The ribs are accurately machined and provide reference surfaces for both the armour and the shell. This ensures repeatable location of the vacuum vessel and greatly reduces the positional requirements for the bellows convolutions.

The symmetry of the liner design is truly a case of design by compromise. Although there are many configurations which would satisfy the requirements of the liner alone, only a few can do so and still supply the required diagnostic access, and interface with the machine support structure. In brief, the liner was designed to supply 16 stations for diagnostic access and other characteristics were selected in a manner which minimizes conflict with the required access.

The secondary requirements are satisfied by selecting the geometry and thermal characteristics of the interspace based on thermal analysis of the front end. This does not include the aspect ratio of the liner which was selected to meet physics requirements. The secondary requirements are dependant on the geometry of the front end and can only be determined after the configuration that satisfies the primary requirements is known. A large range of thermal conductivity is available with the numerous materials

suitable for use in the interspace and this will allow the thermal response of the front end to be taylored to meet varying requirements. The major limitation is the approximately 250°C continuous use temperature limit of available electrical insulators.

The Design

The ZTH liner will be constructed entirely of Inconel 625 and will be composed of 16 equal bellows subassemblies. Figure 1. Each bellows

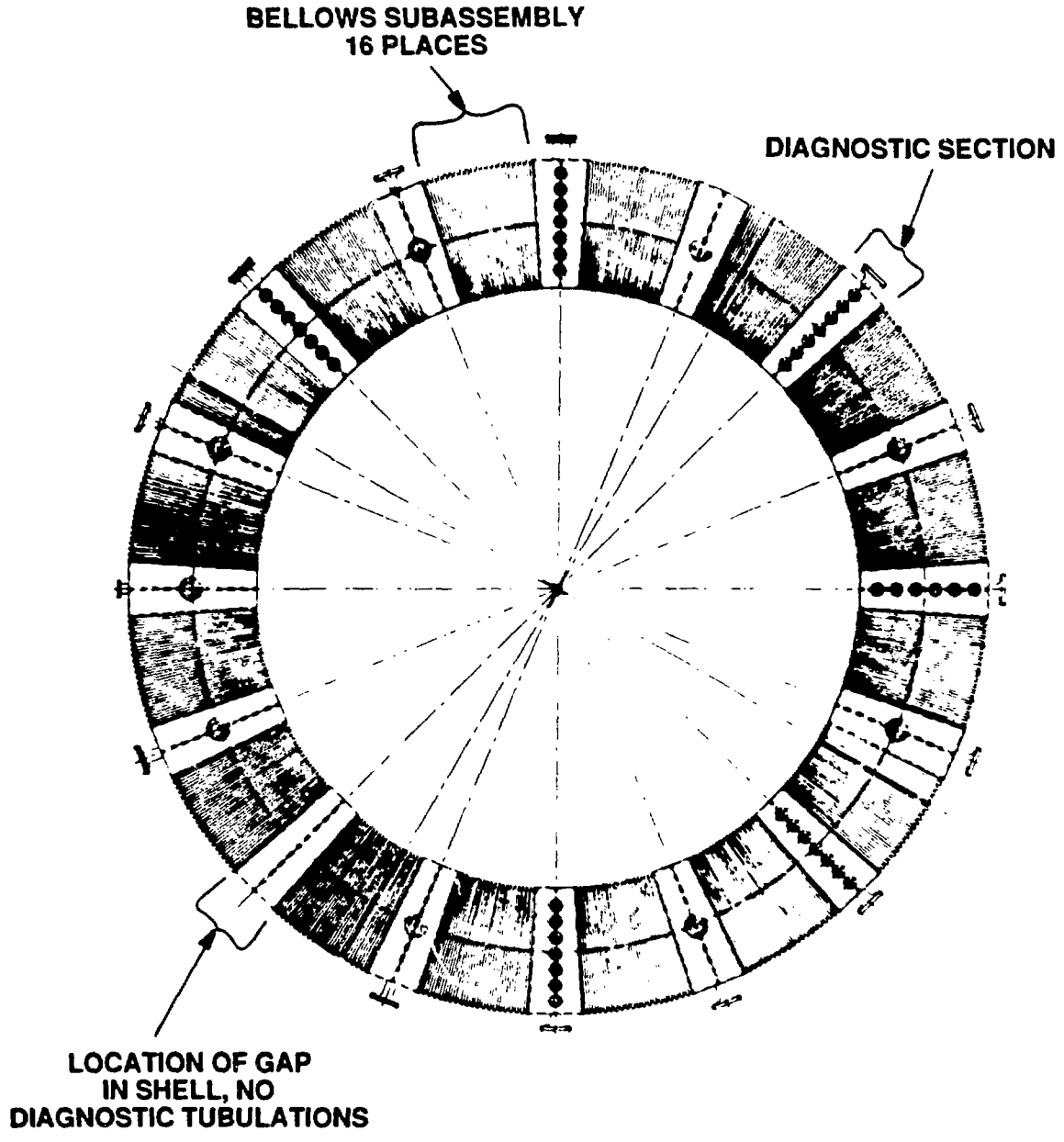

Fig. 1 ZTH Liner Concept
ribs not shown

subassembly consists of 5 equal length bellows sections connected by 6 support rings. Figure 2 & 3. The Bellows geometry was chosen as it increases the toroidal path length to 3300 cm which is 2.2 times the mean circumference. The long path length coupled with the 1.6 mm thickness of the bellows skin produces a toroidal resistance of 8 milli ohms. A second reason for selecting the bellows geometry is that its area moment of inertia is equivalent to that of a cylinder with a uniform wall thickness of 1.8 cm. This provides the rigidity necessary to resist the radial compressive magnetic and vacuum loading. The fabrication of bellows is a well established technique and the manufacturers are able to provide consultation on the strength of a given design based on their empirical data. But, the diagnostic skin and its interaction with the ribs and tubulations is more complicated and its strength is currently being estimated using the finite element method.

The rings are included between the bellows sections to provide attachment points for the armour and to provide for a reference surface by which the conductive shell can be located. These rings are not assumed to contribute to the stiffness of the bellows but do contribute to the strength of the

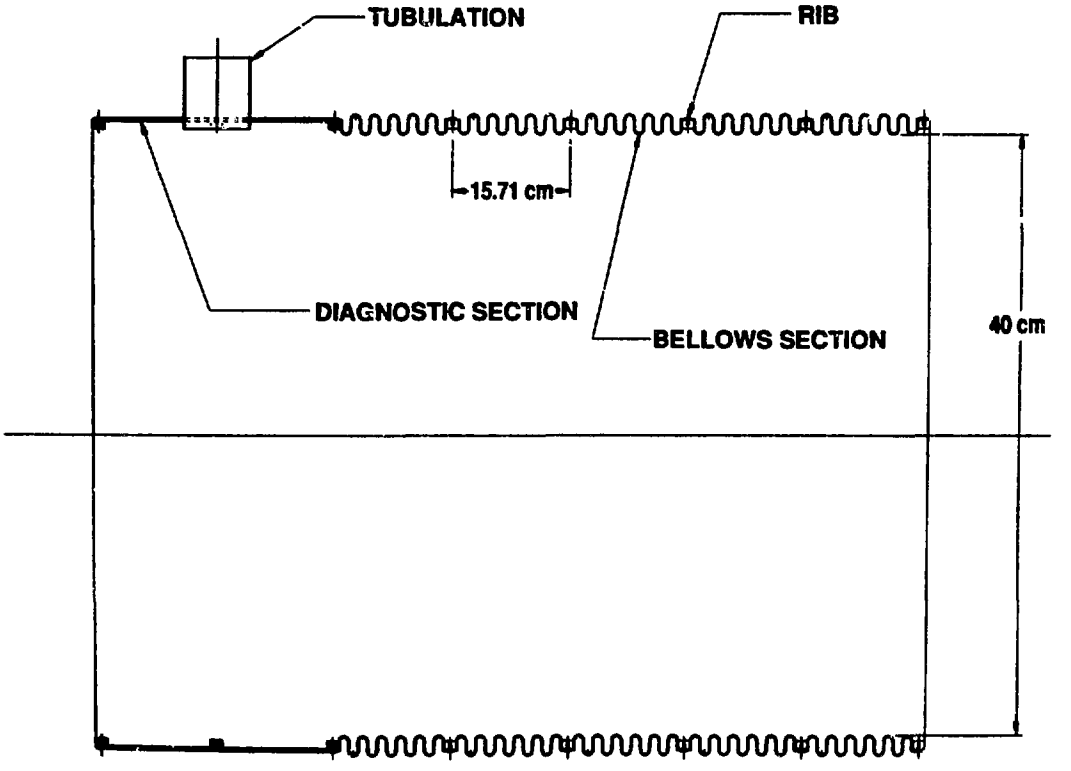

Fig. 2 ZTH liner subassembly non arced, shown attached to diagnostic section.

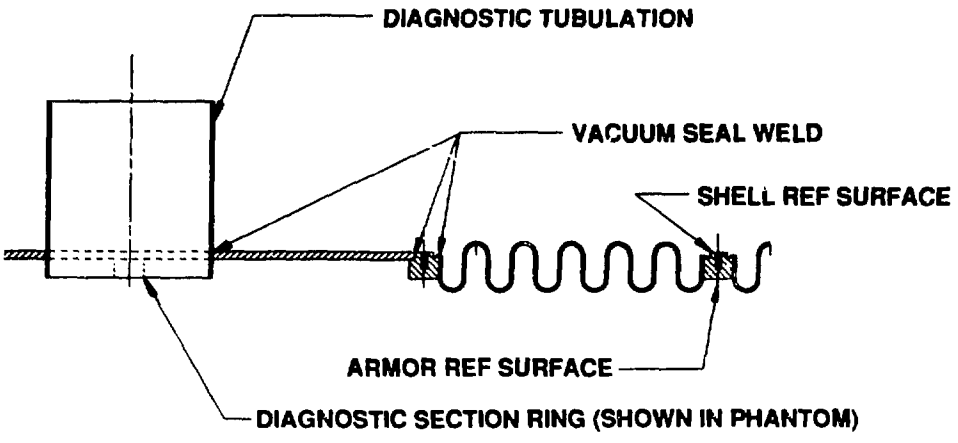

Fig. 3 ZTH Liner Detail

diagnostic section. Although the liner assembly contains 112 ribs (16 subassemblies with 6 ribs in the bellows section and 1 bisecting the diagnostic section) and each rib serves as an attachment for an armour section only 96 of the 112 resulting poloidal gaps are assumed to contribute to the stand off voltage required to prevent a toroidal current from developing in the armour. The remaining 16 gaps occur adjacent to diagnostic sections where the resistance of the thicker inconel skin is insufficient to allow a substantial buildup of potential. Each rib is designed to allow for the attachment of 44 armour sections along a poloidal diameter resulting in a total of 4928 tiles. Since the rings are equally spaced, the tiles for any given poloidal position are identical in size which will greatly facilitate the installation of such a large number of tiles. In an effort to reduce the effect of the rings on the resistivity of the liner the rings are scalloped to reduce their cross section. Figure 4.

The overall geometry of the liner and ZTH in general was set by the decision to have 16 diagnostic stations. For the liner this resulted in the bellows sections being replaced by a 1.6 mm thick, single wall, chord section, diagnostic skin. This skin was chosen as its uniform surface enables the diagnostic tubulations to be attached to the liner using conventional welding techniques. Even though the skin section reduces the total liner resistance and are less rigid then the bellows section, the weld reliability was selected as the controling factor due to the mechanical loading and thermal stresses expected in that location.

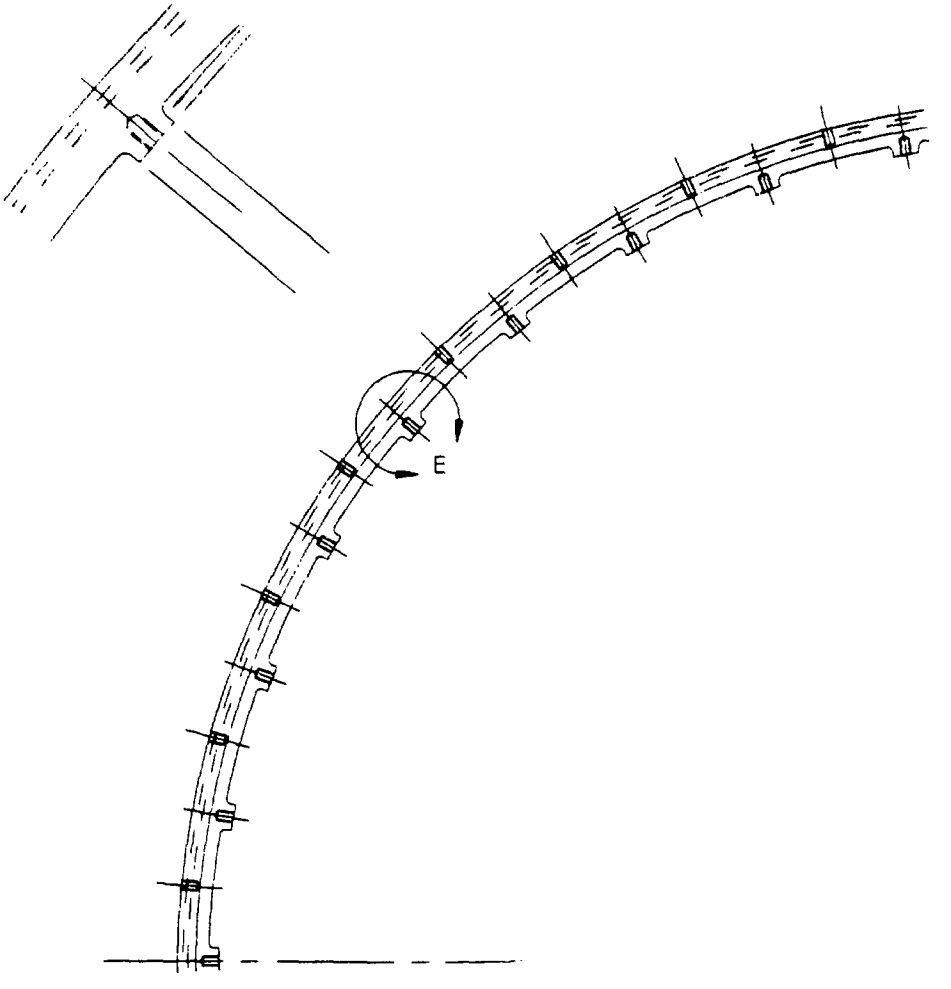

Fig. 4 ZTH Vacuum Liner Rib Detail

Although the liner has 16 axis of symmetry and has 16 diagnostic sections, only 15 of the sections will provide diagnostic access. The other section is located under gap region of the shell, where for structural and electrical insulation reasons, no penatrations are allowed through the gap and this precludes diagnostic tubulations at this station. There are 5 different diagnostic tubulation configurations which occupy the 15 available diagnostic stations. Figure 5. All tubulations were designed to minimize the required hole in the conducting shell in an effort to reduce the field errors which occur due to non uniformities in the conductor.

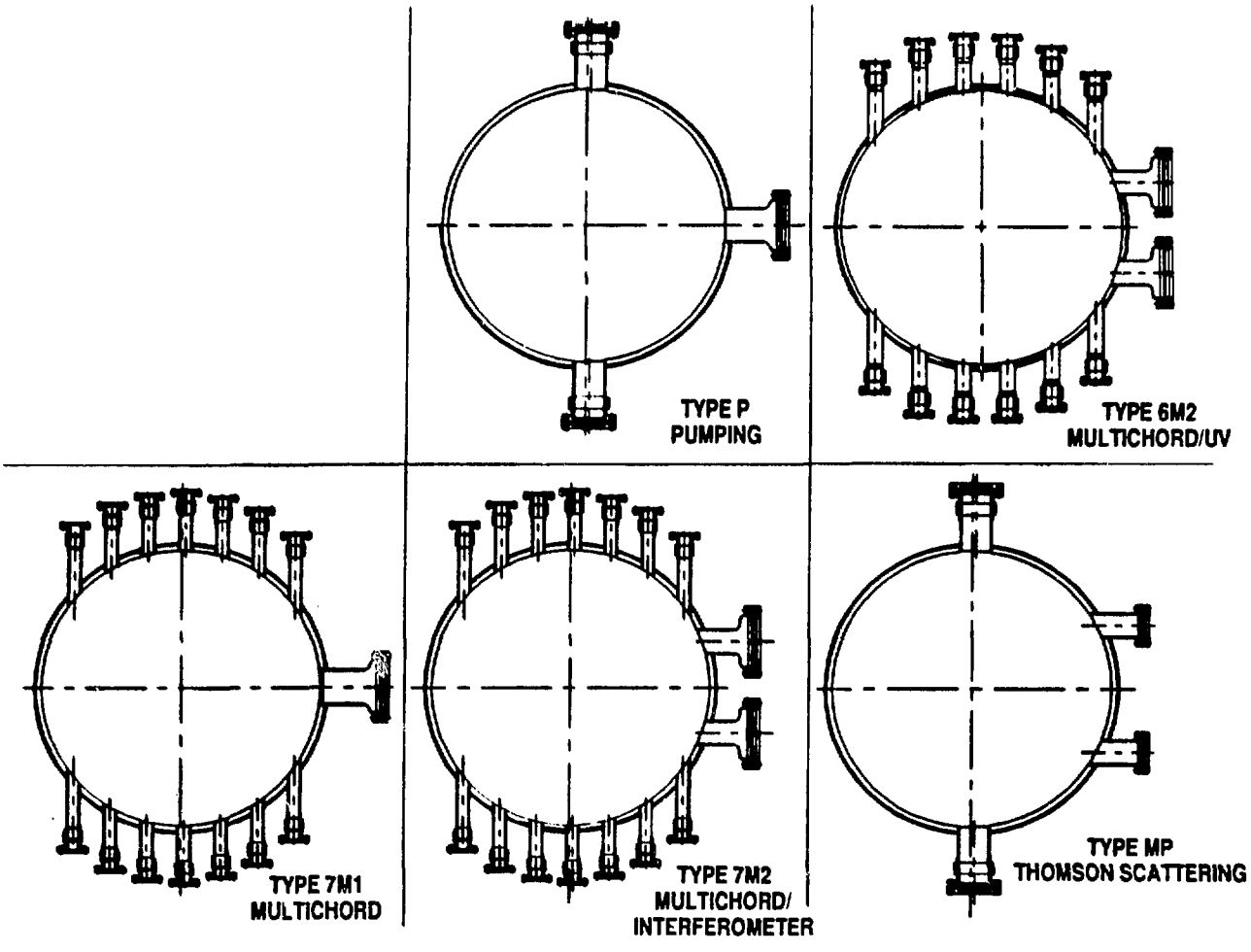

Fig. 5 ZTH Diagnostic Station Configurations

The horizontal tubulations are one piece tubes, 1.8 mm wall, which are welded to the diagnostic skin and are of sufficient length to penetrate the shell. Each tube terminates with a welded on CONFLAT(T) flange which allows interface with the diagnostics. A simple hole is provided in the shell for tubulations which are located on the horizontal centerline while a keyhole and insert plate are required for off axis tubulations. The keyhole is required to enable the shell sections to pass over the liner tubulation during assembly and the insert plate is installed to regain toroidal electrical continuity in the shell across the keyhole.

(T) Registered trademark of Varian Associates.

If the same design were used for the vertical tubulations, the shell would have to pass over the entire tubulation, including the CONFLAT flange and required shell hole would be too large. Insert plates were considered but were rejected due to structural considerations. As a result a different approach was selected which has the tubulations constructed of two pieces connected with a HELICOFLEX(T) seal, Fig. 6. During shell assembly the upper portion of the tubulation which includes the CONFLAT flange is removed. As a result the shell hole only needs to be large enough to clear the male portion of the HELICOFLEX seal. After assembly the upper portion of the tubulation is installed and the shell is now captive. Lacking experience with HELICOFLEX seals the program has opted to build prototypes of these tubulations and test them for reliability. The required parts are currently being fabricated.

The vacuum liner interface with the conducting shell occurs in the innerspace region. The innerspace is the void between the liner OD and the shell ID. In ZTH this space has a nonconstant width as the liner center is offset outboard 12 mm from the shell center. This shift equals the anticipated Shavfranov shift of the plasma and results in the innerspace width varying from a minimum of 1.6 cm at the outboard horizontal centerline to a maximum of 4 cm at the inboad midplane.

(T) Registered trademark of Joints Fargére Industrie, France.

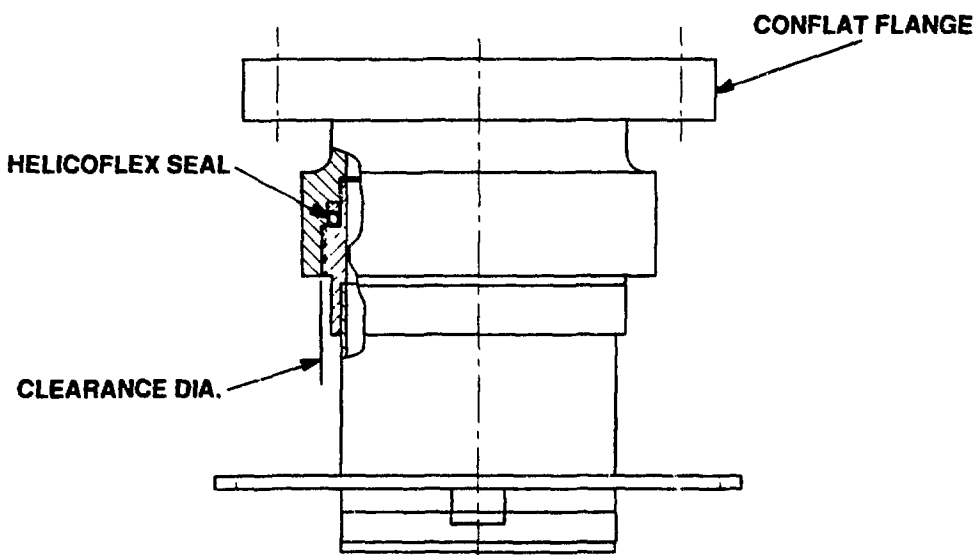

Fig. 6 Helicoflex seal arrangement for ZTH vertical tubulation

The innerspace region contains the liner structural supports and the thermal and electrical insulation. These components must be carefully selected to satisfy the secondary design requirements of Table 1 while still allowing for; 25 kV of isolation between shell and liner, a uniform heat flux from the liner to the shell to prevent temperature gradients from thermally stressing the liner, and protection of the electrical insulation from temperatures exceeding 250°C.

To position the liner within the shell crescent shaped standoffs will be attached to the liner. The standoffs will be made from a liquid crystal polymer such as XYDAR(T) by injection molding and will be machined to final shape. Fig. 7. Due to the expected thermal expansion of the minor diameter of the vacuum liner the standoffs cannot fill the innerspace completely, but must be undersized by approximately 3 mm to allow for the expansion. This does not mean that there is 3 mm of uncertainty in the position of the liner as the vacuum loading will always load the inboard standoffs and the expansion will move the liner center outboard. As a result the location of the liner is always known but is dependant on temperature.

The electrical insulation will consist of silicone rubber sheets glued to the shell ID to ensure good thermal contact with the cooling capacity of the water jacket and KAPTON(T) inserts providing increased tracking distance at joints between the rubber sheets. The thermal insulation will be a glass fiber blanket enclosed mat of ceramic fiber. The thermal resistance of the insulation layer will not be constant due to the non uniform innerspace width and will be kept to a minimum to maximize the experiment rep rate. The primary purpose of the thermal layer is to prevent excessive temperatures at the electrical insulation and to keep the liner at a uniform temperature.

Design Uncertainties

The design detailed in this report is still preliminary in some aspects. Still pending are results of; a diagnostic skin stress analysis, a transient heat transfer analysis of the front end cross section, and a vacuum test

---

(T) XYDAR is a registered trademark of Dart Industries, Inc.

(T) KAPTON is a registered trademark of E. I. Dupont, Inc.

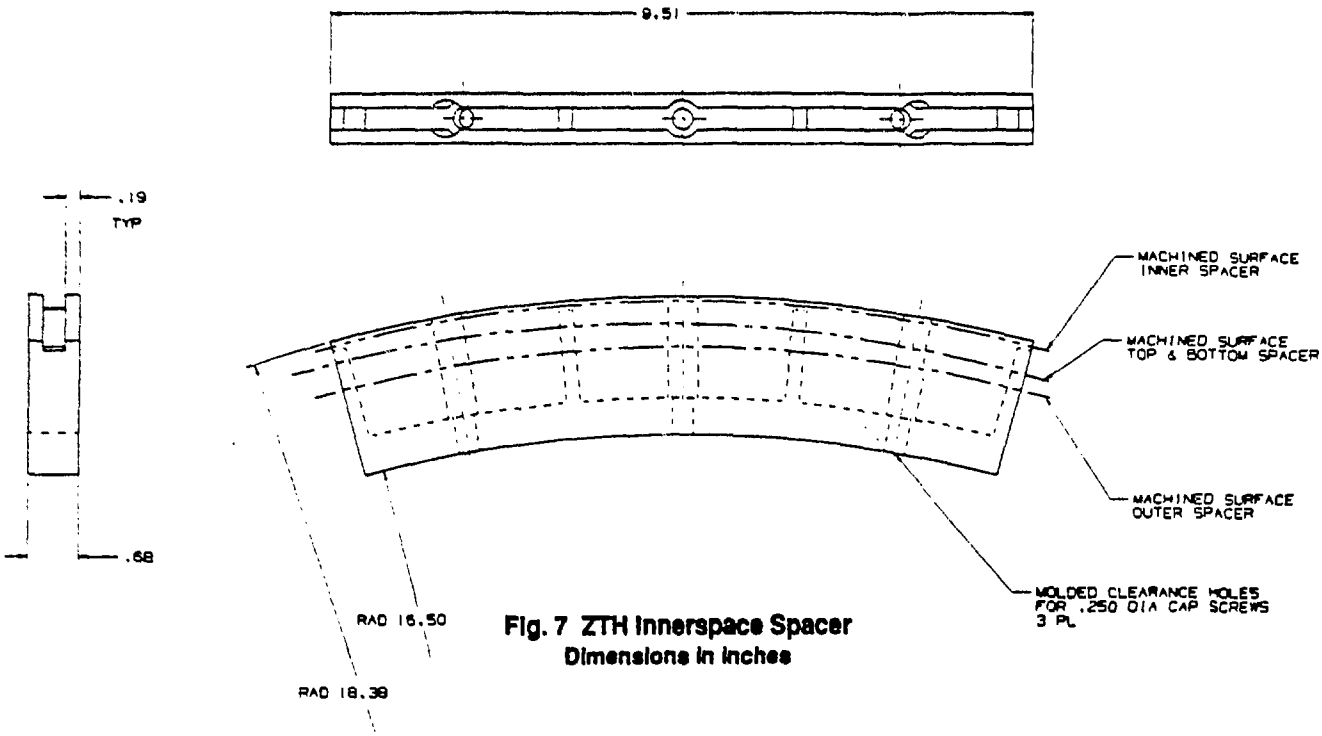

Fig. 7 ZTH Innerspace Spacer
Dimensions in Inches

program for the helicoflex seal. Some areas of the design could change as a result of these studies.

DESIGN CRITERIA FOR A GRAPHITE FIRST WALL

F. Gnesotto
Istituto Gas Ionizzati - Progetto RFX
Associazione EURATOM-ENEA-CNR

ABSTRACT

The reasons that led to the choice of covering the RFX vacuum vessel with a full graphite armor are firstly outlined and a comparison is made with other possible first wall configurations. The main design features of the graphite tiles and the material properties are described, with particular reference to the calculation of mechanical stresses due to clamping forces and electrodynamic actions, and to the thermal transient analysis.

Finally, the effect of a 40 m^2 plasma-facing graphite surface on particle recycling and impurity production is discussed and PWI control criteria are proposed.

1.INTRODUCTION

In the original RFX design, approved in 1983, the toroidal, all-metal liner was together a vacuum vessel and a first wall for the plasma. During the RFX preliminary design, in fact, the operating experiments were performing quite satisfactorily with a bare metallic wall, probably owing to the very short pulse length and to the low plasma currents and associated energies.

Afterwards, the pulse length, as far as the plasma current, were increased to levels at which liner damage and impurity contamination were found on all the medium-sized RFP experiments /1/ /2/ /3/. For this reason, various liner protection schemes were installed and tested: poloidal rings, toroidal rails and discrete tiles in ZT-40M /4/, again discrete tiles on HBTX-1B /5/ and a full armor in OHTE /6/. In all these experiments, polycristalline, high purity graphite was adopted for the plasma-facing components.

On the basis of the experimental results from the abovementioned RFP devices and by taking into account the large amount of data coming from the behaviour of graphite components in Tokamaks, a decision was taken of covering the RFX vacuum vessel with graphite tiles. The following paragraph discusses the choice of a full armor, whereas the other ones describe the main aspects of the design.

2. DEVELOPMENT OF THE FIRST WALL DESIGN

A scheme of the engineering development is shown in fig. 1.

First, a thermal analysis of the bare metallic wall was performed for a full-power, well controlled plasma pulse. The first and second columns in Table I give, for the different pulse phases, their duration and the energy dumped onto the toroidal wall.

TABLE I

	Duration (ms)	Dumped Energy (MJ)	Max Power Density (MW)
Current rise	30	6.0	27
Current flat-top	250	9.0	5.0
Soft landing	30	5.0	22

We conservatively neglected radiation and neutral transport and assumed an outward plasma column shift δ of 30 mm, constant during the pulse. This is consistent with the actual design of the vessel-shell system, in which they are concentric and the equilibrium position can be hardly moved from the natural Shafranov's one.

Larger uncertainties characterize the evaluation of the heat flux distribution on the wall. We assumed it to be axisymmetric, by neglecting the magnetic effects from the gaps and the discrete toroidal field coils. As far as the poloidal distribution is concerned, the results from ZT-40 M /4/ and HBTX-1B can be extrapolated to RFX on the basis of the relationship

$$\lambda_n = (DL/V_s)^{1/2} \equiv T^{1/4} L^{1/2} B^{-1/2}$$

in which D is the Bohm's diffusion coefficient, L is the connection length and V_s is the ion sound speed; the lower limit for the scrape-off characteristic length for density, λ_n, results to be, for RFX, roughly equal to that found in ZT-40 and HBTX-1B. By assuming the same scaling for the temperature dacay length, we find for RFX $\lambda_q \geq 0.5$ cm.

The calculated peak power density is shown in the third column of Table I for the three pulse phases, where any asymmetry between ion and electron-drift directions is neglected.

A simple, one-dimensional calculation, shows that the temperature increase during the pulse is about 1000 °C in the most stressed zone. By accounting for some

intensification due to field errors or wall discontinuities (e. g: pumping ports, diagnostic accesses), a substantial melting of Inconel could probably take place.

But the situation is even worse in the case of a fast, uncontrolled plasma current termination. By assuming an energy deposition time of 0.1 ms, melting is produced even with a uniform heat distribution (1400 MW/m^2); if energy is deposited on half of the wall, the melted layer would be about 30μm thick.

The conclusion was that, besides the need of minimizing the high-Z impurity influx into the plasma (that could also be obtained by wall carbonization), the metallic, vacuum tight wall should be protected from the plasma.

Two alternative solutions have been considered

A) four toroidal limiters, each of them made by 72 graphite tiles, plus wall carbonization;

B) a full graphite armor, made by 2016 trapezoidal tiles.

For solution A), the limiters should significantly protrude into the plasma to maintain their effectiveness for λ_q larger than the minimum expected. In a configuration being fully compatible with diagnostic access to the chamber, the limiters cover about 22% of the torus surface and the peak power density is about five times higher than on a smooth toroidal surface, with the same λ_q and δ . The graphite temperature increase may locally exceed 3000°C, so that a significant erosion of the limiter blades may be expected by evaporation. Moreover, fast terminations may additionally stress the limiters if plasma energy is supposed to be mainly transported by charged particles to the limiters; on the contrary, if the energy is quite uniformly dumped on the torus wall, the carbonized metal could locally melt as discussed before.

On the basis of these simple calculations and by taking into account the fact that the effectiveness of toroidal rings in acting as limiters for an RFP plasma is still in doubt, the vessel has been designed to allow limiter installation and metal wall carbonization, but the reference solution is a full graphite armor, whose main features are discussed in the following paragraphs.

3. MATERIAL PROPERTIES AND OUTGASSING

The RFX full armor will be made by Le Carbone Lorraine 5890/PT graphite. This grade has been extensively tested during the last years on many European Tokamaks, so that its behaviour under vacuum and under particle and heat load is presently well known. Its main properties are listed in Table II. Graphitization will be followed by a

purification process, since the ash content on finished parts is specified to be lower than 100 ppm (averaged over the tiles). After machining, the tiles will be ultrasonically cleaned and finally outgassed under vacuum at 2000°C for 5 hours.

TABLE II

GRAPHITE PROPERTIES

Density	$\geq$ 1.79 g/cm^3
Open porosity	$\leq$ 15%
Shore hardness	= 55
Ultimate tensile strength	$\geq$ 30 MPa
Ultimate compressive strength	$\geq$ 115 MPa
Young modulus	$\leq$ 13 GPa
Thermal expansion coefficient:	
20 to 400°C	$\leq 5 \cdot 10^{-6}$ K^{-1}
20 to 1000°C	$\leq 6 \cdot 10^{-6}$ K^{-1}
Thermal conductivity:	
20°C	$\geq$ 70 W/mK
400°C	$\geq$ 50 W/mK

4. TILE AND CLAMP DESIGN

The full graphite armor /7/ is subdivided into 72 tiles in the toroidal direction and into 28 tiles in the poloidal direction. The tiles are individually supported from the vessel poloidal rings (see fig. 2): this avoids current circulation through the supports during the electromagnetic transients.

By subdividing the wall into 72 segments along the toroidal direction, the tile-to-tile voltage is kept below 10 V during rise time and below 30 V in the case of uncontrolled plasma current terminations: these voltage levels seem to be reasonably low to prevent bypolar arcing between adjacent tiles. Moreover, the deviation from toroidality of the 72 cylindrical vessel elements is kept within $\pm$ 1 mm: the same deviation characterizes the plasma facing graphite wall, since the tiles are straigth in toroidal direction. The tiles are 130 to 210 mm long.

The poloidal subdivision into 28 segments (that gives a poloidal length of 95 mm, equal for all tiles) originates from the need of passing the tiles through the pumping ports of the vacuum vessel, since there isn't any man-hole through coils,

shell and vacuum tight wall.

The tile handling will be performed by a robot manipulator, operating in dry air and being mainly designed for maintenance purposes. Modifications of a small fraction of the wall are also foreseen by remote handling, whereas a major modification (e.g.: change of wall material) shall require vessel opening on a meridian plane. Due to the small diameter of the arm (less than 150 mm), its working space is limited to 360° poloidally and 30° toroidally, so that all the 12 pumping ports should be made available for reaching the whole first wall.

Three solutions have been considered for the tile clamping system:

A. the tile is bolted onto a stainless steel plate; the four bolts are screwed onto two cylindrical pins that clamp the graphite tile onto the plate. This is very similar to the conventional Tokamak solution;

B. the tile is brased onto a molybdenum plate;

C. the tile has no backing plate and it is directly clamped on the vessel ring (see fig. 3).

Table III schematically shows a comparison among the three solutions.

TABLE III

	A	B	C	
Plasma-vessel distance	25	18	18	mm
Graphite weight	1100	650	810	Kg
Extraction force during fast terminations	300	600	60	N
Number of components of a tile-plate assembly	12	2	1	
Mechanical stress on the graphite for clamping the tile	medium	very low	high	
Cost	medium	high	low	

The force that tends to pull out the tiles, due to the interaction between the toroidal field and the poloidal currents flowing through the vessel ring, the plate and the tile, strongly depends on the electrical conductivity of the plate; solution C is by far the best from this point of view. Since solution C is the simplest and the cheapest one, but the clamping stress is relatively high due to the small clamping area, thorough stress analysis has been performed, by taking into account the electromagnetic forces due to fast terminations, the possible machining and mounting

errors and the brittle behaviour of the graphite.

As far as electrodynamic actions are concerned, the peak extraction force is 60 N, whereas the torques along the three axes of the tile are always less than 1 N·m.The extraction force gives rise to a shear stress on the graphite, always lower than 0.2 MPa, whereas the torques give rise to negligible compressive stresses inside the foot of the tile.

The clamping key, through four Belleville washers, pushes the tile onto the vessel ring with a force of about 100 N; the associated stresses are about 0.3 MPa (compressive) and 0.13 MPa (tensile).

Higher stress levels are obtained if the radius of curvature of the tile root is not perfectly matched with the poloidal ring radius; the worst case is when there is a clearance under the clamping point even with the full clamping force (100 N).

In this case, a flexural stress state is produced, with a maximum of 1.5 MPa (tensile) and 0.65 MPa (compressive): Fig. 4a shows the tile quarter which has been analyzed by a F.E. method /8/ and its deformed shape, whereas Fig. 4b shows the distribution of the principal stresses (segments with arrows = tensile stresses) around the central hole.

As far as the clamping system is concerned, particular attention has been paid to the following aspects:

- the system should be simple and reliable, to allow remote handling;
- seizure under vacuum should be avoided.

The system is composed (see fig. 3) by a key that will be inserted into a restraint bush (welded to the vessel ring) and rotated by the robot hand to fix the tile.

The key will be alternatively built from molybdeum (or TZM) with a brazed graphite cap and a TiN coating on the contact area, or from a C-C composite; the decision will be taken at the end of an extensive test program, now under way, on the strength and seizure probability (under thermal cycling) of the proposed solutions.

5. THERMAL ANALYSIS

The thermal analysis of the first wall has been performed by means of numerical 1D and 2D methods /7/. Since the thermal conductance between tile root and vessel ring is largely unknown (the test program will also give this information), heat conduction from tile to vessel has been conservatively neglected.

The RFX armor acts as a toroidal limiter, so that the thermal loads are still given by Table I (no radiation, λ_q= 0.5 cm, δ = 3 cm, no flux asymmetry).

A 1-D thermal analysis has been carried out for a duty-cycle of one 2 MA pulse every ten minutes, by considering the hottest toroidal row of tiles and by neglecting the radiative cooling towards the other, colder rows. The vessel can be kept at a constant temperature of 90°C by its cooling system: starting from ambient temperature, the thermal régime is reached after about 10 shots. Fig. 5 shows the temperature waveform during and immediately after the pulse, for various depths inside the graphite. Immediately before the pulse, the tile temperature is about 400°C, then the tile surface reaches about 700°C during the pulse and about 850°C during the soft termination.

A 2-D thermal analysis has been then developed to investigate the tile - to -tile radiative cooling during the dead time between pulses. The results of this calculation are summarized in fig. 6 , where the skin temperature as a function of the poloidal angle is given for various instants during and after the pulse. It is worthwhile to point out that the temperature of the hottest tiles before the shot is now about 270°C, instead of 400°C. A further decrease in base-temperature is expected from the effect of the thermal conductance between tiles and vessel rings.

Finally, the thermal effect of a fast current termination, with a full energy (5MJ) release in 0.1 ms, has been evaluated. Only for very high flux peaking factors (>5) the graphite erosion by sublimation may be significant ($>1\,\mu$m): since the energy input is much less than required for crack formation, the full armor is thought to be capable of withstanding a reasonable number of uncontrolled current terminations (see also paragraph 4).

6. IMPURITY PRODUCTION. RECYCLING

For well-controlled pulses, the wall temperature is so low that evaporation is expected to be negligible: the main sources of C impurities shall be physical and chemical sputtering and unipolar arcing. As far as other light impurities are concerned (H_2O, CO .....), their production will be minimized by annealing at high temperature, proper storage, in situ baking up to 350°C, glow discharge cleaning, pulse discharge cleaning.

Control of plasma density will certainly be a critical issue in determining the confinement properties of next RFP devices. The presence of a large amount of graphite shall play a major role in controlling the global recycling coefficient of plasma ions. A relatively cold wall, saturated by H/D during previous pulses or wall loading procedures, can act as a large particle source, due to thermal or ion-induced desorption, giving rise to a high recycling coefficient . This effect has been found to

be beneficial /6/ for sustaining the plasma density in RFP discharges, otherwise characterized by "pump out" on timescales of the order of some ms.

In next-step devices, the pulse length will be much longer and the wall temperature during pulse much higher: a recycling coefficient larger than unity would prevent density control by gas puffing and pellet injection. Wall temperature regulation between pulses seems to be the best way for controlling, via thermal desorption, the H/D amount on the graphite and thus the recycling coefficient: at high temperature (>300°C) a large faction of the previously trapped H/D can be desorbed before the pulse, so that a wall pumping effect is to be expected, whereas at lower temperatures the wall may act as a particle source.

7. CONCLUSIONS

Although the thermal loads in next-step RFP devices are expected to be relatively high due to the short energy confinement time (compared with Tokamaks) and to the possibility of very fast plasma current terminations, a full graphite armor is fully adequate to withstand them for a large number of pulses. If tiles are individually supported, without large low-conductivity backing plates, the electrodynamic actions can be easily withstood by the clamps. Owing to the relatively short pulse duration, inertial cooling between pulses is sufficient even without accounting for heat conduction.

H/D recycling can be controlled by wall temperature regulation. Finally, physical sputtering and unipolar arcing are considered to be the main C sources, so that control of plasma boundary conditions is thought to be an essential feature for improving the confinement quality.

8. REFERENCES

/1/ D. A. Baker et al: Proc. 9th Int. Conf. on Plasma Physics and Controlled Nuclear Fusion Research, IAEA, vol. I, p. 641 (1983).

/2/ T. Tamano et al, ibid., p. 609.

/3/ H. A. B. Bodin et al, ibid., p. 641.

/4/ J. N. Downing, et al, Journal of Nuclear Materials 128 & 129, p. 517 (1984).

/5/ A. A. Newton et al, Journal of Nuclear Materials 145 - 147, p. 487 (1987).

/6/ G. L. Jackson et al, Journal of Nuclear Materials 145 - 147, p. 470 (1987).

/7/ F. Elio et al, Proc. of the 14th Symposium on Fusion Technology, Avignon, 1986.

/8/ F. Elio, private communication.

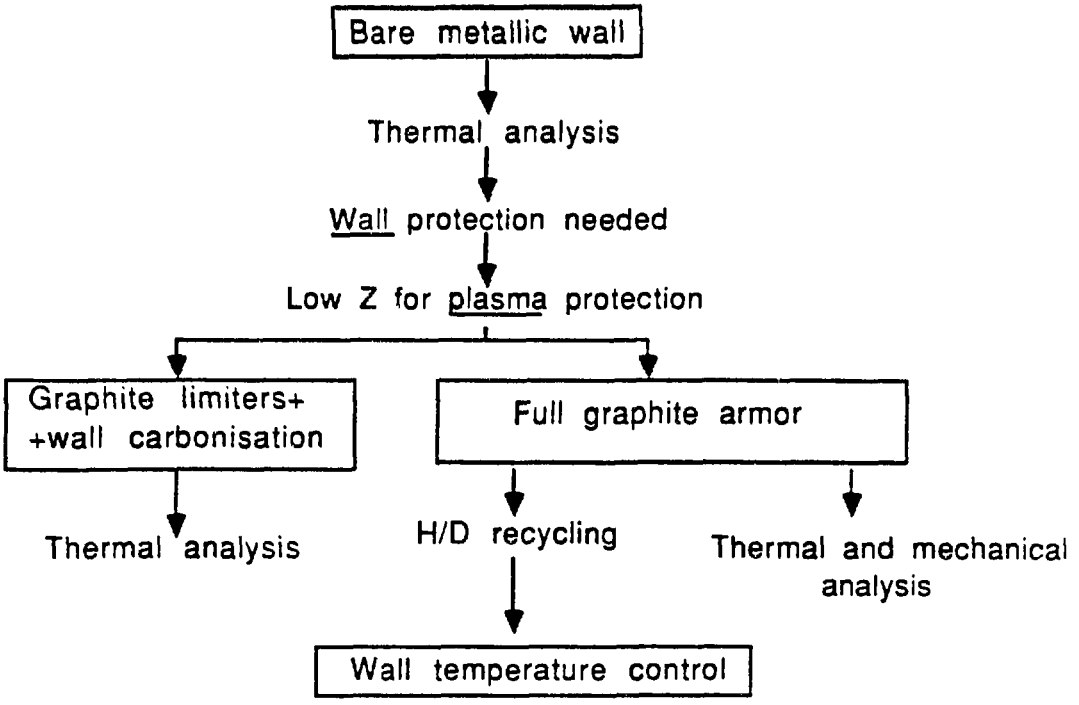

Fig. 1: Development of the RFX first wall design

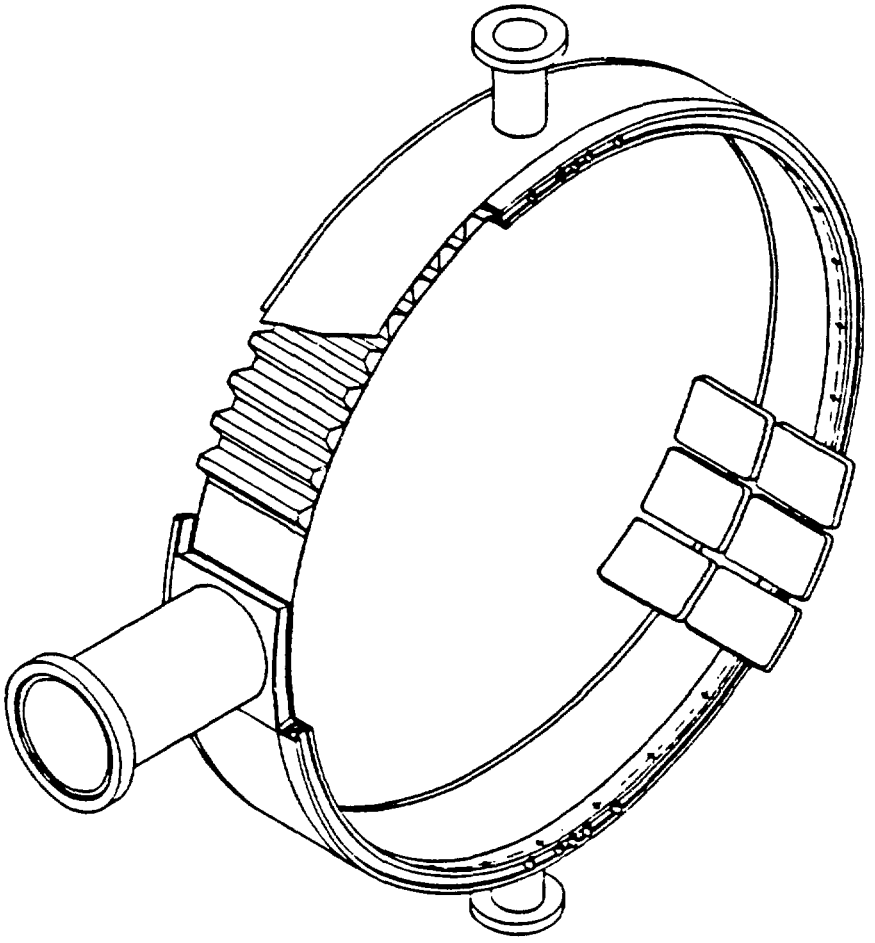

Fig.2: RFX vessel and first wall

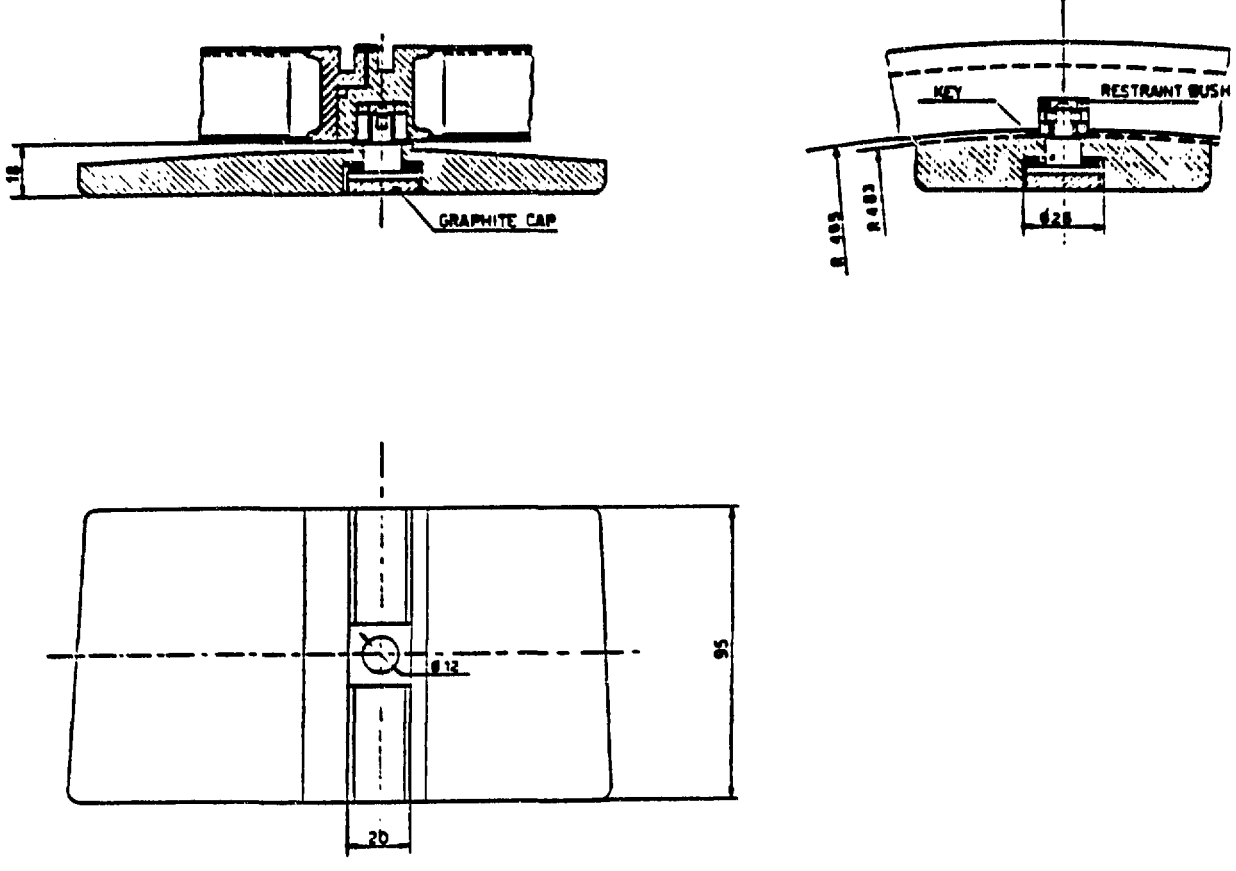

Fig.3 Tile design

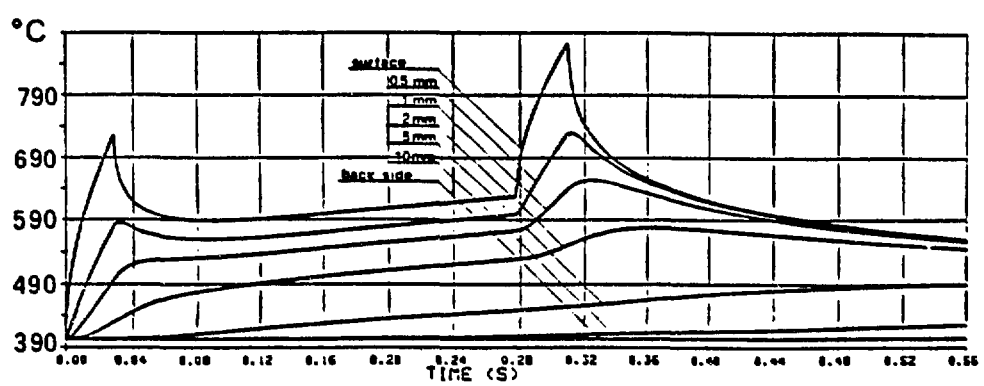

Fig.5: tile temperature during the shot: maximum heat flux

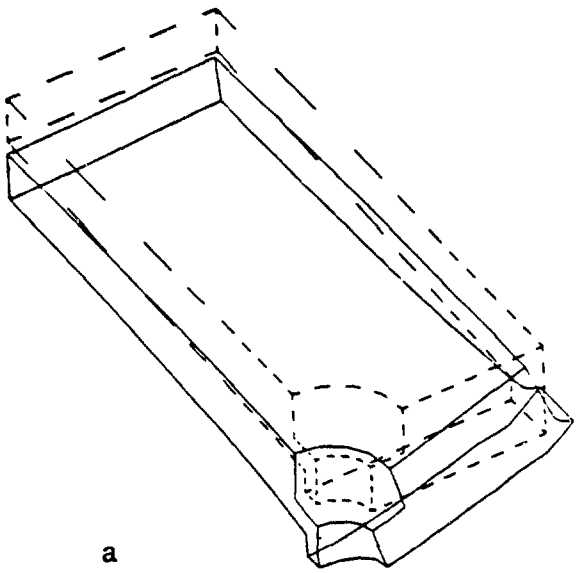

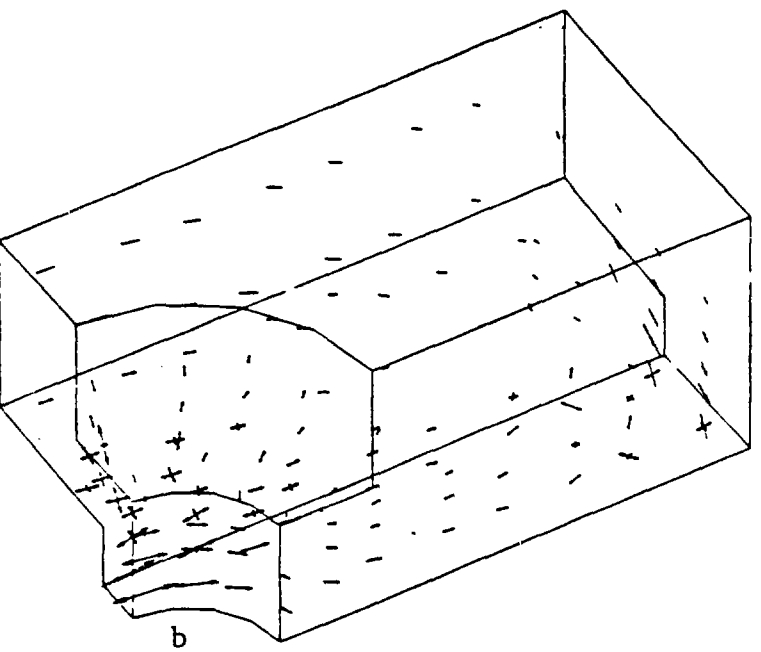

Fig. 4: Tile stress analysis
a: undeformed and deformed shape
b: stresses in the central zone

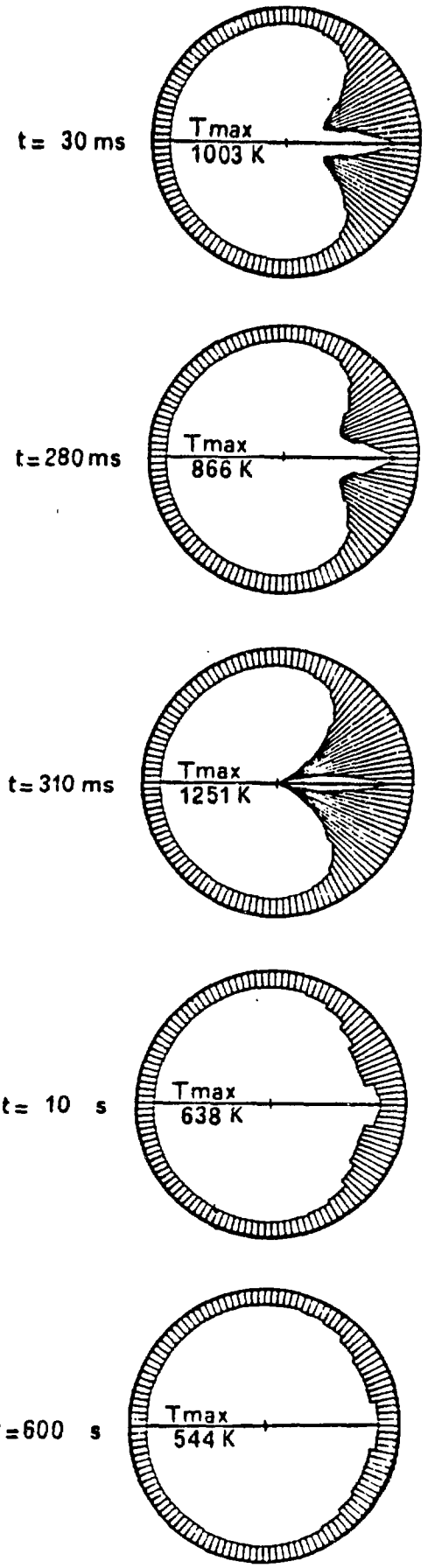

Fig.6: Inner surface temperature for various instants

RFX VACUUM VESSEL AND SHELL

F. Gnesotto
Istituto Gas Ionizzati - Progetto RFX
Associazione EURATOM-ENEA-CNR

ABSTRACT

The design of the RFX toroidal vacuum vessel and shell is described. The main characteristics of both components are reported, as well as the most significant technological aspects of their construction. The main results of mechanical and electromagnetic calculations are then discussed in terms of reliability of the load assembly and influence on plasma behaviour. Finally, the torus temperature control system is described.

1. INTRODUCTION

The main purposes of the RFX vessel-shell assembly can be summarized as follows:

a) to provide the vacuum environment for the plasma;
b) to support the first wall;
c) to support the toroidal field winding and the field shaping coils;
d) to provide an electrically conducting wall for MHD stabilization;
e) to help plasma horizontal equilibrium control with a selected vertical field diffusion time constant.

In RFX, since a relatively long vertical field time constant has been specified (300 ms), the shell should be thick (65 mm of aluminium or 30 mm of copper), so that it lends itself to be the main mechanical structure of the inner torus. For a shell with shorter time constant, that will be installed in a second experimental phase, the two functions d) and e) can be separated from function c), giving more flexibility to the choice of the electromagnetic parameters.

The vacuum vessel, besides performing roles a) and b), gives a substantial contribution to stabilization of MHD modes at high frequency ($\gtrsim$ 1 KHz).

Reliability in assuring vacuum tightness has been fixed as primary objective in designing the toroidal chamber /1/. A rigid, double walled vessel (fig. 1) has thus been

preferred, even if it presents some drawbacks in terms of electromagnetic effects on plasma (see later on) and of larger thermal expansion. The 72 solid poloidal rings offer an ideal support for the graphite tiles, whereas the double wall adds very much in terms of vessel stiffness and strength, ease of leak testing, possibility of direct cooling.

Located as near as possible to the vacuum vessel, the thick shell (fig. 1) is built from four 180° x 180° aluminium alloy pieces /2/.

The shell is insulated on the two equatorial and the two meridian cuts: metal-to-metal joints have been excluded since, in the case of poor equilibrium control, they would be crossed by linear current densities of the order of one MA/m for tens of ms.

The shell houses the 48 toroidal field coils, the 24 poloidal rings that support the field shaping coils and the torus itself, and the vessel supports.

Tables I and II summarize the main vessel and shell characteristics.

Table I: main vessel characteristics

Material	Inconel 625	
Major radius:		
- at ambient temperature	1995	mm
- at 350°C	2003	mm
Internal minor radius		
- at ambient temperature	475	mm
- at 350°C	477	mm
Wall thickness	30	mm
Vacuum volume	9.2	m^3
Maximum operating temperature	350	°C
Cooling	dry air, CO_2	
Toroidal resistance	1.1	mΩ
Vertical field diffusion time constant	1.0	ms
Toroidal field diffusion time constant	2.1	ms

Table II: main shell characteristics

Material	Aluminium alloy	
Major radius	2000	mm
Inner minor radius	535	mm
Thickness	65	mm
Maximum operating temperature	40	°C
Cooling	deionized water	
Vertical field diffusion time constant	300	ms

2. Mechanical aspects of the design

2.1 The vacuum vessel

The vacuum vessel (fig. 2) is made by 72 cylindrical, wedge shaped elements having circular cross-section (fig. 3).

They consist of a sandwich structure: the inner skin, 2 mm thick, and the outer skin, 1 mm thick, are linked by a 0.5 mm thick, corrugated sheet. Resistance spot welding has been preferred to other possible welding processes (TIG, resistance seam welding) for joining the skins to the corrugated sheet, since it gives the best repeatability (with ease of quality control) and it minimizes the extent of the heat affected zone. The two skins are then TIG welded at both ends to solid poloidal rings.

Six elements, welded together both on the inside and on the outside of the rings, build up a vessel sector, which includes a pumping section and a diagnostic section. The interspace of each sector is a vacuum tight chamber, with a double access at the top and the bottom (see figs. 2 and 3), for gas cooling and leak testing.

Finally, 12 sectors are welded together to form the whole torus; these final seals are made only from the outside, so the vessel can be opened on six vertical planes by grinding and rewelding the lips.

The vessel is supported from the shell on the equatorial plane by 48 stainless steel elements, allowing free radial expansion of the torus and equipped with ceramic insulators.

The vessel is evacuated through twelve, 150 mm diameter circular ports (fig. 2); each port is connected to a pumping unit, including a 1000 l/s turbomolecular pump and a 1500 l/s cryogenic pump. The expected pumping speed at the vessel is about

5000 l/s for N_2.

An extensive stress analysis /3/ by means of finite-element methods has been performed on the vessel structure, which is loaded by the atmospheric pressure, acting either on the inner skin or on the outer skin, by temperature gradients and, during the plasma pulse, by electrodynamic forces.

During normal operation, when the interspace between the two skins is vented, the atmospheric pressure mainly produce membrane compressive stresses acting both along toroidal and poloidal directions. A maximum stress of -10 MPa is found on the inner sheet, whereas a shear stress of 7 MPa appears on the corrugated sheet.

A temperature difference between inner (warmer) and outer sheet gives rise to a tensile stress of 2.4 MPa/°C in the outer sheet and to a compressive stress of -1.8 MPa/°C in the inner skin. The real temperature difference will depend very much on the operating conditions (power from plasma, cooling etc.), but the relatively high figures evidence the usefulness of the vessel rings as thermal bridges and the importance of heat conduction from the tiles to the rings.

The electrodynamic loads are significant only in the case of a fast plasma current termination: if the characteristic decay time is assumed to be as low as 0.1 ms, a toroidal current up to 1.5 MA is induced on the vessel. The peak inward pressure (due both to toroidal current and to magnetic pressure from B_φ redistribution) reaches about 0.36 MPa and is substantially axisymmetric, due to the absence of bellows. The total inward force on the vessel is 2.0 MN during a fast termination.

The electrodynamic loads have a pulse length of less than one ms, so the inertia effects should be accounted for. Nevertheless, for reference purposes a 3-D static analysis has been first performed: the stresses result to be again mainly compressive, with a maximum value of -30 MPa in the inner sheet. A 3-D dynamic analysis followed /4/, including a careful examination of the stress and displacement amplification factors; the frequency response analysis resulted in an amplification factor of about 1.5 for the stresses. Also the buckling analysis evidenced a very high safety factor with respect to applied external pressures, so that the overall stress state of the vessel, even under the worst conditions, seems to be well within reasonable limits.

2.2 The shell

Each one of the four shell pieces (fig. 1) will be built from laminated plates, toroidally shaped by pressing and welded to obtain the required toroidal extent (180°).

The shell is fully machined, with poloidal grooves on the outside for toroidal

coils and supporting rings and variously shaped recesses on the inside for magnetic pick-up coils, cooling channels, vessel supports.

The most critical aspect of the electromechanical design is related to the vertical gaps: each of them should withstand a voltage of about 1 kV (during fast current terminations) and very large tensile and shear stresses due to the electrodynamic actions, mainly produced by the shell toroidal currents interacting with the poloidal and radial field components. In the case of abnormal operating conditions (loss of control on the field shaping currents), a maximum normal force of about 1100 kN tends to open each gap, together with a vertical shear force of about 50 kN /2/. These forces, caused by the high conductivity and large thickness of the wall, should be withstood by the insulated vertical joints, whose design has been optimized also with reference to the needs of avoiding any topological interference with vessel and coils and of minimizing the gap amplitude.

Fig. 4 shows an exploded view of the vertical joint tightening system. The main insulation is made by a 5 mm thick epoxy-glass layer, whereas the clamping system is composed by threaded epoxy-glass bushes, which insulate the steel studs from the opposite shell half: 22 clamping elements are provided for every joint. The bushes, in which the glass fibres lie perpendicular to the thread axis, should withstand the stud preload and the dynamic forces during the pulse. Extensive tests, whose results have been compared with structural calculations, have demostrated /5/ the reliability of this system: the breaking load is higher than 200 kN, no fatigue effects have been evidenced after 100.000 pulses and the preload relaxation is limited to 8% after about one month. All dielectric tests, performed under d-c conditions, resulted in breakdown voltages higher than 14 kV, or higher than 37 kV when the bush was bonded by epoxy resin inside the nut screw to remove any air pocket.

Except from the gap tightening elements, the stress state inside the shell is very low, even when substantial forces are transferred to the shell by the supporting rings in the case of faults on the field shaping coils.

3 ELECTROMAGNETIC ASPECTS OF THE DESIGN

During electromagnetic transients, induced currents on vessel and shell produce magnetic fields in the plasma region. These fields are positively employed in counteracting MHD instabilities and in contributing to plasma equilibrium, but they have also some negative effects on the plasma: these effects are briefly reviewed in the following.

The finite toroidal conductance of the vessel reduces the loop voltage by about

10% during the plasma current rise phase; the total loss in flux swing is about 2.5% of the available 15 Vs.

When the pulse is starting, the toroidal current (up to 550 kA at the peak loop voltage) produces a vertical field inside the vessel, that may prevent gas breakdown.

This field depends on the relative vessel/shell position, and thus on the vessel temperature. Fig. 5 shows the vertical field amplitude at breakdown on the equatorial plane, as a function of the radius and for various vessel temperatures.

Finally, the finite poloidal resistance gives rise to vessel currents during the toroidal field reversal phase. They introduce a delay of 2.1 ms and, due to the presence of the solid rings, they produce a field ripple inside the plasma region. The ripple is maximum on the plasma boundary, reaching about 8 mT when the fastest field reversal time is assumed; however, it should be pointed out that this field ripple lasts for a few ms and is negligibly low during the flat-top phase.

The shell effect in determining the RFX plasma horizontal equilibrium has been the subject of extensive work in the past /6/ and the activity is continuing with reference to the design of the position feedback control and of the "thin" shell.

The calculations have been performed with the aid of a computer code modelling the whole RFX electromagnetic system. The plasma model assumes realistic current density profiles and accounts for dynamo effects; the shell is simulated by a lumped-parameter network obtained by developing into a Fourier series along both toroidal and poloidal direction the surface current densities. The 10 independent power supply voltages are the model inputs, whereas plasma parameters like toroidal current and horizontal position as well as the non-axisymmetric poloidal field configuration are the output variables. As expected, the results confirm that, with an accurate programming of the input voltages, it is possible to keep the stray fields at the gaps within some 0.1% of the total magnetic field. On the other hand, there isn't any chance to significantly reduce during the pulse the plasma column shift from its initial value (3 to 4 cm) without producing unacceptable field perturbations.

An accurate control of the stray fields at the gaps also results in the reduction of field errors due to shell holes, since both kinds of perturbations are produced by the same induced current. An assessment has been made /7/ of the relative importance of the two field errors; the results showed that, for equatorial holes having a diameter of 170 mm, the field ripple at the plasma boundary due to the holes is about six times smaller than due to the gaps. Vertical holes have an even weaker

effect on the field configuration.

4. TEMPERATURE CONTROL

The vessel is thermally insulated from the shell by a 10 mm thick blanket made of a microporous, low-thermal conductivity material.

The vessel is also provided with a temperature control equipment, composed by an electrical heating and a forced gas cooling system. The vessel temperature control is considered to be a very important feature to improve pulse repeatability, to control impurity influx into the plasma and particle recycling, to avoid excessive thermal cycling on the vacuum seals.

The vessel operating temperature range shall be from ambient temperature to 350°C. To remove the power deposited on the tiles and transferred from the tiles to the vessel (up to 33 kW with one 2 MA pulse every 10 minutes) gas circulates in poloidal direction through narrow channels on the sides of the vessel stiffening rings (see fig. 3). The efficiency of this system has been tested on a full-scale prototype of a vessel element: with a dry air flow of 40 m^3/h, which doesn't produce any noise or vibration and requires a reasonable pumping power, the vessel temperature can be kept below 74°C (with a temperature difference of 42°C between outlet and inlet ports) at the full plasma power; by pressurizing the air to 1.5 bar, the maximum temperature can be lowered to 40°C (and the temperature difference to 16° C). Even better results have been obtained by replacing air with carbon dioxide.

The vessel heating system consists of electrical cables fixed by small clips on the external vessel surface. With a total power of 60 kW and owing to the modular construction, it is capable of keeping the vessel at its maximum baking temperature (350°C) even in the case of a cable fault. Compared with eddy current heating methods, this solution gives the advantage of a better temperature uniformity (it can be actively controlled); moreover, the system is completely independent of the main power supplies, so there is the possibility of heating the vessel also during the experimental phases.

To prevent agein of the electrical insulating materials, the shell is cooled by deionized water flowing inside copper tubes, which are bonded inside grooves machined on the internal shell surface. In this way, the shell temperature can be kept within 40°C even when the vessel is heated up to 350°C.

7 REFERENCES

/1/ F. Elio, F. Gnesotto, P. Sonato: "RFX First Wall and Vacuum Vessel Design"

Proc. of the 11th Symp. on Fusion Engineering, pp. 866-871, 1985.

/2/ M. Fauri, F. Gnesotto, P. Sonato: "Electromechanical Design of the RFX Stabilizing Shell". Proc. of the 11th SOFE, pp. 1167+1170, 1985.

/3/ F. Elio, C. E. Majorana, P. Zaccaria, F. Zaupa: "Structural and Thermal Analysis of the RFX Vacuum Vessel. Proc. of the 11th SOFE, pp. 825-829,1985.

/4/ F. Elio, C. E. Majorana, M. Pauletti, P. Zaccaria, B. A. Schrefler: "Dynamic and Buckling Analyses of a Toroidal Vessel for Fusion Experiments. MSC/NASTRAN European User's Conference, 1986.

/5/ M. Fauri, private communication.

/6/ F. Gnesotto, M. Guarnieri, A. Santagiustina: "Dynamic Control of the Equilibrium Field Configuration in RFX", Proc. of the 10th SOFE, pp. 316+320, 1983.

/7/ F. Gnesotto, G. Miano, G. Rubinacci: "Numerical Analysis of Time dependent Field Perturbations due to Gaps and Holes in the Shell of a Reverse Field Pinch Device". IEEE Trans. on MAG, vol. MAG-21, N. 6, pp 2400+2403, 1985.

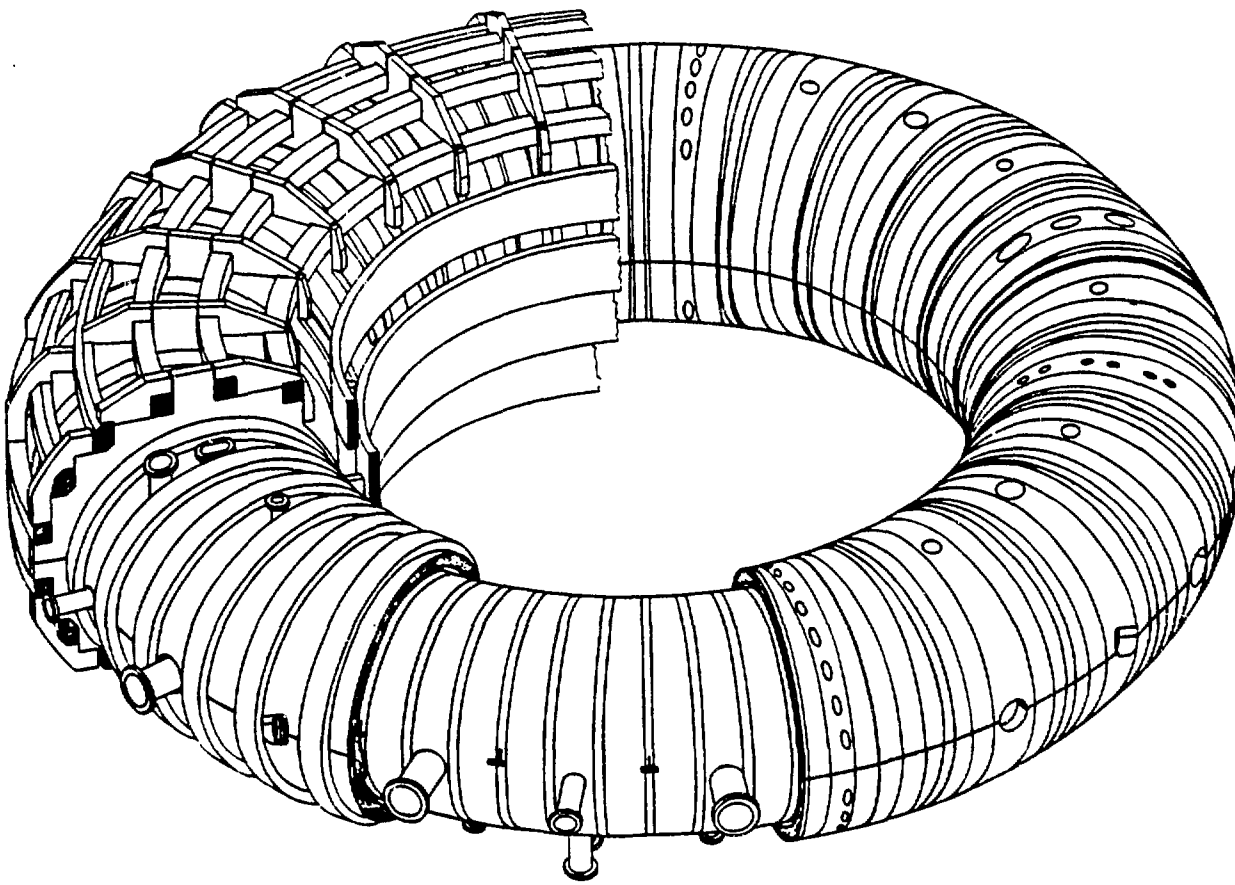

Fig. 1: The RFX toroidal assembly

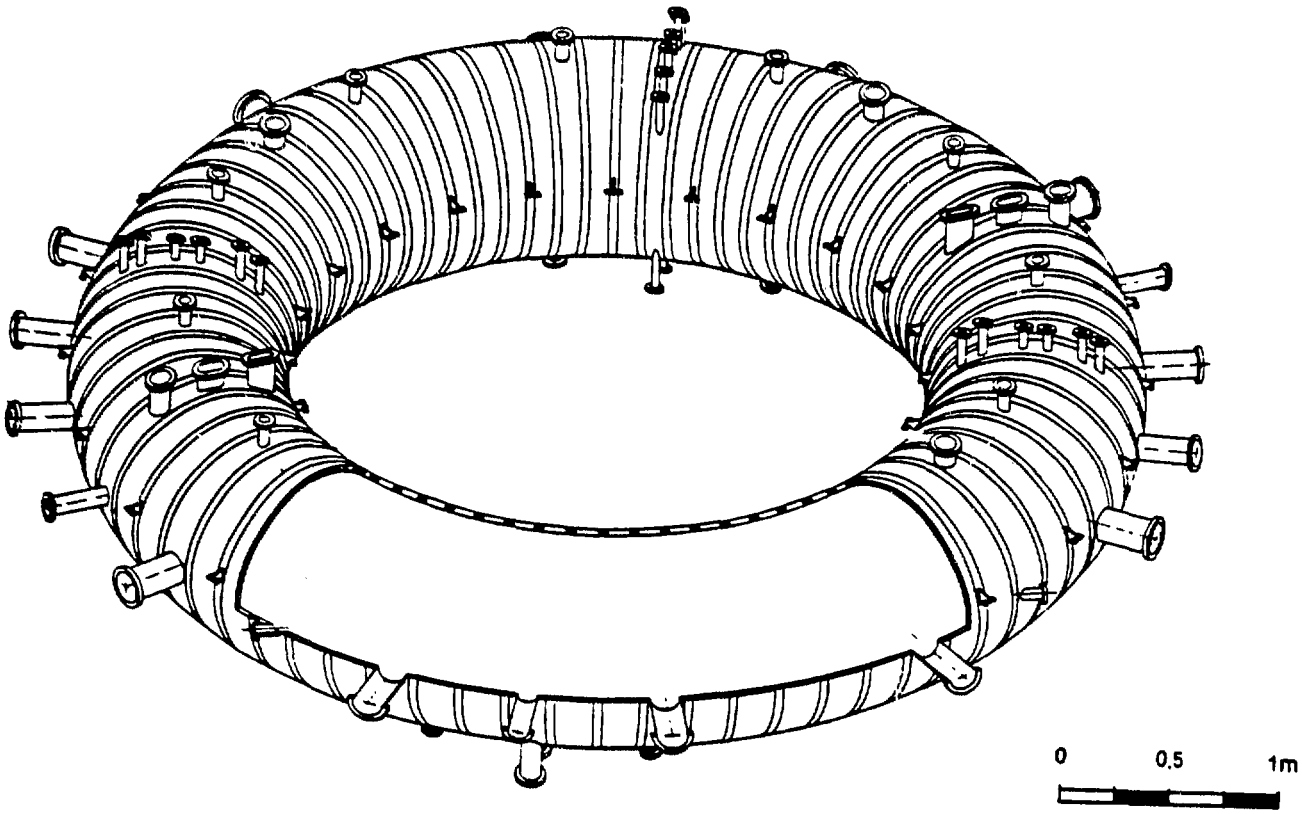

Fig. 2: The RFX vacuum vessel

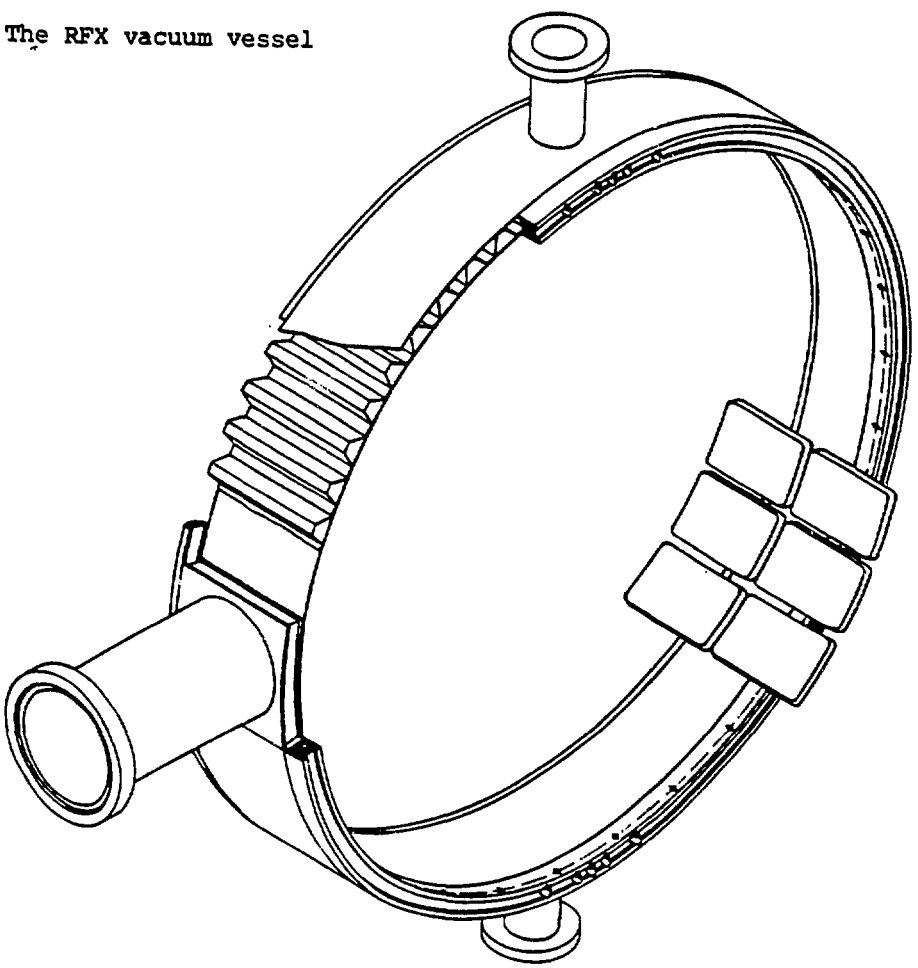

Fig. 3: a vessel element (pumping section)

ZTH BASIC MACHINE STRUCTURE

A. Giger

Coil configuration and coil forces are of paramount importance in selecting a concept and designing a structure to support the ZTH machine. Figure 1 shows the arrangement of ohmic heating and equilibrium coils selected for ZTH after lengthy analyses. The maximum forces they produce during machine operation are shown graphically on figure 2. Figure 2 corresponds to operation at the end of the machine pulse.

For the ZTH machine, a rule has been adopted that the coils will sustain their own individual hoop (circumferential) loading. This will be made possible by ensuring a low coefficient of friction between each coil and its mounting structure. The remaining component of coil forces are in the "z" direction. These vertical components are summarized in table 1.

The most reasonable way of dealing with the large "z" direction forces, since they are symmetrical about the machine horizontal plane of symmetry is to react them against their symmetric twin. A system of 16 vertical fiberglass epoxy bulkheads radiating from the machine vertical centerline has been selected to do this. The bulkheads in relationship to the field coils are shown in figure 3.

Since "z" forces are orders of magnitude larger than the gravity loads, structure to support the machine weight is fairly simple. Machine weight is supported on a center cylindrical pier and 16 outboard stanchions. Appropriate cross bracing is used. This structure is shown as figure 4.

The 4 inch thick bulkheads are held in position by 4 ring beams supplemented by diagonal bracing. Each bulkhead assembly is comprised of 6 sections to allow for assembly and disassembly. Fairly rapid disassembly of the machine down to the front end is planned by crane removal of 3 sub-assemblies. Each of these sub-assemblies is comprised of coils, bulkhead sections, and ring beams.

Figure 4.1 is a plan view of one of the bulkheads that shows some details of joining the several sections together, the ring beams, coil clamps, and location of trim coils. Also depicted inboard of the front end is an inner stainless steel semi-box structure that allows coils 2 and 3 to be continuously supported. This box section will be connected to the inner ring beams to assist is stabilizing the bulkheads. Not shown, but being allowed for, are the front end mounting pads and electrical leads from the coils. The latter are tentatively being supported directly on the bulkheads at 90 degree intervals around the machine.

Bulkhead sections will be held together by shear plates bolted thru inserts on either side of the seam line. Figure 5 shows a cross section of such a fastener. The large radial clearances for the planned 1.25" diameter high strength bolts will allow quick assembly of the machine sections. A full scale component test of the joint design has been started.

The front end will be mounted to the bulkheads by a spline arrangement allowing differential radial motion without transmission of forces other than gravity loads to the bulkheads. This will be done by mating the front end to each bulkhead by two vertical pins or keys. One key will be on top of the torus, the other, with the same axis, on the bottom. The keys will slide in radial slots of a pad , the bottom pad assembly will have a sliding contact surface that will bear the weight of the front end. The top assembly will be positioned with small clearances to prevent any upward motion of the torus. Because the front end assembly will be a considerably more precise structure than the bulkhead system that supports it, the x-y location of the support pads on the bulkhead will be adjustable and lockable. This will allow quick mounting of the front end on the structure. The front end shell will internally resist liner vacuum loads and toroidal field coil forces.

Individual coils will be precisely located optically and their position verified by magnetic measurements. They will be held in these positions by blocking in the "z" and "x" directions at the points where they transfix the bulkheads. In the case of the "x" direction, coil restraint will be only on the inside of the coil. Alignment of the coil set will be held by 32 clamps on each coil. A typical clamp arrangement is shown in figure 6. Clamps will abut both sides of each bulkhead and allow only radial motion, e.g. the coils will be splined to the bulkheads. This will also ensure constant radial alignment of the coils to the front end.

Build up and alignment of the machine starts with the center pier which is constructed from concrete and fiberglass reinforced rebar. Sixteen bearing plates for the bulkheads are precisely located atop the pier by means ofa large diameter jigging ring. The plates (and attached ring) are leveled by nuts on tie bolts which have been emplaced in the concrete. After grouting beneath the plates the jigging ring is removed and the plates securely bolted down.

With the outboard stanchions in place the lowermost bulkhead sections are set in position. An adjustable head on the stanchions allows leveling in the radial direction for the 16 individual bottom bulkhead pieces. With a modicum of care this method will easily allow the bottom course of bulkhead sections to be set level within .030", thus ensuring an accurate base upon which to construct the balance of the machine.

Modest deviation of the bulkheads from their theoretical true radial positions will not be critical because coil and front end positioning and alignment is insensitive to this.

A finite element analysis scoping the ZTH machine has indicated the bulkhead concept is feasible. A new analysis of the presented design is in progress by CTR-4. No detailed design of the presented structure other than the base will be undertaken until the analyses indicate reasonable stresses and deflections will be present.

Earthquake resistance of the machine has been investigated by Tom Butler of MEE-13. A report on this aspect is to be prepared.

Moderate revisions to the current design are expected to accommodate results of finite element analyses of the structure, electrical lead routing,or unforseen factors.

TABLE 1

VERTICAL COMPONENT
OF COIL LOADS

COIL Nº	FORCE (LBS X 10^{-6})
1	- 1.82
2	- 1.24
3	- 3.76
4	- 2.21
5	- 1.13
6	.345
7	.628
8	.612
9	.766

ZTH COIL CONFIGURATION

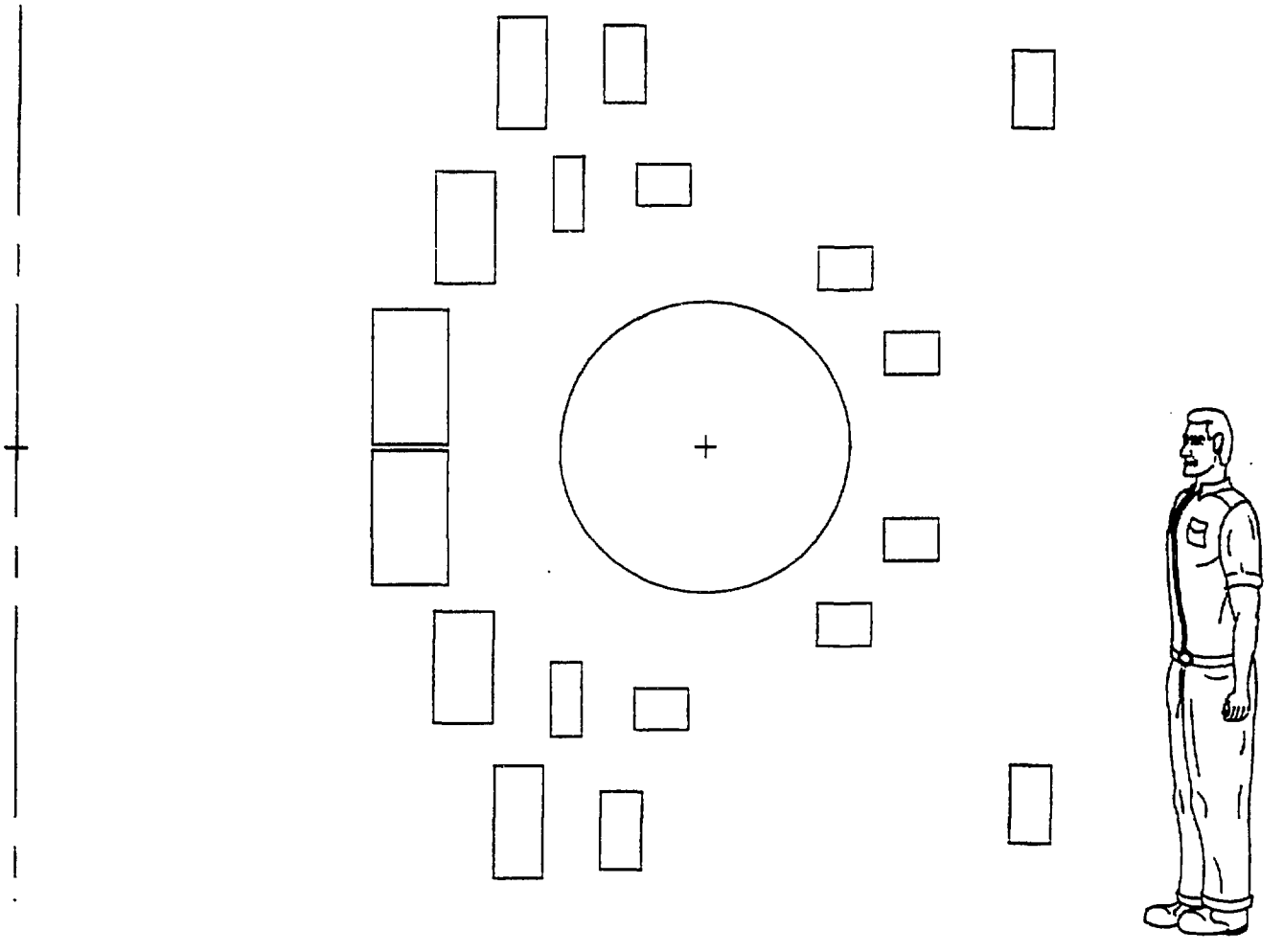

MACHINE
CENTERLINE

FIGURE 1

TOTAL COIL FORCES

(LBS X 10-6)

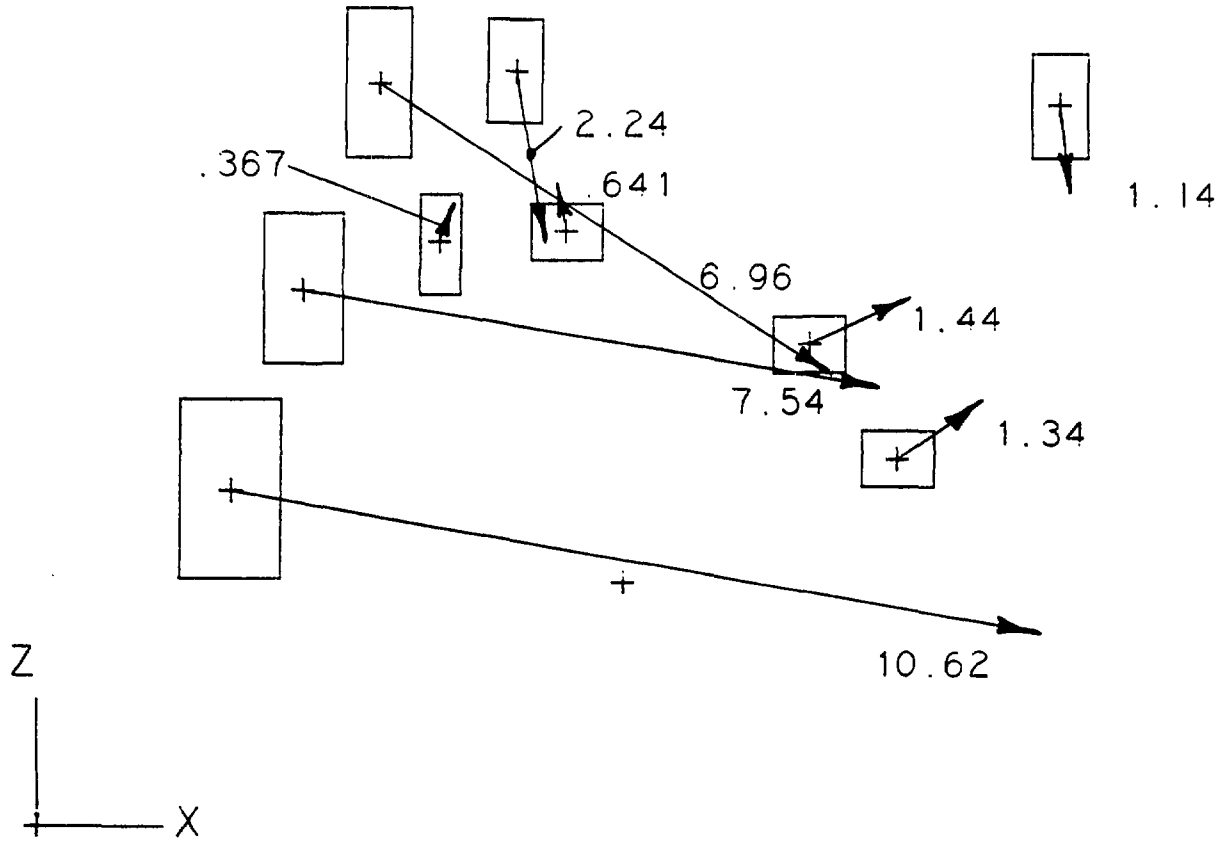

FIGURE 2

ZTH BULKHEAD SYSTEM

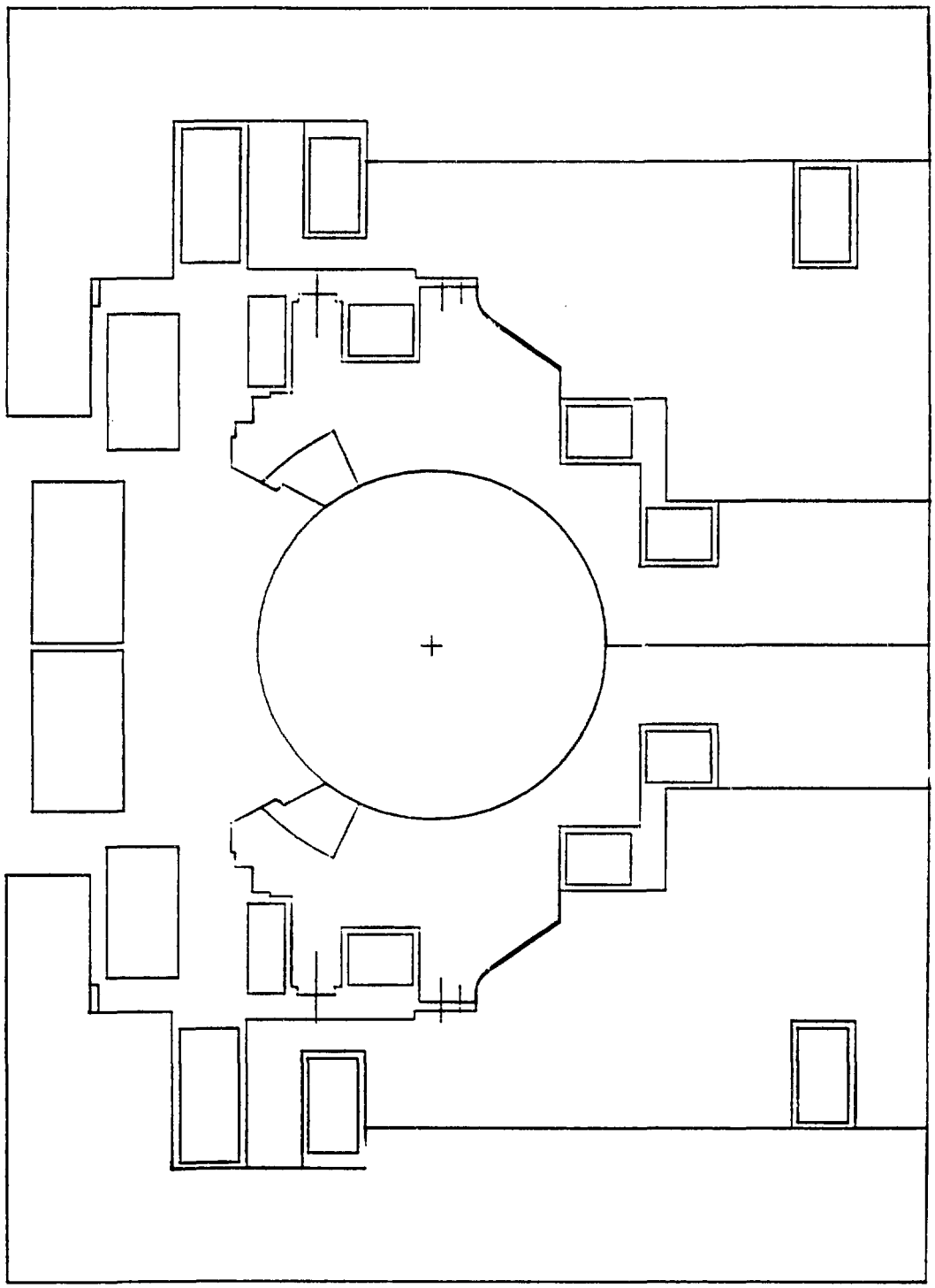

FIGURE 3

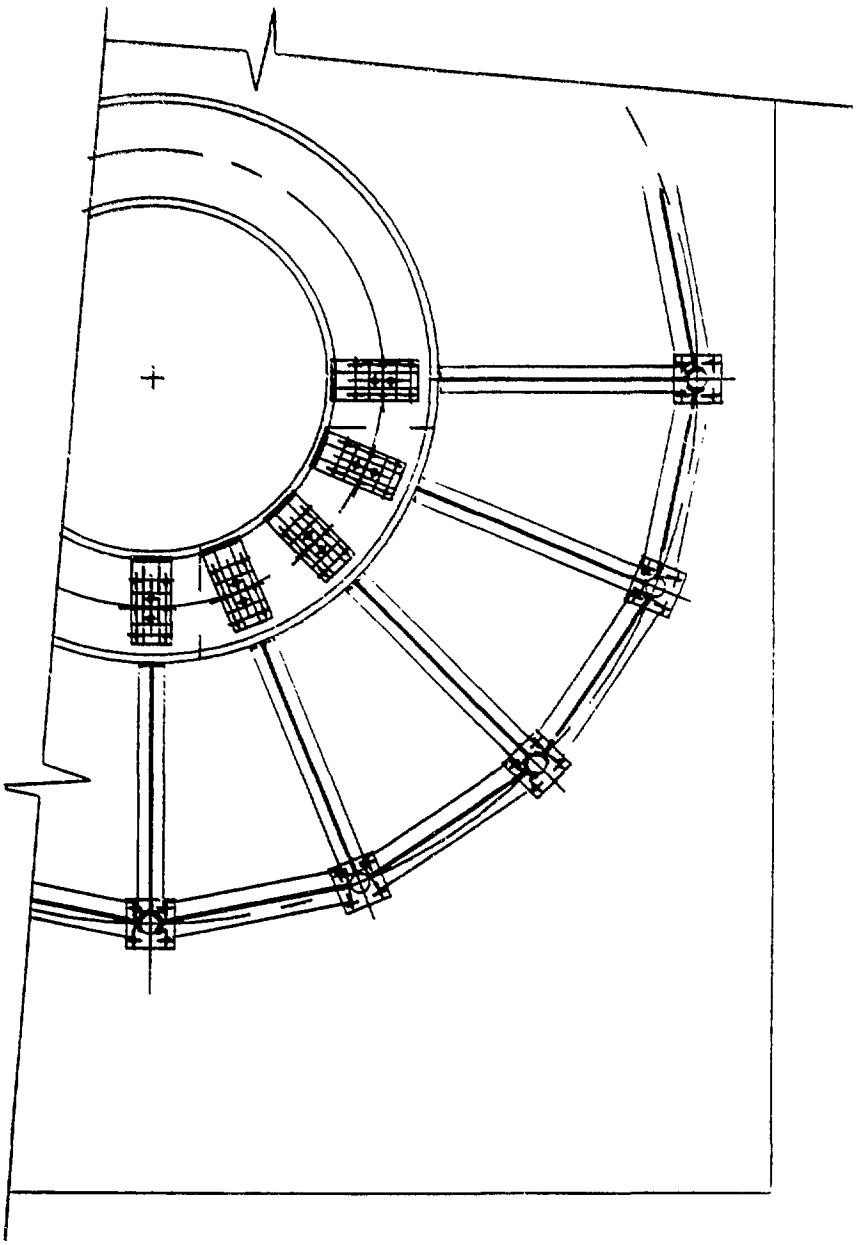

ZTH
MACHINE BASE
REF R1E27C0
6-1-87

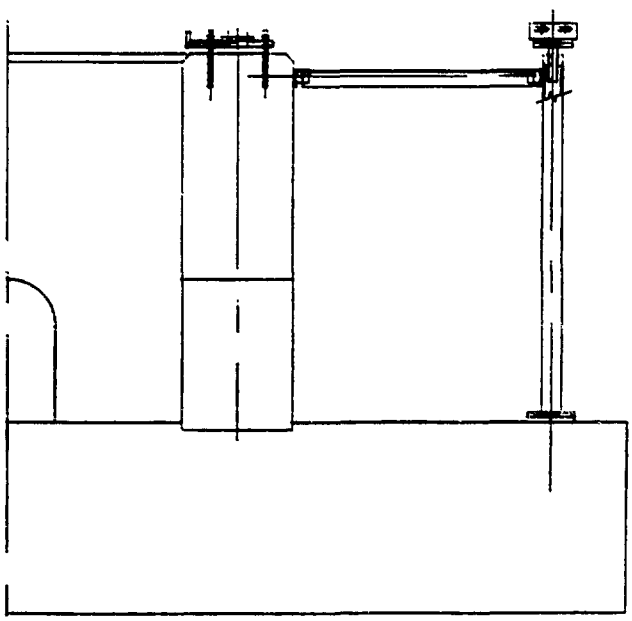

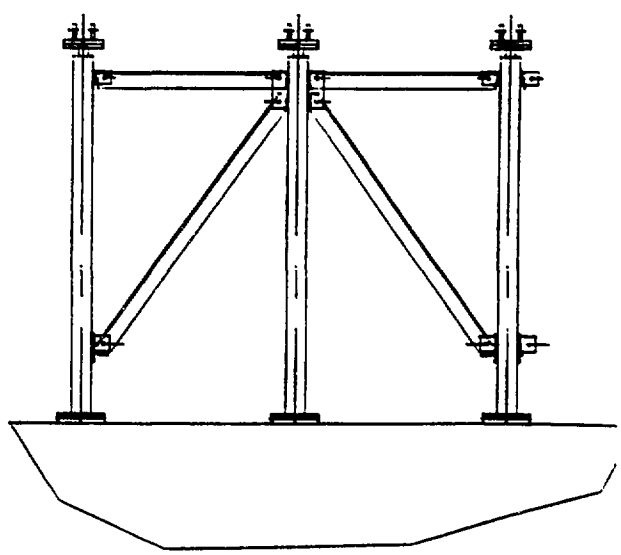

FIGURE 4

ZTH BULKHEAD
PLAN VIEW

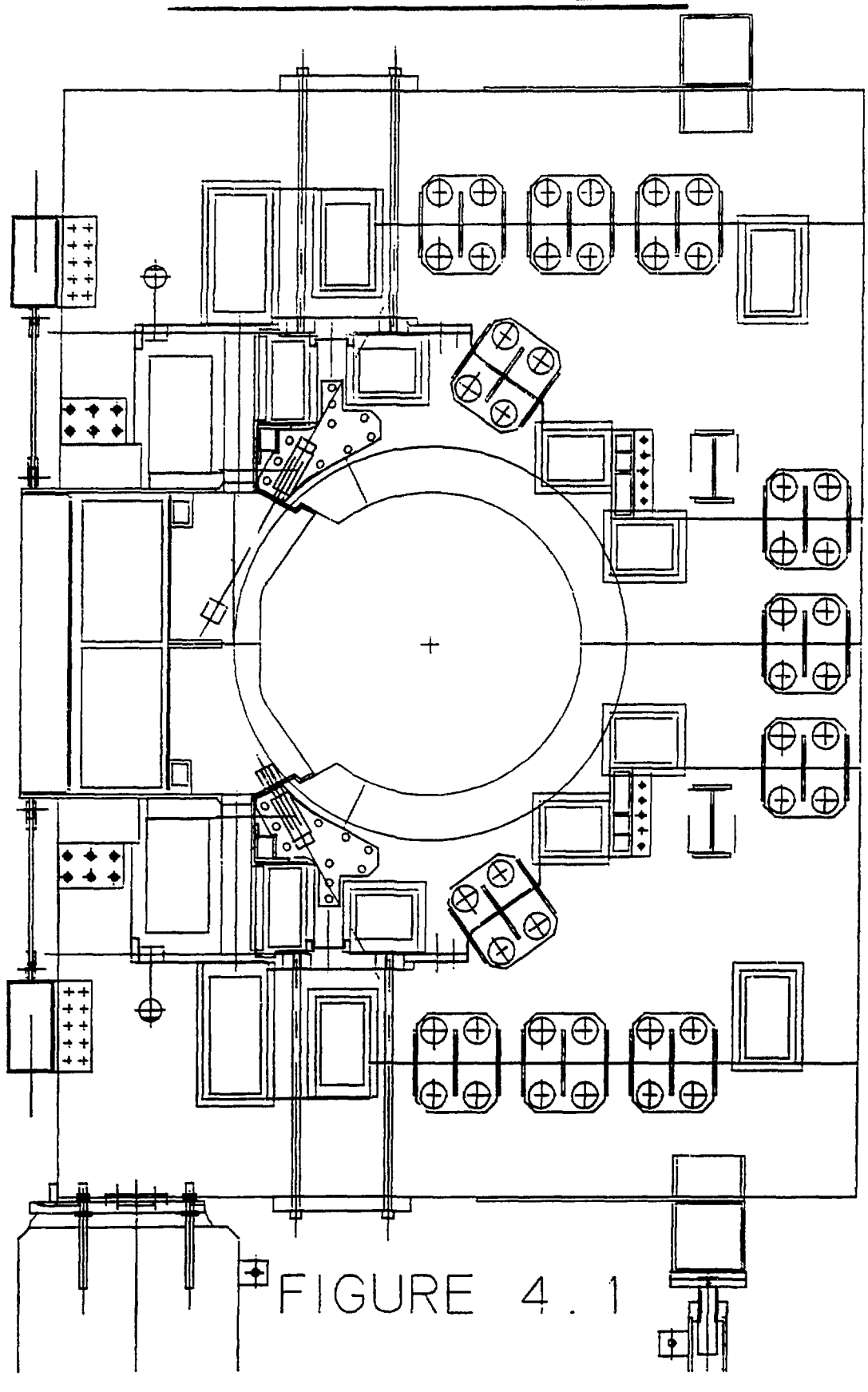

FIGURE 4.1

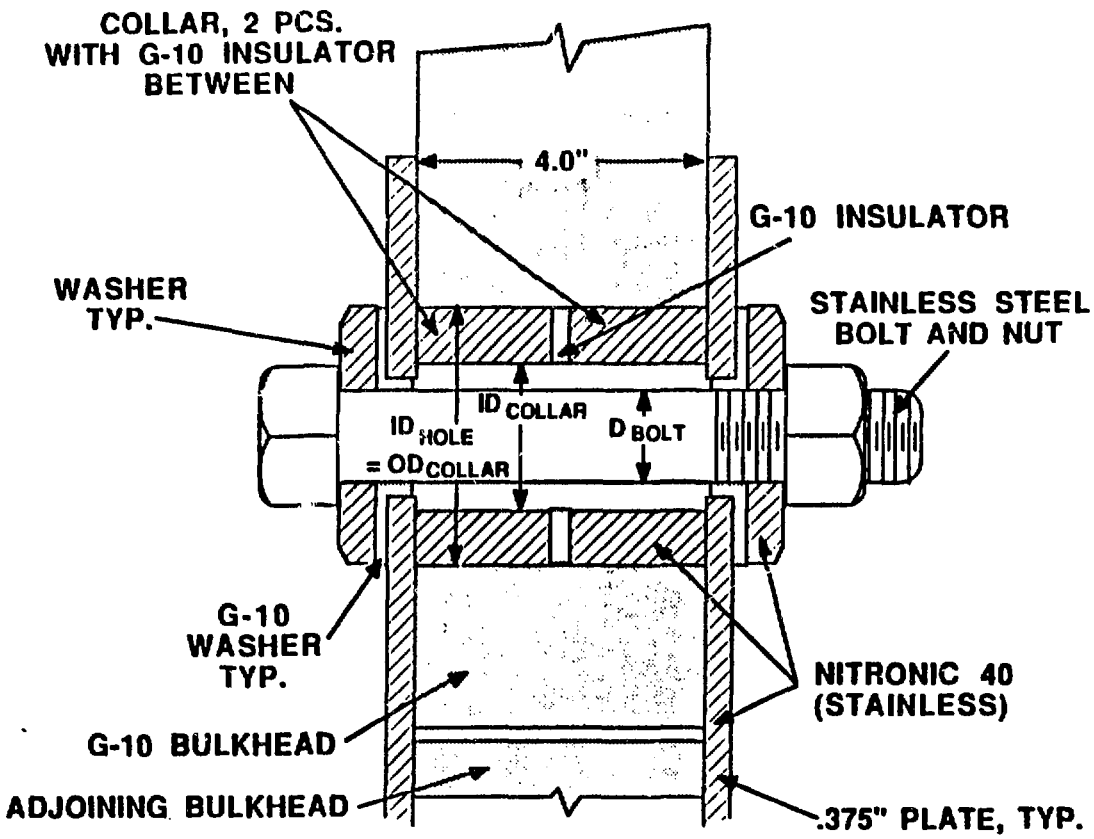

FASTENER DETAIL CROSS-SECTION

FIG. 5

COIL CLAMP DETAIL

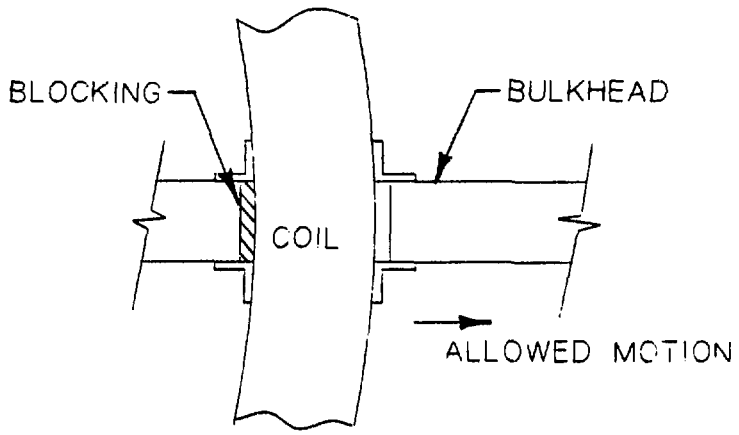

SECTION A-A

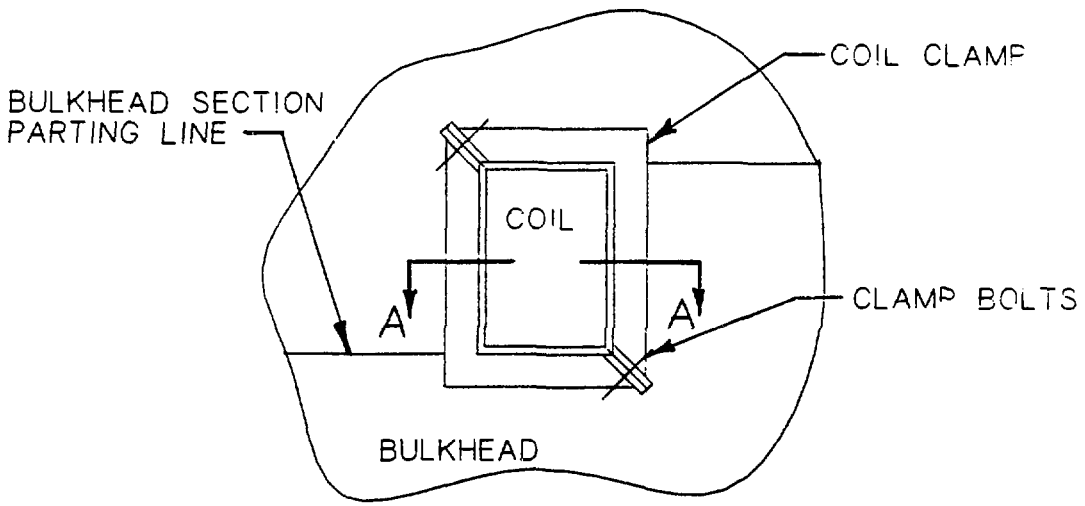

FIGURE 6

STRUCTURAL ANALYSIS OF VACUUM CHAMBER

N.Suzuki, M.Uesaka, and K.Ogawa*
Ishikawajima-Harima Heavy Industries Co.,Ltd. (IHI)
*Electrotechnical Laboratory (ETL)

Structural analysis of vacuum chamber of an RFP, which consists of thin bellows and straight cylinder is presented. Considered electro-magnetic force is due to eddy currents in a vacuum chamber and a shell. The eddy currents were simulated with a system that involves both vacuum chamber and shell. The eddy current induced in the shell rises with characteristic time of plasma current disruption approximately. While the eddy current induced in the vacuum chamber reaches its peak value in much shorter time than the shell current. According to the results of the eddy current analysis, a stress analysis of the chamber is carried out. It is confirmed that a bellows section tends to bulge outward of torus.

1. Introduction

In this paper, eddy current and stress problems in a vacuum chamber with a shell of RFP are analyzed.

These analyses were carried out by using 'INCANET' (IHI Induced Current Analysis Code by Network Mesh Method) and 'BELLOWS' code. 'BELLOWS' is based on the finite element method for axi-symmetric structure with non-symmetric load. Therefore, a bellows and a cylinder were assumed as straight ones. Additionally, the stresses were calculated at every time step under the assumption that electro-magnetic forces were static forces in every time step.

The calculatin was carried out by VAX 11/780 in which the CAE(Computer Aided Engineering) system was installed. Especially, the post proccesor of CAE was used for the graphic display of the numerical results.

2. Formulation of Eddy Current Analysis

The basic principle in the network mesh method lies in representing a conducting surface as a network comprised of a number of branches. The area surrounded by the center lines of branches is defined as a mesh. The branch resistances are obtained as the resistance of those plate, and branch inductances are obtained to integrate a magnetic vector potential, due to unit flowing in a branch(active), along the center line of another branch(passive). The resulting branch resistance and branch inductance matrices are transformed into mesh matrices. By using these meshes, a set of simultaneous differential equations can be written in the following form ;

$$[L_m](\dot{I}_m) + [R_m](\dot{I}_m) = (V_m) \qquad (1)$$

where $[L_m]$, $[R_m]$ are the mesh inductance and resistance matrices, respectively. (I_m) is the mesh current vector and (V_m) is the time-dependent voltage vector resulting from time-dependent external current source. Equation (1) is solved by the Newmark-β method in the computer code.

'INCANET' has also the functions to calculate the following items.

1. total magnetic field due to external sources and eddy currents
2. spatial distribution and a total value of Joule power loss
3. spatial distribution and a total value of electro-magnetic force

3. Outline of Finite Element Method for Axi-symmetric Bellows with Non-symmetric Load

If a conventional finite element method for s shell is applied to the stress analysis of the bellows, too many unknowns appear to be easily handled. However, nodes, elements and physical quantities on them are defined only in the cross section of the bellows in the

r-z plane in this scheme. The Fourier analysis is introduced to calculate the azimuthal distribution of loads and deformation. Thus, the memory of computer used in calculation can be remarkably reduced.

As a complete description of non-symmetric deformation of the axi-symmetric shell, not only meridional and normal displacements have to be considered but also a tangential component associated with an angular direction must be included. In addition, a rotation around the meridional axis has to be added. Generalized forces corresponding to the displacements and rotation are expanded into Fourier serieses with respect to an azimuthal angle.

4. Results and Discussion

The eddy current and stress problens in a vacuum chamber and a shell in RFP are analyzed.The vacuum chamber and the shell supposed in this paper are shown in Fig.1. The major radius of this RFP is 1.5m and minor radii of the vacuum chamber and the shell are 0.3m and 0.4m, respectively. The vacuum chamber has an conventional shape that consists of bellows and cylinders. their material is INCONEL 625 (Young's modulus = 2.19×10^{7}MPa, Poisson ratio = 0.3, electrical resistivity = 1.3×10^{-6} Ωm). Fig.2 shows a concept of a cross section of joint between the bellows and the cylinder. The shell is made of SUS316L (Young's modulus = 1.98×10^{7}MPa, Poisson ratio = 0.3, electrical resistivity = $7.2 \times 10^{-7}\Omega$m) and its thickness is 20mm. Electrical insulators are put on the two intersecting circles between the shell and the y-z plane and on the outer intersecting circle between the shell and the x-y plane, respectively(see Fig.1). Mechanical supports between cylinders of chamber and the shell are placed at every 22.5° sector.

Characteristic time of plasma current disruption supposed in this paper is 1ms. Namely, plasma current of 2 MA goes to zero in a couple of miliseconds.

This plasma current is assumed as a source of eddy current. And electro-magnetic forces on the chamber and the shell are calculated.

For the eddy current analysis, 77 meshes and 177 branches, 24 meshes and 58 branches are set on the chamber and shell, respectively. The imaginary meshes and branches which are interconnected by the center of the coordinate are used for taking into account of the magnetic flux change surrounded by the vacuuum chamber. In the stress analysis, it was assumed that the vacuum chamber and the shell are perfectly constrained at the mechanical supports. Therefore, sectors can be analyzed independently.

Fig.3,4 and 5 show the flow patterns of eddy current at t=0.4ms,0.8ms and 2.4ms(after the plasma current disruption). It can be understood that the eddy current induced in the chamber(one turn in toroidal direction) tends to shield the magnetic flux change caused by the plasma current disruption during the first 1ms.
As this chamber current decays, a saddle-shaped eddy current begins to be induced in the outer shell. The peak values of the eddy currents are 74.0kA(chamber) and 75.8kA(shell).The times at which the eddy currents reach its maximum value are 0.4ms(chamber) and 2.4ms(shell). (see Fig. 6)

The stress analysis of 11.25° sector (33.75°-45°) of the vacuum chamber at 0.4ms was carried out. The deformed geometry and the spatial distribution of maximum principle stress are shown in Fig.7 and 8,respectively. The maximum nodal displacement is 0.157mm. The maximum stress is 170MPa.

5. Concluding Remarks

The eddy current and stress analyses in the system involving the bellows and cylinder for RFP were carried out. It was confirmed that one-turn eddy current is

induced in the vacuum chamber immediately after the plasma current disruption, and a saddle-shaped eddy current begins to be induced in the shell as the chamber current decays. This results indicate that one must consider both a vacuum chamber(liner) and a shell in case of analyzing of eddy current and/or stress for RFP machine.

Address:

IHI ... Tokyo-Chuo Bldg. 6-2,Marunouchi 1-Chome, Chiyoda-Ku,Tokyo 100 Japan

ETL ... 1-4,Umezono 1-Chome,Sakura-Mura, Niihari-Gun,Ibaraki 305 Japan

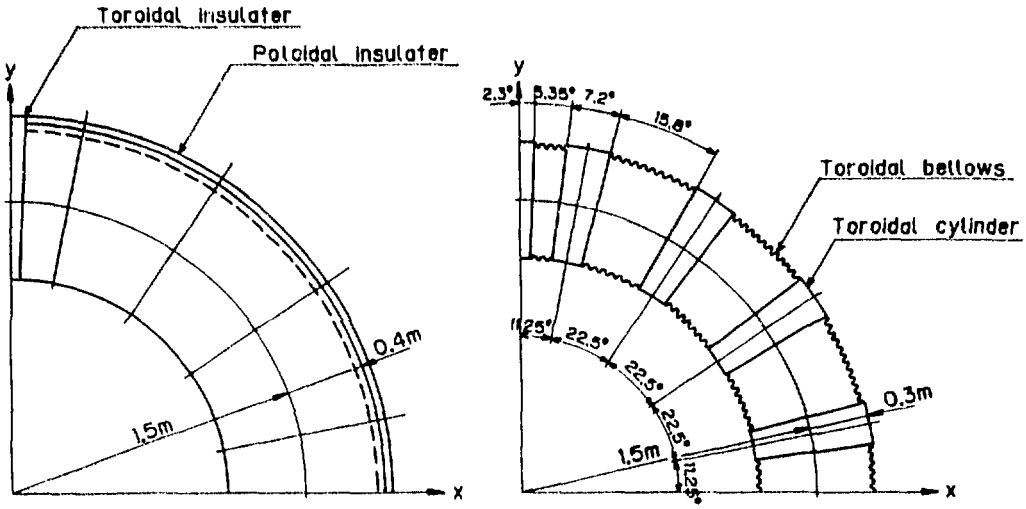

(I) Toroidal shell (II) Vacuum vessel

Fig. 1 Toroidal shell and Vacuum vessel of a Reversed Field Pinch device.

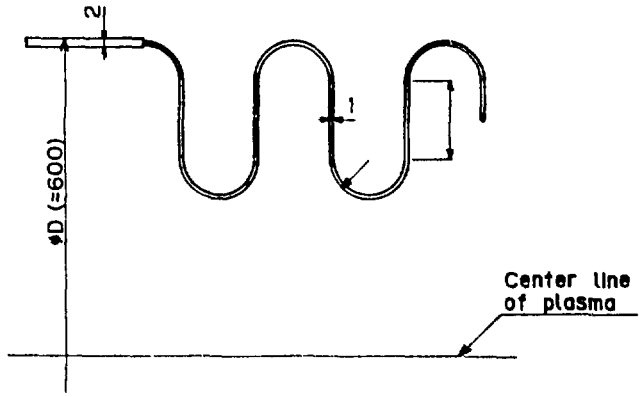

Fig. 2 Joint between toroidal cylinder and bellows.

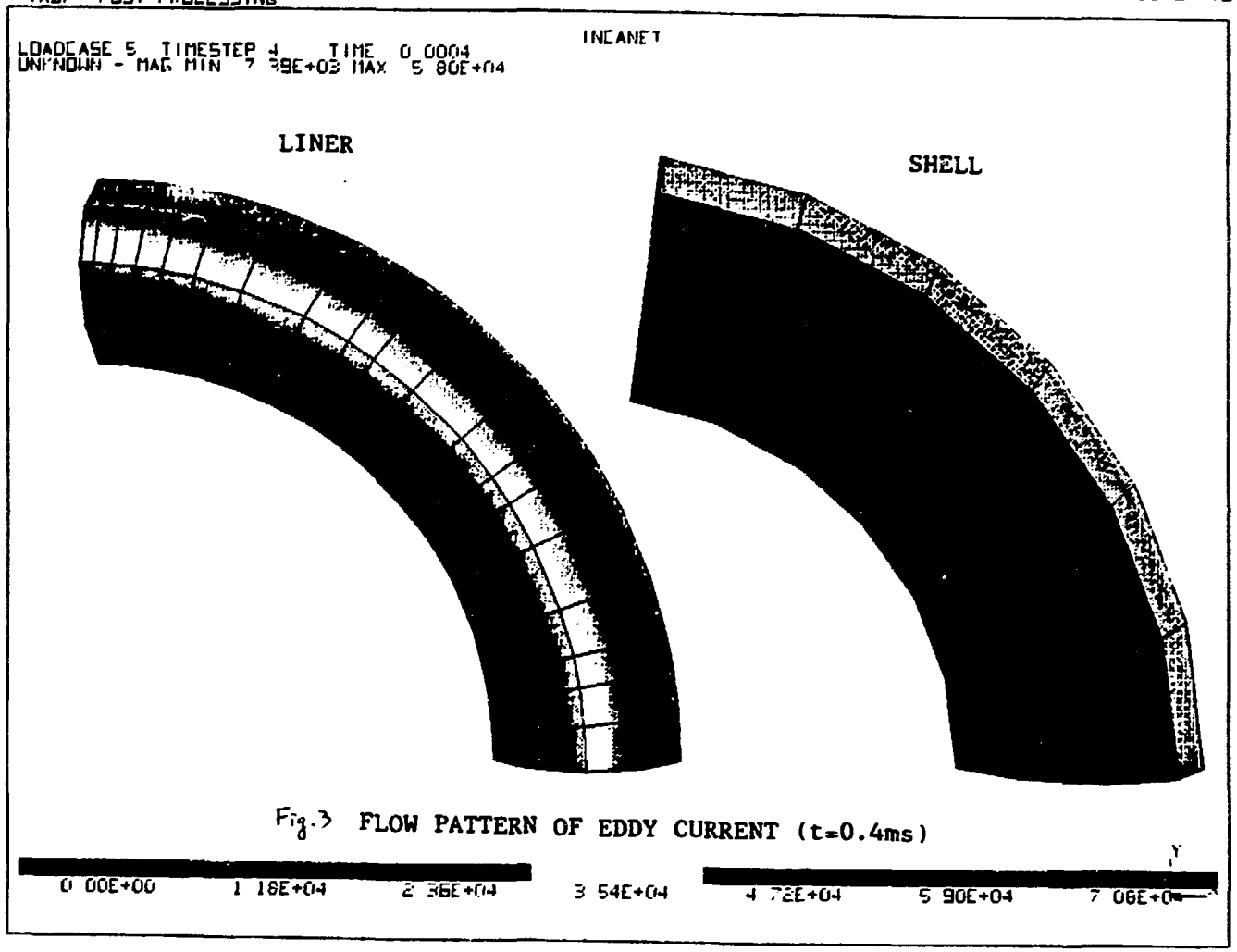

Fig.3 FLOW PATTERN OF EDDY CURRENT (t=0.4ms)

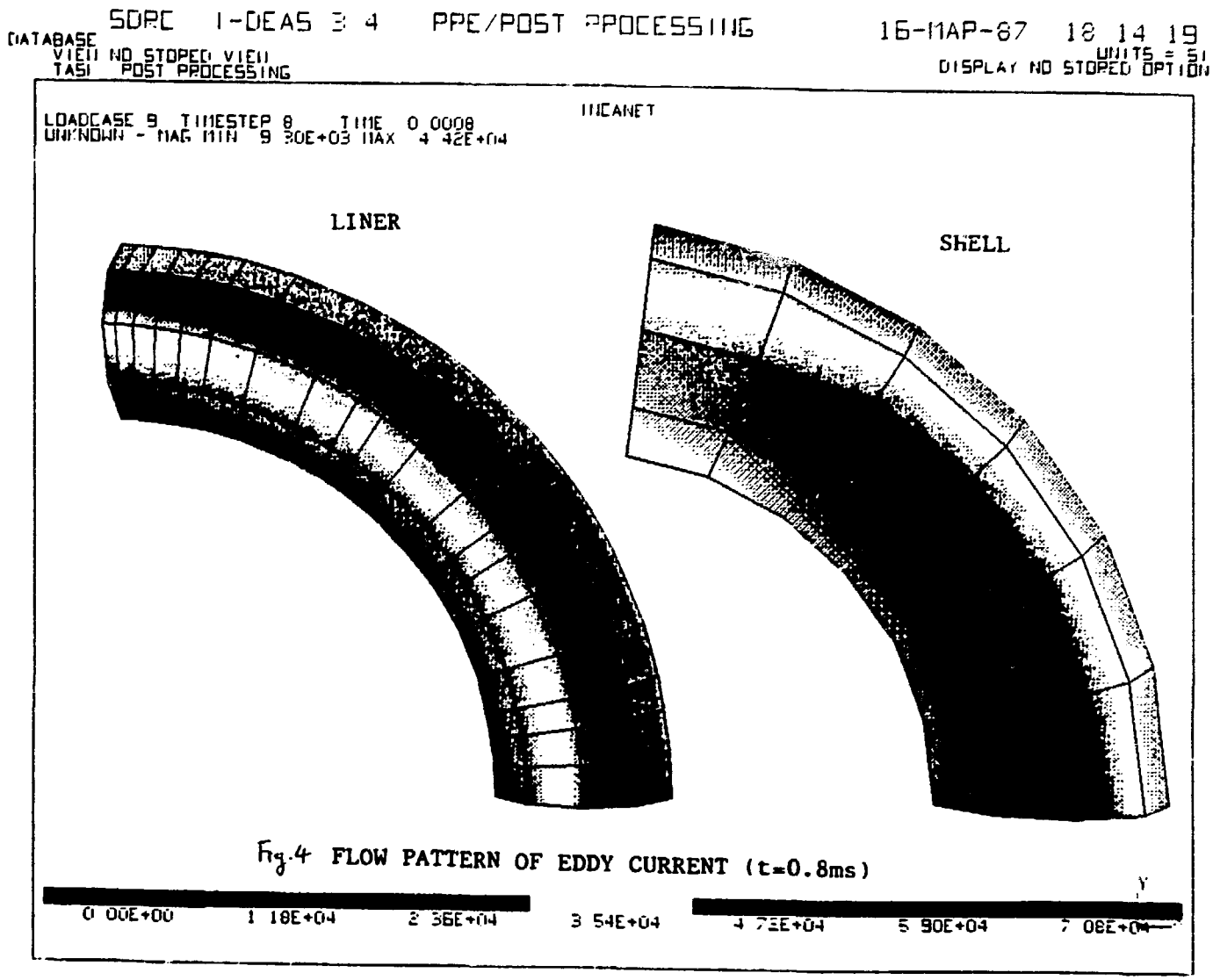

Fig.4 FLOW PATTERN OF EDDY CURRENT (t=0.8ms)

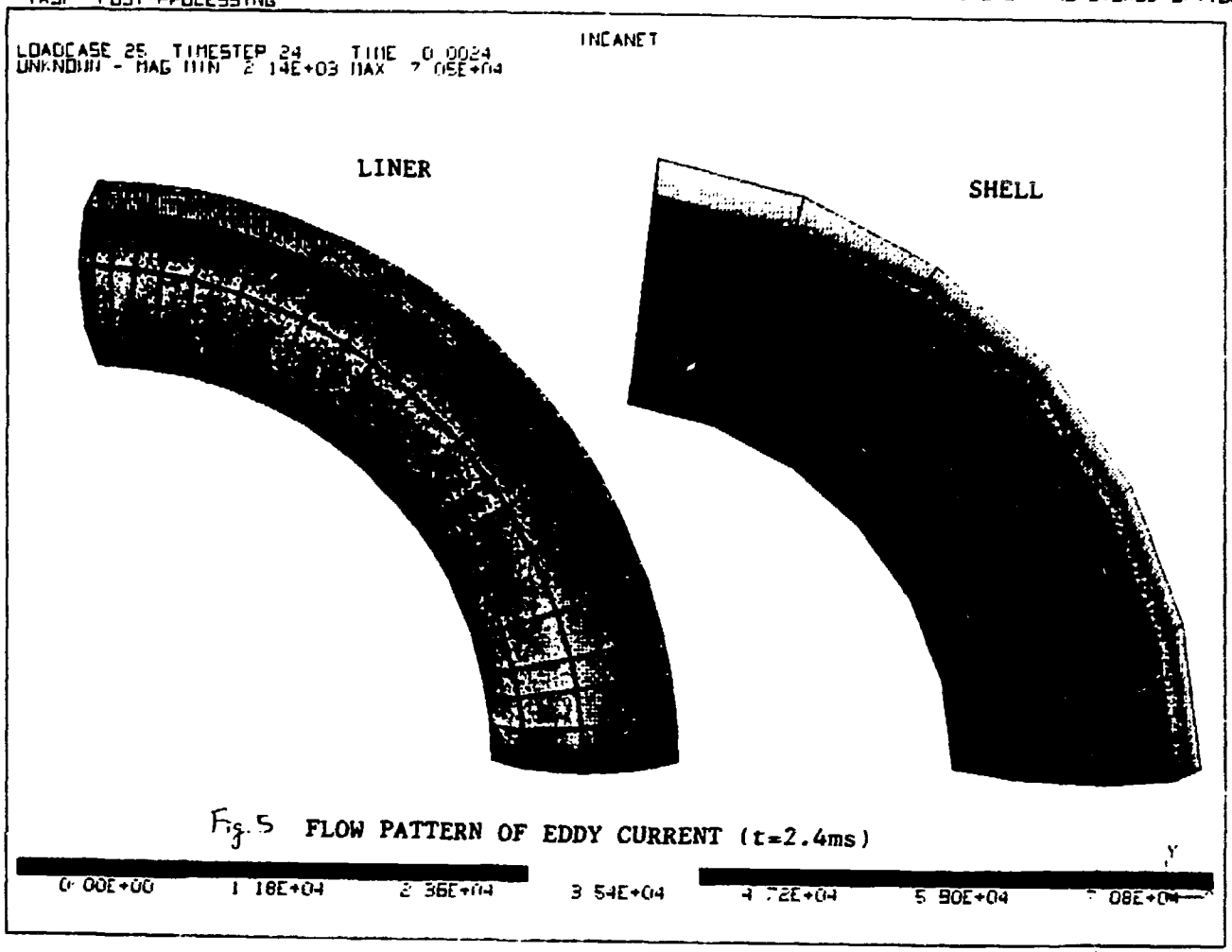

Fig.5 FLOW PATTERN OF EDDY CURRENT (t=2.4ms)

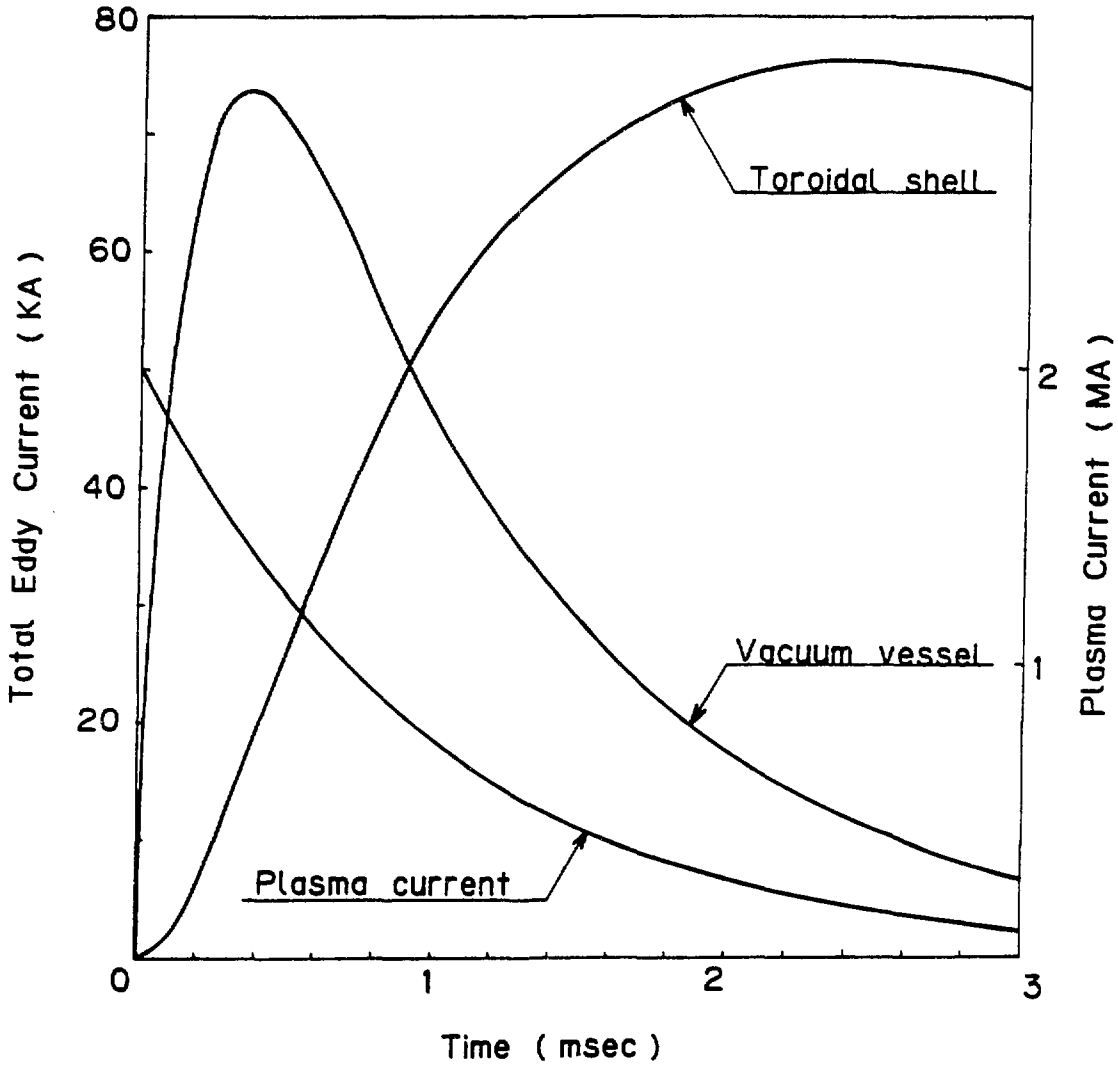

Fig. 6 Total Eddy Currents

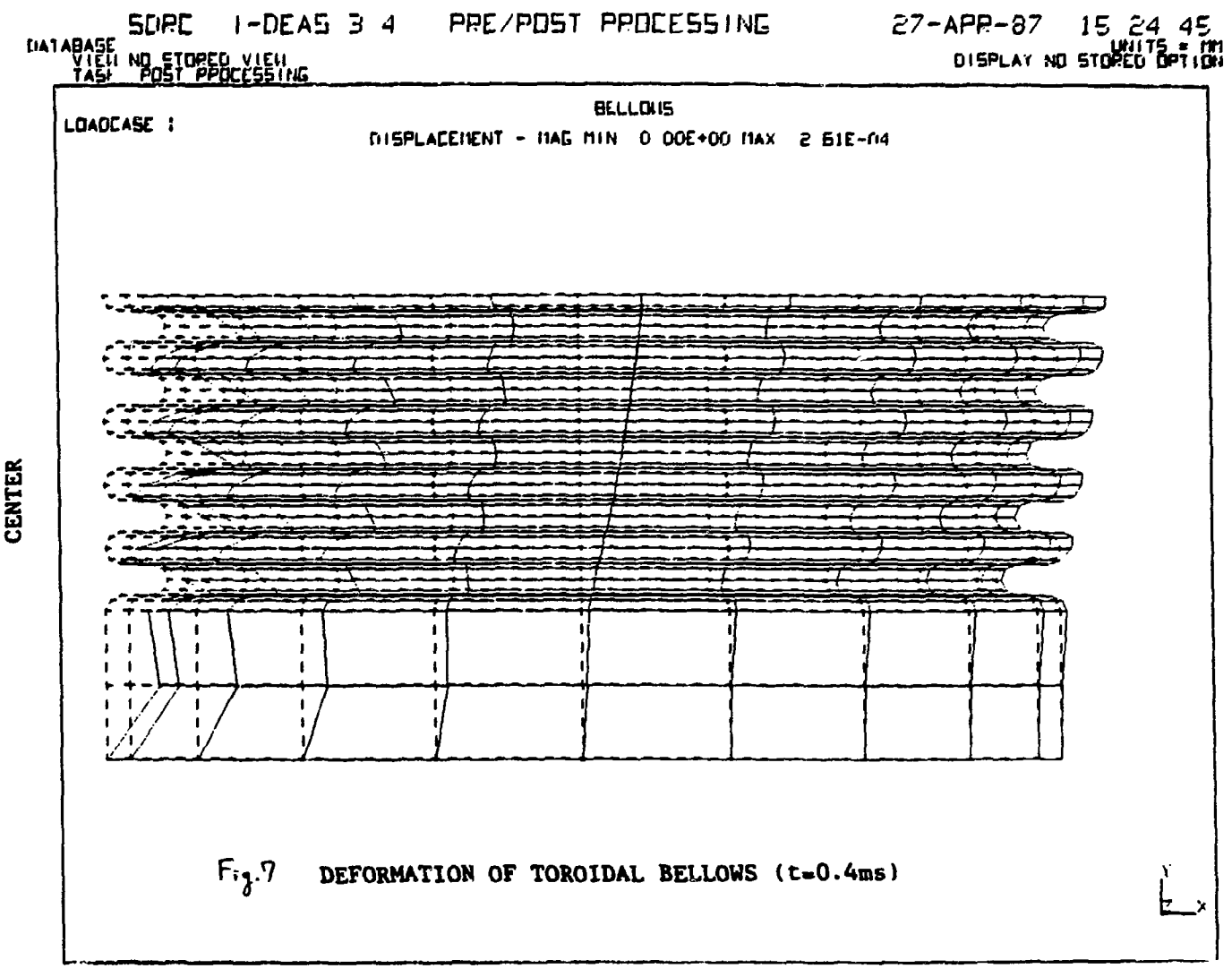

Fig.7 DEFORMATION OF TOROIDAL BELLOWS (t=0.4ms)

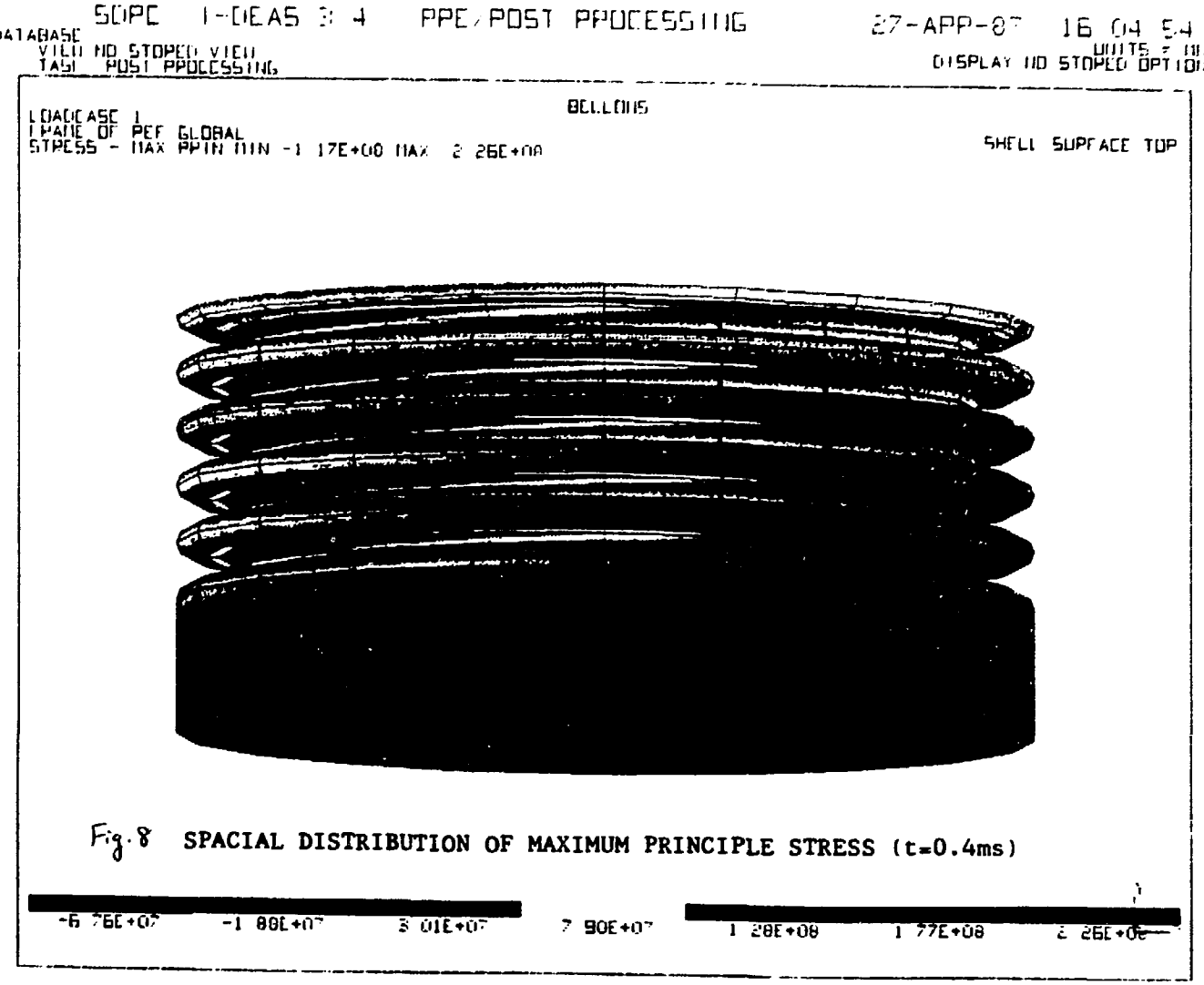

Fig.8 SPACIAL DISTRIBUTION OF MAXIMUM PRINCIPLE STRESS (t=0.4ms)

COMPUTER CONTROL AND DATA ACQUISITION

R.W. Wilkins and L.W. Mann

Los Alamos National Laboratory, Los Alamos, New Mexico 87545

*

The computer control and data acquisition system for CPRF/ZTH is now being designed. The control system will be based on an industrial process control system using off-the-shelf components as much as possible. The data acquisition system will be CAMAC based and will be developed in-house making extensive use of existing systems from Los Alamos and other fusion laboratories.

Introduction

The development of the CPRF/ZTH computer control and data acquisition system is now in the design phase. Preliminary estimates have been made for the number and types of controls needed and for the diagnostics requirements. Various ways of meeting these requirements are presently under evaluation.

Control

The control system is being planned as a distributed system. The machine has been broken down into various subsystems such as vacuum, power supplies, motor generator, and front-end. Each subsystem will be under the control of a subsystem controller capable of sequencing the subsystem through a shot, providing critical protection, doing local trending of subsystem parameters, and being operated in a stand-alone mode from a local console. The present estimate is that there will be a total of about 2000 control points. Fiber optic control interfaces developed for ZT-P will be used to interface the controllers to the equipment being controlled.

The subsystems will be networked together and to a central operator console by means of fiber optic network. The central console will have three or four CRT screens for displaying subsystem status, alarms, and trend plots. Real-time trends will be displayed with one second screen

* Work performed under the auspices of DOE.

updates. In addition, historical trends, such as hourly averages of selected parameters may be logged to disk and recalled for display at a later time. The operator will interact with the system primarily by using a pointing device such as a mouse and/or touch screen.

A survey of commercially available industrial process control systems has shown that there are several systems that have the capability of meeting these design requirements. There is not, however, an ideal system . Different vendors have strengths in different areas such as ease of programming the operator interface versus programming the control logic. The final choice will inevitably involve some tradeoffs.

A supervisory computer may be required in addition to the process control system, depending on the system selected (some use equipment that might serve this function). This computer would be used to archive the shot setup parameters for each shot, carry out computation intensive setup calculations, and provide communications to the data acquisition system. The shot setup archive will be used to automatically download the process control system to recreate any previous shot.

There are some requirements that are beyond the capabilities of existing process control systems. A fault detection system will be developed separately and interfaced to the process control system. This system will take immediate action to protect the machine and then inform the process control system of the nature of the fault. A fast timing or trigger system will also be developed to provide micro-second timing . This system will probably be CAMAC based.

Data Acquisition

The overall organization of the data acquisition/analysis system is shown in Fig. 1. One or more fiber optic CAMAC serial highways will link the data acquisition computer to data acquisition stations located around the machine in the torus hall. These stations will house clusters of CAMAC crates. Diagnostics that are inherently isolated from the machine may be linked to these stations by hardwired data links. Other diagnostics will use fiber optic data links. An estimate of the initial data acquisition requirements are shown in Fig. 2. These requirements are expected to grow rapidly and the system must be designed in a modular fashion to easily

accommodate this growth.

We are evaluating the use of micro-processors located in each CAMAC crate to do preprocessing of the data. In the proposed scheme each processor would readout and compress the data from all of the modules in its crate. Our experience indicates that this compression would reduce the volume of data to be transferred to the data acquisition computer by about a factor of five. Since the readout and compression would be performed in parallel in all creates, this scheme may significantly reduce total data readout time.

The data acquisition computer will be linked to the control system and to data analysis machines by Ethernet. A VAX computer will be used for compatibly with the MFE User Service Center computer system. Immediate post shot data analysis will be done on a local area cluster of workstations such as VAXstations and IBM micro-computers. A larger dedicated data analysis computer on a clustered disk with the data acquisition computer will be added when funding allows.

Key design features are fast data readout with priority for designated channels, automatic generation of selected displays, and a friendly user interface. An existing data acquisition system in use at Los Alamos could form the basis of this system. The Los Alamos system needs a number of extensions, however, and so other options are being considered. One attractive option is the MDS package developed at MIT. This system is already used by a number of the smaller fusion laboratories, and we feel that a move to standardization in data acquisition software would be a positive development. The Event Control System developed at Princeton for TFTR is also of great interest and will probably be incorporated into our system.

Summary

While the detailed design of the control and data acquisition system is not yet clear, its general characteristics have been determines. Most of the control requirements can be met by industrial process control systems and it is our intention to procure such a system. The data acquisition system will require some in-house development but will make use of existing software wherever possible to minimize development effort.

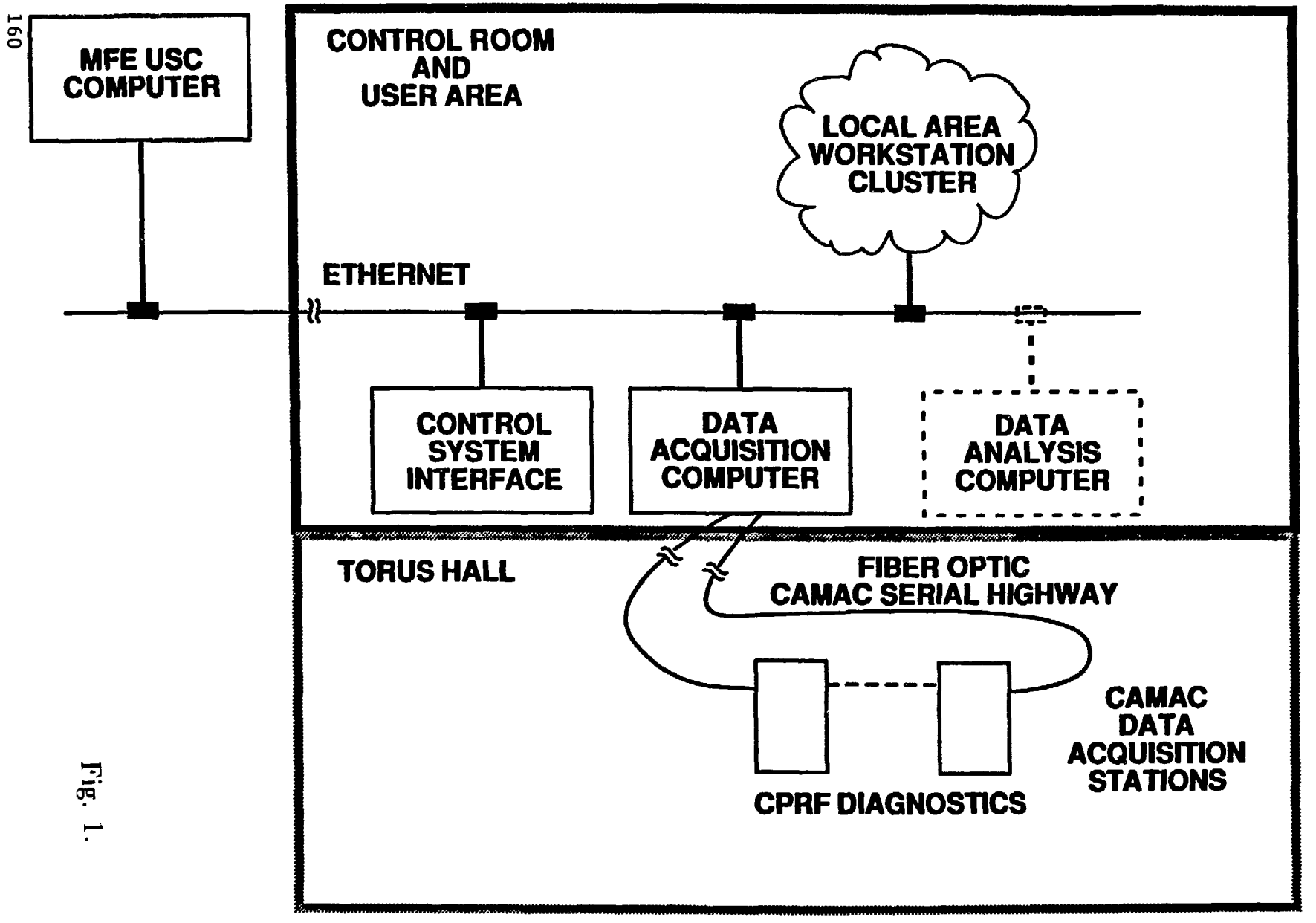
160
MFE USC COMPUTER
CONTROL ROOM AND USER AREA
LOCAL AREA WORKSTATION CLUSTER
ETHERNET
CONTROL SYSTEM INTERFACE
DATA ACQUISITION COMPUTER
DATA ANALYSIS COMPUTER
TORUS HALL
FIBER OPTIC CAMAC SERIAL HIGHWAY
CAMAC DATA ACQUISITION STATIONS
CPRF DIAGNOSTICS

Fig. 1.

Data Estimate

		#chan	link
Electrical	Internal	6	1 MHz optic
"	Interspace	25	100 KHz optic
"	External	10	100 KHz optic
Optical &	Particle	70	hardwired
"	"	93	100 KHz optic
		204	

16 - 32 K samples per channel

4 - 5 M Items per shot

Fig. 2.

ZTH MAGNETICS DESIGN*

by

Robert F. Gribble

UNIVERSITY OF CALIFORNIA
LOS ALAMOS NATIONAL LABORATORY
LOS ALAMOS, NEW MEXICO 87545

Introduction

ZTH is to reach 2 MA by inductive energy transfer in 0.05 seconds followed by power supply ramping to 4 MA in 0.4 seconds. Major and minor radii are 2.4 and 0.4 m. Copper for the poloidal field coils weighs 48 metric tonnes, the oneturn equivalent ohmic heating (OH) coil inductance is 1.90 microhenries, and the OH coil rating is 15.4 MAT, 225 MJ, and 29.3 volt-seconds at 60 kA. The normal operating OH current is 50 kA. Design of the coil for 60 kA provides a margin for uncertainties.

OH coils are connected in series and the combination is connected in parallel with four equilibrium field (EF) coils. With optimized location of all coils, this connection provides decoupling between the OH and EF coil sets so that the changing OH current does not affect EF winding current. This arrangement has many advantages over other PF circuits, including reduction of power supply costs. Optimization of coil locations was achieved with the use of a nonlinear optimizer program to meet the ZTH specifications while also minimizing the cost of both OH and EF coils.

Design Philosophy

The ZTH PF coil arrangement and circuit is similar to that of the RFX experiment(1), and actually grew from the original Padova air core design proposed for the British RFX. In this concept the OH and EF coils are connected in parallel and located so that the two sets are decoupled, and the EF coil induced currents are directly proportional to plasma current with a magnitude to provide an initial passive equilibrium. Power required for equilibrium control in this design is minimized, a highly important consideration for the fast risetime of ZTH.

The Padova concept is similar to the original Doublet design where with proper placement of OH coils and a parallel connection of EF coils located close to the shaped vacuum vessel, the desired flux surface shape was obtained from the EF coil induced currents. In the limit of vanishing coil resistance this ideal geometry would preserve the desired flux surface for all time because with equal turns all coils must have and maintain the same flux, independent of plasma current. With nonzero resistance, the OH coils must be situated so that the OH flux returns outside the toroidal area enclosed by the EF coils to prevent diffusion of OH fields into this area and altering the desired flux surface. As plasma current increases, induced EF coil currents due only to plasma flux changes maintained the flux surface, and small power supplies offset resistive drops and also allowed small changes in the flux surface shape.

---

* Work performed under the auspices of the U.S. DOE.

The RFX EF coils cannot be located on the vacuum vessel (liner) because of the shell and TF coils, but the same Doublet idea is achieved by shifting the circle on which the EF coils are located inwards so that a flux surface coincides with the liner. ZTH specifications on toroidal field (TF) error and diagnostic access prevent placement of any part of an EF coil closer than 30 cm to the liner with the result that location of EF coils on a shifted circle similar to that of the RFX design would require an unacceptably large OH and EF coil configuration. The solution to the ZTH magnetics design problem was the use of a nonlinear numerical optimizer program that simultaneously placed OH and EF coils to minimize both equilibrium power supply and coil costs.

ZTH Magnetics Design Constraints

There were many specifications (constraints) that strongly influenced the ZTH magnetics design. The effects of most of the constraints were not mutually exclusive. Some of the more important constraints in roughly the order of impact are listed below.

1. Programmed current changes in the OH and EF coils must be capable of generating a 4-MA plasma current using reasonable models for plasma parameters. This reduces principally to specifications on the plasma current risetime and available volt-seconds in the OH coils.
2. The diagnostic access must be adequate where the term adequate was the result of a compromise. The original specification that there be clear access to the liner looking in horizontally at the midplane and vertically above the minor axis was too expensive for the equilibrium control system. The compromise chosen is 25 cm above (and below) the midplane looking horizontally in from the outside of the torus and 2.5 cm about the minor axis looking vertically.
3. Maximum radial deviation of the flux surface at the liner is ±5 mm. This limit is imposed to control plasma/wall interactions and erosion of the graphite armor, and applies to all sources of field errors such as holes in the shell and the flux gap. In this paper the flux surface deviation (d) is defined as the greatest radial distance from the liner to the largest flux surface within the liner. The specification of ±5 mm above is equivalent here to a d value of 10 mm.
4. The size of the radial field error in the toroidal field is specified as a function of the toroidal mode number to control magnetic island size at the reversal surface.
5. The coil voltage and current must be within boundaries set by conventional high voltage and switching technology.
6. At plasma initiation there must be a field null near the axis and the field throughout the vacuum vessel must be less than 100 G. An externally applied magnetic field may be used to achieve the necessary null.
7. A structure to support coils and load assembly must be low cost, easy to assemble, and allow modular placement of coils.
8. Within all other constraints, the total cost of the coils, switchgear, and power supplies should be minimized.

The ZTH Magnetics Design Compromise

The specification that most influenced the design of ZTH is the risetime requirement of about 50 ms arising from specification number 1. Scaling results from ZT-40M show that the risetime for inductive energy transfer should be as fast as reasonably possible to reduce the consumption of poloidal flux (volt-

seconds) required to reach 2 MA. Because of the fast current rise, power necessary to control equilibrium during the rise tends to be very large unless the Doublet equilibrium scheme is employed so that equilibrium supplies only compensate for resistive losses and provide small adjustments to allow for variations of internal plasma energy. If the risetime were several seconds, the Doublet scheme would not be necessary because EF energy could be supplied over the longer time with only power supplies of modest size. A nondecoupled PF magnetics configuration for ZTH with 50 ms risetime would require more than 600 MW of equilibrium power. The chosen geometry requires 16 MW of equilibrium power to reach 2 MA and 70 MW for 4 MA plasma current. An advantage of a decoupled system over one that is not is that the OH and EF controls are independent of each other.

A 50 ms risetime requires about 1-kV in the toroidal direction. To stay within reasonable state-of-the-art technology of large coil fabrication and switching (specification 5), the maximum coil voltage should be limited to about 50-kV. Hence the number of OH coil turns should be about 50. But simulations argued the need for more than 10 megampere-turns in the OH coil to obtain required volt-seconds or with 50 turns the OH coil current must be about 200-kA, a value too large for presently available, reasonable cost, opening switches. The solution to this dilemma, borrowed from the Padova RFX design, consists of four interleaved coil sections in series, with each section made up of 64 OH turns in parallel with 64 turns from each of the four EF coil pairs. The number 64 was a compromise in meeting the constraints of the design.

The combination of specifications 2 and 4 forced the selection of the number and size of the TF coils. With 48 coils, access was sufficient but the mean minor coil radius to meet specification 4 is 60 cm. Because of the large radius of the TF coils and specifications 2 and 3, the EF coils could not be placed close to the liner, and simple methods for locating EF coils to optimize coupling and passive equilibrium from induced EF currents could not be employed. An advantage of the outward location of the EF coils is that fewer are needed to meet specification 3. Only three coil pairs (three above and three below the midplane) could have been used. The decision was to use four pairs to improve the capability of the equilibrium control system.

There are several important consequences to the placement of EF coils relatively far from the liner compared to the ideal location on the liner. The greatest disadvantage of the ZTH EF coil location is a nonnegligible increase in OH coil and energy system cost over an ideal configuration, but a significant advantage is the reduction in the size of EF coils allowing required diagnostic access. A large leakage inductance results from this EF coil location that reduces the ZTH transfer efficiency to 60 per cent of the ideal maximum value, requiring a 40 per cent increase in OH coil volt-seconds and power over that for the ideal geometry. The leakage inductance also reduces the induced ampere-turns in the EF coils, and for ZTH this results in forces on the EF coils that are less than one-half that for the ideal configuration. As a consequence, the ZTH EF coils are smaller and require less equilibrium power to supply resistive losses compared to the ideal. EF coils of the early conceptual design were nearly the same size as the 4 MA ZTH design and an early attempt to scale up the conceptual design to 4 MA resulted in EF coils that weighed almost as much as the OH coils. Because of the large separation of the EF coils from the liner, the EF coils cannot act as a shell to limit plasma motion on the short time scale as for Doublet or RFX. An accurate

equilibrium control system with fast power supplies or the combination of a thin shell and slower supplies are required. ZTH EF coils could provide equilibrium for a plasma current of 6 MA with additional support against bending.

Selection of the plasma major radius required many iterative calculations to satisfy the specifications. During the past seven years it grew at a monotonic but unsteady average rate of 10 cm each year. It would have been desirable to accurately calculate the total experiment cost as a function of major radius R. But many functions required for this calculation are difficult to quantify. For example, the effort required to design the coil and load assembly tend to increase with decreasing R but in quantized jumps. A recent attempt to decrease R from 2.4 m would have caused interference between TF coils and the support bulkheads, requiring a different and more expensive structure of greater complexity.

Opening switch rating had the greatest effect on the determination of R. Volt-seconds consumed by the plasma during current rise probably varies directly with R. Magnetic energy transfer efficiency for configurations that meet the specifications increases with R to a power slightly less than one. Optimized OH coil inductance varies approximately as R(OH coil) to the 3/2 power. Combining these approximations leads to the conclusion that the required OH coil current varies roughly as 1/R, a result with important implications regarding opening switch rating. At the onset of the ZTH magnetics design there was one proven opening switch design of reasonable cost rated at 25 kA, 50 kV. Testing of two of these switches in parallel for a 50 kA rating had been carried out at Los Alamos successfully. A 75 kA switch is less reliable than the 50 kA tested switch and characteristics were not known. Selecting the ZTH opening switch rating at a nominal 50 kA set the OH coil inductance and hence the OH coil radius. The value of R then was determined by the spacing required for EF and TF coils and access specifications.

PF Coil Optimization

The problem of upgrading the ZT-H conceptual design to 4 MA has been mentioned. Equilibrium power of this design was excessive at even 2 MA. Required was a procedure that would provide:

1. Low magnetic field in the liner region from the OH coils,
2. Decoupling of OH and EF coils so that induced EF currents would be proportional only to plasma current,
3. Smaller EF currents for reduced forces leading to reasonable coil size,
4. Induced EF coil current distribution that would meet flux surface deviation specifications for a specified Shafranov Λ value, and
5. A coil arrangement that would meet the diagnostic access specification and allow a reasonable structure.

Separate optimization of OH and EF coils did not yield the required decoupling of the two sets. Both had to be optimized simultaneously. It would have been desirable to minimize only one function (residual), the total cost of the experiment. But optimizer routines that minimized the sum of squares of residuals did not work, implying that working only with the total cost likewise would not also, even if unlimited time and resources were available to construct such a routine. A linear optimizer did not work. Nonlinear optimizer routines that minimized only one residual tended to get stuck in the maze of valleys and bayous of the hyperspace of the many variables.

The nonlinear optimizer subroutine that obtained satisfying results, written by Ken Klare of group CTR-8 at LANL, is a modified Gauss-Newton procedure that operates on all of the residuals simultaneously, using both Jacobian and Hessian matrices. The modifications included the addition of a hook feature that allowed the routine to bypass Jacobian singularity difficulties. Previously tried optimizer routines were unsatisfactory because solution residuals and variables depended on the initial values, requiring many different starting points to approach the best. The Klare routine arrived at the same solution for a wide range of starting values, a result that provided confidence that the solution was the best possible for the constraints of the problem.

About 80 per cent of the optimizer programs evaluated the residuals, and most of the rest was the optimizer subroutine. The program was run in several different forms with 13 to 20 variables. Several different sets of variables were tried. Initially a set of 16 OH coil pairs obtained a field within the liner of less than 1 mT. But interleaving was difficult and the cost of 16 sets of tooling for fabrication would have been too expensive. With a proper set of 15 variables and 69 weighted residuals the optimizer obtained a reasonable compromise that met the specifications with only 5 OH coil pairs.

Figure 1 shows the coil locations. OH coils are 1 through 5 and EF coils are 6 through 9. Variables were the radius of coils 1 through 4, and 6, the height above the midplane of coils 2, and 4 through 8, and the four EF coil induced currents. The radius of coil 7 and height of 9 were fixed by access requirements. Because the optimizer tended to increase the radius of 5 beyond that which would fit through the torus hall door, its radius was fixed. Similarly, the height of 3 was fixed because the optimizer wished to locate it where it interfered with the torus hall crane. To minimize leakage inductance, coils 8 and 9 were placed as close to the TF coil as tolerance requirements would allow. Height of 1 was fixed to allow adjustment for tolerance variations.

The residuals were:

1. magnitude of B resulting from OH coil current at 23 points on the liner,
2. variation of flux due to EF and plasma currents at 23 points on the liner,
3. variation EF and plasma current flux at the EF coils,
4. variation of the elements of the first column of the inductance matrix from a specified input parameter, the desired OH value,
5. four coupling coefficients between OH and EF coils,
6. difference between induced EF currents and those required for minimum deviation of the flux surface at the liner,
7. difference between induced EF currents and a specified distribution,
8. two penalty functions to prevent the optimizer from causing structure problems by placing coils 2,3,6 too close to each other.

The redundancies in some of the residual functions were necessary. Transfer efficiency is approximately proportional to the OH coil inductance of 4 above. This parameter was as large as possible in the compromise to meet the specifications. For calculating the flux surface deviation, (d) the plasma current was represented as a single filament located at a radius equal to 1.003 times R. This location was chosen to obtain the least d with EF coil currents that provided an index of 0.3 and a vertical field (Bv) calculated from the Shafranov formula for A equal to -0.3. A solution of the full Grad-Shafranov

equilibrium equations confirmed the adequacy of the approach. The immobile single wire plasma representation provides the best test of the capability of the EF coils to form a minimum deviation flux surface. Effects of the shell and liner on flux surface deviation were not included. The inductance matrix was calculated with the liner forced to be a flux surface. Residuals 7 above were used to reduce current in the outer EF coils to minimize forces and hence size of these coils.

Results of the Optimization

The Gauss-Newton-hook optimizer routine of Ken Klare worked so extraordinarily well that it not only solved the required problem but also allowed the reduction of the number of OH coils to five pairs, simplifying the structure and reducing the total OH coil cost. With fewer OH, coils assembly and disassembly time is reduced. The greatest optimizer weight was placed on decoupling and achieving passive equilibrium at the initiation of plasma current. This weighting and the reduction of the number of OH coils did not obtain an ideal low value of residual B field within the liner due to OH coil current. Maximum calculated B within the liner is 10.4 mT. However, with 28 k-amp-turns in the trim coils or the EF coils at initiation of plasma current, a hexapole null (Fig. 2) can be obtained on the midplane near the minor axis for ideal plasma breakdown conditions.

Table 1a lists the oneturn equivalent reduced inductance matrix, and table 1b lists the coupling coefficients for the EF coils in functional form for vanishing coil resistance. The numbers of column 1 (decoupling coefficients), which should ideally be zero for complete decoupling, are unrealistically small because of tolerance and nonideal winding effects. Induced EF coil currents caused by plasma current are given by the coefficients of column 2. These induced currents are within a few per cent of those from a Grad-Shafranov equilibrium calculation.(2)

Table 1c lists sensitivity factors for errors in coil fabricated radius or in placement. The first 9 rows of 1c are for a 1 cm increase in coil radius and the last 9 rows are for a 1 cm increase in height location above the midplane, all taken one at a time. The first 4 columns are multipliers of the decoupling coefficients, and the next 4 columns apply similarly to the coupling coefficients between EF coils and plasma. The last two columns are multipliers of the residual B within the liner due to OH coil current and multipliers for flux surface deviation. For example, if the radius of coil 2 were increased by 1 cm over the design value, the decoupling coefficient would change sign and increase in magnitude by a factor of 464. Similarly, the coefficient of coupling between plasma and coil 6 would decrease 1 per cent, magnitude of B within the liner due to OH current would increase 10 per cent, but flux surface deviation would not change.

A 50 per cent increase in B within the liner because of a 1 cm error in the radius of coil 1 can be offset by initial trim current. Obviously, the decoupling factors are most sensitive to coil errors, yet the equilibrium supplies can take care of decoupling factors as large as 0.004 with the 50 mS shell time constant. The mean copper radius of each coil will be determined as accurately as possible and the optimizer will be rerun to determine offsets in the coil heights above the midplane to recover the best realistic decoupling. A calculation showed that such adjustment would be successful. All coils can be adjusted 2 cm in height from the midplane to correct for radius

errors and in eccentric displacement to compensate for eccentric location of copper within the mold. Each coil block shown in fig. 1 actually consists of four sections with separate leads for interleaving. In each block the coil sections are rotated 90 degrees with respect to each other to reduce nonaxisymmetric effects such as crossovers and leads. Copper conductor skin effects were not included, but preliminary calculations show that skin effects are probably not a problem.

Table 1a

[L] (One turn equivalent)

1.904E-06					
1.904E-06	4.549E-06				
1.904E-06	3.078E-06	5.767E-06			
1.905E-06	2.355E-06	3.174E-06	8.016E-06		
1.904E-06	2.270E-06	2.931E-06	5.369E-06	9.484E-06	
1.903E-06	2.538E-06	3.064E-06	4.030E-06	4.205E-06	5.484E-06

Table 1b

Ioh, I-phi coefs of Ief:

I-ef1= 3.139E-06 * Ioh + -1.768E-03 * I-phi
I-ef2= -1.328E-05 * Ioh + -2.345E-03 * I-phi
I-ef3= -1.109E-04 * Ioh + -3.182E-03 * I-phi
I-ef4= 4.234E-05 * Ioh + -2.887E-03 * I-phi

Table 1c

Sensitivity factors for a 1 cm increase in R taken one at a time

	Ioh coefs of Ief				Iphi coefs of Ief				max |B| liner	flux surface deviation
	1	2	3	4	1	2	3	4		
1	327.8	-30.1	-0.3	3.2	0.99	1.00	1.00	1.00	1.5	1.0
2	-463.5	-11.6	0.1	2.8	0.99	1.00	1.00	1.00	1.1	1.0
3	56.8	20.3	-0.1	4.1	1.00	1.00	1.00	1.00	0.8	1.0
4	144.1	50.5	2.9	-1.0	1.00	1.00	1.00	1.00	0.8	1.1
5	38.5	-9.1	-0.5	-1.4	1.00	1.00	1.00	1.00	1.0	1.0
6	-95.8	-6.1	1.0	1.0	1.01	0.99	1.00	1.00	1.0	1.0
7	-31.8	-18.3	1.4	0.7	1.01	1.00	1.00	1.00	1.0	1.0
8	1.5	-0.7	2.0	2.2	1.00	1.01	0.97	1.00	1.0	1.1
9	1.0	1.1	1.1	1.3	1.00	1.00	1.02	0.97	1.0	1.3
	Factors for a 1cm increase in Z									
1	-268.7	14.5	1.5	0.3	1.00	1.00	1.00	1.00	0.9	1.0
2	-302.4	13.2	0.8	2.1	1.01	1.00	1.00	1.00	0.7	1.0
3	263.0	21.9	2.5	-1.6	1.00	1.00	1.00	1.00	0.9	1.0
4	110.3	-38.4	1.9	-0.5	1.00	1.00	1.00	1.00	1.0	1.0
5	-28.0	6.7	-0.3	6.4	1.00	1.00	1.00	1.00	1.1	0.9
6	42.3	3.9	1.0	1.0	0.94	1.01	1.00	1.00	1.0	1.0
7	12.5	7.7	0.9	1.1	1.03	0.96	1.01	1.00	1.0	1.0
8	0.8	1.3	0.8	0.8	1.00	1.00	0.98	1.02	1.0	1.1
9	1.1	0.6	0.7	-0.5	1.00	1.00	1.00	0.99	1.0	1.2

A large number of 0-D Culham coupled model simulations were carried out during the magnetics development to insure that SCR type power supplies of reasonable size could be used. The CTR circuits program SCAT was employed for all simulations. Figure 3 shows some of the outputs of one simulation where supplies attempted to maintain a constant plasma current (I-phi) of 4 MA following inductive energy transfer and attempted to maintain a constant value of θ by feedback control of the B-phi SCR supply. Figure 3d shows d, the flux surface deviation, where I-phi is represented as a single filament as discussed above. An ad hoc plasma resistance function was chosen so that I-phi reached 2 MA at the end of inductive energy transfer (14 volt-seconds at the liner). This function was inversely proportional to I-phi (constant resistive voltage) and decreased as F passed through zero, characteristic of ZT-40M data. Variable name Imag of Fig. 3f is the OH coil current where the four sections are in parallel for a more simple circuit representation (maximum OH current is 4 times 50 kA). The negative spike in the B-phi supply current is unrealistic and will not be allowed in the final TF supply design. Eq #1 refers to coil number 6 (EF6).

Characteristics of the interleaving are illustrated in Figs. 4 and 5. Each of the four series sections consists of a 64 turn OH set in parallel with four 64 turn EF coil sets where the sets are chosen to obtain the best match of induced current and voltage between the sections. The computer tried some 992,000 combinations of the most logical choices to find the best. Figure 4 shows circuit currents with EF supplies turned off. Variable VL1 refers to voltage across section 1. Supplies are turned on for the calculation of fig. 5 where they attempt to obtain matching of the sections and force EF currents corresponding to equilibrium. The upper right plot, Fig. 5b, shows satisfactory matching of the sections of EF6, similar to that of the other EF coils. Required supply voltages are shown in the lower 4 plots. It would appear that the EF supplies can easily obtain a good match of the section currents.

The last test of the magnetics design was the simulation using a model that approximated plasma motion to determine if the EF coils and supplies could control equilibrium if, for example, the Shafranov Λ changed rapidly. For this model the shell, liner, and plasma were each represented by 24 pairs of filaments or wires located symmetrically about the midplane. To reduce the inductance matrix to a manageable size the wires were connected in series in groups of 3 above and 3 below the midplane to obtain 8 inductive circuits each for the shell, liner, and plasma models. A resistance equivalent to a section of the shell or liner was placed in series with the corresponding inductor. Shell elements are connected in parallel with no closed path so that the net toroidal shell current must be zero. Liner and plasma element connections allow net toroidal current. With one OH and 4 EF coil sets, there are 29 inductors coupled by 406 mutual inductances.

Because the single ring of plasma wires cannot adequately represent the actual radial current distribution of a real plasma and the resulting internal plasma inductance, an ad hoc inductor and resistor was placed in series with the parallel plasma wires to obtain a more realistic plasma current risetime. The purpose of the simulation was to verify the adequate response of the EF coils and SCR supplies in controlling equilibrium, not to simulate the real internal plasma equilibrium problem. However, a future simulation could employ a radial distribution of plasma wires where the wire current distribution is determined such that the force on each wire is minimized.

Horizontal motion of the plasma is simulated by shifting the current distribution in the plasma wires (inductors) by using voltage sources in series with each inductor. Source coefficients are chosen so that the net plasma current is not changed by action of the sources. Source voltage is proportional to the difference between actual Bv due to all wire and coil currents and the Shafranov Bv calculated using the value of plasma current and an input Λ. The initial Λ is -0.3, corresponding to li of 1.4 and β-p of 0. Constant li is used due to the assumption that a constant Θ mode is employed during current rise. Shifting plasma wire current distribution induces currents in the liner and shell, producing a restoring Bv before the equilibrium control system can respond.

Figure 6 shows the location of coils and wires. Note that the shell wires are shifted inward 8 mm to limit the initial flux surface deviation. Equilibrium supplies are modeled using realistic SCR characteristics of control delay, turnoff delay, and chopping.

Equilibrium feedback control is accomplished with an algorithm that continuously estimates from several liner flux loop signals, the least change in each EF coil current necessary to minimize flux surface deviation. Calculating the least change in current minimizes EF power and tends to prevent driving EF coil current beyond the rated value. In the experiment, liner flux signals are obtained from flux loops and correction coils. In the model they are calculated from all of the wire and coil currents. Use of only four flux loop pairs resulted in an exact match of flux at the four locations but allowed unacceptable deviation of the flux surface between them. Sixteen loops provided the least flux surface deviation but eight were satisfactory.

The feedback algorithm requires calculating (measuring) the 8 by 4 mutual inductance matrix [L] that relates the flux at the eight loops to the four EF coil currents. A solution to these equations that supplies the ΔI that minimizes the $\Delta\psi$ ($\Delta\psi$ is the difference between a flux loop signal and the average of the signals) is not satisfactory because under many conditions the ΔI is so large that the time required for the change allows the flux surface deviation specification to be exceeded. Increasing the power supply voltage rating is too expensive. The difficulty is resolved by adding 4 rows to [L] to minimizes the ΔI and obtain the $\Delta\psi$. These added rows are a diagonal matrix with weights for minimizing the ΔI as the diagonal terms. The generalized inverse of the resultant 12 by 4 matrix (equivalent to a least squares solution of the 12 equations for the 4 ΔIs) is a 4 by 12 matrix, the first 8 columns of which are the summing weights for the equilibrium control circuit. For example, the control input to EF supply 2 consists of the weighted sum of flux loop signals where the weights are the first 8 elements of the second row of the inverted matrix.

The above algorithm is unstable because of the delays introduced by shell diffusion, EF coil inductance, and the SCR supplies. However, as was found for the Asdex experiment, the addition of a preprogrammed reference signal to the above control output, can stabilize the system. A faster response is obtained by adding the time derivative of the control signal to the above sum. Previous history or a best guess of the required EF coil current as a function of plasma current may be used for the preprogrammed signal. This equilibrium control algorithm can be implemented with either digital or analog circuits. The weighted sum of flux signals could consist of a simple summing amplifier. There are obvious advantages and disadvantages to either approach.

Of concern was whether [L] above was ill-conditioned as a result of the optimized location of the EF coils. Such was not so, and in fact the elements of the inverted matrix have a relative narrow range allowing simple choice of summing resistors for the analog implementation of the control logic and integer logic without level shifting for a digital implementation, probably.

Figure 7 depicts the results of the wire model simulation employing the above control scheme. The ΔI weight was 0.25 and the preprogrammed reference was obtained from simulations of the single wire model for a constant Shafranov Λ of -0.3. Each EF power supply was requested to provide a voltage proportional to the control signal Ec.

$$Ec = 0.2(Ip-Ia) + \Delta I + .001\ d/dt(\Delta I),$$

where Ia is the actual EF coil current, Ip is the preprogrammed estimate, and ΔI is the algorithm output estimate of the change to improve the flux surface deviation. The equilibrium system simulation was not optimized. It was run only to show that the system could perform satisfactorily. A simulation that included the trim coils showed that they could further improve the system by reducing flux surface deviation to less than 2 mm, a result that is probably meaningless considering dimensional tolerances of the liner, shell, flux loops, and coils.

For the simulation of Fig. 7, a low resistive loop voltage was used to reduce the time span of the calculation. Plot (b) is the flux surface deviation, (d) is the poloidal β input function, (e) and (g) are the shell currents per 7.5 degree sector spaced 22.5 degrees apart, (i) through (l) show the actual and demand EF currents on the left scale and supply voltage on the right, and (m) and (n) show four of the liner and plasma wire currents. Note that aliasing obscures the detailed structure of the EF supply voltages. Maximum EF supply voltage was 1.2 kV.

Conclusion

A method devised to optimize ZTH OH and EF coil locations has provided a design that meets specifications including minimizing costs. Several types of circuit simulations show that the design will with high probability be capable of plasma boundary flux surface control with EF supplies rated at a power level only slightly greater than that required to supply resistive losses for the maximum current rating of the EF coils. EF coil current rating is 25 per cent greater than the currents required for equilibrium at 4 MA and Shafranov Λ of -0.1.

Acknowledgments

We acknowledge the contributions of the Los Alamos RFP team for discussions and reviews of this effort, in particular that of D.A.Baker, J.N.DiMarco, H.J.Boenig, A.J.Giger, K.A.Klare, L.W.Mann, J.G.Melton, G.Miller, J.A.Phillips, M.M.Pickrell, and K.F.Schoenberg.

References

1. G. Malesani, G. Rostagni, "The RFX Experiment," Proc. of the 14th Symposium on Fusion Technology, Avignon, 1986. pp173-184
2. D.A.Baker et al, "Plasma Equilibrium for ZTH," This conference

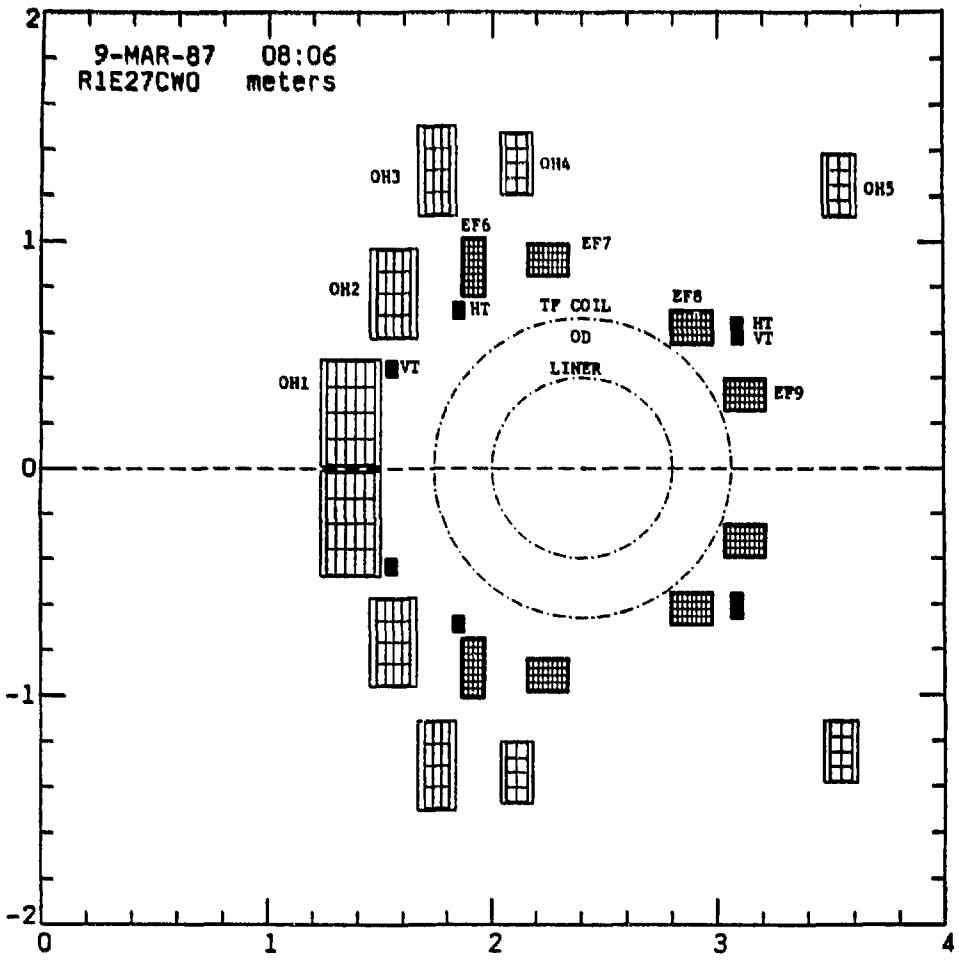

Fig. 1

PF Coil Configuratio

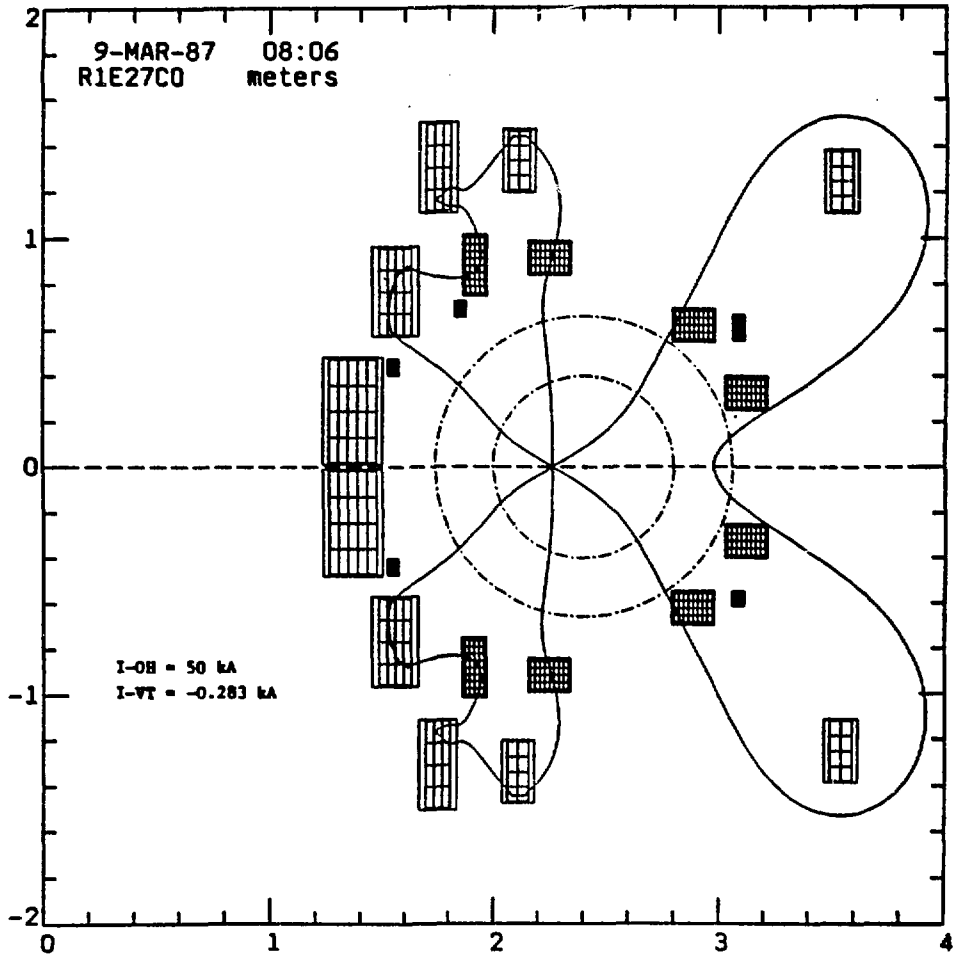

Fig. 2

Flux Surfaces

Fig. 3

O-D Culham Coupled Model Simulations

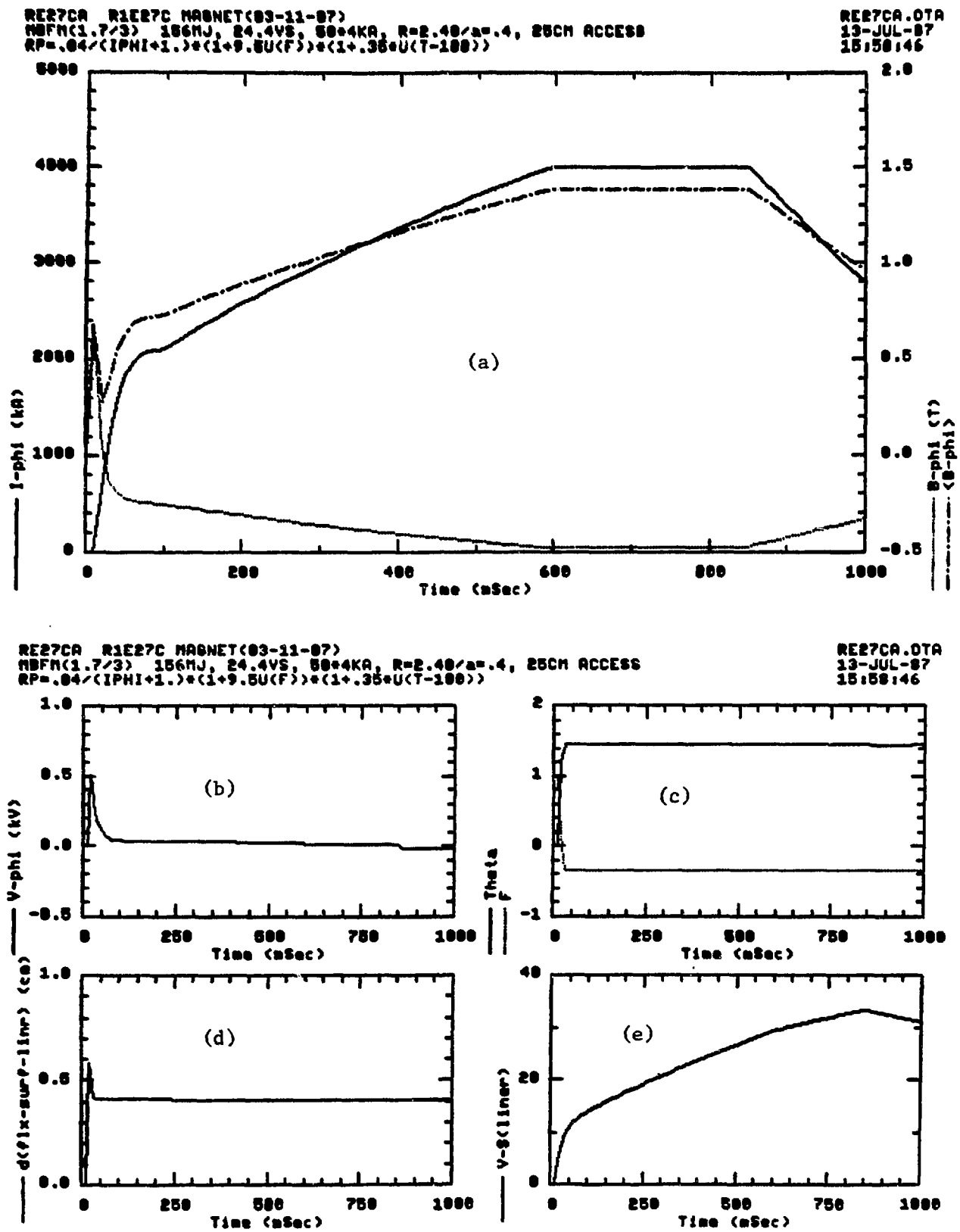

Fig. 3
O-D Culham Coupled Model Simulations

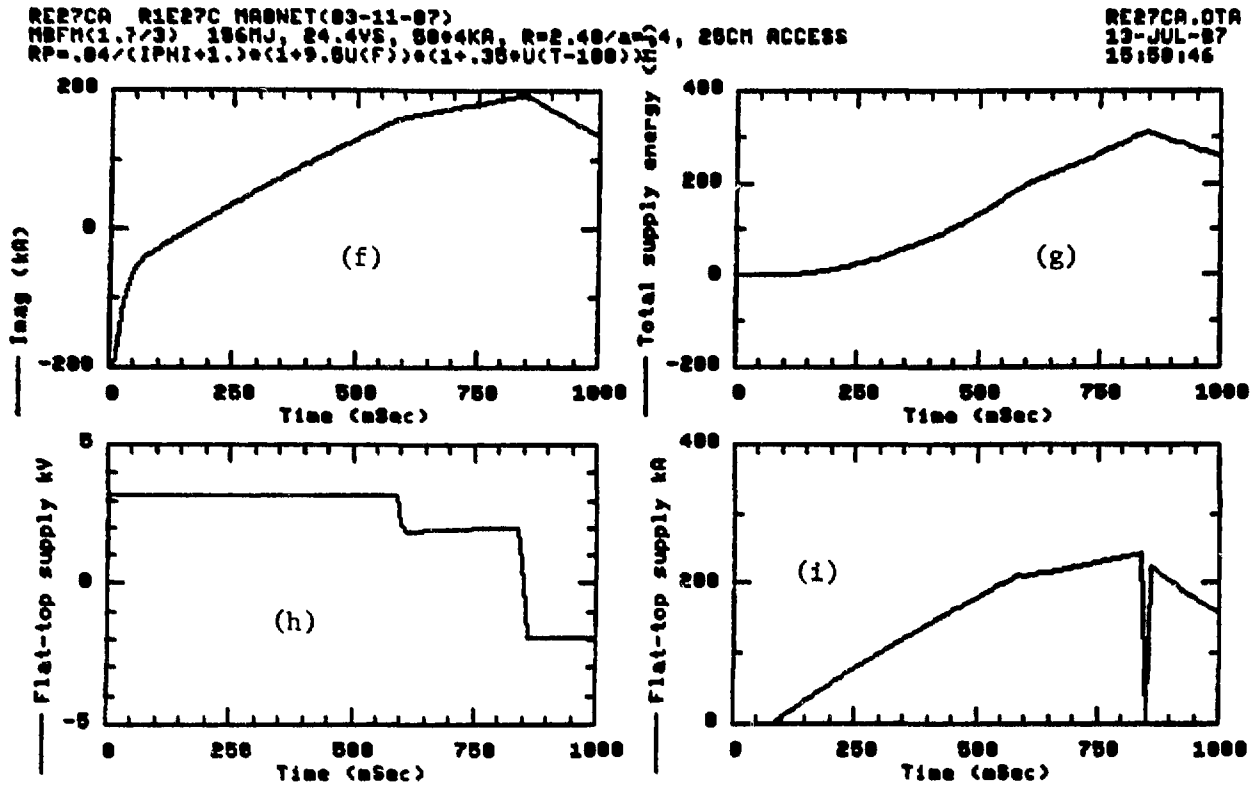

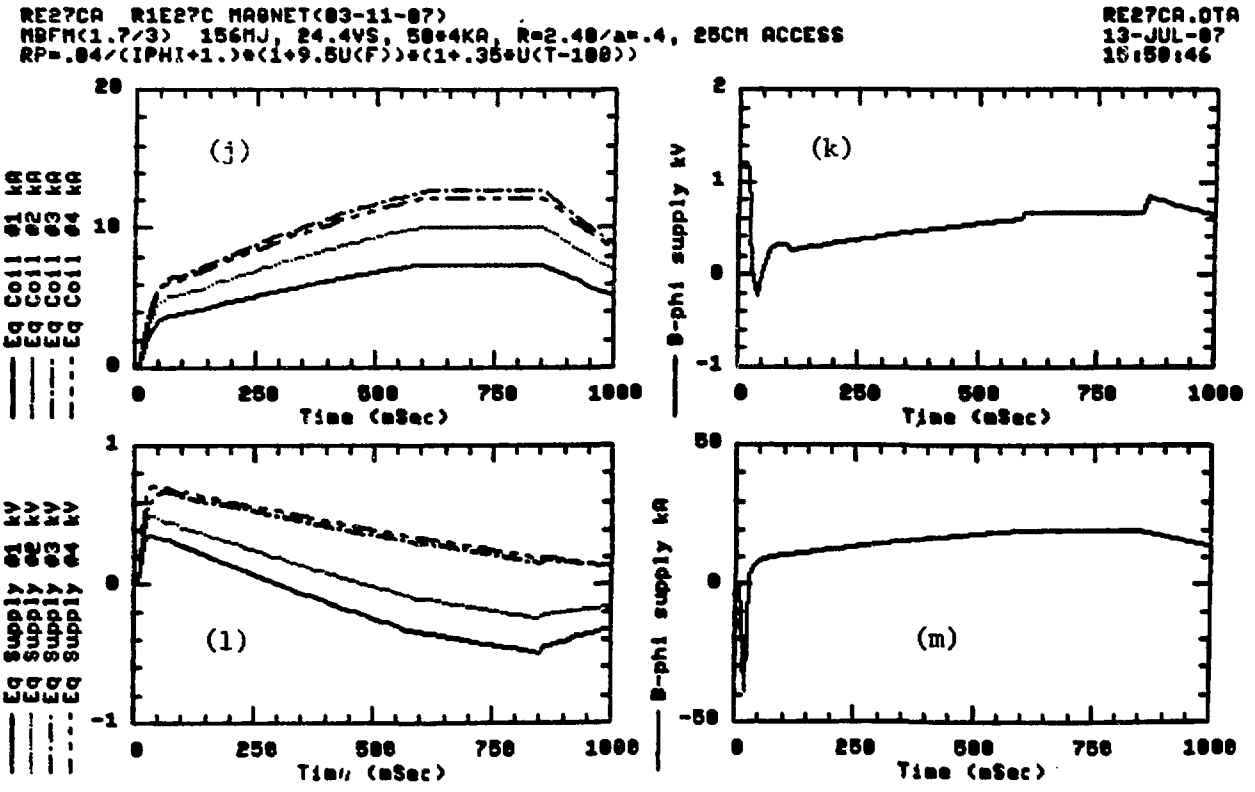

Fig. 4
PF Circuit Simulations for Four Interleaved Sections with EF Supplies Turned Off

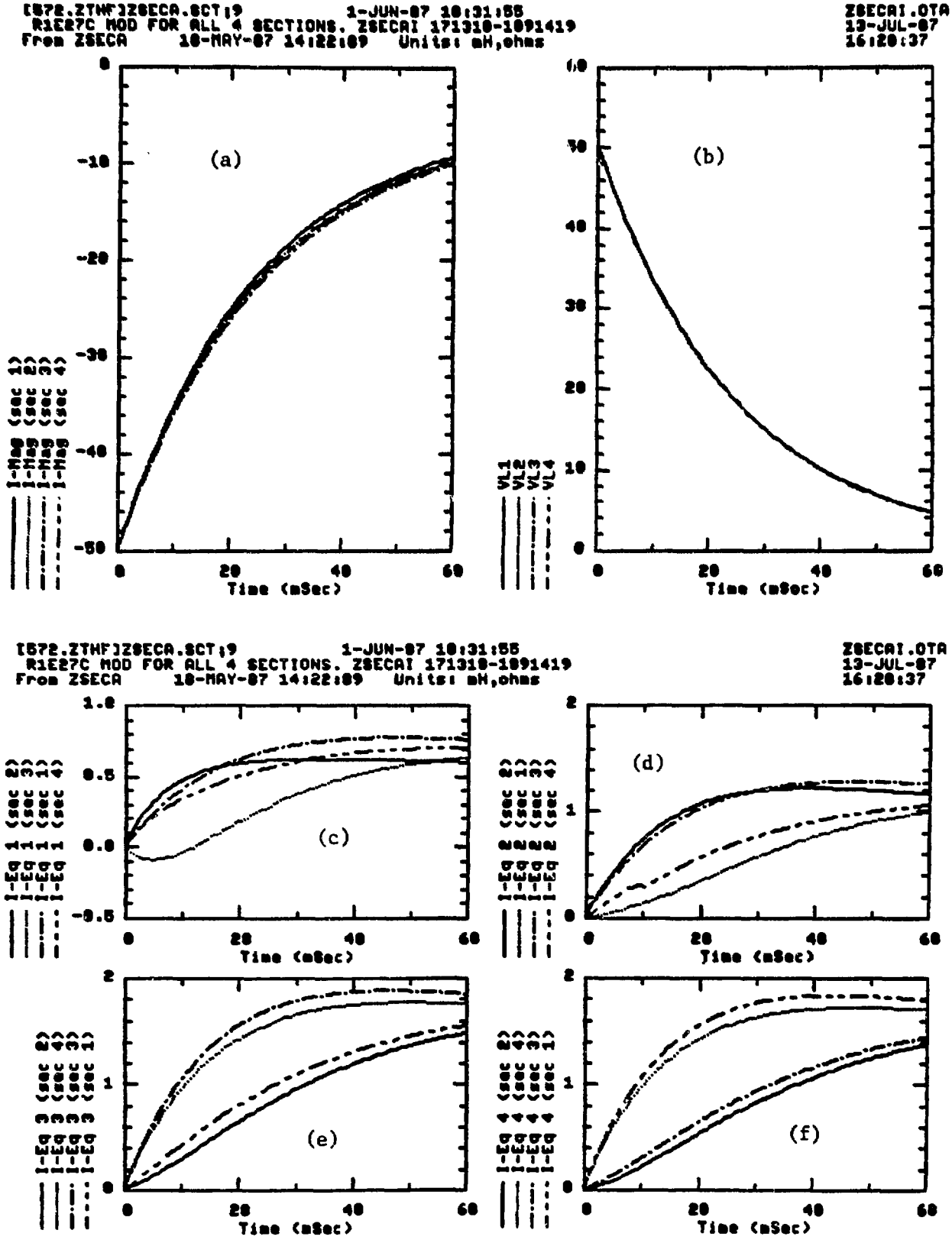

Fig. 5
PF Circuit Simulations for Four Interleaved Sections with EF Supplies Turned On

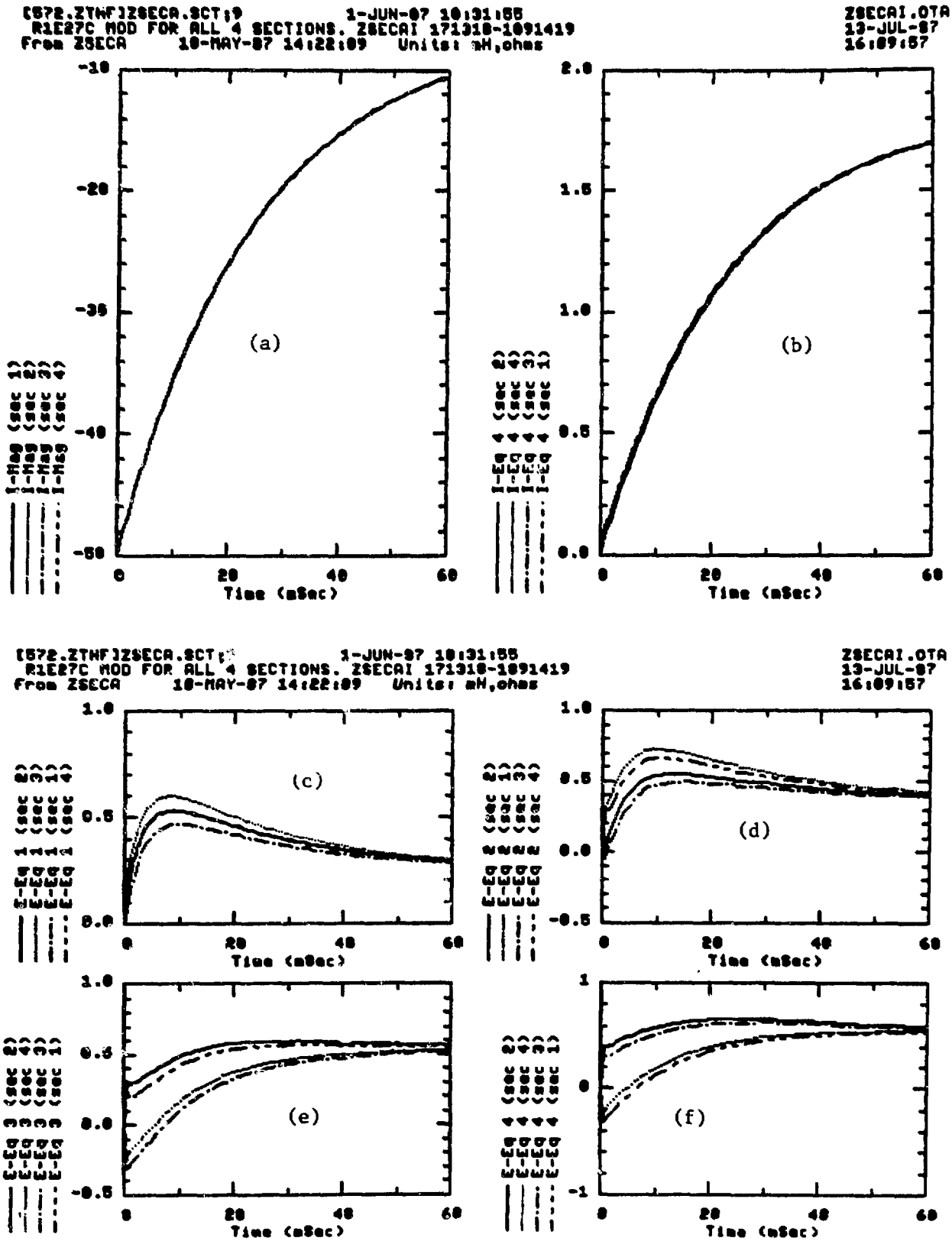

Fig. 6

Wire Model Configuration

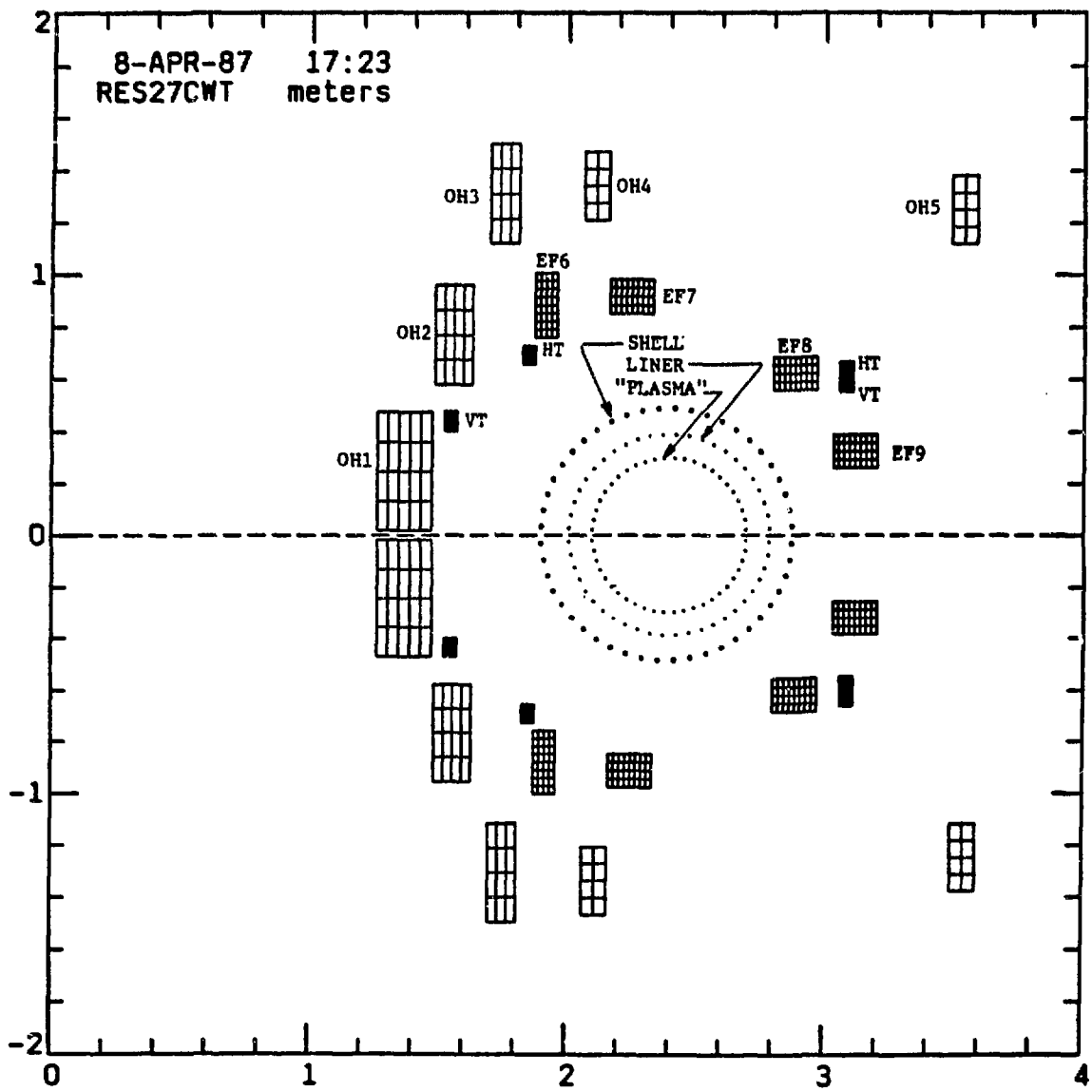

Fig. 7

Wire Model Simulations

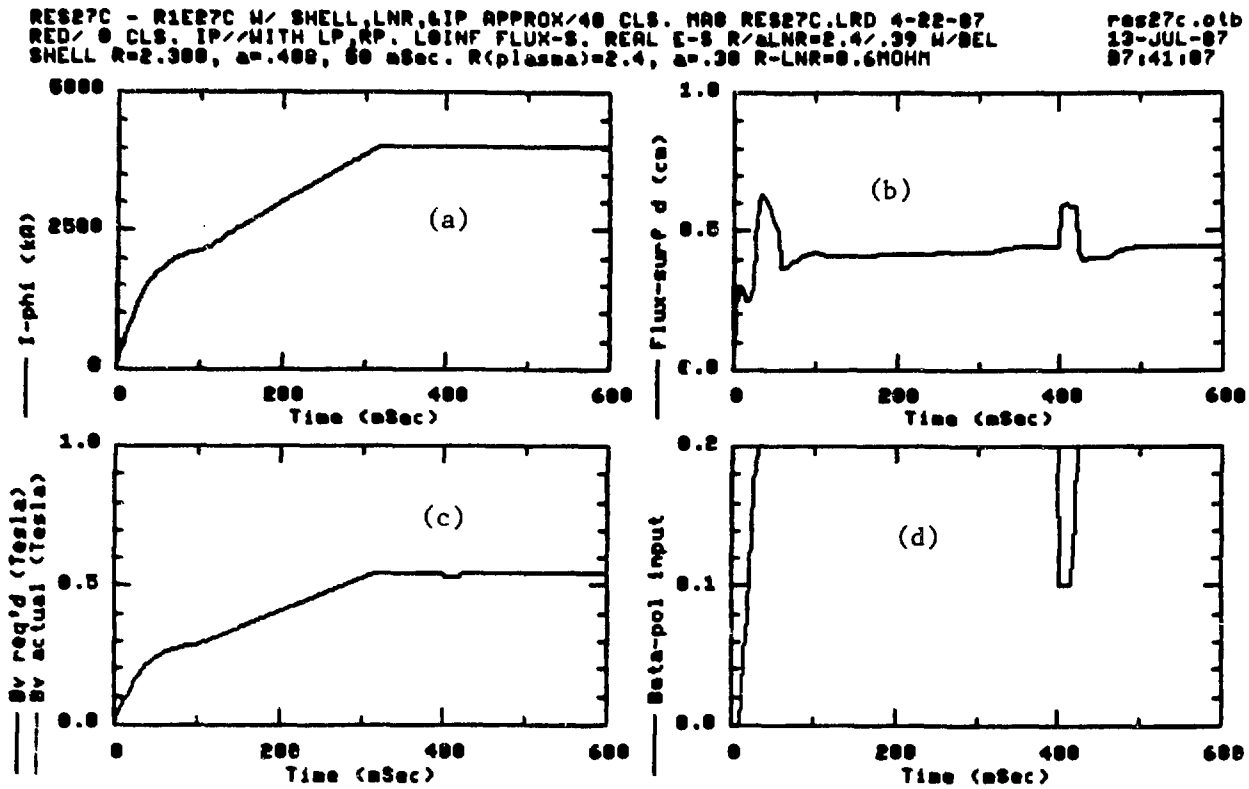

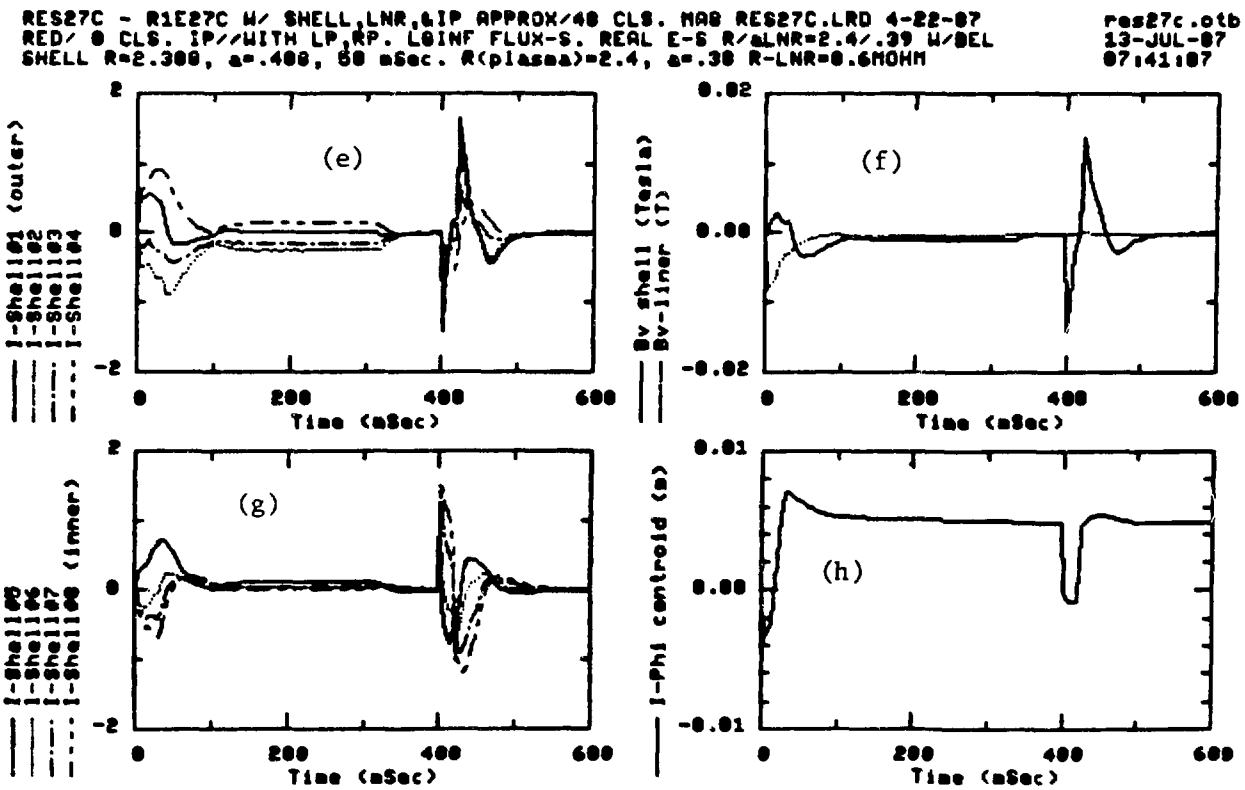

Fig. 7
Wire Model Simulations

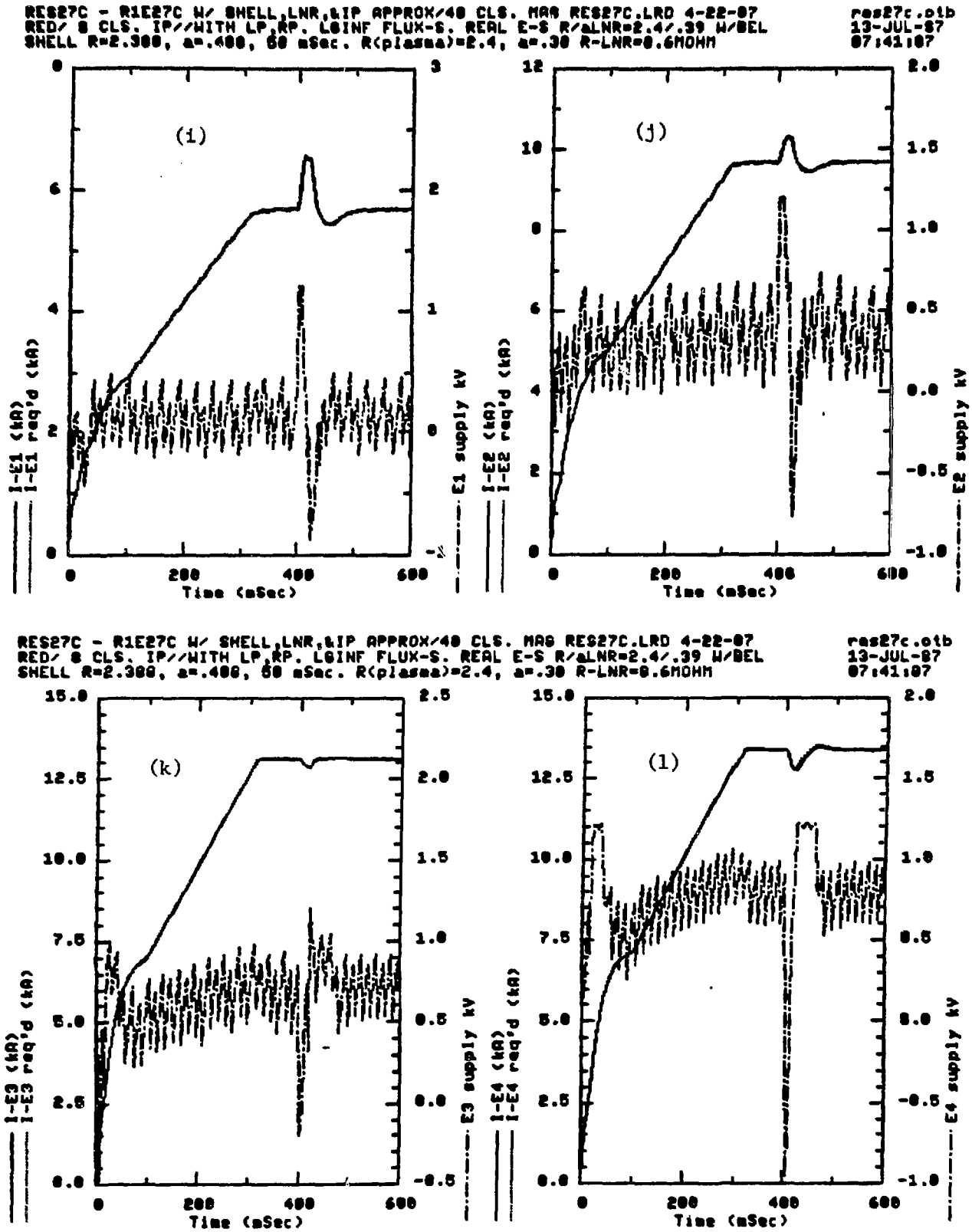

Fig. 7

Wire Model Simulations

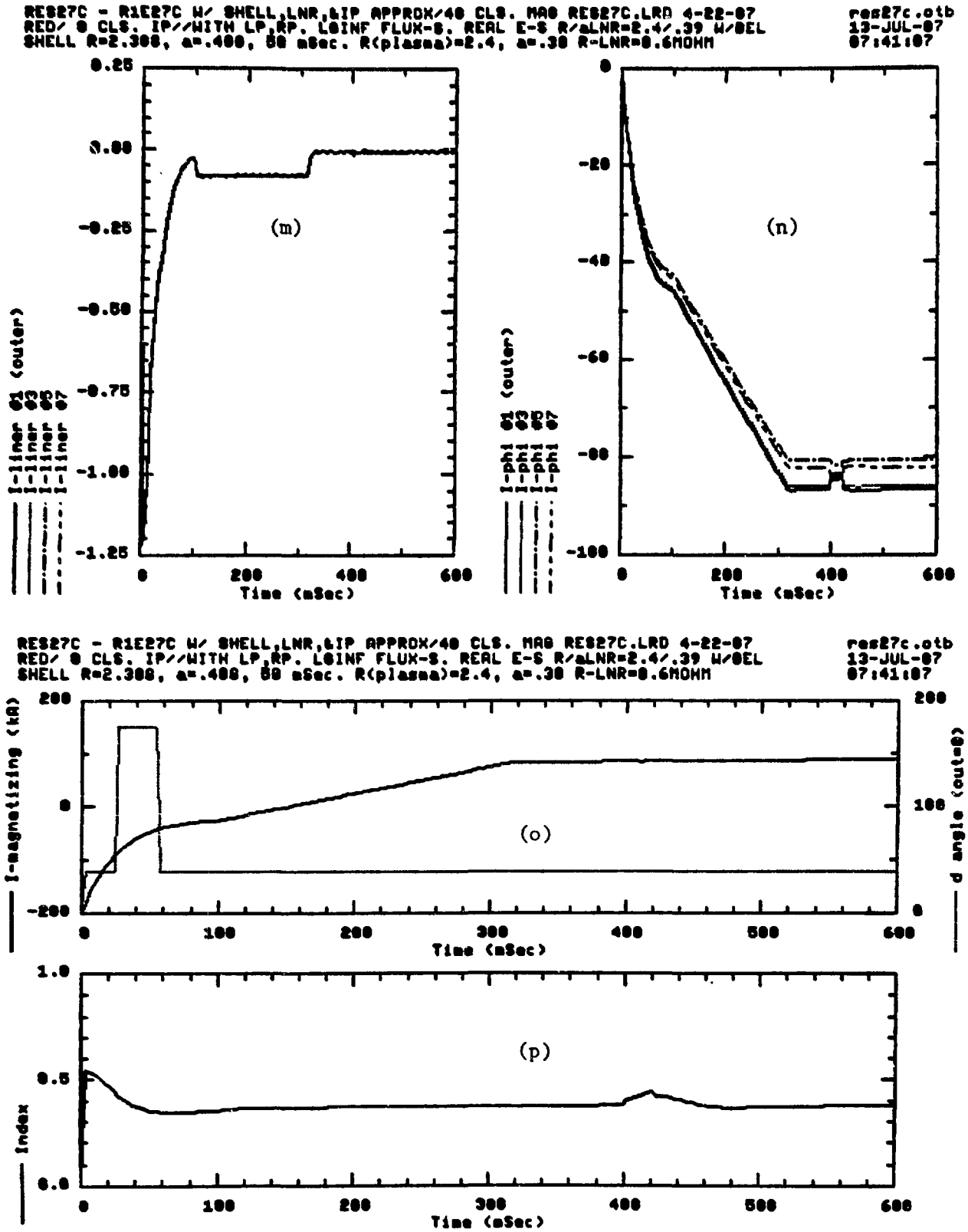

PLASMA EQUILIBRIUM FOR ZTH

D.A. Baker, R.F. Gribble, M.S. Hoyt and K.M. Ling
Los Alamos National Laboratory

I. Introduction

We present here the rationale and considerations concerning the equilibrium and feedback used in the design of the ZTH experiment. In this paper, the ohmic heating (OH) and equilibrium (EF) coil locations are prescribed. Their locations have been determined to satisfy many constraints as described in the magnetics paper by R. Gribble.[1] In particular the arrangement has been chosen so that the OH coils produce a negligible field in the plasma region and, with the plasma present, the induced currents in the EF coils produce the correct vertical field for a nominal equilibrium.

The general class of static scalar pressure MHD equilibria are described by solutions of a pair of Maxwell equations and pressure balance:

$$\text{Div } \mathbf{B} = 0, \tag{1}$$

$$\text{Curl } \mathbf{B} = \mu_0 \mathbf{J}, \tag{2}$$

$$\mathbf{J} \times \mathbf{B} = \nabla p, \tag{3}$$

where **B** is the magnetic field, **J** the current density and p the plasma pressure (mks units). We can eliminate **J** by substituting from Eq (2) into Eq (3)

$$\text{Curl } \mathbf{B} \times \mathbf{B} = \mu_0 \nabla p \tag{4}$$

A second form of the equilibrium equation is obtained by taking the vector product of **B** with Eq. (3) and solving for **J**:

$$\mathbf{J} = \mu_o^{-1} \lambda \mathbf{B} + (\mathbf{B} \times \nabla p) / B^2 \equiv \mathbf{J}_{\parallel} + \mathbf{J}_{\perp}. \tag{5}$$

λ is a function of space but must satisfy a condition [2] so that Div **J** = 0 as required by Eq (2).

We then again eliminate **J** by substituting this form of **J** into Eq. (2).

$$\text{Curl } \mathbf{B} = \lambda \mathbf{B} + \mu_o(\mathbf{B} \times \nabla p)/B^2. \qquad (6)$$

II. One Dimensional Cylindrical Equilibria

For design purposes one-dimensional-cylindrical equilibrium models are particularly useful because of their simplicity. Toroidal corrections to the circular cylindrical case describing the toroidal shift and toroidal equilibrium vertical field are readily obtainable from the Shafranov formulas.[2,3] The shift formula has been shown to give $\leq 15\%$ accuracy for an RFP configuration provided the toroidal aspect ratio > 2, poloidal beta $\leq 50\%$ for shifts less than 10% of the minor radius of the boundary circular cross-section.[4] As discussed in Sec. III, these solutions can be used as input to compute corresponding fully 2-D equilibria.

A. Models with Pressure and/or Field Components Specified

For a 1-D equilibrium depending only on the radial coordinate of a cylindrical coordinate system (r,θ,z) the zero divergence condition and boundedness on **B** and **J** are easily satisified by setting B_r and J_r to zero. We then seek solutions for Eq (4), or alternatively Eq. (5). In the first instance Eq. (4) becomes first order differential equation containing the three functions $p(r)$, $B_\theta(r)$ and $B_z(r)$:

$$\mu_o dp/dr + d/dr(B_z^2/2) + r^{-1}B_\theta d(rB_\theta)/dr = 0 \qquad (7)$$

Mathmatically there is a lot of freedom in the choice of equilibria. In particular, one is free to choose any pair of these functions and solve for the third using eq. (7). More generally one is free to choose two additional relationships between the three functions to define the problem for appropriate boundary conditions. Specifying B_θ, B_z and solving for p has often been done in the past when the field components were measured with internal magnetic probes. We avoid this choice in our modelling since the $p(r)$ function is very sensitive to the variations in the field components and rather unlikely pressure profiles can easily result. Many trial and error choices for B_θ and B_z may be needed before a desirable pressure function results. In the past we have used both combinations of the choices of pressure and one

field component. Specifying B_θ and p leads to solving for B_z^2 and an explicit choice of the sign of a square root is required when the field reverses. We used the specifications of p and B_θ for the modeling of the ZT-40M design.[4] For the RFP, a particular advantage of specifying p and B_z is that the amount of field reversal can be chosen apriori.

B. Models with λ Specified

When one is interested in equilibria obtained by specifying the parallel current parameter $\lambda(r)$, Eq. (6) is useful. For the cylindrical 1-D case under discussion, this vector equation leads to the following equations describing the field components.

$$dB_z/dr = -\lambda B_\theta - \mu_o(B_z/B^2)dp/dr, \tag{8}$$

$$dB_\theta/dr = \lambda B_z - B_\theta/r - \mu_o(B_\theta/B^2)dp/dr. \tag{9}$$

For a choice of λ (r) and p(r) this set can be integrated to obtain the magnetic field.

1. Force Free Models

The class of 1-D cylindrical force-free models are the solutions of Eq. (8) and (9) with $dp/dr \equiv 0$. The choice $\lambda(r)$ = constant leads to the Bessel Function Model (BFM). The choice λ (r) = constant out to a cut off radius r_c and zero for $r_c < r < a$ (a is the plasma radius) leads to the truncated Bessel Function Model[5] (TBFM). When the BFM is modified so that $\lambda(r)$ falls linearly to zero as r varies from $r = r_c$ to r = a, the Modified Bessel Function Model (MBFM) is generated.[6] See Figure 1. The TBFM and MFBM allow freedom to fit experimental F-θ diagrams while retaining λ = constant inside the radius $r< r_c$. They do, however, contain nonphysical discontinuities in J or its derivative. The choice $\lambda = \lambda_0(1-(r/a)^\gamma)$ has been used to give smooth behavior but both this model and the MBFM require numerical integration to obtain the fields.

A force-free RFP model which has analytic expressions for the fields and has no discontinuous behavior has been obtained.[7] This model allows a generalization with many parameters to accomodate a wide choice for $\lambda(r)$. For

low current discharges in ZT-40M, where internal probe data are available, there are indications [8] that λ (r) may peak away from the minor axis so that the above models with flat λ(r) on the interior may be to restrictive.

2. Models with λ(r) and Plasma Pressure Specified

Plasma pressure can easily be added to the above models by adding a pressure function keeping the same λ(r) and integrating Eqs. (7) and (8). There is a wide choice of equilibria if λ(r) and p(r) are freely chosen. It should be borne in mind however, that with this approach the amount of field reversal is not an input and non-RFP profiles can easily result. There is a wide choice of functions for pressure. A pressure profile using a two-piece cubic with a continuous dp/dr and prescribed derivatives at r=0 and r=a has proven to be versatile.[4] This pressure model allows hollow, flat, and monotonic profiles. The pressure profile $p(r) = p_o\ (1-(r/a)^\gamma)$ has also been used for analyzing ZT-40M data.[9]

III. Two Dimensional Axisymmetric Equilibria

A. Diffuse Profiles

The general two dimensional axisymmetric equilibria are solutions of the vector equation (4). For this case this equation can be written in terms of a poloidal flux function $\psi = rA_\phi$ where A_ϕ is the toroidal component of the vector potential with **B**= Curl **A**. The cylindrical coordinate system (ρ, ϕ,z) has z aligned along the major toroidal axis. The toroidal angle is ϕ and ρ is the major radial coordinate; the ψ function satisfies the Grad-Shafranov Equation

$$\rho\frac{\partial}{\partial\rho}\left(\frac{1}{\rho}\frac{\partial\psi}{\partial\rho}\right)+\frac{\partial^2\psi}{\partial z^2}+\mu_o\rho^2\frac{dp}{d\psi}+I\frac{dI}{d\psi}=0, \tag{10}$$

where $p(\psi)$ and $I(\psi)$ are specified functions. When ψ has been obtained the magnetic field is computed from

$$\mathbf{B} = \mathbf{B}_{pol} + \mathbf{B}_\phi = (1/\rho)\nabla\psi \times \hat{\phi} + (I/\rho)\hat{\phi} \tag{11}$$

where the caret denotes a unit vector.

For a prescribed boundary where ψ is constant (casing problem), we solve Eq. (11) using the Baker-Mann toroidal equilibrium code [4] which has been used for many CTR problems in the past. For a free boundary with external coils, one must iterate between Green's functions for the coils and the solution including the plasma currents, to produce a self-consistent ψ on the boundary of the computational mesh. For this part of the problem we use a Grad-Shafranov equation solver developed for the case of the unidirectional toroidal fields of Tokamaks at Princeton[10] and later modified[11] to allow toroidal field reversal needed for RFP solutions. The present design calculations use a combination of Los Alamos codes and the Princeton code. In particular, a preprocessor code has been developed (see appendix of Ref (4)) to allow inputs from 1-D cylindrical models for computing a corresponding toroidal solution. This code generates $p(\psi)$ and $I(\psi)$ functions from 1-D cylindrical solutions discussed in Sec. II. One then studies the simpler 1-D problem first and when a cylindrical solution of interest is obtained, a corresponding fully toroidal solution is then computed using a 2-D code in a straightforward manner. This eliminates the time-consuming step of trying to guess $p(\psi)$ and $I(\psi)$ functions to give a solution with the properties desired. This code also generates, from the 1-D solution, a very good starting ψ function to load on the 2-D mesh for iterating to a final solution. A sample comparison of the pressure and field profiles for the 1-D and corresponding 2-D case is given in Fig. 2.

B. Thin Wire Model

For the large number of calculations needed for the exploration and optimization of the field coil configuration with many constraints, a much faster running code is used in which the plasma is represented by a single thin current loop. The vertical field B_v value is the Shafranov value for a specified $\ell_i = < B_\theta^2 > / B^2(a)$ and $\beta_p = \langle p \rangle / (B_\theta^2(a)/2\mu_o)$. ($< >$ denotes an average over the plasma cross-section). The EF coil currents are calculated to provide the Shafranov B_v and a given vacuum field index of about 0.5. The location of the filamentary current that represents I_ϕ is chosen ($> R$) such that the deviation of the largest flux surface within the liner (resulting from the filament and all of the coil currents) from the liner is minimized. This model has been compared with the results of the 2-D equilibrium code using the same coils and agreement with the vertical field value was found

to be within a few percent. This simplified model was used to optimize the coil geometry with the many constraints as discussed in the magnetics paper.[1] The constraints of interest for equilibrium were (1) minimum deviation of the flux surface at the liner, (2) field index in the stable region, between 0 and 1.5 (3) fields of the OH coils negligible in plasma region (4) the mutual self inductances of the system are chosen so that the induced EF coil currents produce the required vertical field for a nominal equilibrium and scales with the plasma current. The optimized coil configuration is shown in Fig. 3.

IV. Feedback Control of the Equilibrium

The general approach being used is to have many toroidal flux loops at the liner which can measure the poloidal flux changes due to displacement of the plasma toroidal current. These signals are then analyzed by analog or digital equipment which determine changes in EF coil current requiring least power to minimize the deviation of the flux surface at the liner.

A. Multiwire Model

The model consists of the actual OH and EF coils with 48 thin circular loops (wires) to represent the shell (thin skin), 48 wires to approximate the plasma, and 48 wires to represent the liner (see Fig 3.). For all three, six wires are connected in series, 3 above and 3 below the midplane, symmetrically, to reduce the number of inductors to a manageable number: one OH, 4 EF, 8 shell, 8 liner, and 8 plasma. The 29 inductors are mutually coupled by 406 mutual inductances, a rather large number for use in the general circuit solver SCAT (many more can be handled by the VAX but input files become bulky).

A fairly accurate model represents the SCR equilibrium control power supplies. The ODE solver time step of .25 msec models the inherent SCR controller delay. The power supplies being modelled have an output voltage limited to +1.5 and -0.9 kV with a maximum power of 35 MW for 2 MA I_ϕ and 70 MW for 4 MA (less than 16 MW is necessary for 2 MA - the 35 MW is for compatibility with upgrading to 4 MA operation). The SCR supply characteristics of a fast ouput voltage increase after the delay and a slow (10 msec worse case) response to input demand for a decrease

in output voltage is included. The model output follows a sine wave down from the previous output value to the new demand value for a decreasing input signal.

Equilibrium (or lack thereof) shift in plasma current is modeled by voltage sources in series with the "plasma" wires proportional to the difference between the desired Shafranov vertical field B_v and the actual B_v due to currents in the liner shell and EF coils. These source values are scaled with the cosine of the poloidal angle and factors that prevent a change in the total "plasma" current to effectively shift current in the wires. Shifting "plasma" wire currents change the flux at the liner and induce currents in the shell and liner wires. New EF coil current values are calculated to reduce flux deviation at the liner with minimum power. The feedback algorithm consists of a linear weighted sum of flux loop signals and their derivatives added to a pre-programmed input signal. The weights are obtained from a generalized inverse of the measured inductance matrix augmented by terms to minimize EF coil power.

The plasma wires with their shifting sources are all connected in parallel with a series R and L to represent the internal plasma current (and to obtain the correct risetime), but the fields are calculated only from the wire current. Shell wire inductances are connected in series with a resistance determined by the equivalent shell sector resistance. The shell resistance and inductances are connected in parallel with no closing path so that the net shell current must be zero. This corresponds to a shell gap of zero width as required for a 2-D model. Gap and hole field diffusion effects are ignored in this axisymmetric model.

B. Time Dependent MHD Model

In order to check the simplified multi-wire feedback model we are using a toroidal, time dependent, resistive MHD code[12] developed at Princeton which has been used for modelling tokamaks and spheromaks[13]. The original tokamak code used flux surface-averaged transport quantities for the transport part of the calculation. In the absence of transport descriptions for an RFP sustained by dynamo action, the ohmic heating term is retained but the transport terms affecting the losses have been eliminated. Instead, a constant beta assumption is modelled by keeping the pressure profile scaled

so that p_{axis}/I_ϕ^2 = constant. The effect of the relaxation is modeled by adding a "hyper-resistivity" term[14] to Ohm's law as follows:

$$\mathbf{E} + \mathbf{v}\times\mathbf{B} = \eta\mathbf{J} - (\mathbf{B}/B^2)\nabla\cdot[\mathbf{D}(\psi)\nabla(\mathbf{J}\cdot\mathbf{B}/B^2)] \qquad (12)$$

The magnitude of the coefficient D controls the amount of relaxation. The code allows the use of the same coil configuration, shell and liner modeling as used in the multiwire model. Feedback from sensor loops outside the liner center the plasma. The external circuits can also be connected but this has not yet been implemented.

V. Conclusions

A. Conclusions from the Wire Model

The design configuration including OH coils, EF coils, trim coils, and wire models for plasma, liner, and shell are shown in Fig. 2. Wire model simulations with a 50 msec shell show that, for magnetic energy transfer of plasma current to 2 MA, less than 16 MW of installed equilibrium power is necessary to maintain a flux surface deviation at the liner of less than $\pm$ 3 mm for a change in beta from 0 to 0.2. For 4 MA operation this becomes 70 MW. However, to maintain stability of the equilibrium system, a pre-programmed signal consisting of a best guess or previous data must be added (about 20%) to the feedback signals from the flux loops, and for faster response the derivative of the flux signals must be added. During a constant plasma current of 4 MA a sudden decrease in beta of 0.1 requires about 33 MW of EF coil power to maintain a flux surface deviation of less then $\pm$ 3mm. Ninety percent of this power is consumed in ohmic heating the EF coils. Sample results are shown in Fig. 4. Under most conditions even at 4MA plasma current the flux surface deviation can be controlled to less than $\pm$5mm.

B. Conclusions from Equilibrium and the Time Dependent MHD Codes

These calculations provide checks on the wire models. The flat-top toroidal current value in both sets of EF, OH coils and the plasma obtained from the single wire model is input to the equilibrium code with a diffuse current and pressure profile having the same B_p and ℓ_i values. The EF coil currents were

all allowed to vary by a constant factor in order to center the equilibrium. In the cases studied so far this correction factor was always less than 10%. This provides a reasonable check on the adequacy of the wire model. Sensitivity tests for various plasma profiles are still in progress. A sample toroidal equilibrium is shown in Fig. 5.

The time dependent code is being used to verify that a 4 MA current ramp can be carried out with the field coil design. The concern is that additional axisymmetric modes might cause a problem when the multiwire model is replaced by an MHD plasma model. The general observations with this code to date are as follows:

(a) The modified Ohm's law does allow a steady reversed field state after ramping and flat-topping the current.

(b) Without the dynamo term the plasma minor cross section contracts as the positive toroidal flux is lost.

(c) In all cases studied $\mathbf{J}\cdot\mathbf{B}/\mathbf{B}^2$ did not remain flat but peaked on axis.

(d) Numerical instability was observed for

(1) D values in the mean field dynamo term > 0.7.

(2) The radial profile of the $D(\psi)$ term going to zero at $> 95\%$ of the limiter radial position.

(3) The reversed field ramped proportional to the toroidal current.

(e) The main effect of adding the shell was a change in the index of the vacuum field and production of a more circular flux surfaces during the current ramping.

(f) For a pair of feedback flux loop sensors the plasma remained horizontally centered but its cross-section became flattened as the current ramped up. An additional pair of vertical motion flux sensing loops stopped the flattening (See Figs. (6) and (7)). It takes at least 8 pairs of sensing loops to keep the flux surface deviation within $\pm$ 5mm at the liner position.

VI. Acknowledgements

We acknowledge the contributions of the Los Alamos RFP Team for discussions and data relevant to the equilbrium aspects of this design. We particularly acknowledge the contributions of C.J. Buchenauer, J. N. DiMarco, R.C. Grimm, S.C. Jardin, K.A. Klare, J. Manikam, L. W. Mann, G. Miller, M.M. Pickrell, N. Pomphrey and K.F. Schoenberg. Work performed under the auspices of the US DOE.

References

1. R. F. Gribble, "ZTH Magnetics Design" This Conference

2. V.D. Shafranov, Rev of Plasma Physics Vol 2, edited by M.A. Leontovich (Consultants Bureau New York 1966) p 103.

3. V.S.Mukhovatov and V.D. Shafranov, Nucl. Fusion 11, 605 (1971).

4. D.A. Baker, L.W. Mann and K.F. Schoenberg, Los Alamos National Laboratory Report LA-9162-MS (1982).

5. R.L. Hagenson and R.A. Krakowski, Los Alamos National Laboratory Report LA-9389-MS P. 17 (1982).

6. K.F. Schoenberg, R. F. Gribble, and J.A. Philips, Nuclear Fusion **22,**1433 (1982).

7. K. M. Ling and D. A. Baker, Mathematical Modelling **7,**429 (1986).

8. J. C. Ingraham, private communication.

9. T. Cayton, private communication (to be published).

10. J.L. Johnson et al., Journal Comp. Physics **32,** 212 (1979).

11. We are indebted to J. Manikam and R.C. Grimm for the transfer and assistance in the adaptation of a modified code for RFP equilibria.

12. S.C. Jardin, N. Pomphrey, and J. DeLucia, Journal Comp. Physics **66,** 481 (1986).

13. S.C. Jardin, A. Janos, and M. Yamada, Nuclear Fusion **26,** 647 (1986).

14. A. H. Boozer, Journal Plasma Physics **35,** 133 (1986).

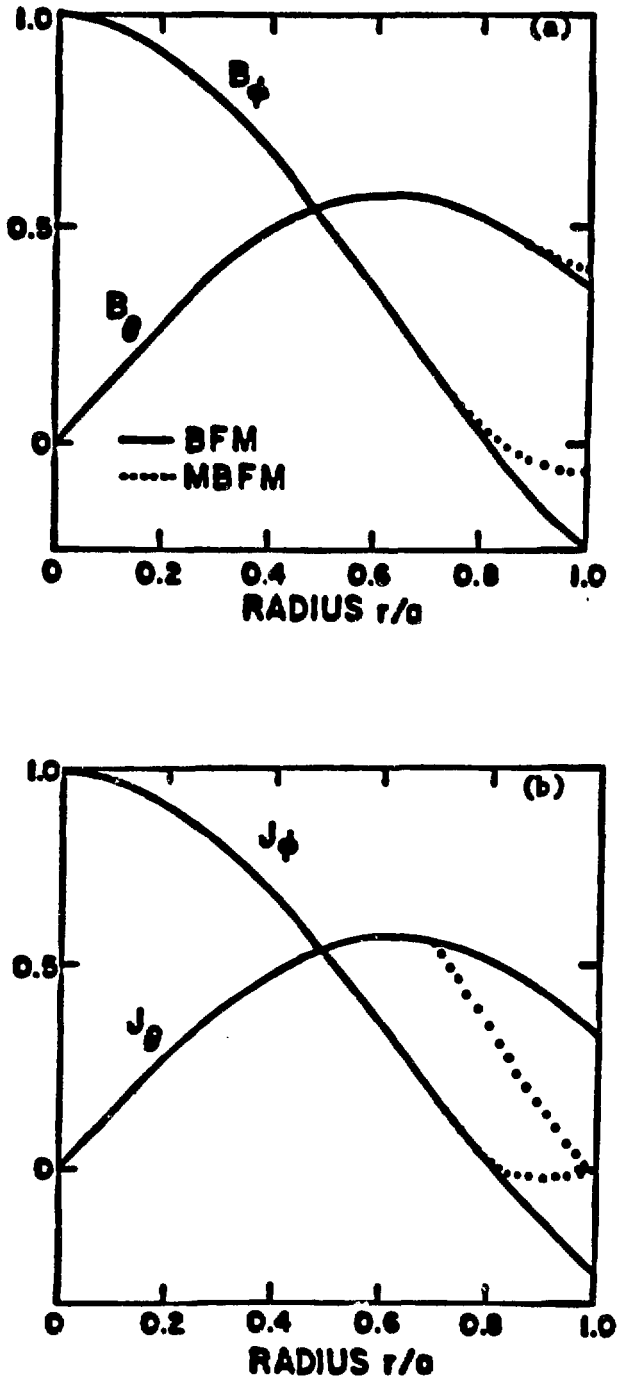

Fig. 1 - Toroidal and poloidal spatial profiles for the BFM and MBFM.

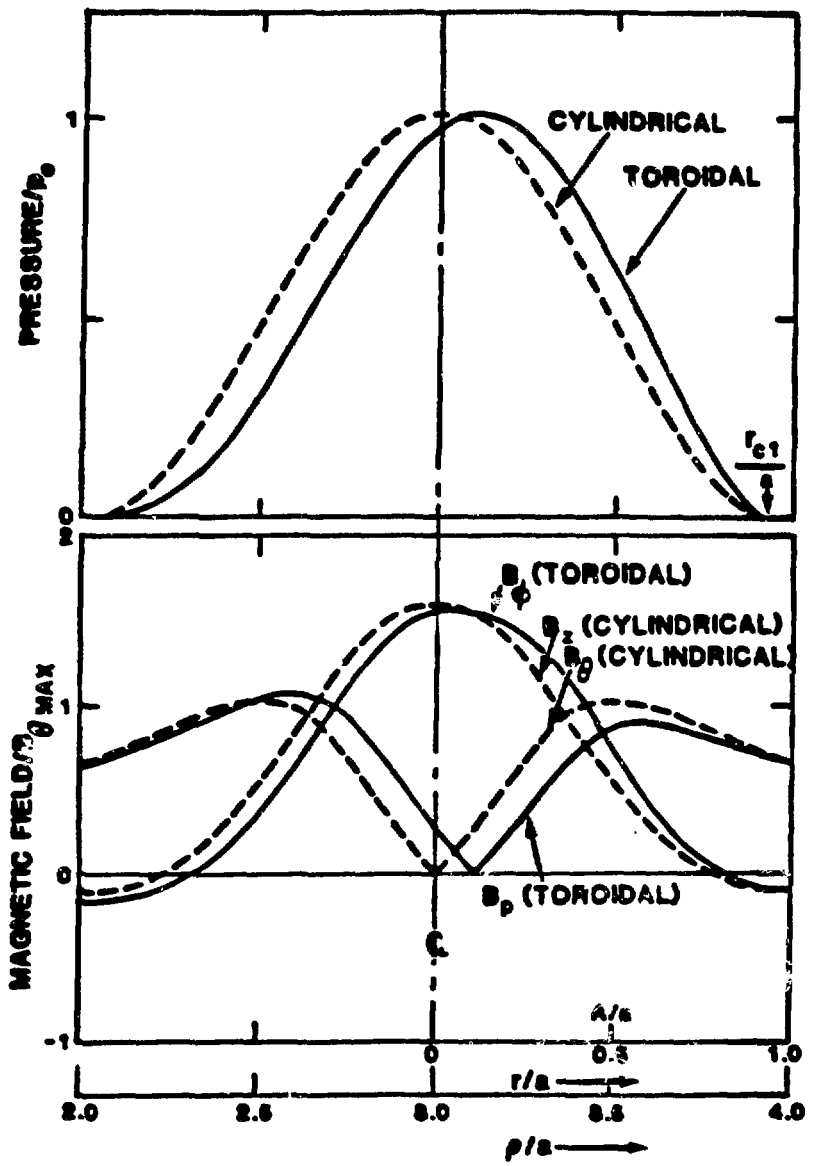

Fig. 2 - Comparision of the pressure and field profiles from the toroidal calculation and the corresponding 1-D calculation from which it is derived.

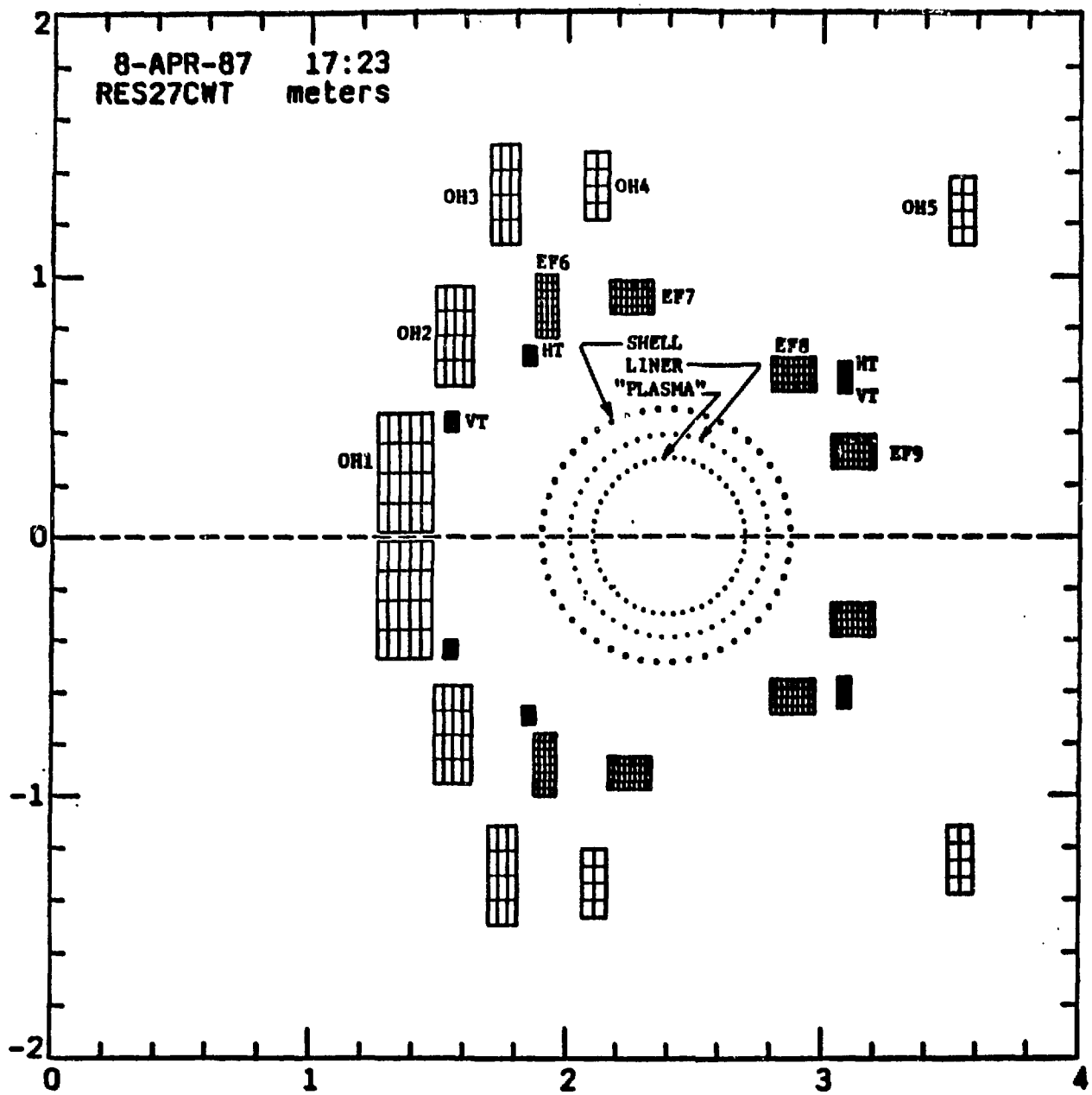

Fig. 3 - Optimized coil configuration for ZTH using the thin wire model. OH, EF, HT and VT distinguish the ohmic heating, equilibrium horizontal trim and vertical trim coils respectively. Shown also are the loops used to model the shell, liner and plasma.

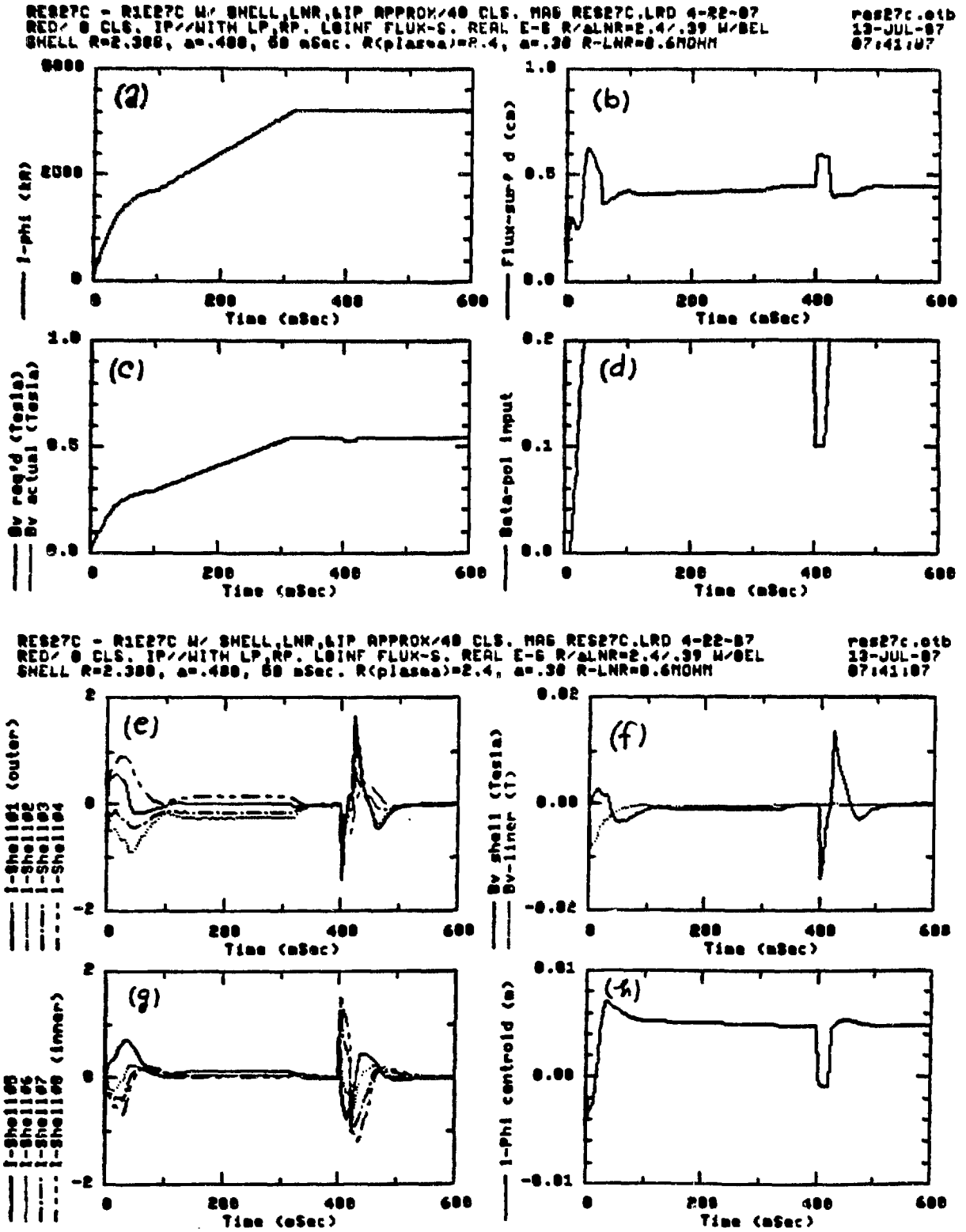

Fig. 4 - Sample reponse of the ZTH feedback system where the system is subjected to a β_t decreasing pulse from 0.2 to 0.1. (a) plasma current, (b) flux surface deviation, (c) vertical field, (d) the specified β_t pulse, (e) and (g) the currents in the shell model (counting clockwise from the inboard-midplane), (f) vertical field due only to the shell and the liner, and (h) centroid of plasma wire currents.

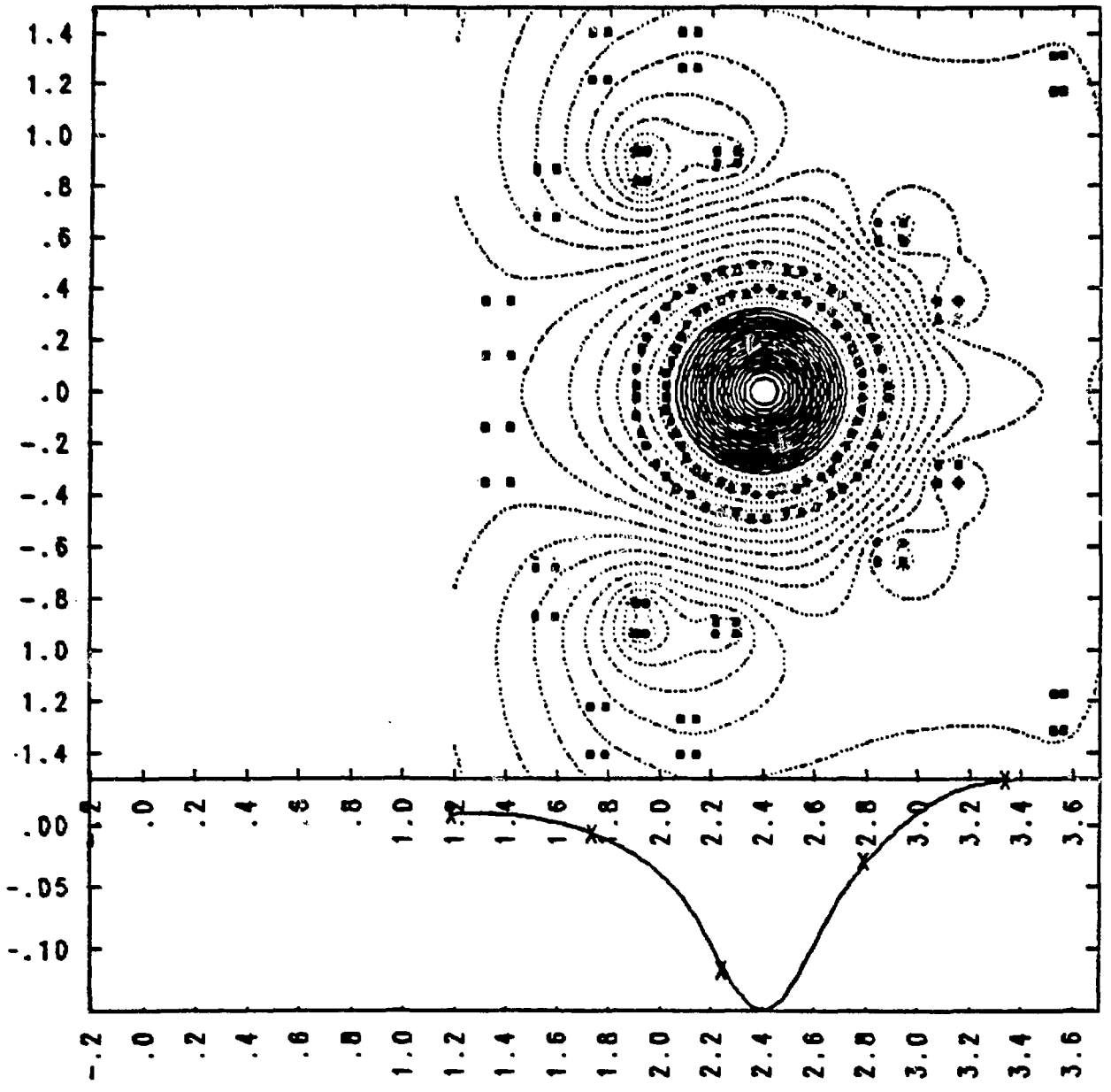

Fig. 5 - Sample toroidal equilibrium for the ZTH coil design ($\ell_i = 1.4, \beta_p = 0.1$).

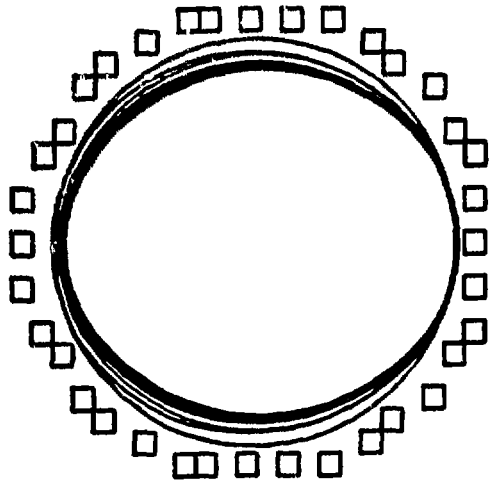

Fig. 6 - Flux evolution plot showing the flattening the flux surface at the limiter at increasing times as the current is ramped to 1.2 MA in 20 msec with feedback control using only two flux loop sensors

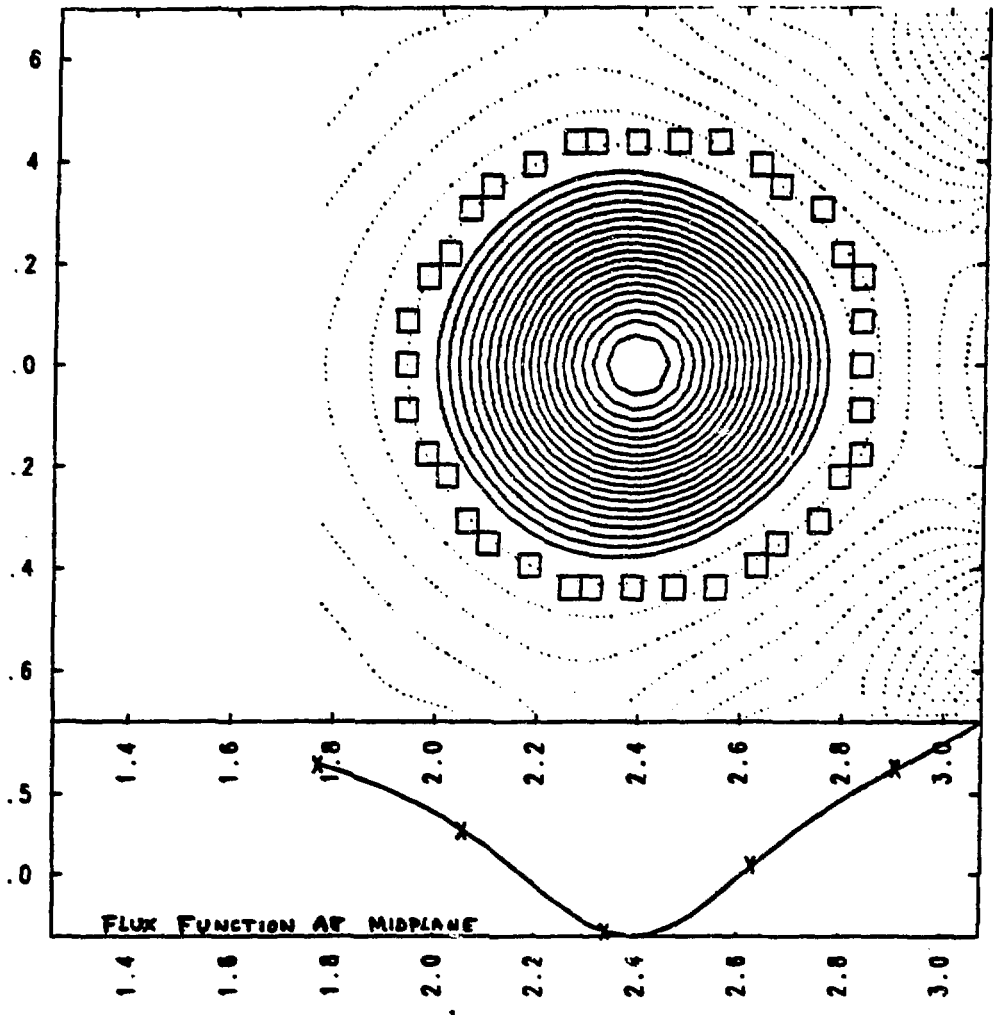

Fig. 7 - Final flux plot for same conditions as Fig. 6 except a pair of vertical feedback sensing loops is added greatly improving circularity.

APPENDIX

Codes Used in Equilibrium Design Studies

Equilibrium

1-D Cylindrical	Baker, Hoyt (LANL)
2-D Toroidal Wire-Model	Gribble (LANL)
2-D Toroidal/Casing	Baker, Mann, Hoyt (LANL)
2-D Toroidal/Coils	Grimm, Manikam (PPPL)
2-D Toroidal/Coils	Ling, Jardin (LANL)
2-D Preprocessor	Baker, Hoyt (LANL)
2-D Postprocessor	Baker, Hoyt (LANL)

Time Dependent MHD

2-D Toroidal Multi-wire Model	Gribble (LANL)
2-D Toroidal	Jardin, Pomphrey (PPL) Ling (LANL)

CPRF/ZTH POLOIDAL AND TOROIDAL FIELD COIL SETS

by
John D. Rogers,
Robin Gribble,
and Ted Linton

The ZTH is a reverse field pinch fusion machine being designed for construction and operation at the Los Alamos National Laboratory (LANL). The plasma magnetic confinement and reversed field is accomplished by poloidal field and toroidal field coils. These coils are to be made of copper conductor with water cooling and are to be vacuum/pressure epoxy impregnated with insulating materials - fiberglass, G10 epoxy fiberglass laminate, Kapton, and possibly Mylar. The poloidal field coils are divided into two subsets according to their function and are called ohmic heating (OH) and equilibrium field (EF) coils. They are symmetrical in geometrical arrangement across a horizontal midplane, thus, the coils are mirror image pairs. The coils are to be made of OFHC CDA 104 copper. The physical arrangement of the coils is shown in Fig. 1. The coordinate scales are in meters.

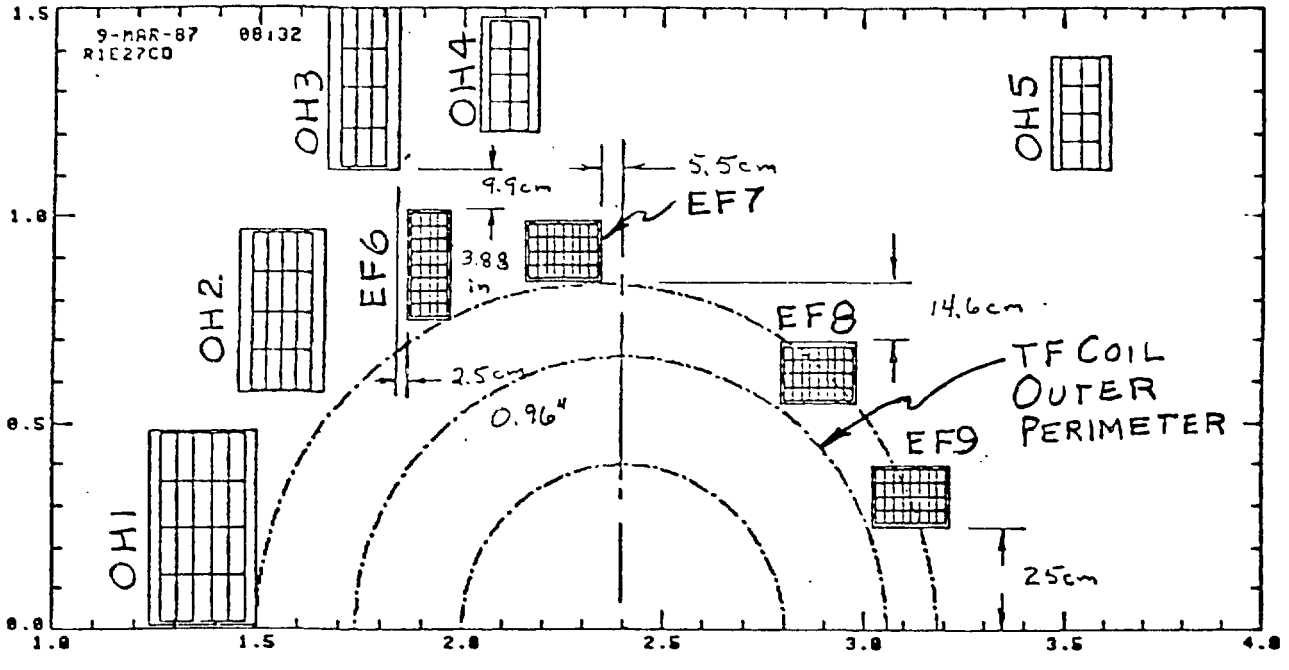

Fig. 1. ZTH poloidal field coil arrangement.

The engineering parameters-dimensions, currents, voltages, resistive energy dissipation, tolerances are given in the tables.

The PF coils are each made of four independent electrical sections. The OH coils are connected, one section of each coil, in series. Each EF coil electrical section connects directly to the power supply system.

Table I gives the coordinates of the PF coils with repect to the machine center, size of the conductor winding pack, the number of electrical sections, number of turns, winding type, maximum current, I^2t, and the length of the support at the 16 bulkheads that support the coils. The machine structure is made of 16 radially extended sheets of 4 in. (10.16 cm) thick G10 that lie in vertical planes and intersect the PF coils at equal angles for support. Support lengths for the coils at the bulkheads are also given and are determined by a coil stress limit of about 17,000 psi (116 MPa) in the conductor.

TABLE I

PF COILS

Coil	Centroid Mean Radius m	Width m	Height m	Electrical Sections	Turns/ Section	Turns/ Layer	Layers/ Section
OH1	1.3683	0.2523	0.4560	4	10	5	2 spiral
OH2	1.5577	0.1966	0.3798	4	8	4	2 spiral
OH3	1.7530	0.1597	0.3798	4	6	3	2 spiral
OH4	2.1124	0.1330	0.2613	4	4	4	1 spiral
OH5	3.5400	0.1330	0.2613	4	4	4	1 spiral
EF6	1.9166	0.0875	0.2444	4	32	16	2 helical
EF7	2.2500	0.1708	0.1294	4	32	8	4 helical
EF8	2.8860	0.1708	0.1294	4	32	8	4 helical
EF9	3.1192	0.1708	0.1294	4	32	8	4 helical

Coil	Total Number Turns	Current max kA	I^2t kA^2s	Discharge Cleaning kW	Support Length m
OH1	40	60	6800	negligible	continuous
OH2	32	60	6800	negligible	continuous
OH3	24	60	6800	negligible	continuous
OH4	16	60	6800	negligible	0.1
OH5	16	60	6800	negligible	0.1
EF6	128	2.25	3.9	0	0.1
EF7	128	3.00	7.0	0	0.1
EF8	128	4.00	11.1	0	0.3
EF9	128	4.00	10.3	0	0.3

TABLE I continued

PF COILS

Coil	Centroid Mean Radius in.	Width in.	Height in.
OH1	53.872	9.932	17.951
OH2	61.328	7.735	14.951
OH3	69.017	6.288	14.951
OH4	83.167	5.235	10.288
OH5	139.370	5.235	10.288
EF6	75.458	3.444	9.622
EF7	88.583	6.724	5.094
EF8	113.623	6.724	5.094
EF9	122.802	6.724	5.094

Maximum Dimensions with Outer Ground Plane Insulation

Coil	Width in.	Height in.	Centroid Distance to Midplane, in.
OH1	10.432	18.451	9.646
OH2	8.235	15.451	30.254
OH3	6.788	15.451	51.529
OH4	5.735	10.788	52.730
OH5	5.735	10.788	49.165
EF6	4.194	10.372	34.745
EF7	7.474	5.844	36.038
EF8	7.474	5.844	24.454
EF9	7.474	5.844	12.756

Table II gives some of the same information for the TF coils. The TF coils are helical wound with the conductor on edge. The radius to the TF coil inner conductor surface is 22.834 in. (0.58 m).

TABLE II

TF COILS

Turns Coil	Current Max kA	I^2t kA^2s	Voltage kV/turn	Voltage kV/coil	Discharge Cleaning kW/coil	Machine Major Radius in.
6	39.9	134	1.67	10.0	12	94.488(2.40 m)

Table III gives the conductor dimensions.

TABLE III

Conductor Dimensions

Coil	Width, in./cm	Height, in./cm
OH1	1.500/3.810	1.875/4.763
OH2	1.375/3.493	1.500/3.810
OH3	1.375/3.493	1.500/3.810
OH4	0.875/2.223	2.000/5.080
OH5	0.875/2.223	2.000/5.080
EF6	0.250/.635	0.500/1.270
EF7	0.250/.635	0.500/1.270
EF8	0.250/.635	0.500/1.270
EF9	0.250/.635	0.500/1.270
TF	0.563/1.430	1.625/4.128

Table IV gives the tolerances to which the coils are to be manufactured.

TABLE IV

FINISHED COIL TOLERANCES

TF Coils	
Radius tolerance, in./cm	±0.125/.318
Height tolerance, in./cm	±0.030/.076
Width tolerance radially, in./cm	±0.030/.076
Flatness tolerance, in./cm	±0.125/.318
Ohmic Heating Coils	
Radius tolerance, in./cm	±0.250/.635
Height tolerance, in./cm	
Height < 5.0 in./<12.70 cm	±0.030/.076
5.0 in./12.70 cm ≤ height ≤ 7.88 in./20.02 cm	±0.040/.102
7.88 in./20.02 cm ≤ height ≤ 20.0 in./50.80 cm	±0.060/.152
Width tolerance radially, in./cm	
Width < 5.0 in./<12.70 cm	±0.030/.076
5.0 in./12.70 cm ≤ width ≤ 10.0 in./25.40 cm	±0.040/.102
Flatness tolerance, in./cm	±0.125/.318
EF Coils	
Same tolerances as for the ohmic heating coils.	

Table V gives the normal and transient voltages for the PF coils. The transient voltages are the peak fault voltages expected with voltage supression devices in the power supply circuits. The voltages are for turn to turn, across each coil section, between independent electrical sections in a given coil, and from the coil to ground.

TABLE V

NORMAL COIL VOLTAGES

Coil	kV/turn	kV/section	kV between sections	kV to ground
OH1	0.9	9	9	±25
OH2	0.86	7	7	±25
OH3	1.0	6	6	±25
OH4	1.25	5	5	±25
OH5	1.25	5	5	±25
EF6	0.78	25	25	±25
EF7	0.78	25	25	±25
EF8	0.78	25	25	±25
EF9	0.78	25	25	±25
TF	1.67	10	NA	±10

TRANSIENT COIL VOLTAGES

Coil	kV/turn	kV/section	kV between sections	kV to ground
OH1	2.0	20	20	±25
OH2	2.0	16	16	±25
OH3	2.33	14	14	±25
OH4	3.25	13	13	±25
OH5	2.5	10	10	±25
EF6	1.25	40	40	±25
EF7	1.25	40	40	±25
EF8	1.25	40	40	±25
EF9	1.25	40	40	±25
TF	1.67	10	NA	±10

Tables VI and VII give the properties for the conductor material and the allowable static load stress levels.

TABLE VI

CDA 104 COPPER PROPERTIES

	Annealed	Quarter Hard	Half Hard
Ultimate Tensile Strength, MPa	205	260	277
kpsi	30	38	40.5
Yield Strength, MPa	23	205	275
kpsi	3.4	30	40.2
Elongation, %	48	25	13
Hardness, R_F	53	70	80
Modulus Elasticity, GPa	128	125	123
Shear Modulus, GPa	48	48	47
Poisson Ratio	0.35	0.35	0.35

TABLE VII

COPPER ALLOWABLE STRESS LIMITS

Stress limit, combined allowable principle stress

Tensile/compressive	<2/3 ultimate tensile or 0.6 yield strength
Bending/membrane	<2/3 ultimate tensile or 0.6 yield strength
Shear	<1/2 yield strength

Proposals for design and manufacture of the coils are presently being solicited. The expected period to design the coils is five months and the period to manufacture is believed to be 80 weeks. However, some overlap in design and manufacture, particularly material procurement might reduce the total lapsed time.

Poloidal Divertor Design for Next Step STE-RFP Device

H. Oshiyama
Department of Electrical Engineering,
Kyoto Institute of Technology

Abstract

This paper presents a brief summary of a poloidal field divertor design for the next step STE-RFP device. The magnetic field lines which form the diverted magnetic flux are calculated by solving the equation of field lines in terms of a usual Runge-Kutta fourth order method. The factors determining plasma flow into the divertor are discussed and the exhaust and screening efficiencies characterizing the divertor scrape-off layer are also considered.

1. Introduction

It is well known that the presence of a relatively small density of impurity ions prevents a plasma from being heated to thermonuclear temperatures owing to large radiative power losses. Thus some methods of impurity control must be developed. One method is using a magnetic divertor.

Various kinds of a magnetic divertor, for example the bundle divertor used in DITE[1], the poloidal divertor in DIVA[2] and the toroidal divertor in C-stellarator[3], have been proposed for toroidal plasma discharges. In regard to a divertor design for RFP, for example, a toroidal-field poloidally symmetric divertor and a toroidal-field bundle divertor have been proposed by Los Alamos team[4].

This paper presents a poloidal field divertor design for next generation STE-RFP[5] at Kyoto Institute of Technology. STE is an abbreviation of Separatrix Test Experiment for RFP which started in 1981.

2. Analysis of a Poloidal Field Divertor

The concept of our poloidal divertor is illustrated in Fig.1.

It consists of two parts; one is a divertor hoop carring the current in the same direction as that of the plasma current, the other is a divertor shell which has a circular cross section surrounding the divertor hoop and also has a small cut with an open angle 2β.

The divertor shell carries reverse currents with respect to the divertor-hoop current. This axisymmetric divertor system has a magnetic separatrix, inside which all flux remain within the main plasma; outside the separatrix all flux are diverted to the divertor chamber. Magnetic topology of the diverted field lines has been calculated numerically.

In the computations, the magnetic field components in the main plasma region are assumed as

$$\begin{aligned} B_r &= -\{B_o J_o(\alpha r)/2\alpha R + b_1 J_1(\alpha r)/\alpha r\} \sin\theta \\ B_\theta &= B_o J_1(\alpha r) - \{b_1 J_o(\alpha r) + B_o J_o(\alpha r)/2\alpha R - b_1 J_1(\alpha r)/\alpha r \\ &\qquad + B_o r J_1(\alpha r)/2R\} \cos\theta \\ B_z &= B_o J_o(\alpha r) + \{b_1 J_1(\alpha r) - B_o r J_o(\alpha r)/2R\} \cos\theta \end{aligned} \tag{1}$$

where a is the minor radius, R the major radius, α a Lagrange multiplier, $b_1 = -B_o a J_o(\alpha a)/2R J_1(\alpha a)$, and $J_o(\alpha r)$ and $J_1(\alpha r)$ are the Bessel functions of the zero and the first order.

Equation (1) is a toroidal expression for the force-free field of $\mathrm{rot}B = \alpha B$, which is analyzed by using the quasi-cylindrical coordinates (r,θ,η) shown in Fig.1.

The plasma chamber has the major radius R and the minor radius a, whose center passes through a point O'. The divertor hoop carring current I_D intersects at a point O" with the radius of R+D. The divertor shell with radius a_o carries the reverse current I_R .

The magnetic field components created by the divertor hoop current I_D are given by

$$\begin{aligned} B_{Dx} &= \mu_o I_D (R+D) r \sin\theta\cos\phi \{ K(k) - (F/F-G)E(k) \}/\pi G(F+G)^{1/2} \\ B_{Dy} &= \mu_o I_D (R+D) r \sin\theta\sin\phi \{ K(k) - (F/F-G)E(k) \}/\pi G(F+G)^{1/2} \\ B_{Dz} &= -\mu_o I_D (R+D) E(k)/\pi(F-G)(F+G)^{1/2} - \mu_o I_D \{ K(k) - FE(k)/(F-G) \} \\ &\qquad /2\pi(F+G)^{1/2} \end{aligned} \tag{2}$$

where $F=R^2+r^2+2rR\cos\theta+(R+D)^2$, $G=2(R+D)(R+r\cos\theta)$, $k^2=2G/(F+G)$ and, $K(k)$ and $E(k)$ are complete Elliptic Integrals of the First and Second kinds, respectively.

Next the magnetic field created by the divertor-shell current I_R which is distributed uniformly in the divertor shell is given by

$$B_{Rx} = \int_{\beta}^{2\pi-\beta} \bar{B}_x(\theta')d\theta'$$

$$B_{Ry} = \int_{\beta}^{2\pi-\beta} \bar{B}_y(\theta')d\theta' \qquad (3)$$

$$B_{Rz} = \int_{\beta}^{2\pi-\beta} \bar{B}_z(\theta')d\theta'$$

where $\bar{B}_x(\theta')$, $\bar{B}_y(\theta')$, $\bar{B}_z(\theta')$ have similer expressions in eq.(2), for example,

$$\bar{B}_x(\theta')=\mu_o I_R(R+D-a_o\cos\theta')(r\sin\theta-a_o\sin\theta')\cos\phi \times\{K(\bar{k})-\bar{F}E(\bar{k})/(\bar{F}-\bar{G})\}/\ \bar{G}(\bar{F}+\bar{G})^{1/2} \qquad (4)$$

Here the symbols in eq.(4) are given by

$$\bar{F}=R^2+2rR\cos\theta+r^2+(R+D)^2-2(R+D)a_o\cos\theta'+a_o^2-2a_o r\sin\theta\sin\theta'$$
$$\bar{G}=2(R+r\cos\theta)(R+D-a_o\cos\theta') \qquad (5)$$
$$\bar{k}^2=2\bar{G}/(\bar{F}+\bar{G})$$

Now we can design the magnetic configuration of the divertor system by summing up the three kinds of fields given by eqs.(1),(2),and (3).

The main design requirements are: first a minimum perturbation of the main plasma region, second a weak magnetic mirror along the diverted field lines, and third a completely diverting the magnetic flux outside separatrix into the divertor region without being in contact with the plasma chamber.

To satisfy the above requirements, we have looked for the suitable values of D/a and I_D/B_o under the fixed conditions of aspect ratio $R/a=2.5$ and a Lagrange multiplier $\alpha=60\ m^{-1}$.

The computation result is shown in Fig.2, with the normalized coordinate of $X=r/a$. The position of the $B_z=0$ is indicated by the dotted line. It has been verified that if $I_R=0$, almost all magnetic

lines of force outside the main plasma intersect the plasma chamber and we can not obtain a good divertor configuration.

The field strength along a typical diverted field line is shown in Fig.3 and the mirror ratio between points A and C is about 2. The divertor collector plate may be located near the point C. This small mirror ratio helps plasma particles to come into the divertor chamber and to be exhausted to great extent. The field intensity is minimum at the point B, and this fact will be expected to give the advantage of minimum-B configuration.

3. Exhaust and Screening Efficiencies in Divertor Scrape-off Layer

In this section we consider the plasma flow into the divertor region and calculate both exhaust and screening efficiencies, ξ_{ex} , ξ_s .

These efficiencies can be defined by

$$\xi_{ex} = 1 - \frac{\Gamma_i^+ (r=a_w)}{\Gamma_i^+ (r=a_s)} \quad \text{and} \quad \xi_s = 1 - \frac{\Gamma_i^- (r=a_s)}{\Gamma_i^- (r=a_w)} \tag{6}$$

respectively, where Γ_i^+ denotes the outwards ion flux and Γ_i^- denotes the inward particle flux, a_s and a_w are radii of separatrix and wall, respectively.

In calculating ξ_{ex} and ξ_s, we assume one-dimentional model of the divertor scrape-off layer, in which the diffusion equation for ion density is written simply as

$$\frac{d}{dy} \left(D_{\perp s} \frac{dn_i}{dy} \right) = n_i / \tau_{//} \tag{7}$$

where $y=r-a_s$, $\tau_{//} \sim L_d f_m / v_s$, $v_s=(2\kappa T_e/m_i)^{1/2}$ and f_m is a factor related mirror ratio.

Here $\tau_{//}$ is the characteristic time for the diversion of ions which are removed along the diverted field lines, and L_d is the average geometrical path length along field lines outside the separatrix into the divertor.

Neglecting the parametric dependence of $D_{\perp s}$ and v_s, we get a solution of the eq.(7), namely

$$n(y) = n(s) \exp(-y/\Delta) \tag{8}$$

where $\Delta=(D_{\perp s} \tau_{//})^{1/2} = (D_{\perp s} L_d f_m / v_s)^{1/2}$

The neutral impurity density, n_o satisfies

$$\frac{d}{dR}(n_o v_o) + n_e n_o \langle\sigma v\rangle = 0 \qquad (9)$$

where $\langle\sigma v\rangle$ is the electron-impact ionization rate, v_o is the velocity of the incident neutral impurity which we assume to have an energy of 1eV, and R is measured from the wall.
The solution for eq.(9) is

$$n_o(R) = n_o(0)\exp\left(- \int_o^{R_s} \langle\sigma v\rangle / v_o \, dR \right) . \qquad (10)$$

By using eqs.(8) ,and (10), we get

$$\xi_{ex} = 1 - \exp\left(-(a_w - a_s)/\Delta \right)$$
$$\xi_s = 1 - \exp\left(-\xi_{ex} \langle\sigma v\rangle \, \Delta n_s / v_o \right) . \qquad (11)$$

Calculated values of both Δ and ξ_{ex} for densities and temperatures are plotted in Fig.4. We have assumed that the cross-field diffusion coefficient follows the Pfirsch-Schluter dependence, but with $D_{\perp s} \sim 100 D_{ps}$. We have plotted the screening efficiencies for typical light impurities oxygen. The calculated values of ξ_s are close to unity for oxygen when $n_s > 4 \times 10^{13} cm^{-3}$.

In summary we have considered the poloidal divertor system for next step STE-RFP by choosing the appropriate values of parameters.

References

1) P.E.Stott, C.M.Wilson and A.Gibson:Nucl.Fusion 17(1977)481.
2) DIVA Group:Nucl.Fusion 20(1978)1619.
3) C.R.Burnett, D.J.Grove et al. :Phys.Fluids 1(1958)438.
4) C.G.Bathke, R.L.Miller,and R.A.Krakowski:10th Symposium on Fusion Engineering, Dece.5-9,1983,1259.
5) H.Oshiyama and S.Masamune:Memoirs of the Facu. Engi. and Desi., Kyoto Institute of Technology 33(1984)19.

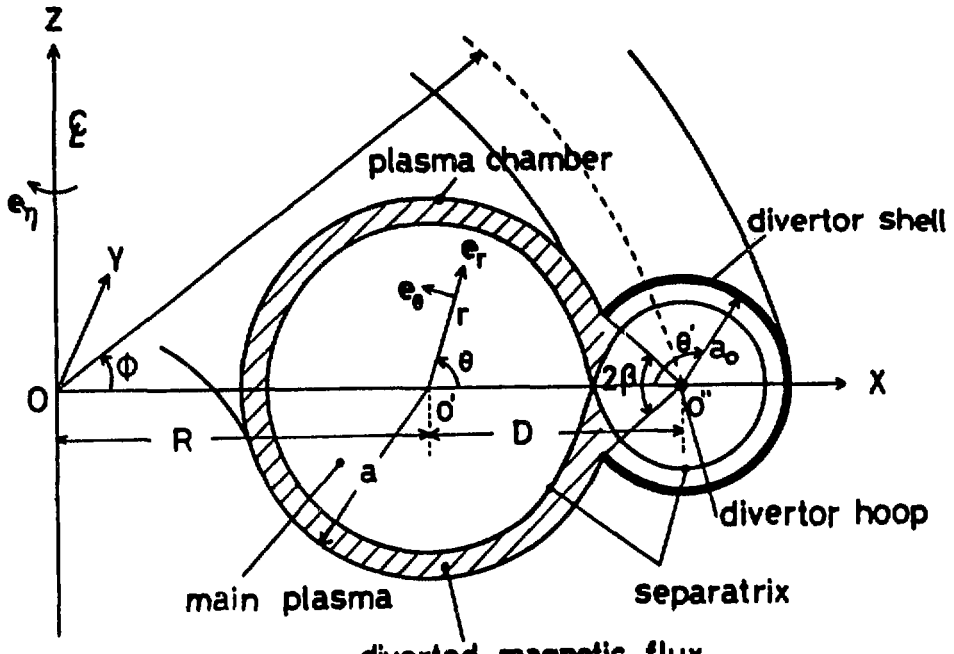

FIG.1

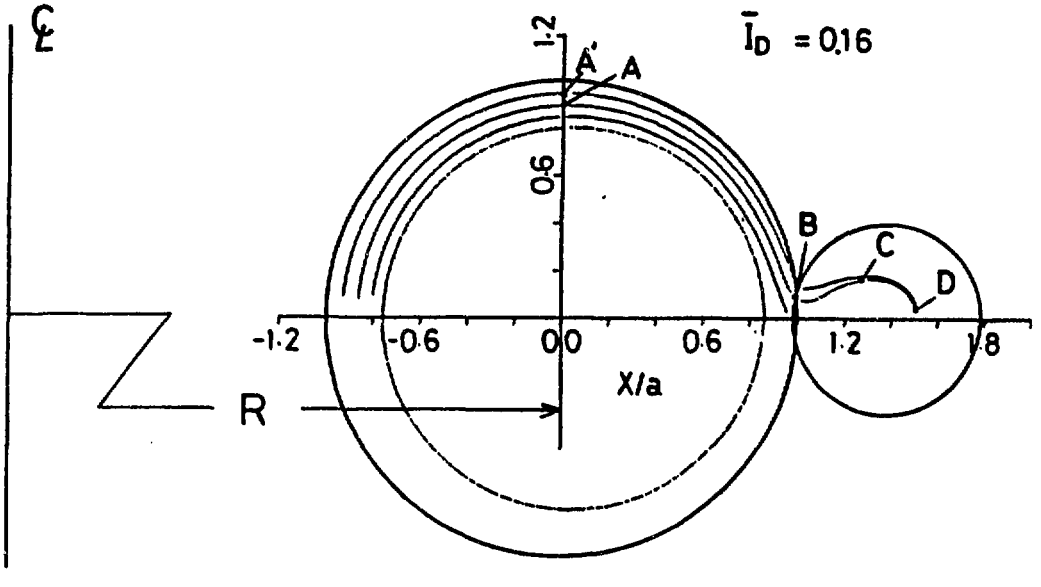

FIG. 2 Magnetic configuration of the divertor system

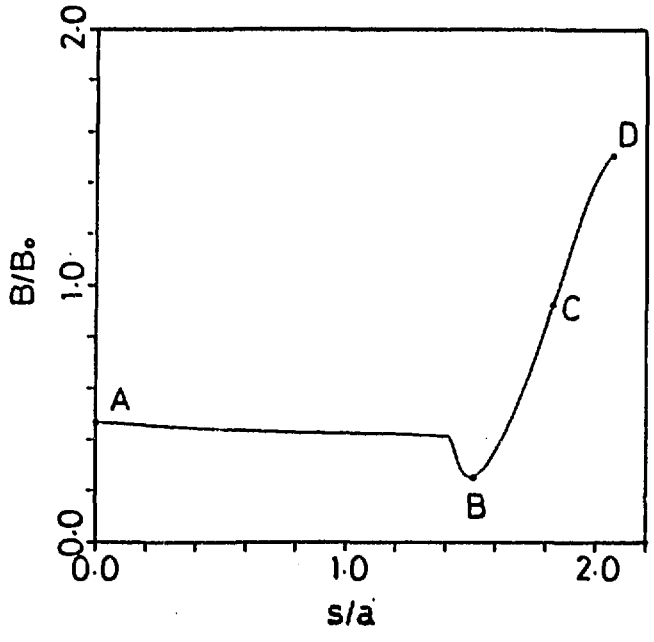

FIG.3 Field strength along a typical field line

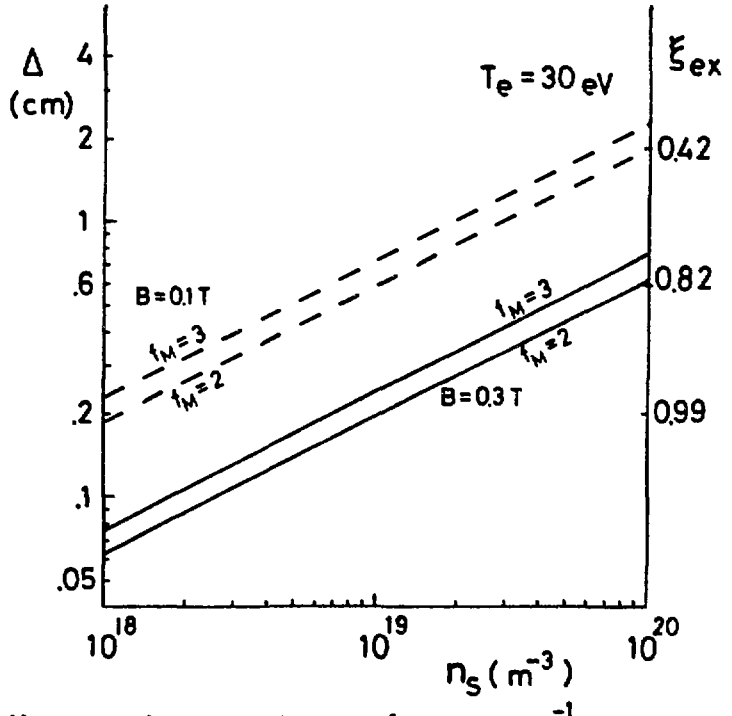

FIG.4
Density scale length, $\Delta=(d \ln n/dx)^{-1}$, in the scrape-off layer assuming $y_{wall}/a=(a_w-a_s)/a=0.1$

MAGNETICS AND WINDING DESIGN IN RFX

A. Stella
Istituto Gas Ionizzati - Progetto RFX
Associazione EURATOM-ENEA-CNR

ABSTRACT

The present contribution deals with both Poloidal Field (PF) and Toroidal Field (TF) Systems in RFX. After a short revew of the basic concepts representing the theoretical background of the PF System a number of considerations are made on the specified physical constrants which lead to the choice of the engineering parameters among a very narrow range of possibilities.

The PF coils design is then presented pointing out the most peculiar features and in particular those aspects which may affect the overall field performance.
A number of technological and manufacturing aspects of the magnetizing winding are also given.

The Toroidal Field Coils are designed as well to tight physical specifications but their most tricky engineering problems come mainly from constraints specified in order to provide easy and quick accessibility and maintenance. The paper describes the TF coil design, made to cope with the requirements above, the field operation and performance. The paper anticipates also a number of technological problems which will have to be taken into account during detailed design and manufacture.

2. POLOIDAL FIELD SYSTEM

2.1 Introduction

The RFX PF system, consisting of Magnetizing and Field Shaping winding, is characterized by the parameters and the features given in Table I. As it will be described below most of the given parameters represent a direct consequence of specified requirements.

TABLE I - PF System parameters and Features

Magnetizing winding	
Stored flux	15 Wb
Maximum stray field	5 mT
Loop voltage	700 V
Number of sectors	4
Number of turns per sector	25+25
Total number of turns	200
Total resistance	18 mohm
Total inductance	58 mH
Maximum current	50 kA
Insulation level to earth	17.5 kV
Field Shaping Coils	
Loop voltage	700 V
Number of coils	8+8
Number of turns per coil	24
Average current per turn	5.2 kA
Insulation level to earth	17.5 kV
Common Features	
Inductive decoupling	
Equatorial Symmetry	
Diagnostic Accessibility	

2.2 Concept review

The RFX poloidal Field System /1/ has two functions: to create the magnetic flux necessary to initiate and sustain the plasma current (up to 2 MA) and to produce the magnetic field configuration for the plasma equilibrium. The induction values required, above 4 T, would completely saturate an iron core, thus RFX is designed with an air core. Two separate Poloidal Field Windings are provided: the Magnetizing (M) Winding and the Field Shaping (F) Winding (Fig. 1). The first is required to create the magnetic flux (15 Wb at 50 kA) with negligible stray field in

the plasma region. The second has to provide the equilibrium field and to counterbalance the plasma magnetomotive force, so that the flux swing requirements from the M winding are minimized.

The RFX poloidal basic system includes the M and F windings and the plasma P (Fig. 2).

The overall circuit behaviour can be fully described by the following set of equations.

$$v_M = L_M \frac{di_M}{dt} + M_{MF} \frac{di_F}{dt} + M_{MP} \frac{di_p}{dt} + R_M i_M \tag{1}$$

$$v_F = M_{MF} \frac{di_M}{dt} + L_F \frac{di_F}{dt} + M_{FP} \frac{di_p}{dt} + R_F i_F \tag{2}$$

$$v_P = M_{MP} \frac{di_M}{dt} + M_{FP} \frac{di_F}{dt} + L_p \frac{di_p}{dt} + R_p i_p = 0 \tag{3}$$

In order to obtain operational flexibility in the Field Shaping current control, M and F windings must be decoupled from each other. This is obtained through a proper magnetic and circuit design of both M and F coils.

Under ideal conditions (winding resistances equal to zero) full decoupling is achieved with

a) parallel connection of M and F windings;

b) $L_M = M_{MF}$, which can be satisfied by a proper choice of the turns of M and F windings /2/.

In fact from equations (1) and (2) we get

$$v_M - v_F = (L_M - L_{MF}) \frac{di_M}{dt} + (M_{MF} - L_F) \frac{di_F}{dt} + (M_{MP} - L_P) \frac{di_p}{dt} \tag{4}$$

which, with the two conditions above, reduces to

$$(M_{MF} - L_F) \frac{di_F}{dt} + (M_{MP} - L_P) \frac{di_p}{dt} = 0 \tag{5}$$

This means that (if a plasma with constant magnetic parameters is considered), i_F and i_P are proportional. In particular if we consider the "no plasma" condition $i_P = 0$, must be also $i_F = 0$, independently of the behaviour of the magnetizing current i_M.

Furthermore from the two conditions above also follows that M and F windings are always linked with the same flux and the space between them is, in principle, free of any magnetic field (except for leakages).

In the real operating conditions, when the resistances cannot be neglected, the decoupling can still be obtained by means of a suitable control system to offset the effects of the resistive voltage drops.

2.3 Physical specifications

RFX is designed with a toroidal vessel of 2 m and 0.5 m major and minor radius respectively.

A Poloidal Air Core Transformer, as shown in Fig. 1, provides the flux swing as required to ionize the gas within the vacuum vessel, to cause the plasma current to rise up to 2 MA and to maintain it during flat-top. A $\psi = 15$ Wb magnetizing flux to be initially stored corresponds to the total flux swing requirement for both current rise and flat top. RFX operation is supporsed to require most of the flux to be released during fast rise only, so that a symmetric flux swing operation, as usually done in Tokamaks, is not applicable. In any case a plasma current setting up, consisting of fast rise and ramping (or slow rise), is compatible with the machine design and may be possibly implemented at a later stage, would RFX operation require it.

The magnetic field produced by the magnetizing windings is required to be bound outside the vacuum vessel to prevent magnetic configuration distortions inside the plasma: an upper limit of 5 mT on the stray field was chosen as design specification. Moreover for plasma breakdown and subsequent current rise a loop voltage up to $V_T = 700$ V on the vacuum vessel was specified.

2.4 Engineering consideration

In a first and very rough approximation the magnetizing winding can be though as a short and thick solenoid with length H = 2.4 m and radius R = 1.2 m: its one turn inductance can be extimated as $L_M = 1.5$ microH so that the total amperturns required to give 15 Wb are

$$A_T = \psi / L_M = 10 \text{ MAT} \qquad (6)$$

Taking into account the voltage per turn V_T above, the poloidal system power rating can be simply estimated as

$$P = V_T \cdot A_T = V_T \cdot N \cdot I_M = V_M \cdot I_M \qquad (7)$$

where $V_M = V_T \cdot N$ is the total feeding voltage at the winding terminals and I_M represents the magnetizing current.

This very high figure is a fixed technical constraint, coming directly from the physical specifications mentioned above, and represents a critical aspect of the overall RFX design.

In order to achieve such a power rating we can only play with the total feeding voltage V_M at the winding terminals, and the magnetizing current I_M according to equation (7).

In our case for example we might have chosen

V_M = 70 kV, I_M = 100 kA, N = 100, or

V_M = 140 kV, I_M = 50 kA, N = 200, or

V_M = 280 kV, I_M = 25 kA, N = 400 and so on.

It is clear that a reduced total voltage at the winding terminals requires higher current to deal with. The chosen intermediate solution, with N_M = 200 turns and I_M = 50 kA magnetizing current, is the result of a compromise: a higher number of turns in the winding would allow to reduce the current in the circuit, but would increase the voltage between terminals beyond reasonable limits. On the contrary fewer turns would require an excessive current level, too large copper cross section and very low flexibility in the winding configuration and power supplies. The total voltage over the whole winding remains still rather high (140 kV). To limit the voltage from terminals to earth as well as between terminals an interleaved configuration has been adopted /3/ by splitting the whole winding into four equivalent sectos so that the circuit schematic shown in Fig. 3 is obtained. M_{S1}, M_{S2}, M_{S3} and M_{S4}, represent the four sectors which are permagnetized in series by P_{MAT} (50 kA, V_o = 1700 V) up to 50 kA through the circuit breakers S_T.At t = 0 (Fig. 3) P_{MAT} is switched off and S_T are opened. The current is forced into the commutating R_T resistors, the voltage across them causes the plasma to breakdown and the current to rise up to 2 MA. Each S_T unit is rated for 50 kA, 35 kV and $i^2t = 5 \cdot 10^9 A^2s$. To comply with the vacuum interrupters thermal rating PMAT has to be able to charge the magnetizing winding

within 3 s and this requires to limit the resistance below 18 mohm including busbars and connections. As a consequence the cross section of the copper conductors in the coils results quite large of the order of 2000 mm^2/turn /4/.

Each sector is then connected in parallel to 4 of the 16 field shaping coils F, as shown in Fig. 3, which have the main function of plasma equilibrium control and carry amperturns equal to the plasma current /5/.

2.5 Engineering problems

The physical specifications set for RFX, together with the chosen arrangement, with four sectors, raise a number of engineering problems hard to be solved and additional conditions to be met.

a. First of all the above mentioned decoupling condition $L_M = M_{MF}$ becomes

$$\sum_{J=1}^{4} M_{M_j M_i} = \sum_{J=1}^{4} M_{M_j F_k} = \sum_{J=1}^{4} M_{M_j F_{(9-K)}} \qquad i,k = 1,\ldots,4 \tag{8}$$

In the case the above conditions are not fully satisfied the currents, in the four branches of the magnetizing winding, are not equal to each other (especially during fast rise) so that the magnetic field configuration may become much worst than during premagnetization. In order to meet condition (8) a winding design in which the four sectors are finely interleaved is mandatory. On the other hand with such an arrangement the magnetic field configurations indipendently produced by each one of the four sectors are similar, with relatively low field error in the plasma region, so that, in case of current unbalance among branches the overall field configuration is not dramatically jeopardized.

Unfortunately a finely interleaved arrangement implies a lot of coil terminals, which proved to be among the most effective sources of localized stray fields.

In RFX the coils belonging to each sector have been identified in order to equalize as much as possible the four equivalent self inductances, given by the left side elements in the equations (8). The result of such a procedure is shown in Fig. 4; the corresponding magnetic parameters obtained are given in Table II /6/.

b. Due to the copper cross section of the conductors and the relatively short rise time specified for the plasma current the typical diffusion time of the current within each coil conductor is of the same order of the circuit time constant. In this way the additional transient stray field produced during the early phase of the plasma current rise is significantly high and has to be taken into account . A special purpose code has

been developed in order to account for diffusion phenomena in RFX cois; in particular it has been found that massive conductors, corresponding to the overall cross section required, would be unacceptable as shown in Fig. 5. That is the reason why each turn of the central pancake stack has been subdivided in two conductors, transposed to each other at half winding; the resulting field performance obtained with such an arrangement is shown in Fig. 6.

TABLE II - Decoupling parameters in mH

i	$\Sigma_j M_{M_j M_i}$	$\Sigma_j M_{M_j F_i}$	$\Sigma_j M_{M_j F_{(9-k)}}$
1	14.30	14.11	14.14
2	14.31	14.12	14.14
3	14.37	14.14	14.15
4	14.45	14.15	14.14

2.6 Summary of Field errors

The maximum acceptable field errors in RFX has been specified to be less than 5 mT, in any point of the plasma region.

The coil design is usually performed with fully axisymmetric and static codes, so that no localized field errors, nor diffusion phenomena are taken into account /7/. In other words this approach accounts only for "background" field error, to which all the other effects, sumarized in Table III should be properly added /8/.

2.7 Magnet technology

Magnetizing coil design

All the copper used for RFX magnetizing winding (Fig. 7 and 8) is half hard copper, type OFXLP C10300 (ASTMB 224), specified according to the data given in Table IV. The joints are made by induction heating, using SILFOS (15%Ag, 80%Cu, 5%P) filling material.

The corner radius of all conductors is 2.5 mm, which allows to keep the electric field below about 13 kV/mm during tests. In the pancake corners, where that limit would be exceded, the corner radius is increased to 4 mm.

Extensive use of glass/kapton is made, which allows to keep a relatively thin

thickness of the insulation; 1.4 mm between turns, 3.8 between layers, and 7.4 mm to ground). The resin used for impregnation is Orlitherm (BBC trade mark) which proved to have excellent dielettric and mechanical properties in many former applications to fusion experiments (JET, TFTR etc..). Bonding between copper and resin is improved by using DZ80 primer.

Top and bottom M13 to M16 coils are supported at 12 locations only represented by the radial "C" frames of the mechanical structure. To be able to withstand the magnetic vertical forces, keeping the shear stress below the specified 5MPa, the coils have been designed with massive copper conductors, and shape shown in Fig.8. The main drawback is represented by a very uneven, current density distribution during fast rise; nevertheless calculations have shown that the corresponding field error is still acceptable.

All the coils (and the busbars) are water cooled.

TABLE III - Summary of stray fields

Field produced by (1)	Axysimmetric	Local
Design (background field)	x	
Coil manufacture (tolerances)	x	x
Coil positioning	x	x
Coil displacements (under load)	x	
Turn to turn transition		x
Layer to layer transition		x
Coil feeding terminals		x
Busbars		x
Current unbalance	x	
Diffusion phenomena (2)		
Induced current into non magnetic steel (2) (concrete reinforcement or other)	x	x
Saturation of steel elements (concrete reinforcements or others)	x	x

(1) Vertical Field produced by the vacuum vessel is not considered here

(2) Time dependent effects.

TABLE IV - Technical data for the copper

Composition		
Copper+Silver	minimum	99.95%
Silver	minimum	0.08%
Okygen	maximum	0.12%
Phosphorus	maximum	0.004%
Electrical resistivity	maximum	$1.76 \cdot 10^{-8}$Ohm·m (98%IACS)
Mechanical properties		
0.2 proof stress	minimum	200 MPa
	maximum	290 MPa
Elongation at fracture		14%
Ultimate tensile strenght	minimum	255 MPa
	maximum	315 MPa
Hardness (Vikers)	minimum	70 VHN
	maximum	90 VHN
Surface roughness parameter		
on the surface	maximum	1.6 micro m
in the hole	maximum	3.0 micro m
Average grain size		0.06 mm

3. TOROIDAL FIELD SYSTEM

3.1 Introduction

The required toroidal field, up to 0.7 T is produced by a toroidal field winding whose main technical data are given in Table V. It consist of 48 eight turn coils, evenly distributed around the shell every 7.5°. Each coil is split in two halves at the equatorial plane for assembly purposes, and the electrical continuity is provided by flexible connections to allow thermal expansion, the transition from one turn to the next being located at the outer equatorial joints as well as the current feeders. The coils are placed in grooves machined into the shell and tightly fastened to it by a pretensioned stainless steel belt 6 mm thick. In this way virtually no bending occurs in the coil, neither detachment from the shell.

TABLE V - Toroidal field winding parameters

Toroidal field	0.7 T
Total ampereturns	7 MAt
Number of coils	48
Turns per coil	8
Current per turn	18.2 KA
Copper cross section	24x22 mm^2
Turn rations	32-64-96-128-192-384
Insulation between turns	220 V
Insulation to earth (normal operation)	3.5 kV

3.2 Filed performance and ripple

Portholes wide enough for pumping, diagnostics and first wall protection element handling represent a very limiting constraint on the number of toroidal field coils, so that their arrangement, as described above, represents a compromise between field ripple requirements and accessibility. In this configuration and with steady state conditions and no plasma a maximum flux line deviation of 3.5 mm (compared with the ideal toroidal flux line) is found in the outer region of the vacuum vessel, (R=45 m, ϑ=0) this can be seen from Fig. 9 where flux line deviation have been plotted versus minor radius R for a number of angles.

The corresponding maximum transverse field is found to be B_r/B_{to}=0.03. This filed, shown in Fig. 10 as a function of the radius also for a number of poloidal coordinates, decreases very quickly from outside inwards, and becomes less and less important for a plasma well detached from the wall.

An alternative toroidal winding configuration with 72 coils has been considered to even further reduce the field ripple; in spite of much lower filed errors (one order of magnitude; see Fig. 11) this solution proved to present too many snags to be actually regarded as a workable alternative.

3.3 Coils and their connections

Each toroidal field coil consists of two layers of 4 turns each (Fig. 12), all of them connected in series. Upper and lower half coils are connected at the equatorial

plane.

Turn to turn and layer to layer connections as well as the feeding terminals are located on the outer side (Fig. 13).

The coils are permanently connected in twelve groups of four (Fig. 14), each of them presenting 32 turns (8x4) at its terminals.

Each group of four coils is fed by 500 mm^2 copper cross section cables, (Fig. 15). The number of turns can be change acting on links of a collector plate, located at the machine hall wall.

4. STATUS OF THE CONTRACTS

All the contracts for RFX coils have been placed and are expected to be completed by 1988 as shown in Table VI.

TABLE VI - Status of RFX contracts on magnet

	Supplier	Country	Start	Delivery
Magnetizing coils	Brown-Boveri TIBB	Switzerland and Italy	MARCH 87	NOVEMBER 88
Field shaping coils	Alsthom	France	MARCH 87	SEPTEMBER 88
Toroidal field coils	Jeumont Schneider	France	JULY 87	NOVEMBER 88

REFERENCES

/1/ The RFX Design Team, "The RFX Experiment Technical Proposal", Application for Euratom Preferential Support, Padova, Italy, 1982.

/2/ M. Guarnieri, G. Rubinacci, A. Stella, "Poloidal Magnetic System for a Large RFX Experiment", Proc. of the 11th SOFT, Oxford, 1980, pp 519-526.

/3/ G. Rostagni et al., "RFX 2 MA Project: Padova design studies.", University of Padova Report UPee 80/04, Padova 1980.

/4/ M. Guarnieri, C. Modena, B. Schrefler, A. Stella, "Electromagnetic and Mechanical Design of RFX Magnetizing Winding". Fusion Technology, vol. 8, n. 1, 1985.

/5/ F. Bellina, G. Chitarin, M. Guarnieri, A. Stella, "The RFX Field Shaping Winding Design", proc. of MT-9 Conference, Zurich, Switzerland, 1985.

/6/ G. Rostagni et al., "The RFX project: A design Review", Proc. of the 13th SOFT, Varese, 1984.

/7/ M. Guarnieri, A Stella: "A procedure for Axisymmetric Winding Design under Parametric Constraints: an Application to the RFX Poloidal Transformer", IEEE Transactions on Magnetics, Vol. Mag-21, No. 6, pp. 2449-2452.

/8/ F. Bellina et al., "Field errors in RFX Magnetic Field Configuration", proc. of the 14th Fusion Technology Conference, Avignon, France 1986.

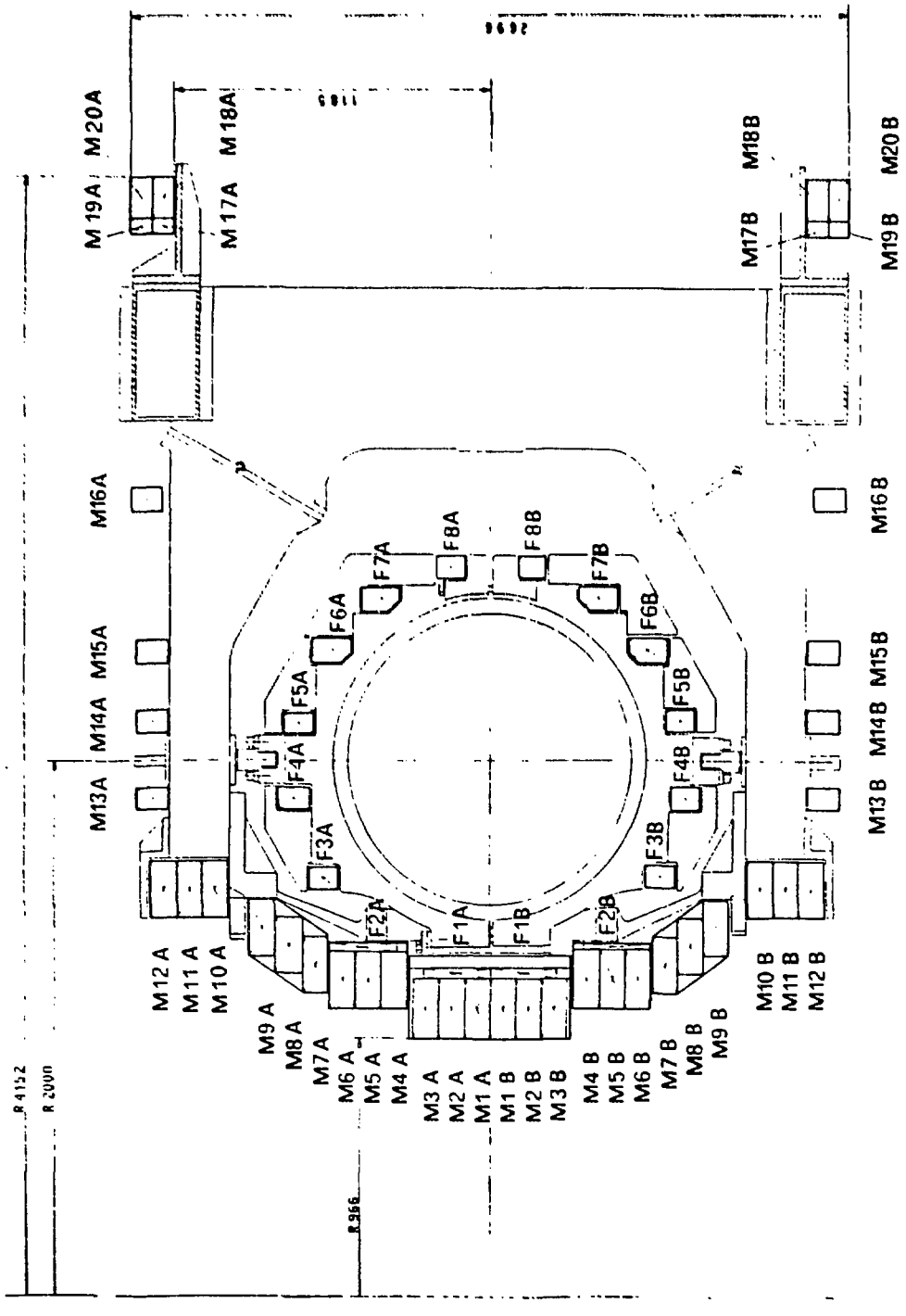
M 19 A
M 17 A
M 18 A
M 20 A
M 17 B
M 18 B
M 19 B
M 20 B
M16A
M15A
M14A
M13A
M16B
M15B
M14B
M13B
F1A
F1B
F2A
F2B
F3A
F3B
F4A
F4B
F5A
F5B
F6A
F6B
F7A
F7B
F8A
F8B
M12 A
M11 A
M10 A
M9 A
M8 A
M7A
M6 A
M5 A
M4 A
M3 A
M2 A
M1 A
M1 B
M2 B
M3 B
M4 B
M5 B
M6 B
M7 B
M8 B
M9 B
M10 B
M11 B
M12 B
R 2000

Fig. 1.

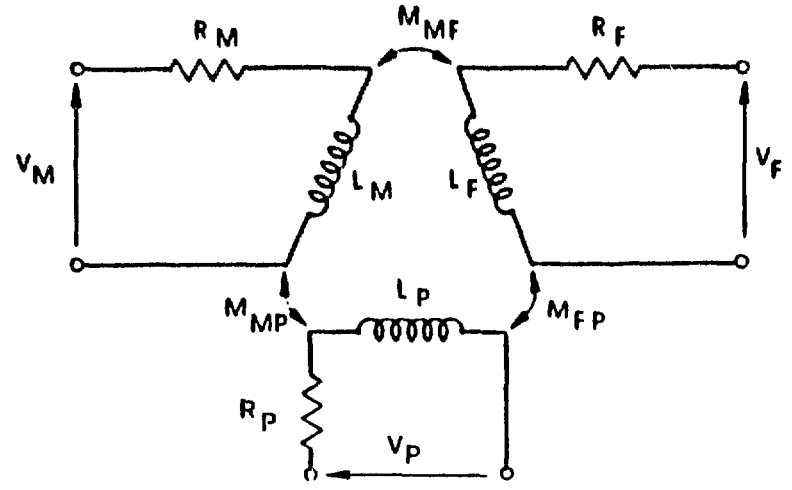

Poloidal system coupled circuits.

Fig. 2.

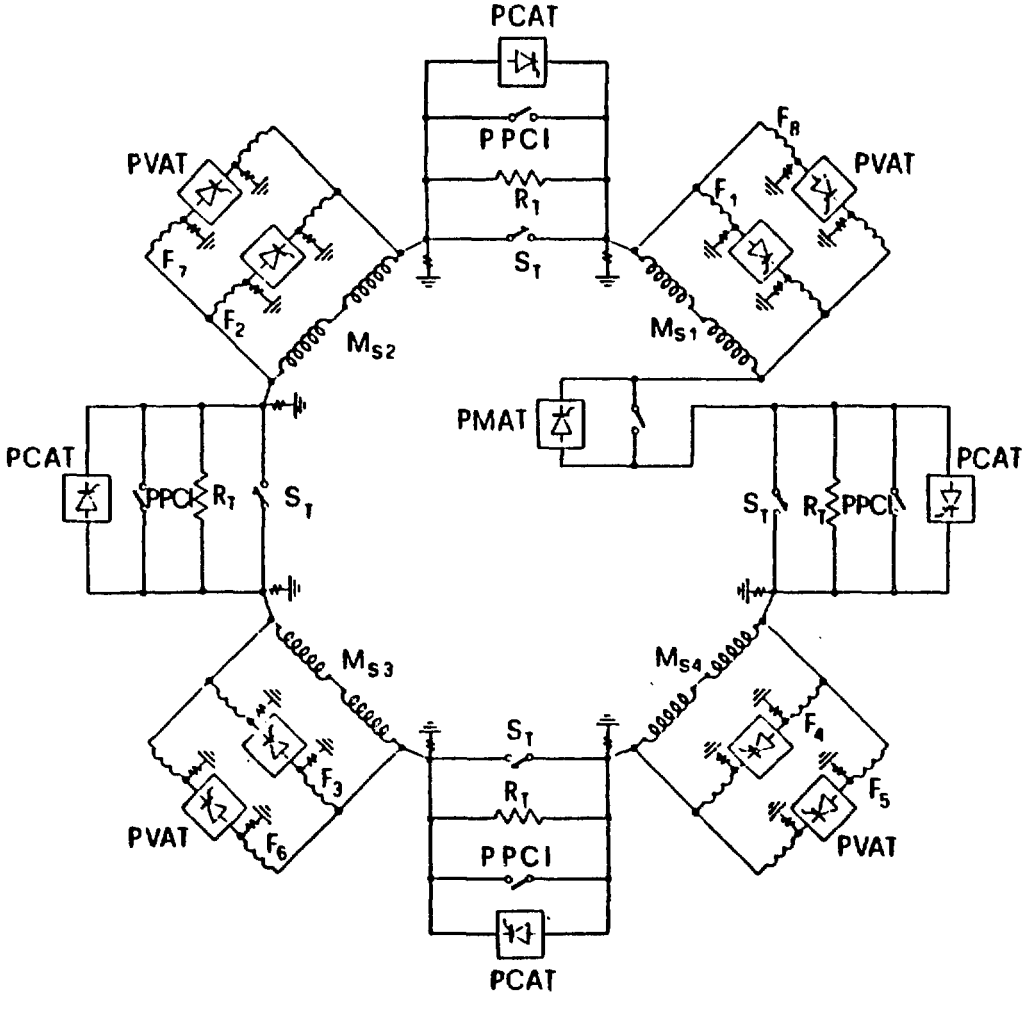

Fig. 3.

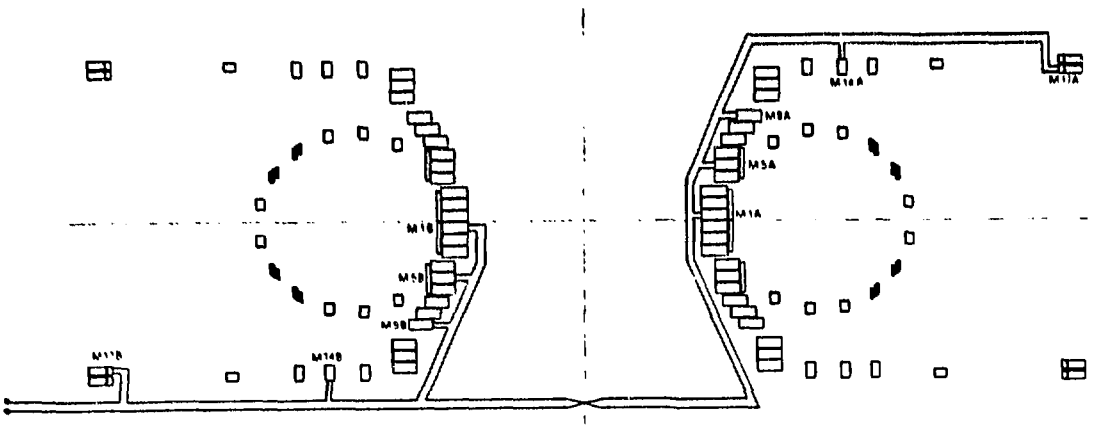

MAGNETIZING WINDING:

SECTOR 1 COIL CONNECTIONS

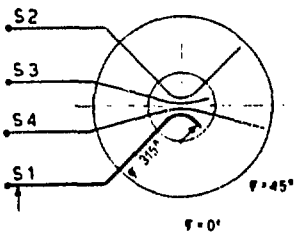

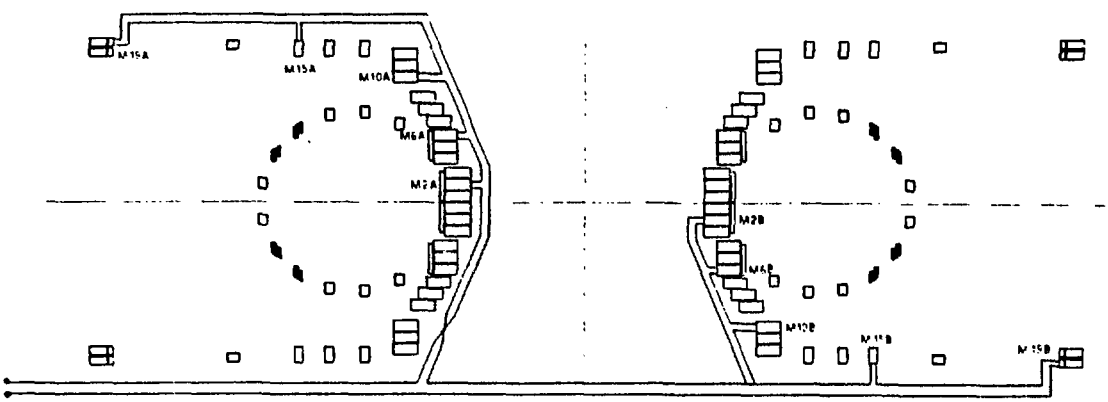

MAGNETIZING WINDING:

SECTOR 2 COIL CONNECTIONS

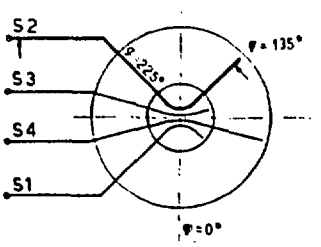

Fig. 4a.

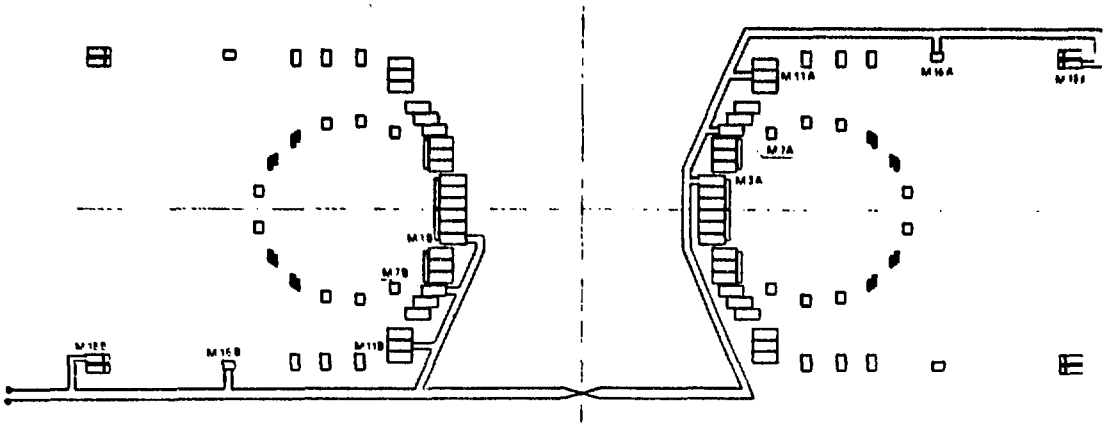

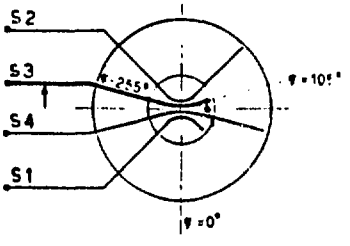

MAGNETIZING WINDING:

SECTOR 3 COIL CONNECTIONS

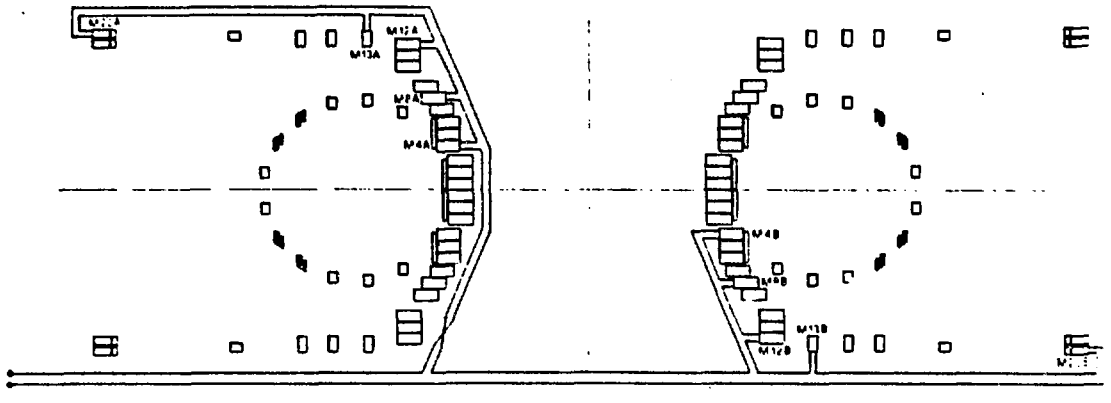

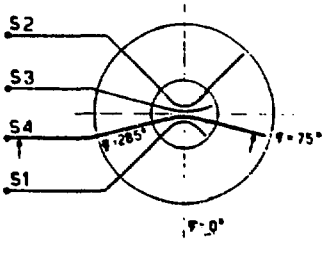

MAGNETIZING WINDING:

SECTOR 4 COIL CONNECTIONS

Fig. 4b.

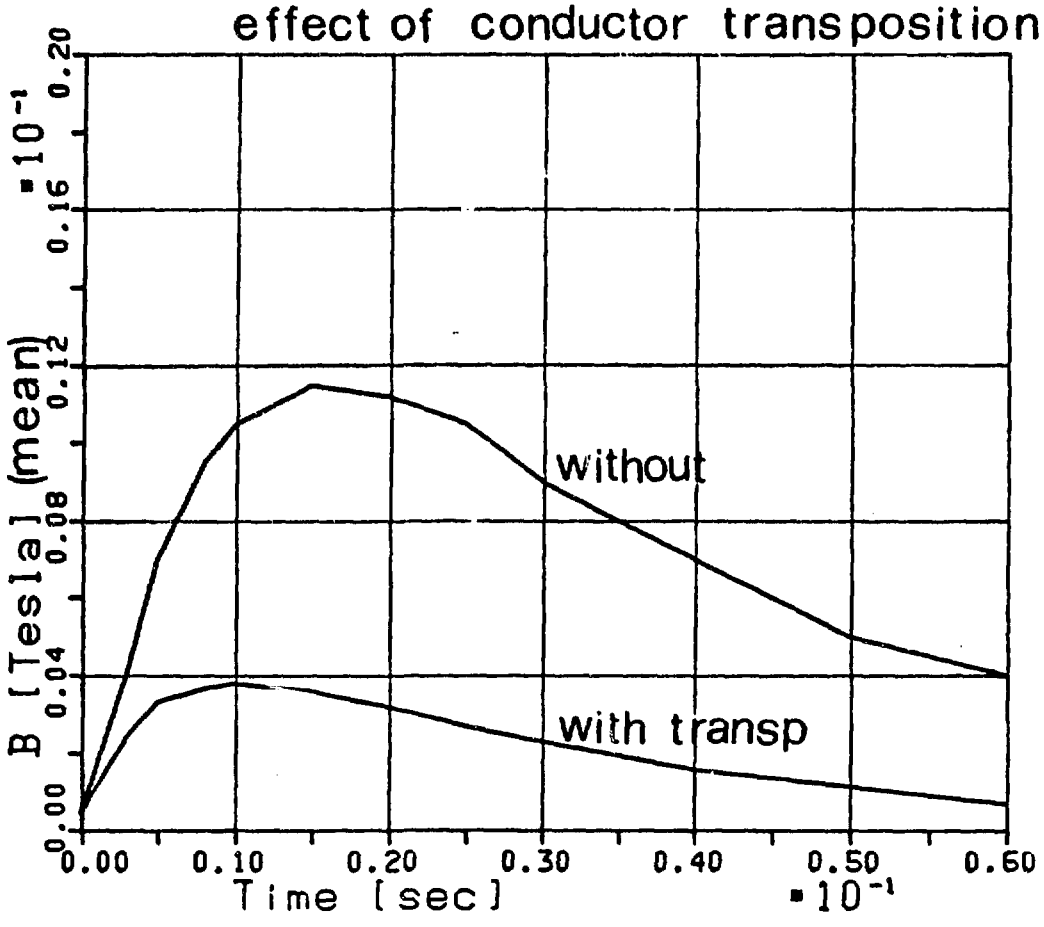
effect of conductor transposition
B [Tesla] (mean)
*10⁻¹
0.00
0.04
0.08
0.12
0.16
0.20
without
with transp
0.00
0.10
0.20
0.30
0.40
0.50
0.60
Time [sec]
*10⁻¹

Fig. 5.

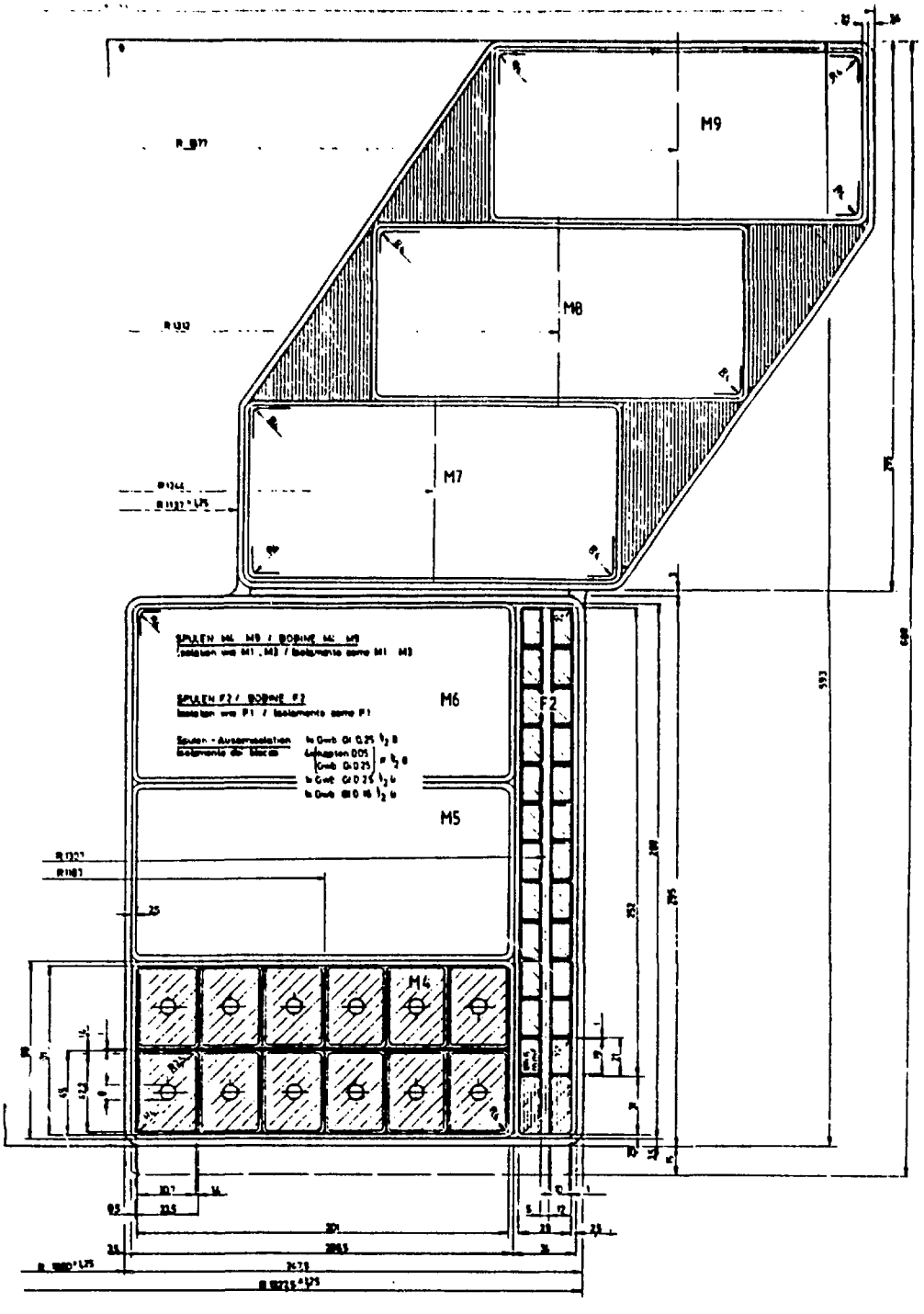

Fig. 7.

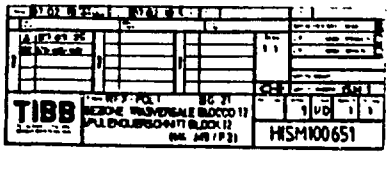

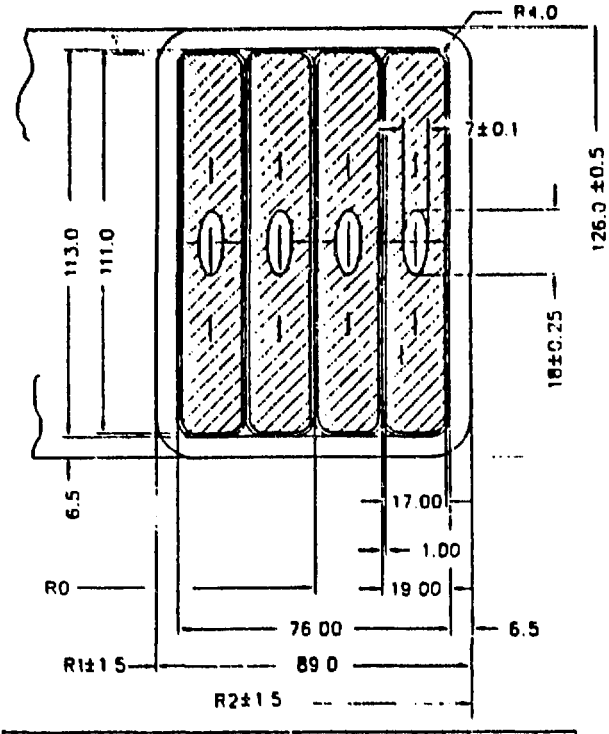

SPULE/BOBINA	I4/M13	I5/M14	I6/M15	I7/M16
R1	1810.5	2100.5	2355.5	2905.5
R2	1899.5	2189.5	2444.5	2994.5
R0	1855	2145	2400	2950

Fig. 8.

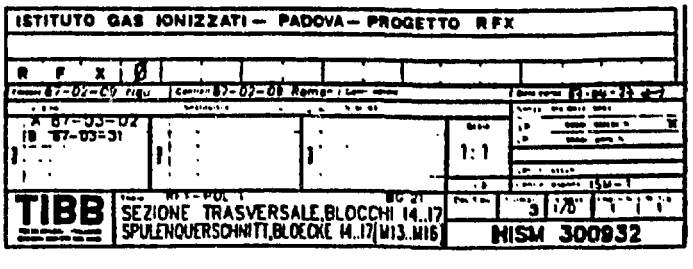

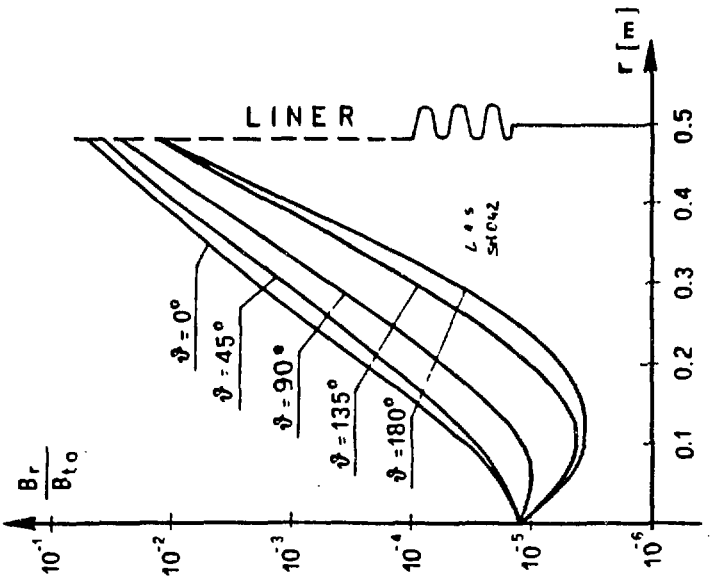
LINER
r [m]
0.1
0.2
0.3
0.4
0.5
$\frac{B_r}{B_{to}}$
10^{-1}
10^{-2}
10^{-3}
10^{-4}
10^{-5}
10^{-6}
$\vartheta = 0°$
$\vartheta = 45°$
$\vartheta = 90°$
$\vartheta = 135°$
$\vartheta = 180°$

Fig. 9.

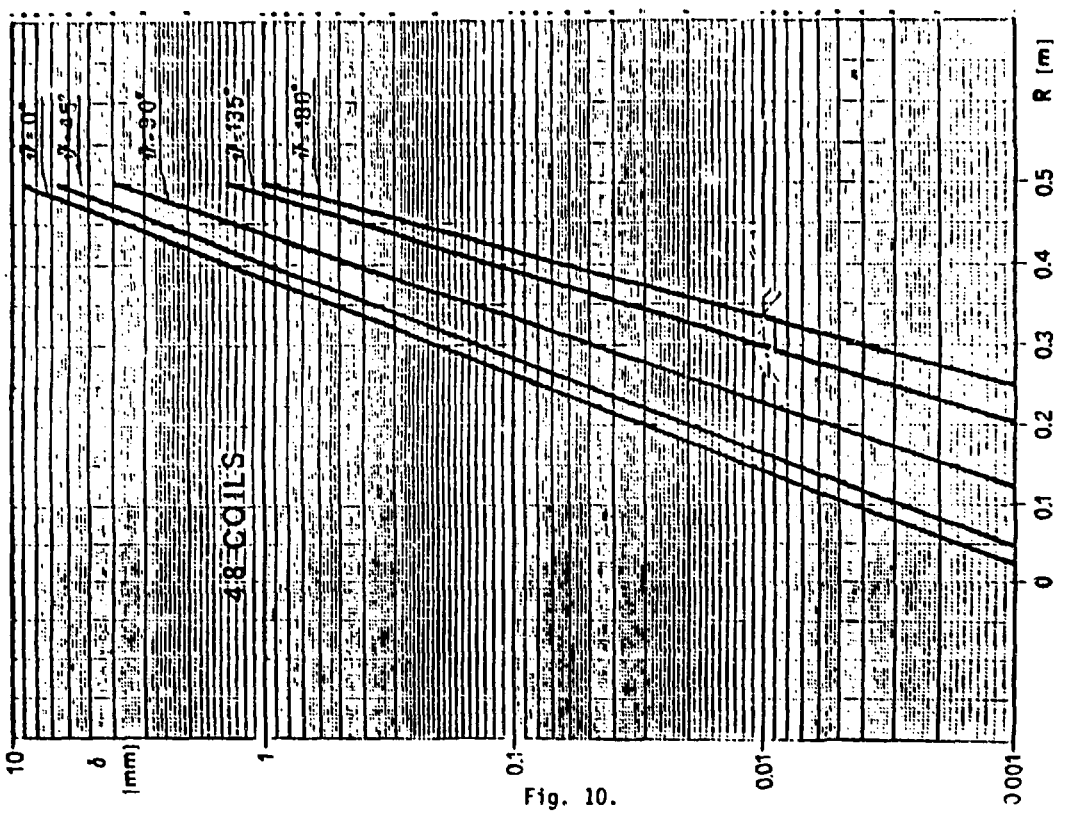
48 COILS
$\vartheta = 0°$
$\vartheta = 45°$
$\vartheta = 90°$
$\vartheta = 135°$
$\vartheta = 180°$
δ (mm)
10
1
0.1
0.01
0.001
0
0.1
0.2
0.3
0.4
0.5
R [m]

Fig. 10.

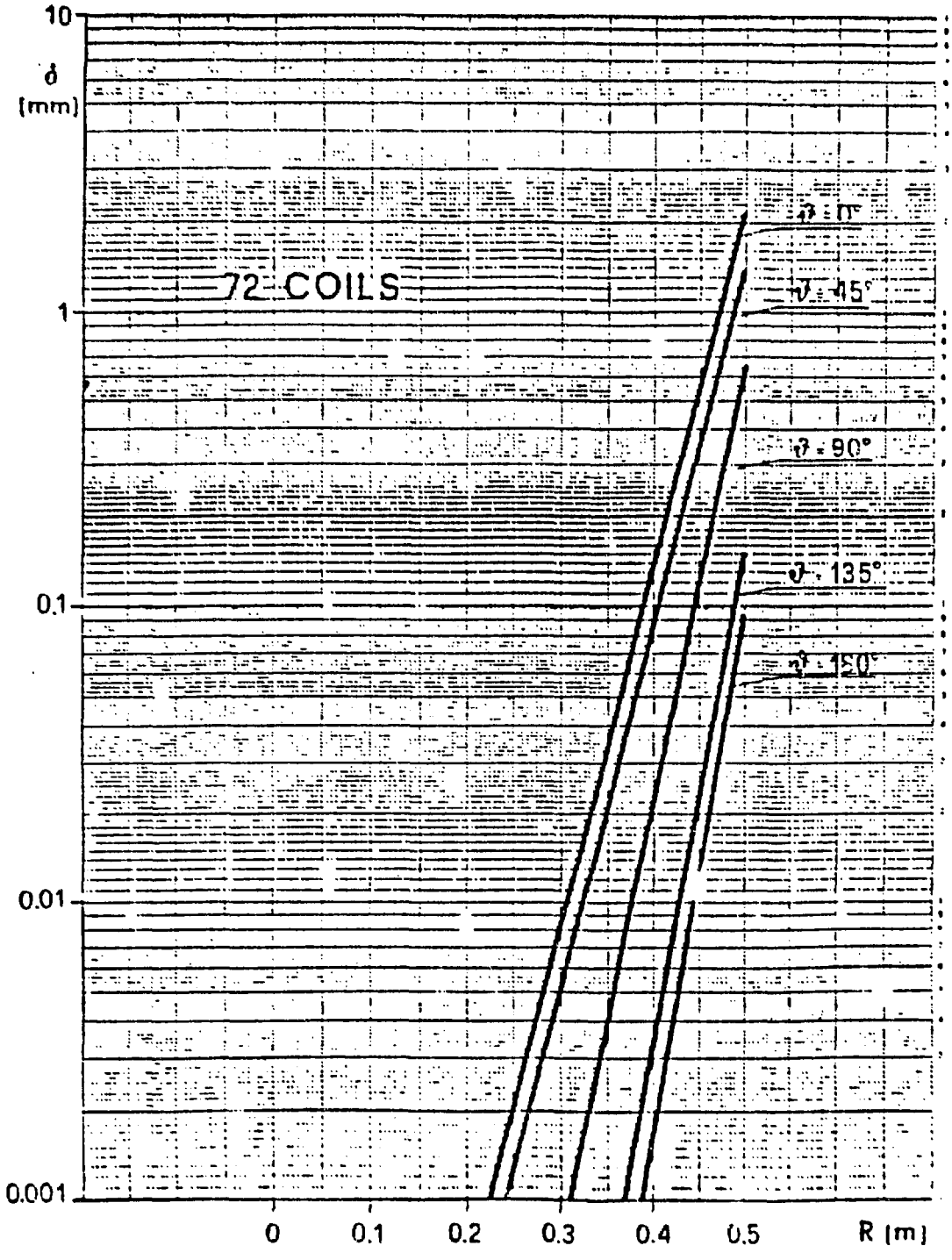
10
δ
(mm)
1
0.1
0.01
0.001
72 COILS
ϑ = 0°
ϑ = 45°
ϑ = 90°
ϑ = 135°
ϑ = 180°
0
0.1
0.2
0.3
0.4
0.5
R (m)

Fig. 11

NOTA LE TOLLERANZE SONO LIMITATE ALLA PARTE DI BOBINA INSERITA NELLA CAVA

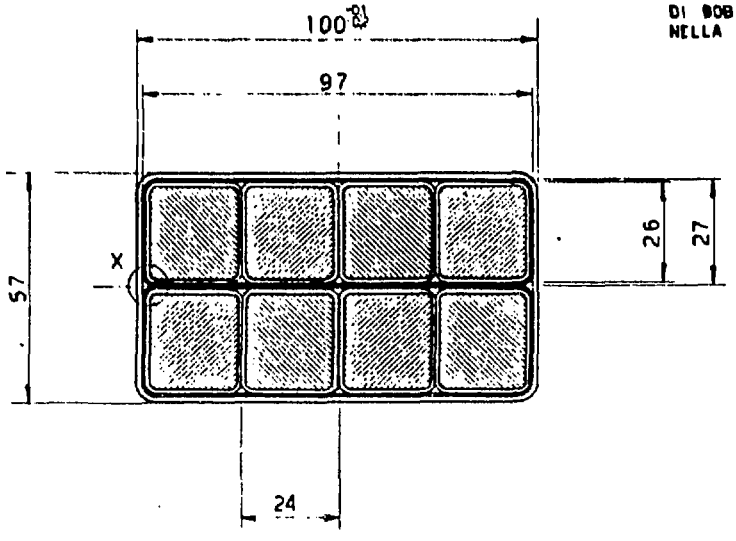

Part X Scala 5:1

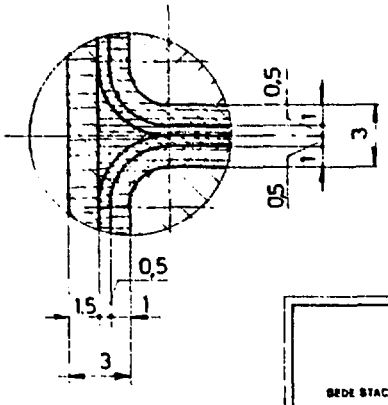

Sezione conduttore: 524,57mm²

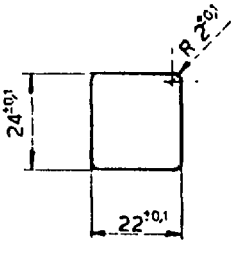

ISTITUTO GAS IONIZZATI – PADOVA (ITALY)

SEDE STACCATA PER PROGETTO RFX P.ZZA SALVEMINI 12/13 - 35131 PADOVA - TEL. (049) 887800 - TELEFAX 881439

CONSIGLIO NAZIONALE DELLE RICERCHE ASSOCIAZIONE EURATOM - C N R

PROGETTO RFX	1:1
SISTEMA MAGNETICO	16-01-87
	2102 87
AVVOLGIMENTO TOROIDALE	Stella-Bellina
	Fabio Leonardo
SEMIBOBINA TOROIDALE: SEZIONE TRASVERSALE	

R F X Ø S M A T P E 0 0 0 3 0 7 0

Fig. 12.

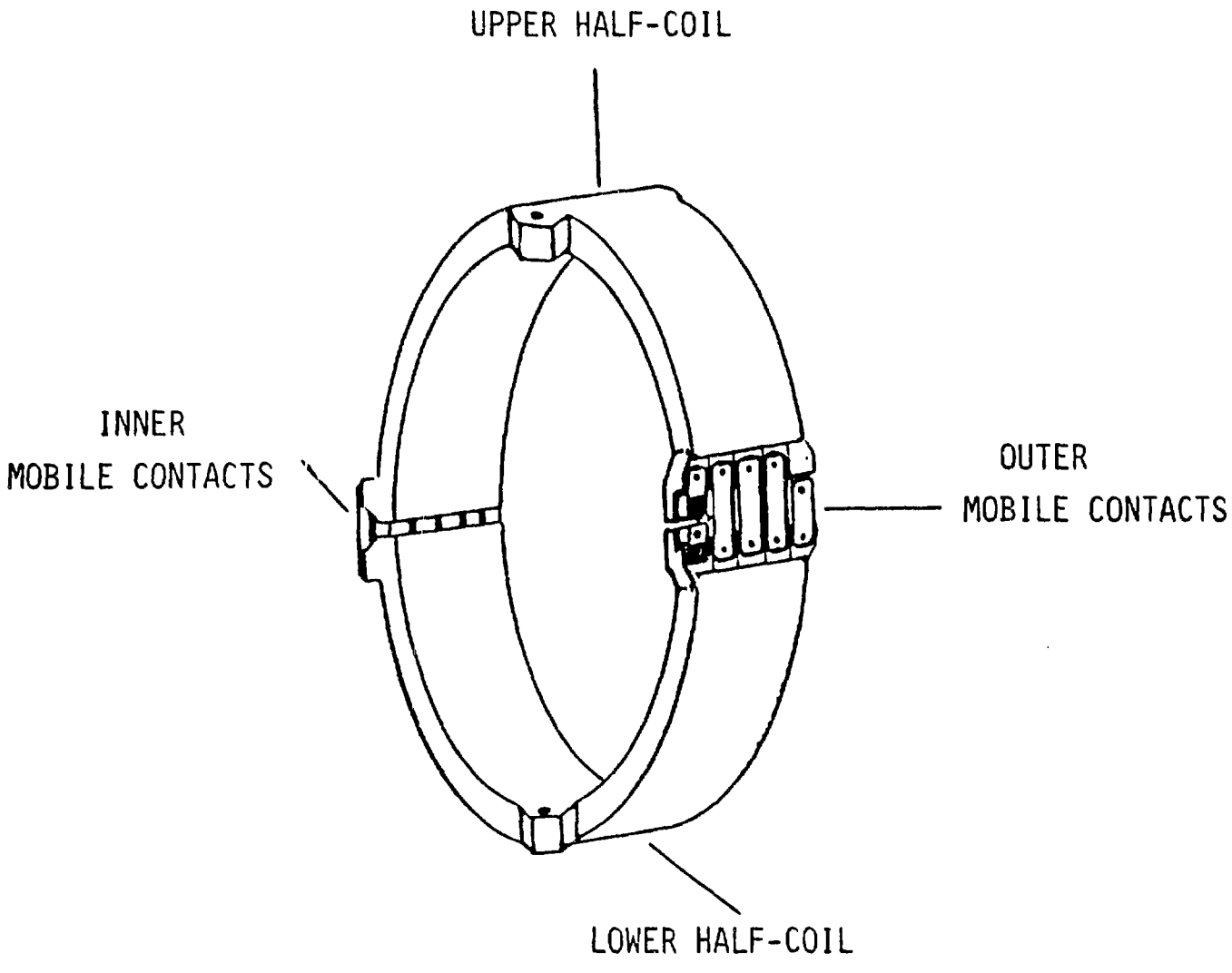

TOROIDAL COIL ELEMENTS

Fig. 13.

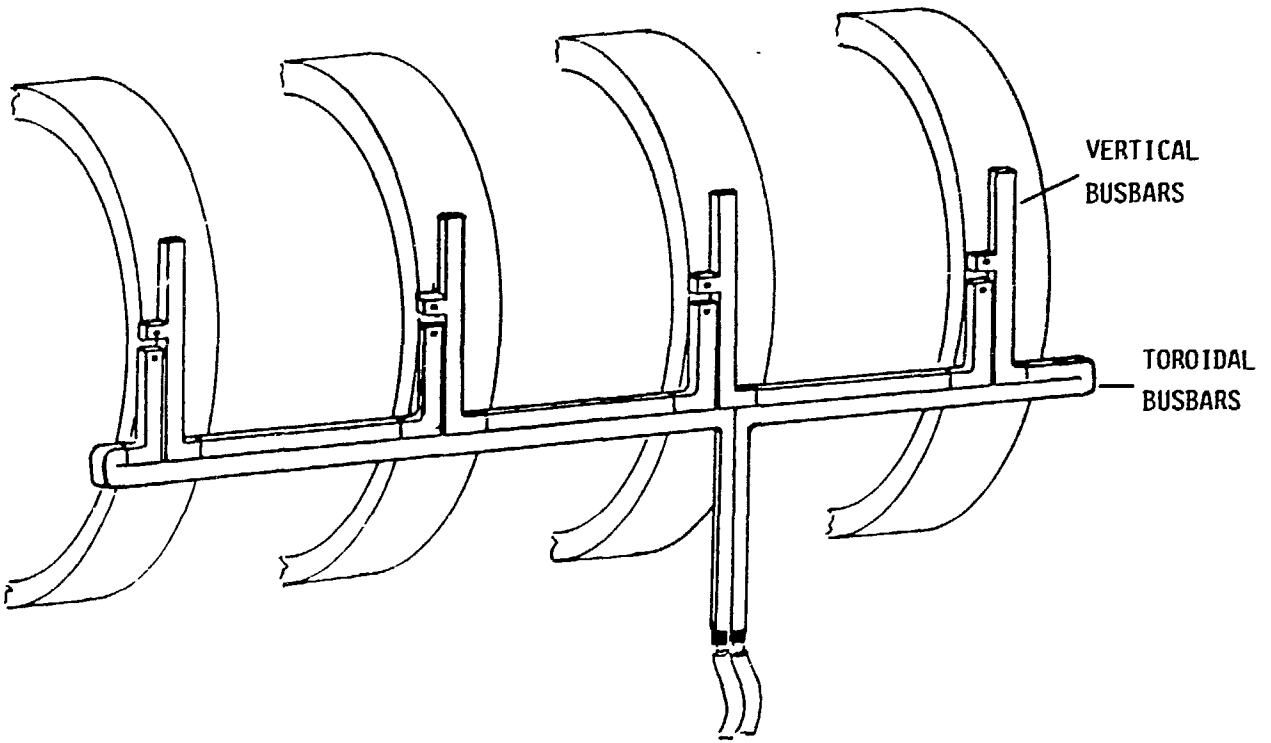

Fig. 14.

TOROIDAL COIL BUSBARS SYSTEM

ZTH GENERATOR

Boris J. Rosev
Los Alamos National Laboratory

SUMMARY

The 4 MA ZTH fusion experiment requires about 800 MW of power and 600 MJ. That amount of power and energy cannot be taken from the local utility system. Inertial energy storage by a pulsed generator is necessary. It is more cost effective to use a surplus generator instead of a specially designed pulsed generator. After discussions with several major turbogenerator manufacturers the recommendation was to use a 1800 RPM machine instead of a 3600 RPM. The 1800 RPM generators built primarily for nuclear applications experience lower dynamic stresses and fit better for our pulse mode operation.

Generator Description

Several available generators owned by U.S. utilities were evaluated. Some had less power capacity than the required 800 MW, the others were above 900 MW capacity. Having a generator with higher capacity than needed is more expensive to transport, install and operate. Our final choice is a new, never used, generator owned by TVA and manufactured by Brown Boveri Corporation (BBC). The generator was designed to provide electrical power in a nuclear power plant which was cancelled. It was designed for a power plant life of 40 years.

The BBC generator ratings are:

Power, MVA - 1,430

Voltage, KV - 24

Speed, RPM - 1,800

Energy at 1,800 RPM, MJ - 1,210

Extractable Energy, MJ - 600

(1,800 RPM to 1,260 RPM)

Cooling Hydrogen, PSIG - 75

Current, KA - 34.4

Frequency, Hz - 60

LANL is working with BBC on modification for air cooling instead of hydrogen cooling. The advantages of air cooling are:

1. Very simple operation. There will be no need of seal oil, stator water cooling, H_2 cooling and CO_2 systems. It will be less expensive and easier to install and operate the machine.

2. Safe operation using dry air instead of H_2. Hydrogen leaks in the generator create potential danger for explosion.

3. Less environmental problems are foreseen.

A disadvantage of air cooling is that during standstill dry air has to be supplied into the generator to avoid humidity problems.

Originally, the generator was designed for steady-state operations. BBC investigated its suitability as a power source for a pulsed loading. Generator loading profile concerning active and reactive power were specified by the Los Alamos National Laboratory.

Brown Boveri investigated the effects of pulsed loading on the machine electrically and mechanically.

The results showed that the required load curve can be obtained. The existing static excitation system, provided with the generator with power supplied from the generator terminals and with a ceiling voltage of 1000 V, is suitable for the pulse mode operation. The stresses to which the generator is subjected during a power pulse are acceptable.

The thermal load on the winding, including the harmonics in the current due to a 12-pulse rectifier operation, is not critical. The average total power loss in the rotor lies below the continuous loss of the field current at rated operation.

Mechanically, high stress areas, such as the rotor teeth, the retaining rings, the rotor body, subjected to pulsed loading, were investigated. It was found that the rotor can take the cyclic stress for 100,000 shots without the flywheel and between 5,000 to 10,000 shots with a 2,800 MJ flywheel.

Once per year, the rotor will be removed from the stator and examined for internal cracks using the latest ultrasonic techniques.

LANL is considering to purchase a spare generator rotor from TVA surplus inventories.

Drive System

The BBC generator will be brought up to speed by motorizing it instead of using a separate electrical motor. The advantages are:

1. Lower energy losses

2. Shorter length of the generator installation train

3. Shorter generator foundation and building

4. Less expensive installation

5. Reduced vibration level

The drive system consists of a transformer rectifier, dc reactor and inverter. In Fig. 1, a circuit diagram of a possible unit is shown. During the acceleration phase, the generator is excited at constant volts/seconds. At synchronous speed, the generator voltage is about 4000 V. This requires a small static exciter with a voltage and current rating of 400 A and 30 V.

In the future when the generator will be furnished with a flywheel, the existing drive system can be connected in parallel with an identical new unit in order to double the drive power.

Transportation

The present location of the generator is Hartsville, Tennessee on the Cumberland River. The generator will be transported on a barge from Hartsville, TN to Houston, TX. From Houston, TX to Lamy, NM, it will continue by rail on a Schnabel car transporter. From Lamy, NM to Los Alamos, NM, a road transporter will be used. The transportation of the generator will take place in February 1988.

Building

The generator building will be located west of the existing ANTARES Target Building (TSL-124) at TA-35. It will be a pre-engineered metal building, 60 ft. wide by 200 ft. long, by 60 ft. high. The building will be erected over the machine immediately after the generator stator is placed on its foundation in March of 1988. The building has two floors. The upper floor is the operating floor, which also includes a small control room.

Spring Loaded Foundation

The generator reinforced concrete foundation will use approximately 5,400 cubic yards of concrete. The design of the foundation for the generator was based on the static loads of the equipment and generator to be supported and the dynamic loads resulting from repetitive pulsed loading of the generator, short-circuit conditions, and a soil movement criterion less than 0.2 by 10^{-3} mm within 200 meters distance of the machine.

Because of the dynamic stresses during the repetitive pulse operation, the generator manufacturer recommended a spring supported foundation. Also, because of the proximity of the generator with laser experiments involving delicate optical equipment at TA-35, it was decided that the generator be isolated from the supporting geological structure by mounting the generator on a spring supported foundation. The concrete structure on which the generator is mounted will be supported by a total of 60 springs (30 springs on each side).

The foundation was designed by Kaiser Engineers with the support of P. W. Stadelmann as a consultant and BBC. The foundation design and the site excavation are 95% complete. Some time this month, the erection of the generator foundation will start. Pan Am Company will perform the construction.

Vibration and Soil Movement

For the pulsed power generator a concrete spring mounted foundation was selected. Below the springs, a concrete slab upon gravel as a spring mass system upon the rock, volcanic tuff was considered. The excitation load is a torque applied by the generator stator upon the concrete surface. To analyze the vibration transmission from the generator, P. W. Stadelmann made computer simulations and vibration levels were calculated at certain distances from the generator.

The results for the machine foundation for forced vibration due to the pulsation torques applied by the stator on top of the concrete foundation result in a foundation movement of 0.6 mm and movement of the gravel of 0.3 mm at a frequency of f = 30 Hz.

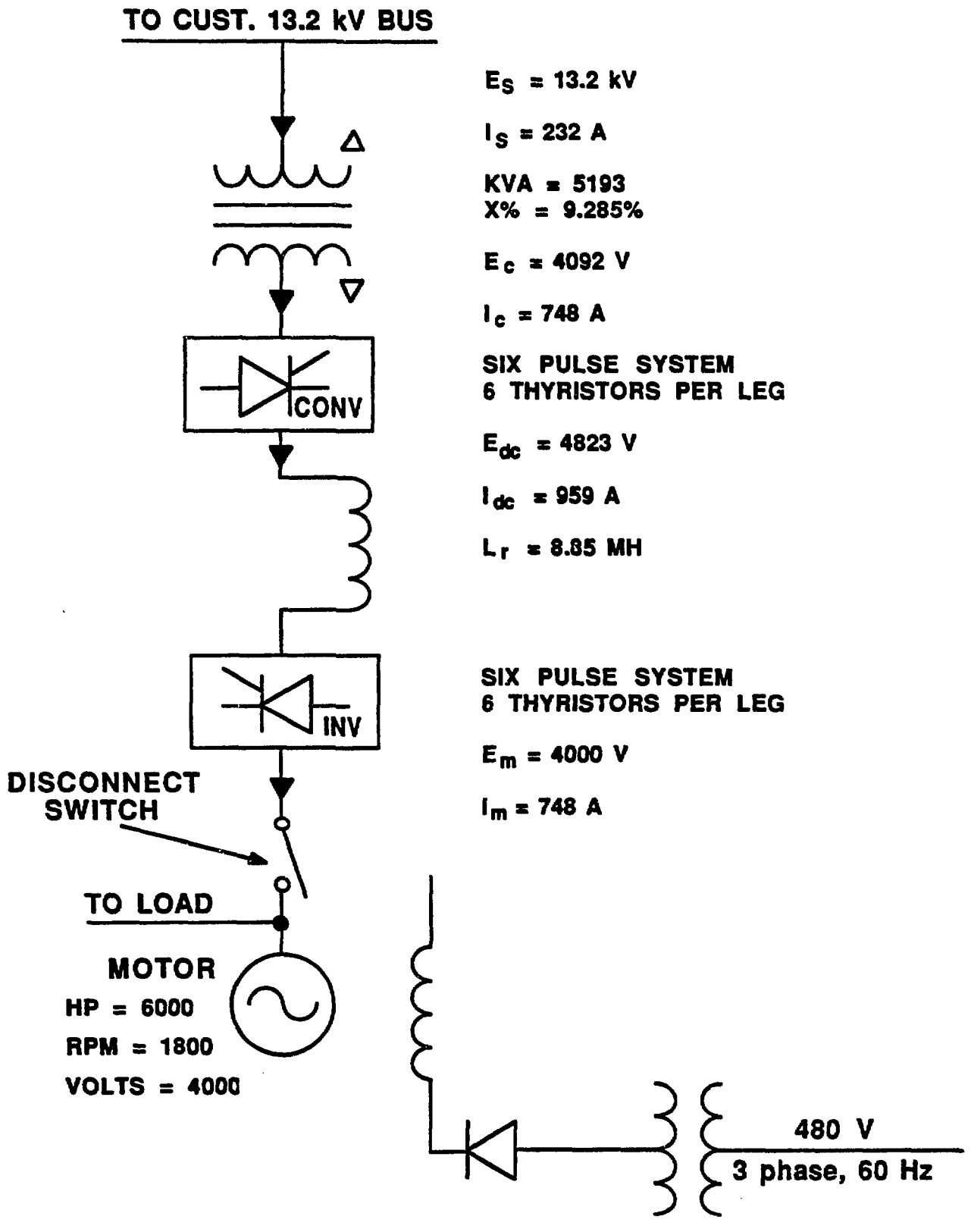

E_S = 13.2 kV

I_S = 232 A

KVA = 5193
X% = 9.285%

E_c = 4092 V

I_c = 748 A

SIX PULSE SYSTEM
6 THYRISTORS PER LEG

E_{dc} = 4823 V

I_{dc} = 959 A

L_r = 8.85 MH

SIX PULSE SYSTEM
6 THYRISTORS PER LEG

E_m = 4000 V

I_m = 748 A

SINGLE LINE DIAGRAM FOR LOS ALAMOS

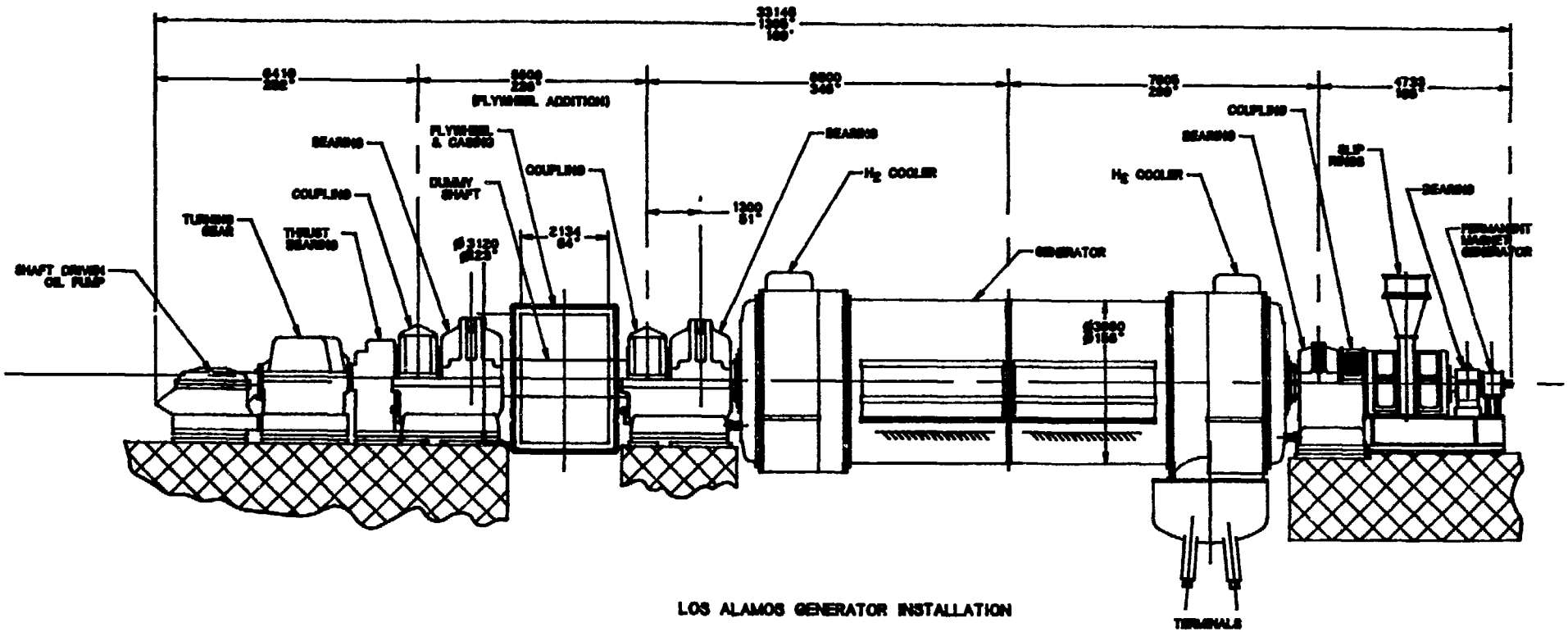

LOS ALAMOS GENERATOR INSTALLATION

A LIGHTNING PROTECTION SCHEME FOR THE CPRF/ZTH SYSTEM COMPLEX

by

HERBERT KONKEL
Los Alamos National Laboratory

ABSTRACT

This paper describes some of the background in the design and the lightning protection and grounding scheme recommended for the CPRF/ZTH system at the Los Alamos Laboratory. Standard power industry practices were applied to minimize the effect on both the system and personnel of a high magnitude, direct lightning discharge in the CPRF/ZTH area. The recommended scheme is in compliance with existing local and national electric and safety codes.

INTRODUCTION

The Los Alamos area with both its high isokeraunic(1) level and high soil resistivity requires special consideration given to its grounding design and protection layout for both environmental and fault conditions. A lightning discharge to earth creates a high earth potential gradient that decreases with distance away from the point of discharge(1,2). This potential gradient causes high both current and voltage magnitudes within the discharge area. If the discharge occurs in the immediate area of the CPRF/ZTH system, then potential damage can result to the hardware and expose personnel to hazardous conditions. These potential hazards are aggravated with the CPRF/ZTH system layout distributed between three separate building areas. The system is interconnected with high capacity current paths which, during a lightning discharge condition in the immediate area, floats at different potentials along the earth gradient profile. Since the system is referenced to ground at several points, the earth gradient is applied directly to its hardware. With the high conductive paths of the system, the high voltage potentials are transferred to other locations within the system. Because of these potentially hazardous conditions, grounding schemes for the CPRF/ZTH system were evaluated to minimize and limit the high voltage potentials within the system to acceptable levels, limit the high magnitude discharge or fault currents that could occur within the system and maintain a safe working environment for personnel under both normal and abnormal conditions. This work will describe the recommended lightning protection and grounding scheme for the CPRF/ZTH system which is indicated in figure 1.

GROUNDING SCHEME INVESTIGATED

With a criteria of a safe environment for both personnel and hardware, digital model investigations were performed using the Bonneville Power Administration's Electromagnetic Transients Program(3) version M43+. Grounding schemes using both single-point and multi-point grounds, low and high impedance common reference

circuits for the system hardware, building air terminals and counterpoise systems and static overhead wires were evaluated for their effectiveness. Any grounding scheme selected would have to adhere to existing local and national safety, electric codes and practices.

In the evaluation of the various grounding and protection schemes a standard ANSI/IEEE waveform of 1.2us X 50us voltage waveform providing a discharge current magnitude of 200kA was used to evaluate the effects of the discharge on the particular protection scheme studied. The voltage magnitude was varied to achieve a consistent current magnitude between each case.

Since the generator location has a greater separation distance than the other system components, it offered the system the highest exposure to earth gradients under both fault and lightning discharge conditions. With a solid earth bond applied to the generator common, high ground fault magnitudes could exist that require a highly conductive earth path for the ground return between the system components. Under discharge conditions, high current magnitudes could exist over this path which exposes both personnel and hardware to high earth potential gradients and potentially hazardous conditions. The early studies showed that voltages as high as 1.2MV and currents as 75kA existed in and around the system. These results indicated that the grounding requirement had to be above the normal grounding application.

The application of a limiting resistor in the generator neutral(4) limits the current to a low magnitude of current under ground fault conditions. With the limited, low magnitude ground fault current, the need for a high capacity current ground return path between the generator and power supply system components is no longer necessary. In the CPRF/ZTH system, a neutral grounding, stepdown transformer is recommended so its secondary provides both the use of a lower voltage resistor circuit and dielectric isolation for the protection hardware. Since the generator winding common is still earth referenced through the transformer, earth potentials are still transferred over the high potential bus connection to the power supply building, but its effect is reduced due to the neutral transformer impedance. Metal oxide surge arrestors will be dielectricly coordinated and applied to limit voltage potentials below the system equipment BIL.

For greater protection from the high earth gradients during near or direct discharge conditions, building air terminals and counterpoise systems were included in the investigation. Most buildings on the Laboratory complex include air terminals and counterpoise to divert lightning discharge energy to earth and away from structures or hardware. Air terminals are intertied by a roof counterpoise and down-links to the earth counterpoise. This integrated system distributes the high discharge potentials over the building area while the earth path diversion takes place. Because of the high soil resistivity in the Los Alamos area, ground wells are added at intervals to the earth counterpoise to improve the

conductive path to remote earth. Earth counterpoise are interbonded to increase the path to remote earth efficiently and to distribute the earth potential gradient over a greater earth surface area. This reduces the potential per unit distance. In the CPRF/ZTH application, by applying a counterpoise around the generator building and then bonding to the existing building counterpoise network in the general area, the earth potential gradients are reduced which reduces the voltage gradients within the system. Additional earth paths between the generator building counterpoise and the existing counterpoise were applied for more efficient gradient distribution due to the separation distance between hardware, the large generator building area, and the high frequency characteristics of a lightning discharge. These paths assure more uniformity in the resulting earth potential gradient.

The building concrete foundation offers a low impedance path to near (local) earth. This necessitates the building concrete reinforcement bar be bonded to the system ground bus to reduce the possible potential gradient between the floor and the system hardware. Bonding the reinforcement bar to the ground bus reduces the step-touch potential to personnel. A single-point ground was selected between the Power Supply and Torus buildings to bond the counterpoise and reinforcement bar of both buildings to the system common ground bus. Bonding is also required at the generator building between the counterpoise, the reinforcement bar and common ground within the generator building for the same purpose. This scheme minimizes the circulating currents due to earth gradient potentials. Although with the single-point ground scheme under high discharge current conditions, a potential gradient does exist between the building floor and system ground bus in each of the buildings, any current flow is limited by the higher impedance of the above surface concrete.

From the investigation of grounding schemes using single and multi-point grounds showed that a single-point ground scheme is preferred over a multi-point scheme. With a multi-point scheme current magnitudes over 4500 Amps were possible along the ground bus. This scheme also exposes personnel to high voltages (greater than 8000 volts under some conditions) between the floor and system hardware. With the single point ground scheme, circulating between the system and earth are reduced to zero. The voltage exposure to personnel increased to almost 50kV but of shorter in energy magnitude and time duration. The hazard still remained for both hardware and personnel mainly in the Torus area during a discharge condition. The high voltages differences existing between the floor and common ground bus were due to the high surface potential gradient existing between the Power Supply and Torus building areas.

Earth gradients could be minimized if earth currents, resulting from a discharge, were diverted away from the area of the system. This effect occurs with the application of static earth wires in the area above the buildings if their earth grounding scheme is properly applied. Each of the static towers earth counterpoise must have a low impedance to remote earth and must be independent of the building's

earth counterpoise network. This type of protection is in common practice in the power industry throughout the world. Accepted design guidelines are outlined in the National Fire Protection Association Code (5) and a number of IEEE/ANSI standards(6,7). The layout of the towers and static wire configuration are illustrated in figure 2.

With a grounding and protection scheme of using static wires and single point grounding described above, the study indicated that, for a lightning discharge to the static wires, voltage differentials between the floor and hardware were reduced to less than 800 volts of 80 us duration, see figure 3.

CONCLUSION AND RECOMMENDATION

In conclusion, the following grounding scheme is recommended for the CPRF/ZTH System at Los Alamos. The scheme is in compliance with existing local and national codes and provides safety to both hardware and personnel during normal operation, fault and lightning discharge conditions.

a. A ground bus common with both the Power Supply and Torus Buildings referenced to ground at a common location (single-point) between the these buildings. The common ground bus would not extend back to the generator building.

b. Single point ground references for the ground bus systems at the Generator Building and between the Power Supply and Torus Buildings. At both locations, the building's counterpoise and reinforcement bar would be bonded to the local system common ground bus.

c. A generator neutral grounding transformer with current limiting resistors applied in the secondary circuit to limit ground fault current magnitudes.

d. The present IEEE recommended generator surge protection scheme be applied to the generator terminals and be dielectricly coordinated with the other system hardware.

d. Static overhead wires connecting four towers located at the perimeter of the buildings. The towers would be at least 80 feet in height.

e. In the immediate area of each tower, independent counterpoise be used with a low value of resistance to remote earth. The low resistance could be obtained with the application of ground wells in a distributed configuration.

The application of these recommendation would divert lightning discharge currents away from the immediate building area and raise the earth potential in the area contained within the static wire towers to a near uniform potential. Because of this reduced potential gradient between buildings resulting from a lightning discharge

condition, voltage differences within the CPRF/ZTH system are limited to safe levels.

REFERENCES:

1. IEEE Std 142-1982, IEEE Recommended Practice for Grounding of Industrial and Commerical Power Systems.

2. ANSI/IEEE Std 80-1986, IEEE Guide for Safety in AC Substation Grounding.

3. Electromagnetic Transients Program (EMTP) Rule Book, May 1986.

4. ANSI/IEEE C37.101-1985, Guide for Generator Ground Protection.

5. NFPA 78-1983, Lightning Protection Code, National Fire Protection Association.

6. IEEE Std 141-1982, IEEE Recommended Practice for Electric Power Distribution For Industrial Plants.

7. IEEE Std 487-1980, IEEE Guide for the Protection of Wire-Line Communication Facilities Serving Electric Power Stations.

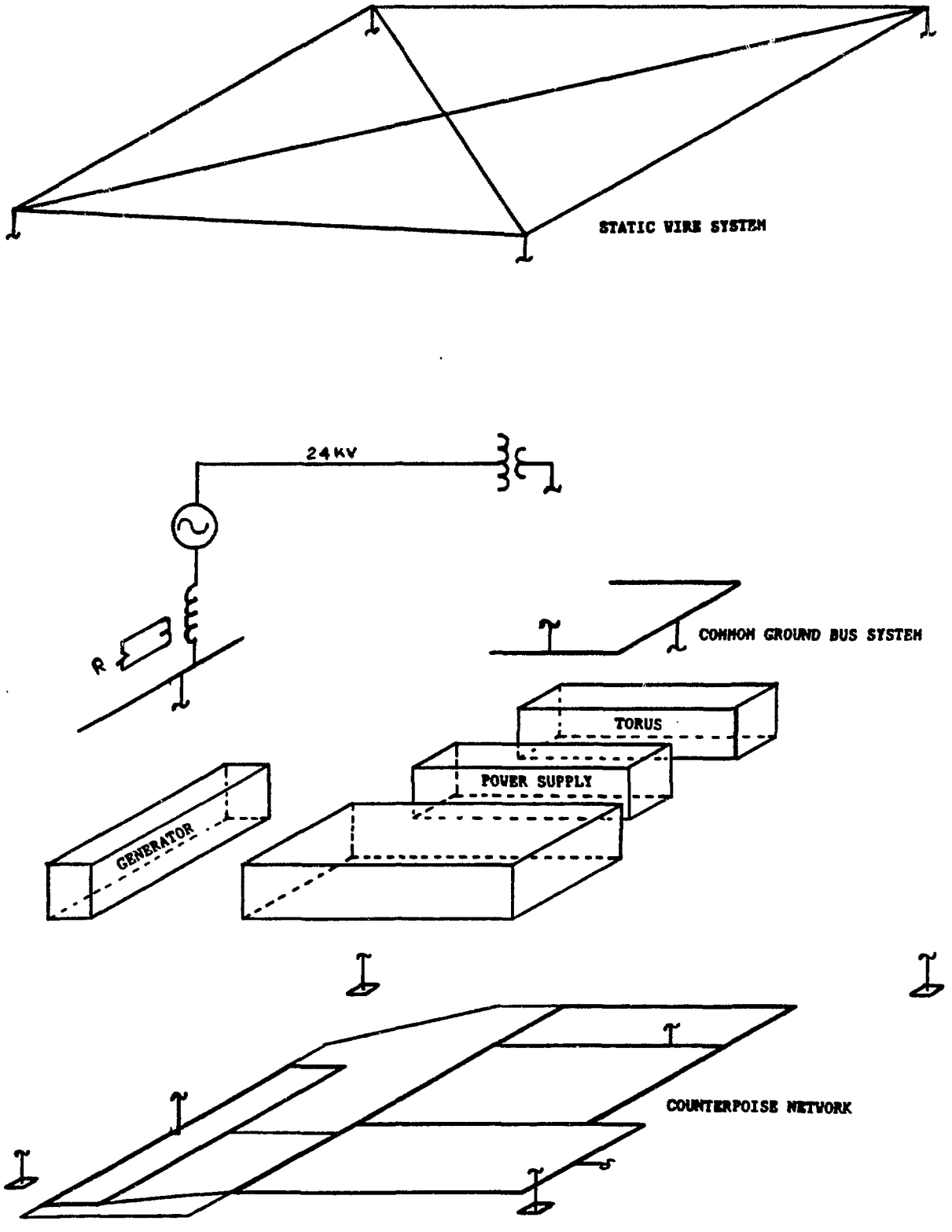

Figure 1. RECOMMENDED LIGHTNING PROTECTION SCHEME FOR THE CPRF/ZTH SYSTEM.

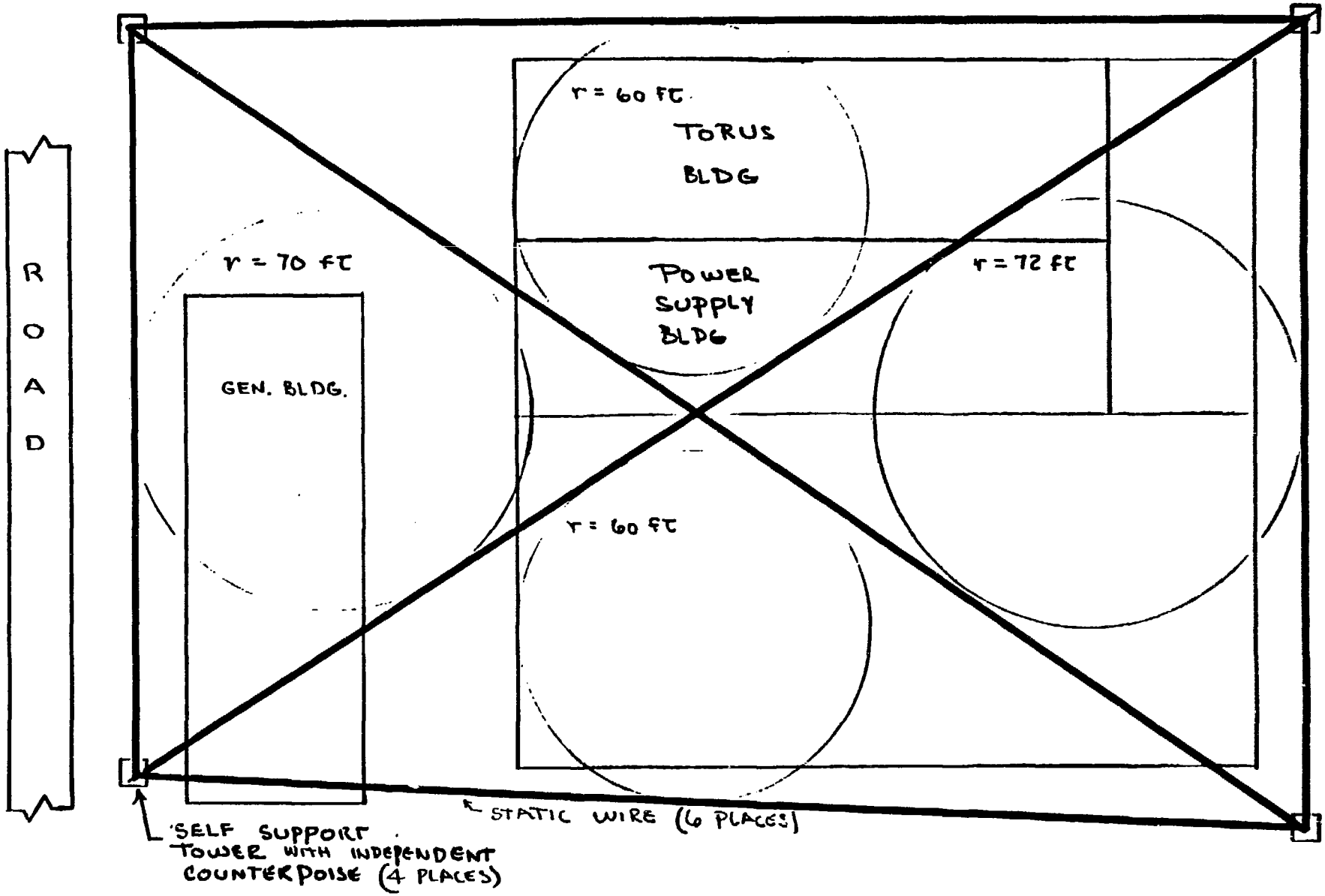

Figure 2. THE APPLICATION OF STATIC OVERHEAD WIRES.

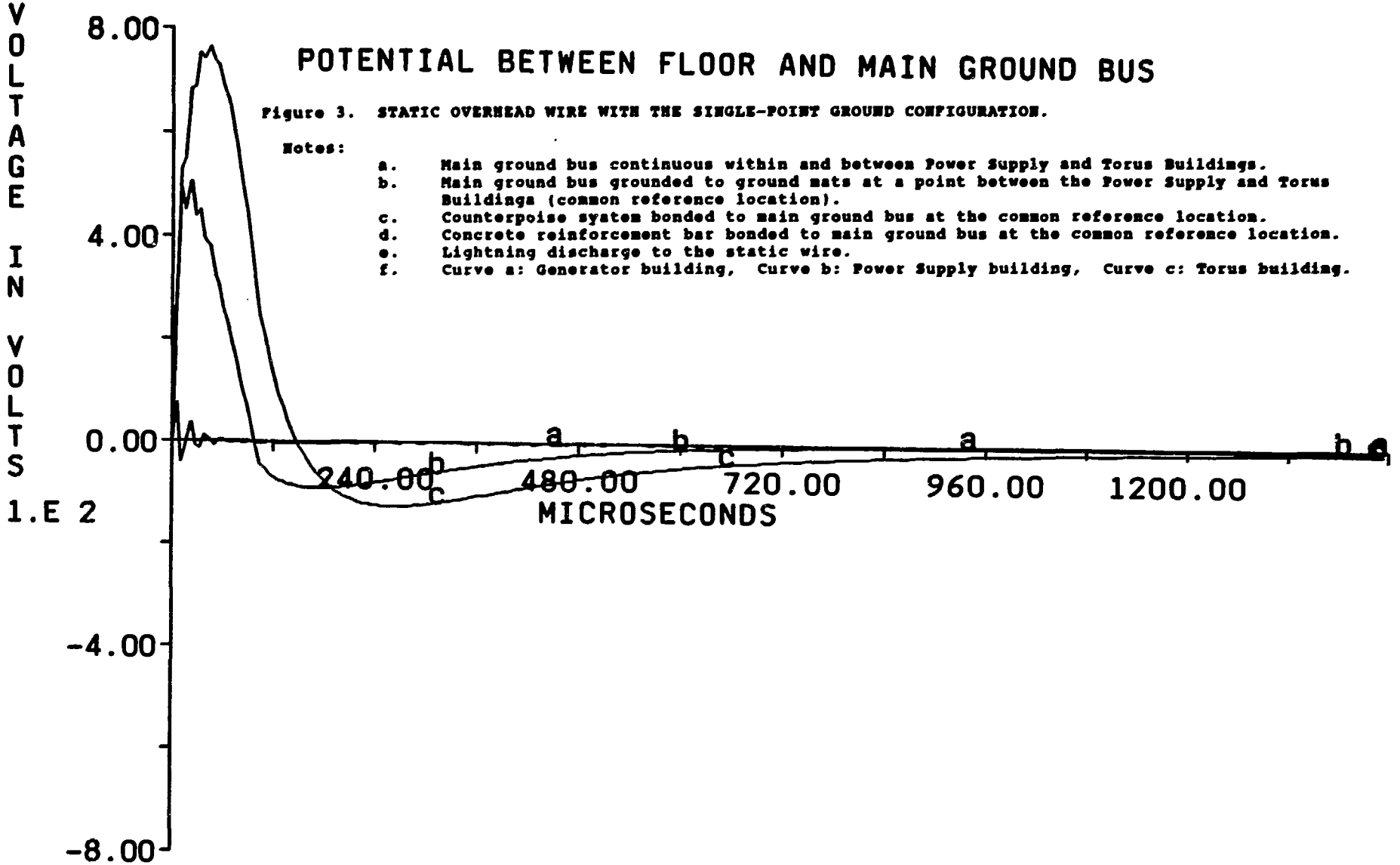

Figure 3. STATIC OVERHEAD WIRE WITH THE SINGLE-POINT GROUND CONFIGURATION.

Notes:

a. Main ground bus continuous within and between Power Supply and Torus Buildings.
b. Main ground bus grounded to ground mats at a point between the Power Supply and Torus Buildings (common reference location).
c. Counterpoise system bonded to main ground bus at the common reference location.
d. Concrete reinforcement bar bonded to main ground bus at the common reference location.
e. Lightning discharge to the static wire.
f. Curve a: Generator building, Curve b: Power Supply building, Curve c: Torus building.

ZTH TOROIDAL FIELD ENERGY SYSTEM

Jimmy G. Melton
Los Alamos National Laboratory

The ZTH toroidal field energy system is in the preliminary design phase. The bias toroidal magnetic field for the RFP experiment will be established by discharging a capacitor bank into the toroidal field coils. The capacitor bank will be allowed to ring during plasma current build-up to aid the reversal of toroidal magnetic field at the wall. During plasma current flat-top phase, the current in the TF coils will be sustained by thyristor converter power supplies. Figure 1 shows representative current waveshapes and power supply requirements.

In addition to the usual features of RFP TF circuits described above, the ZTH TF circuit will have some unusual features. Because we want to be able to reverse the toroidal magnetic field much faster than the plasma current risetime (early reversal), the TF circuit must be capable of a wide and continuous range of reversal times, 0.5 ms to 50 ms. This requires a high degree of modularity of the TF coils and the capacitor banks. The converter power supply system must be capable of controlling the current in the TF coils to within 5% during the flat-top and ramp phases.

I. Toroidal Field Coil Design

The TF coil system has already been designed and an RFQ for final design and construction is being tendered. The design of the toroidal field circuit must conform to the firm constraints of the existing coil system design.

Design of the toroidal field coils was strongly controlled by requirements that magnetic field errors be rigidly constrained to be less than a specified value that depends on the toroidal mode number. This resulted in a design with 48 circular pancake coils, each with six turns, located rather far from the shell and plasma (at minor radius 60 cm). The coils are designed for 10 kV and 20 kA for up to 900 ms. The coils will be installed in 24 groups of two coils in series, to allow various connection possibilities to achieve different field reversal times.

II. Circuit Performance Requirements

The formal Technical Design Criteria for ZTH specifies that the initial bias toroidal field before the plasma current rise will be a maximum of 0.3 Tesla, and that it should be possible to reverse this field to about F = -0.5 in a reversal time that is continuously variable from 0.5 to 50 ms. The specification was adopted after careful consideration of the volt-second consumption of various RFP devices and is based on the projection that the best way to achieve 2 MA plasma operation with limited volt-seconds

available will be to operate in the fast reversal mode, in which toroidal field reversal occurs early in the 50 ms plasma current risetime. This specification allows us to design ZTH with a smaller toroidal field capacitor bank than is customarily used. The smaller bank, however, commits ZTH to operate in the fast reversal mode to reach 2 MA plasma current, because 0.3 Tesla initial toroidal field is consistent with operation in matched mode only to about 0.8 MA plasma current. Matched mode operation to 2 MA could be achieved by increasing the size of the TF capacitor bank.

The TF circuit is required to produce a wide continuous range of reversal times. To achieve this will require that the TF capacitor bank be modular in arrangement and that the TF coil connection scheme be capable of many series-parallel combinations. It will also be necessary to trim the reversal time by changing the number of capacitors within a capacitor module. Figure 2 is a graph that indicates how to combine TF coil connections and capacitor bank size to produce a desired reversal time.

III. Capacitor Bank Description

The TF coils are connected in 24 sets of two series coils each. The capacitor bank is subdivided into 48 modules, each consisting of ten each 170 uF 10 kV capacitors with associated discharge and crowbar ignitrons, mechanical by-pass switches, damping resistors, dump switches, etc. Total bank energy is 4.08 MJ. To accomplish the required switching and reversal of current in the switches will require a total of 192 ignitrons, in inverse-parallel connections to allow current commutation. However, other alternatives such as diodes, thyristors, etc. are being investigated and may eventually be used for nominal and/or special situations.

The modular arrangement will allow connection of the overall circuit in two different ways. In the parallel connection scheme, to achieve the fastest reversal time all of the 24 TF coil sets would be connected in parallel and all of the capacitor modules (arranged in pairs for +/- 10 kV operation) would be connected in parallel. In the series connection scheme, to achieve the same reversal time the coils would be all in series with the capacitor modules interleaved in series between coil sets. Figure 3 shows a basic +/- capacitor bank module and how the coils can be connected in the series and in the parallel scheme.

Both of the connection schemes have disadvantages. The parallel scheme requires the voltage of the flat-top power supplies to be inconveniently low and it does not guarantee equal current sharing among the paralleled coil sets. Even if an individual power supply module were used for each coil set, it would be difficult to equalize the currents to within 0.5% as would be required. The series scheme requires an interleaved circuit, similar to the interleaved PF circuit, to reduce the voltage-to-ground of the circuit components. This scheme is difficult to ground and is subject to possible high overvoltages if any of the series switches fails to close simultaneously with the others.

IV. TF Power Supply Description

To flat-top the current in the TF coils for 2 MA plasma current requires 6 MW of power supply power. When all of the TF coils are connected in series, this power must be supplied at 1000 volts and 6000 amps. With all coil sets in parallel, this power must be supplied at 42 volts and 144 kA. In order to match the flat-top power to all possible combinations of TF coil connections would require 24 separate power supply modules, each rated at 42 volts and 6000 amps output, capable of being connected in series, and each capable of individual control. The series TF coil connection scheme,

on the other hand, allows the TF power supply to be inserted at one position in the circuit loop with voltage and current ratings that do not change with circuit configuration (i.e. turns ratio). This is illustrated in Fig. 4. This advantage will probably result in the use of the series connection. The capacitor bank basic module can be designed the same in either case.

To provide the proper coil current to ramp the plasma current from 2 MA to 4 MA will require increasing the power supply output current from 6 kA to 20 kA. The voltage rating remains about the same at 1 kV. The entire toroidal field energy system is being designed so that the power supply upgrade is the only change required to add the capability to ramp to 4 MA.

V. Status

Circuit analysis of the basic TF circuit operation is nearly completed, but much detailed analysis and design work remains to be done. A detailed fault analysis of the circuit is soon to begin, with an associated design of the necessary overvoltage protection circuits.

Electrical tests are being conducted on Metal-Oxide Varistors (MOVs) for use as overvoltage protection.

A prototype of a capacitor module will soon be built and tested.

Major procurement for the TF circuit may be much reduced by using existing equipment. The capacitor bank will use existing capacitors. Also, an existing 12 MVA thyristor converter (owned by LANL) appears to be adequate for 2 MA flat-top operation, provided the series connection scheme is used. This leaves only switching, controls, and miscellaneous hardware to procure.

Fast switching will probably be done by size-D NL-5553BF ignitrons, since LANL has over 10 years of successful operation of these tubes. Where ignitron commutation is required, NL-37207 ignitrons will be used, since they have been used successfully in ZT-40M and ZT-P. Thus, it is anticipated that no development work is needed in this area.

A search is underway for a suitable commercially available mechanical switch to by-pass the crowbar ignitrons. It is planned to conduct electrical tests of this switch before final procurement, because it is a non-standard application and because 48 switching units will be required in the TF circuit.

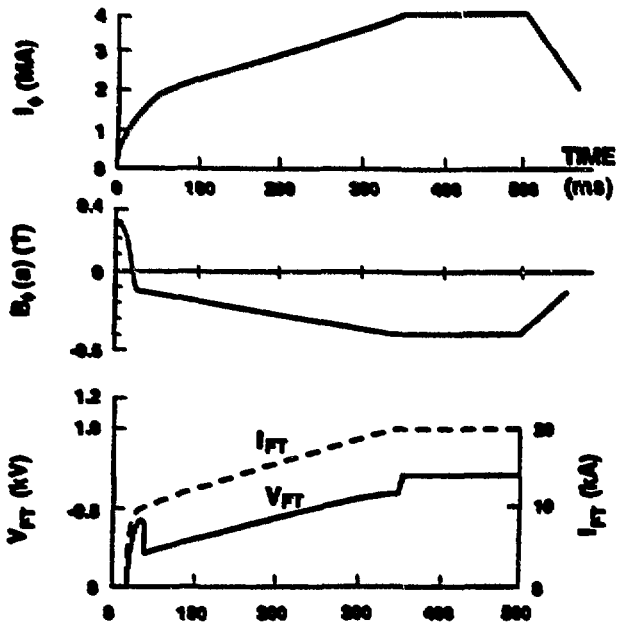

Fig. 1
Required magnetic fields waveshapes and TF power supply requirements.

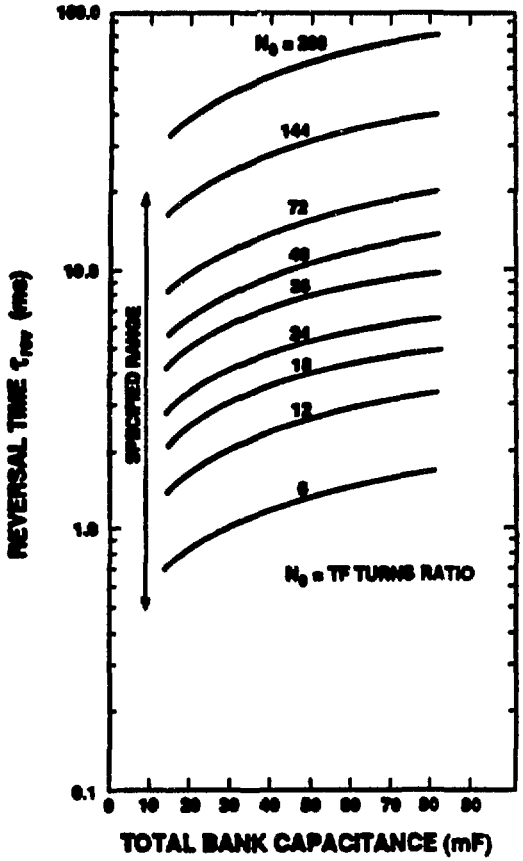

Fig. 2
Available reversal time range

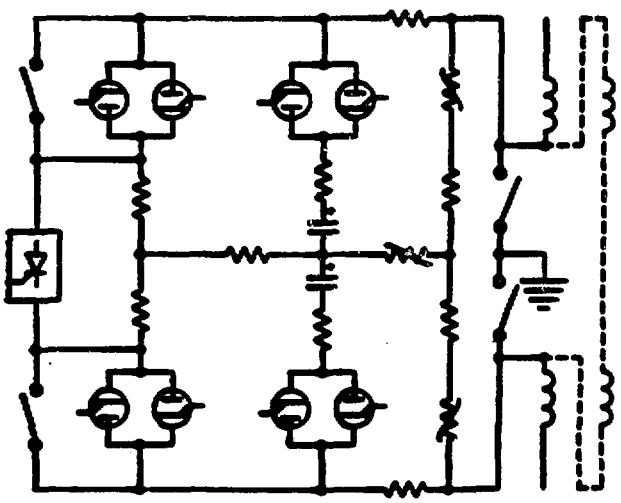

Fig. 3
Capacitor bank module

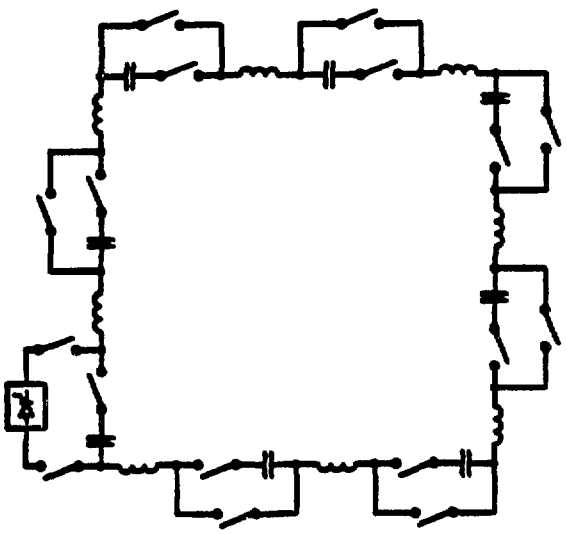

Fig. 4
Representative series connection of toroidal field current for N_θ = 36 turns

RFX TOROIDAL FIELD POWER SUPPLY

J W Gray

UKAEA Culham Laboratory, Abingdon, Oxfordshire
(Euratom/UKAEA Fusion Association)

1. INTRODUCTION

RFX is a large RFP experiment designed to operate at up to 2MA plasma current with a toroidal vessel of major and minor radii of 2m and 0.5m respectively [1]. RFX is currently under construction at Padova, Italy.

The toroidal field is provided by a 48 coil 8 turn winding evenly distributed around the major circumference as close as possible to the outer surface of the conducting shell which coaxially encloses the plasma vacuum vessel (liner). The poloidal field system consists of a set of magnetizing coils distributed around the torus to produce 15Wb flux swing with very low stray field in the plasma region, and also a set of 16 field shaping coils located just outside the toroidal field coils. These coils are connected in pairs and are fed by eight independent power supply modules to provide accurate field control at the shell surface. The power supply system is essentially based upon a modular system of converters and capacitor banks.

2. TOROIDAL FIELD POWER SUPPLY

The general arrangement of the toroidal field power supply is shown in fig 1. The

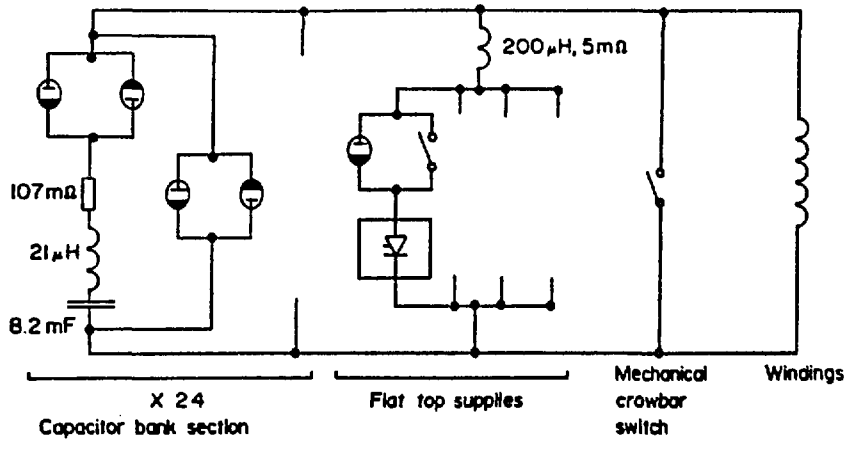

Fig. 1. Simplified toroidal field circuit

capacitor bank consists of up to 24 parallel connected 200kJ sections, configurable into a maximum of six groups. Each group may consist of 1 to 24 sections and is chargeable to an initial voltage within the range +/-7kV. The flat-top supply consists of four parallel connected AC/DC thyristor converters each of 1700V no-load maximum voltage, 12.5kA maximum 25

current. During the rise phase of the plasma current the capacitor banks are discharged and begin to oscillate with the windings. The first three quarter cycles create the characteristic RFP reversal of toroidal winding current. At around peak reverse current flat-top supplies are inserted and retain the reversed field until the end of the pulse (fig 2). The accurate control of the toroidal field at the wall during the reversal phase is a critical feature of the toroidal field power supply. To achieve this it is required to insert different sections of the bank charged to different voltages, either positive or negative, throughout the plasma rise phase t_1 (fig 2). Ignitron switches are used in

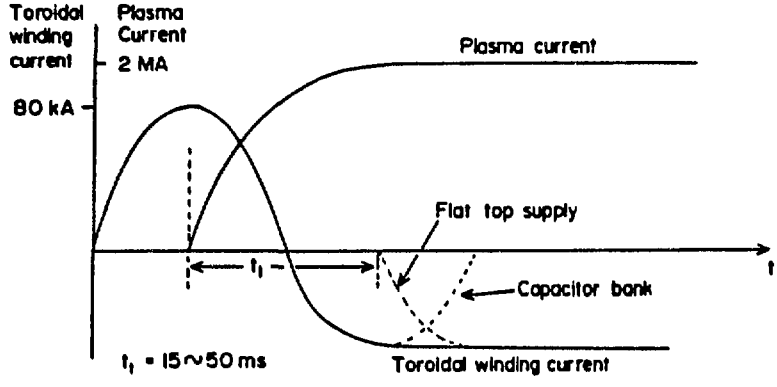

Fig. 2. Typical current waveform

series with each 200kJ section to allow the precise pre-programmed insertion times, accurate to within 10 microseconds. These size E ignitrons are mounted in inverse parallel pairs to allow for current commutation from one ignitron to its inverse parallel partner when the current reversal occurs [2].

A further mode of operation requires that at peak forward current, a short-circuit be applied across the toroidal windings. For this purpose an anti-parallel pair of size E ignitrons is connected across each 200kJ section. The trigger signals for these are arranged such that all of the crowbar ignitrons of the sections which are being used trigger simultaneously from a common signal. The bank has been designed so that if insertion and crowbar ignitrons are simultaneously fired on a fully charged section no damage occurs. The ignitrons are well within their nominal 400C charge carrying limit in discharging the 57 coulombs stored in each capacitor section, and passive current limiting components are mounted in series with the start ignitrons to limit the current passed to 50kA. However, in the event of a plasma failing to form, the toroidal field does not reverse and the winding current decays with a time constant of about 350ms. To cope with the charge flow (maximum possible is 17000C) a backup mechanical switch is included in the circuit which has to close within 20ms to avoid overloading the crowbar ignitrons assuming that at least two capacitor sections' ignitrons are in circuit.

The flat-top converters must be protected from the initial capacitor voltage of up to 7kV, and therefore require a series switch. However, they must be inserted precisely at the correct moment when the winding voltage has fallen to the point at which the converters are required to take over the supply of current. To achieve this a size E ignitron switch is used in series with each module. A parallel mechanical switch is also required to avoid coulomb overloading of the ignitrons, and this must close within 30ms.

3. PLASMA DISRUPTION

If, after the toroidal field at the wall has reversed, a plasma disruption occurs, the flux which was originally trapped within the plasma column is suddenly released. This tends to induce currents in the toroidal winding in the original pre-reversal direction. The effects of this from a circuit analysis point of view can be approximated using the circuit of fig 3, a current I_d being produced at the time of the disruption in the direction shown.

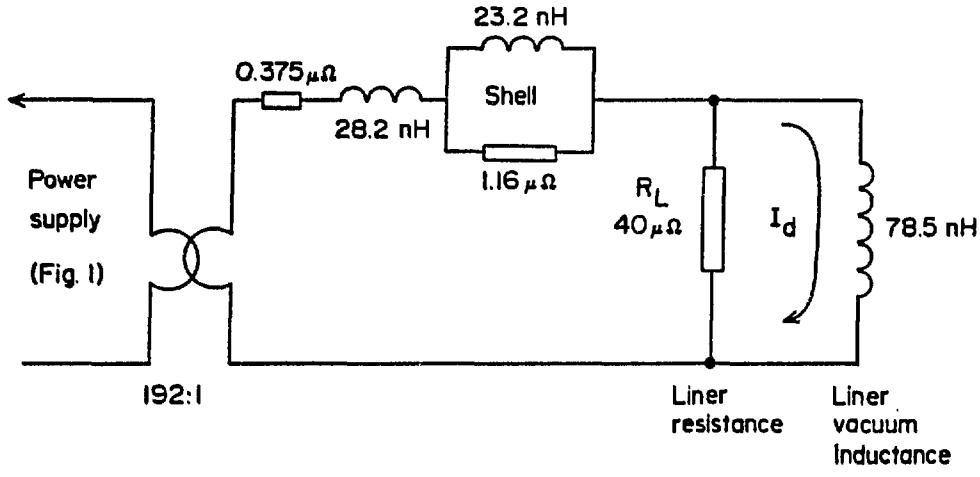

Fig. 3. Single turn equivalent circuit

Estimates of the field produced by the released flux during disruption are somewhat speculative but 0.55T is regarded as a pessimistic worst case. This corresponds to a current I_d of 5.5MA. Should the disruption occur during the flat-top phase of the pulse with all the capacitor insertion ignitrons extinguished, then the full voltage generated across the liner R_L, referred to the primary side, would be applied across the converters, ie, some 40kV. The method adopted to prevent this happening is to make sure that either one or two 200kJ capacitor sections remain connected throughout the pulse. Whether one or two sections will be needed will depend on the plasma current, extent of field reversal and operational experience on the severity of disruptions. Two further mechanical switches S1 and S2 are used (fig 4). These switches are each three pole devices mounted on common

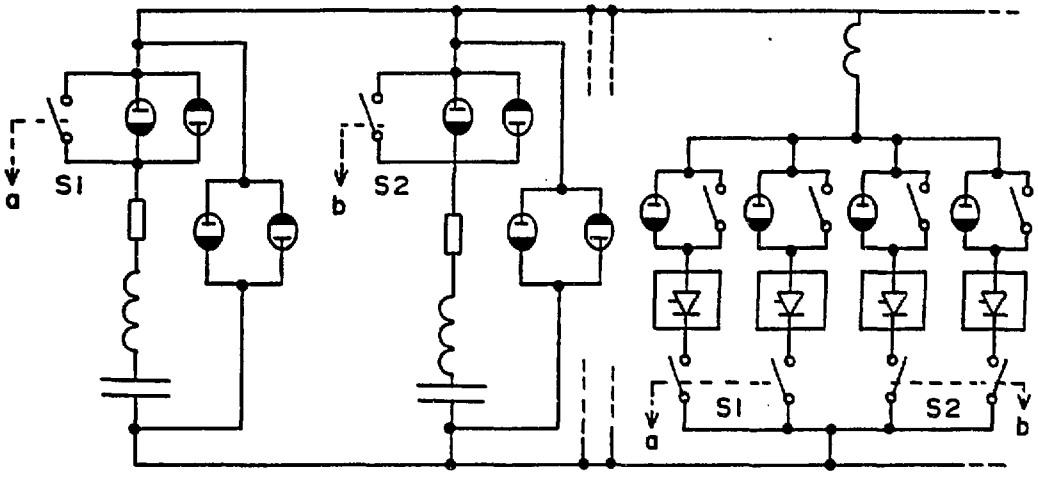

Fig. 4. Toroidal field circuit showing connections of interlock switches S_1 and S_2

operating shafts. Two poles of each switch are connected in series with the four flat-top supply modules, and the remaining pole is connected across the start ignitrons of two of the sections (or alternatively both across one section's start ignitrons). The switches ensure mechanically that it is impossible to connect the flat-top supplies without at least these two capacitor sections also conducting. In operation, they receive a trigger signal to close at the same time as the capacitor section insertion ignitrons, and they must operate within a period of 20ms to ensure that they are fully closed before flat-top operation starts.

If a disruption occurs before the flat-top insertion switches have been closed, in the worst case disruption (0.55T), the voltage reached on the two connected banks is 7.8kV (fig 5). (If other capacitor sections are still conducting, then the maximum recovered

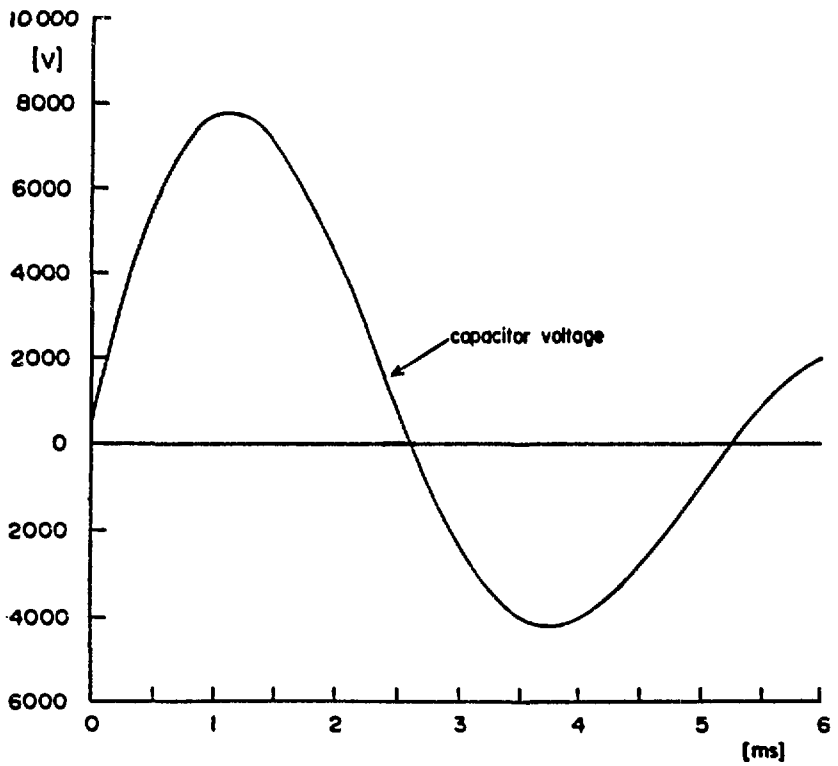

Fig. 5. Disruption before flat-top phase

voltage by the bank is correspondingly reduced). If however, the flat-top phase is underway then an overvoltage protection circuit installed locally to the converters comes into operation (fig 6). This device is essentially a thyristor crowbar which automatically

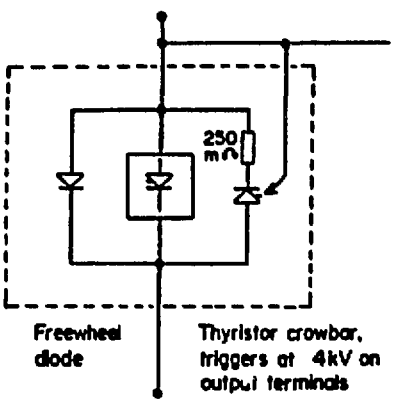

Fig. 6. Flat-top convertor module with protection components

triggers whenever the voltage across the terminals of the converters exceeds a preset voltage of about 4kV. In this case the converter protection circuit comes into operation once the capacitors are re-charged up to 4kV by the disruption, giving waveforms shown in fig 7. The converter protection circuit is designed to handle this current pulse (15kA peak), so that operation of the main crowbar is unnecessary.

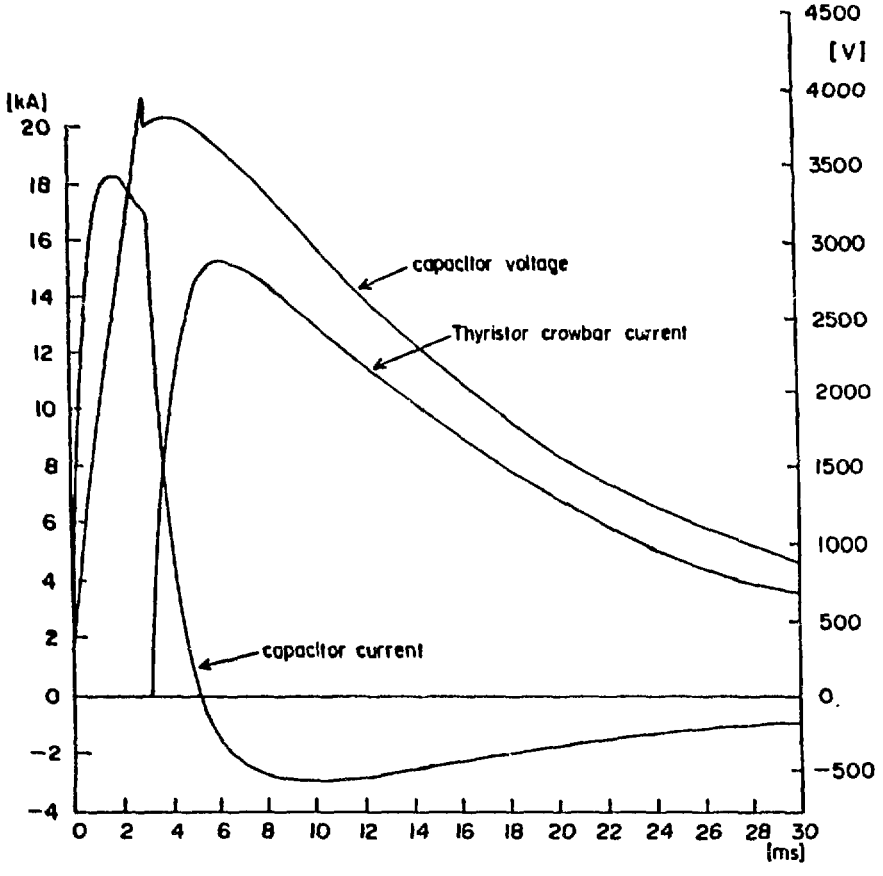

Fig. 7. Disruption during flat-top phase

4. REFERENCES

[1] G ROSTAGNI et al, "The RFX Project: A Design Review", Proc. of the 13th S.O.F.T., Varese, 1984, pp. 189-201.

[2] P M BARNES, R A BURDEN and J W GRAY, "Ignitron Switching Problems Associated with a Large Reversed Field Pinch Experiment", Proc. of the 10th S.O.F.T., Padova, 1978, pp. 413-418.

A Preliminary Study of a Power Supply System for REPUTE-II

Y. Ishigaki Y. Itou
(Hitachi Ltd., Hitachi Works, Japan)

The outline of the power supply for REPUTE-II has been studied by the digital computer simulation (EMTP M32 Version). The constants of the RFP coil system are shown in table 1.

Table 1 Inductance Matrix

For loop current

	Inductance (H)					Resistance(Ω)
	Plasma	OH Coil	VF Coil	V.Vessel	Shell	
Plasma	4.3E-6	83.0E-6	2.1E-6	3.5E-6	-0.8E-6	Fig.1
OH Coil		8.3E-3	-10.0E-6	83.0E-6	—	5.3E-3
VF Coil			2.74E-3	1.3E-6	13.0E-3	5.5E-3
V.Vessel				3.0E-6	—	12.0E-3
Shell					1.05E-6	—

For toroidal current

	Inductance (H)		Resistance(Ω)
	Toroidal Field Coil	V.Vessel	
Toroidal Field Coil	0.30E-3	0.18E-5	1.0E-3
V.Vessel		0.40E-7	0.3E-5

Two cases of the plasma resistance model shown in Fig.1 and Fig.2 were adopted to compare the characteristic of the power supply system.

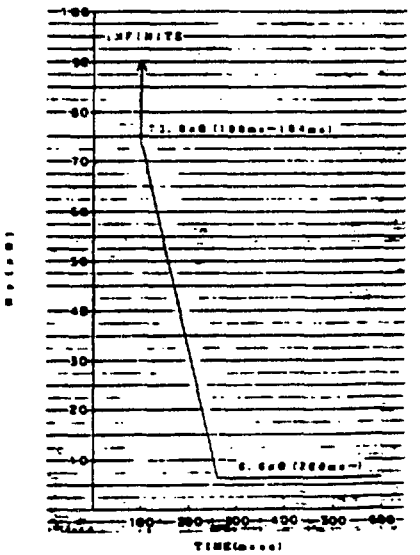

Fig.1 Model 1

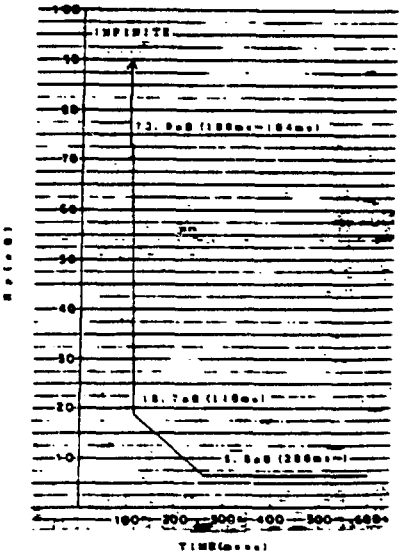

Fig.2 Model 2

The power supply system was modeled as shown in Fig.3 to analyse its characteristics. In this model,R1 and R2 shown in the OH power supply system are used to reduce loop voltage in the plasma circuit.

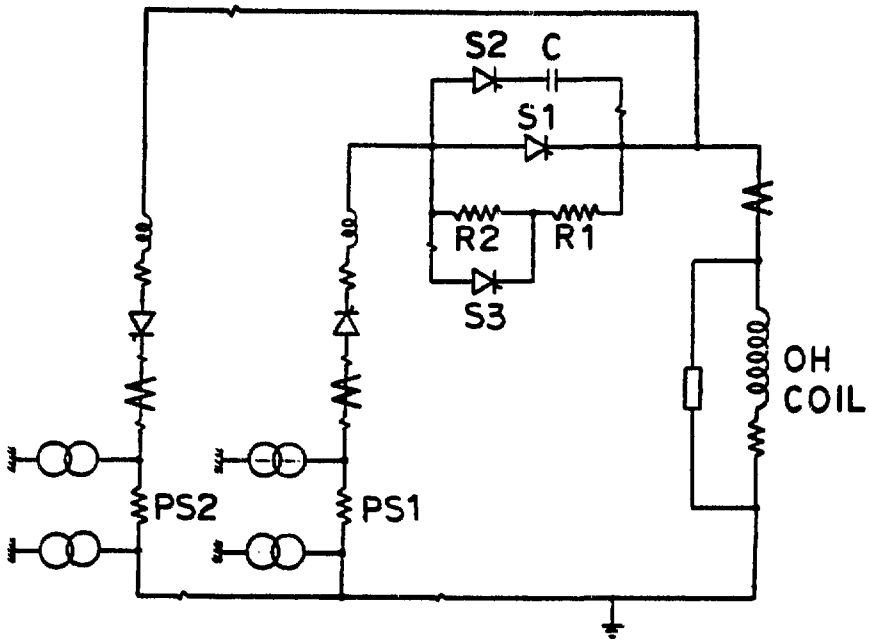

Fig.3 Simulation Model

With these resistances, several cases of parameter survey were conducted. The typical simulation results are shown in Fig.4 and the peak power of each case is also obtained as in Table 2.

Table 2 Simulation results (peak power)

NO	PLASMA CURRENT BUILD UP CONDITIONS	PLASMA RESISTANCE MODEL	R1/R2 (Ω)	PEAK POWER (MW)
1	0.4MA/4ms	Fig.1	0.200/0.363	1,145.8
2			0.400/0.163	1,058.1
3			0.563/0.0	1,035.4
4		Fig.2	0.563/0.0	420.6
5	0.2MA/4ms		0.258/0.0	485.7

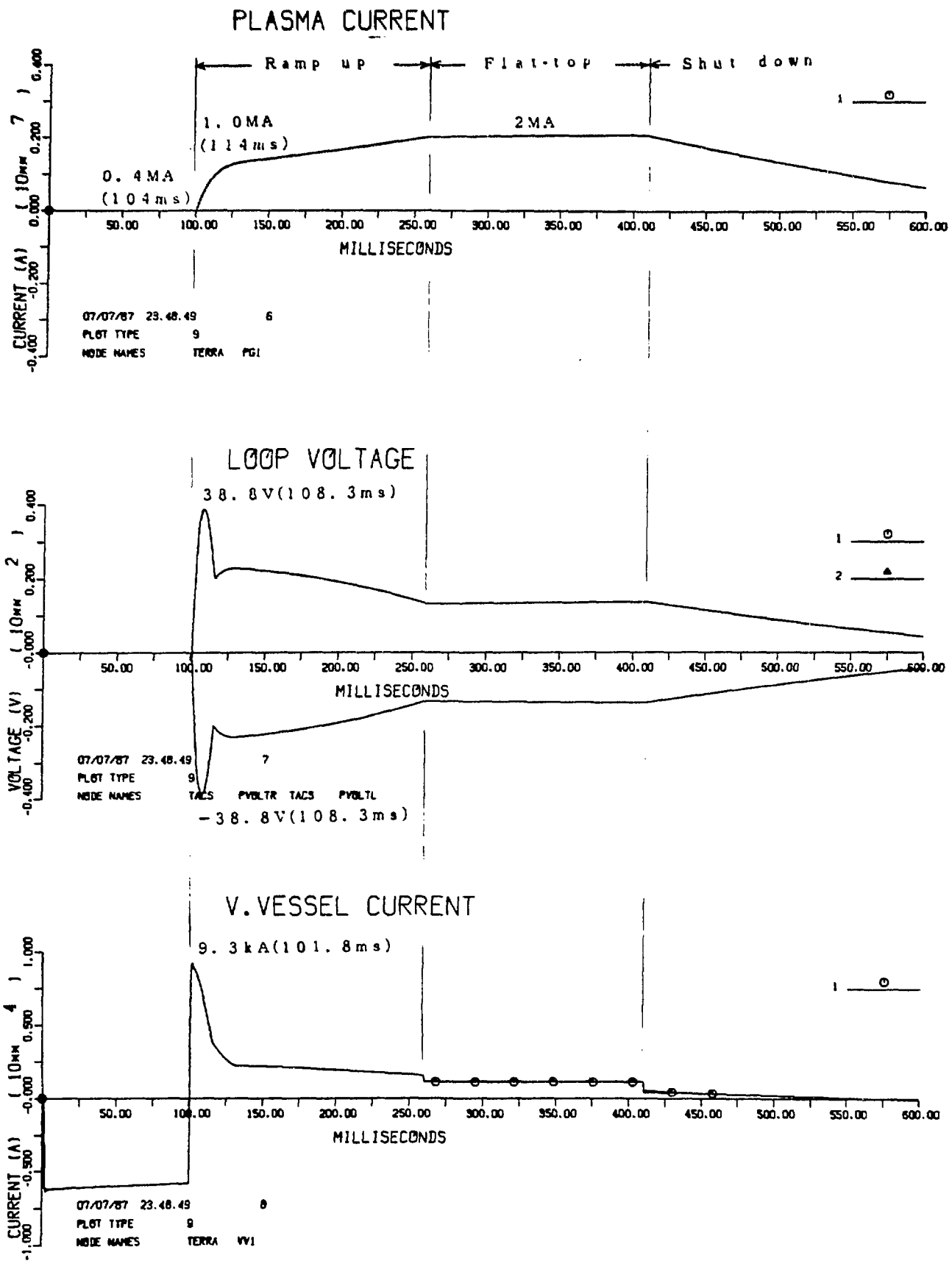

Fig. 4 (1) SIMULATION RESULT (Rp ; Fig.2 , R1/R2 ; 0.563/0Ω)

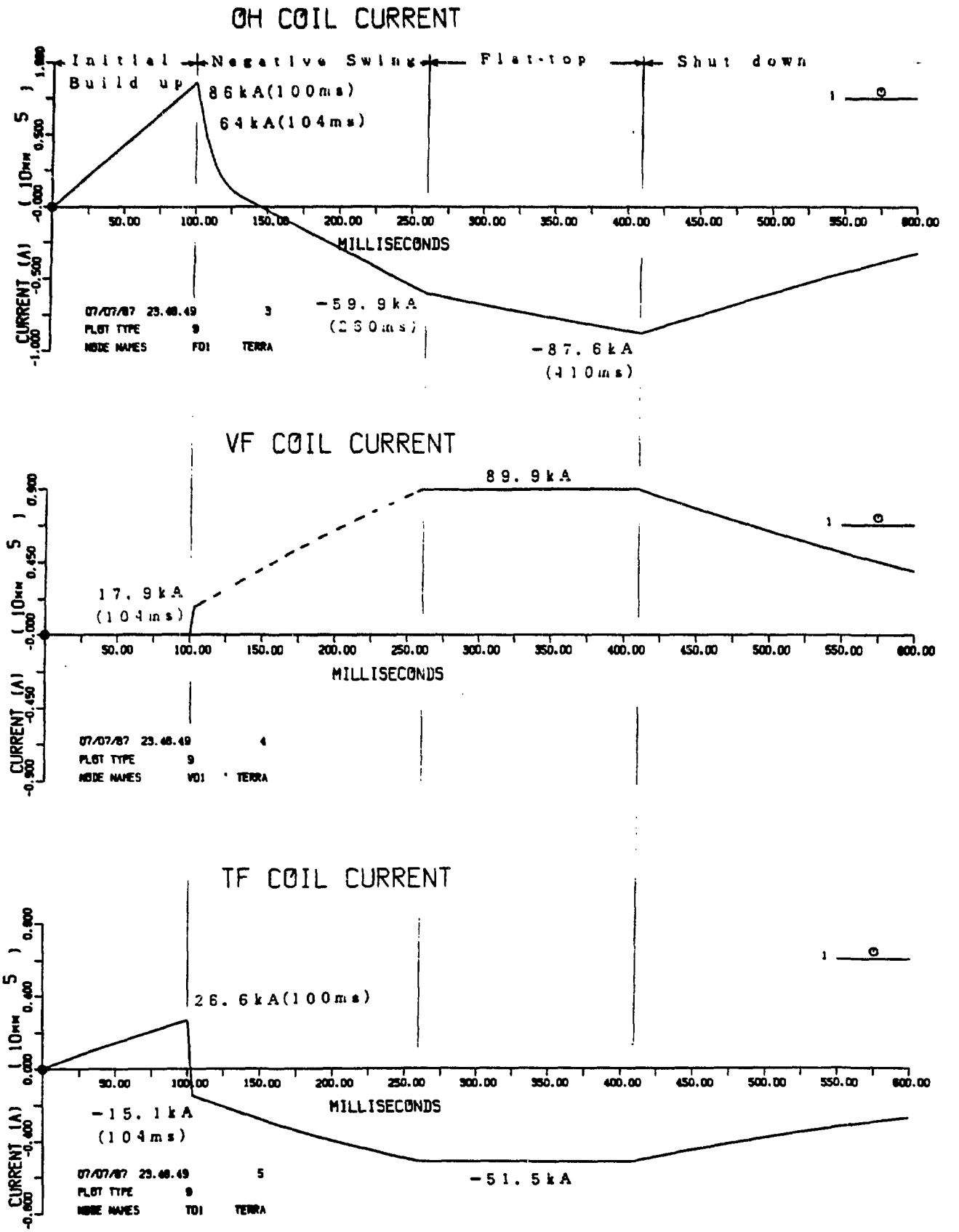

Fig. 4 (2) SIMULATION RESULT (Rp; Fig.2 ,R1/R2; 0.563/0Ω)

Power Supply System

for

TPE-RX1 & TPE-RX

K. Ogawa, T. Shimada, Y. Hirano, Y. Yagi

I. Oyabu*), S. Yamaguchi*) and M. Yamane*)

Electrotechnical Lab.

*) Mitsubishi Fusion Center

1. Introduction

The TPE-RX1 is a medium-size RFP. The status and the objectives are as follows;

1) Plasma parameters located between present experiment (TPE-1RM15) and next large experiment(TPE-RX).
2) Extension of present scalings.
3) Effects of shell on plasma confinement.
   with conducting shell ⟶ with resistive shell ⟶ without shell.
4) Test of several kinds of feedback system.

TPE-RX corresponds to the ZT-H(CPRF) size experiment in Los Alamos.

The technology of the power supply system holds the key to the construction and performance of the experiments. At first the machine and plasma parameters are summarized, then the preliminary design of the power supply system is presented.

2.Machine and Plasma Parameters

The plasma and machine parameters are summarized in Table-1, and the cross sectional views of each machine are compared in Fig.1. The parameters of the TPE-1RM15 are the present values which are achieved in the experiment. The parameters of the TPE-RX1 & TPE-RX are designed values. The principle in these designs are as follows;

1) Reflection of an updated plasma parameters from the latest experiment.

2) Current density : 5 ~10MA/m^2

3) In engineering (not rigorous) acceptable parameters determined by taking the previous conditions into acount.

Parameters are checked consistently in each machine.

An promising scaling law leading to the Lawson parameters are shown in Fig. 2.

3. Power Supply System

The power supply system of the TPE-RX1 is shown in Fig.3. The capacitor bank is the mainly adapted, and this system is similar to that of the TPE-1RM15. The resistive shell experiment is being planned now and in this stage the vertical field coil and its power supply system will be improved.

The power supply system in the TPE-RX is shown in Fig.4. The scale of this power supply is the same as that of the present large tokamak (JT-60, JET, TFTR). Thyristers and openning switches are the mainly adapted here. The key points in this system are the break down voltage at the start up phase and the sustain voltage at the flat top phase. The one turn voltage is desinged to be 30 volt by the thyrister system, so this has high potentiality to perform the Fθ pumping and other experiments. If the break down voltage is up to 1.0 kV, then new openning switch system should be developed. From engineering point of view, the lower break down voltage is favorable, and also may give good effect to do the physics experiment.

Table-1 Parameter in TPE-1RM15, TPE-RX1 and TPE-RX

	TPE-1RM15*)	TPE-RX1**)	TPE-RX**)
1) Torus Major Radius R(m) :	0.7	1.05	1.55
2) Torus Minor Radius r(m) :	0.135	0.2	0.3
3) Plasma Current Ip(MA) :	0.18	0.5~1.0	2.0
4) Current Duration τ_p (ms) :	8.	$\gtrsim$ 30.	$\gtrsim$ 50.
5) Current Rising Time τ_r (ms) :	2.0	5.~10.	10. 20.
6) Vloop Initial (Volt) :	400.	500.	500.
Flot top (Volt) :	20.0(160kA)	20.0	20.0
7) Flux Swing (VS) :	0.74	2.8(500kA)	15.
8) Shell :	Ideal	Ideal Resistive	Resistive
9) OH/Coil Energy (MJ) :	1.0	~15.	~100.

*) present experimental value, and the blank means under measurement.

**) design value

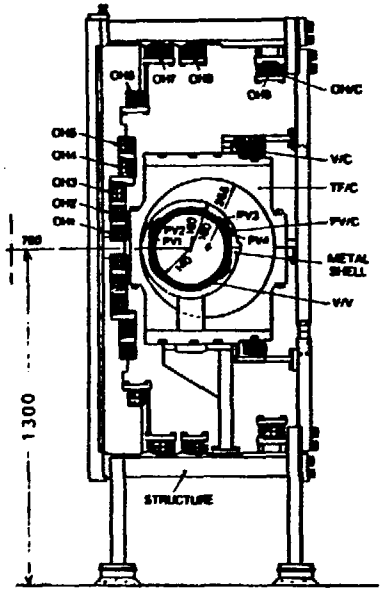

TPE-1RM15 Cross Sectional View

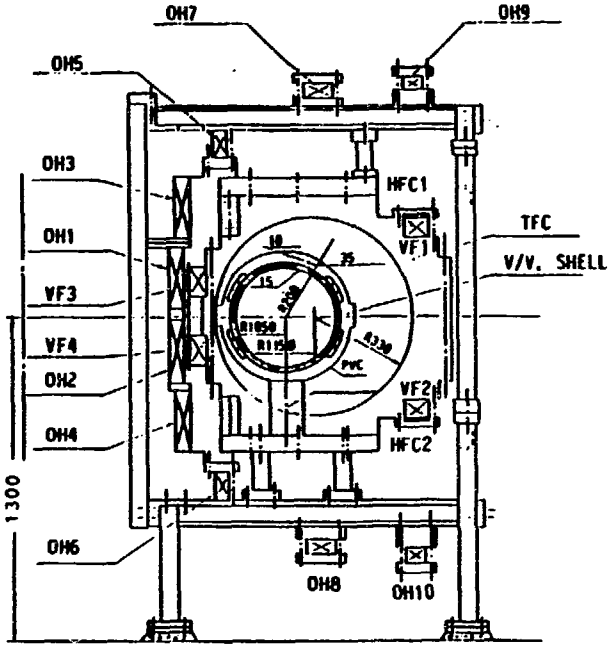

TPE-RX1 Cross Sectional View

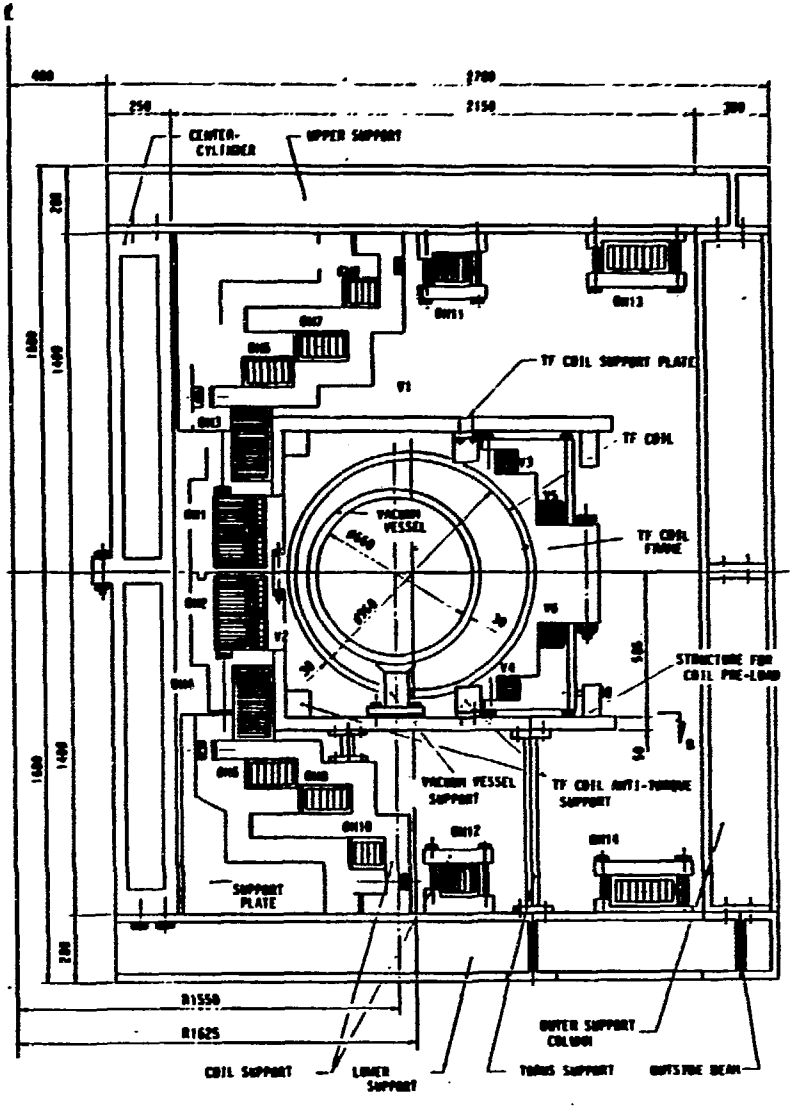

TPE-RX Cross Sectional View

Fig.1

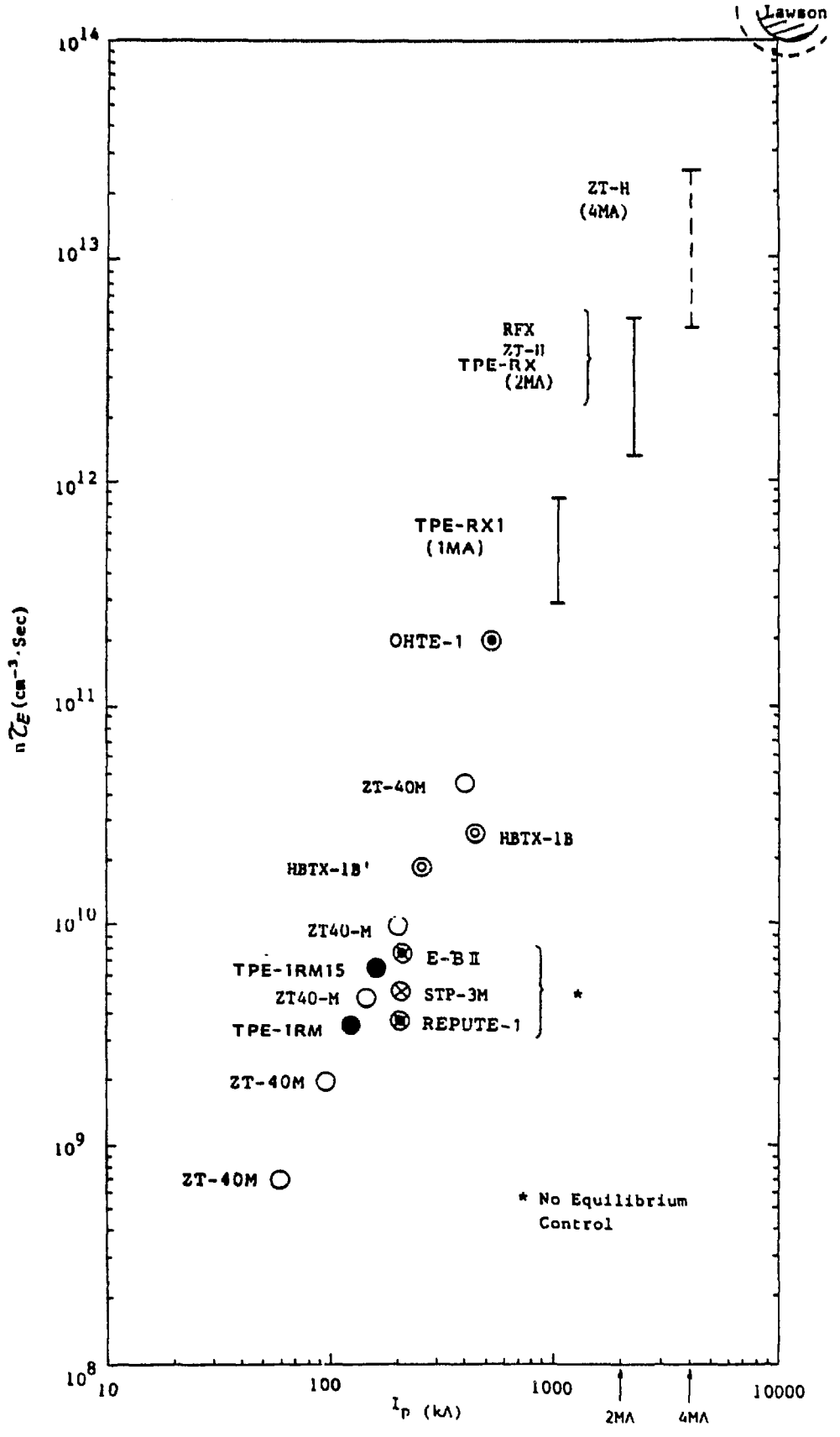
Lawson
10^{14}
10^{13}
10^{12}
10^{11}
10^{10}
10^{9}
10^{8}
$n\tau_E$ (cm^{-3}·Sec)
ZT-H
(4MA)
RFX
ZT-II
TPE-RX
(2MA)
TPE-RX1
(1MA)
OHTE-1
ZT-40M
HBTX-1B
HBTX-1B'
ZT40-M
E-B II
TPE-1RM15
ZT40-M
STP-3M
TPE-1RM
REPUTE-1
ZT-40M
ZT-40M
*
* No Equilibrium Control
10
100
1000
10000
I_p (kA)
2MA
4MA

Fig. 2

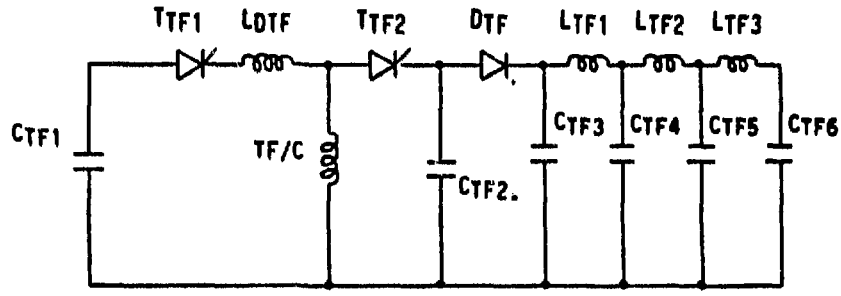

C_{TF1}: Condenser for initial excitation
L_{DTF}: Reactor for decoupling
C_{TF2}: Condenser for field inversion
$L_{TF1} \sim L_{TF3}$
$C_{TF3} \sim C_{TF6}$: PFN (Pulse Forming Network)
$C_{TF1} \sim 0.44MJ$
$C_{TF2} \sim 0.45MJ$
$C_{TF3\sim6} \sim 0.018MJ$

TPE-RX1 Circuit of TF/C Power Supply

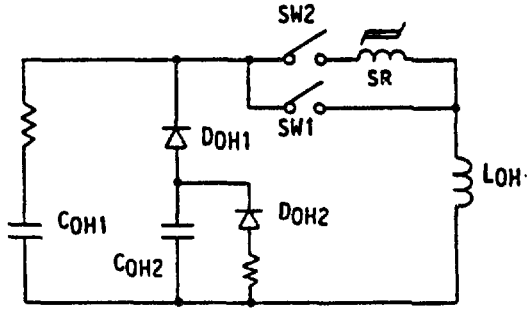

C_{OH1} : Start-up Condenser
C_{OH2} : Flat-top Condenser
SW1 : Ignitron
SW2 : High Power Closing Switch
SR : Saturable Reactor
$C_{OH1} \sim 4.4MJ$
$C_{OH2} \sim 2.4MJ$

TPE-RX1 Circuit of OH/C Power Supply

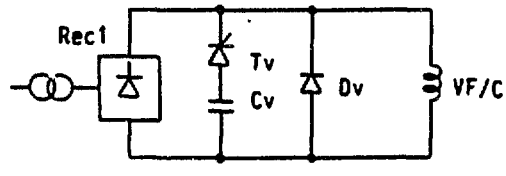

Rec1 : DC power source
Cv : Condenser for raising
Dv : Diode for flywheel
Tr : Current transformer
Rec2 : DC power source

$Cv \sim 0.138MJ$

TPE-RX1 Circuit of DCV/C Power Supply

Fig.3

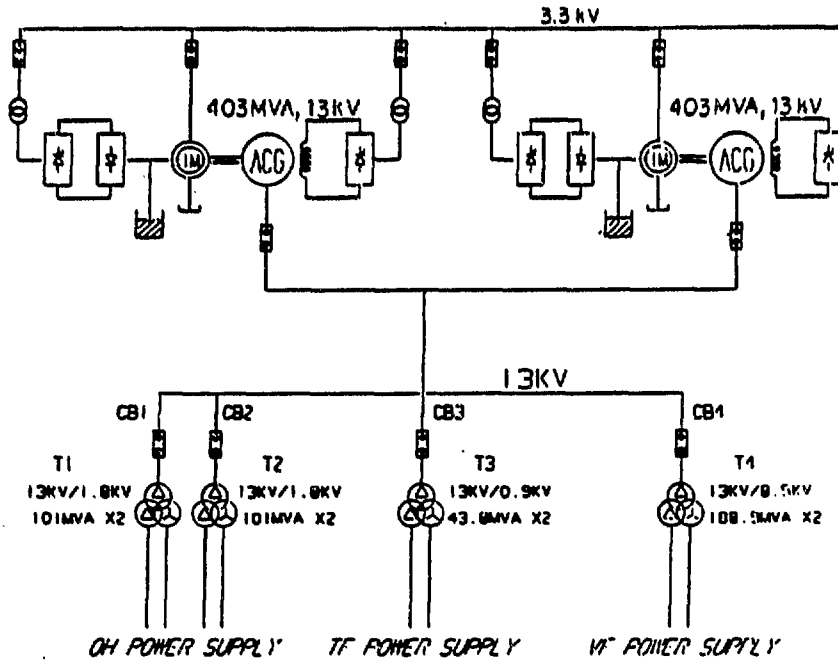

TPE-RX Circuit Diagram of AC Line

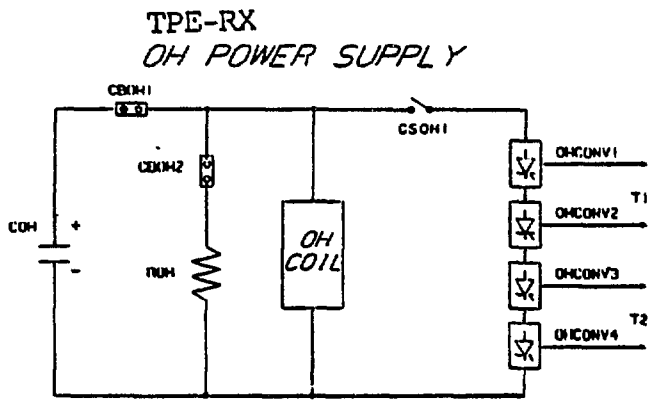

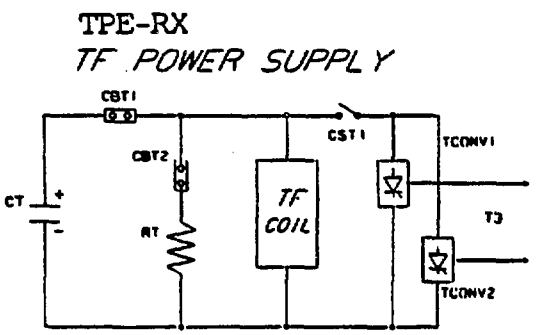

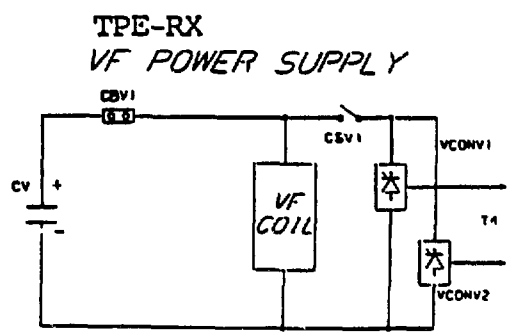

Fig.4

A.C. POWER STATION: LAYOUT AND INTERACTION WITH THE GRID

L. Fellin
Università di Padova - Italy

ABSTRACT

The layout of the AC network, which is fed by the Italian 400 kV grid is presented. The design of the step-down transformers, which are the most critical components, is briefly discussed. The criteria followed in the analysis of the interaction of the power system with the grid are discussed and the employed calculation tools, with their main results, are presented.

1. INTRODUCTION

The RFX experiment is directly fed from the 400 kV Italian commercial electrical grid; in fact, no obstacles came from the total power requirement (Fig. 1) neither from the nominal duty cycle (one pulse every 10 minutes).

Moreover, the RFX site is very close to a big link derived from the most important network in Italy, not far away from the big thermal power stations as Fusina, Porto Tolle, Ostiglia and Sermide (Fig. 2).

The Italian electrical company (ENEL) gave its permisson to the connection after knowing the results of the simulations referred later. Moreover ENEL proposed to study a special contract in which the peak power demand and the energy consumption may be paid under a conventional evaluation, with notable reduction of the energy measurement problems.

2. THE A.C. SYSTEM LAYOUT

Fig. 3 and 4 show a schematic diagram of the AC system and a general layout of the substation respectively.

The 400 kV section includes two step down transformers, not working in parallel, and only one SF6 circuit breaker.

This arrangement assures a small voltage drop during the pulse, without increasing the short circuit current level in the 21.6 kV side; moreover, it allows to work at reduced power in case of fault of one of the transformers. A further reduction in the cost was obtained using only one 400 kV circuit breaker instead of the three that would be normally employed in similar plants, due to the fact that the continuos service is not required.

The parameters of the step-down transformers are:

-	Peak power	150 MVA
-	Maximum time at peak power	4 sec
-	Thermal power rating	50 MVA
-	V_1/V_{20} Voltages	400/21.6 kV
-	Winding connections and group	star/delta, 11
-	Neutral point connection	directly grounded
-	On load tap changer range	+12%Vn ÷ -8%Vn
-	Short circuit voltage	6% at 50 MVA - 18% at 150 MVA
-	Short circuit current 400/21,6 kV side	26/22.3 kA

The transformer design showed some specific problems /1/ due to the unusually small thermal power in comparison with the maximum fault level of the network (18 GVA) and due to the peculiar use of the machine. In fact, the transformers must be connected and disconnected from the grid many times in the year (possibly every day); moreover the short circuit at their terminals is very likely. Finally their short circuit impedance is lower than usual of a factor two. Therefore, many precautions were adopted to prevent serious failures inside them; in particular an accurate analysis of the coil geometry was carried out, in order to avoid critical points in the potential distribution (Fig. 5); furthermore, to limit the in-rush currents in the transformer, an unipolar closing on the maximum voltage of the SF6 circuit was adopted, with fairly good approximation.

All the other components of the AC substation appear more conventional than the transformer; they are the 400 kV overhead line (2 km long coming out from ENEL station), the isolating switches, SF6 circuit breaker, ZnO lightning protections, voltage and current transfomers, bus-bar, protection devices, etc.

In order to increase the protection against the short circuit, all the equiprnent on the 21.6 kV side was designed for a nominal voltage of 33 kV.

3. INTERACTIONS OF RFX WITH THE 400 kV GRID

Some effects of the RFX experiment on the 400 kV grid were analyzed; in particular:

1) voltage drop due to pulsed load (Fig. 1);
2) electromechanical transients in the alternators of the power stations electrically close to the area of RFX experiment plant;
3) harmonic distortion of the grid voltage (400 kV side).

A preliminary evaluation of the voltage drop and of the electromechanical

transients was carried out by simulating the 400 kV network as in Fig. 2 and 6 by utilizing two alternative codes.

The first one (NEWDYN program, built up by ENEL, /2/) represents each power generator with a 5-state-variable dynamic model (i.e. two mechanical and three electromagnetical). The second one /3/ is a 2-state-variable model based on CSMP III code.

The results appear in good agreement: with the more conservative methods, and assuming a power demand of 100 MW active power and 170 MVAR reactive power, the following results have been obtained:

- maximum voltage drop: 1.1% (at Camin station)
- maximum peak to peak change of active power on generators 0.9% (at Fusina power plant with some electrical lines out of service)
- maximum peak to peak angular speed variation 0,05 Hz
- maximum variation on the voltage phase angle $5.6 \cdot 10^{-3}$ rad

Typical power transients onto the nearest power generators with different start-up time of RFX experiment are shown in Fig. 7

In order to evaluate the harmonic content on the grid, a steady state analysis was initially carried out, based on a simplified diagram of the converter modules utilizing the Fourier analysis of the current in every 3-phase converter bridge. Six operating modes of the bridges were examined and the results are reported in /4/. Only the classical harmonics could be evaluated in this work; abnormal harmonics may be taken into account only when the detailed converter design is defined.

The limited time duration of the pulse (the nominal plasma life is 250 ms) made more convenient a transient analysis of the converter system behaviour, which was carried out by imposing ideal current and voltage waveforms at the different converter terminals /5/, with the aim of evaluate the harmonic content on the 21.6 kV bus-bars and the level of interaction among the different converters.

The results confirmed the negligible harmonic content on the 400 kV grid (of the order of 2-3% of nominal voltage).

4. COMPLETE SIMULATION OF THE MACHINE SUPPLY SYSTEM

At the end of the design phase, the need was felt for a more complete simulation tool, which was able to take into account all the interactive aspects among grid, transformers, converter system, machine windings and plasma.

Therefore the RIPA (RFX Integrated Performance Analyzer) program, based on EMTP code, was developed /6/ which allowed to evaluate for the first time

interactive phenomena, such as the effect of the converter ripples on the toroidal and poloidal plasma loop voltages and the complete harmonic spectrum of the currents absorbed from the 400 kV and 21.6 kV grids taking into account the effects of the control system and of the construction differences of the circuit components, which might create anomalous harmonic content; this program is supposed to be very useful also during the commissioning and the operation of the machine.

5. STATUS OF THE ART

The step-down transformers are already built and their erection will start as soon as the civil works in the electrical substation will end.

The 400 kV overhead line is completed and commissioned and the installation of the other components will begin together, with that of the transformers.

The substation is scheduled to be ready before the end of the year.

REFERENCES

/1/ Nuova I.E.L. - Project report on the 150/50 MVA step down transformer - Legnano (MI), 1986.

/2/ ENEL - Comportamento dinamico della rete Enel a seguito del disturbo introdotto dall'alimentazione dell'impianto RFX a Camin, 1984.

/3/ I. Benfatto, L. Fellin - L'Energia Elettrica, n. 2, 1985.

/4/ I. Benfatto, L. Fellin - 10th Symposium on Fusion Engineering, Philadelphia, 1983.

/5/ I. Benfatto, R. Piovan, P. Tenti - 5th IEEE Pulsed Power conf., Arlington, 1985.

/6/ I. Benfatto, et al. - 11th SOFE, Austin, 1985.

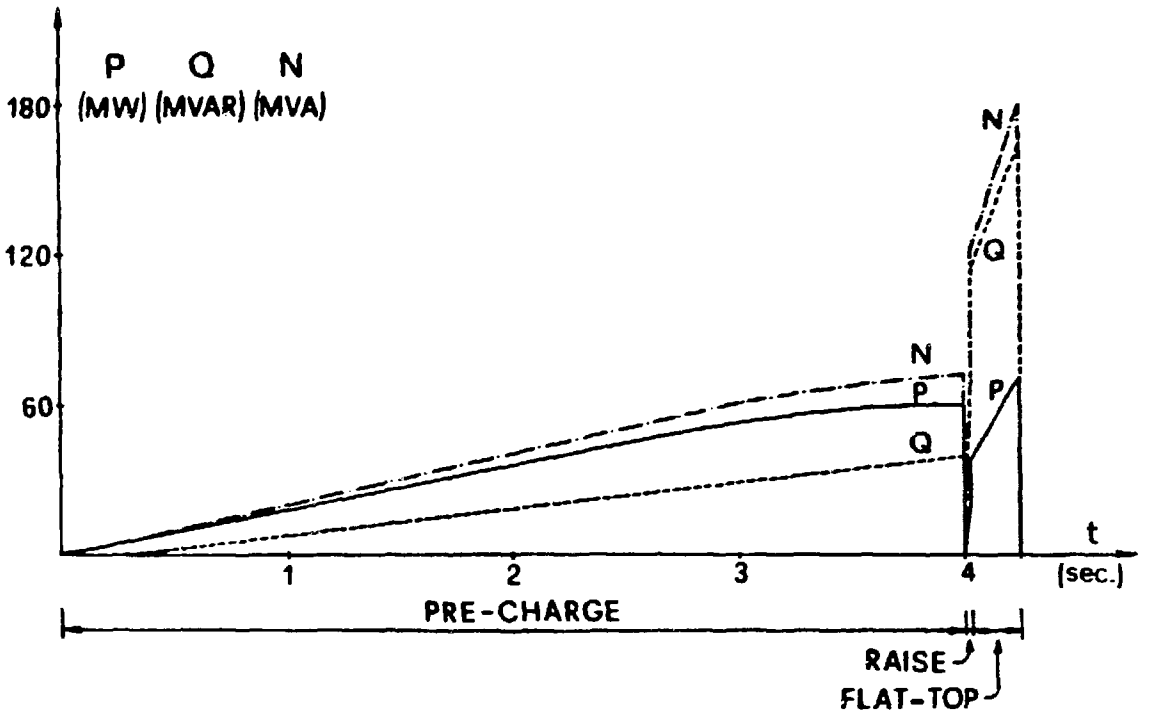

Fig.1 - Typical RFX power consumption at full performance.

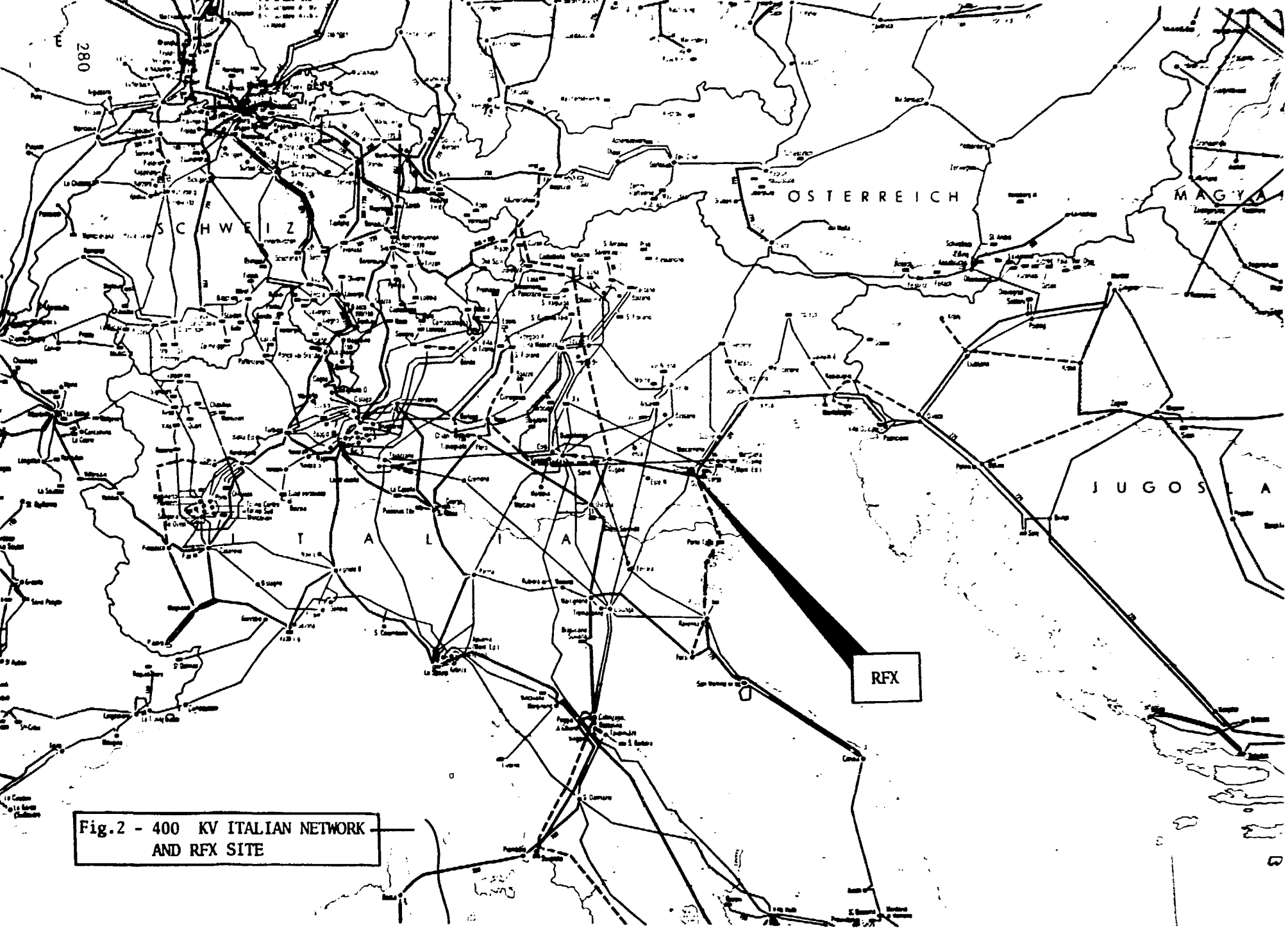

Fig.2 - 400 KV ITALIAN NETWORK AND RFX SITE

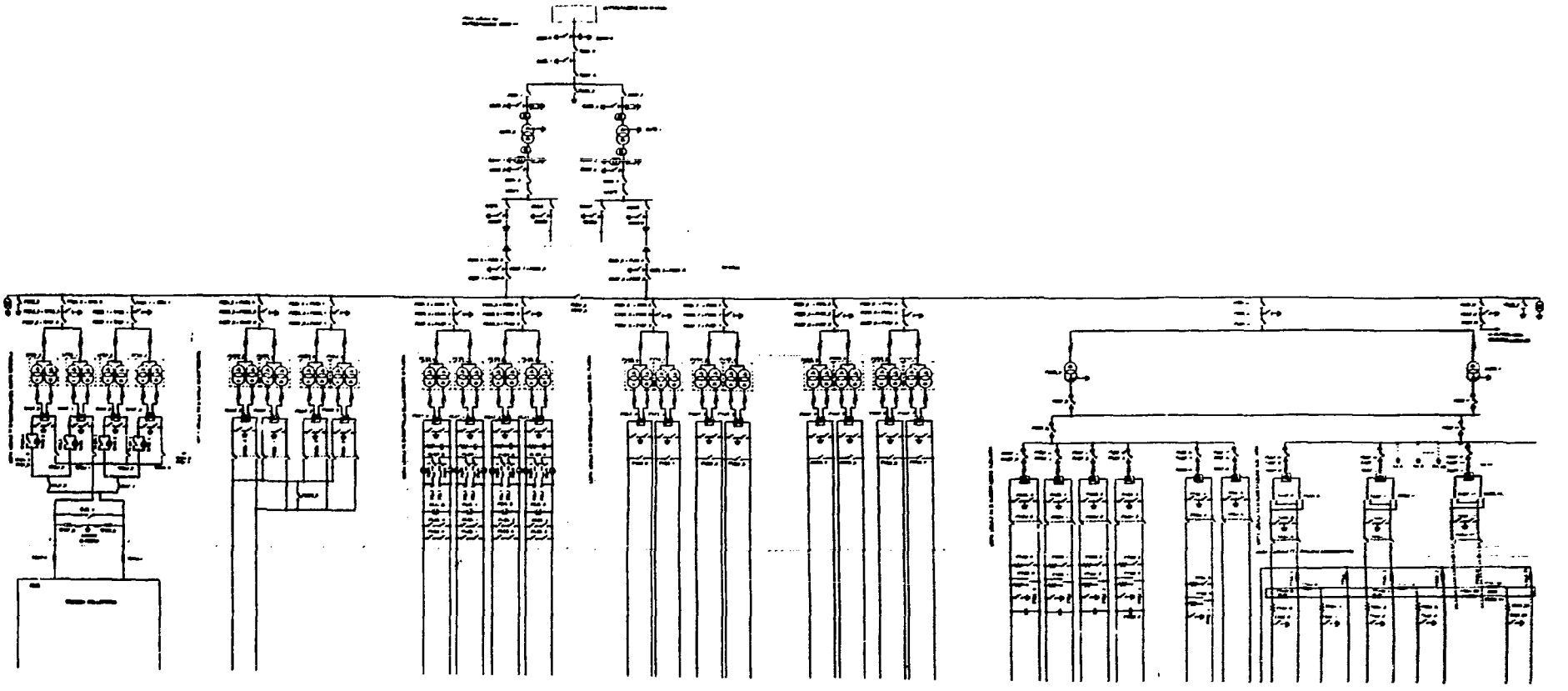

Fig. 3 - ELECTRICAL SCHEME OF SUBSTATION AND POWER DISTRIBUTION

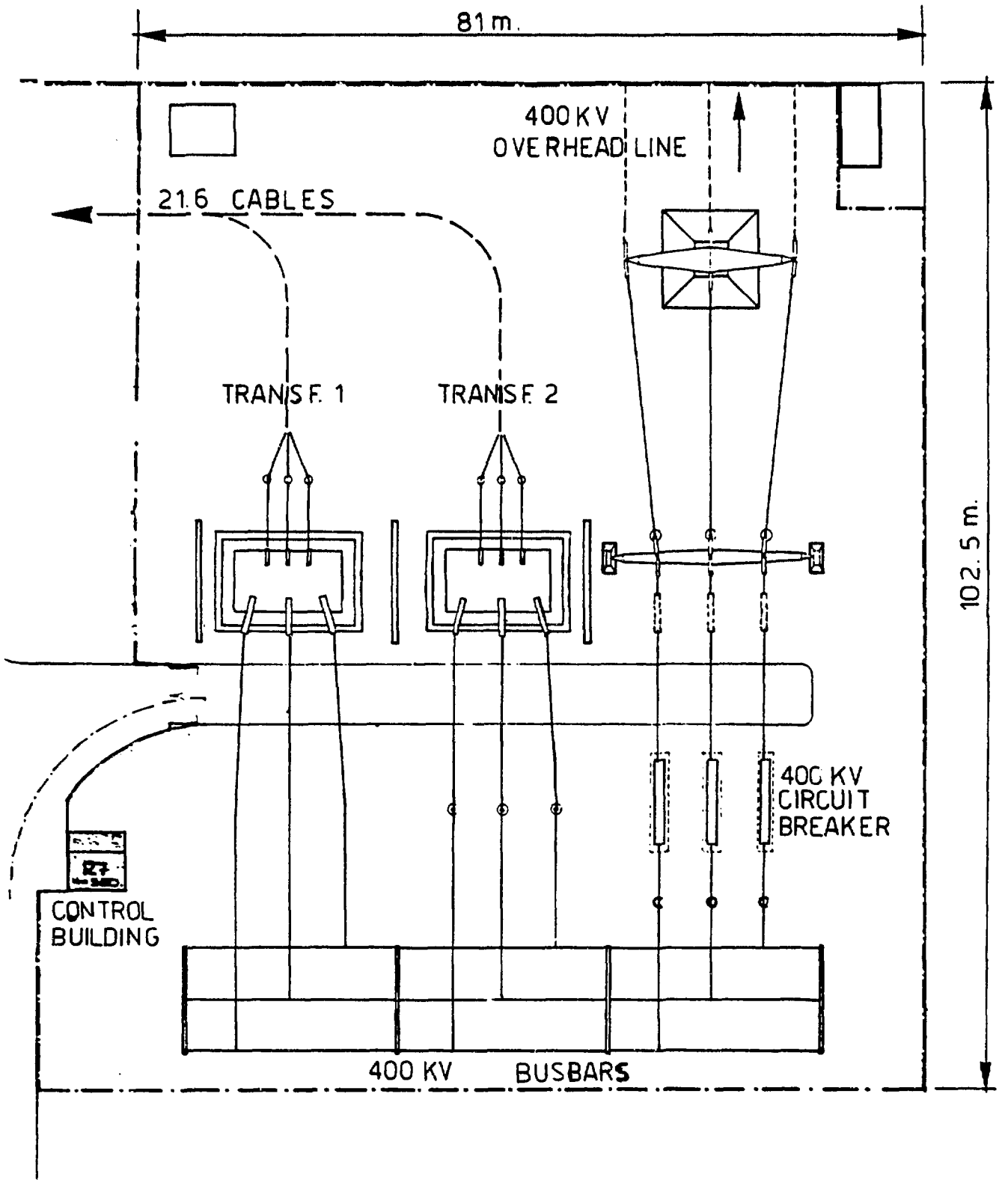

Fig. 4 - POWER SUBSTATION LAYOUT

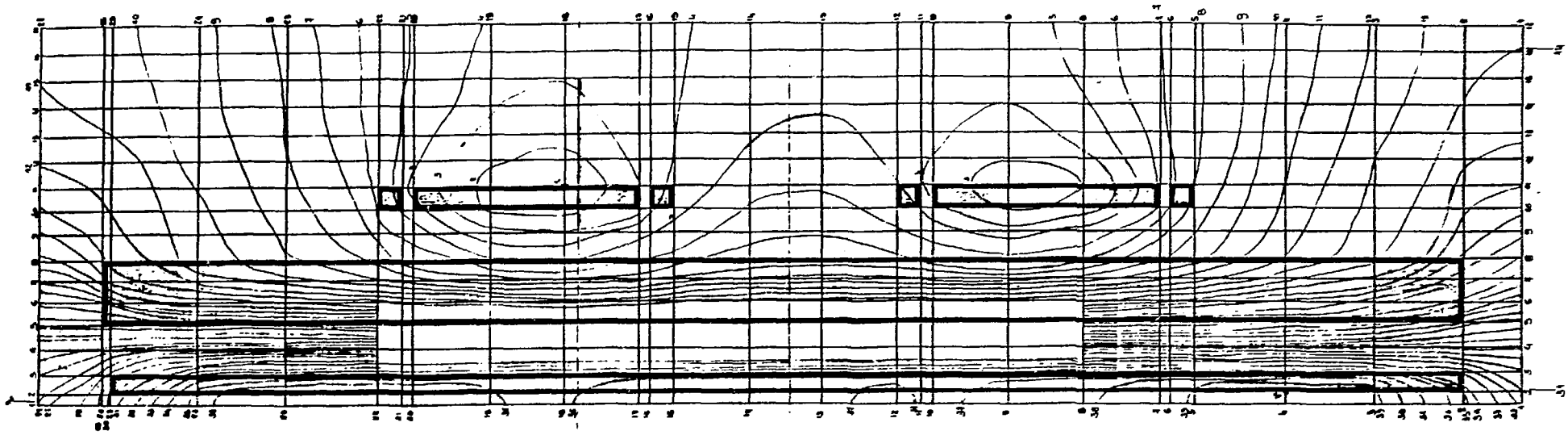

Fig. 5- POTENTIAL DISTRIBUTION IN THE STEP DOWN TRANSFORMER

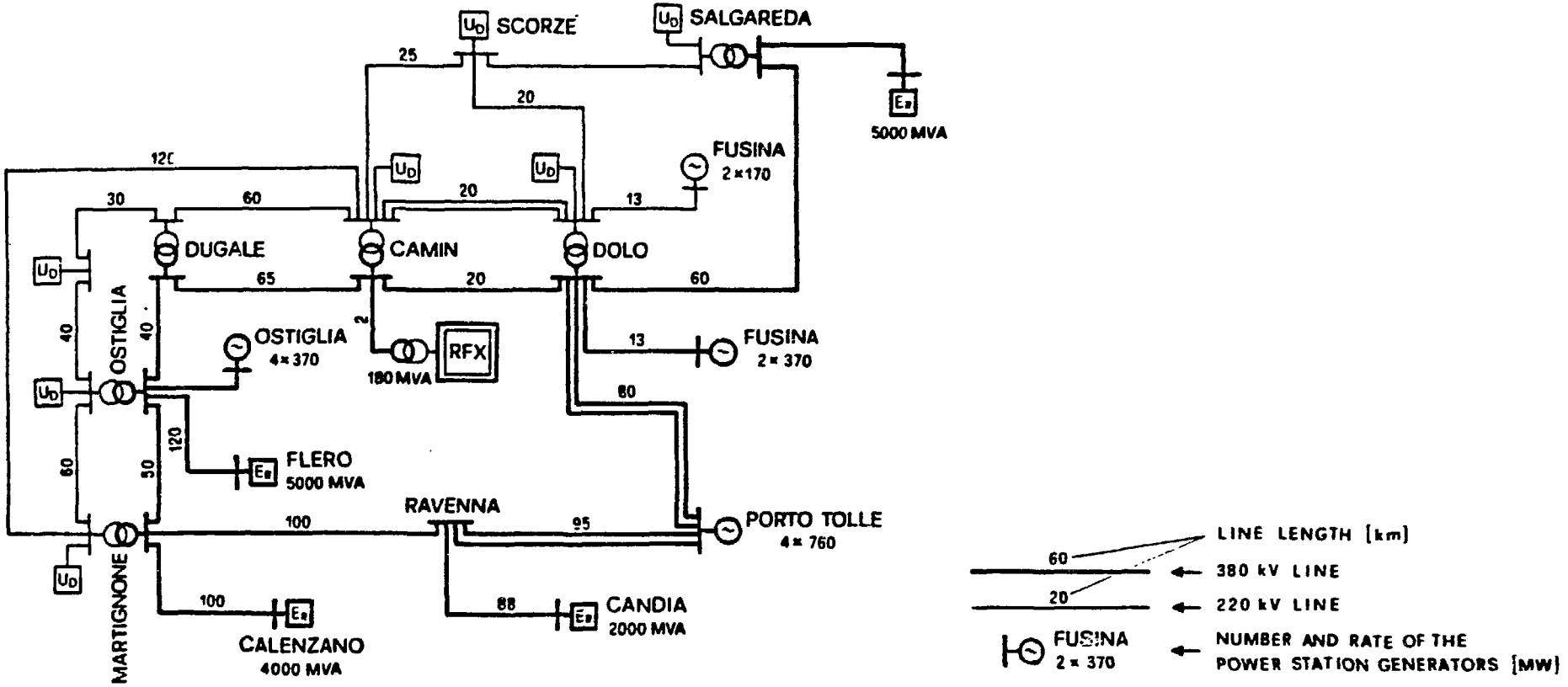

Fig.6 - Transmission and interconnection power grid near the RFX site

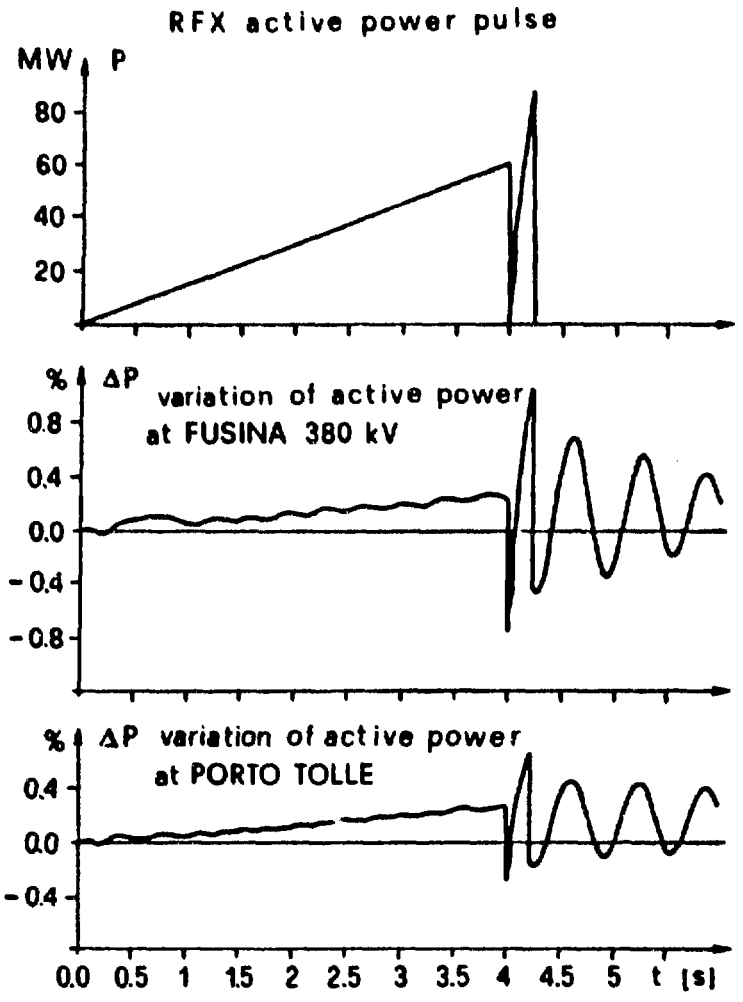

Fig.7 - Variation of active power supplied by the generators of FUSINA and PORTO TOLLE, during the RFX pulse.

PRELIMINARY DESIGN OF THE POLOIDAL FIELD ENERGY SYSTEM FOR ZTH

Heinrich J. Boenig

Los Alamos National Laboratory
Los Alamos, New Mexico 87545

SUMMARY

The design of the poloidal energy system is in the preliminary stage. For a plasma current of 2 MA four ohmic heating power supplies with a rating of 3840 V at 12.5 kA are required. For a 4 MA plasma current the supplies must be expanded to provide 3840 V at 50 kA. The present design makes use of the four charging supplies also as ramping and flat-top supplies. The total switch requirement in the poloidal energy system has been specified. A prototype 50 kA/50 kV dc current interrupter has been developed and tested in the laboratory in over 100 shots and in 12 shots at 55 kV/55 kA. The sixteen equilibrium supplies require a total power installation of 60 MW for 4 MA operation. The current transfer resistor design calls for a linear, water cooled resistor. Development of a non-linear MOV based transfer resistor is being undertaken.

1. Generator and ac Distribution System

The poloidal energy system requires about 800 MW of power and 600 MJ of energy for a 4 MA plasma current. Power and energy are provided by a 1430 MVA, 600 MJ, 1800 rpm pulsed generator. This energy pulse will cause the generator speed to fluctuate between 1800 and 1260 rpm (60 to 42 Hz). According to our present thinking, the ac power distribution system consists of six branches, each feeding converter transformers. As shown in Fig. 1, four branches are connected to the ohmic heating supplies, and one each to the toroidal flat-top supply and the sixteen equilibrium supplies. The high short circuit capacity (5800 MVA) of the generator with the absence of a generator circuit breaker makes the protection for the generator difficult. To keep the generator short circuit current at an acceptable level, the options of a line reactor in series with a 40 to 60 kA ac breaker or of a smaller line reactor in series with an explosive fuse are being studied. Because the line reactor inhibits the voltage regulation during the current pulse, thus increasing the converter cost, we will design the reactance for the largest available ac breaker or explosive fuse. The design of the ac components is underway, using the Electromagnetic Transient Program (EMTP) developed by Bonneville Power Administration (BPA).

2. Poloidal Energy System - Overview

The main components of the poloidal energy system as shown in Fig. 2 are:

a) Four ohmic heating power supplies rated at 3840 V and 12.5 kA for 2 MA operation and 3840 V and 50 kA for 4 MA operation;

b) Sixteen equilibrium coil supplies, consisting of two sets with eight identical units, rated at 1 kV/3 kA and 1.25 kV/4 kA;

c) Cold and isolation switches;

d) Four 50 kV/50 kA dc current interrupters;

e) Four one ohm transfer resistors.

The ohmic heating power supplies serve as both the charging and ramp/flat- top supplies. During the charging mode at 2 MA converter capability, four 3840 V, 12.5 kA supplies are connected in parallel and bring the ohmic heating coil current up to 50 kA in 2.6 s. When the 4 MA converter capability is installed, the charging time is reduced to 0.45s. Before the energy transfer phase is initiated, the power supplies are bypassed and disconnected, and the coil current circulates through the bypass switch as well as the dc current interrupters. By opening the dc current interrupters, the current transfers into the 1Ω resistors. Simultaneously the equilibrium supplies are connected to the respective coils. The four main power supplies are reconnected for ramping/flat-top operation in the series mode. At the end of a plasma discharge part of the magnetic energy in the coils is converted into inertial energy by reversing the power supply output voltage at a comfortable voltage level (0.6pu) thus avoiding converter failures.

3. Converters

Each of the four ohmic heating supplies can be subdivided into four six-pulse, 960 V, 12.5 kA supplies. The no-load voltage should be about 1300 V. While a 12-pulse supply shows a slight cost advantage over a 24-pulse supply, the ripple requirement during flat-top operation may require 24-pulse operation of an ohmic heating supply. This question is being studied. The addition of power supplies for 4 MA operation is achieved by adding identical ohmic heating supplies in parallel. To reduce cost, we are investigating the possibility of using four excitation systems of large surplus generators as ohmic heating supplies. The steady state rating of the excitation systems is 16 kA full load current and 1052 V no load voltage. The excitation system manufacturer is currently under contract to investigate the suitability of the rectifiers as pulsed load converters. Preliminary results are encouraging.

The sixteen equilibrium coil supplies can be divided into two sets of eight each. One set requires a full load rating of 3 kA at 1 kV and the other set a full load rating of 4 kA at 1.25 kV. Because of the similarity of the supplies, one basic mechanical construction can be used.

The transformer should have a 25% voltage tap and the rectifiers should have SCRs with different voltage ratings and different numbers of parallel paths. This would accommodate the 25% different voltage and current requirements of one set of supplies.

4. Switches

A great number (about 200) of isolation, disconnect, metal-to-metal and grounding switches are required for proper operation of the poloidal field energy system. The switch requirements, such as voltage, current, I^2t, closing and opening time etc. have been determined. It is anticipated that many of the switches can be installed using commercially available ac circuit breakers, probably of the vacuum interrupter type. To meet some application requirements which cannot be met by a single switch, a combination of two switches will suffice. In some instances the parallel operation of a fast ignitron switch with a slower metal-to-metal switch can solve a fast closing time and high I^2t requirement. A detailed fault analysis of the system using the EMTP code will check the correctness of the assumed switch parameters.

5. Dc Current Interrupter

A 50 kV/50 kA DC current interrupter is at the present time not readily available at a reasonable cost from the electrical equipment manufacturers. Based on previous experience with 25 kA/25 kV breakers which were developed at Los Alamos for other US fusion experiments, we felt confident to develop the ZTH current interrupter in-house. A breaker, as shown in Fig. 3, was assembled and tested. Major components were: six vacuum bottles in a 2 parallel/3 series arrangement; 90 μF, 60 kV counterpulse bank; saturable reactors; MOV transfer resistor. The load current is provided by a 10,000 μF, 10 kV capacitor bank in series with a 240 mH inductor. The vacuum bottles are of the axial magnetic field type.

To this date 100 interruptions at 50 kV/50 kA and 12 at 55 kV/55 kA have been accomplished with limited reliability (Fig. 4). We are designing a new switch test facility to do switch life testing (2,000 shots) with the rated I^2t requirement. In addition, the test facility will incorporate all the switch support systems such as control and data acquisition systems, ignitron switches, etc. which are needed for ZTH. Also, these auxiliary systems are being tested. Recently, we learned that a higher current carrying vacuum interrupter is available at a reasonable price from a different manufacturer. We intend to test these bottles and the actuator in the test facility. These higher current bottles may reduce the number of parallel bottles from two to one.

6. Transfer Resistor

A stainless steel, water cooled, linear resistor is our first choice as transfer resistor. However, work is proceeding on a non-linear, metal oxide varistor based transfer resistor. A non-linear resistor would increase the transfer efficiency for ZTH. Tests are being conducted to

determine a safe energy absorption limit for MOVs. Discs of two different manufacturers are being tested, some of the discs to destruction.

ACKNOWLEDGEMENT

The author thanks R. Gribble, J. Melton and W. Reass for assistance provided in preparing this paper.

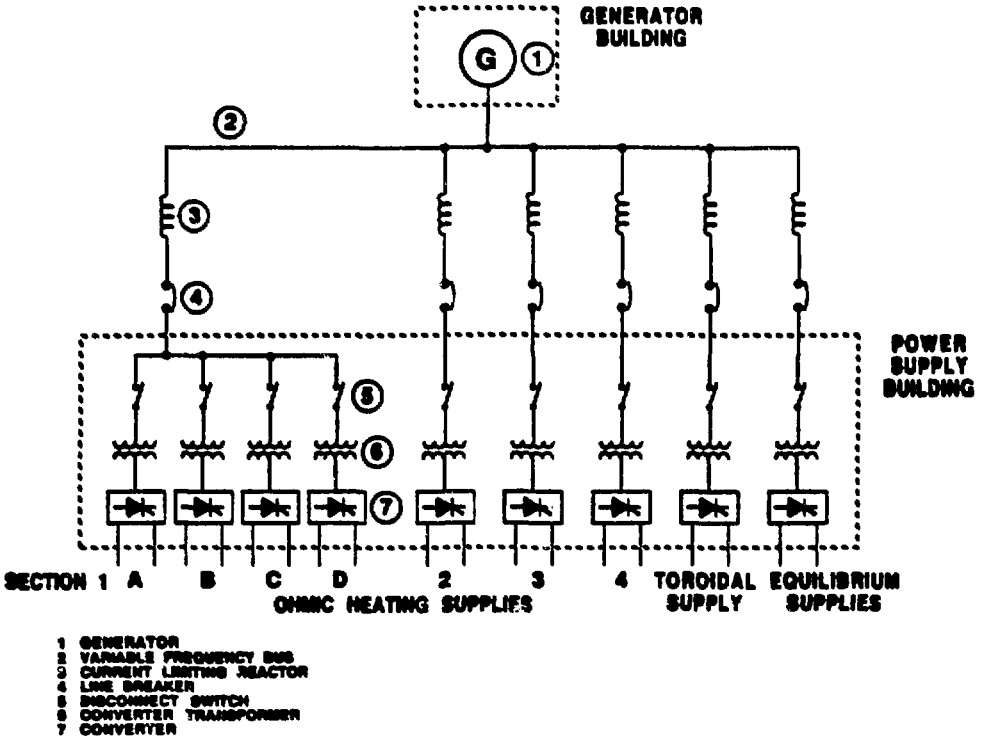

Fig. 1 ZTH Power Distribution System

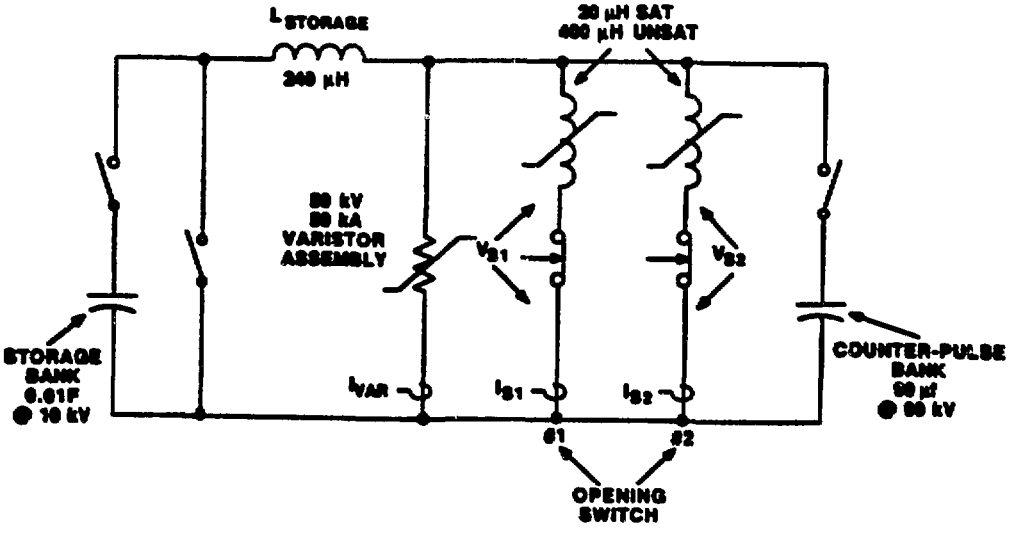

Fig. 3 Simplified Electrical Diagram of Switch Test Facility

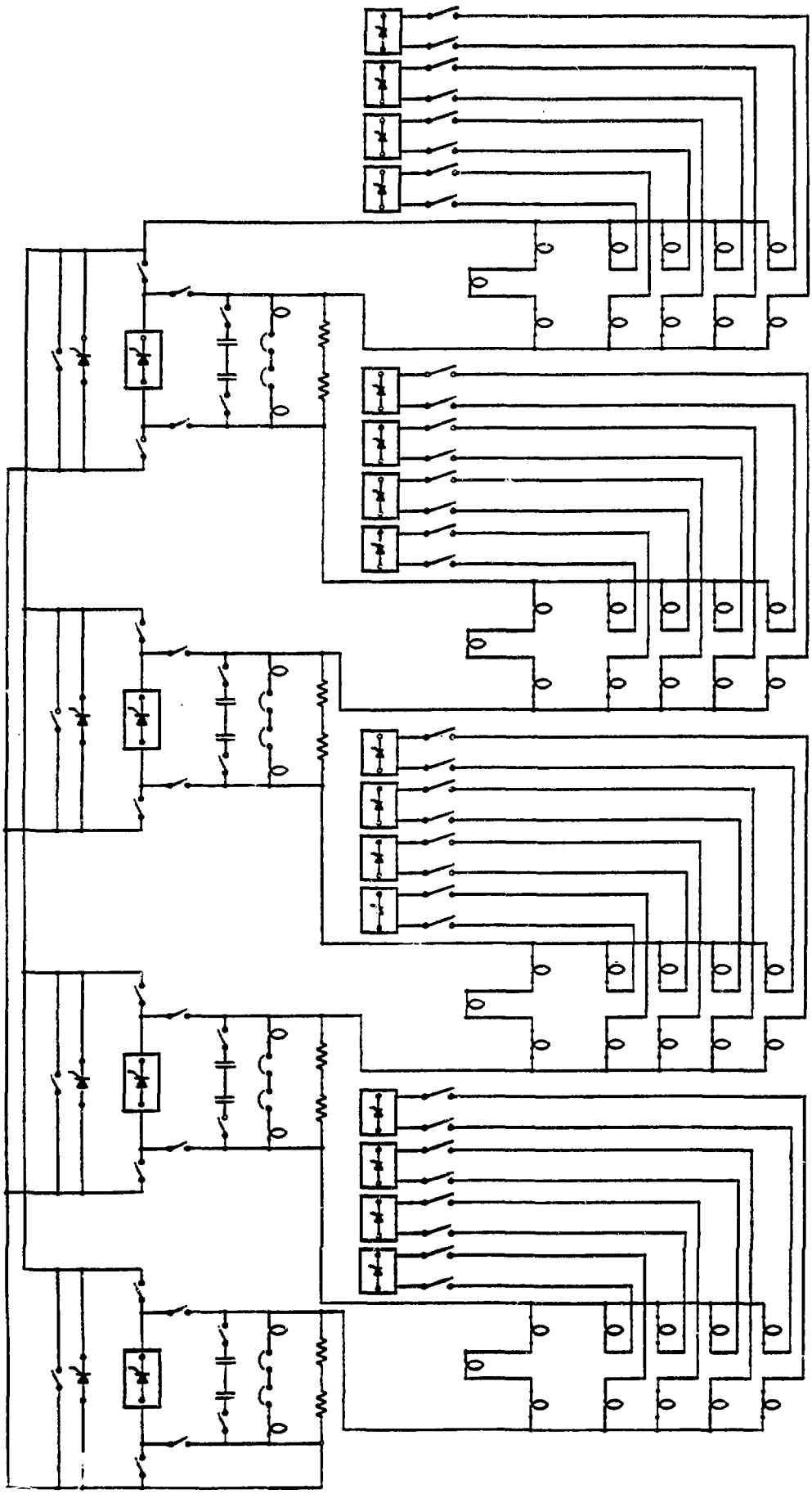

Fig. 2 Poloidal Field Energy System

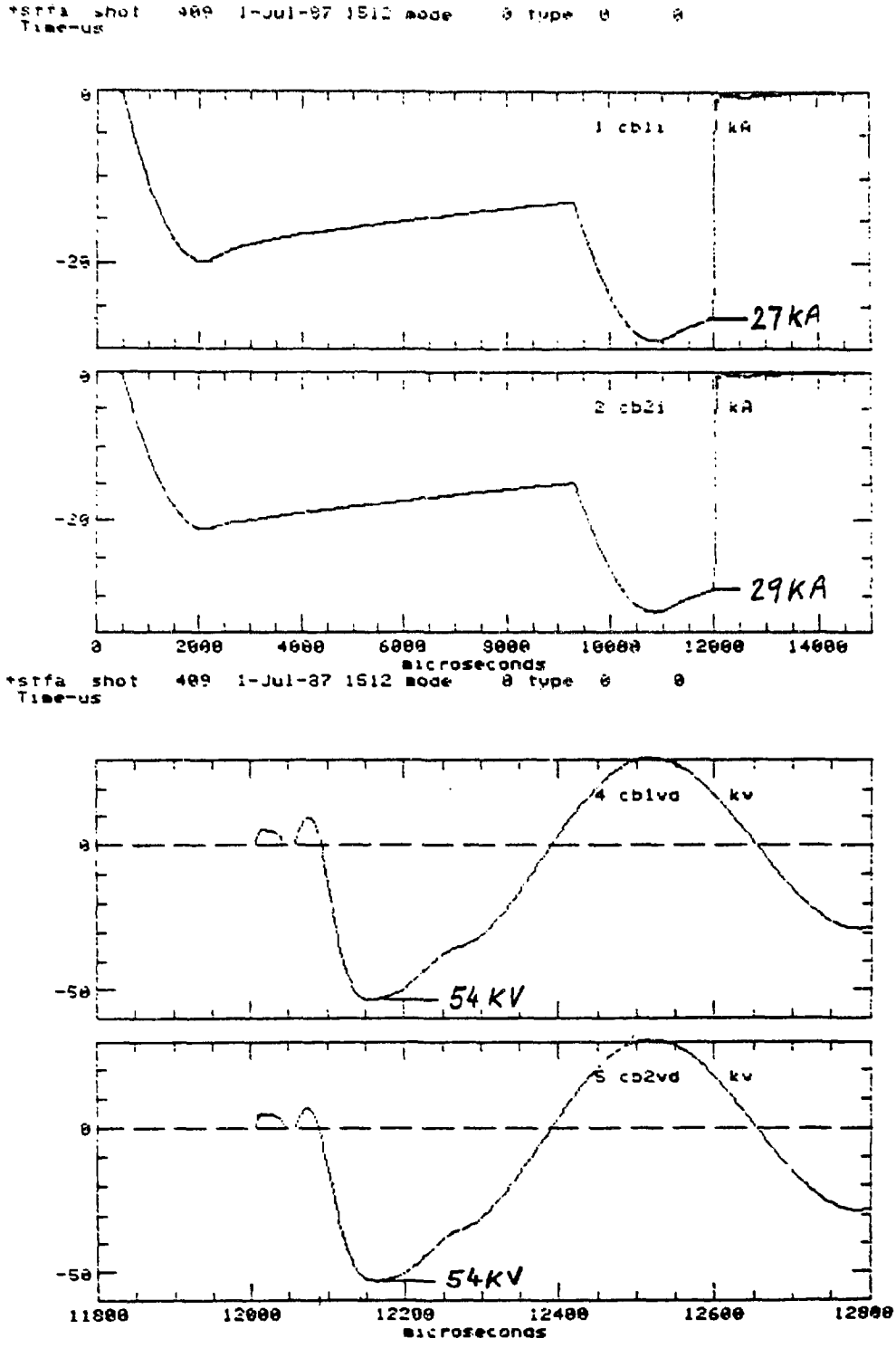

Fig. 4 Current and voltage traces for a 55 kA/55 kV dc current interruption
a) cb1i current through breaker 1
b) cb1i current through breaker 2
c) cb1vd voltage across breaker 1
d) cb2vd voltage across breaker 2

RFX POLOIDAL FIELD POWER SUPPLY

A. Maschio*
Istituto Gas Ionizzati - Progetto RFX
Associazione EURATOM-ENEA-CNR

ABSTRACT

The scheme and the operating principles of the poloidal field circuit of RFX are presented. The final structure of the different components of the power supply system is presented and the major problems met during the design phase are discussed. Finally the calculation tools set up for the study of the overall system are briefly described, while large reference is made to the already existing literature on these subjects.

1. INTRODUCTION

The poloidal field circuit of RFX must provide (not differently from in a Tokamak) the magnetic flux linked with the torus whose variation is used to set up the plasma current. But quite different from in a Tokamak are the characteristic times for this flux variation (only some tens of ms); relatively high voltages in the circuit (up to 35 kV) were required though splitting the magnetizing winding in four parts, as explained in /1/.

The overall scheme of the circuit is shown in Fig. 1; at the beginning of the shot the PMAT converters charge the magnetizing winding M and are then disconnected; afterwards the PTSO switching units are operated and the magnetizing current is diverted into the PTRB resistors, then decaying in few tens of milliseconds. The voltage induced by the flux variation is applied to the gas, causes its ionization and gives rise to the plasma current.

At the end of the rise phase, the PCAT converters keep constant the plasma current, by controlling the derivative of the current (and therefore of the magnetic flux) in the M winding; in the meanwhile a proper distribution of the currents among the field windings F is assured by the PVAT converters to control the field errors at the gaps of the shell and to maintain decoupled the M and F winding systems.

* Now with Università di Catania - Italy

2. THE AC/DC CONVERTERS

Due to the uncertainties related to the plasma behaviour, which can require a heavy change in the parameters and in the configuration of the system, a modular approach in the design of the converter system was adopted. The basic element is a 6-thyristor bridge TB, whose rating is shown in Tab.1. The thyristor used in the converters is the type AT 874 of Ansaldo, Italy, which is 78.6 mm of diameter and rated 4.4 kV.

TABLE 1 - Rating of the elementary bridge TB

No-load voltage	2 kV
Load voltage	1.4 kV
In (for 5 s)	3.13 kA
I (for 0.5 s)	4.07 kA

The improvement in the performances, compared with the initial design ones /2/, has been made possible without increasing the cost due to the progress in the construction of large thyristors. Two different types of converter units, called respectively A and B, are used. Type A units employ 4 TB in parallel, so that the current rating is 12.5 kA for 5 s or 16.3 kA for 0.5 s and type B units employ 2 TB (6.25 kA for 5 s or 8.13 kA for 0.5 s). Each unit is equipped with free-wheeling diodes and DC side reactors.

Both units employ a 3-winding transformer with the two secondary windings star and delta connected respectively, so that they can operate in the 12-pulse configuration; furthermore, the primary winding of the transformer is of the extended-delta type, so that an even number of converters working in parallel can operate in the 24-pulse configuration, with a proper connection of the primary terminals (Fig.2).

The converter system consists of 12 type A units and 8 type B units, for a total nominal power of 400 MVA (280 MW): 4 A units are used in the PMAT converters, 4 A units are used as PCAT converters and the type B units are used as PVAT; the last 4 A units (called TFAT /3/) are used in the toroidal field circuit.

A detailed analysis of the arrangement and the connection on the AC side is presented in /4/.

3. PROTECTION OF THE CONVERTER SYSTEM

In case of untimely operation (or fault) of the relative protection switches /3/, a voltage can appear at the terminals of the converters PCAT and TFAT with a maximum value of 35 kV or 7 kV respectively.

In both cases the intervention of a protecting crowbar /3/ is expected, but with a delay of about 1 ms. In addition, overvoltages of smaller amplitude, but with a much higher repetition rate, can be originated in both circuits by sudden disruptions of the plasma.

Therefore a system to protect the converters from both events has been designed. Solutions employing either ZnO varistors or thyristor crowbars with series resistor were examined /5/. The first one has the advantage of operating in an only passive way, which guarantees high reliability; on the other hand, the energies involved are quite high (up to 0.5 MJ), so that the use of many varistors in parallel should be required; though some positive indications came from recent experimental results /6/, there is no enough knowledge on the real reliability of such a system.

At the end the second solution has been chosen for RFX (see Fig. 3), with different resistors according to the different converters, with the aim to use the highest possible value of resistance for each converters, so reducing the fault current in the converter transformer. The protecting thiristors are directly fired through a breakover diode system which is very reliable.

4. ENERGY TRANSFER UNITS

RFX will use four energy transfer units, whose rating is given in Tab. II. The solution originally proposed was based on four vacuum circuit breakers per unit (2 in series and 2 in parallel), being the limits of a single breaker of the order of 25÷30 kA and 20÷25 kV for the interruptible current and the recovery voltage respectively.

TABLE II - Rating of the energy transfer units

Nominal current	50 kA
Recovery voltage	35 kV
I^2t before opening	$5 \cdot 10^9 A^2s$

The high number of breakers that had to be employed made critical the problems of mechanical synchronization of the different units: a too high jitter in the

opening times leads to the requirement of very long arcing times in the breakers, which in turn reduce the breaker life. In addition, the impact on the cost of the replacements of the breakers was not negligible.

For these reasons an alternative employing thyristors was examined and considered practicable /7/; therefore, at the time of the tender, the manufacturers were left free to propose a solution based either on vacuum circuit breakers or on thyristors.

What resulted at the end was that the cost of a thyristor based solution was considerably higher (about a factor two) than the vacuum breaker one, even when the cost of the spare parts was taken into account. Furthermore, a vacuum circuit breaker able to interrupt more than 50 kA DC was then available on the market and this fact made more reliable the solution using these components. Having been increased the level of the current supplied by the counterpulse bank and of its derivative, the ignitrons, which are used to fire the counterpulse network, were no more able to interrupt their current after its zero crossing. Therefore a diode (built up with fast recovery components) was put in series with the ignitrons themselves to make sure the current extinction.

5. DEVELOPMENT TESTS

Some tests were carried out directly by the RFX design group on components recently developed or used in a different than the standard way.

In particular tests were done on ZnO varistors connected in parallel, to check if this particular use of these components is reliable, considering also their ageing due to the numerous interventions which are expected during the machine life /6/.

The current sharing among the different varistors in parallel kept constant during the life tests, for a number of shots which, in the best components, was some order of magnitude higher than the manufacturer expectations. Nevertheless, explosion of some varistors was random observed, without finding a criterium to predict it. It was only found that the degradation of the varistor before the explosion took place in no more than two shots.

Interruption tests were carried out on the vacuum breaker chosen for the energy transfer units. The breaker has a self-produced axial magnetic field, with a typical value of 8 mT/kA, and is produced by Siemens, West Germany. A limited number of shots (about 200) was initially carried out, aimed manly at understanding its limits in DC operation. Currents up to 55 kA were reliably interrupted with recovery voltages up to 40 kV. The arcing time was varied between 4 and 12 ms /8/.

Due to the limitation of the test circuit, the $I^2 \cdot t$ before the interruption was of the order of some 10^6 $A^2 \cdot s$ but the $I^2 \cdot t$ is expected to effect the performance of the breaker only towards the end of its life. Fig. 4 shows typical waveforms of the interrupted current and of the recovery voltage during the tests.

A life test of 2.000 interruptions at 55 kA is scheduled in the next winter in the framework of the manufacturing contract.

6. CALCULATION TOOLS

A 0-dimensional plasma model, utilizing the CSMP code, was initially set up /9/to evaluate the adequacy of the power supply system for the expected behaviour of RFX. Both poloidal and toroidal circuits were represented only with their equivalent one-turn scheme, and the analysis of the machine performances was emphasized. Later on, the need was recognized for a more complete analysis of some particular design aspects which could effect the machine operation; they were the interaction, through the 20 kV grid, among the different converters; the effect of the ripple in the output voltage of the converters on the plasma loop voltages in both poloidal and toroidal directions; finally, the disymmetries in the construction of the different transformer (e.g. in the short circuit impedances) which could give rise to an anomalous harmonic content, with respect to the ideal case.

Therefore a new simulation tool was set up, based on the EMTP code, called RIPA (RFX Integrated Performance Analyser) /10/. It includes a model for the AC network, with individual transformers and thyristor bridges, the control system and the previous 0-dimensional plasma model, whose equations were represented by a block scheme to be simulated by TACS routines of EMTP. Through possibly less accurate than the previous model, it gave very interesting results for the particular problem for which it was derived.

Of course many other simulations, based in general on CSMP code, were carried out to solve particular problems of some component.

7. STATUS OF THE ART

The tenders for the converter system and for the energy transfer units have been already assigned, to Ansaldo, Italy and Siemens, West Germany respectively. The construction phase should begin for both contracts in the next October and the final erection will take place in the spring and summer 1988. The protection switches and the crowbars, which have been designed by the Culham Laboratory, will be

probably ready at the end of summer 1988, together with the busbar system. The integrated commissioning of the power supply system should start at the beginning of 1989.

REFERENCES

/1/ Stella, this Workshop

/2/ Rostagni et al. Univ. of Padova Report UPee 80/04, Padova 1980.

/3/ Gray, this Workshop.

/4/ Fellin, this Workshop.

/5/ De Lorenzi et al., Proc. of 5th IEEE Pulsed Power Conf., 1985.

/6/ De Lorenzi, Gaio, Piovan, pres. at 6th IEEE Pulsed Power Conf., 1987.

/7/ Maschio, Piovan, Proc of 14th Symp. on Fusion Techn., 1986.

/8/ Benfatto, Maschio, Manganaro, to be published.

/9/ Maschio, Ortolani, Piovan, Proc. of 10th Symp. on Fusion Engin., 1983.

/10/ Benfatto et al., Proc. of 11th Symp. on Fusion Engin., 1985.

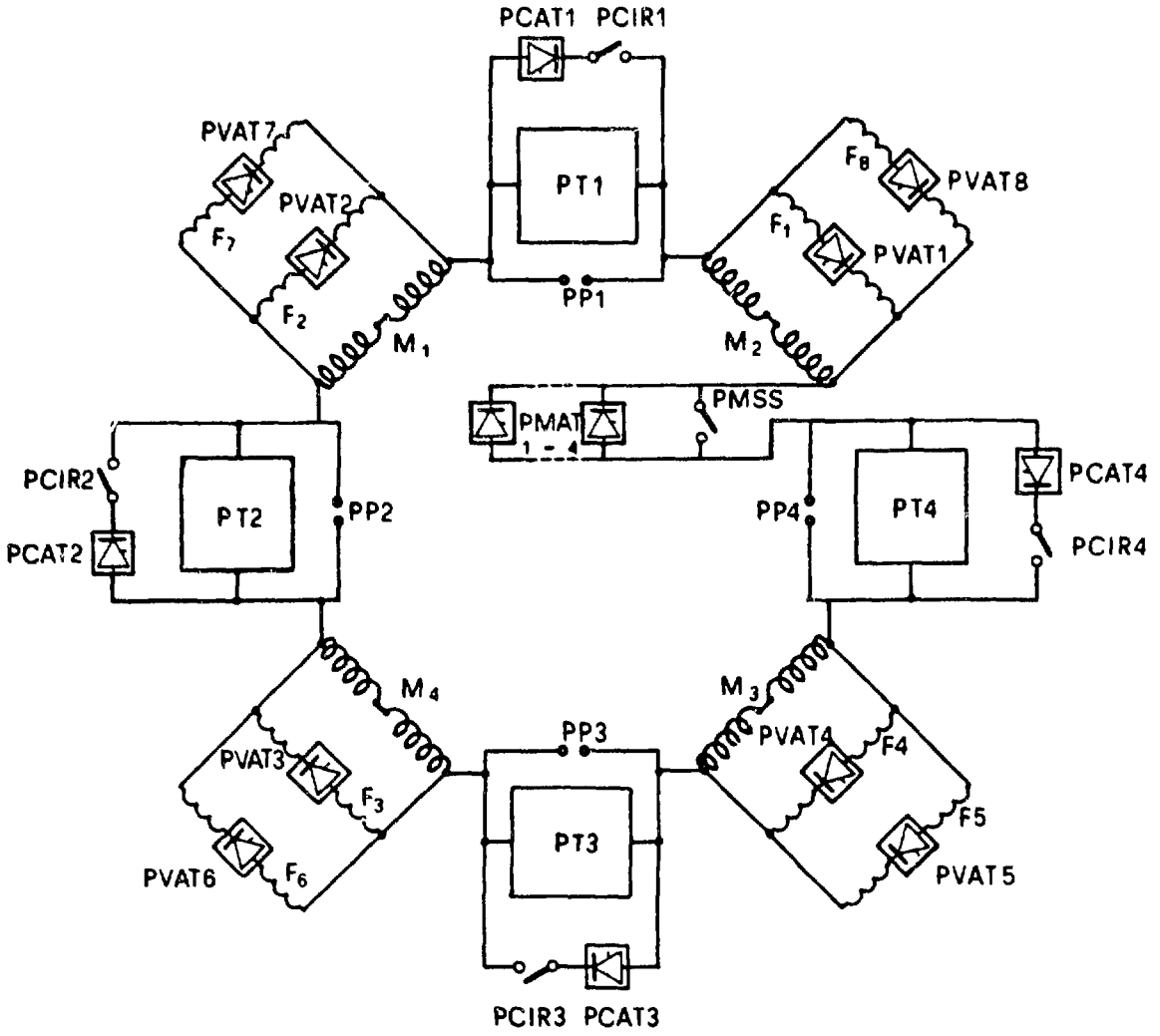

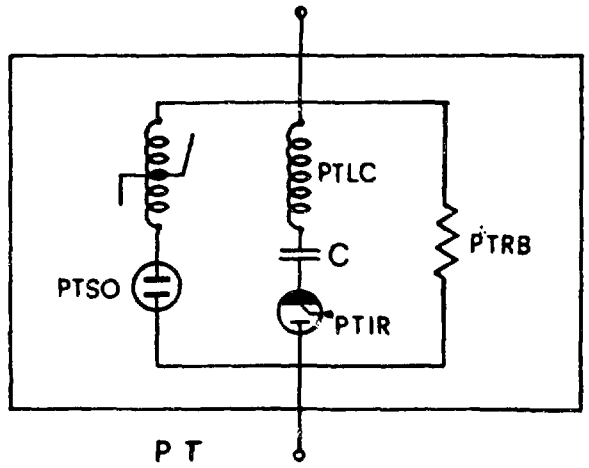

Fig. 1: a) RFX poloidal field circuit

b) Scheme of an energy transfer unit

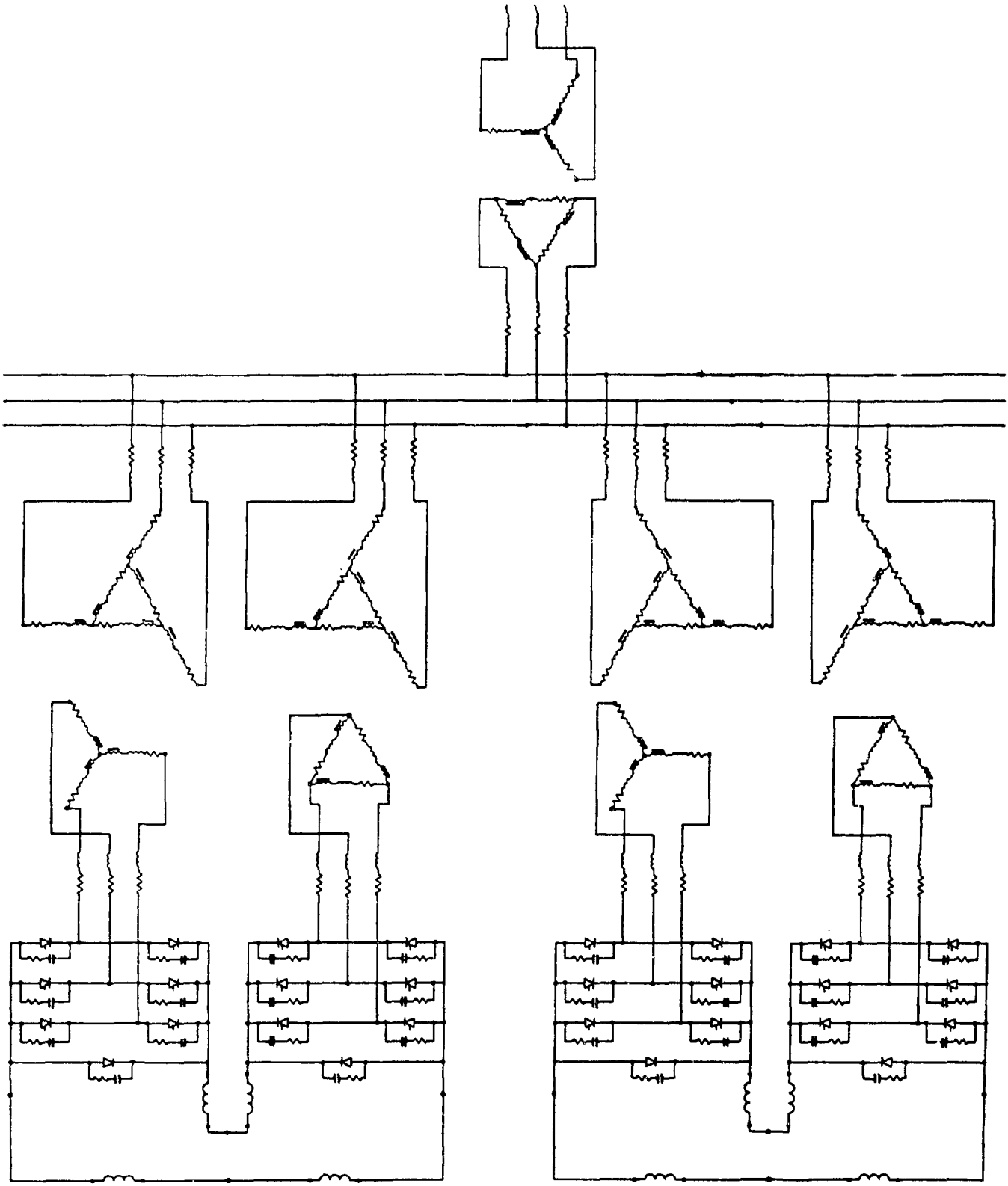

Fig. 2: Two converter units connected for 24-pulse operation

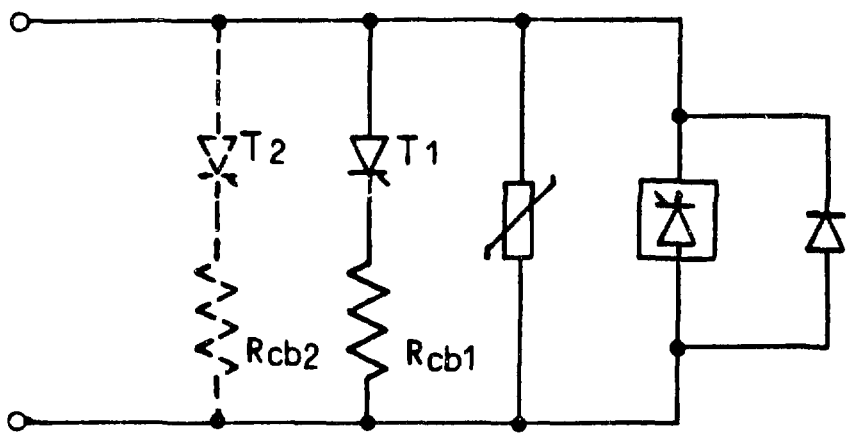

Fig. 3: Thyristor crowbar protection system

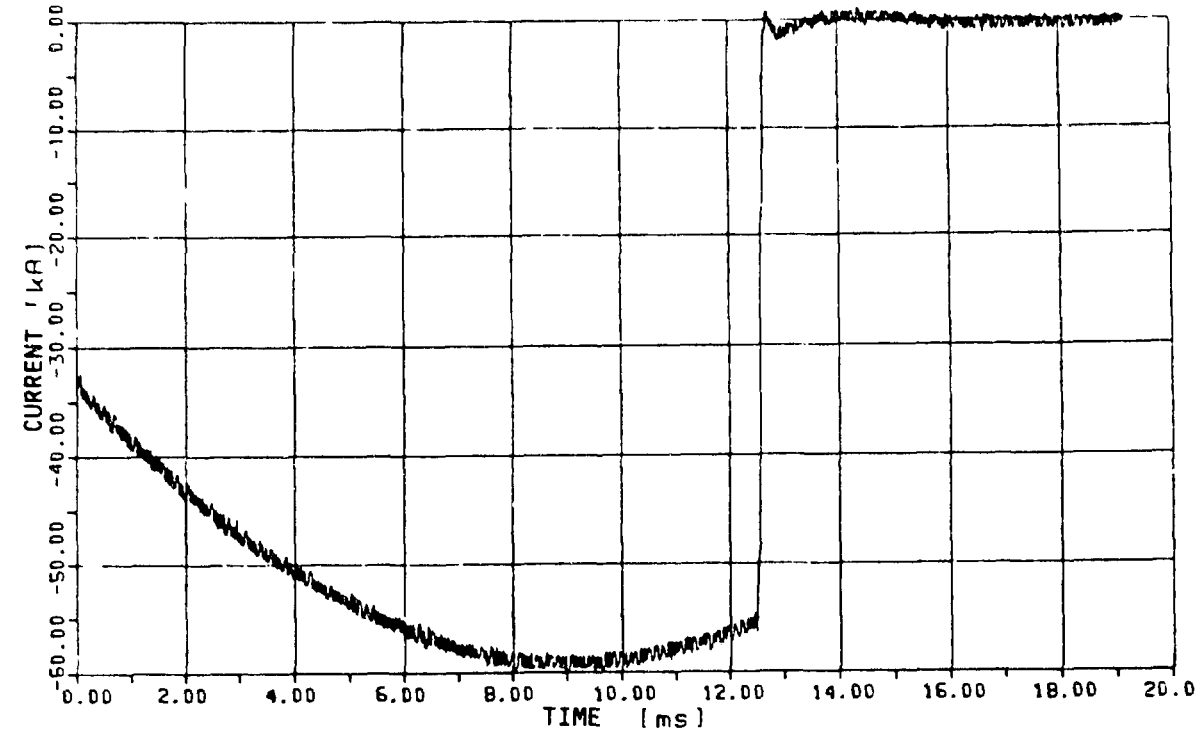

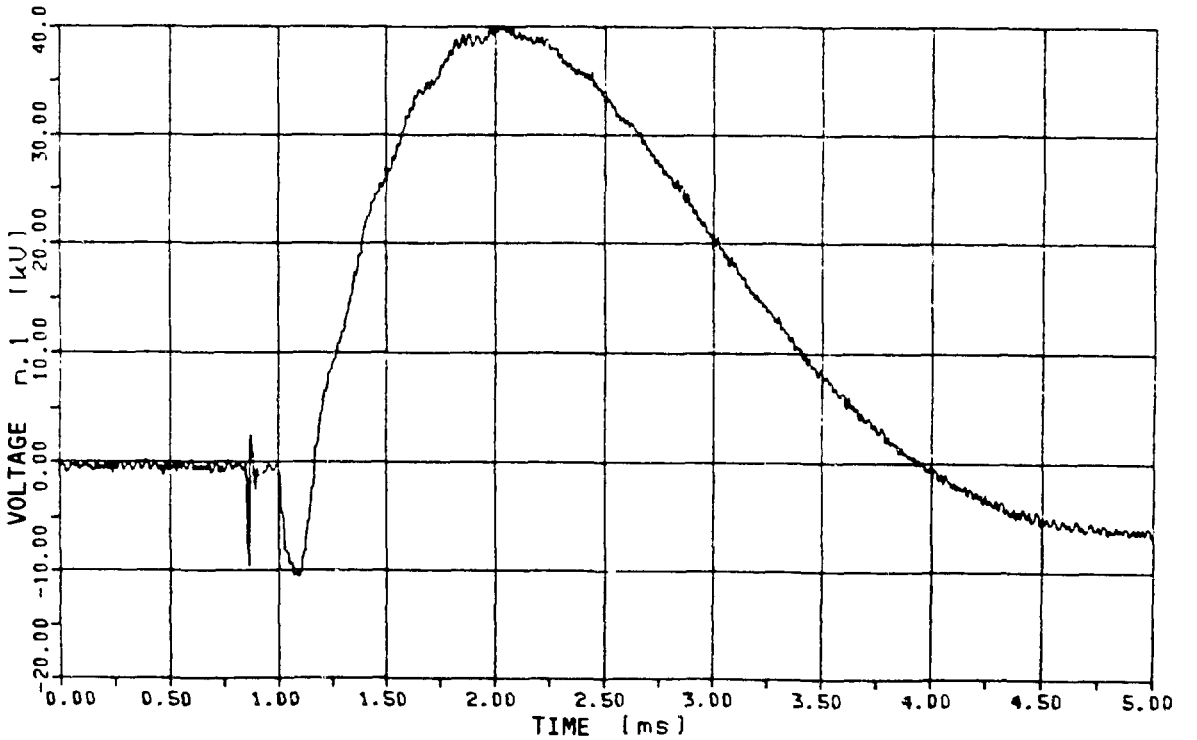

Fig. 4: Current and voltage wave forms during the tests

RFP OPERATIONS WITH A RESISTIVE SHELL IN OHTE

GA Technologies Inc.

and

Istituto Gas Ionizzati del C.N.R.

Presented by
T. Tamano, GA Technologies, Inc.

The attached paper is a copy of the EPS abstract presented at the 14th European Conference on Controlled Fusion and Plasma Physics, Madrid, 22-26 June 1987.
(Volume 11D, Part II, page 447)

REVERSED FIELD PINCH OPERATION WITH A THIN SHELL

S. Ortolani, V. Antoni, and S. Martini
Istituto Gas Ionizzati del C.N.R.
EURATOM-ENEA-CNR Association, Padova, Italy
and
R. LaHaye, M. Schaffer, T. Tamano, and P. Taylor
GA Technologies, San Diego, California, USA

Reversed Field Pinches (RFP) have typically been studied in experiments where a thick conducting shell tightly surrounds the plasma. This feature has been dictated by the theoretical belief that MHD plasma instabilities would otherwise grow and destroy plasma confinement. On the other hand, the presence of the thick conducting shell prevents accurate active plasma position control, which is important for minimizing plasma-wall interactions. Furthermore, in a reactor the discharge length will of necessity be longer than the shell time constant and the possibility of using a thin conducting shell will make the prospect of the fusion reactor more attractive.

Already in the design of the new generation of devices such as RFX [1], ZT-H [2], OHTE II [3], TPE-RX [4], the decision of whether or not to continue installing thick conducting shells is a very important and difficult one to make. In particular, it is now believed that accurate equilibrium control, edge plasma properties, plasma-wall interactions and impurity contamination can play a dominant role in determining the loop voltage necessary for maintaining the RFP distributions, and therefore the energy confinement time, since for an ohmically heated system like the RFP, the simple relationship holds: $\tau_E = 3/8\mu_0 R\beta_\theta I/V$.

The present OHTE device has the unique feature of utilizing an electrically thin conducting shell in which discharge lengths much longer than the shell time constant for the vertical field have already been achieved [5].

Due to the interest in the construction and operation of future larger experiments, a joint Padova/GA experimental program was therefore carried out to further examine the scientific and technical features of the OHTE thin shell operation. In particular, an attempt was made to prolong the pulse lengths through finer tuning of the equilibrium control using an additional B_v circuit thereby further assessing the plasma sensitivity to position control as opposed to inherent MHD stability limitations due to the lack of a perfectly conducting shell.

The OHTE device ($R = 1.24\ m,\ a = .18\ m$)[5] has been operated in the RFP mode. The thin shell is made of brass ($\eta = 6 \cdot 10^{-8}\Omega \cdot m$) and is 0.8 mm thick with a minor radius of 0.2 m. The vertical field time constant is 1.5 ms whereas the toroidal field time constant is $\lesssim 0.25\ ms$. The experiments reported here have been made at currents of 150-200 kA. Typical plasma parameters are $\bar{n} = 5 \cdot 10^{19} m^{-3}$, $T(0) \sim 150\ eV$ corresponding to $I/N \simeq 3\text{–}4 \cdot 10^{-14}\ A \cdot m$ and to the OHTE temperature scaling of approximately 1 eV/kA[5]. The loop voltage is of $\sim$ 100 volts corresponding to plasma resistances $V/I \gtrsim 0.5\ m\Omega$.

The total vertical field necessary for centering the OHTE plasma is approximately $1.6 \cdot 10^{-7} I\ T$ (i.e., $\sim 0.03T$ at the current level we operated). The basic toroidal equilibrium control is achieved by mismatching the currents in the primary poloidal field coils [5]. In addition, an independently powered vertical field coil system was used for fine B_v tuning and plasma positioning. In this vertical field control experiment, variations of a few gauss in B_v were explored and the corresponding plasma pulse lengths were analyzed. In particular, we present here two sets of measurements:

a) a comparison between discharges with and without the use of vertical field control.

b) a comparison between discharges with opposite orientation of the toroidal field.

This last experiment was done to examine the existence of any direct coupling with the external helical coils leading to effective stabilization.

RESULTS

An example of a typical current waveform and of the corresponding plasma displacement is shown in Fig. 1 for a case without and one with the vertical field control where B_v was ramped at the rate of 10G/ms starting at 3 ms. Systematic prolongation of the current pulse is achieved, typically from 6-8 ms to 10-11 ms. An example of a discharge where the vertical field was initiated before current start is shown in Fig. 2. This mode of operation resulted in general in more reproducible discharges and on average gave even longer pulse lengths of $\sim$ 12 ms. The addition of a second bank to maintain the current flattop has already been used in the past, resulting in the longest pulse lengths previously reported[5]. In the recent measurements, after having done some B_v optimization, the second flattop bank was again applied and resulted in discharge lengths $\approx$ 14 ms (see Fig. 3). A summary of the results is presented in Fig. 4 in which the plasma displacement at the beginning of the current termination is plotted versus discharge duration. The results for the discharges without vertical field control are shown in Fig. 4a. In this case, the plasma is always displaced outward and terminated. Fig. 4b shows the results with

vertical field control demonstrating the prolongation of the discharges compared to the case without B_v control. The large number of discharges with small displacement indicates that termination is caused by insufficient sustaining voltage while a smaller set of discharges is terminated because of excessive inward displacement.

In the present OHTE set-up, just outside the shell at $r = 0.215\ m$, there are 4 cm thick helical coils. In order to examine whether or not these coils can provide some plasma stabilization by acting as a sort of discrete thick shell, the sign of the B_ϕ field was changed to reverse the relative pitch between magnetic field lines and external coils. The coil q is 0.2 and it is nowhere resonant in the plasma, which is characterized by q values $\lesssim 0.1$. Indeed, the change in sign did not apparently change the MHD stability properties of the discharge, and fluctuation spectra were very similar in both cases. It should also be noted that resistive MHD stability theory indicates that increasing the size of the vacuum interspace between the plasma and the conducting wall rapidly cancels the stabilizing effect of even a perfect wall [6]. It seems therefore unlikely that with an approximately 20% vacuum interspace from the plasma the discrete coils could produce a significant effect.

CONCLUSIONS

The pulse length in OHTE, operating with a thin conducting shell, has been prolonged by finer control of the plasma position. The plasma sensitivity to equilibrium control further proves the absence of any intrinsic limitation on the plasma performance due to the lack of the perfectly conducting shell. The addition of the external vertical field control has extended the discharge lengths from ~8 ms to ~14 ms, with a simultaneous increase in discharge reproducibility. Although MHD linear theory predicts that RFP plasmas are unstable with a resistive shell boundary, no change in gross MHD modes is observed experimentally. However, a toroidally localized kink mode ("slinky" mode) due to non-linear couplings of several internal kink modes has been found [7]. The experimental indication that a relatively resistive shell ($\tau_{shell} \approx 1/10\ \tau_{pulse}$) can provide an adequate MHD stability boundary introduces the possibility of major simplifications and optimizations in the design and construction of the next generation of RFP experiments. In particular, field error constraints on gaps and portholes become much less important and active accurate plasma positioning becomes possible. The latter may prove to be a crucial issue in RFP research where the dissipation in the outer plasma regions can largely determine the loop voltage and therefore the energy confinement time.

This work was supported by the U.S. DOE under Grant No. DE-FG03-86ER53228.

REFERENCES

[1] Malesani, G. and Rostagni, G., Proc. 14th Soft, Avignon (1986)

[2] Los Alamos Internal Report, LA-UR842601 (1985).

[3] T. Tamano, private communication

[4] K. Ogawa, private communication

[5] R.R. Goforth, et al., **Nuclear Fusion**, 26, 4 (1986)515

[6] D. Merlin, S. Ortolani, R. Paccagnella, this conference.

[7] T. Tamano et al., GA-A Report 18821 (19[illegible]7)

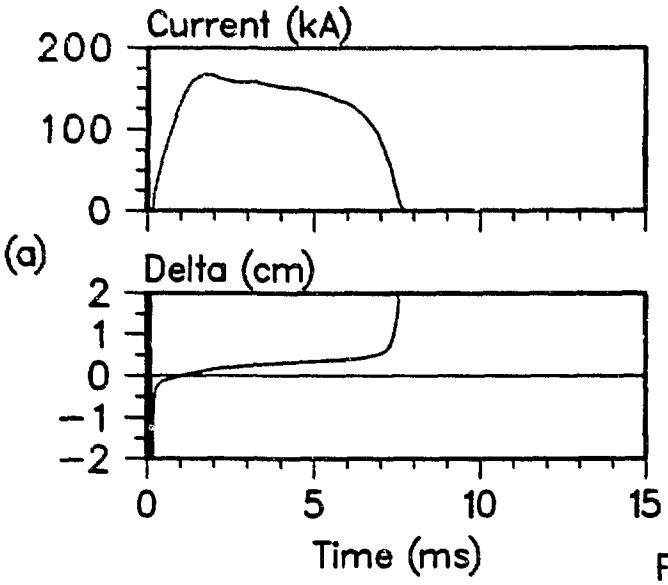

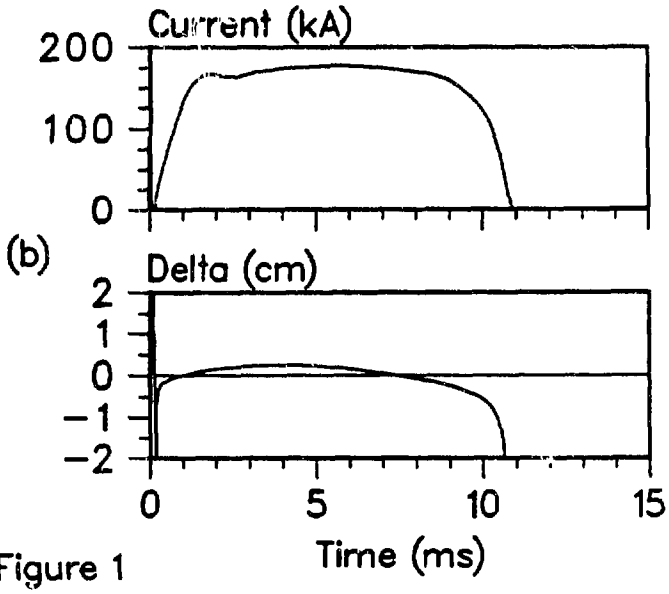

Figure 1

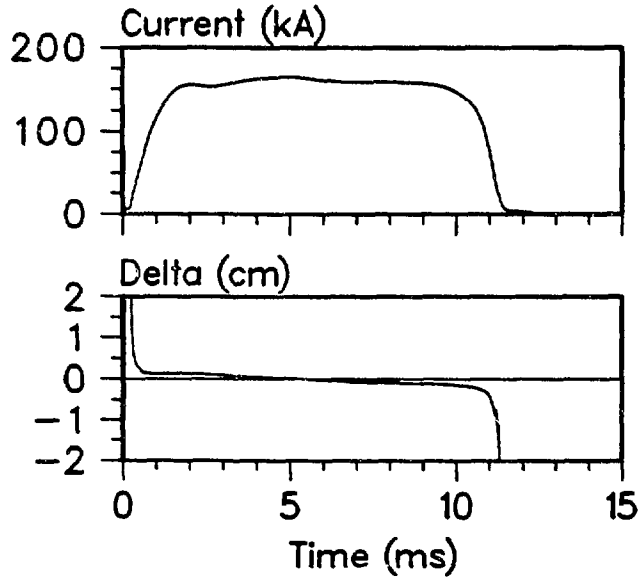

Figure 2

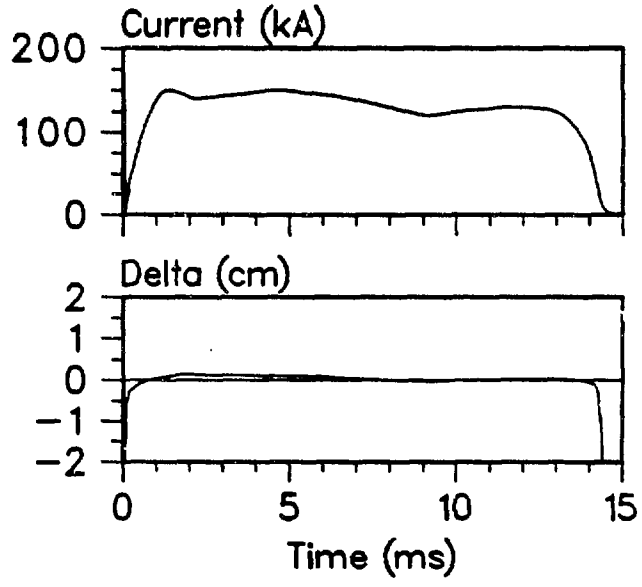

Figure 3

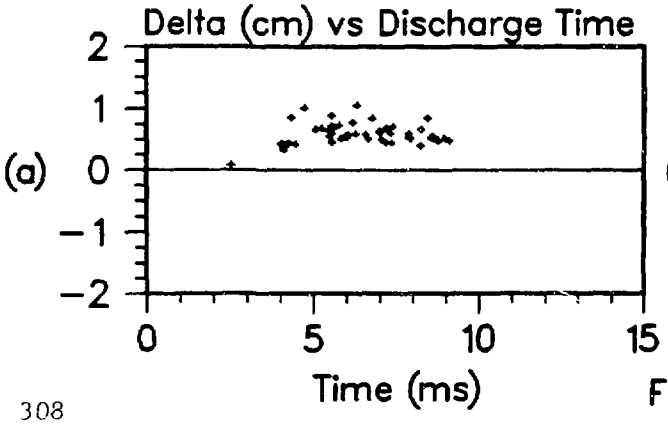

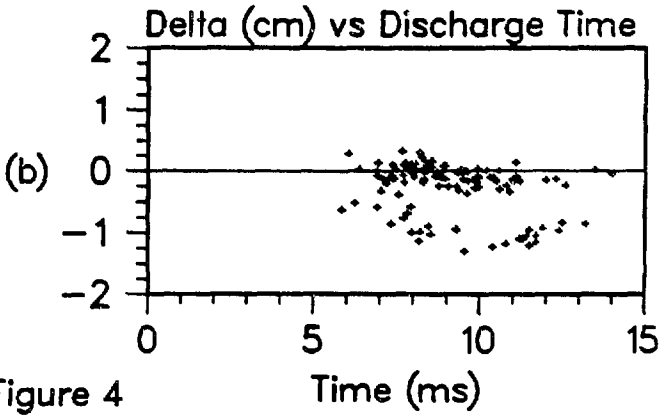

Figure 4

Operation of an RFP with a Modular Shell

Peter Schmid and Scott Robertson

University of Colorado, Boulder, CO 80309-0391

Abstract

A shell having many gaps will allow modular construction of an ignition-scale RFP. Modular shells with cuts every 20° in toroidal angle are being tested on the Reversatron. A very thin shell of 0.3 mm aluminum with a 40 μsec penetration time gives a higher plasma resistance and shorter discharge duration than is obtained with a thick conventional shell. Performance is better than with no shell, however. The experiment is to be repeated with a 1.25 mm modular shell.

Recent data indicate that the RFP can be operated with a thin shell having a time constant shorter than the duration of the discharge.[1-3] It appears, however, that the shell cannot be entirely eliminated. A modular shell of many sections not linking the toroidal coils will simplify the design and construction of an ignition-scale RFP. In this paper we describe experimental tests of a thin, modular shell which were performed on the Reversatron.

The Reversatron (Fig. 1) is a small (R/a = 50 cm/8 cm) air-core RFP constructed to allow relatively rapid removal and replacement of the shell.[4] When the shell is removed the equilibrium is provided by a preprogrammed vertical field. Discharges are made in 18 mTorr of He and the line-averaged density is typically 5×10^{14} cm^{-3}. The modular shell is fabricated from 0.3 mm aluminum sheet metal cut into sections and bent to cover the metal bellows of the vacuum chamber. Each section spans 20° in toroidal angle and is cut in the equatorial plane. The cuts generate an m = 2, n = 18 field perturbation. The measured penetration time of the vertical field is 40 μsec which is shorter than the penetration time of a one-piece shell of the same thickness due to the large number of cuts. The penetration time of the metal bellows alone is 4 μsec. Discharges with no shell and a conventional 22 mm thick shell are described in detail elsewhere.[2,3]

In Fig. 2 we compare discharges with the thick shell, the thin modular shell, and no shell. In the thick shell case, the discharge duration is determined by the ohmic heating capacitor bank and is 400 μsec. With no shell the duration is reduced to 220 μsec. The reduction is associated with the appearance of m = 1 modes with low toroidal

mode number.[3] With the modular shell, the duration is increased slightly to 250 μsec.

The longer discharge duration is associated with an increased plasma current and a reduced loop voltage. The time dependence of the plasma resistance in the three cases is shown in Fig. 3. The resistance rises most rapidly when there is no shell and the rise is delayed by the modular shell.

Fluctuations in the poloidal field can be divided into two categories. Within the vacuum chamber a B_θ probe at the wall records a fast oscillation of 1-5% having a period of 15-50 μsec. This oscillation modulates the F-Θ trajectory and is probably associated with the dynamo.[5,6] Outside the bellows are coils sensitive to m = 1 oscillations. The m = 1 probes are oriented to measure up-down asymmetry and are located at seven positions in toroidal angle. The signals are predominately at lower frequency due to shielding by the vacuum chamber walls. These fields reverse sign only a few times during the discharge and have no clear periodicity. Fourier analysis indicates toroidal mode numbers of n = 1,2 and 3. Higher modes cannot be resolved due to the limited number of probes.

In Fig. 4 we show the amplitudes of the m = 1 perturbations at seven locations for no shell and for the modular shell. Note that the signals are nearly twice as large with the shell. We interpret the larger B_θ perturbations as being due to the image currents in the shell. If we model the plasma as a thin wire, a displacement of the wire will give twice the m = 1 perturbation to B_θ when there is a shell.

The displacement of the plasma column can be inferred by assuming that B_θ varies inversely with minor radius (Fig. 5). With no shell, the

r.m.s. displacement indicated by the seven probes is 8-10 mm. With the modular shell and with the assumption that the probe signals are doubled for a given displacement by the image currents, the r.m.s. displacement is reduced to 5-7 mm. Without the assumption, we are unable to explain why the shell results both in an increased m = 1 fluctuation level and an improved performance.

Although the thin modular shell has improved the performance over that obtained with no shell, the performance is not as good as obtained with the thick shell which has cuts at only four toroidal locations. The reduced performance may be due to the short time constant rather than the larger number of cuts. A modular shell of 1.25 mm thickness and ~200 μsec penetration time has been constructed and is to be tested to determine whether or not performance with the modular shell can be made equal to the performance with the thick shell.

This research is supported by the U.S. Department of Energy.

References

1) R. Goforth, T. Carlstrom, C. Chu, B. Curwen, D. Graumann, P. Lee, E. Nilles, T. Ohkawa, M. Schaffer, T. Tamano, P. Taylor, T. Taylor, and D. Register, Nucl. Fusion 26, 515 (1986).

2) S. Robertson and P. Schmid, Phys. Fluids 30, 884 (1987).

3) S. Robertson and P. Schmid, Nucl. Fusion 27, 267 (1987).

4) P. Schmid and S. Robertson, IEEE Trans. Plasma Sci. PS-14, 267 (1987).

5) R.G. Watt and R.A. Nebel, Phys. Fluids 26, 1168 (1983).

6) V. Antoni and S. Ortolani, Phys. Fluids 30, 1489 (1987).

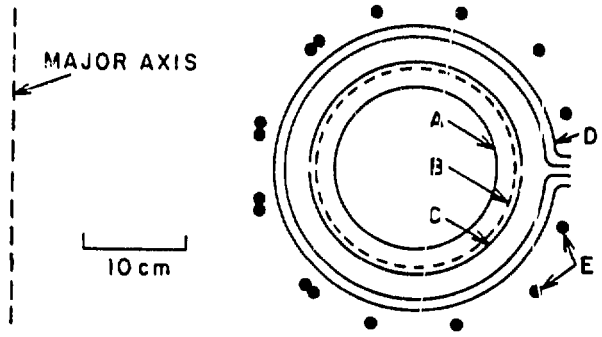

Fig. 1. Cross-section of the Reversatron: A. Inner diameter of bellows. B. Outer diameter of bellows. C. Thin, modular shell. D. Toroidal field windings. E. Poloidal field windings. The vertical field windings are not shown.

Fig. 2. Discharges with (a) thick shell (40 msec time constant), (b) modular shell (40 μsec time constant), and (c) no shell (4 μsec time constant).

(a) Thick shell

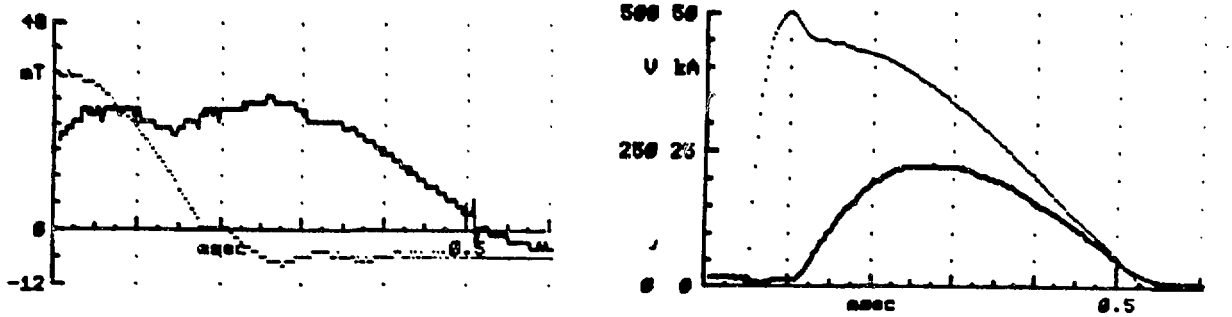

(b) Modular shell

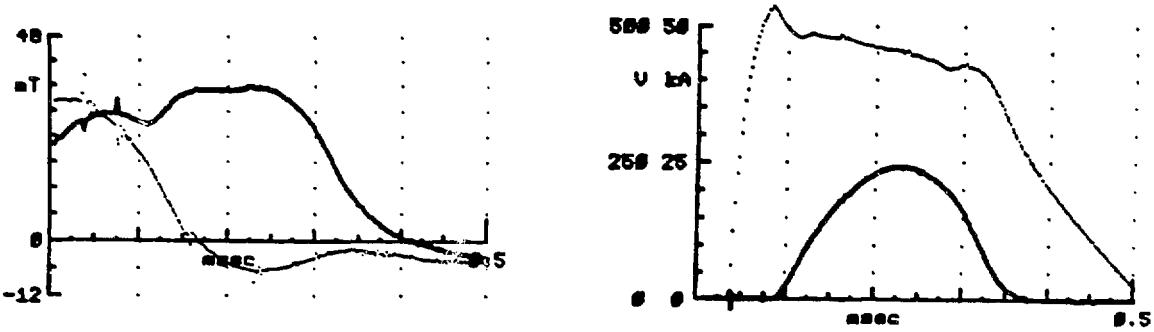

(c) No shell

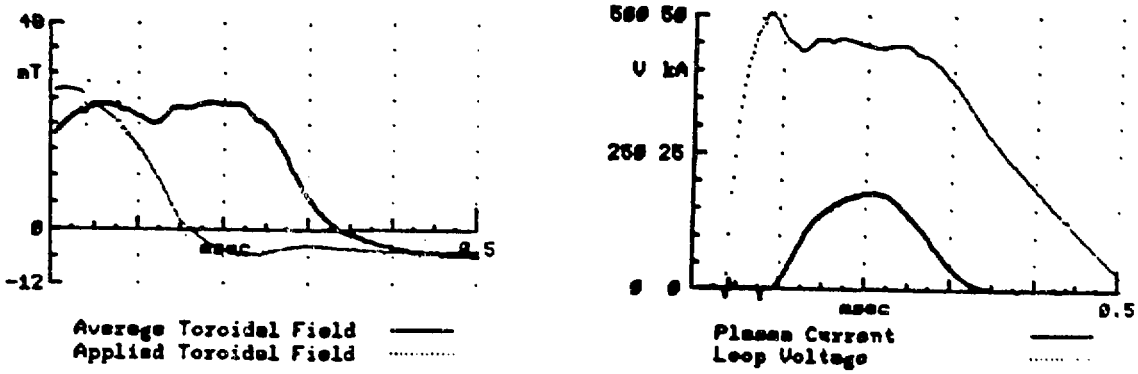

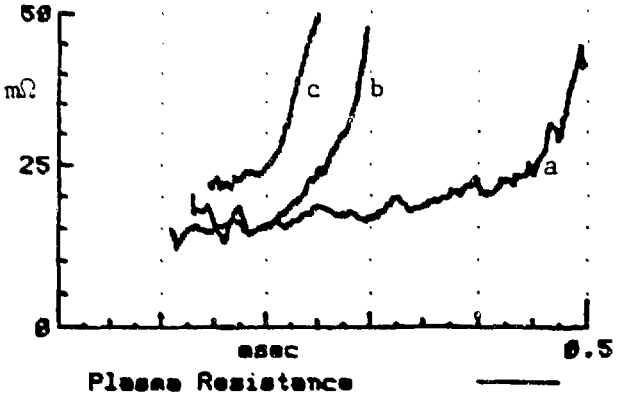

Fig. 3. Plasma resistance in milliohms for the three discharges in Fig. 2.

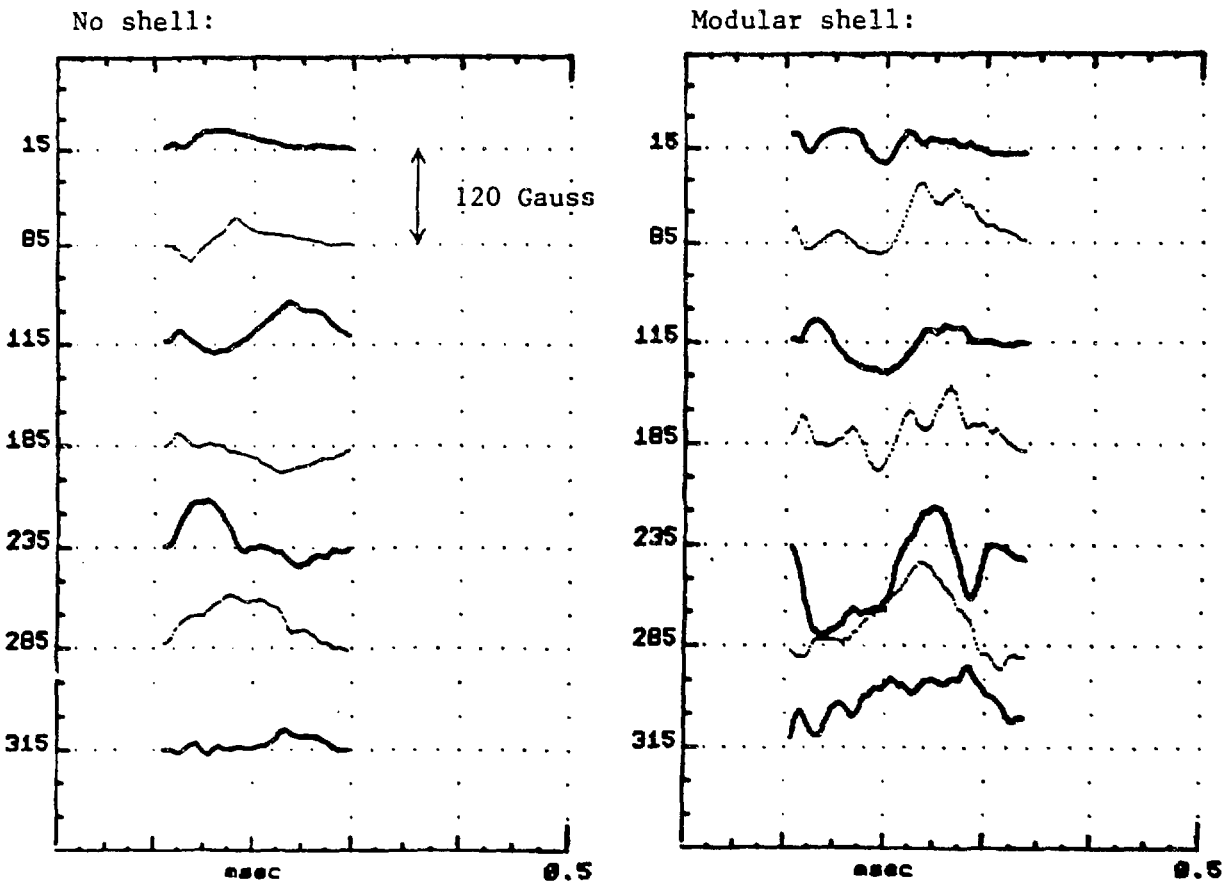

Fig. 4. The amplitude of the m = 1 component of the poloidal field at seven toroidal locations with no shell (left) and with the modular shell (right). The vertical scale is 40 Gauss per small division. The seven signals are labelled by their position in toroidal angle.

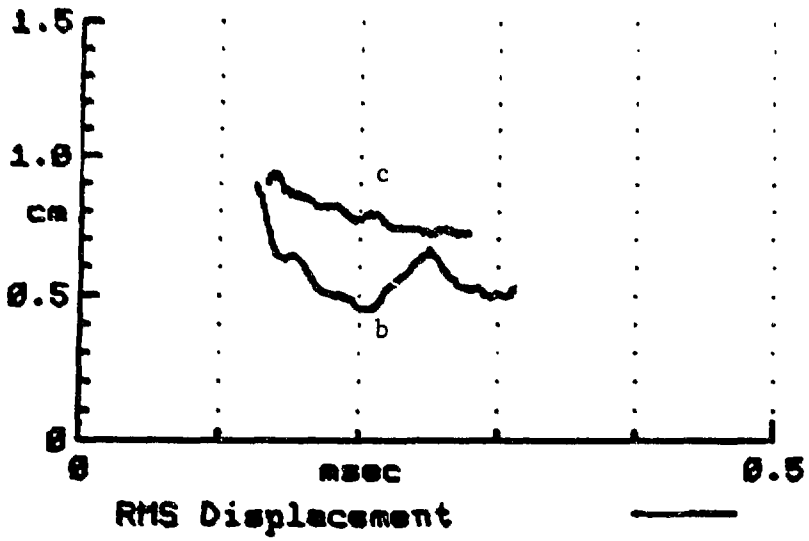

Fig. 5. Root-mean-square displacement of the plasma as a function of time b) with the modular shell and c) with no shell. The displacement is averaged over seven probes and over ten shots. The assumed relationship between the probe signals and the displacement is explained in the text.

International Workshop on Engineering Design of next Step RFP devices, Los Alamos, 13-17 July 1987

LOOP VOLTAGES, FIELD ERRORS, FIELD CONTROL, MANIPULATORS AND OTHER EXPERIENCE FROM HBTX1B RELEVANT TO NEXT STEP RFP

A A Newton
Culham Laboratory, Abingdon, Oxon, OX14 3DB, UK
(Euratom/UKAEA Fusion Association)

INTRODUCTION

There has been considerable progress in achieving high electron temperatures and confinement on HBTX1B (R/a=0.8/0.26m, I=80-520kA) by the reduction of magnetic field errors and control of equilibrium by vertical field. [1] The best parameters achieved to date are the loop voltage falling to 8v with I=80kA, T_e=800ev at the end of a 10 ms pulse, and $\tau_{Ee} \sim$ 1ms. The X-ray spectrum shows an energetic electron component with characteristic energy of 8keV indicating that some electrons are now confined for 10^3 circuits of the torus. The toroidal field $B_\phi \sim$ 8mT contrasts strongly with ohmically heated Tokamaks of similar current, dimensions and temperature which require ~2T.

These improvements have been produced after minimising the magnetic flux intersecting the wall and limiters (error flux, $\phi_n = \int \underline{B}.\underline{ds}$) by minimising the magnetic field errors (gap flux and ripple), centering the toroidal equilibrium with a vertical field [2] and finally removing the limiters. [3] The error flux is found to contribute an extra term to the loop voltage $V_A \propto \phi_n$ which is dominant in many conditions on HBTX1B [4].

The main objective in this note is to examine the implication of this effect for next step RFP and to suggest criteria for their magnetic design.

Other work at Culham important for large RFP includes the control of the toroidal field. Start up at constant θ (ramping) has been demonstrated on HBTX1B with V_{loop} < 100v and 150kA is reached in a risetime, $\tau_I \sim$8ms. Matched mode start up was attempted and possible with $\tau_I \sim$3ms. The quality of the plasma degraded with increasing τ_I and it was not possible to obtain τ_I=5ms or longer. In these condition the plasma resistance increased with time. The results underline the importance of constant θ start up for $\tau_I/a^2 \gtrsim 50$ ms/m^2 [5]. RFX has $\tau_I/a^2 > 120$ ms/m^2.

Experimental demonstrations of controlled rundown of the current pulse show that catastrophic termination due to loss of reversal can be prevented [6]. After shorting the loop voltage the reversal was deep-end and the current fell to 15% of the peak value before termination occured; feedback control should further reduce the current at termination.

The thin shell HBTX1C is under construction to test the control of equilibrium and the effect of a resistive shell on stability; the main features are summarised in the final part of the paper. The manipulator used to remove tiles from HBTX1B is briefly described.

FIELD ERROR CALCULATION

A simple technique to calculate field errors based on analytic and empirical formulae has been developed [7]. Field errors are defined by the field line deviation

$$\delta = \int B_{\perp} dl/B$$

and the effective area of an error is given by $A=\delta$ x characteristic width x number of occurences. For inter machine comparison this is normalised to the toroidal surface area $A'=A/(4\pi^2 aR)$.

There are many sources of field error and their size can be calculated with the semi-empirical formulae (see table 1). Data for Culham medium sized RFP are given in table 2 with predictions for RFX (design as 1986). The reduction in errors in the HBTX1 series of experiments and the importance of equilibrium centering with a vertical field can be clearly seen.

LOOP VOLTAGE

The additional loop voltage, V_A, caused by dissipation by helicity when field lines intersect the wall or limiters is directly related to the "error flux" defined:-

$$\phi_n = AB_{\theta}(a) \quad \text{or} \quad AB_{\phi}(a)$$

depending on which field component is in error. The voltage is proportional to $\Delta\chi\ \phi_n$ where $\Delta\chi$ is the potential drop along the magnetic field line caused by the obstruction to current flow due to the field lines intersecting the wall or limiters [4]. Using sheath theory Tsui

gives $\Delta\chi=1.8kT_{ee}$ where T_{ee} is the local electron temperature and then

ie. $$V_A = \Delta\chi \frac{\Theta}{\pi a^2} A$$

is proportional to the area of the field error.

The historic formulation (Jarboe-Alper effect [8]) gives V_A proportional to the volume of the scrape off layer (V_{edge}) defined by the field error and

$$V_A = E''(\Theta/\pi a^2)V_{edge}$$

These formulations are equivalent for HBTX1B results with $\Delta\chi$=18v and E"=27v/m.

The scaling of V_A with dimensions is different for the two formulations and can be estimated by comparing HBTX1B with TPE-1RM15 (R/a=0.7/0.135m) [9]. A similar variation of V_A with equilibrium displacement is seen in both experiments when the correcting DC vertical field is varied. Tsui's formulation fits both experiments with $z_i \sim 2$ in TPE-1RM15 which is plausible (z_i was not measured in the first investigations) and the Jarboe-Alper formula fits with a less plausible $z_i \sim 1$.

EXTRAPOLATIONS TO RFX

When extrapolating to RFX the expected plasma resistance due to coulomb collisions (including the dynamo effect supporting poloidal currents in the plasma) and its loop voltage are low and the loop voltage will be dominated by V_A if the phenomena seen in HBTX1B are present. Predicting the loop voltages for RFX (R/a=2.0/0.5m) I adopt Tsui's value as the expectation and find $V_A \sim$ 16v/1% field error and I take the Jarboe-Alper value as the upper bound with the $V_A \sim$32v/1%.

The toroidal equilibrium displacement Δ is an important source of additional loop voltage and $V_A \sim 5v/(\Delta/a\%)$. The Δ is readily calculated for the shell determined equilibrium using the Shafranov formula giving V_A= 40 v with an 80v upper limit.

Toroidal field ripple has been shown to be an important source of error (ZT-40M, HBTX1A, REPUTE-1) but has not been established on the same quantitative basis as equilibrium shift. Toroidal field ripple has a magnetic connection length $L_c \sim (2\pi R/n_{coil})(\theta/F)$ (where n_{coil} is the number of toroidal field coils) which is the same order as that for the toroidal equilibrium displacement $L_c \sim 2\pi a$. The ripple error is 1.8% in RFX. Including a factor to account for the fact that B_ϕ is the minor field component gives a V_A of a few volts.

Gap errors due to the mismatch of poloidal field inside and outside the shell can be measured directly with saddle or local coils. On RFX if the first harmonic poloidal of B_θ is matched to 1% as specified for feedback control the gap error is similar to that on HBTX1B and the additional loop voltage is estimated as ~1v. The main effect of the gap error in HBTX1B is to shorten the pulse duration rather than increase the loop voltage significantly and to localize the plasma wall interaction around the gap.

NEW THIN SHELL APPARATUS

HBTX1C installation began on 1 June 1987. Fig. 1 shows the nesting of the vessel, thin shell in the GRP I_θ and B_θ windings bobbins. This machine uses the same vessel (without tiles), iron core and power supplies as HBTX1B [10]. The new features are:-

(a) A Thin shell made of 5 layers of copper gauze each having 10 poloidal gaps to give $\tau_{sBV} \simeq$ 2ms. The gaps are staggered for each layer giving a flux maze to suppress the localised vertical fields normally associated with vertical gaps. The gauze is held in epoxy and there are 2 equatorial gaps. (Baking will now be limited to <110°C compared to 200°C previously).

(b) To give zero order toroidal equilibrium the I_ϕ windings are mounted eccentrically (b=0.33m, Δ_b=0.035m) so that the outer magnetic flux surface is aligned with the vessel (see crossection diagram in Fig 2).

(c) Equilibrium correction is provided by currents in trim coils. A switching type feedback system (f< 3kHz) has been developed to control gross horizontal and vertical shifts and has demonstrated control of the gap flux on HBTX1B. The I_ϕ windings and trim coils are in series and with the iron core operated in the linear region this arrangement ensures that plasma, windings and total trim currents are proportional which is important for achieving a good quality equilibrium.

(d) The centre limb of the iron core is close to the I_ϕ windings and there is a risk that flux spilled from the windings will be attracted to the core resulting in positional instability. Calculations show that the range of index $n=-(R/B_v)\, dB_v/dR$ to guarantee both vertical and horizontal stability is very small. The attraction effect of the core is suppressed by a 6 turn bandage (swiss-roll or foil winding) on the core centre limb having an effective time constant ~50ms. The bandage is part of the core back bias system.

 The time constant of the plasma to tilting modes $(R/a)^2\, \tau_{sbv}$~20ms

so that the tilt mode, if present might be observable if the presently achievable duration current pulses (up to 15ms) can be extended somewhat.

Manipulators and Limiter removal

All 156 Graphite limiter tiles (secured by dovetail clips) in HBTX1B were detached using a simple manipulator (see Fig 3) and removed from the vessel through ports at the bottom. The manipulator arm is inserted through a horizontal port on the outside equator and the three horizontal joints allow positioning in toroidal angle. The joints are set and locked with a tool through the top and bottom vertical ports. The rotary arm is turned manually by a flexible drive in the poloidal direction to apply the 2kg force required to unclip the tiles. A Pearpoint minature TV camera (ϕ = 42 mm) held in a simple manipulator (top left in Fig 3) and mobile lamp (bottom right in Fig. 3) enables the operator to view the vessel interior.

CONCLUSION

Many of the problems of large RFP such as startup, terminations, field errors, manipulator, etc have been investigated on HBTX1B. If the additional loop voltage seem in HBTX1B occurs also in RFX then the toroidal equilibrium displacement will add a few tens of volts to the plasma loop voltage.

ACKNOWLEDGEMENTS

The author is grateful to many colleagues who contributed to this work including M K Bevir, P G Noonan, R E King, R Peacock and R K Hall.

The author acknowledges many colleagues in the RFP community for discussions and giving details of their appartus for the assessement of field errors.

REFERENCES

1 H A B Bodin, Invited paper EPS Madrid (1987)

2 P G Noonan, H Tsui and A A Newton, Plasma Physics 27 (1985) 1307

3 A A Newton, IEEE Meeting on Plasma Science, Arlington (1987) and B Alper et al., to be published

4 H Y W Tsui EPS Madrid (1987)

5 P G Noonan, C G Gimblett and A A Newton EPS Madrid (1987)

6 A A Newton and P G Noonan, Nuc. Inst. and Methods A245 (1986) 167

7 A A Newton and others, Internal Report TPGN/207

8 T R Jarboe and B Alper, Phys. Fluids 30 (1987) 1107

9 T Shimada et al., IAEA Conf. Kyoto (1986). Post deadline paper

10 R E King and A A Newton, SOFT, Avignon (1986)

Table I

Approximate Expressions for Calcualtion of Field Errors

Source of Error	Field Line Displacement δ	Total Effective Area A
Equilibrium Toroidal displacement	$\delta_e = 2\Delta$	$A_\Delta = 2\pi R\delta_e$
Gap Flux	ϕ_g	$A_g = 2\phi_g n_g/B_o$
Initial Errors Portholes (in shell)	$\delta_p \simeq 0.06\, r_p{}^3/h^2$	$A_p = \delta_p r_p n_p$
Flat Top Errors Ripple	$\delta_r \simeq \frac{p}{2\pi} \exp(-\frac{2\pi h}{p}) f$	$A_r = 2\pi\delta_r L n_r$
Portholes (Windings deviation)	$\delta_h \simeq \frac{p}{\pi} \frac{As}{h^3}$	$A_h = \delta_h p\, n_h$
Iron Core Bias (Horizontal field)	$\delta_c \simeq 2a\, (B_{RC}/B_o)$	$A_c = 2a\delta_c n_c$

Notes

f = 1 for B_θ ripple and 0.2 for B_ϕ ripple

L = R for B_θ ripple
  = a for B_ϕ ripple

Normalised form $(A/A_T) \times 10^{-2}\%$ where $A_T = 4\pi^2 aR$ is used in Table 2.

r_p = porthole radius
p = windings pitch
h = distance from shell or windings to plasma surface
n = number of windings or occurence of source

Table 2 - Field Errors
Area as % of torus (shell area)

	HBTX1A 81-84	HBTX1B 85-87	RFX
Windings ripple and port distortion ($\gtrsim$ 4 ms)	0.20	0.01	1.8
Shell gap	0.03	0.015	0.02*
Shell port holes (0-4 ms)	0.03	0.03	0.04
Core bias stray field	0.05	0.01	-
Sub totals of above errors			
On short timescales	0.11	0.055	>0.6
On long timescales	0.28	0.035	>0.12
Sub Total	0.31	0.065	0.16
Equilibrium with vertical field centering	NO YES	NO YES	NO
Toroidal displacement	1.5/0.15	1.5/0.15	1.5
Grand Total	1.8/0.44	1.6/0.21	3.2

*Estimated fromm specification for the control of $B_1/B_o < \pm 1\%$

I-C	IRON CORE
I	I_ϕ COIL
L	VACUUM VESSEL
S	SHELL
T	B_ϕ
T-R	B_ϕ COIL
	RETURN LOOP
B	BANDAGE

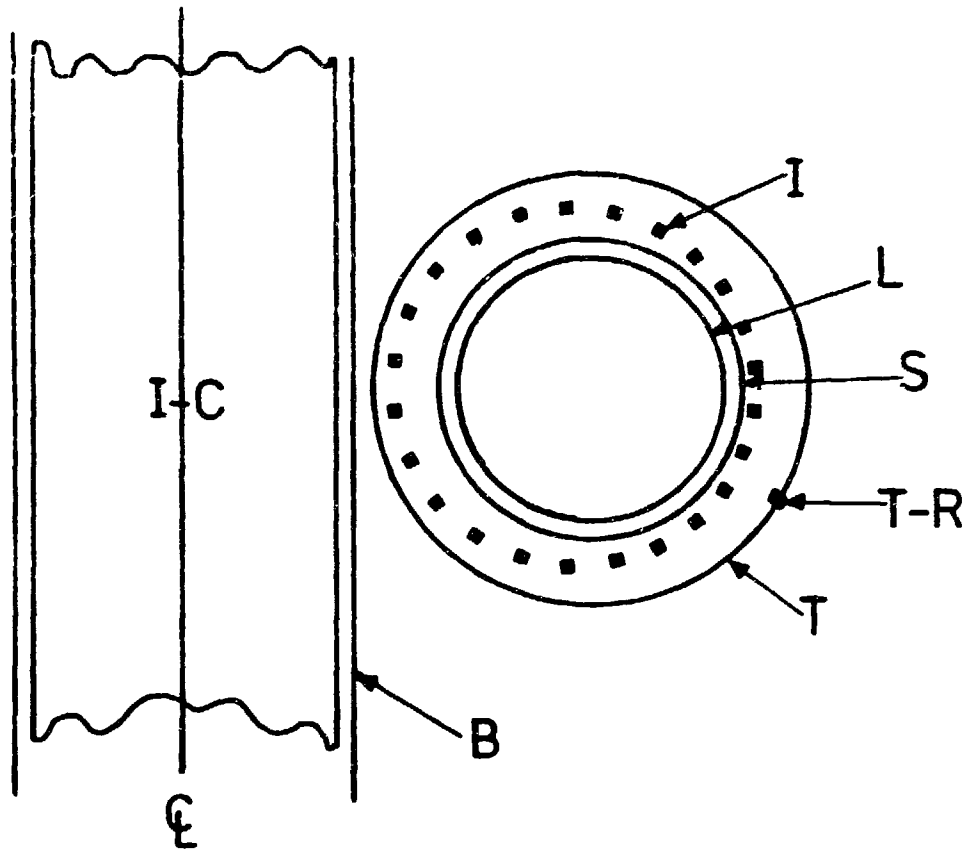

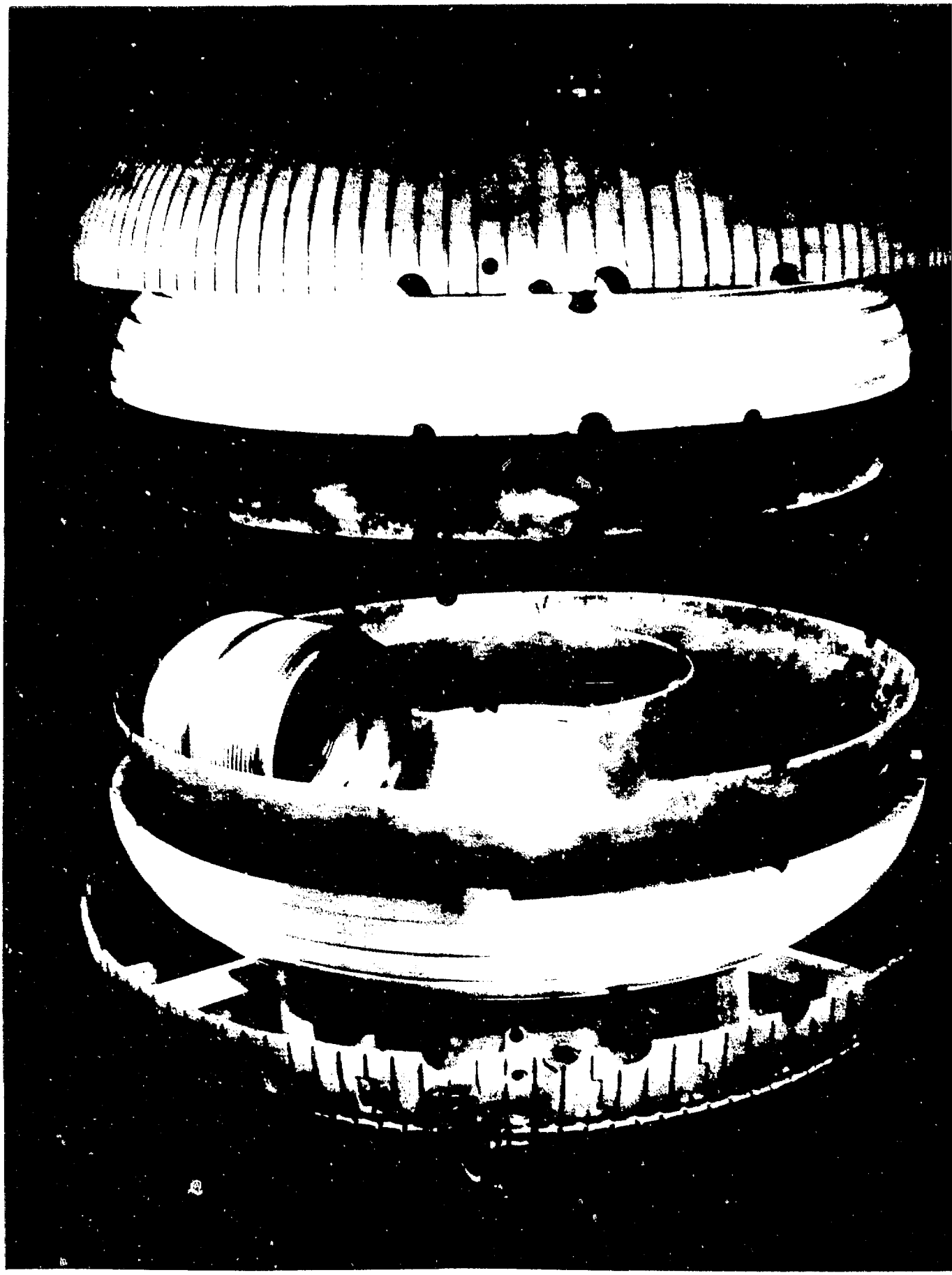

Reversed-Field-Pinch and Ultra-Low-q Discharges in REPUTE-2

N. Inoue, Z. Yoshida, Y. Kamada, M. Saito, and K. Miyamoto

Depratment of Nuclear Engineering, Faculty of Engineering
University of Tokyo, 113, Hongo, Bunkyo-ku, Tokyo

International Workshop on Engineering Design of Next Step RFP Devices

July 13 - 17, 1987
Los Alamos National Laboratory

1. Background

REPUTE-2 is a toroidal current-carrying device which is designed to cover wide range of the discharge safety factor q, *i.e.*, $q_a < 0$ (RFP), $0 < q_a < 1$ (ultra-low-q discharge) and $1 < q_a < 2$ (very-low-q tokamak), where q_a is the surface q value. Realizing the stable confinement in these q regime is important from the view point of the economical reacotor design. The reversed-field-pinch reactor is evaluated as one of the most economical thermonuclear reactor[1], *i.e.*, the cost of the RFP reactor is as low as that of the light water reactor (LWR). The progress of confinement physics of RFP is, however, much less than that of the tokamak at the present stage, and intensive study on the behavior of the RFP plasma is necessary. On the other hand, the tokamak reactor is less economical in comparison with the LWR, and study on lowering the reactor cost is required. The ultra-low-q (ULQ) discharge posesses the characteristics common to both the RFP and the tokamak. The possibility of Ohmic ignition of the ULQ reactor has been suggested by Kamada, *et.al.* [2], and they have shown that the ULQ reactor is sufficiently simple and compact. Operation of the tokamaks in very low q (VLQ) regime is being tried in many of middle-size and big tokamaks, such as, JFT-2M and JET, for the purpose of increasing the confinement efficiency. If the excellent characteristics of the tokamak confinement is maintained in the VLQ regime, it contributes to the decrease of the tokamak reactor cost.

ULQ and VLQ discharge experiments have been done using the REPUTE-1 RFP. It was found that in these q regime, the plasma density and beta are fairly high, and the confinement property is less sensitive to the error field compared to the RFP. However, since the temperature of the REPUTE-1 discharge is limited in low value because of the small plasma current due to the small toroidal field, its magnetic Reynolds number is too small to simulate the reactor plasma behavior. The radiation barrier has not

been overcome yet, and consequently the energy confinement time is very short. In order to improve these aspects of the REPUTE-1 experiment, the REPUTE-2 is designed to produce higher toroidal field of 2T. The toroidal field increases slowly to the final value as in the case of the ramp-up mode of the RFP operation.

The first stage of the REPUTE-2 project will be devoted to study the confinement physics of RFP, ULQ, and VLQ. In the second stage, innovation of these configurations, such as, resistive shell RFP, neutral beam current drive, and higher current density is planned.

2. RFP parameters

Parameters of the RFP discharge are calculated using modified Bessel function model (MBFM) described by equations

$$\frac{dB_\phi}{dr} = -\mu(r)\cdot B_\theta - \mu_0\cdot\frac{dp}{dr}\cdot\frac{B_\theta}{B^2} = \mu_0\cdot j_\theta$$

$$\frac{1}{r}\cdot\frac{d}{dr}(r\cdot B_\theta) - \mu(r)\cdot B_\phi - \mu_0\cdot\frac{dp}{dr}\cdot\frac{B_\theta}{B^2} = \mu_0\cdot j_\phi,$$

where notations have usual meanings. Pressure and μ profiles are assumed as follows,

$$p(r) = p(0)\cdot[1 - (\frac{r}{a})^m]^2$$

$$\mu(r) = \mu(0)\cdot[1 - (\frac{r}{a})^n].$$

Input parameters are plasma minor radius a, major radius R, indices m and n, effective charge number Z_{eff}, and central values of density n_0, temperature T_0, current density j_0, and toroidal field $B_{\phi 0}$. For given values of a, R, n, m, Z_{eff}, n_0, and T_0, j_0 and $B_{\phi 0}$ were adjusted to obtain designed values of I_p, F, Θ, and β_p. Results of calculation are summarised in Table 1.

3. Ultra-Low-q Discharge

Figure 1 shows the q profiles of RFP, ULQ and tokamak discharges. The ULQ q profile is produced by fast rise of the plasma current followed by the relaxation processes, as in the case of RFP setting-up phase. The ULQ configuration is a quasi-steady state with the flat current profile, and it transits to the tokamak state as the current profile peaks[3)-5)]. The flat current profile can be maintained utilizing the skin effect produced by the gradual increase of the plasma current. In the REPUTE-1 and the TORIUT-6, the plasma current was increased slowly while keeping q value constant, and the maintenance of quiescent ULQ state was observed during current ramp-up

phase.

The time evolutions of the toroidal field and the vertical field of the REPUTE-2 are synchronized to the ramp-up of the plasma current. The maximum plasma current attainable is limited by the strength of the coil structure and expressed by the relation $I_{p,max} \cdot B_\phi = 0.8$ MA-T. For $q_a = 1$, the maximum I_p is 0.5 MA with $B_\phi = 1.6$ T. In this case, the average current density is 1.8 MA/m^2 and is quite high compared to those of the existing tokamaks.

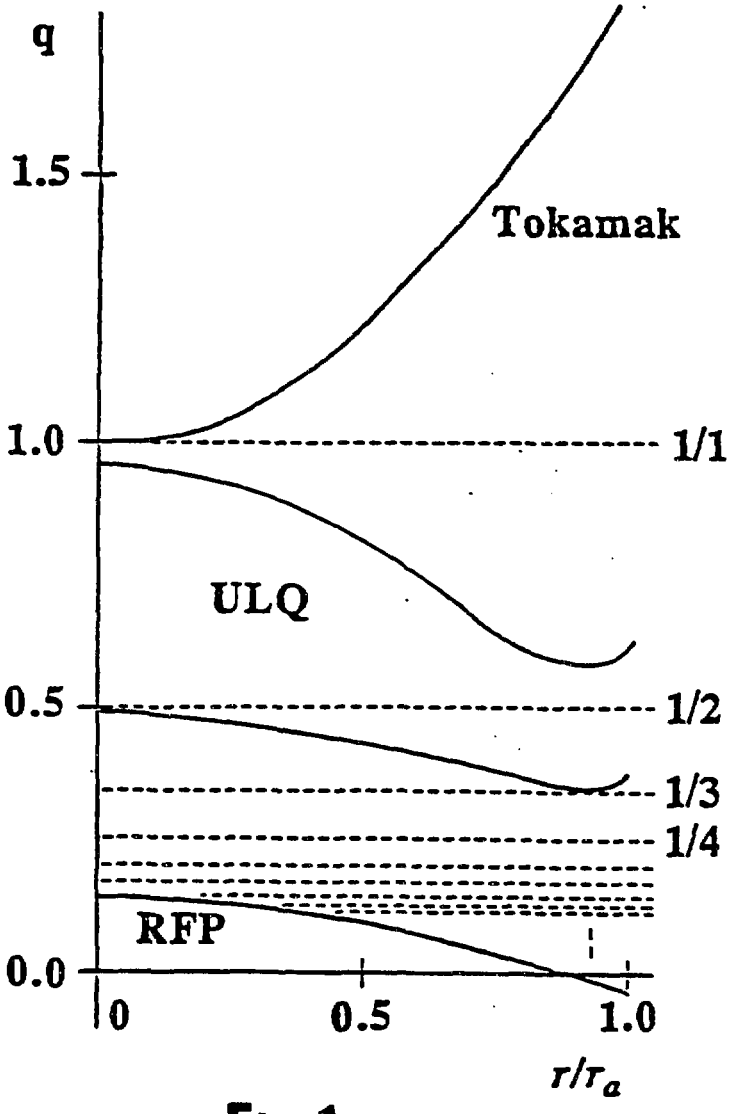

Fig.1

4. Design of ULQ-TCT Intense Neutron Source

As a candidate of the fusion material irradiation test facility the beam-plasma target system or two-component torus (TCT) based on the tokamak configuration have been considered by D.L. Jassby[6]. We have studied an ULQ intense neutron source combined with neutral beam injection[7], where the plasma current is maintained by the beam component[8] which also plays the role of fusion reaction fuel. Advantage of the ULQ-TCT system is:

1. Ionization length of the injected high-energy neutrals is short because of high plasma density of ULQ. Consequently, small-sized device can trap the high-energy beam with high efficiency.
2. High plasma current of ULQ makes it possible to confine the high-energy beam particles in the compact torus system.
3. Since the ULQ is basically the high beta device, the tolerance for beam pressure is fairly large.

Using energy balance equation and particle balance equation, possibility of the ULQ-TCT system has been examined theoretically. Example of parameter set found is described in Table 2. It should be noticed that the energy confinement time is 1/5 of the tokamak L-mode confinement time. Optimization of parameters by parametric survey has not been done yet. The system shown in Table 2, however, is sufficiently compact compared to existing big tokamaks.

References:

1) R.L. Hagenson and R.A. Krakowski, LA-9389-MS,(1982).
2) Y. Kamada, S. Ishida, Z. Yoshida, and N. Inoue, Fusion Research, **54** (1985)567.
3) S. Ishida, Z. Yoshida, K. Hattori, Y. Murakami, J. Morikawa, H. Nihei, and N. Inoue, Fusion Research, **55** (1986)291.
4) Z. Yoshida, S. Ishida, K. Hattori, Y. Murakami, J. Morikawa, H. Nihei, and N. Inoue, J. Phys. Soc. Japan, **55** (1986)450.
5) N. Asakura, *et al.*, in Plasma Physics and Controlled Nuclear Fusion Research, (Proc. 11th Int. Conf., Kyoto, 1986)D-II-4.
6) D.L. Jassby, Nuclear Fusion, **15** (1975)453.
7) M. Saito, Y. Kamada, Z. Yoshida, and N. Inoue, Fusion Research, **57** (1987)241.
8) S. Yamamoto, *et al.*, in Plasma Physics and Controlled Nuclear Fusion Research, (Proc. 11th Int. Conf., Kyoto, 1986)H-I-3.

Table 1. REPUTE-2 Parameters

		A	B	C	D
minor radius	(m)	0.3	0.3	0.3	0.3
major radius	(m)	1.5	1.5	1.5	1.5
index of $\mu(r)$		4	4	8	--
index of $p(r)$		2	2	2	2
n_0	(10^{20}m^{-3})	2.25	4.5	4.5	4.5
T_0	(keV)	0.75	1.5	1.5	1.5
$B_{\phi 0}$	(T)	1.65	3.3	3	--
j_0	(MA/m^2)	14.35	28.7	23.7	--
Z_{eff}		1.5	1.5	1.5	1.5
plasma volume	(m^3)	2.66	2.66	2.66	2.66
I_p	(MA)	1.0	2.0	1.96	2.0
$B_\phi(a)$	(T)	-0.146	-0.292	-0.352	-0.333
$B_\theta(a)$	(T)	0.673	1.345	1.316	1.33
$q(a)$		-0.0434	-0.0434	-0.0535	-0.0626
$<B_\phi>$	(T)	0.409	0.818	0.842	0.833
Φ	(T/m^2)	0.116	0.231	0.238	0.236
F		-0.357	-0.357	-0.418	-0.4
Θ		1.644	1.644	1.563	1.6
β_p		0.10	0.10	0.10	0.10
W_p	(MJ)	0.0720	0.288	0.288	--
W_m	(MJ)	1.15	4.62	4.25	--
P_{OH}	(MW)	29.1	41.2	48.0	--
τ_E	(ms)	2.47	7.0	6.0	8.3
R_{loop}	(μOhm)	29.1	10.3	12.5	6.6
$<\eta>/\eta(0)$		8.81	8.81	10.7	8.0
$V_{loop}(0)$	(V)	13.4	9.46	7.81	--
V_{loop}	(V)	46.0	29.1	24.5	13.2
L_p	(μH)	4.58	4.58	4.48	4.3
$L_p I_p^2/2$	(MJ)	2.30	9.18	8.58	8.6
$\xi = v_{e,dr}/v_{e,th}$		0.035	0.025	0.020	0.013

case A: before ramp up
case B & C: after ramp up
case D: design values

Table 2. ULQ-TCT Intense 14MeV Neutron Source

target plasma		$n_T : n_D = 6 : 4$
beam species		deuteron
aspect ratio		6.25
plasma minor radius	(m)	0.4
plasma major radius	(m)	2.5
effective charge number, Z_{eff}		2.0
q at plasma surface		0.5
toroidal beta	(%)	5.6
electron temperature	(keV)	5.0
electron density	(m^{-3})	1.9×10^{20}
toroidal field	(T)	4.6
plasma current	(MA)	3.0
energy confinement time	(ms)	24.2
beam energy	(keV)	180.0
beam current	(A)	456.4
slowing down time	(ms)	58.4
injection power density	(MW/m^3)	10.4
injection current density	(A/m^3)	57.8
tritium injection rate	(mg/sec)	31.0
fusion power density	(MW/m^3)	7.4
neutron flux at wall	(MW/m^2)	1.4
heat flux at wall	(MW/m^2)	2.4

PLASMA DATA ANALYSIS USING STATISTICAL ANALYSIS SYSTEM

Z. Yoshida, Y. Iwata, Y. Fukuda and N. Inoue
Department of Nuclear Engineering, Faculty of Engineering
The University of Tokyo

1. Introduction

The statistical analysis system (SAS) has been applied to the data analysis of REPUTE-1. The software package SAS has various functions. Here we use the factor analysis routine. The factor analysis [1], [2] is a method of multivariate analysis, which considers no external standard variables. The method explains fluctuations induced by multivariants by using a few representative and hypothetical fluctuations, and gives a scientific simplicity. The factor analysis has been originated in the field of psychology. Nowadays, it is applied not only to psychology but also to other fields of social sciences and natural sciences. We show the applicability of the factor analysis to the plasma data analysis.

2. Method of Factor Analysis

The factor analysis is a method to analyze mutual relations between multivariants. We consider variants which are standardized to standard scares whose values are zero, and variances are one. Now, we indicate n measuring values concerning n variants of N samples as follows.

$$\mathbf{X} = \begin{bmatrix} x_{11} & x_{12} & \cdots & x_{1n} \\ x_{21} & x_{22} & \cdots & x_{2n} \\ \cdot & \cdot & & \cdot \\ \cdot & \cdot & & \cdot \\ \cdot & \cdot & & \cdot \\ x_{N1} & x_{N2} & \cdots & x_{Nn} \end{bmatrix} .$$

The mean value m_j and the variace σ_j of the j-th variant are respectively given by

$$m_j = \frac{1}{N}\sum_{i=1}^{n} x_{ij} \qquad (j=1,2,\cdots,n),$$

$$\sigma_j = \sqrt{\frac{1}{N}\sum_{i=1}^{N}(x_{ij}-m_j)^2} \qquad (j=1,2,\cdots,n).$$

We use the standardized matrix defined by

$$Z_{ij} = (x_{ij}-m_j)/\sigma_j ,$$

namely;

$$\mathbf{Z} = (\mathbf{E}-\frac{1}{N}\mathbf{e}\mathbf{e}')\mathbf{X}\boldsymbol{\Sigma}^{t} ,$$

where

$$\boldsymbol{\Sigma} = \begin{bmatrix} \sigma_1 & 0 & \cdots & 0 \\ 0 & \sigma_2 & \cdots & 0 \\ \cdot & \cdot & & \cdot \\ \cdot & \cdot & & \cdot \\ \cdot & \cdot & & \cdot \\ 0 & 0 & \cdot & \sigma_n \end{bmatrix} ,$$

and E and e indicate unit matrix and unit line vector, respectively, and the superscript t denotes the transposition. In the model of factor analysis, we suppose that Z_{ij} is expressed

by a linear combination of r ($r \leq n$) variants;

$$Z_{ij} = a_{j1} f_{i1} + a_{j2} f_{i2} + \cdots + a_{jr} f_{ir} + d_j u_{ij} ,$$

where $f_{i1}, f_{i2}, \cdots$ and f_{ir} denotes factor scores of factor 1, 2, $\cdots$ r, respectively. The factor load a_{jp} indicates the relation between each measuring variant and each common factor. The independent factor is denoted by u_{ij}. The weight of an independent factor is denoted by d_j. The following conditions are imposed on f_{ip} and u_{ij}.

$$\frac{1}{N}\sum_{i=1}^{N} f_{ip} = 0 \qquad (p = 1,2,\cdots,r) ,$$

$$\frac{1}{N}\sum_{i=1}^{N} u_{ij} = 0 \qquad (j = 1,2,\cdots,n) ,$$

$$\frac{1}{N}\sum_{i=1}^{N} f_{ip}^2 = 1 \qquad (p = 1,2,\cdots,r) ,$$

$$\frac{1}{N}\sum_{i=1}^{N} u_{ij}^2 = 1 \qquad (j = 1,2,\cdots,n) ,$$

$$\sum_{i=1}^{N} f_{ip} u_{ij} = 0 \qquad \begin{cases} p = 1,2,\cdots,r \\ j = 1,2,\cdots,n \end{cases}$$

$$\sum_{i=1}^{N} u_{ij} u_{ik} = 0 \qquad j \neq k .$$

In Matrix expression, we write

$$\mathbf{Z} = \mathbf{F}\mathbf{A}' + \mathbf{U}\mathbf{D} ,$$

where **F** is the $N \times r$ factor score matrix ;

$$\mathbf{F} = \begin{bmatrix} f_{11} & f_{12} & \cdots & f_{1r} \\ f_{21} & f_{22} & \cdots & f_{2r} \\ \cdot & \cdot & & \cdot \\ \cdot & \cdot & & \cdot \\ \cdot & \cdot & & \cdot \\ f_{N1} & f_{N2} & \cdots & f_{Nr} \end{bmatrix} ,$$

A is the $n \times r$ factor load matrix and is called factor pattern;

$$\mathbf{A} = \begin{bmatrix} a_{11} & a_{12} & \cdots & a_{1r} \\ a_{21} & a_{22} & \cdots & a_{2r} \\ \cdot & \cdot & & \cdot \\ \cdot & \cdot & & \cdot \\ \cdot & \cdot & & \cdot \\ a_{n1} & a_{n2} & \cdots & a_{nr} \end{bmatrix} ,$$

and **U** is the $N \times n$ independent factor score matrix, and **D** is the diagonal matrix of independent factor load ;

$$\mathbf{D} = \begin{bmatrix} d_1 & 0 & \cdots & 0 \\ 0 & d_2 & \cdots & 0 \\ \cdot & \cdot & & \cdot \\ \cdot & \cdot & & \cdot \\ \cdot & \cdot & & \cdot \\ 0 & 0 & \cdots & d_n \end{bmatrix} .$$

Since the component of the **UD**, which is required to calculate **A** and **F**, is unknown, we should first estimate **UD**. In this study, we use the α-factor analysis method [4] to calculate **UD**. A characteristic of this method is that the confidence of factors is maximized. The

factor pattern is the correlation between a factor and a variant, which implies physical interpretations of the factor.

3. Data Base of REPUTE-1

The Data Aquisition System (DAS) of REPUTE-1 makes records of discharge control parameters and time dependent plasma and circuit data. In this study, we use discharge control parameters as external standard variables. Plasma parameters and circuit parameters measured at the quiescent period (QP) are considered as output variants, which are processed by factor analysis. The relation between the external variables (control parameters) and the output variants (plasma and discharge parameters) are analyzed by using the regression analysis scheme. Totally there are 32 variants for the controll parameters, and 19 variants for the plasma and discharge parameters. The statistical analysis described in the following section used 1890 samples (deischarges).

4. Results of Analysis

We analyzed relations between plasma data and circuit parameters by means of the factor analysis, and obtained a table of factor patterns; see Table.I. The bigger the absolute value of a correlation coefficient is, the more the corresponding factor is effective to the variable. Looking at the factor patterns, we draw an RFP plasma model of REPUTE-1; see Fig.1.

Factor 1 is related to the duration time T_{DC} of discharge. Factor 1 is also correlated to the fluctuations of the current I_{OH} in the primary windings, and the time T_{MX} which is the time when the maximum current is acieved (see Figs.2 and 3). I_{OH} is coupled with the plasma current I_p through T_{MX} (see Fig.1). The relations between I_{OH} and I_p , and between T_{MX} and I_p are shown in Fig.4 and 5, respectively. Figure 5 shows that when the value of I_p becomes bigger, the value of Volt-sec required to form I_p becomes bigger, and the current-rise time becomes longer. In the QP, the toroidal flux F_X and the electron temperature T_e correspond to the value of I_p shown in Figs.6 and 7, respectively. From Figs.6 and 7, we obtain the following scaling laws.

$$F_X \propto I_p^{0.88} , \qquad T_e \propto I_p^{1.0} .$$

Duration time T_{DC} of discharge is strongly dependent on I_p as is shown in Fig.8.

Similarly we have the following physics interpretations of other factors. Factor 2 is a factor which represents the relation between F and Θ , and factor 3 is a one which represents F. Factor 4 represents energy confinement time τ_E . Using this data base, we obtain the relation between the factor score and the plasma and electrical parameters.

5. Conclusion

The factor analysis has been applied to a plasma data base of REPUTE-1. The characteristics of the RFP plasma in REPUTE-1 is shown to be explained by 4 independent factors. The well known scaling laws, $F_X \propto I_p$, $T_e \propto I_p$ and $\tau_E \propto N_e$, are also confirmed.

REFERENCE

[1] Merdia. k. v., *Multivariate Analysis* (Academic Press., London, 1979).

[2] S. Shiba, *Factor Analysis* , Univ. of Tokyo Press, 1979.

[3] REPUTE-1 Annual Report 1984.

[4] Y. Iwata, Master Thesis, Univ. of Tokyo, 1986.

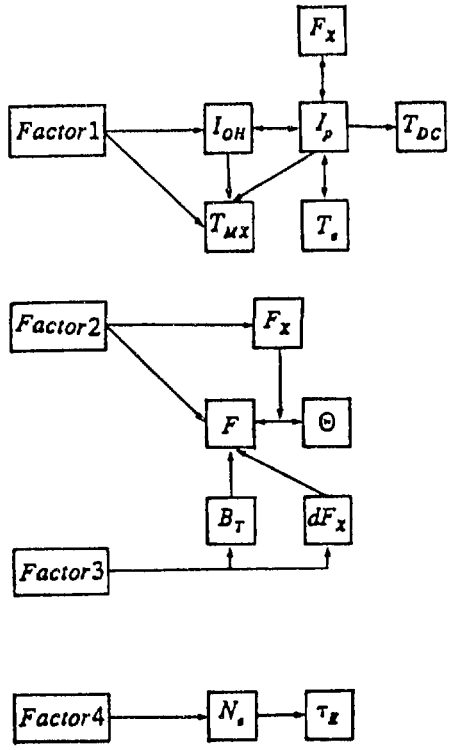

Fig.1: The RFP plasma discharge model of REPUTE-1

	Factor 1	Factor 2	Factor 3	Factor 4	Factor 5	Factor 6
I_p	97 *	-1	2	-17	-11	-2
I_{OH}	95 *	-1	3	-20	1	-3
T_{DC}	91 *	2	1	1	-21	1
T_e	86 *	-1	3	-6	-51 *	1
F_X	85 *	-37 *	17	-20	-2	-2
T_{MX}	79 *	-14	6	13	-28	0
I_V	63 *	-15	8	12	31	-1
dN_e	42 *	-15	7	-22	-35 *	11
V_{OH}	31	6	-4	-22	10	7
τ_E	-15	2	-7	92 *	-22	-1
N_e	-4	5	-8	87 *	21	-7
Θ	-19	80 *	-28	10	-12	-1
F	-16	80 *	45 *	0	-12	1
dF_X	4	-7	85 *	-7	-4	-5
B_T	59 *	41 *	62 *	-12	-14	2
V_t	-23	3	-5	-17	60 *	-4
V_V	0	-11	-1	4	27	3
dI_p	6	13	0	-14	11	66 *
dB_T	-3	-9	-2	3	-5	15

Table 1: Table of factor patterns. Printed value are multiplied by 100 and rounded to the nearest integer values greater than 0.333436 have been flagged by *.

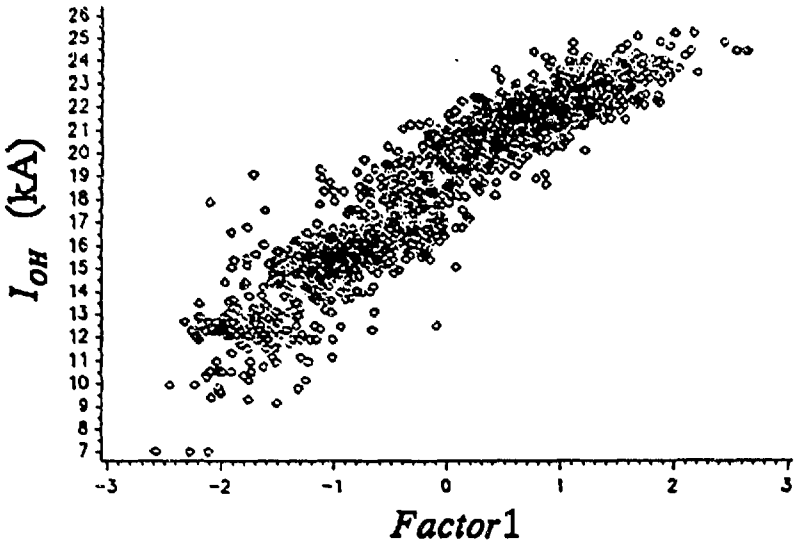

Fig.2: The correlative relation between I_{OH} and *Factor*1

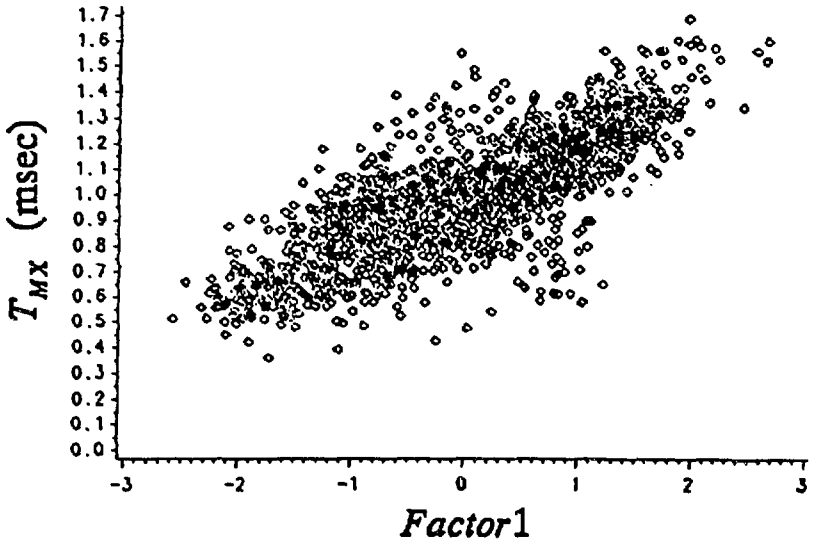

Fig.3: The Correlative relation between T_{MX} and *Factor*1

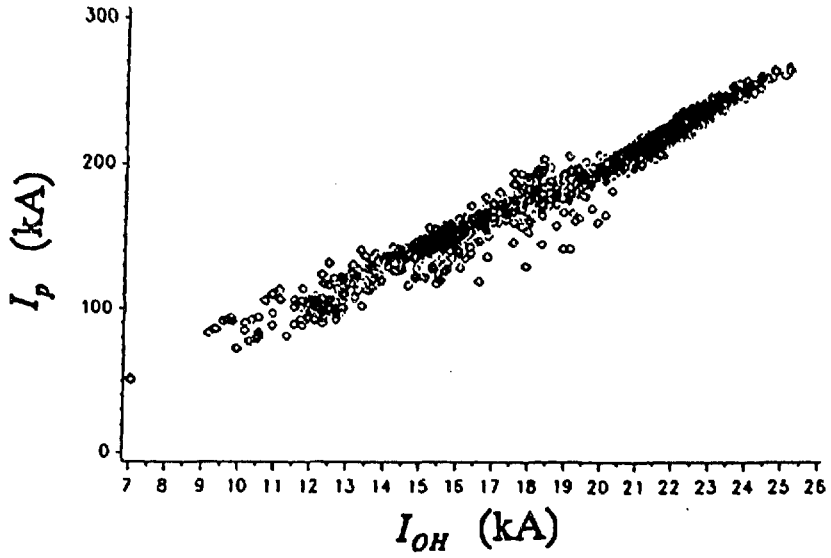

Fig.4: The correlative relation between I_p and I_{OH}

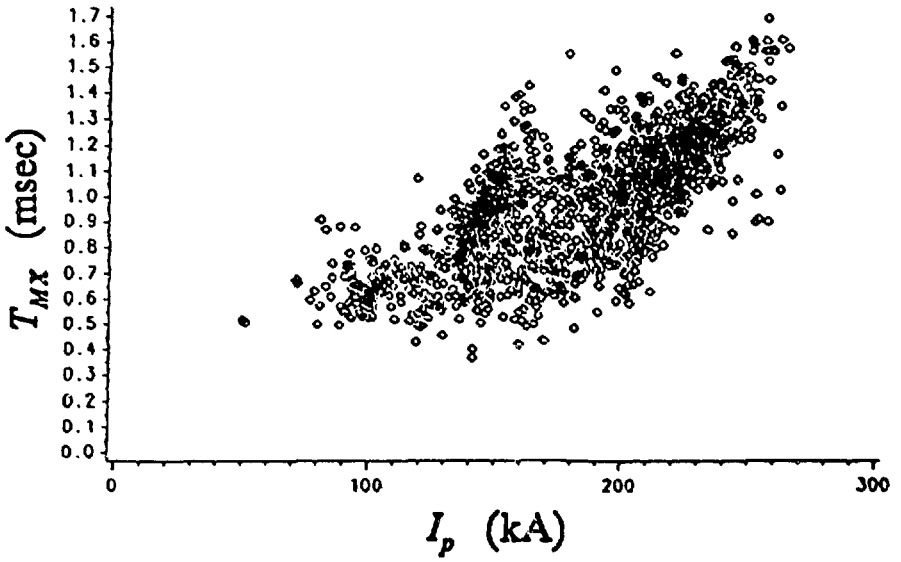

Fig.5: The correlative relation between T_{MX} and I_p

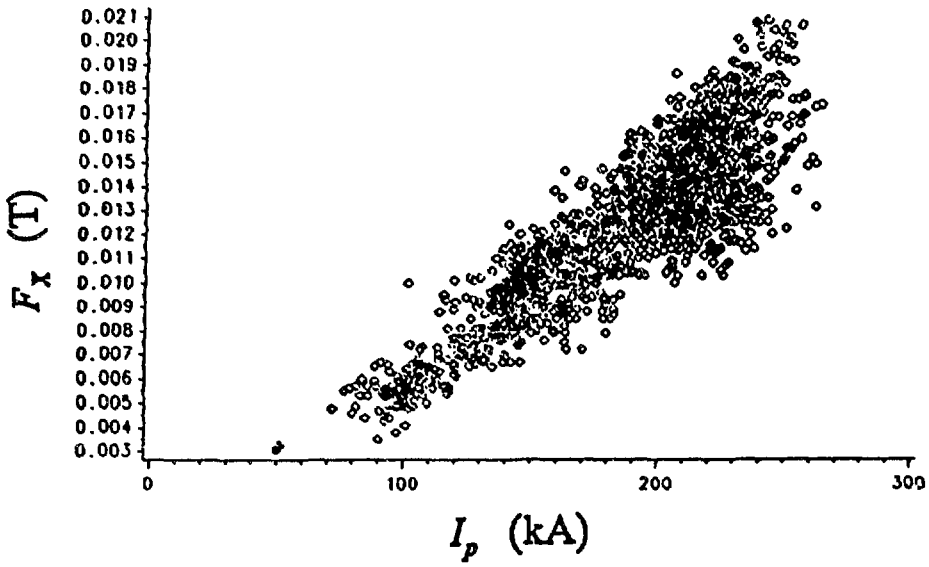

Fig.6: The correlative relation between F_x and I_p

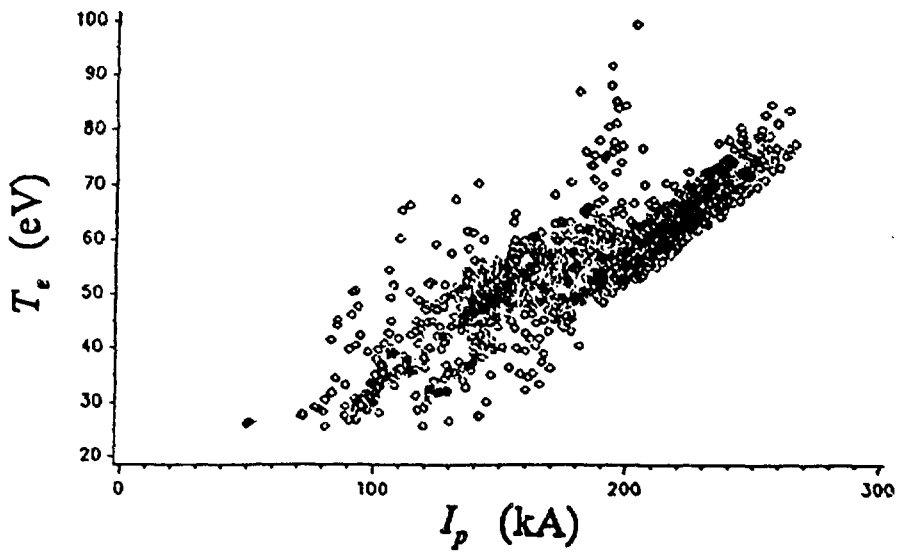

Fig.7: The correlative relation between T_e and I_p

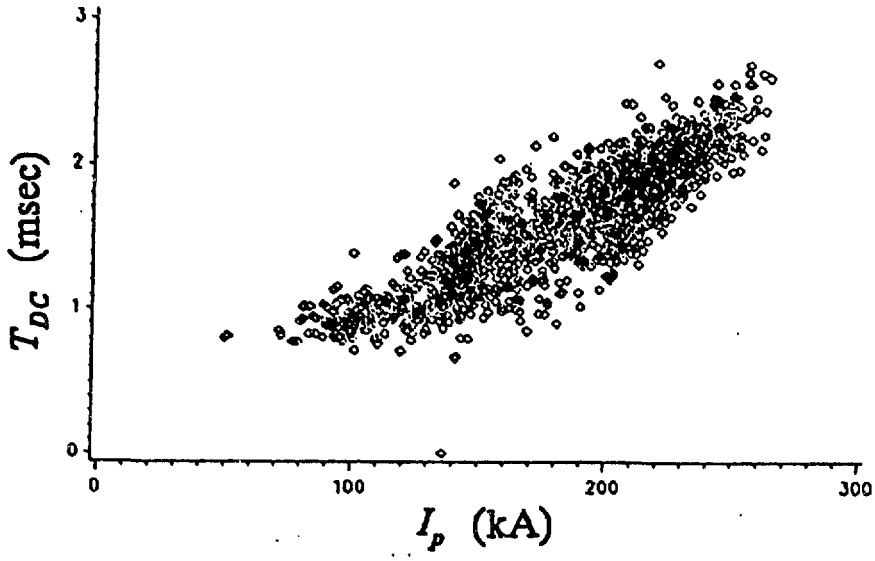

Fig.8: The correlative relation between T_{DC} and I_p

A TAPERED POLOIDAL GAP FOR THE REDUCTION OF FIELD ERRORS†

by

R. W. MOSES

Los Alamos National Laboratory

Los Alamos, NM 87545

The conventional Reversed Field Pinch is surrounded by a toroidal conducting shell that provides wall stabilization for the plasma. Usually, this shell is made of aluminum or copper, and it must have an insulated poloidal gap to permit penetrations of toroidal loop voltage to the plasma. Many magnetic field perturbations will induce toroidal shell currents with poloidal Fourier components having mode numbers $m \geq 1$. A butt-joint poloidal gap will mode convert all of these image currents into potentially damaging magnetic-field errors with large spectra of toroidal-mode numbers. Overlapping tapered gaps have been proposed and partially tested for reducing these field errors.[1,2] The mathematical basis for minimizing the $m = 1$, $n = 0$ field errors for all frequencies using tapered gaps, is presented in this paper.

The details of field errors at a poloidal gap and corresponding plasma effects will be discussed in a future paper.[3] This note describes the theoretical basis for the overlapping tapered poloidal gap that has been proposed for ZTH.

A cylindrical model is used to represent the shell. The z-axis is the minor axis of machine, θ is the poloidal angle, and r is the radial coordinate. The thin shell is of radius a and thickness T_o (away from the gap). All of the shell has resistivity η.

An external vertical field is applied to the shell at a frequency ω,

$$\underset{\sim}{B}_o = B_o(\hat{r}\sin\theta + \hat{\theta}\cos\theta)e^{-i\omega t} \quad . \tag{1}$$

† Work performed under the auspices of the USDOE.

From hereon the frequency term $e^{-i\omega t}$ is assumed to be present but not specified.

The thin shell approximation is used where the skin depth of the shell material is much greater than the shell thickness,

$$\left(\frac{\eta}{\mu_o \omega}\right)^{\frac{1}{2}} \gg T_o \, . \tag{2}$$

Note that this paper is written using SI units.

It is a textbook exercise to show that the total internal and external fields for a straight thin cylinder are

$$\underset{\sim}{B}_i = B_i(\hat{r}\sin\theta + \hat{\theta}\cos\theta), \qquad r \leq a - T_o/2 \tag{3}$$

and

$$\underset{\sim}{B}_e = \underset{\sim}{B}_0 + B_s(\hat{r}\sin\theta - \hat{\theta}\cos\theta)a^2/r^2, \qquad r \geq a + T_o/2 \tag{4}$$

where

$$B_i = B_o/(1 - i\omega\tau_o) \, , \tag{5}$$

$$B_s = i\omega\tau_o B_i \, , \tag{6}$$

and

$$\tau_o = \mu_o a T_o/2\eta \, . \tag{7}$$

The objective of this work is to design an insulated poloidal gap as illustrated in Fig. 1 so that it transmits magnetic fields through the shell according to Eqs (3) and (4). For the purpose of our discussion, an overlapping gap made of two pieces, as in Fig. 1a, will be considered. The metal thickness of the taper attached to the left hand shell is given by $T_1(z) = T(z)$, while the right hand taper is defined to be symmetric, $T_2(z) = T(\ell - z)$.

Subscripts 1 and 2 denote the left and right hand tapers respectively. ZTH has been designed to have a three piece gap as in Fig. 1b, because this design is less likely to interface with the toroidal field of an RFP. In this instance, the top and bottom pieces of taper are each half of the thickness $T_1(z)$.

It is convenient to define the current in the shell in terms of

$$\begin{aligned} T_1(z)\underset{\sim}{J}_1(\theta,z) &= -\nabla\psi_1(\theta,z)\times\hat{r} \\ T_2(z)\underset{\sim}{J}_2(\theta,z) &= -\nabla\psi_2(\theta,z)\times\hat{r}\ . \end{aligned} \tag{8}$$

Away from the gap one has

$$\begin{aligned} T_o J_z(\theta) &= \frac{2B_s}{\mu_o}\cos\theta \\ &\equiv \frac{1}{a}\frac{\partial\psi}{\partial\theta} \\ &\equiv \frac{1}{a}\psi_o\cos\theta\ . \end{aligned} \tag{9}$$

It is assumed that the two (or three) tapers are thin compared to the shell radius and that they are very close together but electrically insulated from one another. Therefore, it is assumed that the shell currents may be superimposed and taken as one. This assumption implies

$$\psi_1(\theta,z)+\psi_2(\theta,z)=\psi_o\sin\theta\ . \tag{10}$$

It is also assumed that radial magnetic field that passes through one taper will also go through the other

$$B_{1r}=B_{2r}=B_{ir} \tag{11}$$

At the surface of each taper the tangential electric field is

$$\underset{\sim}{E}_{1,2t}=\eta\underset{\sim}{J}_{1,2}\ , \tag{12}$$

and Faraday's law relates these to the radial magnetic field

$$\nabla\times\underset{\sim}{E}_{1,2t}=-\frac{\partial\underset{\sim}{B}_r}{\partial t}\ . \tag{13}$$

It is possible to choose a variety of ψ_1 and ψ_2 functions that satisfy Eqs. (9) and (10) and solve for $T(z)$. An obvious but not necessary choice of current distributions is

$$\begin{aligned} \psi_1 &= \psi_o \cos^2 kz \sin\theta \\ \psi_2 &= \psi_o \sin^2 kz \sin\theta \end{aligned} \tag{14}$$

where $k \equiv \pi/2\ell$.

Upon solving Eq. (13) with $T(z)$ as the dependent variable one gets

$$(ka)^2 \frac{\partial}{\partial(kz)} \left[\left(\frac{T_o}{T} \right) \sin(2kz) \right] + \left(\frac{T_o}{T} \right) \cos^2 kz - 1 = 0 \, . \tag{15}$$

Careful analysis of the boundary conditions on Eq. (15) gives

$$\frac{T(o)}{T_o} = 1 + \frac{\pi^2 a^2}{2\ell^2} \tag{16}$$

and

$$T(\ell) = 0 \, . \tag{17}$$

Eq. (15) has been solved numerically, and the results are presented in Fig. 2. Clearly, the length of the tapered pieces is vital to determination of the shape and thickness of the tapers. When the tapers are as long as a shell diameter, their maximum thickness is $\sim$2.25 T_o, but if the taper length is a radius, the maximum thickness is $\sim$6 T_o. If the tapers are made too short and thick, the thin shell approximations could be violated, and the engineering design of the gap would become very complex.

In conclusion, if the tapered gap length is about one shell diameter, this shielded gap should provide a very uniform transmission of $m = 1$, $n = 0$ magnetic fields to the plasma. It is particularly important to note that, with the thin shell assumptions used here, this gap transmits $m = 1$, $n = 0$ fields at **all frequencies** as if the shell were a uniform unbroken cylinder. Although transmission of other m and n components is imperfect, it will surely be superior to a butt joint gap.

REFERENCES

1. M. Bevir, Culham Laboratory, private communication (1983).

2. C. J. Buchenauer, R. G. Watt, J. M. Downing, G. Miller, R. Moses, C. Munson, and P. G. Weber, Paper 2R-31, Bull. Am. Phys. Soc. 30, p. 1404 (October 1985).

3. K. L. Sidikman, R. A. Nebel, J. D. Callen, J. G. Melton, and R. W. Moses, "3-D MHD Simulations of Field Errors in ZTH and ZT-40," to be presented at Varenna International School of Plasma Physics, Varenna, Italy (September 1987).

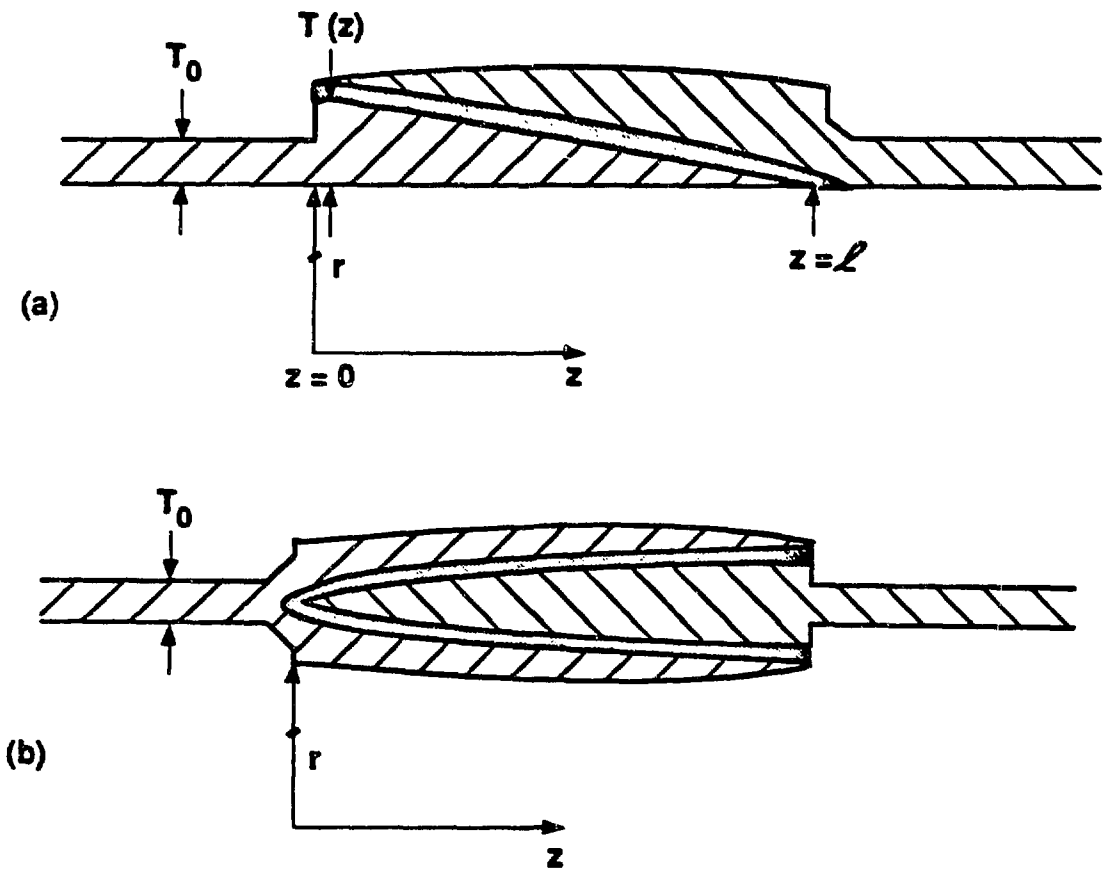

Figure 1. Longitudinal cross section of: (a) a double tapered gap and (b) a triple tapered gap.

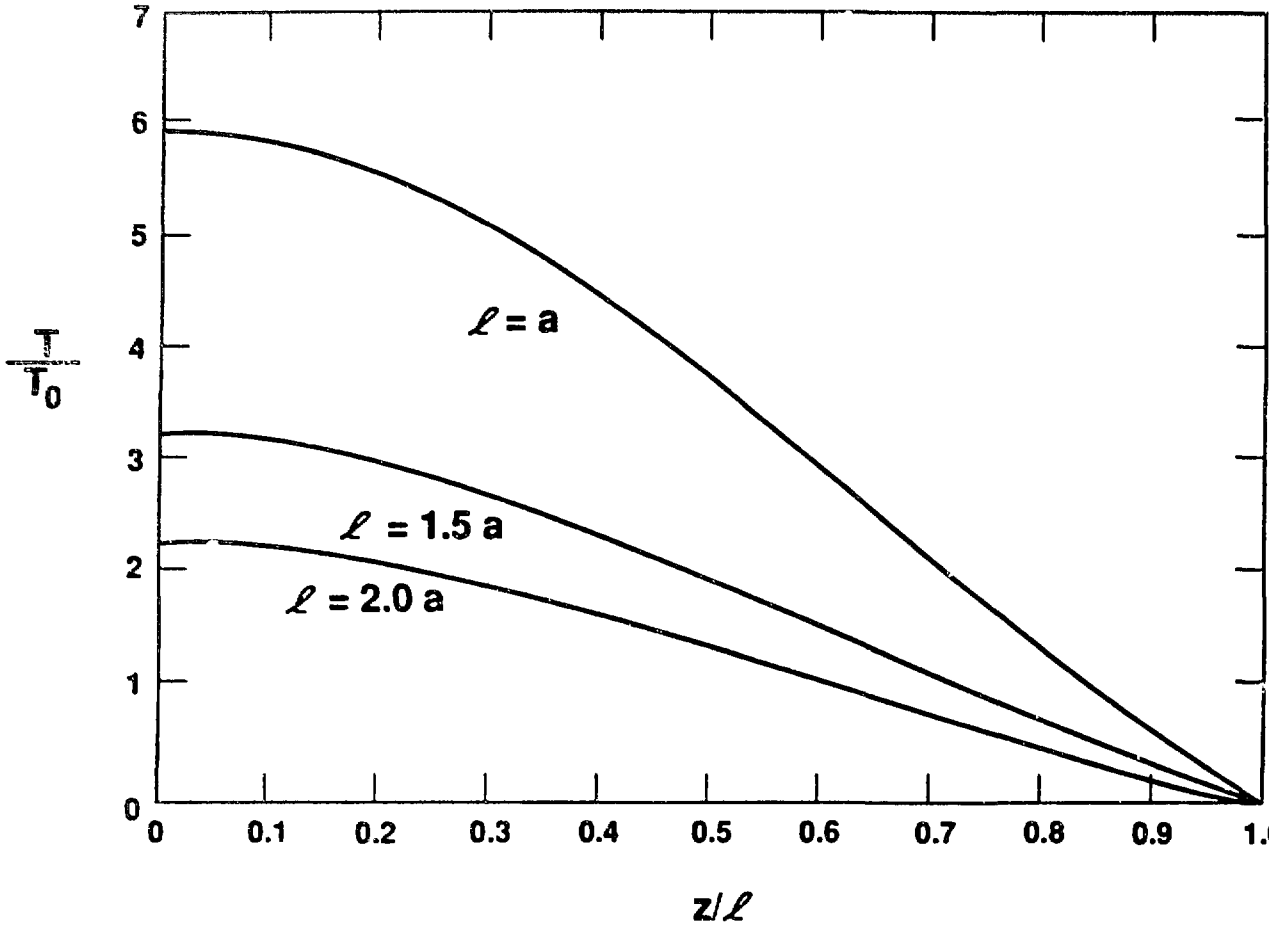

Figure 2. Computed taper thickness as a function of toroidal coordinate, z, and overall gap length ℓ/a.

INSTABILITIES OF AN RFP WITH A RESISTIVE SHELL*

G. Marklin
Los Alamos National Laboratory, Los Alamos, NM 87545

Ideal MHD growth rates have been computed for instabilities of an RFP with a thin resistive shell and a modified-Bessel-function equilibrium in a straight cylinder. In the thin shell model, the growth rate is proportional to the jump in the logarithmic derivative of the helical flux $\psi = irb_r$ across the shell[1]:

$$\gamma\tau_{shell} = \frac{a}{2}\frac{(\psi'_{vacuum} - \psi'_{plasma})}{\psi(a)}$$

where $\tau_{shell} = \mu_0 \delta a/2\eta$ (δ = thickness, a = minor radius, η = resistivity of shell).

The helical flux in the vacuum can be calculated analytically: $\psi_{vacuum} = K'_m(kr)$ where K_m is the modified Bessel function of the second kind. In the plasma, the helical flux is computed by solving the ordinary differential equation:

$$(U\psi'_{plasma})' = UV\psi_{plasma}$$

where

$$U = r/(m^2 + k^2r^2)$$

and

$$V = \frac{m^2 + k^2r^2}{r^2} - \lambda\left(\lambda + \frac{2mk}{m^2 + k^2r^2}\right) - \lambda'\frac{(krB_\theta - mB_z)}{(mB_\theta + krB_z)}$$

which is derived from the linearized momentum equation neglecting inertia [2].

The equilibrium field satisfies

$$\frac{1}{r}\frac{\partial}{\partial r}(rB_\theta) = \lambda B_z \quad \text{and} \quad \frac{\partial B_z}{\partial r} = -\lambda B_\theta$$

with $\lambda(r) = \lambda_0$ for $r < r_c$ and $\lambda(r) = \lambda_0(r-a)/(r_c - a)$ for $r_c \le r \le a$. The parameter r_c is the cutoff radius and λ_0 is determined by specifying the pinch parameter θ.

Figure 1 shows the growth rate of the fastest growing $m = 1$ mode (maximized over k) plotted vs. θ for different r_c. Notice that there exist optimum values of θ for which the growth rate is minimized, resulting in growth times as long as $5 - 10\tau_{shell}$, depending on r_c.

Figure 2 shows a contour plot of $\gamma\tau_{shell}$ vs. θ and ka for $r_c = .7$. The contour spacing is .1 with solid and dotted lines for positive and negative values respectively. The dashed lines are the boundaries between resonant and non-resonant modes. Since most of the unstable modes are non-resonant, the fact that the plasma was described with ideal rather than resistive MHD should not cause serious concern. A more appropriate resistive analysis will only change the results for the resonant modes. This figure shows which k values are unstable at different θ. At the optimum θ of about 1.5, modes with $-1.5 < ka < .9$ are unstable.

REFERENCES

1. C. G. Gimblett, *Nucl. Fus.* **26**, 617 (1986).
2. G. Miller, *Phys. Fluids* **28**, 560 (1985).

* **Work performed by the auspices of the US DOE.**

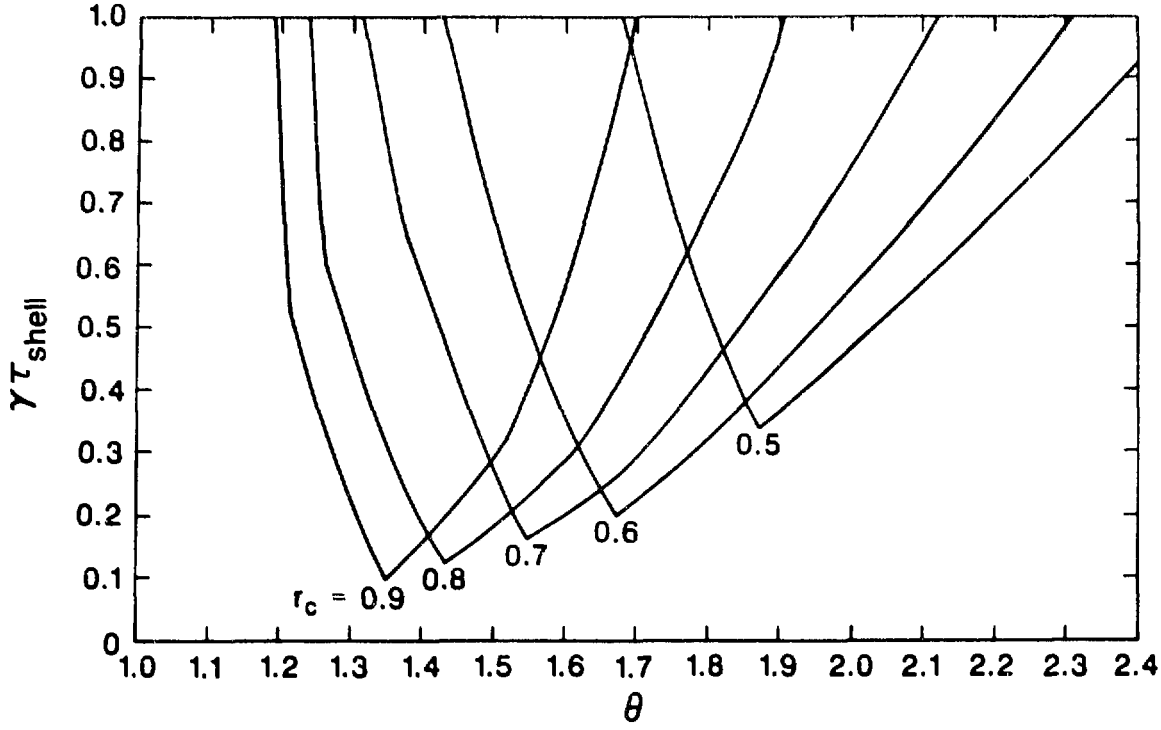

Fig. 1. Growth rate of fastest growing mode vs. θ for different r_c.

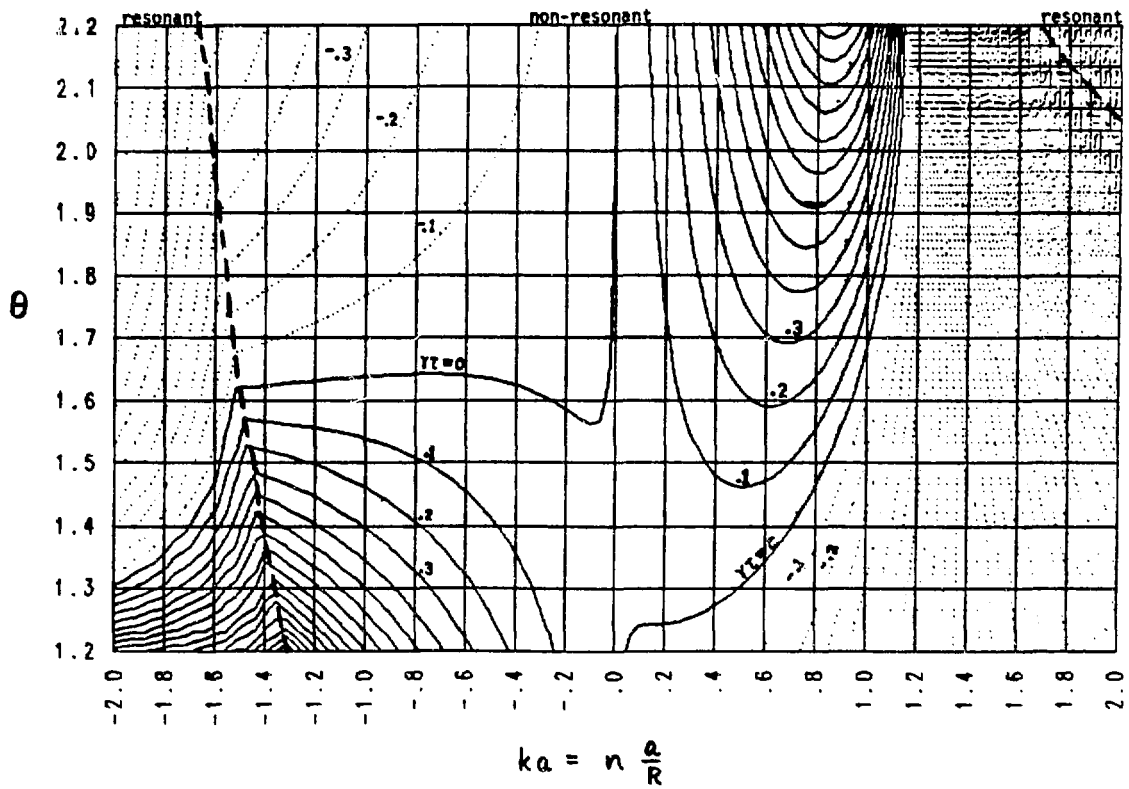

Fig. 2. Contour plot of $\gamma\tau_{shell}$ vs. θ and ka for $r_c = .7$.

3-D MHD SIMULATIONS OF FIELD ERRORS IN ZTH AND ZT-40

by

K. L. Sidikman,* R. A. Nebel, and J. D. Callen*

Los Alamos National Laboratory
Los Alamos, NM 87545

I. INTRODUCTION

Field errors are an important design consideration for any magnetic confinement device. This is particularly true for ZTH (the proposed next-generation Reversed Field Pinch (RFP) at Los Alamos) since part of its mission is to test the confinement properties of an RFP plasma in new, high-temperature regimes. The machine should be designed so that transport is governed by the dynamics of the plasma rather than by losses due to field lines intersecting the vessel wall or field error induced stochasticity.

In order to determine the effects of field errors on a plasma, we have performed numerical simulations which include the 3D dynamical plasma response. Earlier analytic work[1] considered only the effects of $m = 0$, $n \neq 0$ perturbations. (Here m, n are the poloidal and toroidal mode numbers, respectively.) These perturbations are important because they are driven, in part, by an unavoidable field error–the ripple in the toroidal field due to the discreteness of the toroidal field coil set. Moreover, the $m = 0$ perturbations are resonant on the reversal surface ($q = 0$) and result in the growth of islands that may increase transport in the reversed-field region. The plasma response was included by assuming that the plasma had relaxed to a force-free minimum-energy state in the presence of these external perturbations. In the plasma: $\vec{\nabla} \times \mathbf{B} = \lambda \mathbf{B}, \lambda =$ constant, was assumed. This model predicted that the width of $m = 0$ islands would be amplified in the presence of the plasma, as compared to their width if vacuum field perturbations were assumed. (In ZTH, this amounts to a 30% increase of the $m = 0, n = 48$ island resulting from the toroidal field ripple, for example[2].) This rather pessimistic result, along with the limitations of the assumed physical model suggested the need to compute the plasma response directly. In order to model the plasma response, we simulated it with a 3-D MHD code[3] in which the vacuum field errors were imposed at the wall. This included the effects of finite inertia and dissipation as well as a radially dependent λ in the (0,0) components. Thus, the use of a numerical simulation allowed the dynamics to play a role in the plasma response to field errors.

Two types of field errors in ZTH were studied. The first type arises from the currents flowing in the field coil set. The $m = 0$ toroidal field ripple falls into this class. The second type arises from the current induced in the conducting shell by a mismatch of the vertical

* University of Wisconsin - Madison, Department of Physics

field (Bv) needed to maintain the plasma equilibrium. The $m = 1, n = 0$ character of this current is altered as it flows around holes in the shell, such as pump ports and diagnostic ports. This produces localized radial field errors with higher m and n numbers. (This process is often referred to as mode conversion). The remainder of this paper deals with our study of these errors. Section II presents a description of our calculation, including the 3-D code. Sections III and IV will present the model used to represent the field errors and the numerical results for the coil errors and shell errors, respectively. Our conclusions will be given in Section V.

II. COMPUTATIONAL OVERVIEW

A schematic view of our calculation is shown in Fig. 1. Until recently, a simulation of this type would not have been possible. We have taken advantage of two advances in computing: the large memory available in the CRAY II computer and the advent of semi-implicit algorithms.[4,5] These algorithms enabled us to eliminate Alfvén waves and follow the evolution of the field error perturbations using large time steps. Even with these improvements, these simulations taxed the limits of storage and execution time on the CRAY II. Typical jobs were 12,000,000 words in length and required 1000 cpu.

The 3-D code used solves the MHD equations in Fourier space for a periodic cylinder. The version used assumes $\beta = 0$. The dependent variables are the vector potential ($\mathbf{A}$) and the velocity ($\mathbf{U}$). In a normalized form (t scaled to τ_R), the equations are:

$$\frac{\partial}{\partial t}\mathbf{A} = S\mathbf{U} \times \mathbf{B} - \eta\mathbf{J} \tag{1}$$

$$\rho\frac{\partial}{\partial t}\mathbf{U} = -\rho S\mathbf{U} \cdot \vec{\nabla}\mathbf{U} + S\mathbf{J} \times \mathbf{B} + \nu\nabla^2\mathbf{U} \tag{2}$$

$$\mathbf{B} = \vec{\nabla} \times \mathbf{A} \tag{3}$$

$$\mathbf{J} = \vec{\nabla} \times \mathbf{B} \tag{4}$$

$$S = \frac{\tau_R}{\tau_A} \quad \nu = \nu_0(\frac{\tau_R}{a^2}) \tag{5}$$

The times τ_R and τ_A are the resistive and Alfvén times, respectively. The density is taken to be constant: $\rho = 1$. The resistivity profile, η, is taken to be constant: $\eta = 1$. For the results quoted later (exclusive of scaling), $S = 1000$ was used.

Two important approximates were also made. The field errors were assumed to have diffused through the conducting shell. They were not allowed to change in time at the wall. Also, the imposed RFP equilibrium ($m = n = 0$ components) was not allowed to evolve resistively. This was done for several reasons. The equilibrium used (the modified

Bessel function model—see Fig. 2) resembles the observed experimental state. The values of the RFP parameters $F = \frac{B_z(wall)}{\Phi_z}$ and $\Theta = \frac{B_\theta(wall)}{\Phi_z}$ for this model closely match those of the experiment. Finally, the linear growth and nonlinear interaction of unstable plasma perturbations in a resistively-evolving environment may mask the effects of the external field-error perturbations which we wanted to study in isolation. Thus, a stable equilibrium was chosen and maintained, with the RFP dynamo excluded. With these approximations, the plasma response was calculated.

III. COIL RESULTS

The first field errors studied were those from the coil set. The coil design was represented by a set of current elements. The fields at the plasma edge were obtained from the code EFFI,[6] which integrates the Biot-Savart Law. The Fourier transform of these fields was then taken and the symmetric ($m = n = 0$) components were replaced by a plasma equilibrium. The remaining components were used as the field errors. This was done for the coils from both ZTH and ZT-40, the present Los Alamos RFP. The calculation used 65 radial points, $0 \leq m \leq 10$ and $-42 \leq N \leq 42$ for ZT-40 and $0 \leq m \leq 5$ and $-85 \leq n \leq 85$ for ZTH.

In both cases, the combination of field error perturbations and RFP equilibrium advanced by the code reached an approximate steady state. This was observed in the perturbed field and velocity profiles after about $30\tau_A$. In this state, the field and velocity perturbation amplitudes scale linearly with the field errors at the wall. The steady-state perturbation profiles are independent of the type of initial perturbation profiles chosen, for the same field errors at the wall. Most importantly, in the steady state, the amplitude of the radial field for an $m = 0, n \neq 0$ perturbation at its resonant surface ($q = 0$) is reduced compared to the initial vacuum value (see Fig. 3). The reduction is approximately 20% in ZT-40 and approximately 10% in ZTH, for $S = 1000$. In the ZT-40 case, a scaling with S was performed. For the range $500 \leq S \leq 4000$, the percentage of br reduction increased with S. A rough scaling indicates that this percentage

$\%\ (0,n) = (br_{0,n}(q = 0)\ \text{vacuum} - br_{0,n}(q = 0)\ \text{steady state})/br_{0,n}(q = 0)\ \text{vacuum}$

scales like:

$$\%(0,12) \sim S^{.331}$$

$$\%(0,24) \sim S^{.158}$$

(See Fig. 4.)

Island size for $m = 0$ islands is related to $br(q = 0)$. The above results indicate modest $m = 0$ island reduction. However, the overall picture is more optimistic. A flux plot of all the $m = 0, n \neq 0$ perturbations shows only modest islands for ZT-40. For ZTH, the islands are so small as to be unresolvable; some perturbed flux surfaces can be seen (see Fig. 5). A factor of 5 to 8 increase in field error amplitude at the wall in ZTH can be

tolerated before $m = 0$ islands extend halfway between the reversal surface and the wall. (This was taken as the "trouble point" for islands in the ZTH design.) Thus, in the case of $m = 0$ field errors from the coil set (the major threat to ZTH from this source), the plasma responded to the perturbations at the wall by reaching a steady state with reduced islands.

Our results conflict with the analytic results quoted earlier. We believe that this is due to the presence of additional dynamics — flow, dissipation (viscosity and resistivity), non-constant λ in the equilibrium — in our model. There are indications that this is so; the exact mechanisms are still being studied.

As an example, consider the role of flow and viscosity. Perturbed flow is important in our calculation. To see this, consider the momentum equation for our linear perturbations in the steady state:

$$\mathbf{J}_1 \times \mathbf{B}_0 + \mathbf{J}_0 \times \mathbf{B}_1 = -(\frac{\nu}{S})\nabla^2 \mathbf{U}_1 \tag{6}$$

(The 1 subscript indicates the perturbation and the 0 subscript the equilibrium.)

With an equilibrium of the form $\mathbf{J}_0 = \lambda \mathbf{B}_0$, the left-hand side of (6) becomes:

$$(\mathbf{J} \times \mathbf{B})_1 = (\mathbf{J}_1 - \lambda \mathbf{B}_1) \times \mathbf{B}_0 \tag{7}$$

The analytic model has $\mathbf{J}_1 = \lambda \mathbf{B}_1$ and $(\mathbf{J} \times \mathbf{B})_1 \equiv 0$. This is not true in our calculation. Figure 6 shows $| \mathbf{J} \times \mathbf{B} |_1$ and $(\mathbf{J} \cdot \mathbf{B})_1$ for the $m = 0$, $n = 24$ mode. Although $| \mathbf{J} \times \mathbf{B} |_1$ is small compared to $(\mathbf{J} \cdot \mathbf{B})_1$, it is not zero in the plasma edge. At two radial locations, including the vicinity of the reversal surface, $(\mathbf{J} \cdot \mathbf{B})_1$ vanishes and $| \mathbf{J} \times \mathbf{B} |_1$ dominates. A look at Eq. (6) shows that viscosity and flow must be important. Their influence on our results can be seen in the fact that the percentage of $m = 0$ br exclusion defined earlier (% (0,n)) scales with viscosity. Moreover, viscosity does not scale out of the problem. % (0,n) increases and levels off as viscosity decreases (see Fig. 7).

A similar argument can be made regarding the importance of a non-constant λ in the equilibrium in our model. Here, the contrast with the constant $-\lambda$ analytic model is obvious. The effect on the results is striking. When λ is not a constant, $br(q = 0)$ is reduced for $m = 0$ perturbations (see Fig. 3). When we simulate with a constant λ, $br(q = 0)$ is amplified. (See Fig. 8.) This is what the analytic model predicts, although the amplification that we see is smaller than what is predicted. Thus, the plasma dynamics included in our model are important in understanding why our results differ from the previous analytic ones.

IV. SHELL RESULTS

The model for shell errors was based on opposing tangential fields on either side of a hole in a perfect conductor.[7] Field lines bulge into the hole, creating a local radial component. Calculation of the response for a single role required the simplifying

assumption that all the holes are small (hole radius/shell minor radius $\ll 1$) and well-separated. This assumption allowed us to treat the radial fields in one hole while ignoring those in all the others and permitted us to neglect the curvature of the coordinate system.

We considered a single hole in a periodic, perfectly conducting plane. (See Fig. 9.) Given an asymptotically uniform tangential field ΔB above the plane, and no asymptotic tangential field below, the radial field in the plane ($r = 0$) is [7]:

$$b_r = \begin{cases} \frac{2\Delta B}{\pi} \frac{y}{(a^2-\rho^2)^{1/2}} & \rho < a \\ 0 & \rho > a \end{cases}$$

The Fourier spectrum of br was used to calculate the vacuum field errors.

The br spectrum obtained for a single hole was broad in both m and n. Despite the use of the largest grid permitted by machine storage (65 radial points; $-42 \leq n \leq 42$ and $0 \leq m \leq 21$), we were able to cover only one-half of the largest peak. (See Fig 10.) However, although there were many modes, they were all small in size: $br/Bv \sim .1$ and $br(m,n)/Bv \sim .0001$. In addition, most of the spectrum was either non-resonant ($m_{peak} \sim 16$, lower n's) or non-penetrating (large n). Thus, although the single-hole spectrum was broad, it was not likely that large individual islands would grow.

Our simulation used all of the holes included in the ZTH design. (See Fig. 11.) The spectrum shape for each hole was the same, the magnitude for each m and n depending only on hole size. Each Fourier component for each hole was multiplied by a phase factor which accounted for the hole's position in the shell. Thus, the holes were able to interact through interference of these phases.

Δ B was chosen to be the field discontinuity due to the $m = 1$ current induced in the shell by the Bv mismatch. A worst case scenario was assumed: 100% Bv mismatch. The induced currents provide 100% Bv inside the plasma and cancel 100% of the applied Bv outside. Thus, the current produces a field discontinuity of 2 Bv and $\Delta B = 2Bv cos\theta$.

The results from this case showed no visible island structure. As might be expected from the previous arguments, resonant islands were only expected at the lower mode numbers characteristic of constructive interference of the hole phasing. Small islands were observed ($m = 1, n = -16$—corresponding to the $\sim$ 16 toroidal groups of holes) but only when ΔB was increased by a factor of 100. (See Fig. 12.) A field line tracer showed that field lines near a hole received a small radial kick but remained well-confined. (See Fig. 13.) Thus, island growth in ZTH due to shell errors may be expected to be very small. There is a safety factor of about 1000 (100×10—from a reduction of the Bv mismatch to a more likely 10%.)

V. SUMMARY AND CONCLUSIONS

We have performed numerical simulations of the 3-D MHD response of an RFP plasma to external field errors. We have found that neither $m = 0$ perturbations from the toroidal field coils, nor perturbations from shell currents flowing around port holes pose a serious

threat to grow large islands in ZT-H or ZT-40. In fact, the plasma acts to reduce the size of $m = 0$ islands. In particular, this means that ZTH, as designed, is not endangered by large field errors. It should adequately test RFP confinement properties. In general, our results show that MHD dynamics, including flow and dissipation, are important in understanding the plasma response to an external perturbation.

ACKNOWLEDGMENTS

The authors gratefully acknowledge Jim Melton for his efforts in running the EFFI code. We wish to thank Drs. Joe DiMarco and Al Haberstich for providing information about the ZTH design and Dr. Leaf Turner for useful discussions. One of us (KLS) wishes to thank the CTR division of the Los Alamos National Laboratory. The hospitality it has shown over the past two summers has made this work possible. This work was supported by the U.S. Department of Energy.

REFERENCES

1. R. I. Pinsker and A. H. Reiman, *Phys. Fluids* **29**, 782 (1986).

2. Values used in the ZTH calculation:

$$n = 48$$

$$\rho_e = a = 40\ cm \qquad \Theta = 1.4$$

$$R = 215\ cm \qquad \lambda a = 2.8$$

$$\rho_c = 60\ cm \qquad \text{no conducting wall} \quad (\tau_{shell} \ll t_{discharge})$$

3. D. D. Schnack, D. C. Barnes, Z. Mikic, D. S. Harned, and E. J. Caramana, SAIC report SAIC-86/3022-APPAT-83; *J. Comput. Phys.* (1986) submitted.

4. D. S. Harned and W. Kerner, *J. Comput. Phys.* **60**, 62 (1985).

5. D. S. Harned and D. D. Schnack, *J. Comput. Phys.* **65**, 57 (1986).

6. S. J. Sackett, Lawrence Livermore report UCID-17621, (1977).

7. J. D. Jackson, *Classical Electrodynamics*, Second Edition (John Wiley and Sons, Inc., New York, 1975), pp. 201–204.

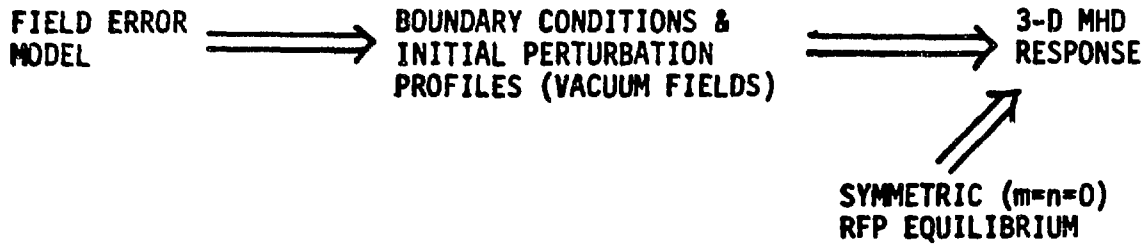

Figure 1. Schematic of the Numerical Calculation

Modified Bessel Function Equilibrium

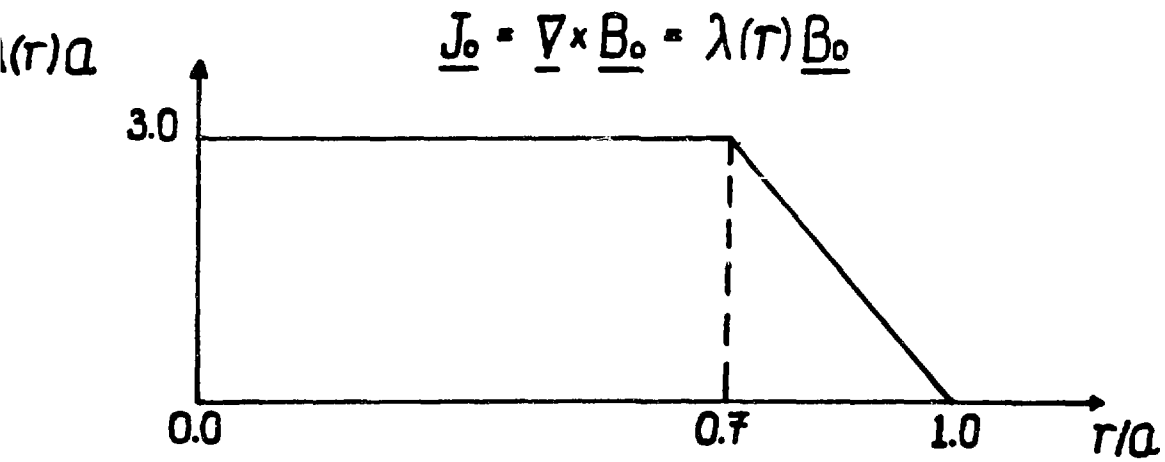

Figure 2.

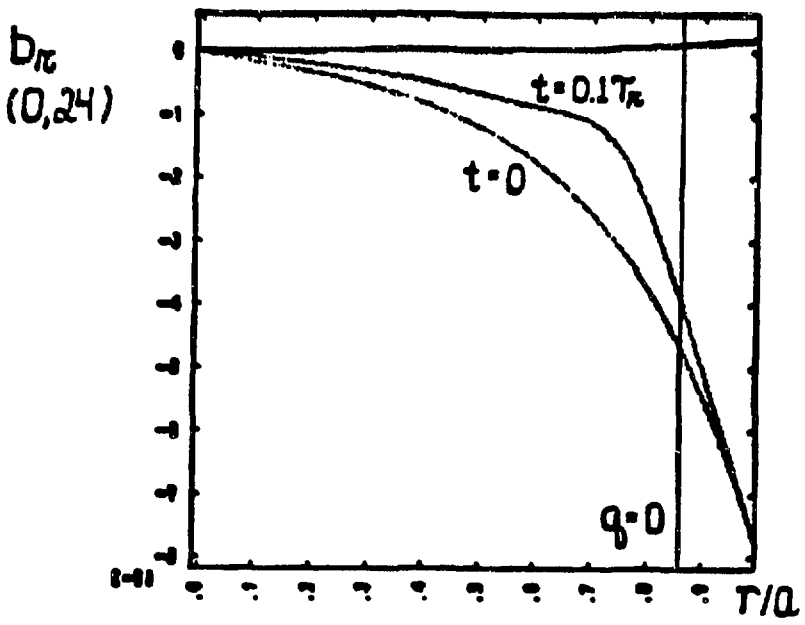

Figure 3. Comparison of $b_r(q=0)$ before (t=0) and after ($t=0.1\tau_R$) the plasma response. Note that $b_r(q=0)$ is reduced in magnitude. (ZT-40 data)

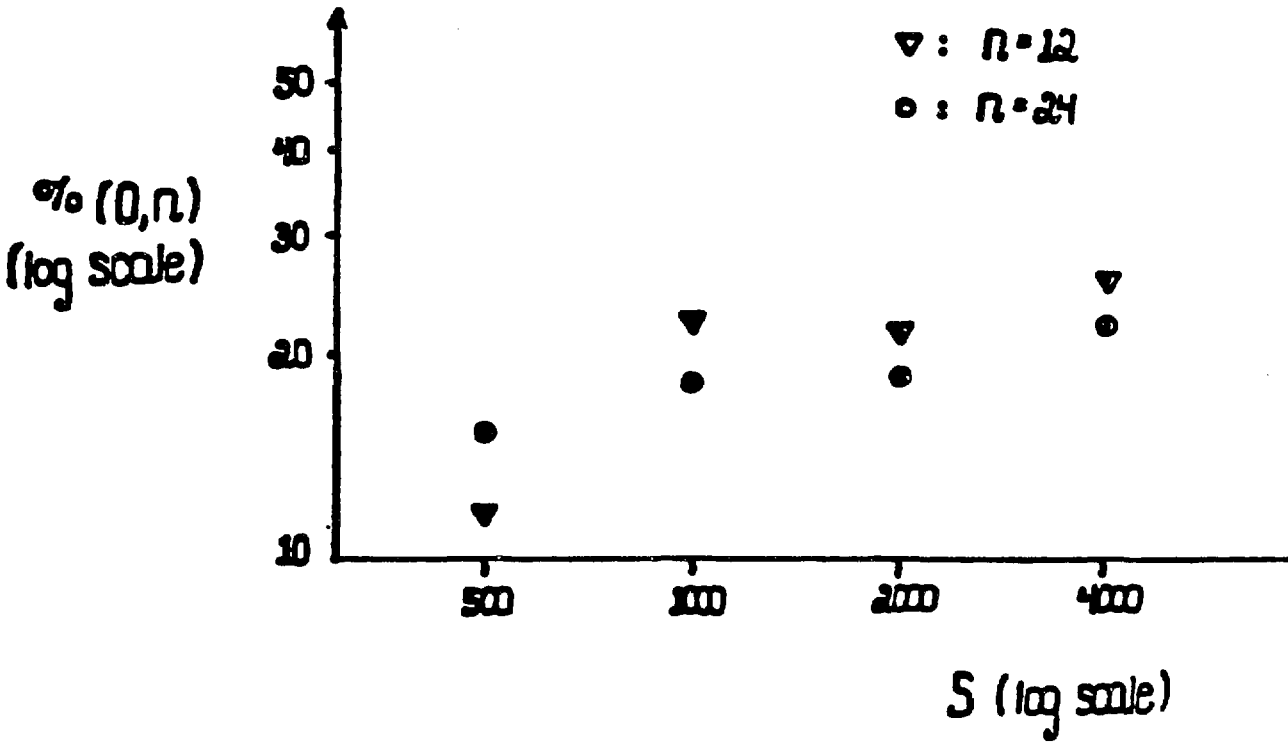

Figure 4. Graph of %(0,n) vs. S

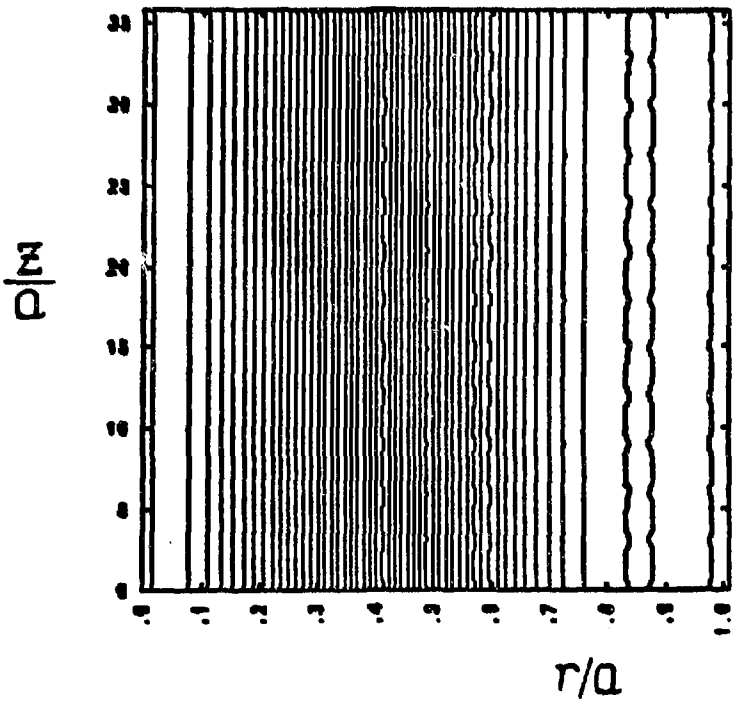

(a) ZT-40 (primarily n=12)

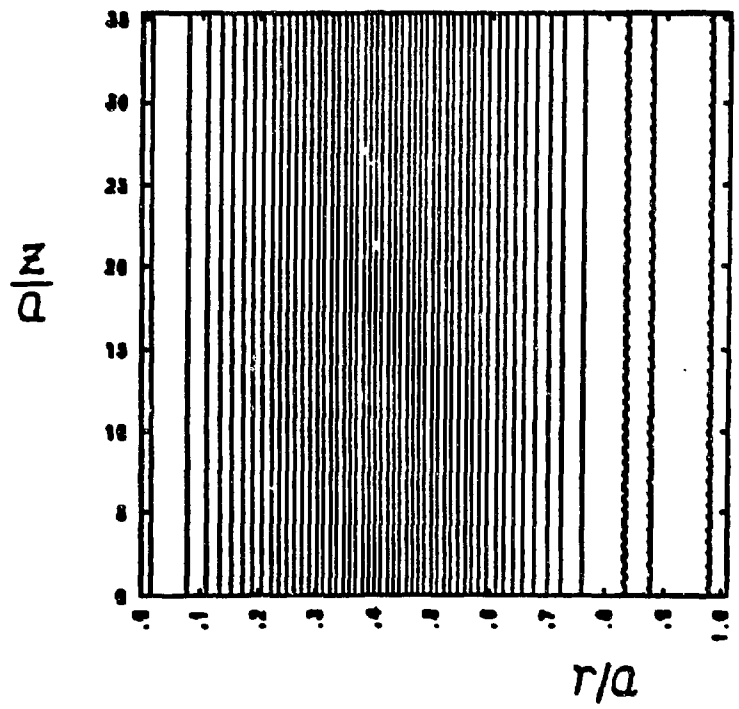

(b) ZTH (primarily n=48)

Figure 5. Plots of helical flux for modes of number (0,n)

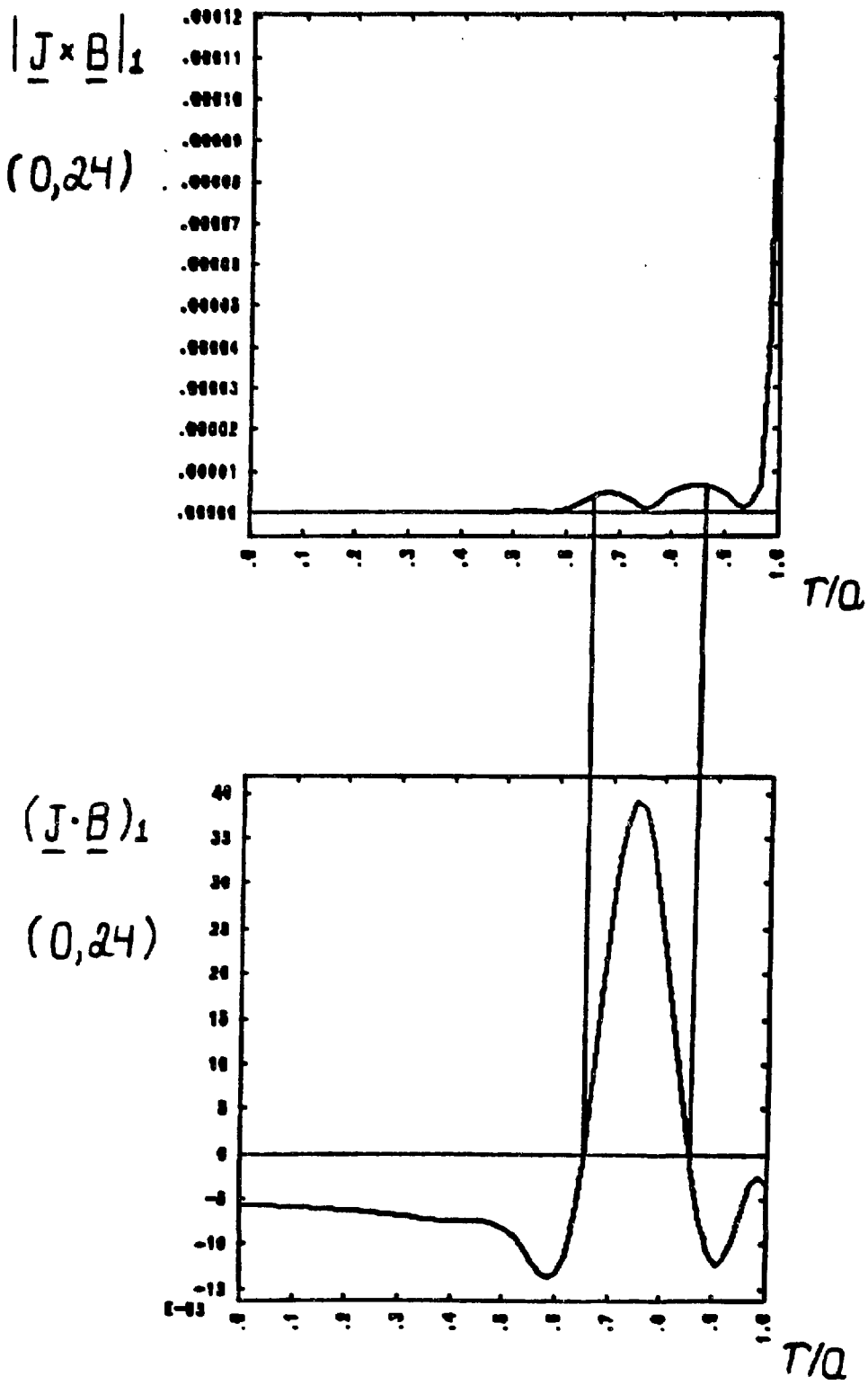

Figure 6. Comparison of $|\underline{J}\times\underline{B}|_1$ and $(\underline{J}\cdot\underline{B})_1$ for the (0,24) mode (ZT-40 case)

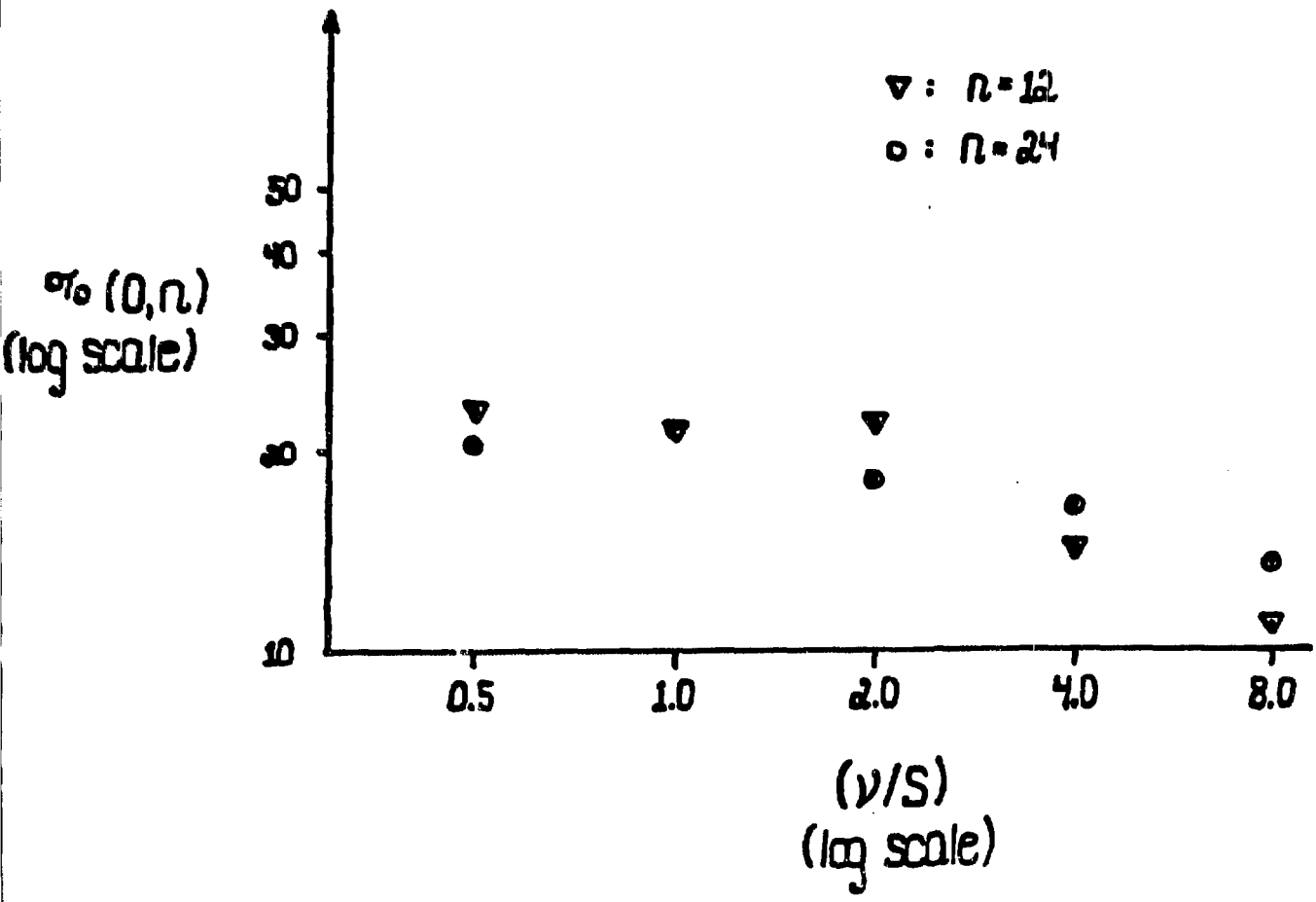

Figure 7. Graph of $\sigma(0,n)$ vs. (ν/S)

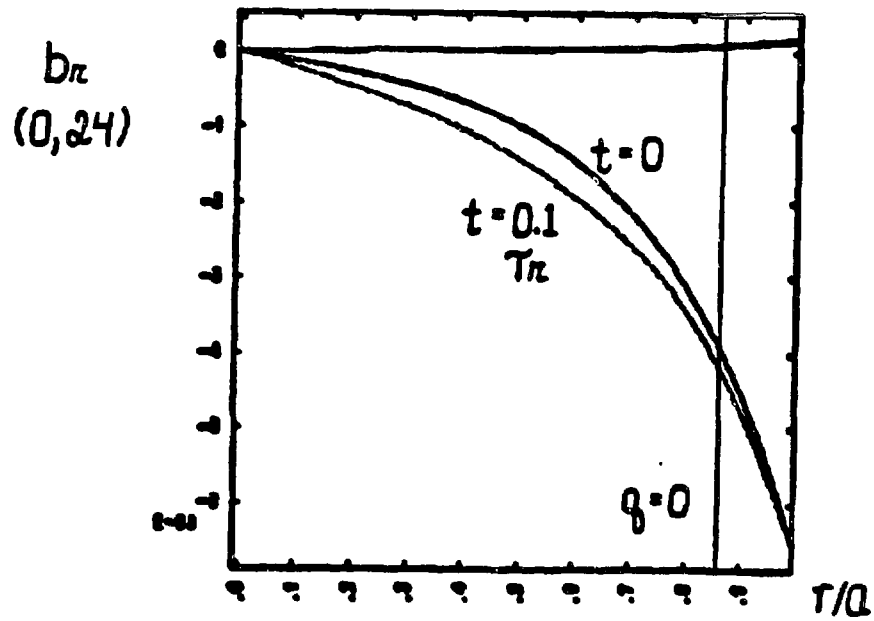

Figure 8. Comparison of $b_r(q=0)$ before (t=0) and after ($t=0.1\tau_n$) the plasma response in the constant-λ case. Note that $b_r(q=0)$ is increased in magnitude (cf. Figure 3.) . (ZT-40 data)

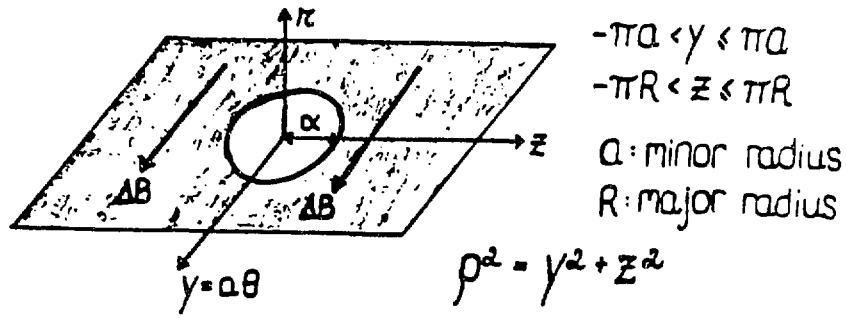

Figure 9. Coordinate system for the calculation of b_r due to a hole in the shell

Figure 10. The Fourier spectrum - $b_r(m,n)$ - of the b_r field due to a hole in the shell
(The shaded areas represent the values of m and n included in the calculation.)

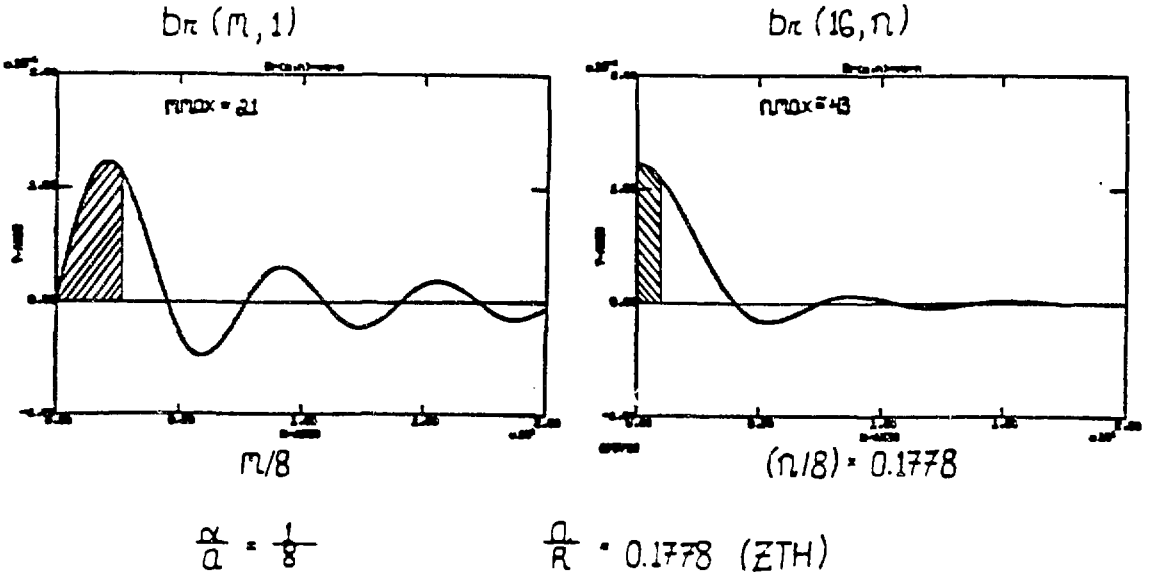

CPRF – DIAGNOSTICS AND PUMPING SECTIONS

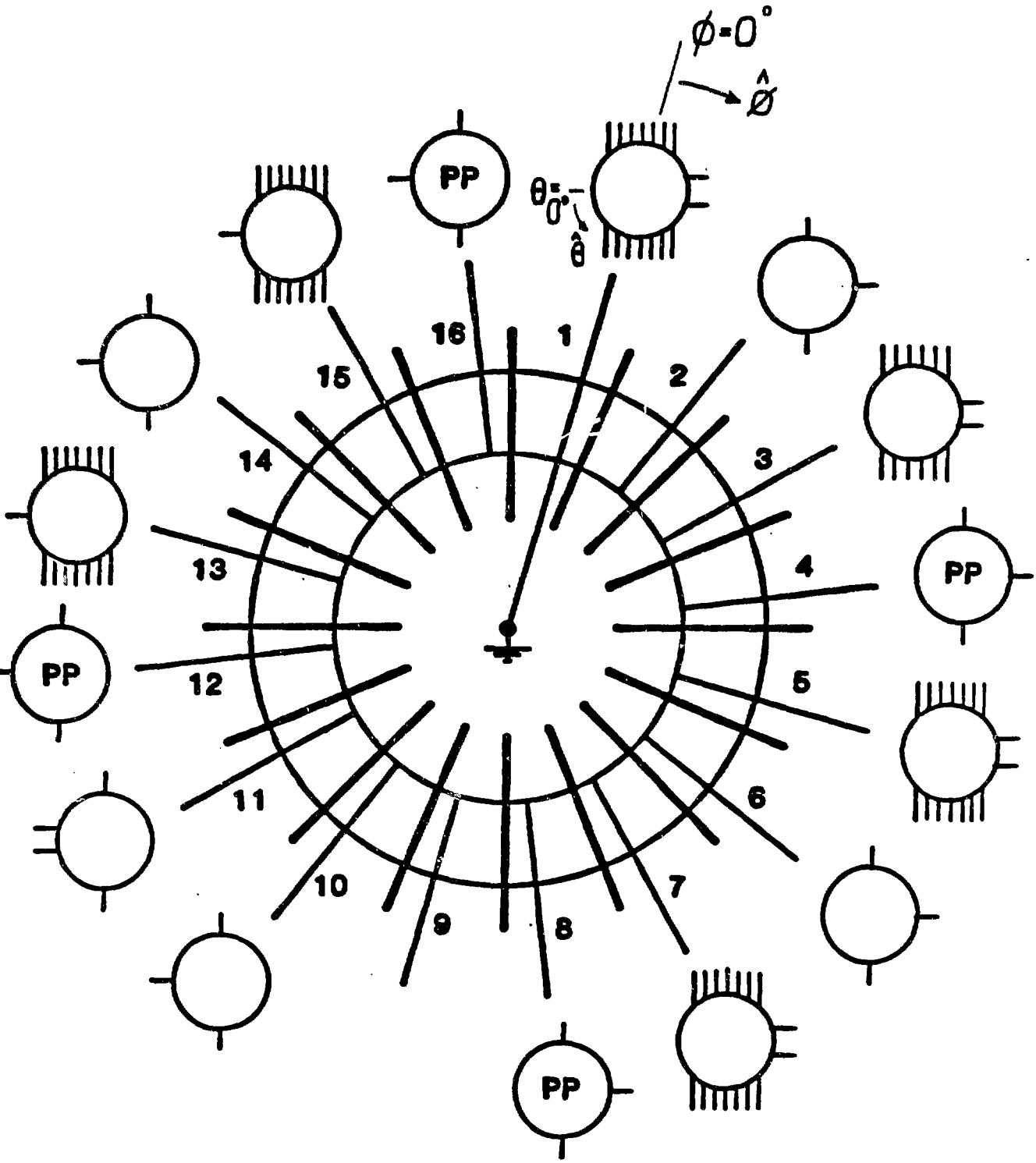

Figure 11. Positions of the holes in ZTH
Shown is a toroidal cross-section with numbers indicating the positions of the hole groups. For each number, a poloidal cross-section (small circle) is shown with the positions of the holes indicated (lines). PP stands for pump port.

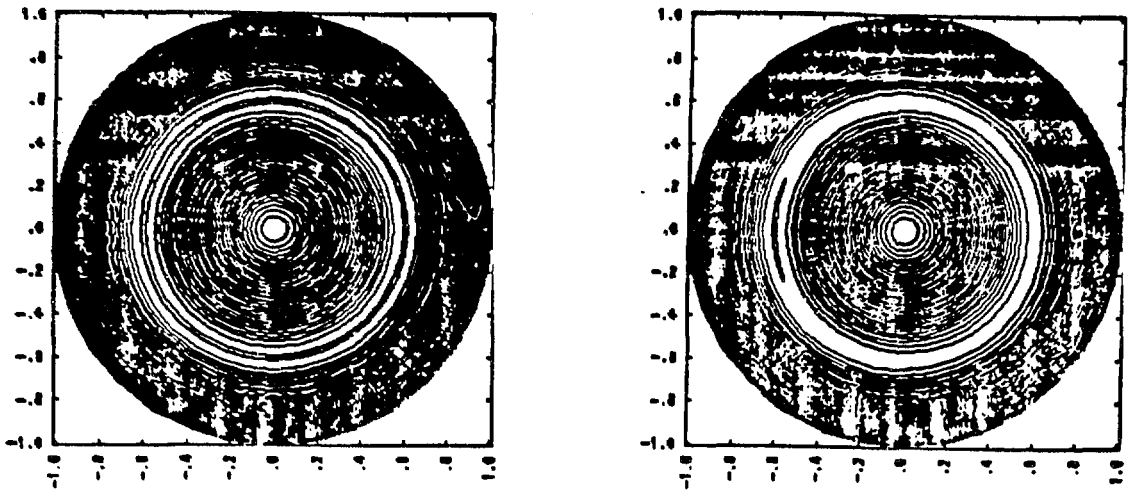

(a) 100% B_V mismatch

(b) 100x100% B_V mismatch

Figure 12. Plots of helical flux for the (1,-16) mode

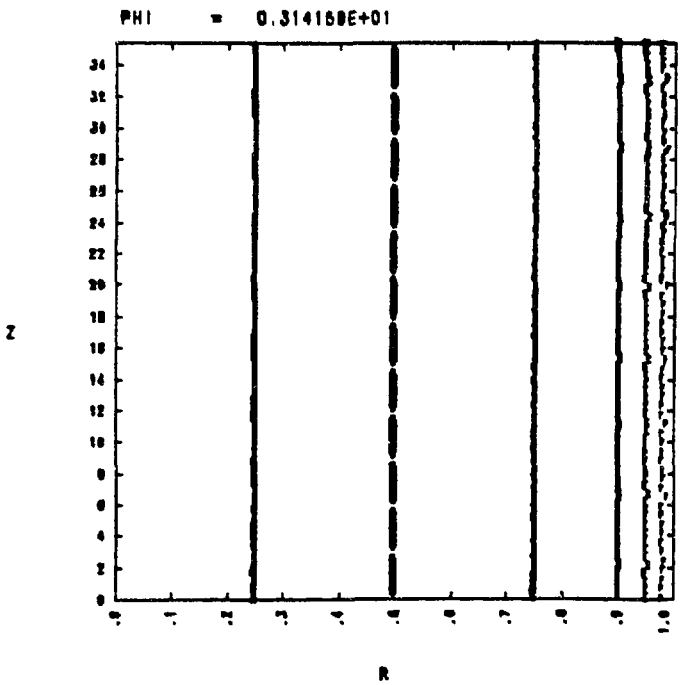

Figure 13. Field-line traces (puncture plot in the r-z plane) for the case of 100% B_V mismatch

RFP Start-Up and ZTH Predictions*

J. Phillips, D. Baker, R. Gribble, and C. Munson

We consider in this short report the start-up[1,2] of the toroidal current, I_ϕ, in a Reversed-Field Pinch (RFP) experiment. The results of a series of runs on the ZT-40M experiment at Los Alamos, and techniques by which the volt-second input, $(\mathrm{V{\cdot}s})_{in}$, can be reduced will be discussed. We also report our preliminary predictions for the start-up requirements for the ZTH experiment now under design and construction at Los Alamos.

I. ZT-40M START-UP.

Several types of start-up modes that are accessable in ZT-40M can be generalized as follows. An RFP discharge begins with the formation of a matched-mode RFP at an initial toroidal current of $I_{\phi i}$, followed by a slow current ramp[3] to a final current $I_{\phi f}$. Examples with three different values of $I_{\phi i}$ are shown in Fig. 1 with about the same value of $I_{\phi f}$. The case for which $I_{\phi i} = I_{\phi f}$, labelled "1" in the figure, is the conventional matched-mode start-up used in most RFP experiments today. The start-up modes in which $I_{\phi i}$ is less than $I_{\phi f}$ we call fast-start ramps. The start-up with the lowest $I_{\phi i}$, driven by the lowest toroidal voltage, V_ϕ, we call the soft-start ramp as the stresses on the windings of the experiment are the smallest.

Examination of Fig.1 shows the following;

1. Matched-mode requires the highest initial $V_\phi \simeq 400\ V$, with $V_{\phi i}$ decreasing as $I_{\phi i}$ is made smaller. Soft start ramps, not shown in the figure, require $\simeq 170$ V.
2. The initial toroidal magnetic field, $B_{\phi i}$, is approximately proportional to $I_{\phi i}$, dropping from $\simeq 0.08$ T to $\simeq 0.02$ T in the figure.
3. The toroidal flux during the current is approximately constant during the current rise in matched-mode operation, and increases by "dynamo" activity during current ramping.
4. For these shots, the depth of the reversal of B_ϕ at the wall, $B_\phi(\mathrm{w})$, is increased as the rate of rise of the ramping current is increased.
5. Theta increases as $B_\phi(\mathrm{w})$ deepens, reaching a value as as high as 2.0.
6. We also note that as theta increases above $\simeq 1.6$ fluctuations and saw-tooth activity become stronger.
7. The $(\mathrm{V{\cdot}s})_{in}$ at peak current increases as $I_{\phi i}$ decreases.

* Work performed under the auspices of the USDOE.

In Fig. 2 the $(V{\cdot}s)_{in}$ required in ZT-40M to reach $I_{\phi f} = 180$ kA for a number of start-up modes and risetimes are shown. We see that the $(V \cdot s)_{in}$ is the smallest for matched-mode and becomes larger as the risetime is increased. The soft-start ramps have the largest $(V \cdot s)_{in}$ with the largest scatter in the data. There is then a trade-off between start-up modes, high voltage and low $(V \cdot s)_{in}$ for matched-mode, and low voltages and higher $(V \cdot s)_{in}$ for ramp discharges.

Attempts have been made to increase the risetime of matched-mode start-up to take advantage of the apparent lower $(V \cdot s)_{in}$. In ZT-40M we were unable to increase the risetime of matched-mode operation to more than 3. ms. We believe this is mainly due to the higher ($\simeq 3.5$) resistance of a stabilized pinch,[4] ($F > 0.0$), over a reversed field pinch, ($F < 0.0$)], Fig. 3. Other factors such as density pumpout before reversal, radiation and temperation behavior are also involved. With the existing system we could not control V_ϕ when passing through the reversal to match the large change in resistance. In Section II we shall report on predictions for matched-mode in ZTH.

In our treatment of the data we calculate a plasma resistance, R_p, using energy balance and a coupled circuit model which assumes the plasma relaxes to a preferred field distribution. The resistive voltage, $V_{\phi res}$, is given by $R_p I_\phi$ and can be calculated during the current rise in ramp discharges.

In the series of ramp discharges reported here, the experiment was operated in the condition that $R_p \simeq I_\phi^{-1}$ or $V_{\phi res}$ a constant, $\simeq 40$ V, independent of I_ϕ. This behavior of $V_{\phi res}$ was fortunate in these runs in that the discharge behavior was relatively simple to describe.

The wide variations in $(V \cdot s)_{in}$ seen in the ramp discharges has been found to be mainly due to variations in theta. In Fig.4, we show variation of $V_{\phi res}$ as a function of theta. Data over the current range $I_{\phi i}$ to $I_{\phi f}$ are included for six discharges with different ramp rates. We also show the average of three studies[5] on flat-top discharges in which theta was varied. Fig. 4 also has the data for four ramp discharges in which the current was flat-topped by adjusting V_ϕ and theta. Differences in the sets of data are probably caused by variations in wall conditioning and plasma density in the sets of data. There is a slight indication in Fig. 4 of a minimum in $V_{\phi res}$ at a value of theta $\simeq 1.45$. This result suggests that if theta could be controlled during the ramp to be a constant at $\simeq 1.45$, the $V_{\phi res}$ would remain a minimum during the ramp with a minimum $(V \cdot s)_{in}$. We have tested this hypothesis by adding a resistance, RTP, in the poloidal current circuit, Fig. 5. This resistance limits changes in the poloidal current during the current rise and variations in theta are kept small.

Figure 6 shows the changes in discharge behavior with RTP shorted, (curves labelled "a"), and with RTP increased to infinity, open circuited, (curves labelled "b"). All other machine conditions are the same. Examination of the figure shows that as RTP is increased;

1. The peak current is increased.

2. The depth of reversal is smaller.
3. Theta is held nearly constant at $\simeq 1.4$.
4. The $(V \cdot s)_{in}$ is reduced.
5. The fluctuation level is markedly reduced.

When the operating conditions are adjusted for constant $I_{\phi f} \simeq 180$ kA, the $(V \cdot s)_{in}$ is reduced for different risetimes as shown in Fig. 7. In some cases the $(V \cdot s)_{in}$ has been reduced by as much as 50%. With these results with controlled theta, the $(V \cdot s)_{in}$ for ramp discharges is close to the sum of $V_{\phi res}$ times the risetime and that needed to increase the magnetic field energy.

II. PREDICTIONS FOR ZTH.

We predict the requirements for ZTH using Gribble's program SCAT. This is a fully developed program using all known electrical parameters for the experiment including such items as equilibrium coils and switch resistances and inductances. The discharge resistance is the only input needed to run the program. For these calculations we have assumed $R_p \propto I_\phi^{-1}$ with $V_{\phi res}$ a constant independent of current. We also assume the discharge resistance before B_ϕ(w) reversal to be 3.5 that after reversal.

The ZTH design requires a current rise to $\simeq 2.0$ MA in $\simeq 50$ ms. This initial current rise is driven by inductive energy transfer. After 50 ms a current ramp driven by a variable power supply raises the current to 4.0 MA in 300 - 400 ms. We examined both a controlled and uncontrolled theta operation in our calculations.

In Fig. 8 we show the behavior of several parameters for the first phase of the current rise to 2.0 MA in 50 ms. In the example the soft-start ramp mode is used with $V_{\phi res} =$ 20 V. The $V_{\phi res}$ of 20 V is calculated using the 40 V for ZT-40M with resistance scaled as R/a^2. The performance of the two discharges are about as expected with the $(V \cdot s)_{in}$ for the controlled theta case being lower than the uncontrolled by about 33%.

Different start-up modes were examined in which I_ϕ was varied from a matched-mode through hard-start ramps to soft-start ramps, Fig. 9. Note the increased power input to the plasma before B_ϕ(w) reversal. Surprisingly the $(V \cdot s)_{in}$ for all modes are about the same. Apparently the power input before reversal in the matched-mode case closely balances that needed to increase the magnetic field energy to ramp up the current. The comparison is made although the matched-mode operation may be impossible for other reasons.

We show in Fig. 10 an example of the second phase of the current rise, from 2 MA to 4 MA in 350 ms. We find in this example in which $V_{\phi res} = 20$ V an initial V_ϕ of $\simeq$55 V is needed to ramp up the current. In ZTH the discharge resistance could be expected to be dependent on the electron temperature and $V_{\phi res}$ to fall with current. The additional

$(V \cdot s)_m$ to raise the current from 2 MA to 4 MA is approximately that which we predict from the results of our study on ZT-40M, i.e. $V_{\phi res}\gamma_{rise} + L(I_{\phi i} - I_{\phi f})$.

These prediction using SCAT and the assumed discharge resistances indicate that ZTH should reach its design operation. Clearly, however, there are provisos that should be mentioned;

1. In ZTH, the dependence of $V_{\phi res}$ on the toroidal current may be completely different from that assumed in our calculations. This will be answered by the experiment.

2. The small I_ϕ used in the soft-start ramps require low initial filling pressures. Although the electron density does increase in ramp discharges, the increase is insufficent to keep I/N constant so that I/N rises. It may be necessary in ZTH to have gas refueling during ramp start-ups by pellet injection or gas puffing.

ACKNOWLEDGEMENTS

The authors wish to thank the CTR-2 staff for their contributions during this work and to the operating staff of ZT-40M. The design changes and modifications to ZT-40M are due to the efforts of Al Schofield and his group.

REFERENCES

1. H. A. Bodin, C. A. Bunting, P. G. Carolan, L. Giudicotti, C. W. Gowers, Y. Hirano, I. H. Hutchinson, P. A. Jones, C. Lamb, M. Malacarne, A. A. Newton, V. A. Piotrowicz, T. Shimada, M. R. C. Watts, "Results From the HBTX1A Reversed Field Pinch Experiment," Plasma Physics and Controlled Nuclear Fusion Research, (IAEA Conference, Baltimore, 1982), 1, 641-656.
2. J. A. Phillips, L. C. Burkhardt, A. Haberstich, R. B. Howell, J. C. Ingraham, E. M. Little, K. S. Thomas, R. G. Watt, P. G. Weber, "ZT-40M Current Risetime Study," Los Alamos National Laboratory report, LA-9717-MS (October 1983).
3. J. A. Phillips, D. A. Baker, L. C. Burkhardt, R. Erickson, A. Haberstich, J. C. Ingraham, E. M. Little, J. G. Melton, K. F. Schoenberg, R. G. Watt, P. G. Weber, G. A. Wurden, "Observations of Ramped Current Operation in ZT-40M," Los Alamos National Laboratory report, LA-10060-MS (May 1984).
4. I. H. Hutchinson, "Plasma Resistance Studies in HBXT1A Reversed Field Pinch," 11th European Conference on Controlled Fusion and Plasma Physics (European Physical Society, Aachen, September 1983),151-154.
5. J. C. Ingraham, P. G. Weber and G. A. Wurden, private communication.

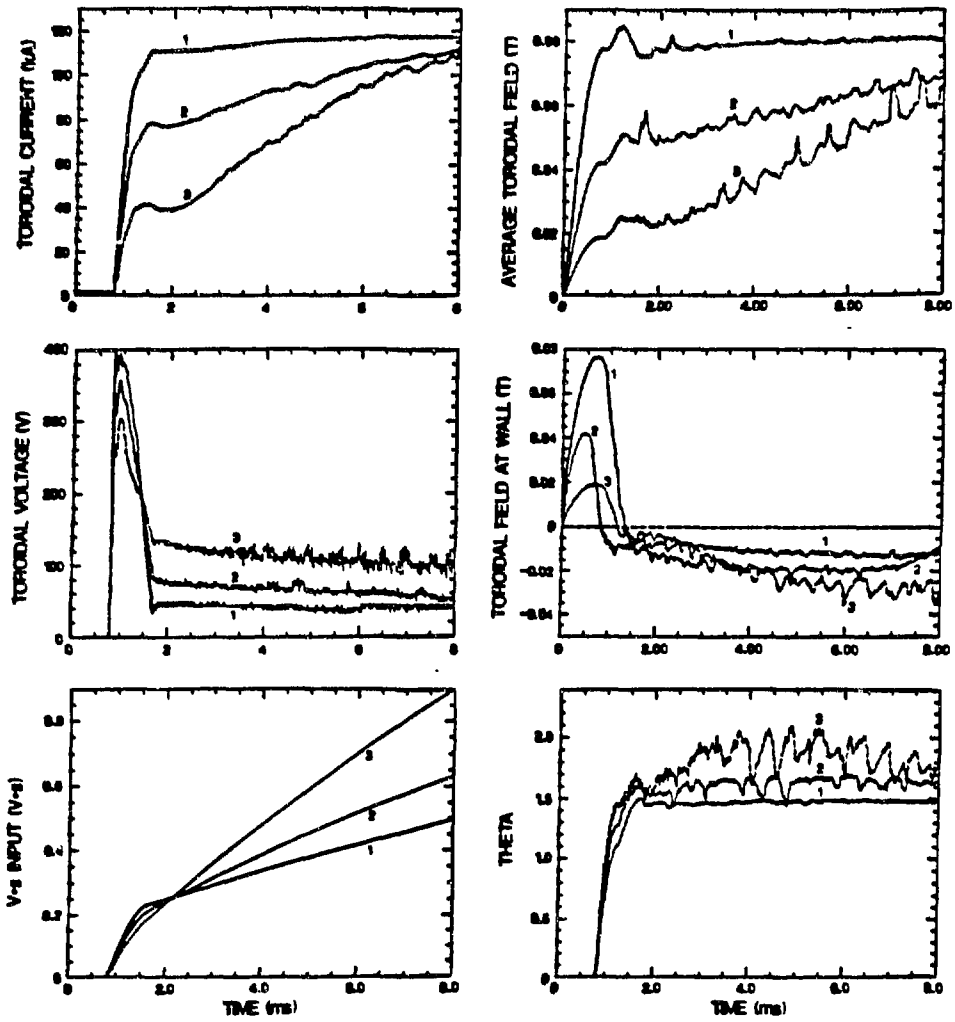

Fig.1. Three examples of ramp discharges with different values of initial fast toroidal current, $I_{\phi i}$.

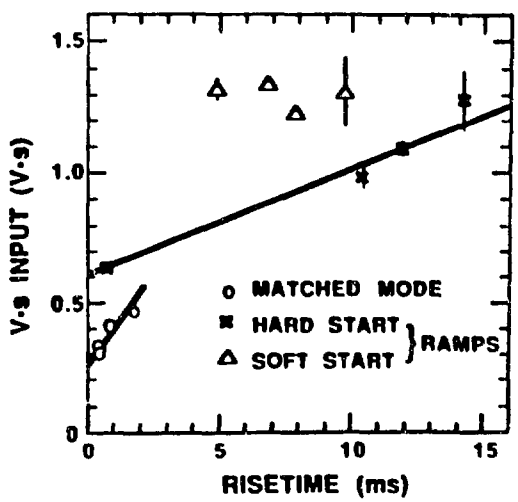

Fig.2. The V·s input vs risetime for three different modes of ramp discharges. The peak current for all discharges is ≈ 180 kA.

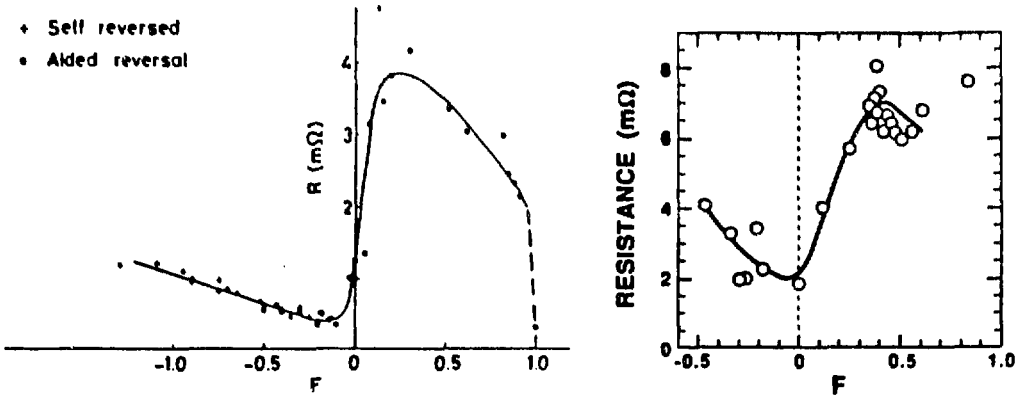

Fig.3. Discharge resistance vs F during start-up. The trace labelled 'a' is from I.H.Hutchinson and trace labelled 'b' from 2T-40M data.

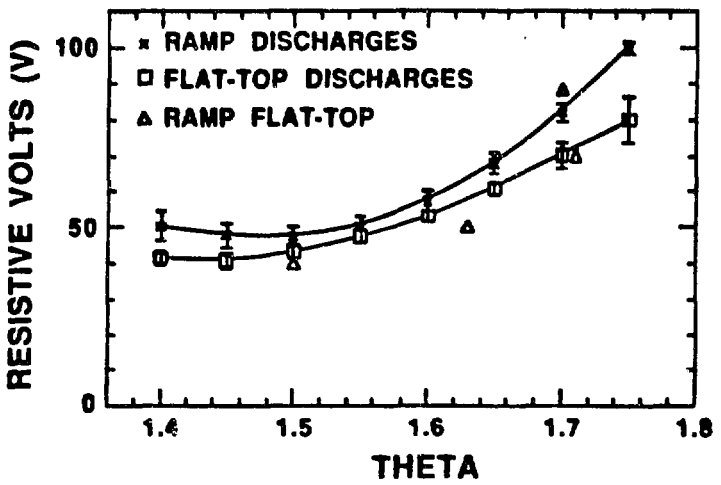

Fig.4. Resistive voltage vs theta for ramp discharges, flat-top discharges and four values of ramp discharges flat-topped at different values of $V_{\phi res}$ and theta.

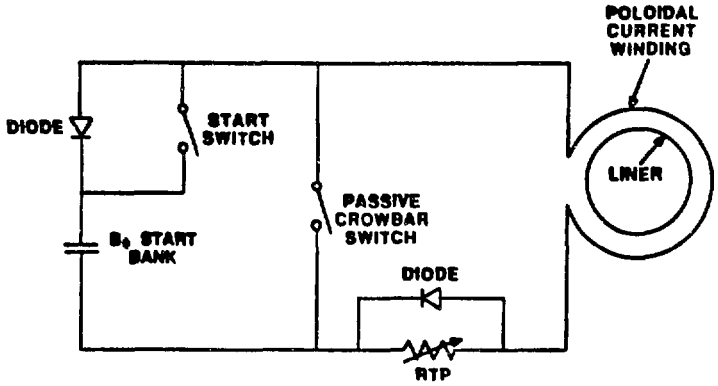

Fig.5. Schematic drawing of the poloidal current circuit showing the location of the resistance RTP.

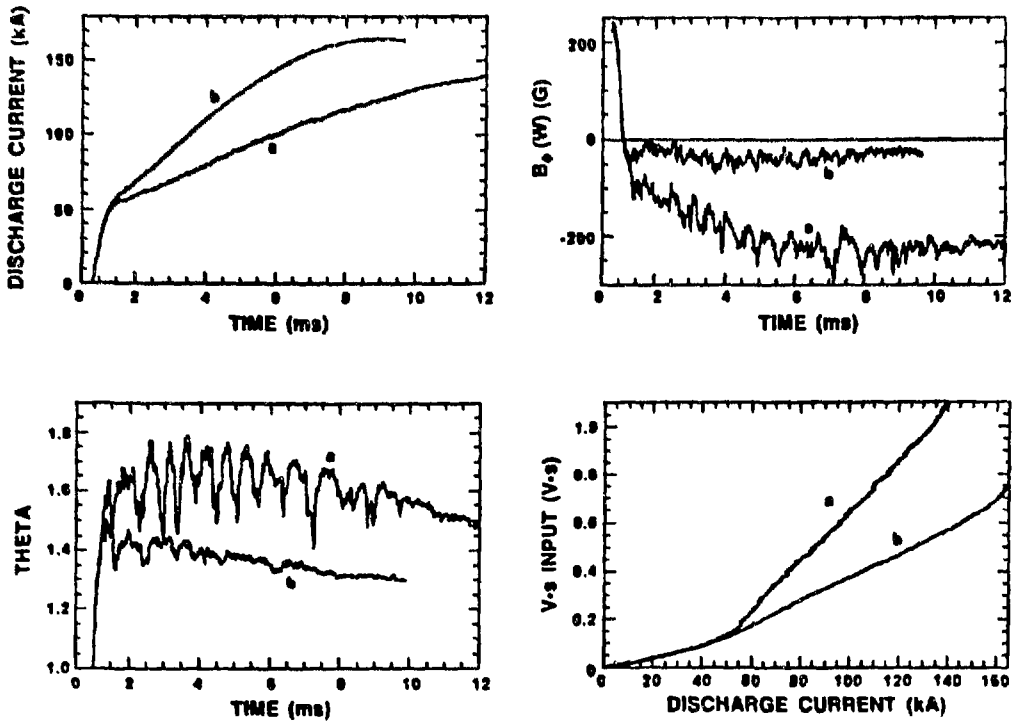

Fig.6. An example of two discharges showing the improved operation when RTP is varied. Traces labelled 'b' are for the case when RTP = 0. Ω and traces 'a' when RTP is open circuited. Note the control of theta at = 1.4, (case 'a') with a reduction of V·s input and a reduction in the fluctuation level.

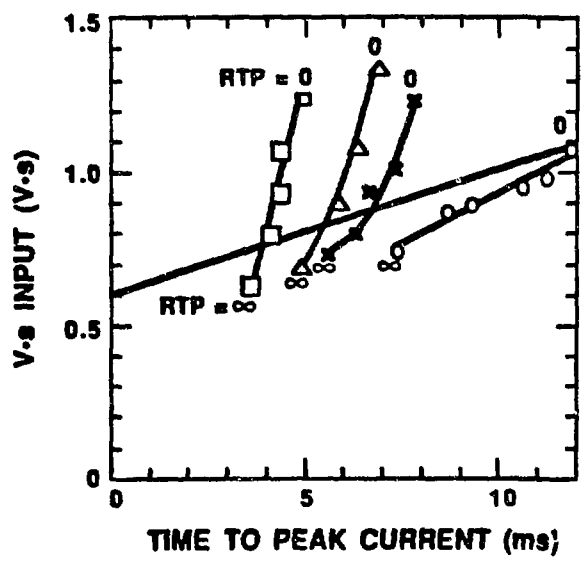

Fig.7. The reduction of V·s input with variations in RTP for ran; discharges with different risetimes. Peak I_ϕ = 180 kA.

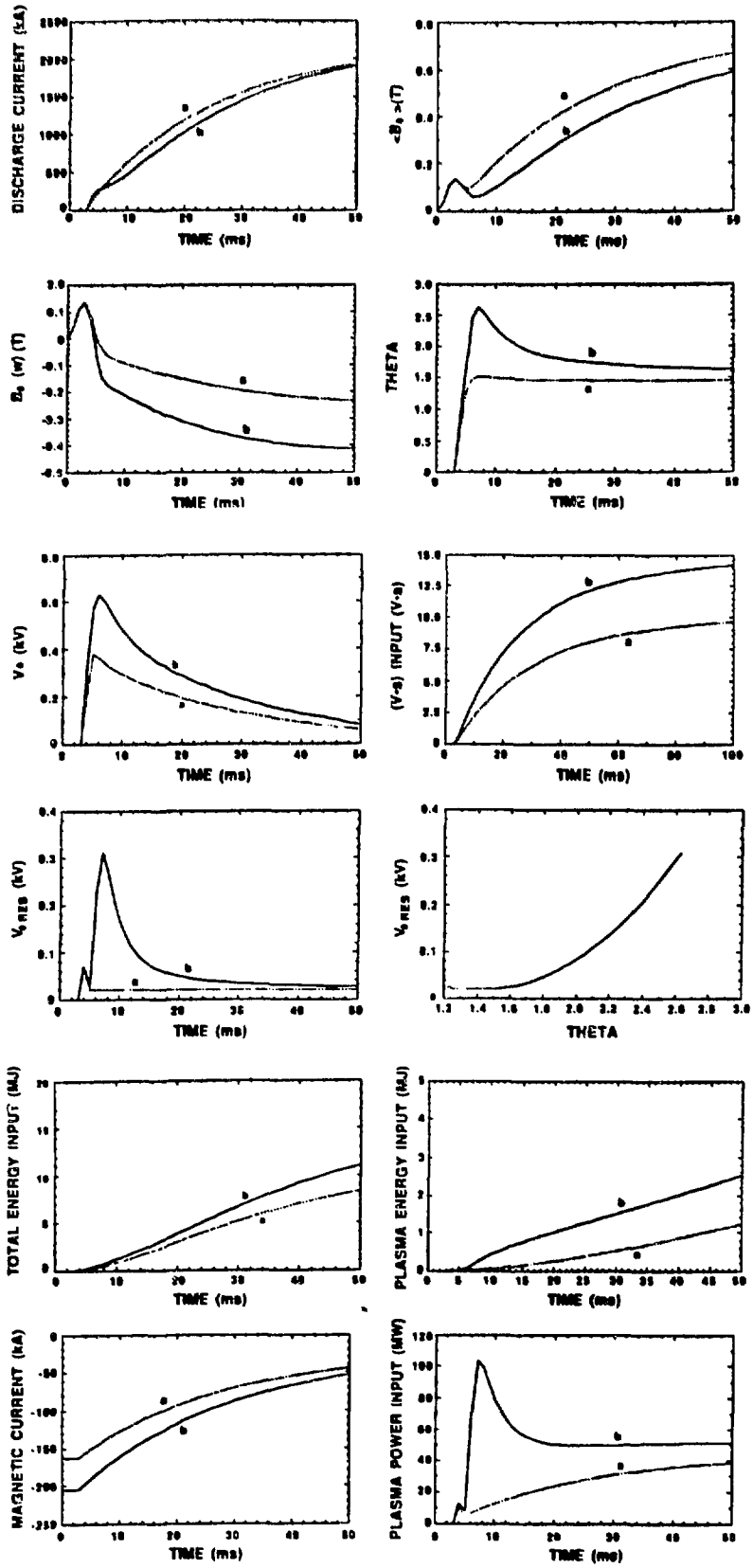

Fig.8. An example of the performance of ZTH predicted by the LANL SCAT program. Curves labelled "a" are for a controlled theta discharge and curves "b" for uncontrolled theta. The starting parameters are adjusted to give = 2MA in = 50 ms.

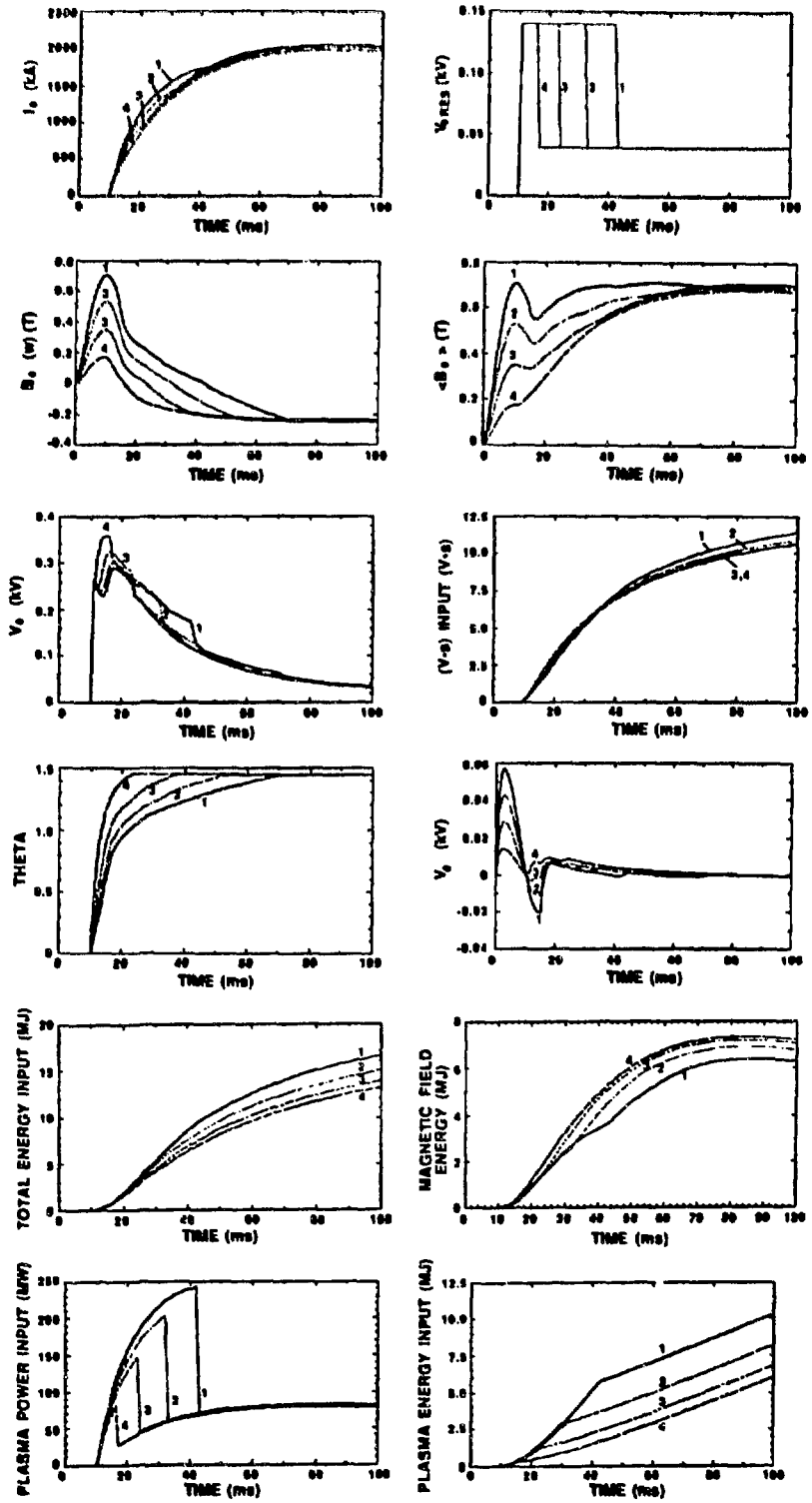

Fig.9. Four examples of ramp discharges as predicted by the LANL SCAT program with different times to reversal. The $B_{\phi i}$ was varied to change the reversal time. The $V_{\phi res}$ before reversal is 3.5 times that after reversal. Curves labelled '1' are for the special case of matched-mode start-up.

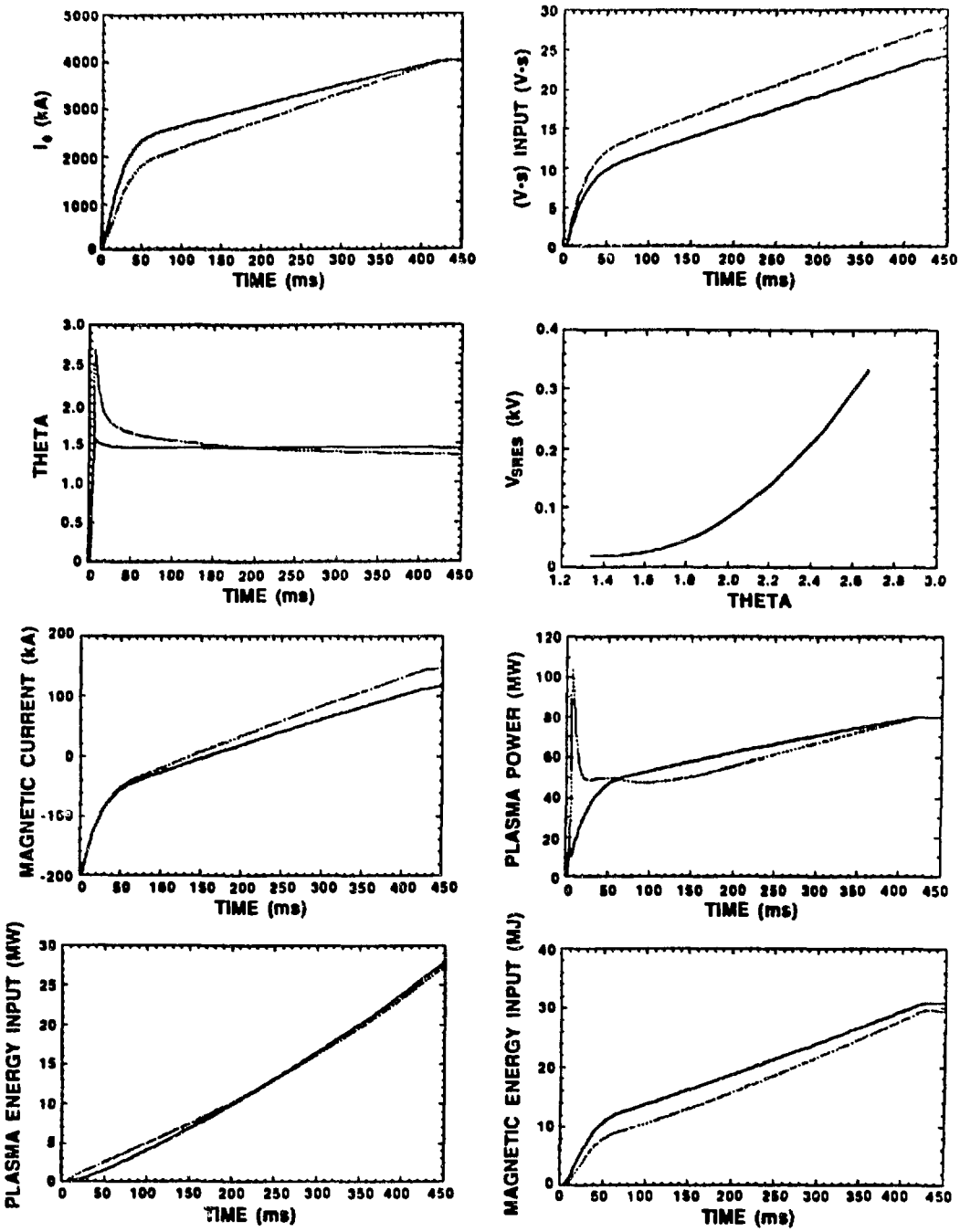

Fig.10. An example of the start-up of ZTH to 4 MA in 0.42 s. Two sets of data are shown, controlled theta (labelled '1') and uncontrolled theta (labelled '2').

CPRF/ZTH SHELL POLOIDAL GAP DESIGN AND FABRICATION

E. J. Yavornik, R. W. Moses, and G. D. Dransfield, Los Alamos National Laboratory.

Introduction

Design is in progress of a new generation RFP machine to be assembled at Los Alamos National Laboratory during FY 86-92. The confinement Physics Research Facility (CPRF) houses the front-end ZTH experiment that contains the Shell Poloidal Gap. Figure I shows the construction of the poloidal gap.

Discussion

The gap design presented in this paper consists of three concentric poloidal stainless steel shells, each appropriately coated with tapered copper and separated within the gap from one another by fiberglass insulation. The center shell is electrically connected to a flange at one end of the conducting shell gap, and the inner and outer shells are electrically connected together to the flange on the opposite side of the conducting shell gap. Optimally, the tapered gap will be as long as the minor diameter of the shell. The boundary dimensions of the gap assembly will be identical to each 22.5° segment of the conducting shell.

At present, it is expected that the required copper will be explosively bonded to flat stainless steel plates. This process forms a bond joint that is stronger than the basic copper material. The taper in the copper will be machined with the bonded assembly held in the flat condition.

The final shell will be die-formed with the same dies as those used for the standard sections of the ZTH shell. Flatness of the tapered part necessary for die-forming will be achieved by placing a second tapered part on to the first to create a uniform-thickness assembly for forming. The die will be capable of accepting spacers of proper thickness to accommodate variable dimensions as required.

In the assembly, the three copper clad gap shells will be separated by fiberglass layers a minimum of 1/4" thick. The layers will probably be fabricated onto the center shell section. After inspection and curing, a heavy coating of epoxy resin will be applied to the center shell and to the inside surface of the two outer shells. They will be pressed together to form the final configuration. Final machining of the flange surfaces and bolt holes can then take place.

Conceptual drawings of the assembly are presented. These include the following figures:

Fig. 1. Toroidal gap assembly
Fig. 2. Typical gap single shell
Fig. 3. Die-formed detail
Fig. 4. Toroidal cross section of gap
Fig. 5. Outer gap vertical section
Fig. 6. Inner gap vertical section

Summary

Because of the difficult fabrication aspects of the overall shell design associated with the rigorous tolerances, a prototype shell segment is planned to help evaluate certain fabrication considerations. Much of the tooling for the shell segments will also be used to fabricate the poloidal gap. It is expected that this prototype fabrication will establish the appropriate process to achieve the desired fabricated hardware in a cost-effective manner.

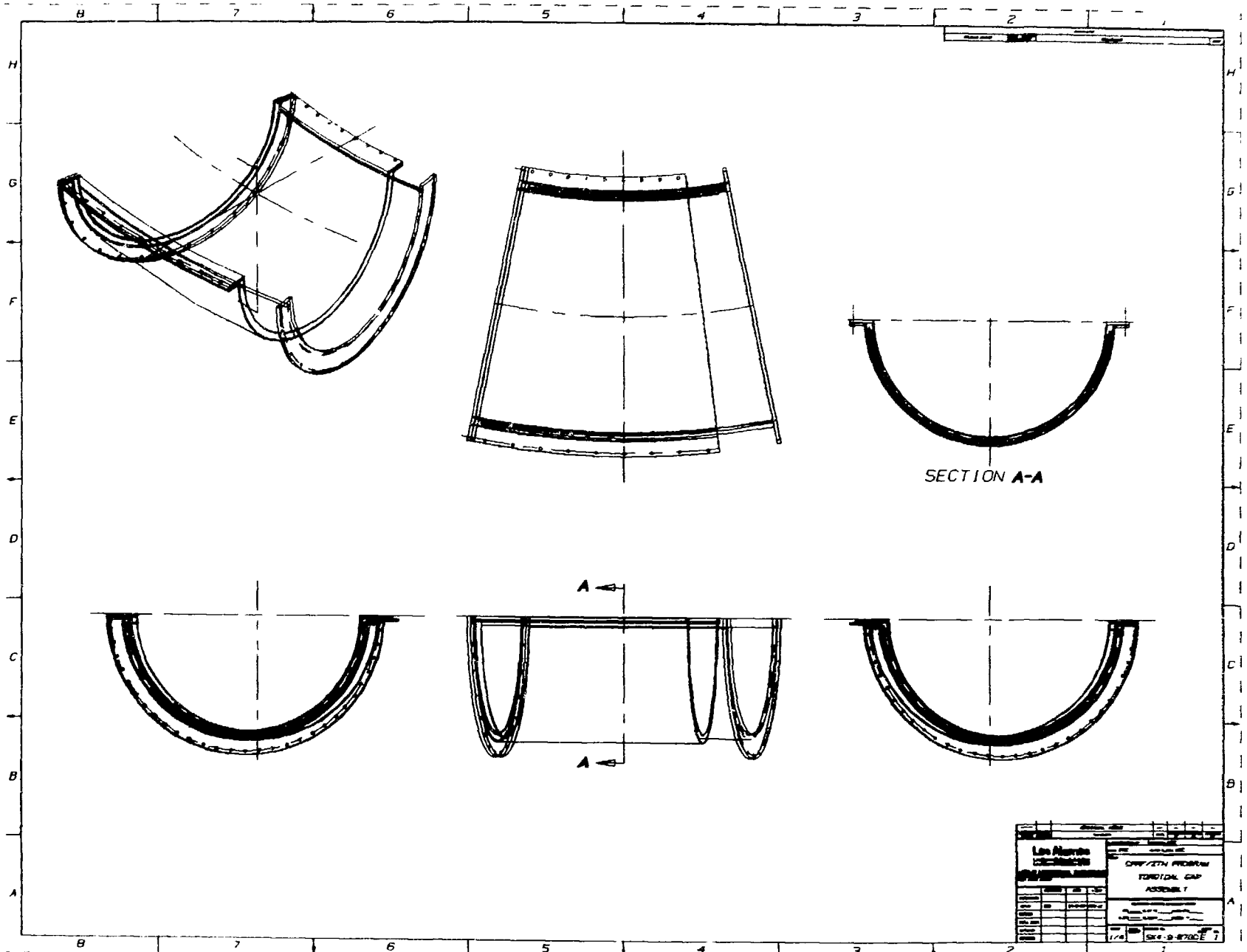

Figure 1

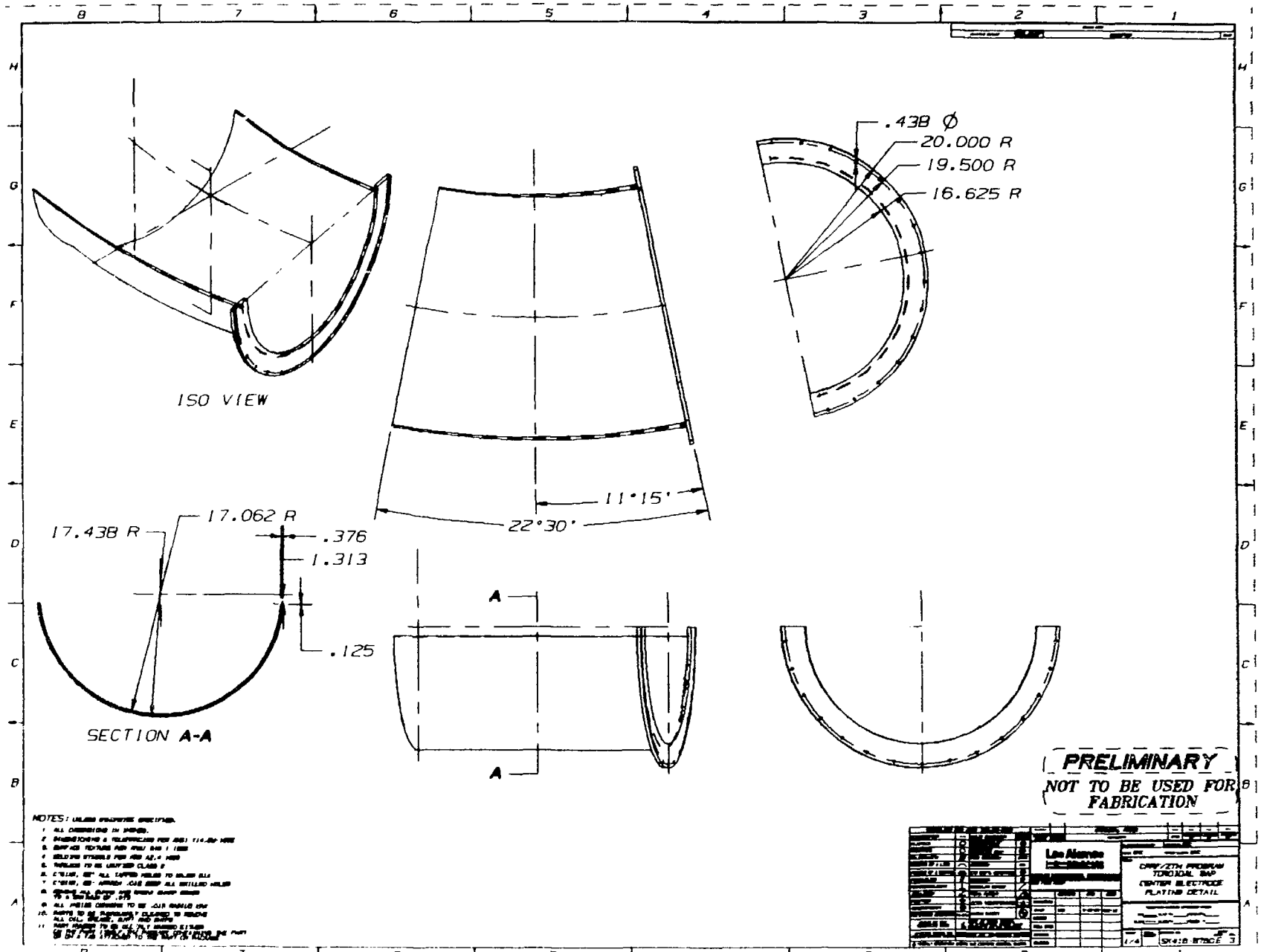
ISO VIEW
.438 Ø
20.000 R
19.500 R
16.625 R
11°15'
22°30'
17.438 R
17.062 R
.376
1.313
.125
SECTION A-A
A
A
PRELIMINARY
NOT TO BE USED FOR FABRICATION

Figure 2

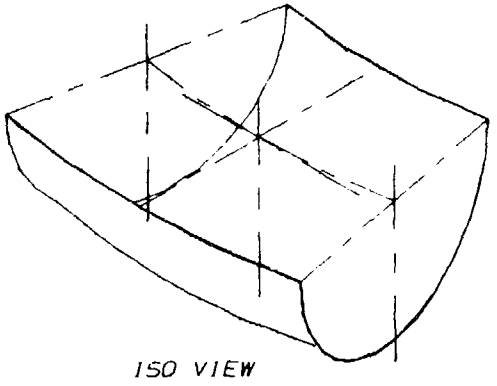

ISO VIEW

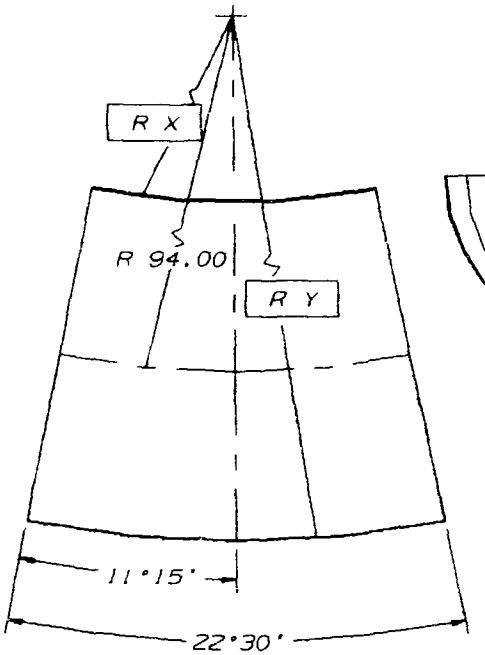

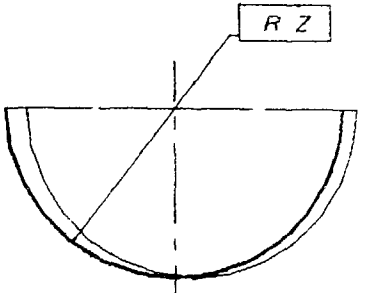

SECTION A-A

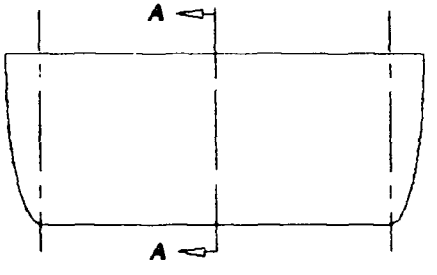

DIMENSION SCHEDULE				
PART NUMBER	R X	R Y	R Z	MATERIAL THICKNESS
SK-415-87-00-E1-1	78.207	111.793	16.625	.125
SK-415-87-00-E1-2				
SK-415-87-00-E1-3				
SK-415-87-00-E1-4				
SK 415 87 00 E1 5				

PRELIMINARY
NOT TO BE USED FOR FABRICATION

NOTES: UNLESS OTHERWISE SPECIFIED.

1. ALL DIMENSIONS IN INCHES.
2. DIMENSIONING & TOLERANCING PER ANSI Y14.5M-1982
3. SURFACE TEXTURE PER ANSI B46.1-1985
4. WELDING SYMBOLS PER AWS A2.4-1986
5. THREADS TO BE UNIFIED CLASS 2
6. C'BORE, 82° ALL TAPPED HOLES TO MAJOR DIA
7. C'BORE, 82° SPOTFACE .015 DEEP ALL DRILLED HOLES
8. REMOVE ALL BURRS AND BREAK SHARP EDGES TO A MAXIMUM OF .015
9. ALL ANGLES CORNERS TO BE .010 RADIUS MAX
10. PARTS TO BE THOROUGHLY CLEANED TO REMOVE ALL OIL, DRAWING, DIRT AND SWARF
11. PART NUMBER TO BE CLEARLY STAMPED ETCHED OR INK MARKED TO THE PARTS SURFACE

Los Alamos

DMF/ZTH PROGRAM
TERMINAL CAP
DIE FORMED DETAILS 1-8

SK-415 STAGE 3

Figure 3

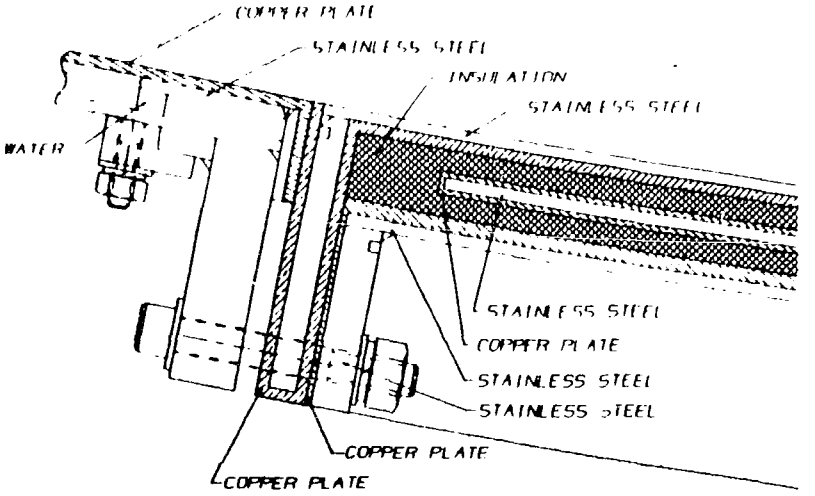

TOROIDAL GAP LEFT SIDE HORIZONTAL SECTION

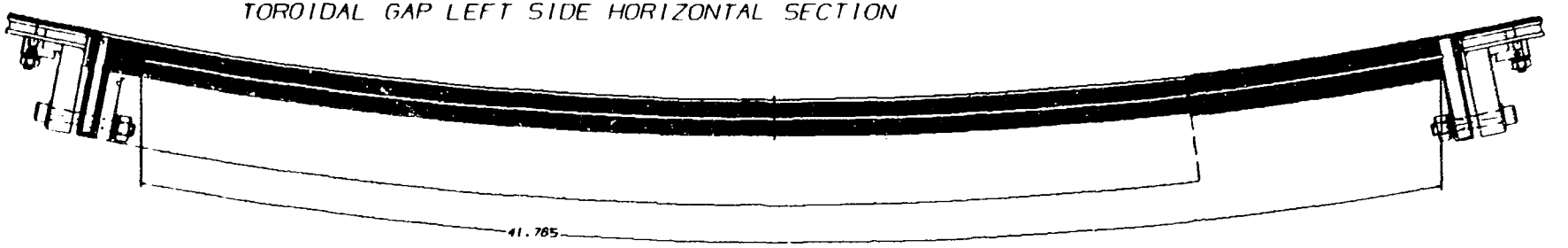

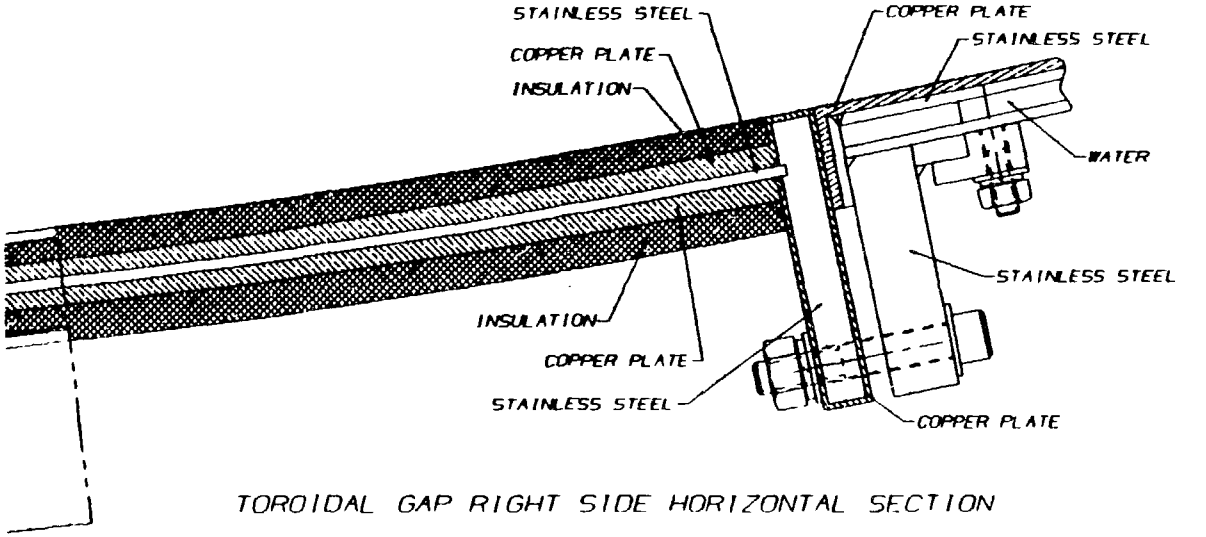

TOROIDAL GAP RIGHT SIDE HORIZONTAL SECTION

TOROIDAL CROSS SECTION OF GAP

FIGURE 4

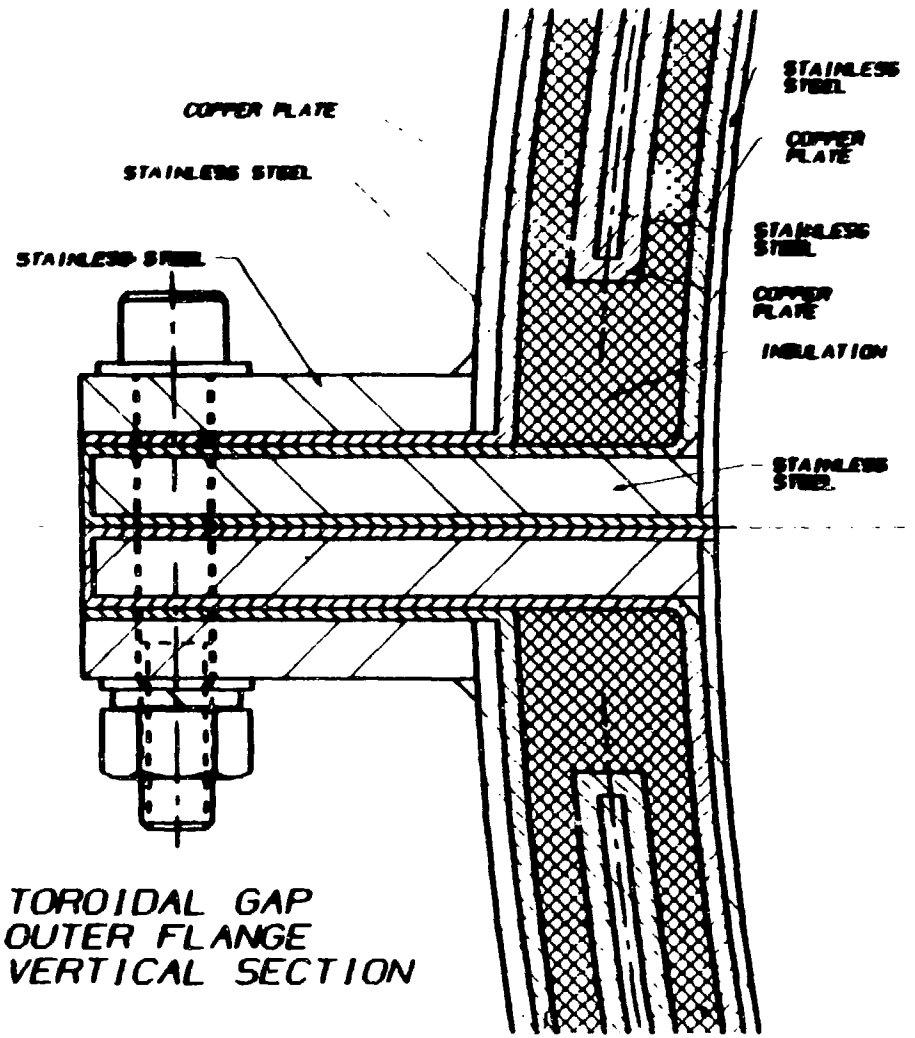
COPPER PLATE
STAINLESS STEEL
STAINLESS STEEL
STAINLESS STEEL
COPPER PLATE
STAINLESS STEEL
COPPER PLATE
INSULATION
STAINLESS STEEL
TOROIDAL GAP
OUTER FLANGE
VERTICAL SECTION

FIGURE 5

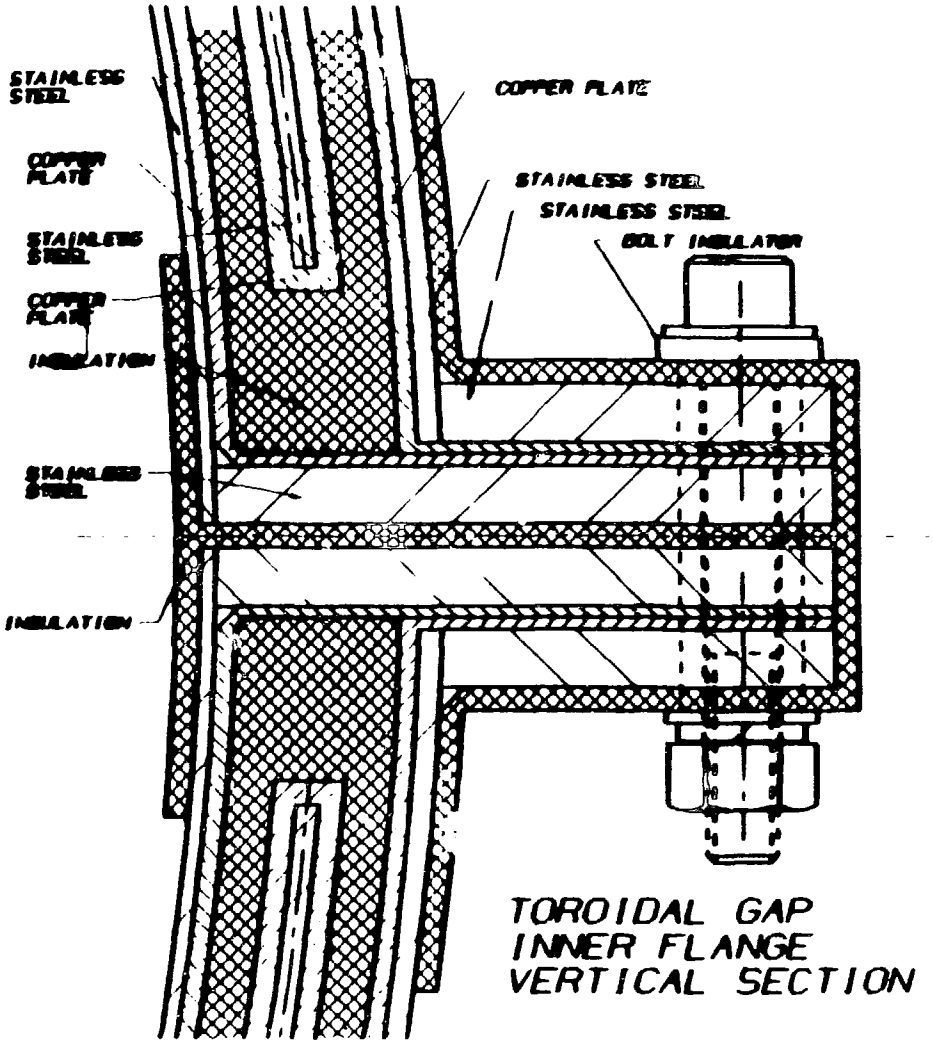
STAINLESS STEEL
COPPER PLATE
STAINLESS STEEL
COPPER PLATE
INSULATION
STAINLESS STEEL
INSULATION
COPPER PLATE
STAINLESS STEEL
STAINLESS STEEL
BOLT INSULATOR
TOROIDAL GAP
INNER FLANGE
VERTICAL SECTION

FIGURE 6

CPRF/ZTH TOROIDAL CONDUCTING SHELL FINITE ELEMENT STRESS ANALYSIS

C. L. Baker, E. O. Ballard, G. D. Dransfield, Los Alamos National Laboratory.

Introduction

Design is in progress of a new generation RFP machine to be assembled at Los Alamos National Laboratory during FY 86-92. The confinement Physics Research Facility (CPRF) houses the front-end ZTH experiment. Figure 1 shows the ZTH in its present configuration without the diagnostic platform surrounding the outer periphery.

Discussion

The ZTH torus, shown by Figure 2, consists of an internal Inconel 625 vacuum liner that contains the high-temperature plasma. The liner is protected by a graphite armor system consisting of 4224 tiles attached to ribs in the liner with Inconel 625 spring clips. The liner is supported by the shell through spacer blocks attached to the outside of the liner ribs. The present design consists of four spacer blocks attached to each of the 80 liner ribs at 90° increments. The spacer blocks encompass 120° around each liner rib, 30° per segment. The magnetic and vacuum loads from the liner are transmitted to the shell through these spacer blocks. Figure 3 shows a 22.5° segment of the shell structure and cooling jacket. The shell consists of an external stainless steel support structure joined to an internal double-walled stainless steel water cooling jacket attached to the structure with bolt on clips.

The finite element model was created directly from Unigraphics II geometry using the Graphics Finite Element Modeling software (GFEM). The geometry was the actual layout of the structural cage and water cooling jacket that had been previously developed. The wire frame 3-D model, shown in figure 4, was created from that layout. Figure 5 shows the wire frame model after it had been surfaced in preparation for the generation of elements. Once the model is surfaced, it is ready for element generation and is meshed, as shown in figure 6. The flanges, channel sections, and liner were modeled using 8-node elements that allow for curved surfaces. The asymmetric magnetic forces that act on the shell were introduced locally in the model using moments, point loads and pressure vectors. Because of the complex interaction of the magnetic loads from the inner vacuum liner to the shell, a second inner shell, representing the vacuum liner, was used to apply the correct loading distribution from the vacuum liner to the shell support structure. The loading is non uniform around the minor diameter and varies from approximately 175 to 195 psi for a worst case plasma termination, during which current flow is transferred from the plasma to the liner. The interaction between the vacuum liner and the shell support structure was accomplished with the use of specialized elements that allow only reaction of compressive forces. This element capability was necessary to provide resultant load transfer from the vacuum liner to the shell support structure in localized areas in which spacer rings are attached to the vacuum liner for positioning within the shell structure.

Magnetic loads are also introduced into the shell from current flow in the copper liner on the inside of the water cooling jacket, These loads vary between 1 to 8 psi around the minor diameter. Additionally, loads are transferred to the shell structure from the poloidal magnets. A net radial inward load of 11,000 lb and an overturning couple of 35,000 ft.-lb is introduced into the shell structure from each of the 48 poloidal magnets. Figure 7 shows a summary of the loading conditions that are presently being considered.

Summary

Because of the complex interactions of the magnetic loads and the modeling of the toroidal shape, the present model is undergoing further development to ensure that the correct approach is used to accurately describe the actual operating system. The combined analytical results with all loads considered should be available soon. The results will be factored into the overall structural design to ensure that the structural design requirements are not exceeded by the operating loads.

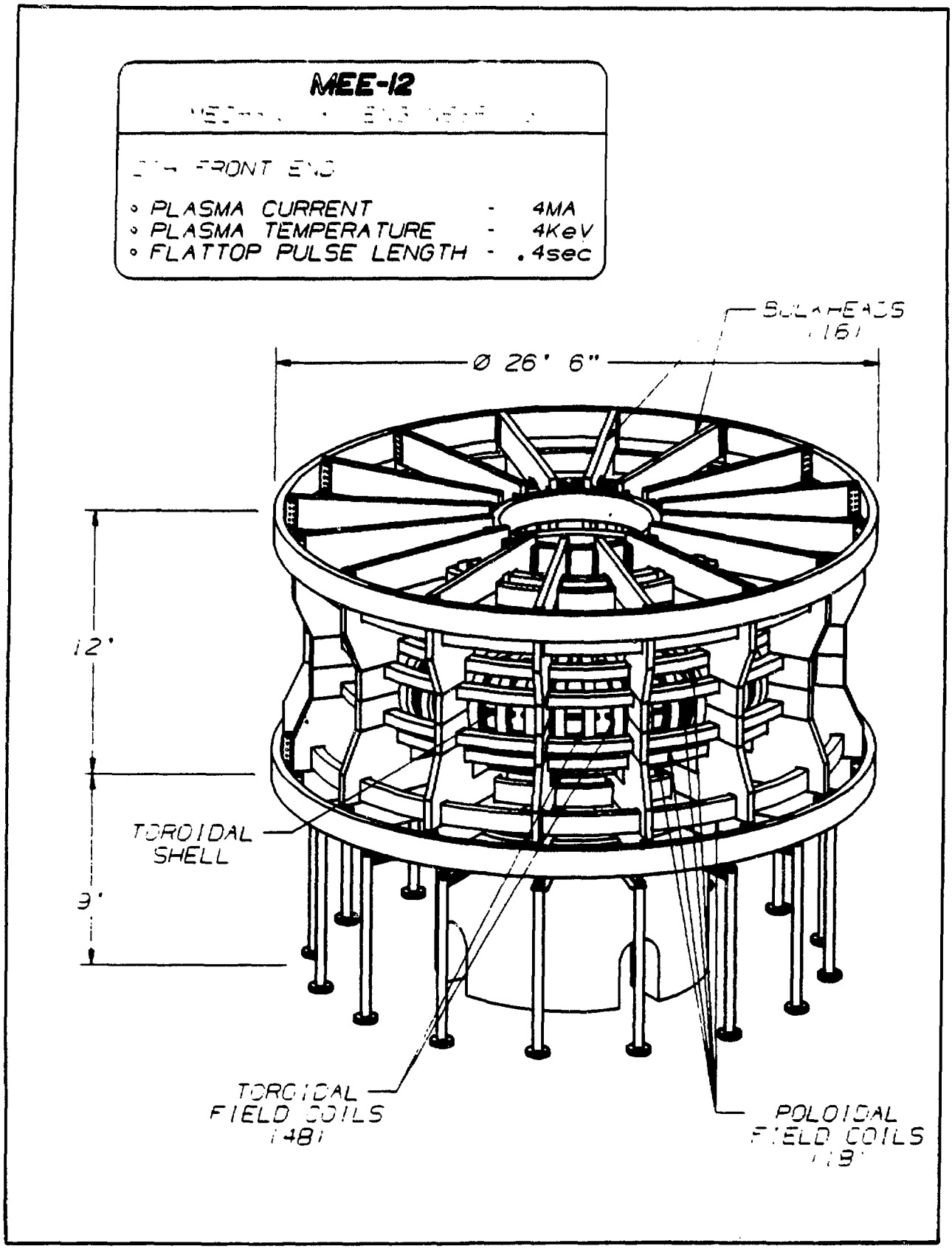
MEE-12
FRONT END
• PLASMA CURRENT - 4MA
• PLASMA TEMPERATURE - 4KeV
• FLATTOP PULSE LENGTH - .4sec
Ø 26' 6"
12'
9'
TOROIDAL SHELL
TOROIDAL FIELD COILS (48)
POLOIDAL FIELD COILS

Figure 1

FIGURE 2

MEE-12
MECHANICAL ENGINEERING
ZTH SHELL

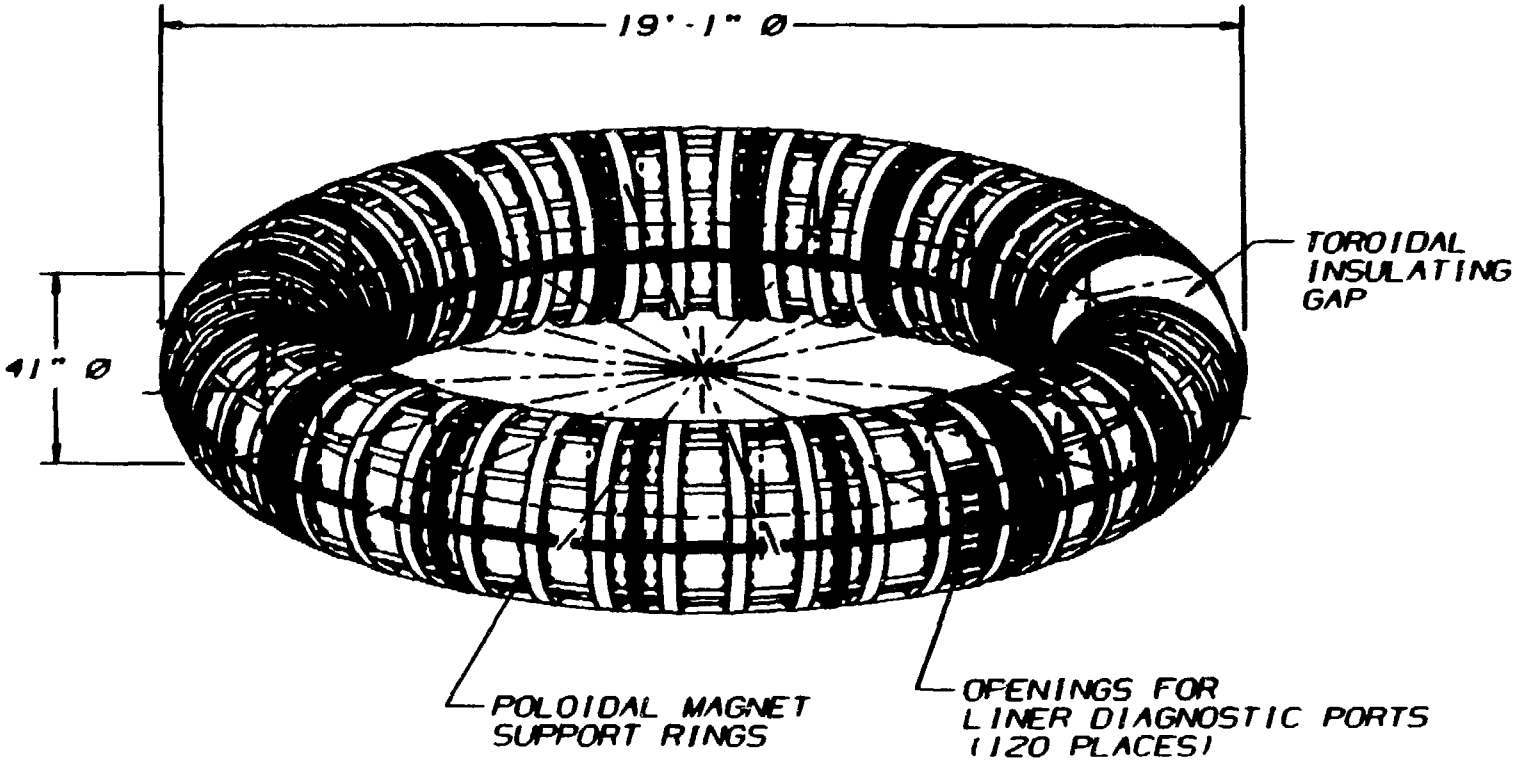

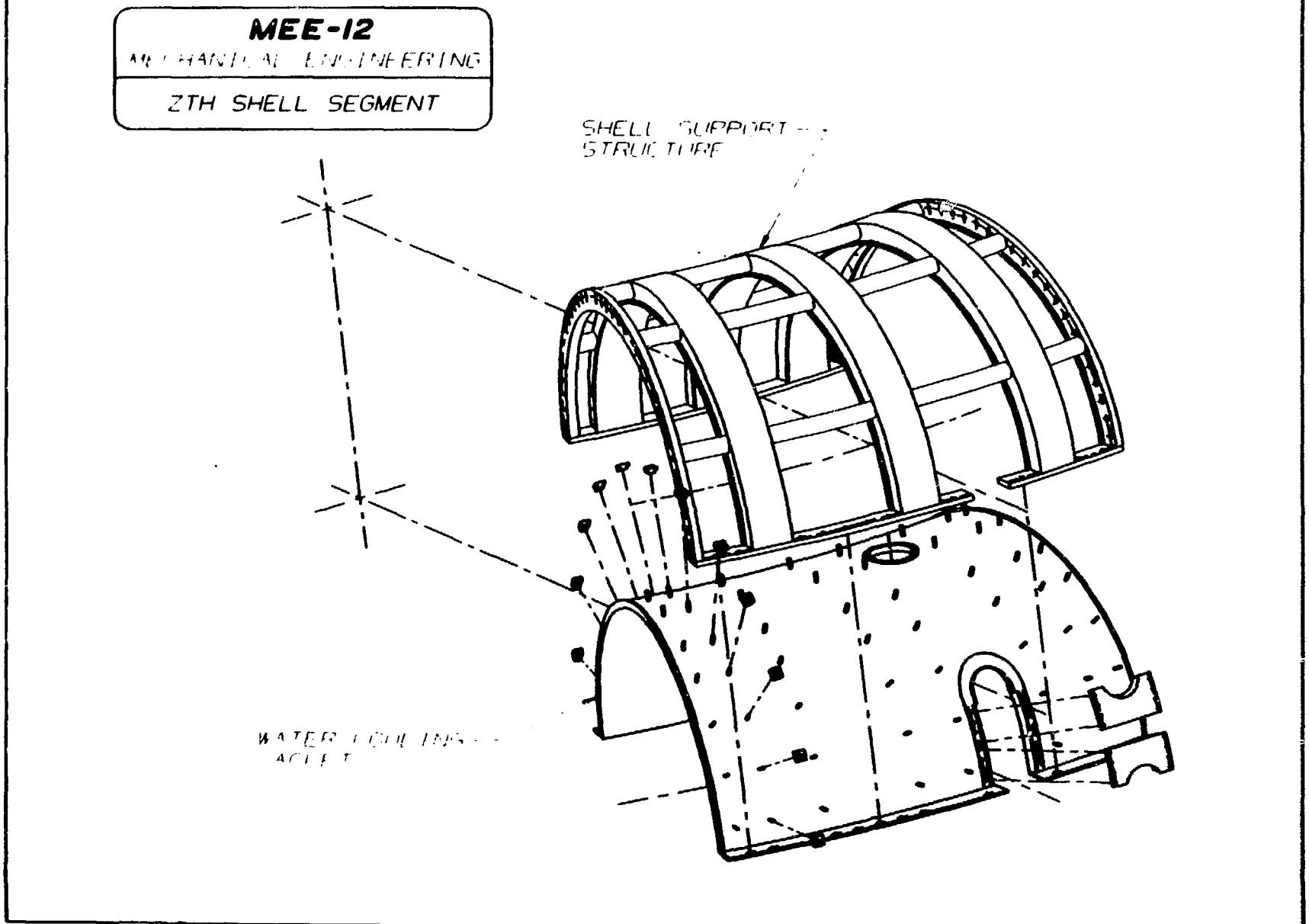
MEE-12
MECHANICAL ENGINEERING
ZTH SHELL SEGMENT
SHELL SUPPORT
STRUCTURE

Figure 3

MEE-12

MECHANICAL ENGINEERING

WIRE-FRAME MODEL OF ZTH SHELL STRUCTURE

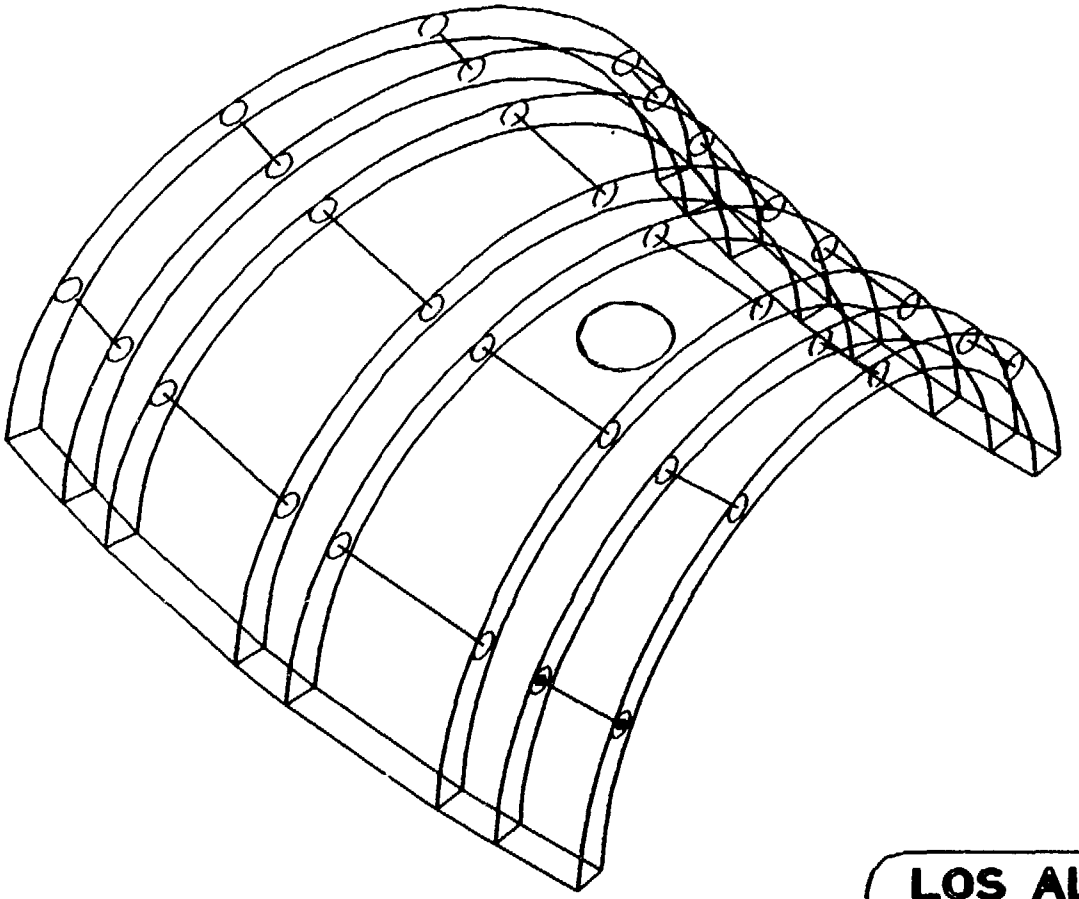

LOS ALAMOS

MECHANICAL AND ELECTRONIC ENGINEERING DIVISION

MEE-12

MECHANICAL ENGINEERING

SURFACES OF ZTH SHELL STRUCTURE

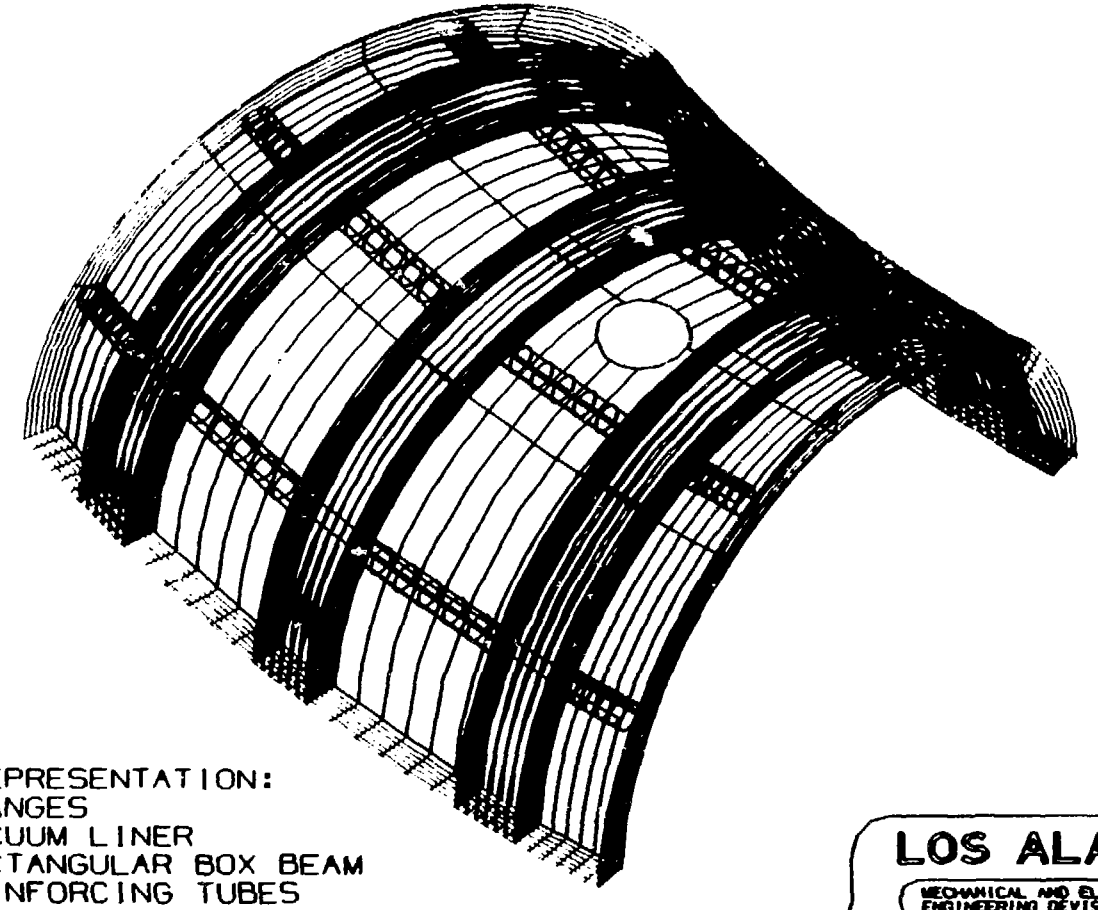

SURFACE REPRESENTATION:
CYAN - FLANGES
RED - VACUUM LINER
GREEN- RECTANGULAR BOX BEAM
BLUE - REINFORCING TUBES

LOS ALAMOS

MECHANICAL AND ELECTRONIC ENGINEERING DIVISION

Figure 5

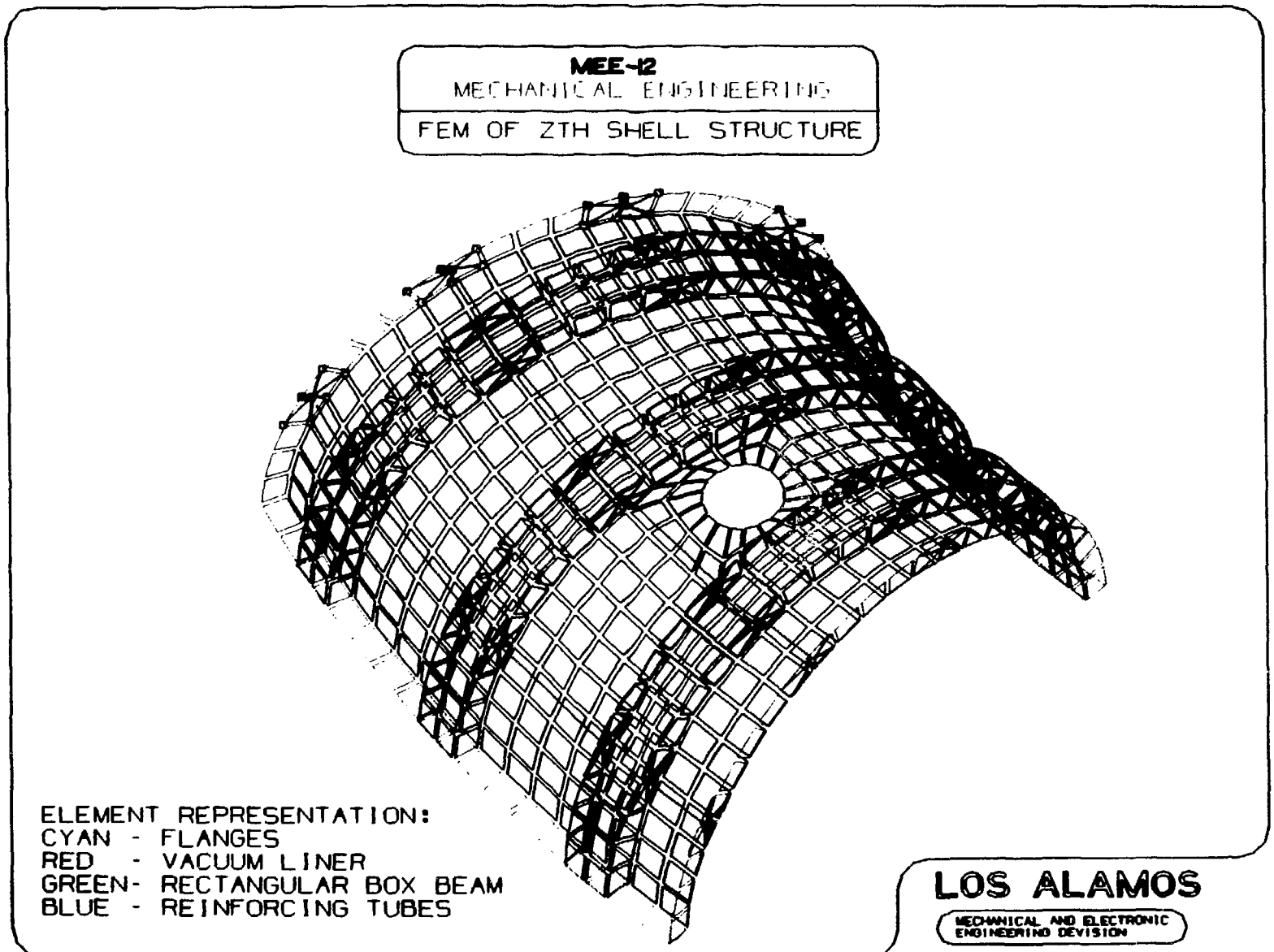
MEE-12
MECHANICAL ENGINEERING
FEM OF ZTH SHELL STRUCTURE
ELEMENT REPRESENTATION:
CYAN - FLANGES
RED - VACUUM LINER
GREEN- RECTANGULAR BOX BEAM
BLUE - REINFORCING TUBES
LOS ALAMOS
MECHANICAL AND ELECTRONIC ENGINEERING DIVISION

Figure 6

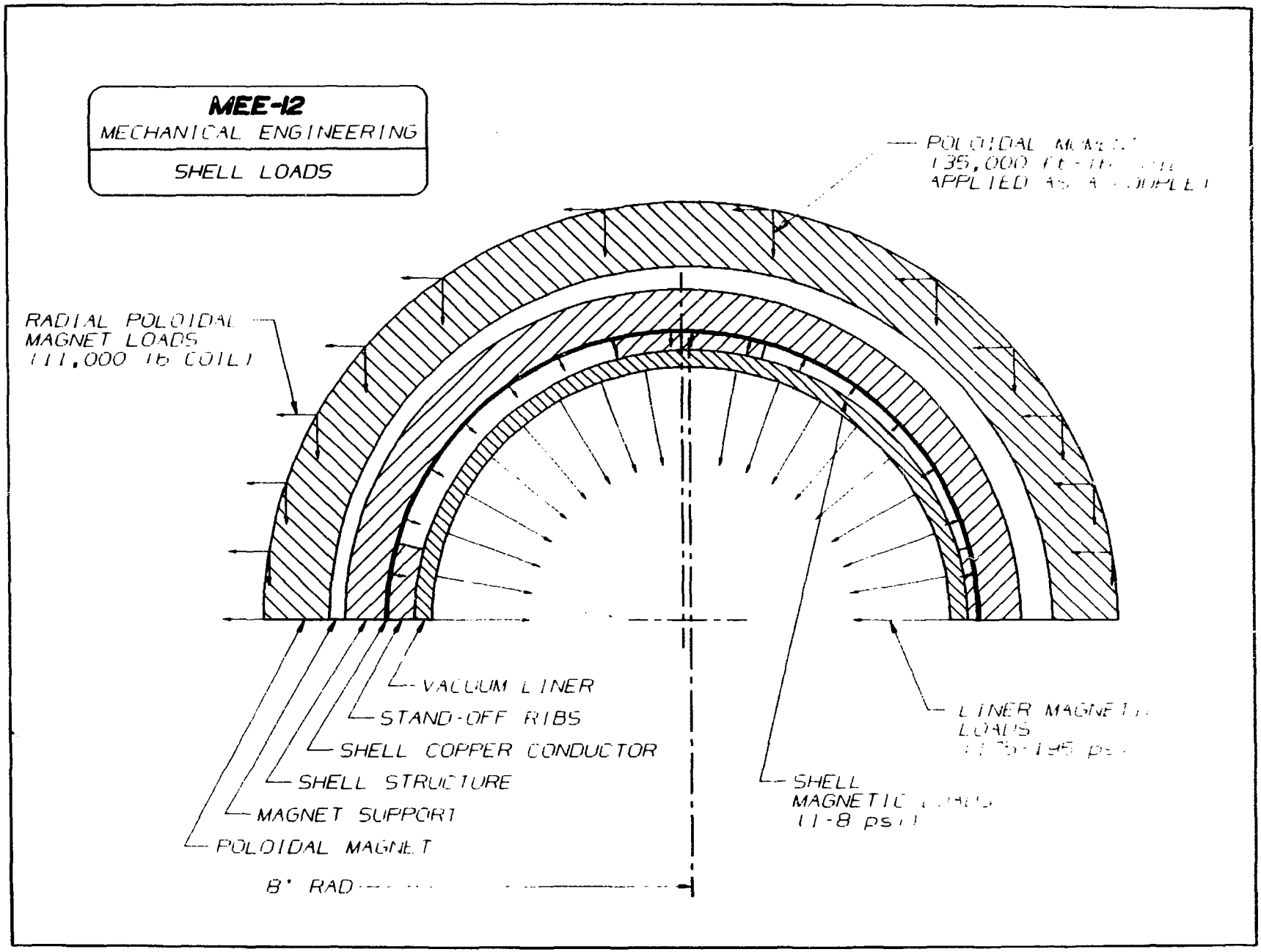

Figure 7

391/3/92

VACUUM/GAS HANDLING SYSTEMS FOR ZTH*

by
J.N. Downing

Los Alamos National Laboratory
P.O. Box 1663, M.S. F648
Los Alamos, NM 87545

Overview

The proposed ZTH vacuum system consists of three (potentially four or more) high-vacuum-pumping-stations (HVPSs), a gas handling system, a roughing system, and a vacuum control system. Figs. 1 and 2 show a plan view of the torus and HVPSs, and Fig. 3 shows an elevation view. A HVPS is shown schematically in Figs. 4. Each high vacuum line consists of a turbomolecular pump (TMP) pumping stack connected to the to the torus through a 29.9-cm-i.d. right-angle valve, a 29.9-cm-i.d., 156-cm-long duct, and a 2 kV insulating break/bellows combination. The HVPSs are designed to be bakeable to at least 150 C. The gate seals on the high-vacuum valves are viton O-rings. Throughout the vacuum liner and high-vacuum pumping system metal sealed joints are used where possible. Any O-ring seals, other than the gate seals, are a double-pumped configuration where a roughing vacuum is maintained between the O-rings.

The insulating break eliminates ground loop currents, and the bellows mechanically decouples the pumping from the vacuum liner. This bellows section will accommodate the dimensional changes caused by heating the liner and/or the high-vacuum system. Expanded views of the insulating break/bellows combination are shown in Figs. 5 and 6. Both a brazed ceramic break and a double-pumped O-ring sealed break are under consideration.

The roughing system for the torus will be located at one of the high-vacuum stations as shown schematically in Fig. 4. This system is also used for pumping the high gas throughput during discharge cleaning procedures at pressures larger than 10^{-1} mbar.

The large magnetic fields near ZTH during operation require that the TMP be located approximately 5-m from the center of the machine. This location will ensure that the magnetic field at the pump location is less than 1300-G for 4.0-s. A cycle time of 600-s gives a duty factor of 0.007 which is within acceptable limits for a TMP in this magnetic field. Depending on the exact choice of TMP and/or the inclusion of flux return conductors in the experiment, these dimensions could change.

The primary danger associated with operating a number of TMPs in parallel is the fault mode where one of the pumps slows down or stops due to an undetected malfunction. The other pumps can maintain the pressure at 67 - 75 % of the original pressure, however, oil can backstream through the non-functioning pump, which causes hydrocarbon contamination of the system before the pressure increases significantly. The control system will monitor the rotaton speeds of the TMPs, and residual gas analyzers will monitor the performance of the system and detect hydrocarbon contamination at the earliest possible stage. If an unacceptable decrease in the rotor speed occurs and/or hydrocarbon contamination is detected, the control system will isolate the pump from the high-vacuum liner, turn the pump off, and vent the pump to atmospheric pressure with dry air or inert gas.

Pumping Ports

The pumping port design can have a significant effect on field errors.

* Work performed under the auspices of the USDOE

The port can cause unacceptable field errors if they are large enough to requires deviation of the toroidal or poloidal field coils, or result in large openings in the shell or liner. A maximum port o.d. in the vacuum liner of 102-mm can be accommodated within the specification for the maximum hole size in the conducting shell established by the Technical Steering Committee. A cross-section view of the pumping port and interface components is shown in Figs. 5 and 6. The tubulations are flared to make use of the maximum space between the toroidal field coils; however, this section is the limiting conductance in the system and has a conductance of 350 l/s (nitrogen at 20 C).

High-Vacuum Pumping Station

The initial configuration will consist of three HVPSs located 90 degrees toroidally apart. A TMP pumping station consists of a TMP, a Roots blower (RB), and a two-stage roughing pump (RP). This pumping stack is connected to the 156-cm long vacuum duct through a 29.9-cm-i.d. right-angle valve and a short ported section. The high-vacuum duct is connected to the torus interface through a 29.9-cm-i.d. bellows and insulating break.

A ported section is provided between the isolation valves and each pump. These ports are used for mounting vacuum diagnostics such as capacitance manometers (CM) and a residual gas analyzer (RGA). The CMs are used for interlock purposes and are constructed so that only stainless steel and Inconel are exposed to the high-vacuum environment. The RGA monitors the performance of the pumping stack. Similar diagnostics are located on the high-vacuum duct.

The TMP pumping station is designed to be a stand-alone sub-system in which the connection to the vacuum liner is the only physical connection between the stations. Rather than sharing a common roughing system this approach uses smaller roughing packages that are dedicated to the stations and provides a separate roughing system for the vacuum liner. Numerous valves, insulating-breaks, pressure sensors, and the interlocks required to operated safely are eliminated. The individual TMP stations require no valves between the TMP and the RP. These simplifications should result in improved overall system reliability.

Anticipated Vacuum System Performance

Estimates of the total pumping speed (S_T), characteristic pumping time (t), and the base pressure (P_u) have been calculated for nitrogen at 20 C and are shown in Table 1. Three pumping stations have been assumed with a TMP pumping speed (S_p)of 2200 l/s.

TABLE 1.

Parameter	Value
S_T (l/s)	735
t (s)	11
P_u (mbar)	1.6×10^{-7}

Equivalent values for deuterium are S_T = 1600 l/s when S_p = 2800 l/s. For

these calculations, the vacuum liner had an estimated volume of 8070 l and a total outgassing/leak rate of 10^{-4} mbar-l/s.

High Vacuum System Figure-of-Merit

During high power discharges and discharge cleaning particles are evolved from the surface and either return to the surface or are removed through the pumping ducts. The ratio of the pumping speed (S_p) at the inside surface of the vacuum liner to the conductance of the torus interface (C_p) is equal the probability of the particle being removed if it enters the pumping duct:

$$(S_p/C_p) = [S_{eff}/(S_{eff}+C_p)$$

where S_{eff} is the effective pumping speed at the torus interface. The conductance, C_p, can be written as

$$C_p = 11.6\ A_p P_{1-2}$$

where A_p is the total area of the pumping ports and P_{1-2} is the probability that a particle which enters the pumping ports will reach the pumping duct. Combining the two equations and dividing by the simple (no convolution factor) surface area of the torus, A, gives

$$(S_p/A) = (11.6)(P_{1-2})(A_p/A)$$

which is a figure-of-merit for the removal of particles from the torus. The quantity (A_p/A) is the probability of the particle entering a pumping port; therefore, the product of the last three terms on the right-hand side of the equation is a measure of probability of a particle being exhausted during a single discharge or cycle of discharge cleaning if the sticking coefficient is equal to 1. If the sticking coefficient is less than 1, then the probability of removal is correspondingly higher. Since A_p/A is usually quite small ($\approx 10^{-3}$), many cycles are required to exhaust the average particle. For tokamaks, S_{eff} would be taken as the pumping speed of the pumps and C_p would be the conductance of the pumping duct. A comparison of the parameter S_p/A for several machines is given below:

MACHINE	S_p/A ($l/s\text{-}m^2$)
DIII	56.3
DIIID	130.0
Textor	184.0
TFTR	13.1
JET	8.0
RFX	131.0
ZTH	19.3
ZT-P	20.8
ZT-40M	4.3(Glow Discharge Cleaning)
ZT-40M	13.2(Pulse Discharge Cleaning)

ZTH compares favorably with the larger machines, but not with the machines that are a similar size (RFX, Textor, DIII). As a consequence, the rate of impurity removal per Discharge Cleaning cycle for ZTH will be similar to that in ZT-P, ZT-40M, and TFTR.

Roughing System

The proposed roughing system has been designed to have: (1) a characteristic pump-down time of less than 25 minutes for a volume of 8070 l, (2) full protection against backstreaming of oil, and (3) electrical isolation of $\geq$ 2 kV. The Roughing System is also shown schematically in Fig. 4. A single stage Roots blower with a pumping speed of 1340 l/s is used with a two stage backing pump(s) that has(have) a pumping speed of 100 l/s (each). This system should reach a pressure of 10^{-4} mbar in approximately 12 - 25 min. depending on the size and length of the vacuum line connecting the pump to the vacuum liner. To protect against the backstreaming of oil in the molecular flow and transition regimes, a liquid nitrogen cold trap is placed between the Roots inlet and the vacuum liner, and a Cu-wool trap is placed between the backing pump and the outlet of the Roots blower. A viscous flow condition is maintained in the roughing line when the Roots blower is off and/or the cold trap is not at the proper temperature with an automatic system which injects nitrogen above the cold trap.

Gas Handling System

The gas handling system is capable of supplying high purity hydrogen or deutrium for (1) the continuous flow during discharges, (2) the gas injection system, and (3) the discharge cleaning procedures. Provision has also been made for supplying dry impurity gases for injection during the discharge or backfilling the torus. The initial fill pressure in the torus prior to discharges is adjustable over the range of 3.2×10^{-4} to 1.3×10^{-3} mbar and reproducible to $\pm$ 2 %. During the discharge, gas injection rates of $\leq$ 130 mbar-l/s-valve is available with provision for programming the pulse shape. The individual units are electrically isolated to prevent current flow in the plumbing.

The gas handling system has its own roughing system, TMP system, and RGA and is fully interlocked to protect the torus during any malfuction. A schematic draving of the gas system is shown in Fig. 7. Palladium purifiers are used to insure the purity of the hydrogen and deuterium gases and a drying system is supplied for the impurity/backfill gas. The content of the gas systems is monitored by the RGA system.

The proposed gas injection system consists of a number of injection valves. These may be utilized as needed for (1) initial discharge pressure control, (2) gas injection during the discharge, (3) the introduction of impurity gases, and (4) gas pressure control during discharge cleaning. By selecting the number and location of the injection valves, gas can be injected in as many places as necessary to achieve uniformity. To achieve the high flow rates necessary for the gas injectors at least one of the supply lines will operate at 1.7 - 6.8 bar (10 - 100 psig). Each gas supply has its pressure regulated automatically by a feedback-controlled servo valve. Each injection valve is electrically isolated by a high-voltage insulating break. The injection valves will be either the piezoelectric

type or the bellows sealed air actuated type which have been used on ZT-40M.

Control System

The control system design for the high vacuum system, roughing system, and the gas handling system is consistent with the overall system control philosophy. A fail-to-safe-condition is applied throughout the design.

A subsystem control computer is used for interlock protection and sequencing events associated with the discharges and discharge cleaning procedures. Digital signals from limit switches on valves, pressure sensors, temperature sensors, power sensors, and the RGAs will be utilized in the interlock sequences. Some analog signals are also used for interlock purposes. Both the analog and digital signals are transmitted to the controller over fiber optic links to provide for electrical isolation. If an interlock sequence is broken at any time, the system will go to a safe condition and notify the operator of the problem.

If the subsystem control computer is not sufficiently reliable to protect the vacuum liner, a programmable controller will be installed in series with the control signals from the computer. A representative subsystem control computer and many of the electrical components are being tested on ZT-P which provides the same type of high magnetic field environment as ZTH.

Residual Gas Analyzer (RGA) System

Mass spectrometric analysis has become a useful plasma diagnostic technique for fusion plasmas. It is the primary diagnostic used for optimizing and process monitoring of plasma discharge cleaning techniques which have been developed for the conditioning of the vacuum vessels of fusion devices and particle accelerators.

On ZTH the residual gas spectra of the vacuum liner and vacuum systems will be monitored continuously with a differentially pumped RGA system. A schematic drawing is shown in Fig. 8 and a line drawing is shown in Fig. 9. Either of two pressure reducing aperatures or a direct connection to the system can be selected. The size of the aperatures are chosen to optimize the sensitivity of the RGA system for the different pressure ranges used for glow discharge cleaning and normal discharges. A 50 l/s TMP is used for the differential pumping, and pressure sensors are used to provide interlock inputs for the control system. The entire system will be temperature controlled for bakeout and/or operation at > 100 C.

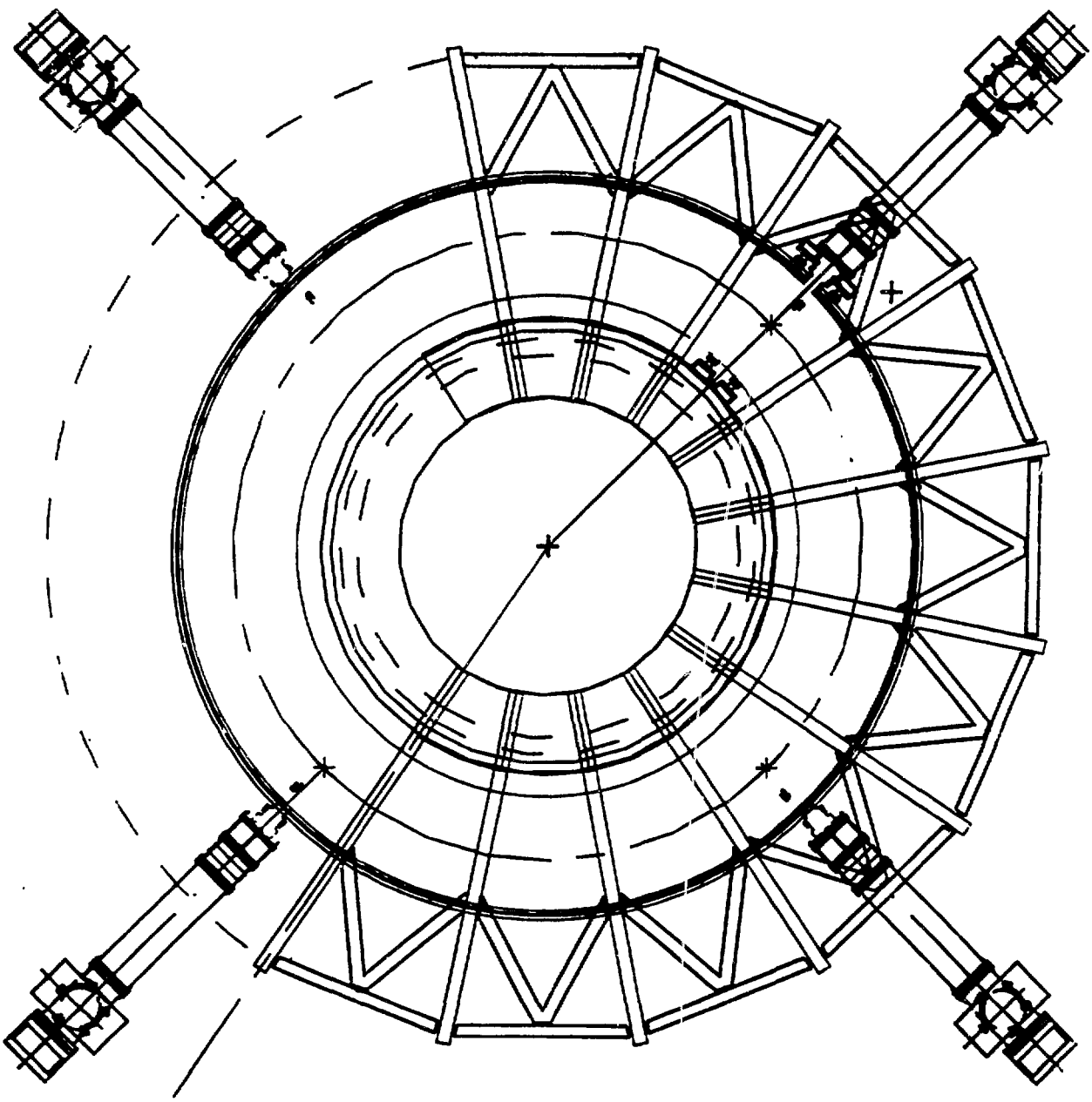

Fig. 1.

A plan view line drawing showing the location of four HVPSs around the torus.

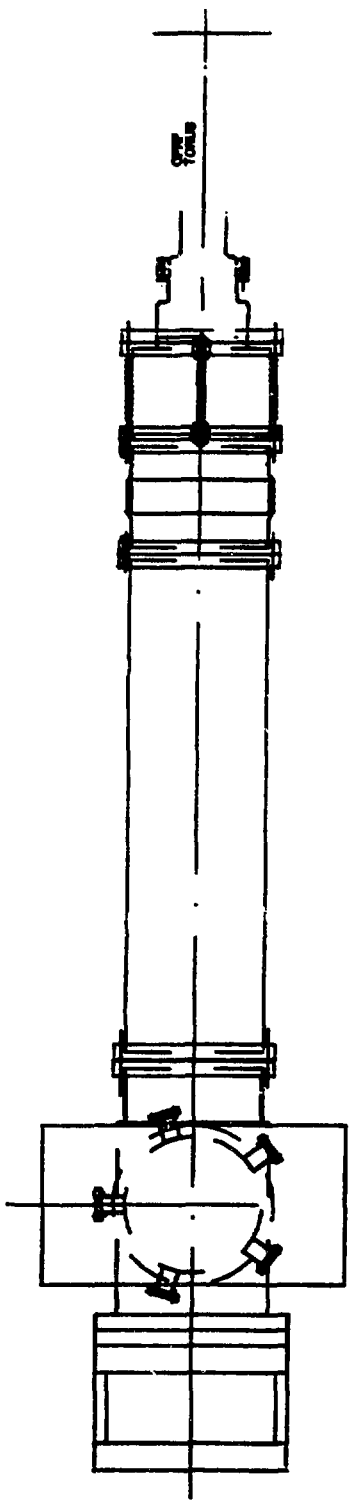

Fig. 2.
A plan view line drawing showing one HVPS.

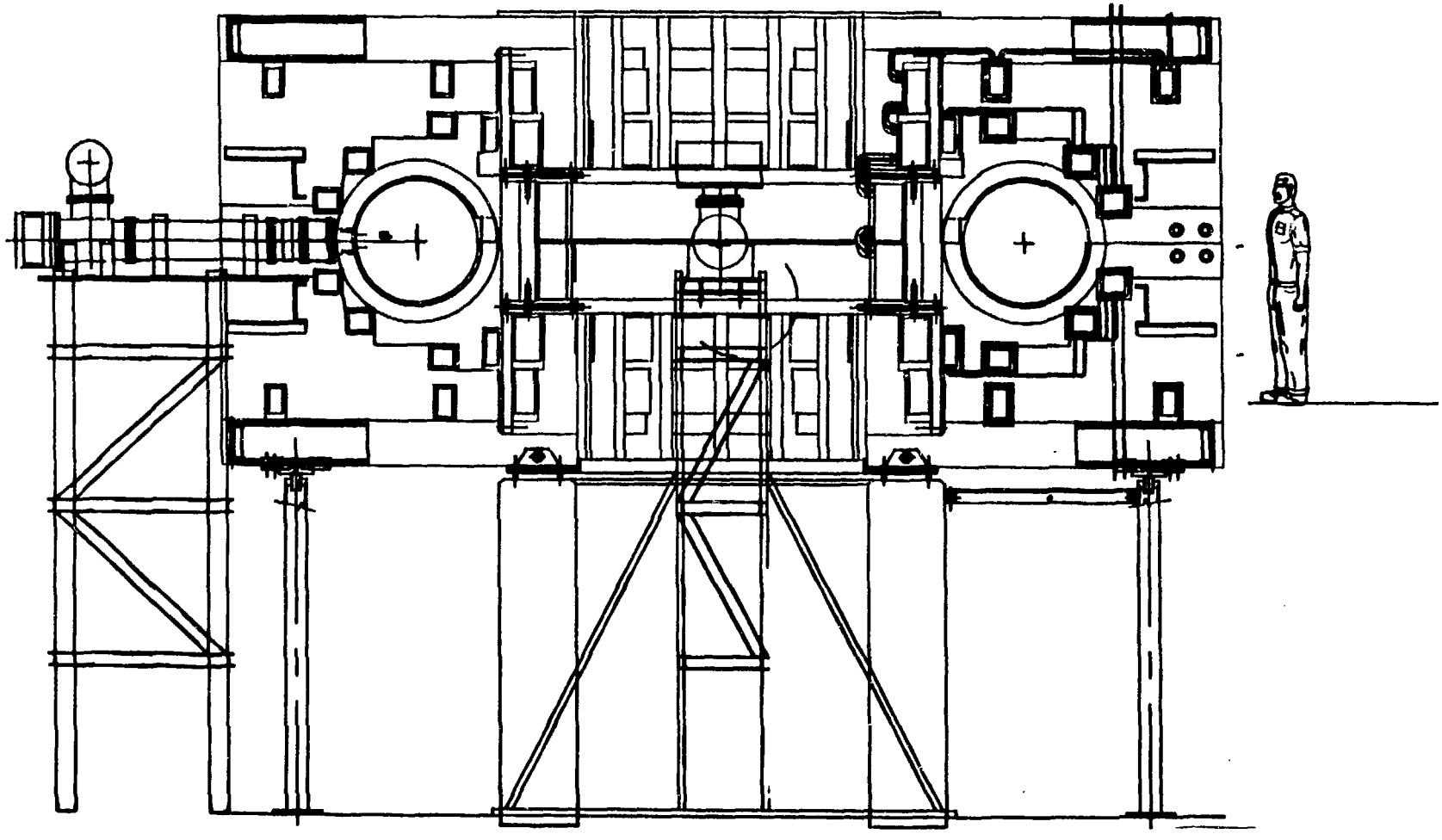

Fig. 3.
An elevation view of ZTH showing the location of the HVPSs.

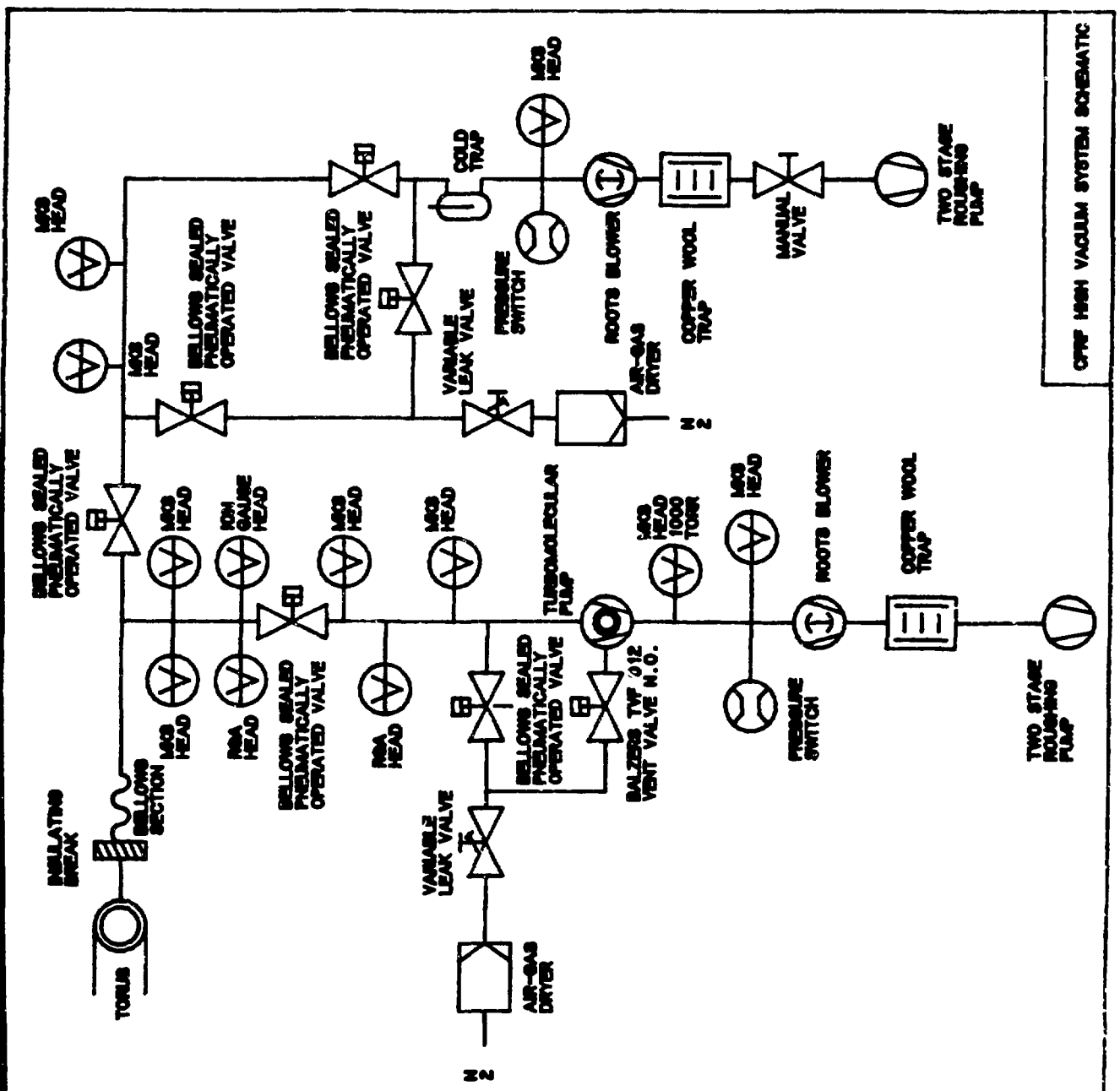

Fig. 4.
A schematic drawing of an HVPS and the Roughing System.

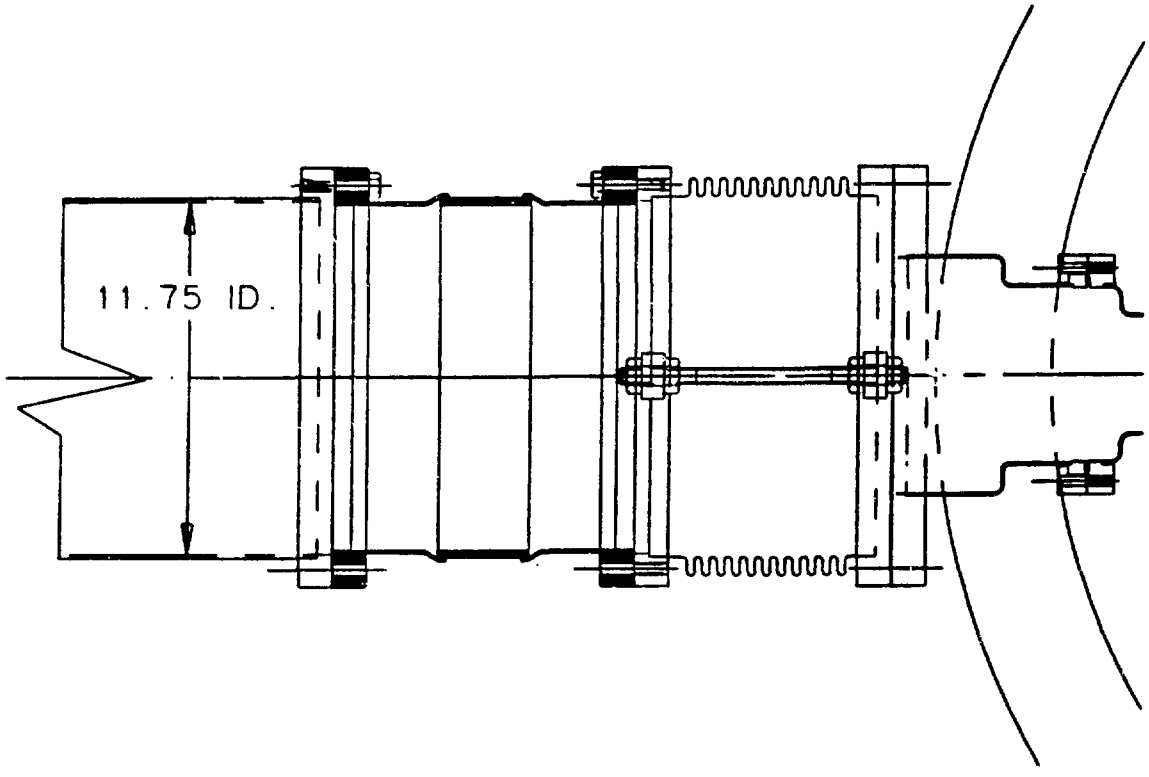

Fig. 5.
An enlarged view of the torus interface components with a brazed ceramic insulating break.

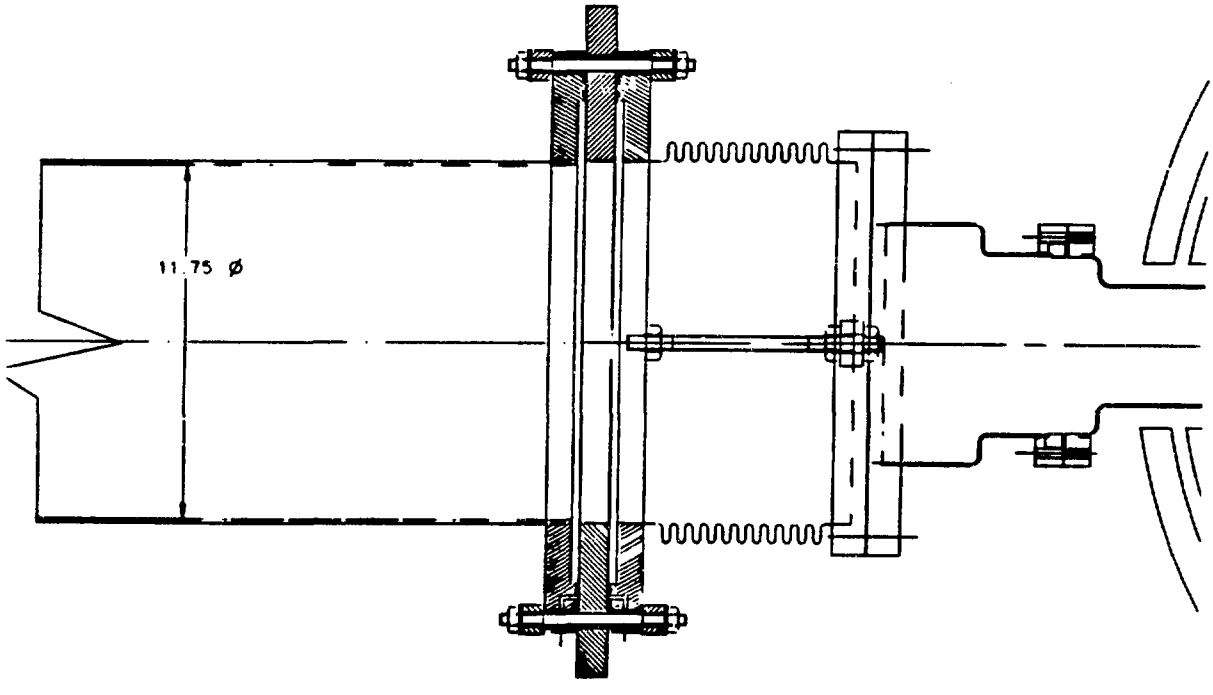

Fig. 6.
An enlarged view of the torus interface components with a double-pumped O-ring sealed insulating break.

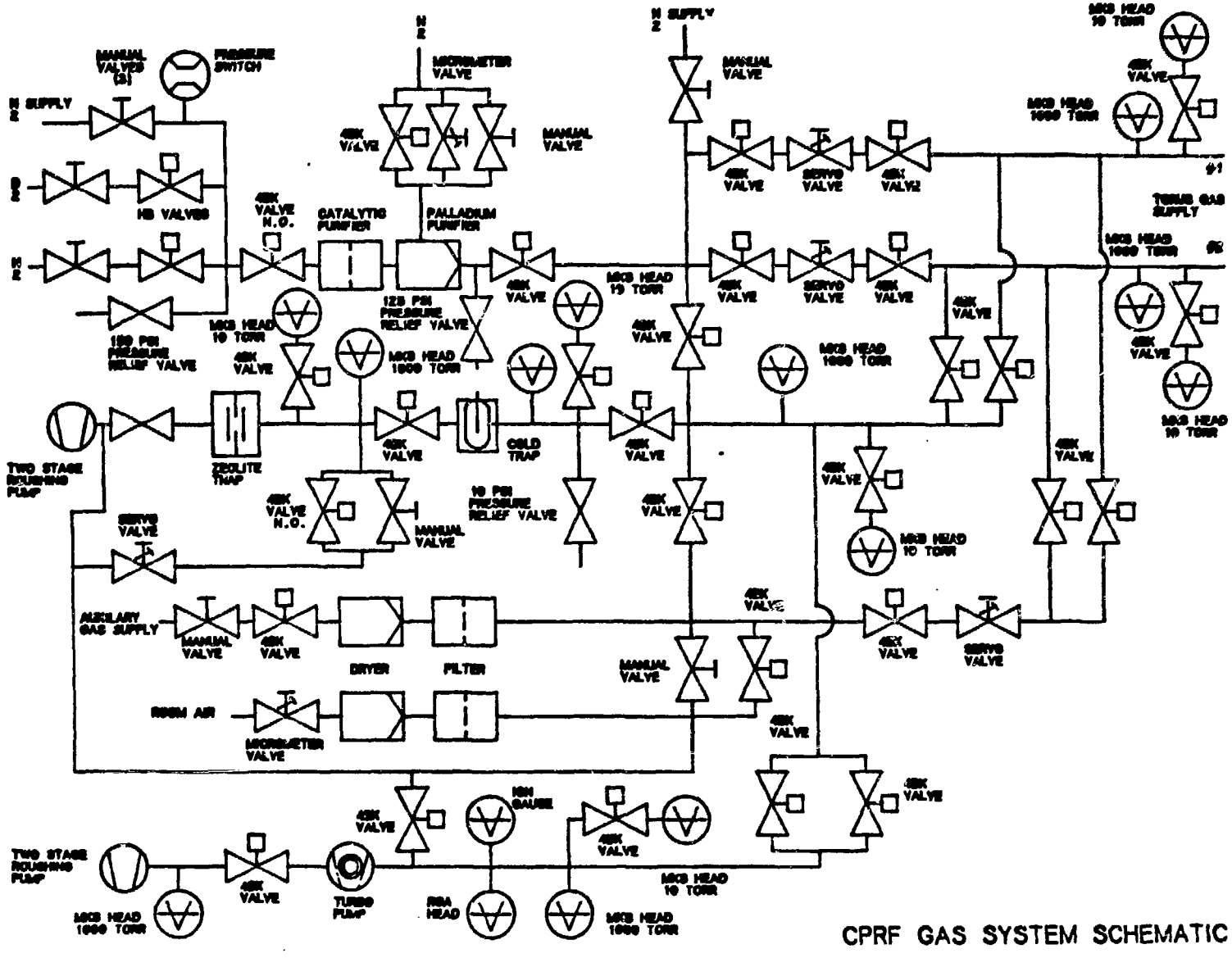

Fig. 7.
A schematic drawing of the Gas Handling System.

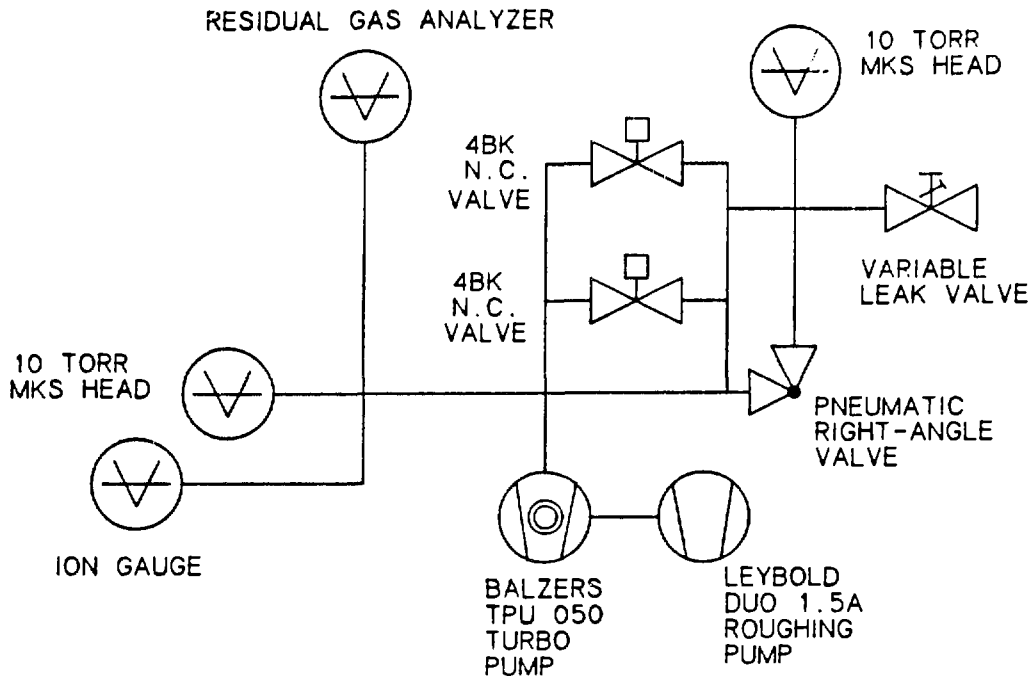

Fig. 8.
A schematic drawing of the RGA System.

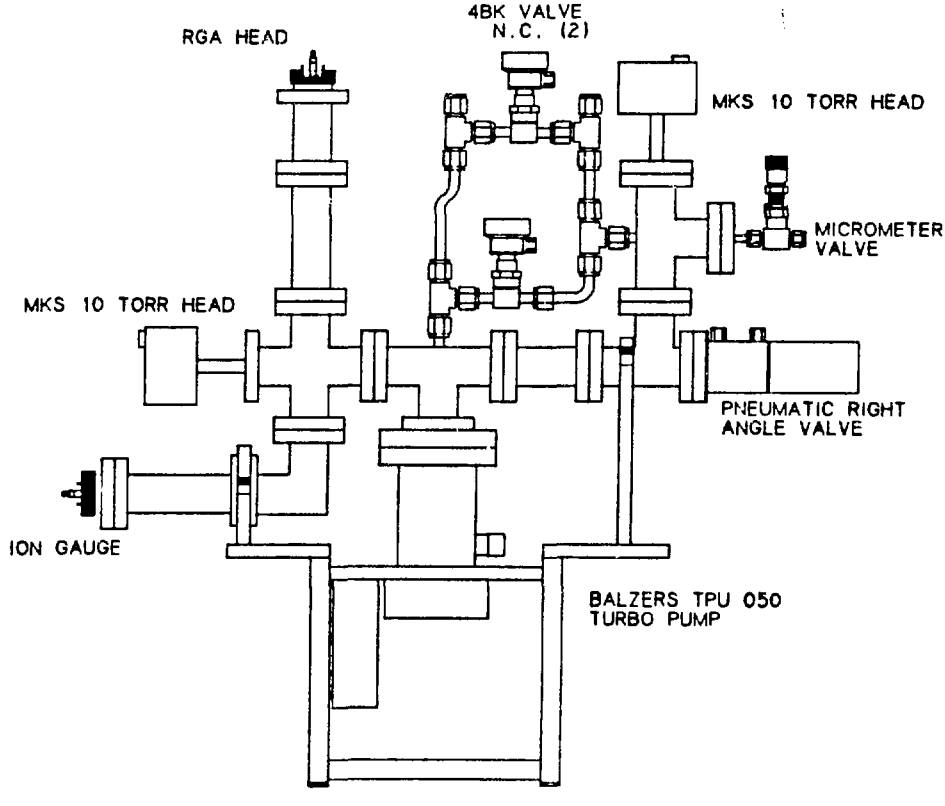

Fig. 9.
A line drawing of the RGA System.

ARMOR/HEAT FLUX DESIGN FOR ZTH

by
J.N. Downing

Los Alamos National Laboratory
P.O. Box 1663, M.S. F648
Los Alamos, NM 87545

INTRODUCTION

A simplified model for the scrape-off layer (SOL) in Reversed-Field Pinches (RFPs) has been developed and applied to CPRF/ZTH. The objectives of this exercise are (a) to determine the sensitivity of the poloidal heat flux distribution as a function of plasma position, (b) to estimate the heat flux enhancement resulting from the removal of armor or wall material, and (c) to estimate the impact of magnetic field errors on the heat flux distribution. The heat flux distribution in the SOL was assumed to be described by an exponential with a characteristic scrape-off length ($\lambda_\perp$ = 0.2 - 2.0-cm). In RFPs a significant electron drift velocity compared with the thermal velocity is observed. This characteristic results in an enhancement in the heat flux by a factor of two for small ($\leq 0.25\lambda_\perp$) equilibrium shifts. Additional peaking of the heat flux results from larger ($\geq 0.25\ \lambda_\perp$) equilibrium shifts and/or the removal of sections of the armor. When a section of the armor is removed (such as in the area of ports) and the equilibrium is shifted, the field lines can intercept the armor segments around the missing segment in small areas and can produce peaking factors (PFs) in the range of 10-1000. The armor above the missing armor element and/or the edges of the armor must be contoured to keep the heat flux to an acceptable level. Radial transport also occurs within the dimensions of the missing armor. This transport was modeled using the same basic assumptions as above and was included in the analysis. The front-surface temperatures have been estimated for flat tiles with the nominal and maximum time-dependent heat fluxes anticipated for ZTH. The maximum front surface temperature is estimated to be 1500 K at the design point.

HEAT FLUX MODEL

The basic assumption of this model is that the heat flux distribution in the scrape-off layer (SOL) can be described by the following relationship:

$$F(r) = F_o \exp[-(r-a)/\lambda_\perp] \qquad (1)$$

where r is the radius of the plasma in the SOL, a is the radius of the last closed field line, $\lambda_\perp$ is the characteristic scrape-off-length, F_o is the uniform equivalent power flux, and F(r) is the uniform power flux through the flux surface at radius r (i.e., normal to the field line). The plasma-wall interaction is modeled as shown in Fig. 1 where the plasma is a cylinder offset from the larger cylinder of the wall armor. The radius of the wall armor is β, Δa is the horizontal shift of the plasma column, and θ is the angle measured from the major radial direction (horizontal). If the plasma flux is primarily along field lines ($V_\parallel \gg V_\perp$), the flux on the surface of the armor (F_w) is given by

$$(F_w \Delta A/F_s) = (2\pi R)(2\pi)[[r_2(1-\theta_2/180)\exp[-(r_2-a)/\lambda_i] - [r_1(1-\theta_1/180)\exp[-(r_1-a)/\lambda_i]] \quad (2)$$

where ΔA is the incremental surface area of the armor on which the heat flux is deposited and R is the major radius of the armor. In RFPs a large electron drift velocity compared to the thermal velocity is observed. This characteristic results in the particle flux being collected on only the upper half of the armor (assuming the electron drift is counterclockwise in Fig. 1). This anisotrophy in heat flow results in an enhancement in the heat flux by a factor of 2 for small equilibrium shifts. Additional peaking of the heat flux results from equilibrium shifts that are $\geq \lambda_i$ and/or the removal of sections of the armor.

For a continuous cylindrically shaped armor segment

$$\Delta A = (2\pi R)(2\pi a)(\emptyset_1 - \emptyset_2)/360). \quad (3)$$

where $\emptyset_2$ and $\emptyset_1$ are the angles corresponding to r_2 and r_1, respectively, with the center of the armor as the reference. The normalized distribution of heat flux and the peaking factor (PF) are shown as a function of poloidal angle, $\emptyset$, in Fig. 2. For this calculation $(\Delta a/\lambda_i) = 1$. Calculations for 2TH are shown in Fig. 3, where the maximum PF and corresponding angle are plotted versus the shift of the plasma column in units of λ_i. The maximum peaking factors vary from $\approx 2 - 8$ for reasonable shifts, and the angle of maximum flux decreases from 90° (for very small shifts) to less than 30° (for the larger shifts).

If the plasma shifts vertically, the heat flux distributions are the same as calculated per Fig. 1, but the symmetry axis is no longer horizontal. The new axis is given by a line through the axis of the armor and the new axis of the plasma. The angle is determined from tan $\Delta x/\Delta a$ where Δx is the vertical shift.

When a section of the armor is removed, the field lines intercept the armor in a much smaller area. This case is illustrated in Fig. 1., where the section of wall armor removed is between angles θ_1 and θ_2. and for the armor immediately below a missing armor segment (in the electron flow direction)

$$\Delta A = ((2\pi R)(r_1 - r_2))/\cos(\theta_2 - \emptyset_2) \quad (4)$$

The enhancement factor is given by

$$\frac{(2\pi a)(\emptyset_1 - \emptyset_2)/360}{(r_1 - r_2)/\cos(\theta_2 - \emptyset_2)} \quad (5)$$

The enhancement of the heat flux resulting from the removal of the armor segment is approximately equal the poloidal length of the missing armor segment divided by the incremental radius $(r_1 - r_2)$ defined by the edges of the missing armor. Enhancements in the range of 10 - 1000 occur; therefore, the tiles above the missing armor and/or the edges of the armor must be contoured to keep the heat flux to an acceptable level.

Radial transport also occurs within the area of the missing armor and the heat flux extends beyound the radius r_1. This transport can be modeled using the same basic assumptions as in Eq. 1:

$$F(r_m) = F(r_i) \exp[-(r_m - r_i)/\lambda_i^*], \quad (6)$$

where $F(r_m)$ is the flux distribution inside the area of missing armor, $F(r_i)$ is the flux calculated from Eq. 1, r_i is the radius corresponding to the top of the missing armor, r_m is the radius of the plasma inside the area of missing armor, and λ_i^* is the characteristic scrape-off length corresponding to the smaller dimension of the missing armor. $F(r_i)$ is the power flux that would have been deposited on the armor that is missing. This effect is large enough that the surfaces must be contoured to keep the heat flux to acceptable levels. Also, on the axis-of-symmetry,

$$(\theta_m = -\theta_i, \ \phi_m = -\phi_i), \quad (7)$$

this is the only heat flux enhancement contribution.

MAXIMUM HEAT FLUX SPECIFICATIONS

For graphite as the armor material, thermal sublimation suggests an upper limit on the front surface temperature, until the end of the flat-top phase, of 2300 K. A more conservative value of 1500 K was chosen as a design point to avoid normal operation near this upper limit. Redeposition of the evolved atoms on cooler areas of the graphite armor will act to lower the contamination level and the local maximum temperature can be larger than 1500 K if the surface area affected is only a small fraction of the total area. The initial armor temperature can be controlled within a range of 23 C to 200 C.

TABLE I. APPROXIMATE PARAMETER VALUES FOR ZTH FOR 4MA OPERATION

DISCHARGE PHASE	TIME SCALE (ms)	AVERAGE POWER INPUT AT THE DESIGN POINT (MW)	MAXIMUM AVERAGE POWER INPUT (MW)
Startup to 2 MA	50	50	140
Ramp to 4 MA	400	21	60
Flattop	200	28	80
Rampdovn	≤400	14	40

For the purposes of evaluation, four phases of the ZTH discharge are identified. Approximate parameter values for 4 MA operation are given in Table I, and the ZTH design point parameters are given in Table II. The average power-to-the-wall is 0.8 MW/m². With a limit on the graphite front surface temperature of 1500 K and with an initial temperature of 473 K, the maximum power flux (for ATJ graphite) is 13 MW/m². Therefore, the allowable PF is 16 for these conditions.

HEAT FLUX PEAKING FACTORS

Examples of types of field errors which will produce a general equilibrium shift with respect to the armor in ZTH are:

1. tolerances in coil construction
2. tolerances in coil placement
3. tolerances in liner construction
4. tolerances in liner support
5. tolerances in shell construction, and
6. incorrect vertical field.

The shift in the flux surfaces from these errors can easily be of order of $1.0\lambda_i$; therefore, as indicated earlier, the PF is ≈ 2.0. Larger variations in the magnetic flux surface will have to be compensated external to the liner and shell.

TABLE II. DESIGN POINT PARAMETERS FOR ZTH

PARAMETER	VALUE
Plasma Current	4 MA
Magnetic Energy in the Poloidal Field	48 MJ
Plasma Kinetic Energy	4.8 - 9.0 MJ
First Wall Operating Temperature	300 - 523 K
First Wall Bakeout Temperature	573 K
First Wall Area	36 m^2
Maximum Front Surface Temperature to the End of the Flattop Phase of the Discharge	1500 K
Minimum Current Termination Time	1.0 ms
Approximate Total Energy To The First-Wall For Full Discharge Duration	40 MJ

In ohmically heated tokamaks, the flux of particles along the field lines is almost equal in both directions, which implies a thermal distribution with no unidirectional drift velocity. In RFPs, however, a significant electron drift velocity compared with the thermal velocity is observed. This characteristic results in an enhancement in the heat flux by a factor of two for small ($\Delta a \leq 0.25\lambda_i$) equilibrium shifts. Additional peaking of the heat flux results from larger ($\Delta a \geq 0.25\lambda_i$) equilibrium shifts and/or the removal of sections of the armor.

If flat tiles are used, the anisotrophy in heat flux will result in most of the heating on the surface of flat tiles occuring on only 1/2 of the surface. The resulting PF is 2. Of course, shaping the tiles would, in principle, eliminate this PF.

In order to obtain relevant physics data, the operating conditions will be varied. In general, this variance will result in an increase in the input power and a corresponding PF of ≈ 2.5.

The sources of the PFs and their approximate values are summarized in Table III. The minimum PF is 10 (if the tiles are shaped) and 20 (if the tiles are not shaped). In the areas of missing armor the PF will be much larger, and it will be necessary to shape the armor in area around the missing segments.

TABLE III. Heat Flux Peaking Factors (PFs)

Source	Value
Anisotrophy in Heat Flux	≈ 2.0
Equilibrium Shifts and/or Liner/Coil Tolerances	≥ 2.0
Operational Variations	≈ 2.5
Tile Shape Factor	≈ 2.0
Missing Armor Segments	10 - 1000

DESIGN OPTIONS

Average power inputs ≤ 1 MW/m² with equilibrium shifts $\leq \lambda_i$ can be accommodated in areas where the armor has been removed by the symmetric contouring shown schematically in Fig. 4. For this approach, the armor tiles around the missing armor are tapered to provide enough surface area to keep the heat flux to an acceptable level. A symmetric arrangement would allow both of the currents to be reversed, which is considered an important physics requirement. If the energy flow in the plasma edge becomes more isotropic in ZTH compared to currently operating machines, this surface modification would be adequate for ≤ 2 MW/m² depending on the degree of isotrophy.

To accommodate the maximum heat fluxes with the anticipated anisotrophy in heat flux, the flexibility of changing the direction of the currents will probably have to be sacrificed. A nonsymmetric contouring of the tiles will be used as shown schematically in Fig. 5. The tile(s) above the missing armor are tapered toward the plasma to produce a shadow in the area of the missing armor, and the tile(s) below the missing armor are tapered away from the plasma to provide enough surface area to keep the heat flux to an acceptable level. If the degree of anisotrophy in heat flux is less in ZTH, this last scheme can be modified as shown schematically in Fig. 6 to accommodate a small fraction of the heat flux in the ion drift direction.

In the current design, the armor has the following characteristics:

1. Rectangular shape with flat surfaces (22 different basic shapes) and 1 cm thickness.

2. 96 gaps in the toroidal direction.

3. 44 gaps in the poloidal direction.

4. Single support which supplies the electrical/thermal connection.

5. Deviation from the ideal flux surface of ≤1.5 mm over the dimensions of the tile.

The tile is mounted to the liner support structure with a metal clip as shown in Fig. 7. The clip extends 90% of the toroidal length of the tile and fits in a machined groove on the edge of the tile. If remote replacement is required the attachment to the liner will be with the self-locking plunger actuated system shown in the drawing. If remote replacement is not required, the clip will be mounted to the support structure with screws.

Each tile is ≈ 6.6-cm long in the poloidal direction. The toroidal length depends on the major radius of the tiles location and varies from ≈ 17.4-cm on the outside major radius to 12.7-cm on the inside major radius. The gap between tiles is ≈ 4-mm. Tolerances in the liner dimensions will be accommodated by custom trimming the dimensions of each tile. Individual tile shapes will be modified as necessary to relieve areas of excessive heat flux. For example, in the area of diagnostic and pumping ports the tiles will be contoured to keep the heat flux within acceptable limits.

An additional feature of this armor system is the optional incorporation of pumping channels for impurity control. The proposed large-area-pump limiter would remove edge-plasma particles through a uniformly distributed system of slots and channels which perforate the first wall armor.[1] In addition to the slots formed by the edges of the tiles, small holes would be uniformly distributed over the tile surface. The size and distribution of the holes would be determined by thermal stress analysis and simulations of plasma exhaust requirements. The volume behind the armor tiles would serve as a "passive" pump during the length of the plasma discharge.

An alternative to individual tiles in the poloidal direction is under consideration. Gore-shaped C-C composite rings are used as shown in Fig. 8. As seen in the drawing, these rings would probably be attached to the liner support rings in fever places (3 are shown). Radial forces such as might occur during current termination would be absorbed in the armor structure itself. Other advantages of this approach are that 1.) the present liner design can be used without modification, 2.) the poloidal shape will reduce the armor PF over that for flat tiles, 3.) the thickness of the armor and/or the distance between the plasma and the liner might potentially(?) be reduced, and .4) the number of individual elements is reduced. The potential disadvantages of this approach are 1.) fever connections to the liner are used which will impare the removal of heat from the armor structure by conduction 2.) to replace or repair an armor segment the torus must be disassembled, 3.) modifications to the armor to minimize the enhanced heat flux around the ports are difficult and, 4.) the removal of the armor in the area of the holes may make the armor too weak.

REFERENCES

[1] J. N. Downing, "A Large Area Pump Limiter Concept," Proc. 11th Symposium on Fusion Energy, 924-927 (1985).

FIGURES

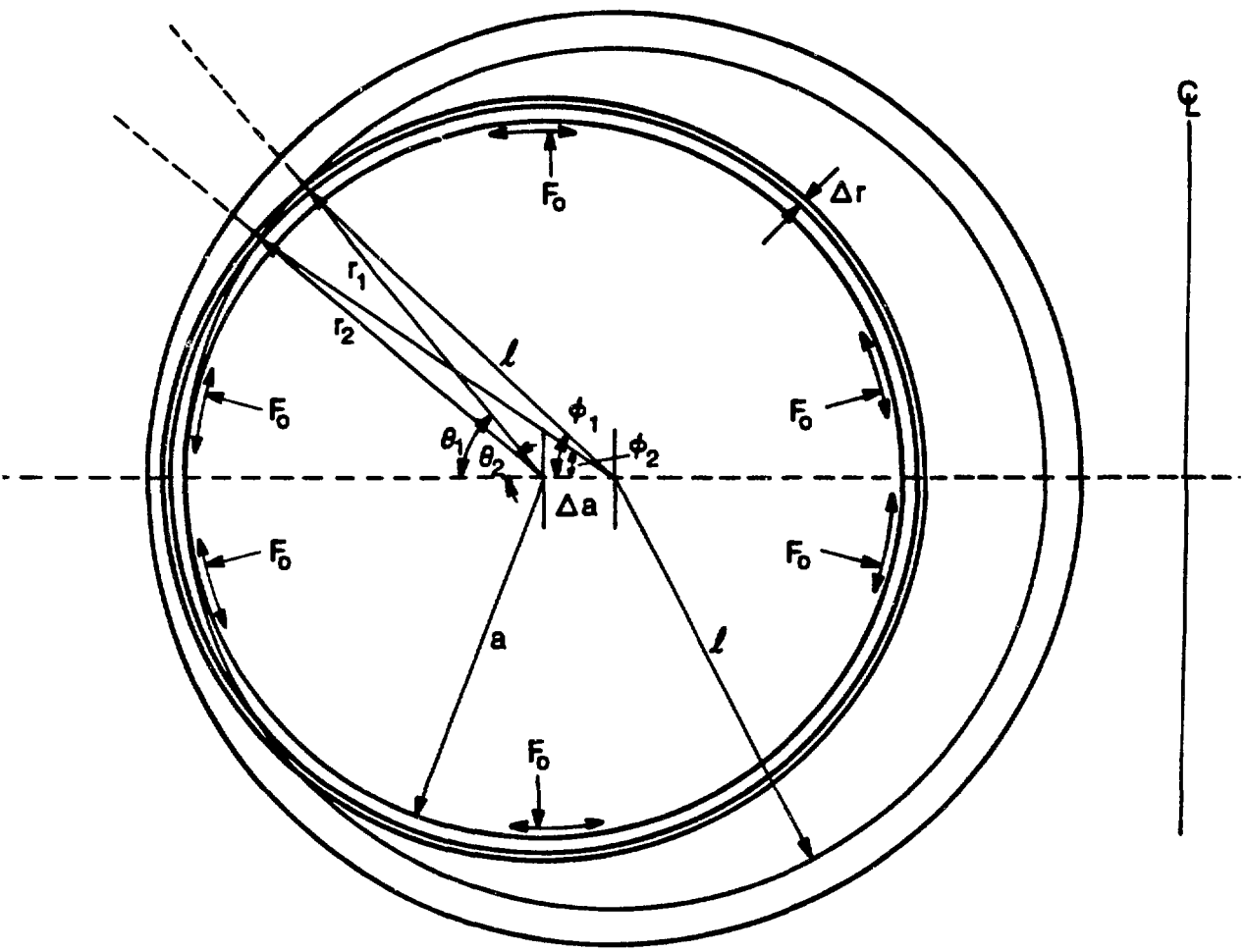

Fig. 1
Model used for calculating the plasma-wall interaction

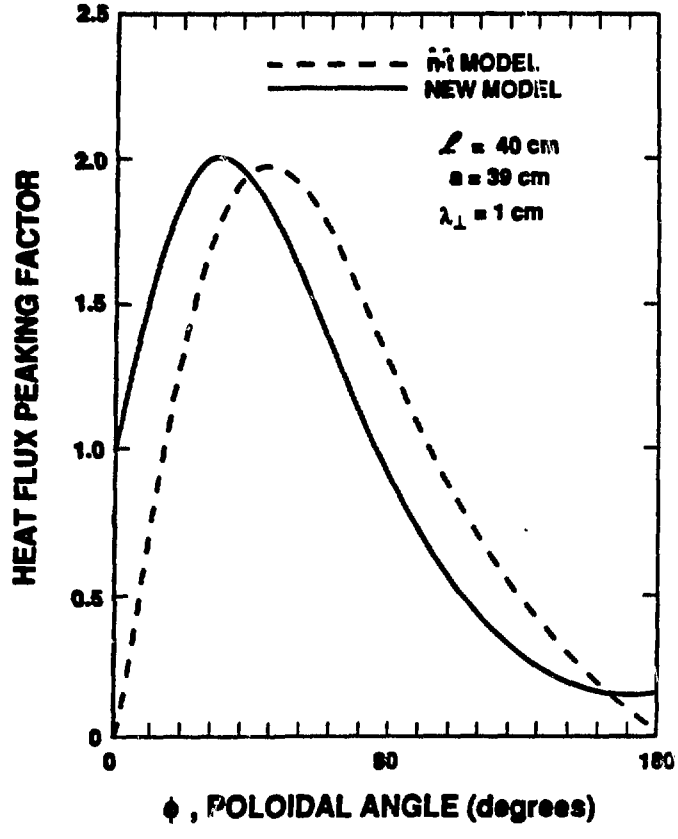

Fig. 2
Normalized distributions of heat flux and the PF as a function of poloidal angle

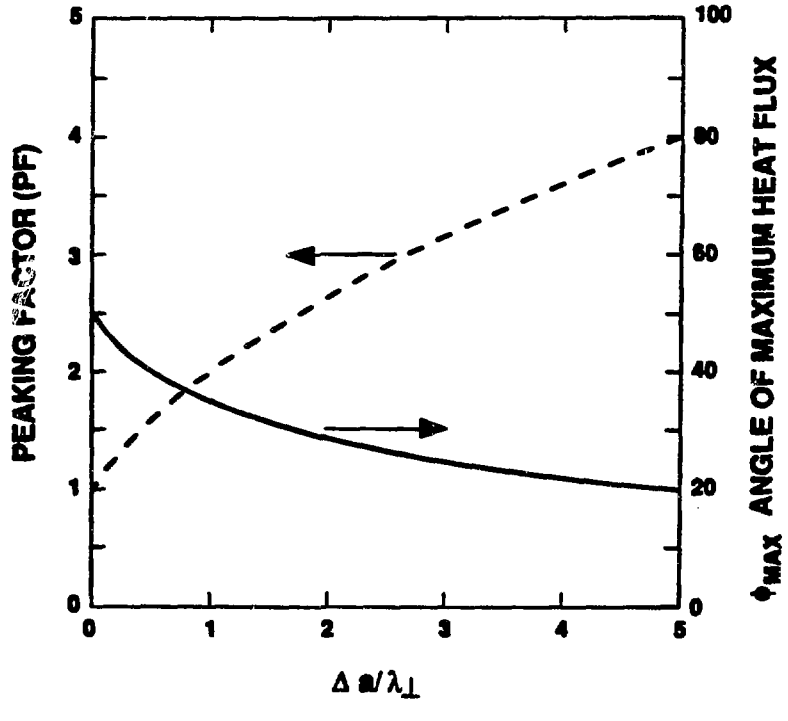

Fig. 3
Maximum PF and corresponding poloidal angle versus the shift of the plasma column in units of $\Delta a/\lambda_\perp$

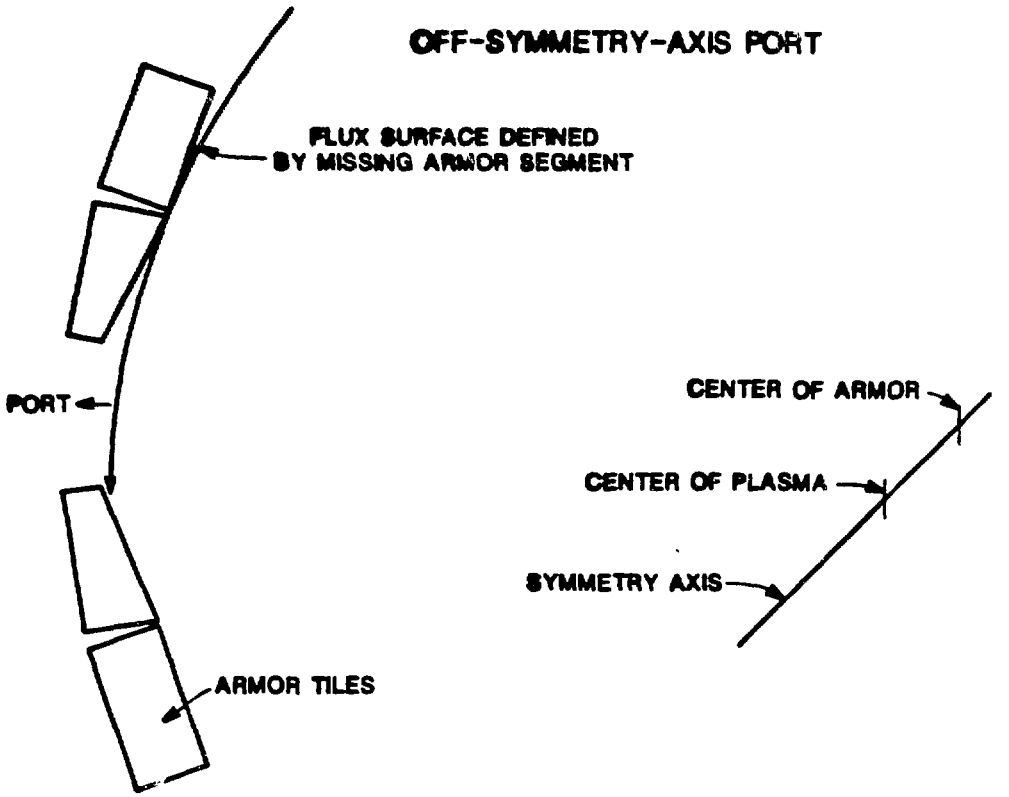

Fig. 4.
Schematic drawing of symmetric contouring for off-symmetry-axis port.

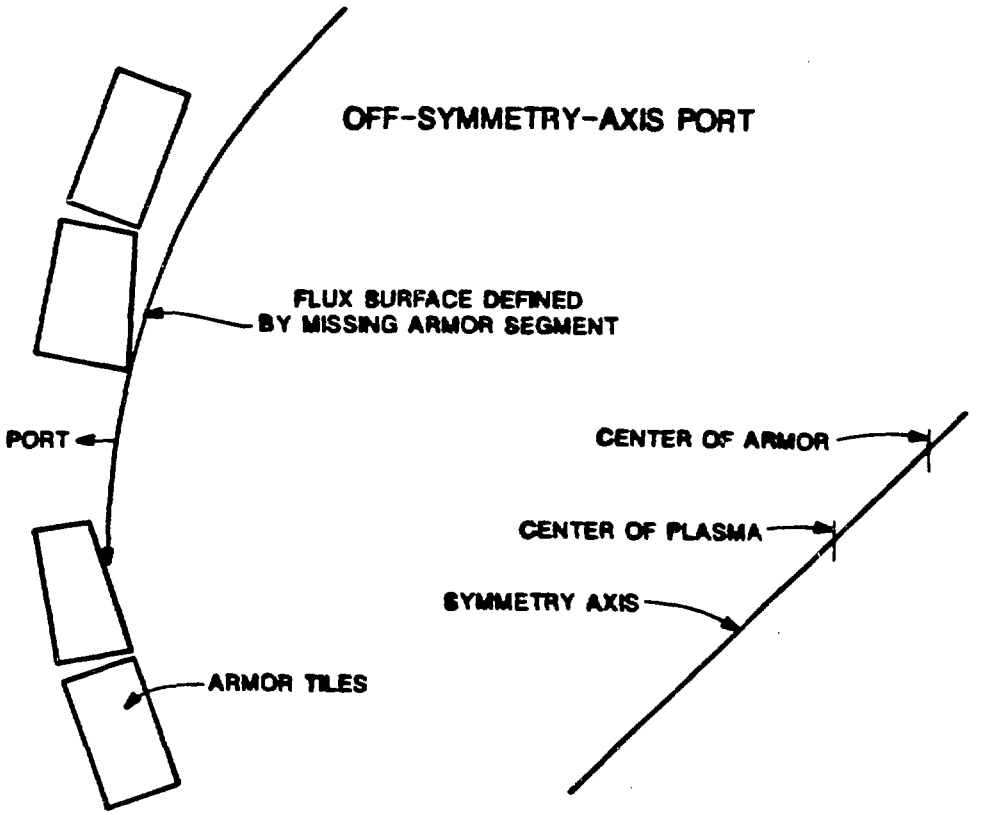

Fig. 5
Schematic drawing of asymmetric contouring for
off-symmetry-axis port with the highest heat flux

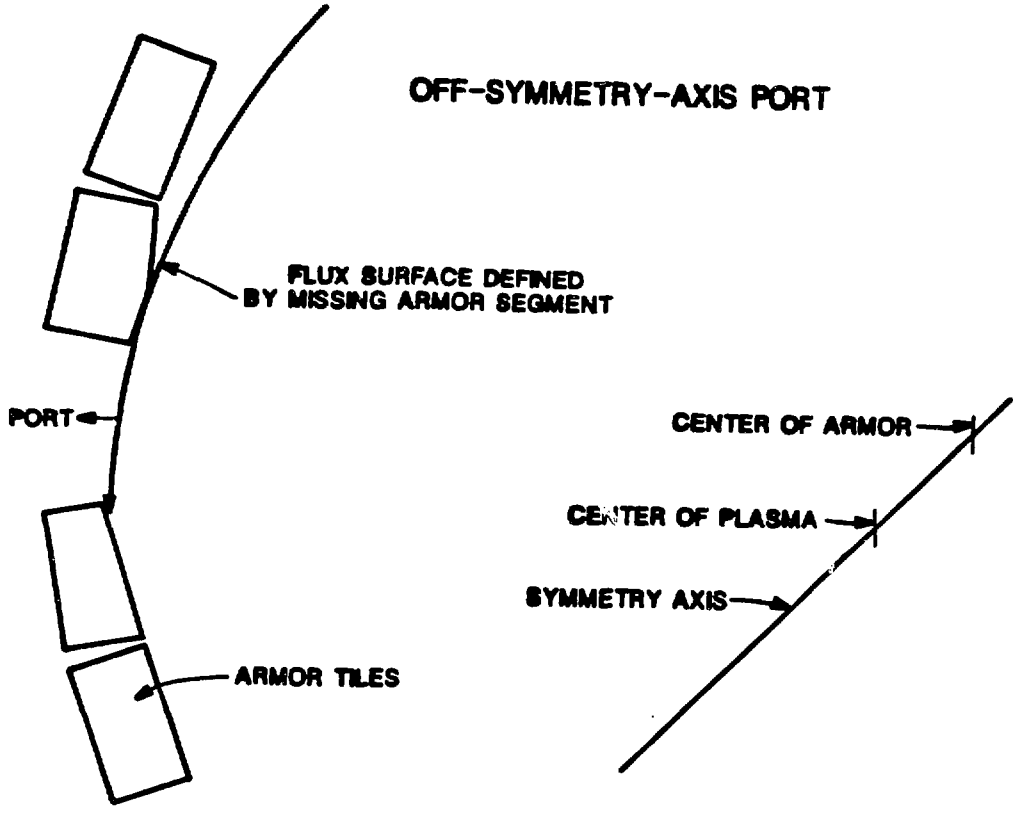

Fig. 6
Schematic drawing in Fig.5 modified for a small amount of heat flux in the ion-drift direction

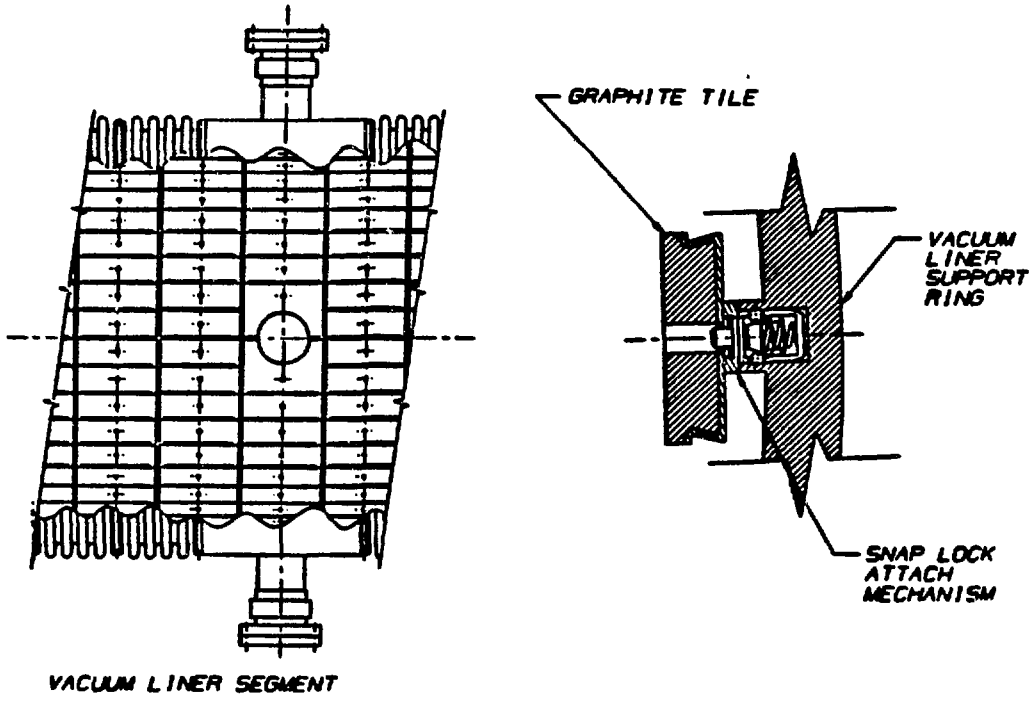

Fig. 7
Schematic drawing of the tile orientation in the liner and the mounting technique

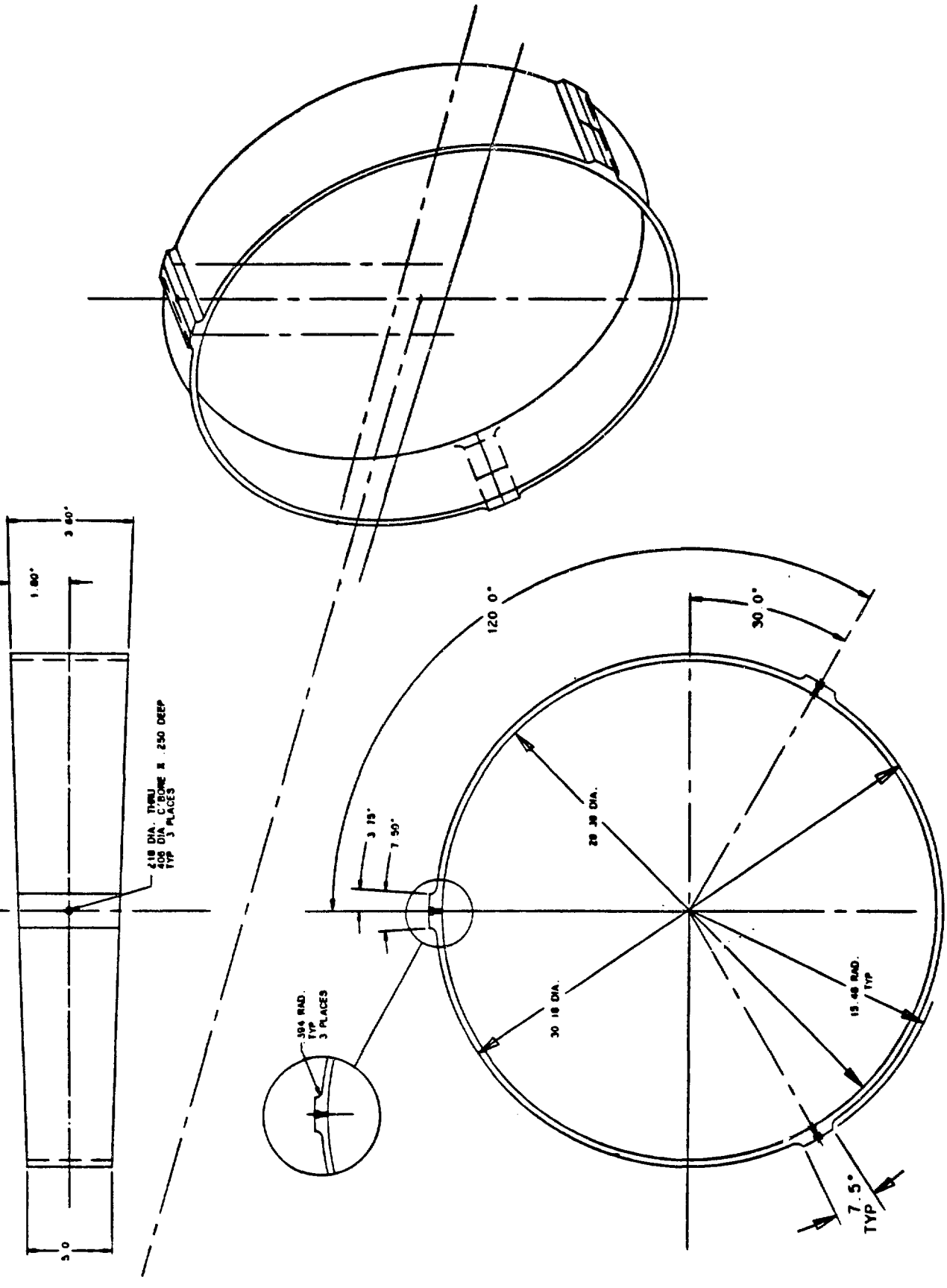

Fig. 8
Schematic drawing of the poloidally continuous C-C composite gore-shaped armor segments

ON PROCEDURE OF ASSEMBLY AND DISASSEMBLY OF RFP APPARATUS

N.Suzuki, K.Odagiri, Y.Miyauchi, H.Oomura,
H.Ukikusa, and K.Ogawa*
Ishikawajima-Harima Heavy Industries Co., Ltd. (IHI)
*Electrotechnical Laboratory (ETL)

An RFP experimental apparatus which has simple structure is proposed. The simple structure makes a term for assembly and disassembly shorter. An accessibility to the machine also becomes better.

1. Introduction

A larger-sized reversed field pinch plasma experimental apparatus(R/a$\sim$1.5m/0.3m, I_p= several MA) has many difficulties for designing. Large electro-magnetic forces, fast start-up, large stored energy(electromagnetic energy, thermal energy), disruption control, etc. become much severer than those of today's machine. However, a big, much rigid, complicated structural apparatus is not desired by most researchers. An RFP apparatus that can be disassembled and assembled easily, and also has good accessibility to various part of machine(favorable to diagnostic equipments, etc.) is so convenient. If it is easy to disassemble and assemble, damaged (by plasma disruption) vacuum chamber can be exchanged with new one so immediately.

A simple structural machine is designed and proposed. And procedure of assembly and disassembly of the machine are introduced.

2. Parameters

The RFP machine envisioned is named 'TPE-RX'. Its parameters are shown in Table 1.

3. Structural Characteristics of TPE-RX

Poloidal cross sectional view and top view of TPE-RX are shown in Fig. 1 and Fig. 2,respectively. This machine has no upper supporting structure constructed by H-section

steels(cf. Fig.5,6). The hoop forces on poloidal field coils(PF coils) are supported by themselves. The axial(torus center axis) forces on PF coils are supported by 'TF(toroidal field) coil supporting plates'(No.17,18 in Fig. 1 ;cf. Fig. 4). Consequently, an accessibility to the machine is kept so easy. Installation of diagnostic equipments is rather easier than in case of full surrounded machine. In this machine, TF coil can be separated to two portions. Also the shell and the insulator that covers the vacuum chamber can be separated to upper and lower parts. These structures are for easy disassemling of the machine.

4. Procedure of Assembly and Disassembly

Fig.7 to 12 show the procedure of assembly of TPE-RX. The procedure is explained below.

(1) Supporting structure is manufactured in works. (It consists of several blocks.)

(2) PF coil supports (for No.1, No.2, and No.5 blocks) are welded on the supporting structure in works. (Fig.7)

(3) PF coils (No.5, No.2, and No.1 blocks) are placed on the coil supports and fixed by bolts.

(4) PF coils(No.3 and No.4) are set on the supporting structure.(not fixed) (Fig.8)

(5) Lower units of TF coil(consists of 2 coils) assembled in works are installed and fixed. These units also fix the PF coils(No.3 and No.4).

(6) The lower units of TF coil are connected together by connecting pipes. (Fig.9)

(7) Vacuum chamber are installed into shell and insulator. (Fig.10)

(8) Assembly of shell with chamber is set on the supporting structure by ceiling crane. (Fig.10)

(9) Upper units of TF coil(consists of 4 coils) are set on the lower units and fixed by bolts.

(10) The upper units are installed on the lower units and connected together by connecting plates. (Fig.12)

The procedure of disassembly is almost inverse to that of assembly explained above.

Address:
IHI ... Tokyo-Chuo Bldg. 6-2,Marunouchi 1-Chome, Chiyoda-Ku,Tokyo 100 Japan
ETL ... 1-4,Umezono 1-Chome,Sakura-Mura, Niihari-Gun,Ibaraki 305 Japan

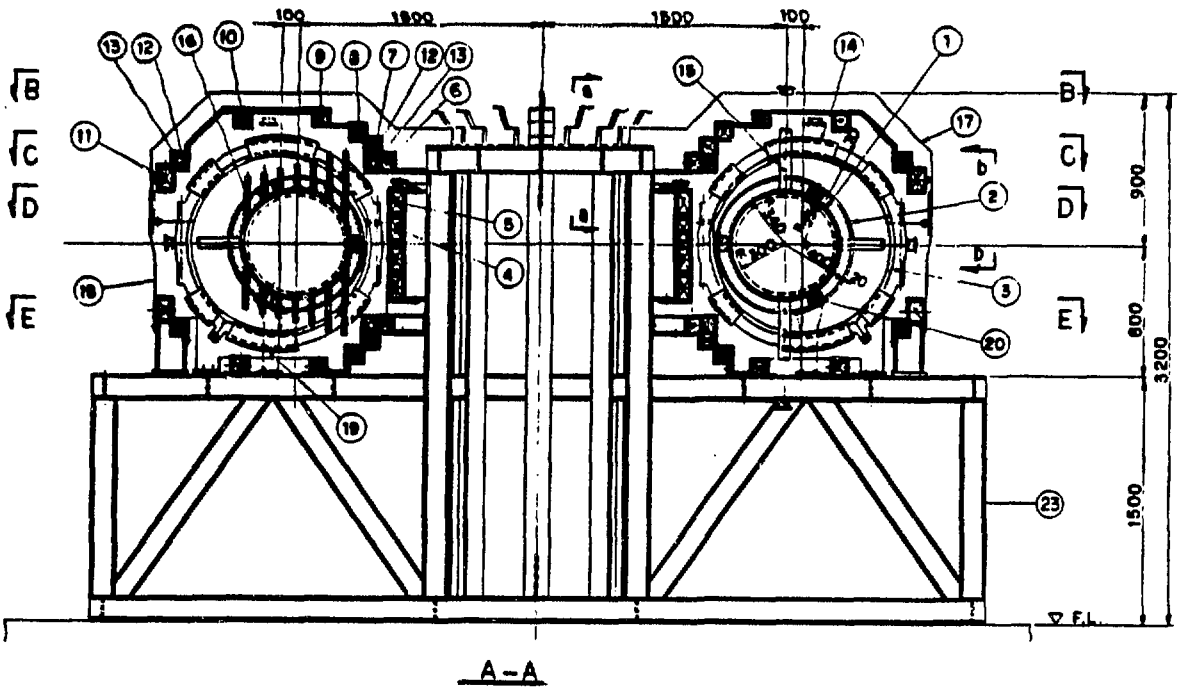

Fig.1 Poloidal Cross Sectional View

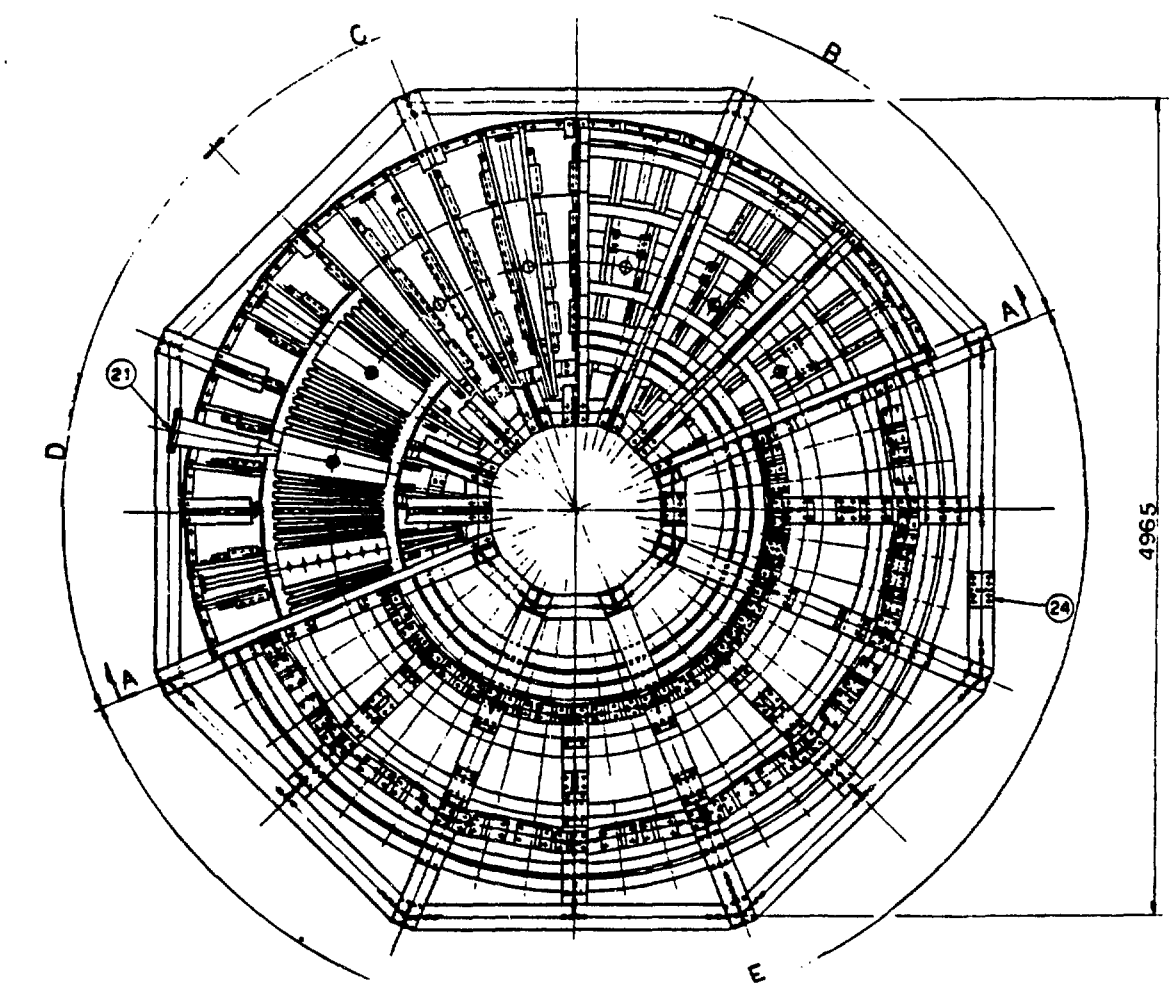

Fig. 2 Top View

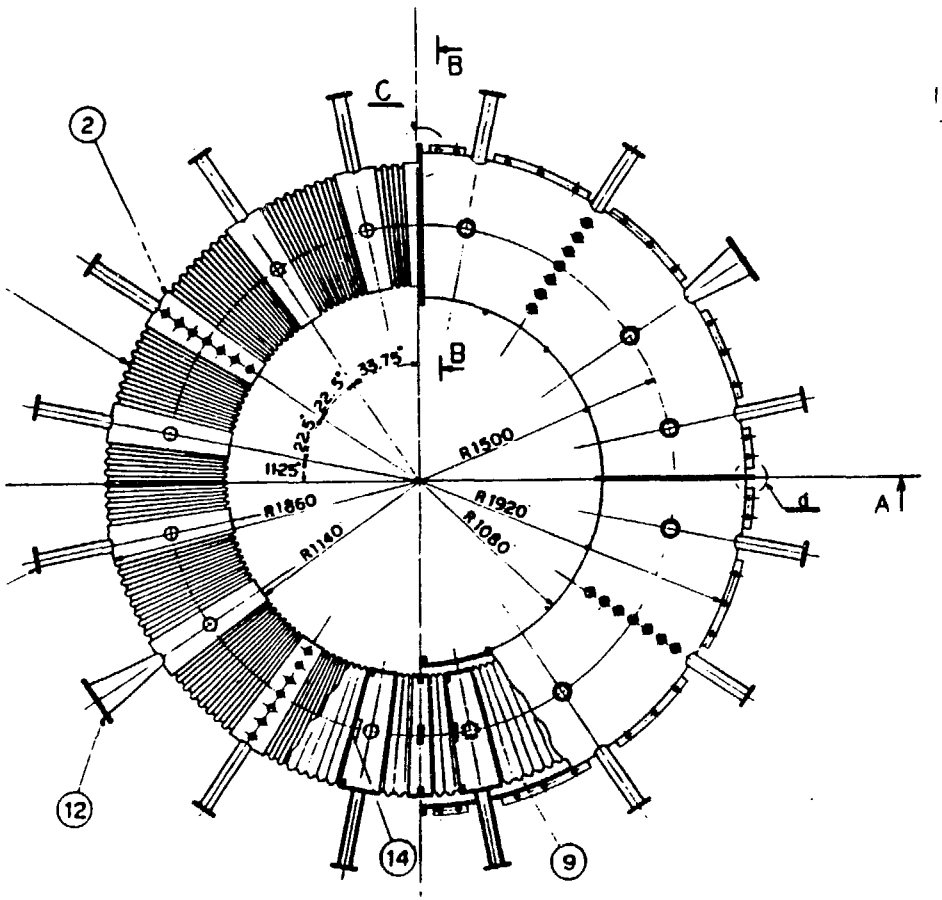

Fig.3 Top View of Vacuum Chamber and Shell

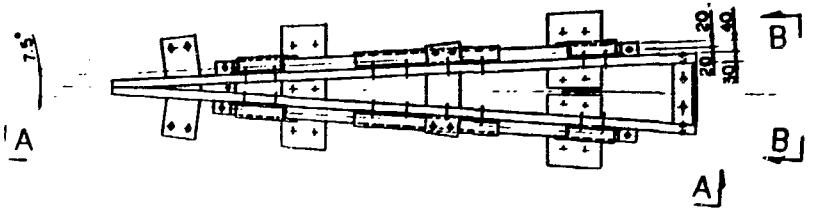

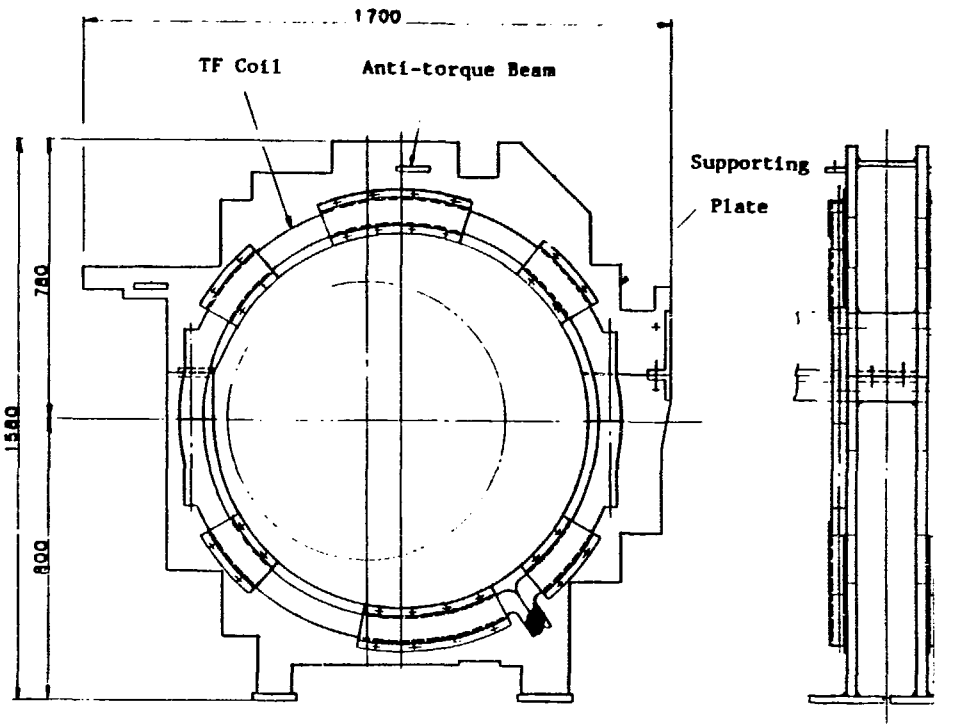

A - A B - B

Fig 4 Supporting Plate for TF Coils

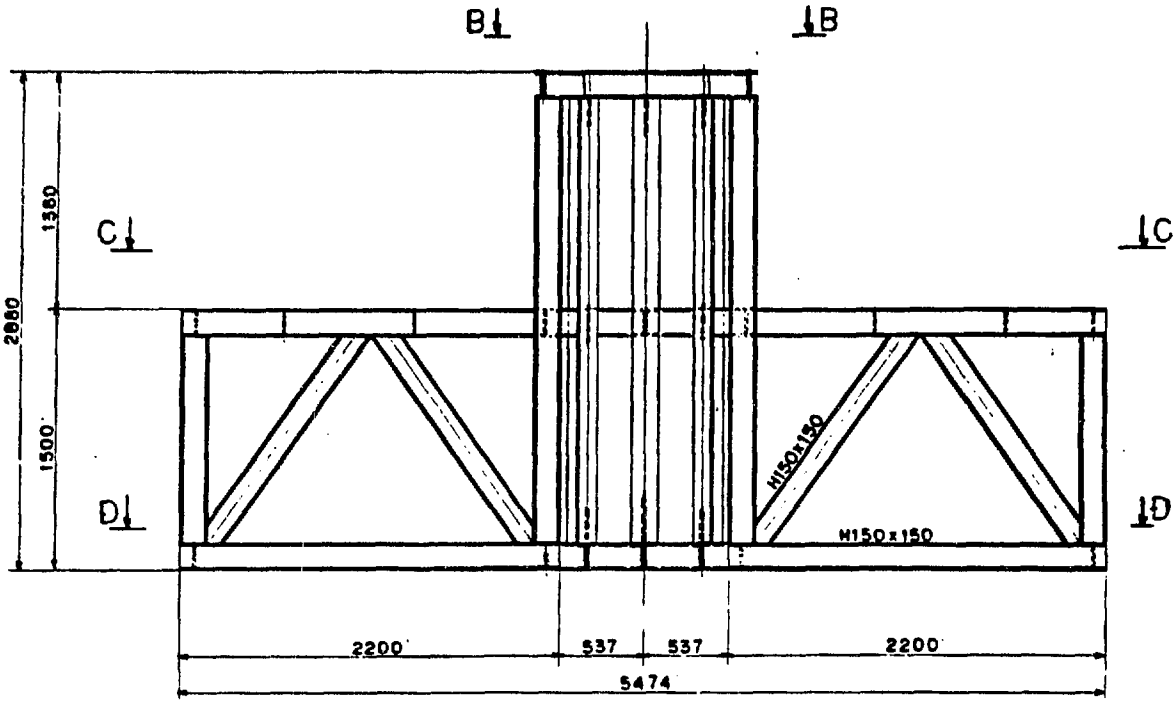

A - A

Fig. 6 Side View of Supporting Structure

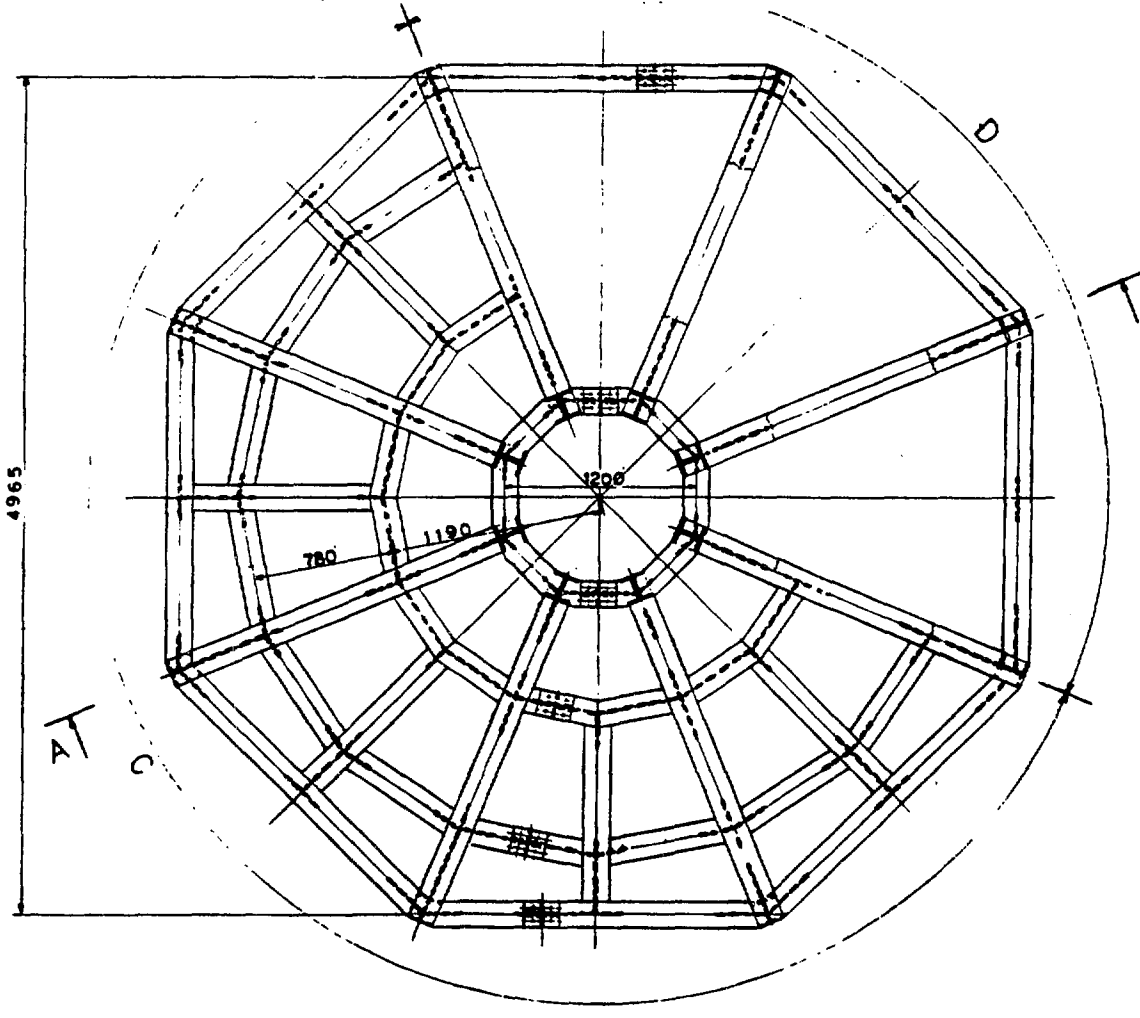

Fig. 5 Top View of Supporting Structure

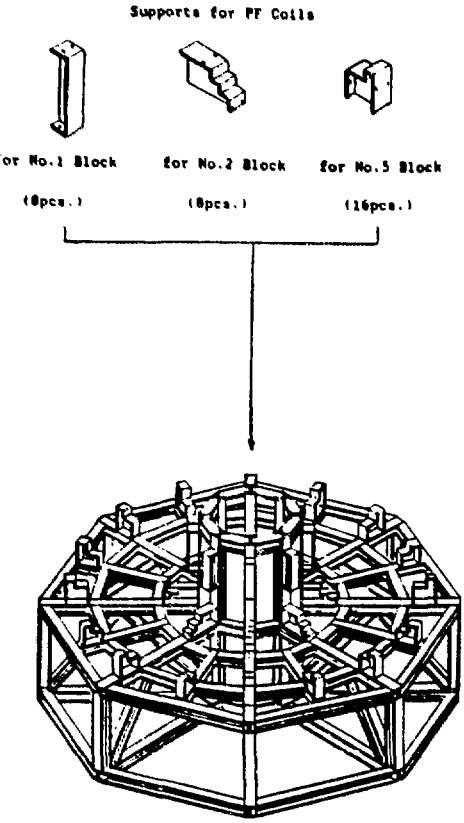

Fig. 7

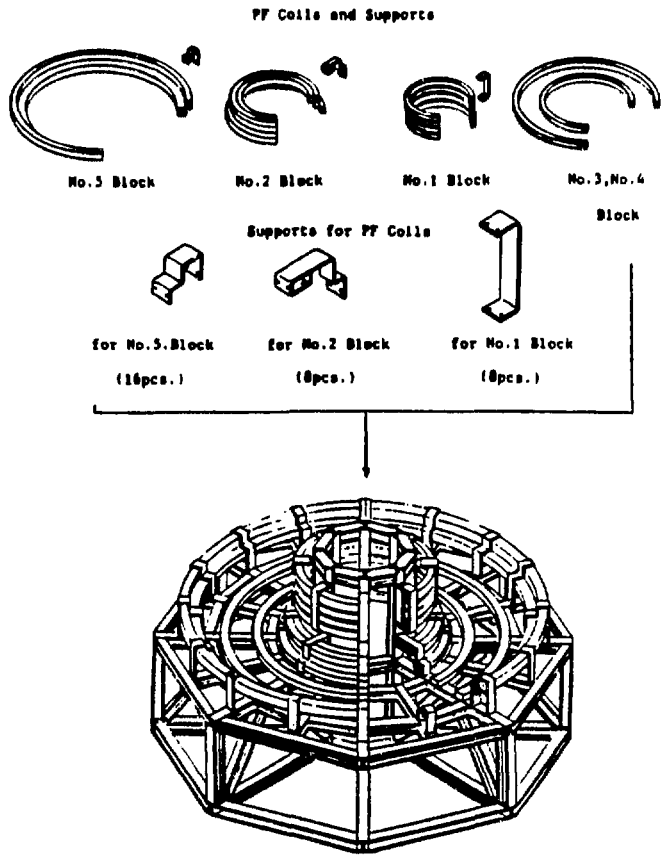

Fig. 8

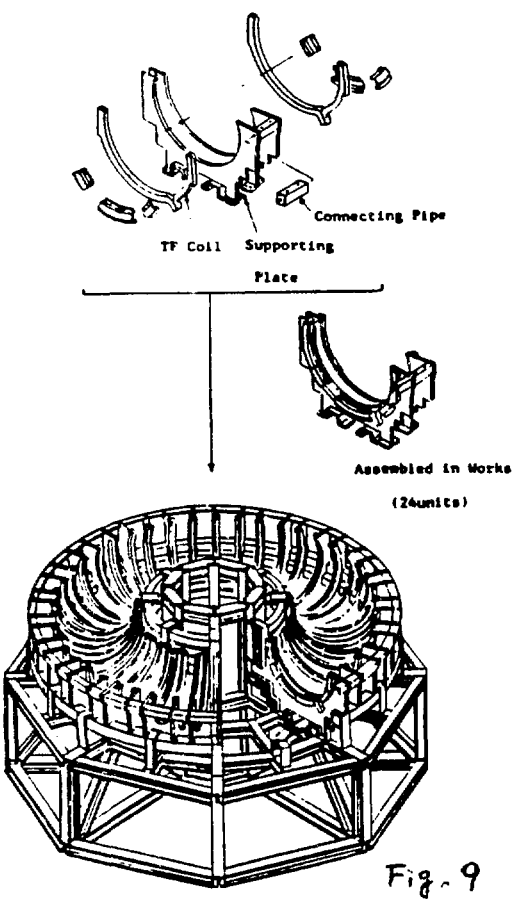

Fig. 9

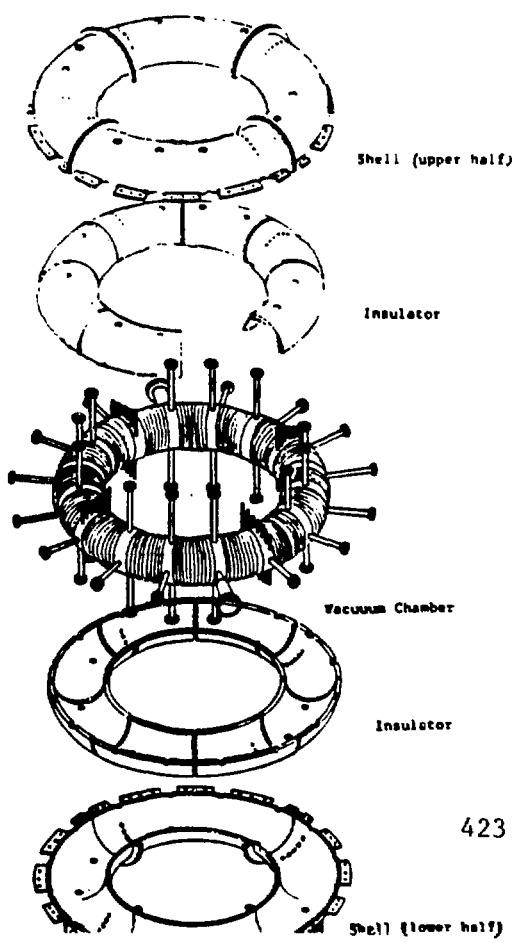

Fig. 10

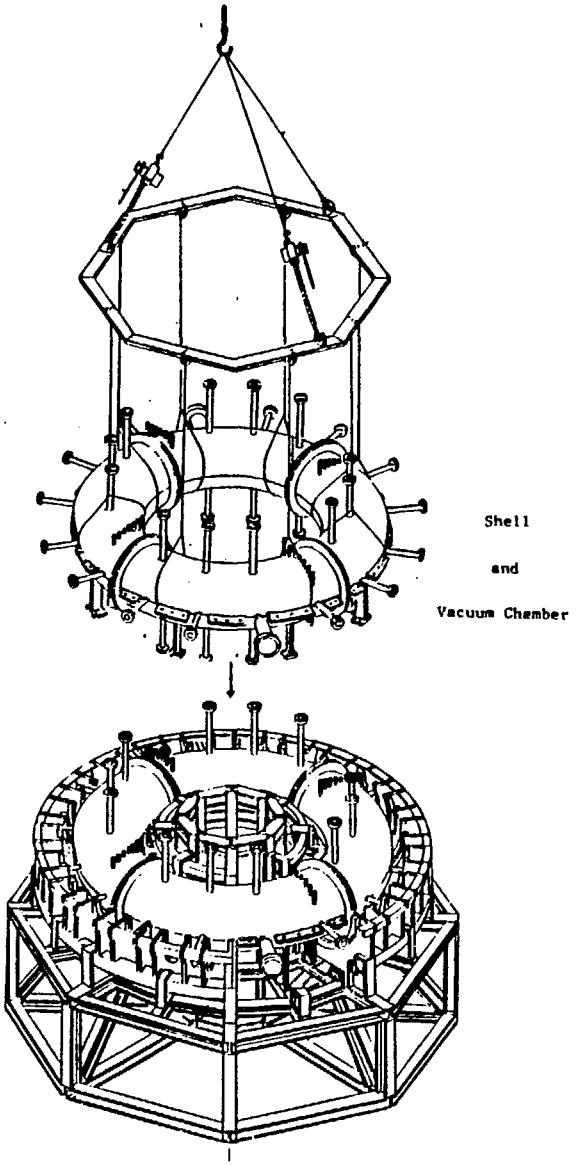
Shell
and
Vacuum Chamber

Fig. 11

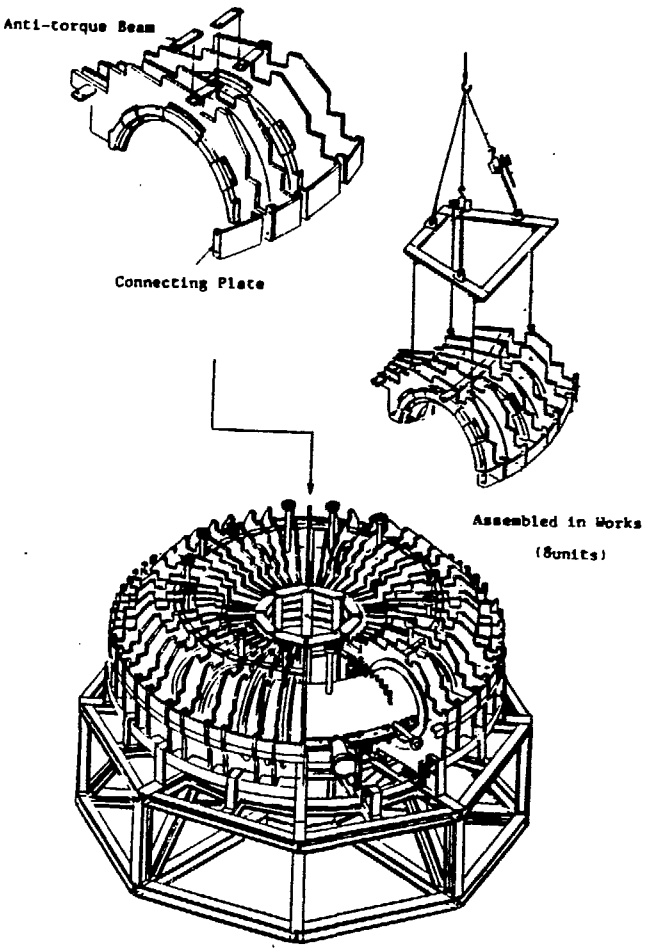
Anti-torque Beam
Connecting Plate
Assembled in Works
(8units)

Fig. 12

Table. 1

PARAMETERS

major radius	R_o	1.5m
minor radius	a	0.3m
plasma current	I_p	2 MA (flux swing 15 V·s)
plasma temperature	$\bar{T}i$, $\bar{T}e$	1.0 keV
plasma density	$\bar{n}_e$	1.5×10^{20} m^{-3}
energy confinement time	τ_E	10 ms
poloidal beta	β_p	0.1
pinch parameter	θ	1.6
reversal ratio	F	–0.2
start-up time	τ_{st}	10 ms
discharge duration time	τ_d	50 ms

CPRF/ZTH SYSTEM THERMAL ANALYSIS

M. T. Gamble, Los Alamos National Laboratory.

Introduction

An indepth thermal analysis is required for the design of the front-end ZTH experiment. The difficulty of this analysis is enhanced by the dual nature of the objectives necessary for this apparatus to accomplish. Primarily, the ZTH front-end must be capable of withstanding a 4 MA plasma. Secondarily, it must sustain long-term bake-outs of the graphite armor at 300°C with only a modest power input. The thermal design of an apparatus to complete the primary objective is nontrivial. However, formulating a design for a device that must effectively act as a thermal conductor, after a plasma burn, and then as a thermal insulator, during bake-outs, requires far more insight and analysis.

Discussion

A schematic representation of a section through the ZTH graphite armor, inconel liner, various insulations, and stainless steel shell is found in Fig. 1. Accompanying this figure is a diagram representing the electrical resistive analogy associated with the ZTH schematic. This model is adequate to predict steady state temperatures for the system when the bake-out condition is simulated. However, many assumptions must be made and parameter studies are limited due to the simplicity of the model.

Several fundamental assumptions were made in constructing the model. The graphite tile was assumed to transfer heat via conduction and radiation to an inconel clip attached to the inconel liner using an inconel post. Perfect thermal contact is not expected at the tile and clip interface. Hence, an interface conductance was chosen to simulate the resistance to heat flow at this joint. This coefficient is primarily a function of pressure and surface quality. Evaluating these parameters, a value of 500 Btu/Hr Ft^2 F was chosen as a baseline for the interface conductance. Perfect thermal contact was assumed at the interface of the inconel clip and the post that secures it to the liner. Minimal inaccuracy is introduced because a skip weld will be employed for this attachment. Appreciable error was not introduced by assuming the convoluted liner to be planar. The depth and number of convolutions per unit area are not excessive. All inconel surfaces are expected to remain free from gross graphite dust collection. A low value of 0.2 was chosen as the standard emissivity characteristic of all inconel components in the front-end. Consistent assumptions were made regarding the resistance to heat flow resulting from poor insulation packing in convolutions. Instead of ascribing interface conductances to the various regions of insulation, an innerspace of still air was chosen to represent this resistance to heat flow. An accurate estimate of pressure and surface contact associated with insulation installation would be difficult to obtain. Hence, any interface conductance chosen would represent a guess, whereas small air gaps may be chosen reasonably and accurately modeled as dead air space. A baseline value of 15 mils was chosen and parameter studies of gap magnitudes were undertaken to bracket results. It was assumed that the explosive bonding process to be used for mating the copper conductor to the stainless steel shell would produce an interface essentially transparent to the heat transfer process. Therefore, no

interface conductance was defined for that region.

To obtain a benchmark for the system, a baseline configuration was defined. Parameter studies of various interface conductances, air gap magnitudes, and material properties were compared to this benchmark. The following enumerates the baseline values of some significant parameters:

Graphite - Inconel clip interface conductance - 500 Btu/Hr Ft^2 F
Graphite emissivity - 0.85
All inconel emissivities - 0.2
All interstitial air gaps - 15 mils
Thermal insulation - 0.5 in.
Electrical insulation - 0.1 in.

This configuration proved acceptable in regards to many important constraints. For example, the temperature of the electrical insulation surface was found to be 54° C while the power input required to maintain system equilibrium was only 21 kW. Fig. 2 provides detailed information for the resistances to heat flow at all points through the section, the heat flux driven through the system, the power required to maintain the system in equilibrium, and the temperatures at each interface through the section. A graph of these temperatures may be found in Fig. 3. The abscissas, labeled position, refer to the nodal positions between resistances of Fig. 1.

Parameter studies were undertaken. Modification of the graphite-inconel interface conductance did not significantly alter solution results due to the higher efficiency of the radiant heat transfer mechanism at that position. Inconel emissivities were altered, in conjunction with the graphite-inconel interface coefficient, only to confirm that, even at low values of inconel emissivity the radiant mode exceeded conduction heat transfer. Protection of the electrical insulation is an important objective. Parameter studies were completed that indicated the presence of 0.5 in. of a thermal insulator, such as min-k, kept temperatures low enough for a variety of electrical insulations. Smaller thicknesses of min-k were also explored to simulate those areas where thermal insulation would be decreased and electronics substituted. In cases where still air was allowed to replace min-k, unrealistically good heat transfer resistance was exhibited by the air. No doubt, some finite velocity should have characterized the air in the space enormously increasing its heat transfer capability.

Summary

The first-order heat transfer analysis of the ZTH system bake-out condition is complete. Useful design results were obtained from the simple one dimensional model. Currently, a finite element model of the front-end is under development. The baseline configuration will provide confirmation of the model's correctitude. However, this more sophisticated approach will facilitate indepth parameter investigations for steady state operations and provide a powerful tool for transient analysis as well.

ZTH FRONT-END SCHEMATIC

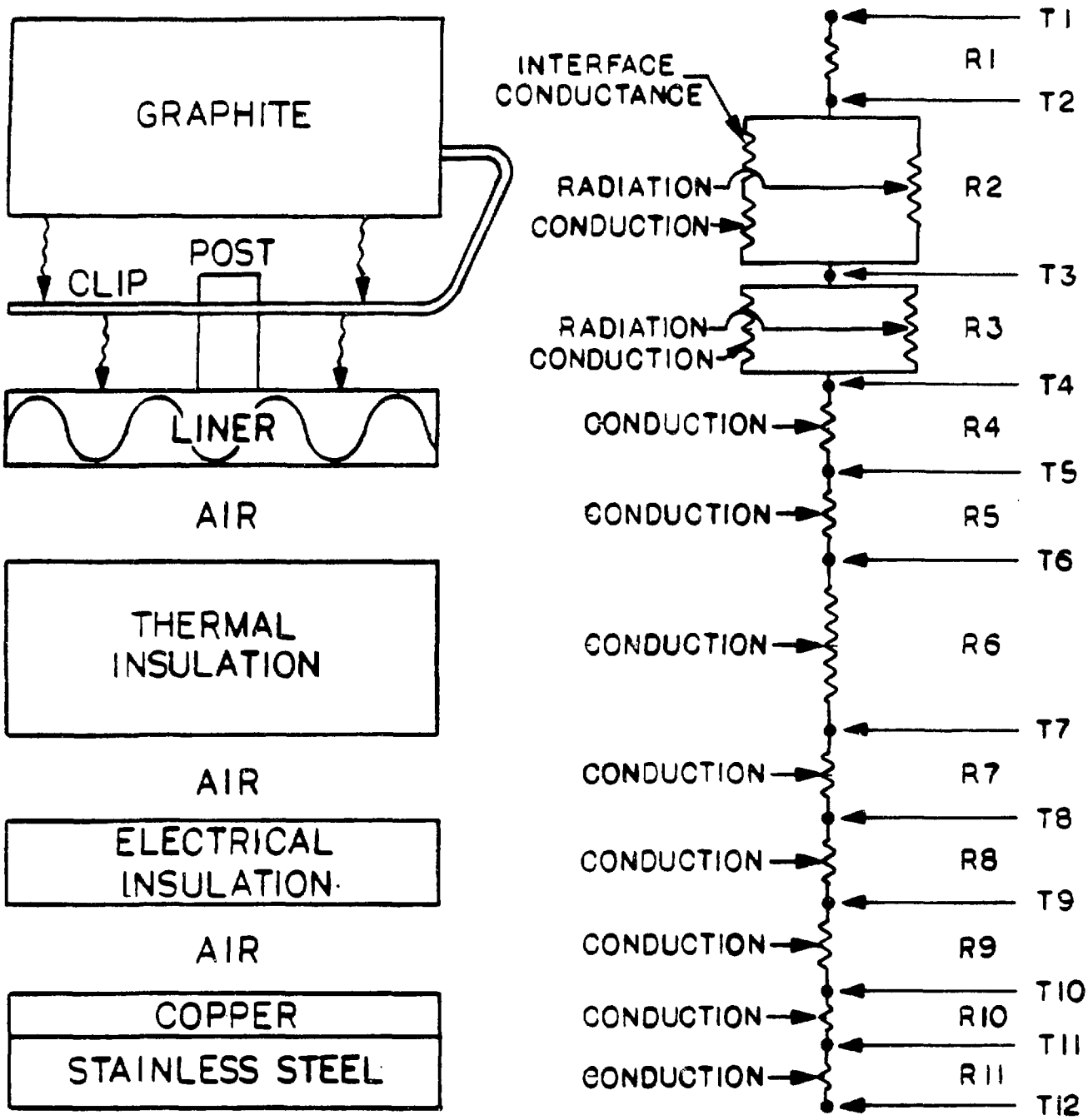

FIGURE 1

CTR HXF BASELINE CASE

R1	R2	R3	R4
7.158182E-04	.3748967	.2729012	4.545455E-04

R5	R6	R7	R8
5.643341E-02	1.947196	6.476684E-02	8.090292E-02

R9	R10	R11
7.022472E-02	4.333334E-05	.00104

OVERALL HEAT XFER COEFF [B/HR*FT2*F] = .3484836

TOTAL SYSTEM HEAT FLUX [B/HR*FT2] = 163.0903

TOTAL POWER REQUIRED FOR AREA OF 40M**2

POWER [B] = 70221.88 [KW] = 20.57483

T1	[F] =	572	[C] =	300
T2	[F] =	571.8833	[C] =	299.9352
T3	[F] =	510.7412	[C] =	265.9674
T4	[F] =	466.2337	[C] =	241.2409
T5	[F] =	466.1596	[C] =	241.1998
T6	[F] =	456.9558	[C] =	236.0866
T7	[F] =	139.387	[C] =	59.65943
T8	[F] =	128.8241	[C] =	53.79117
T9	[F] =	115.6296	[C] =	46.46091
T10	[F] =	104.1767	[C] =	40.09815
T11	[F] =	104	[C] =	40.09422

FIGURE 2

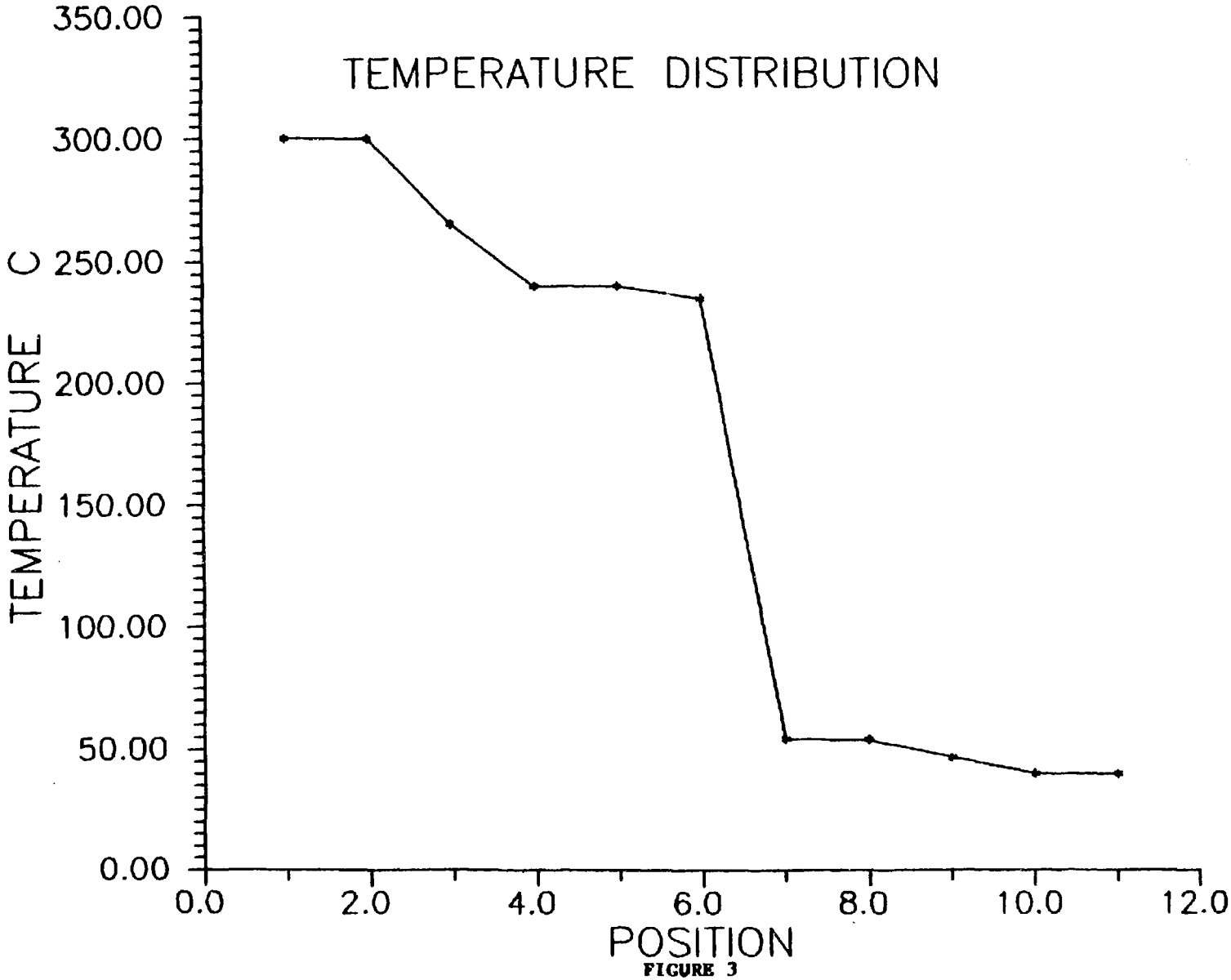
TEMPERATURE DISTRIBUTION
TEMPERATURE C
350.00
300.00
250.00
200.00
150.00
100.00
50.00
0.00
0.0
2.0
4.0
6.0
8.0
10.0
12.0
POSITION

FIGURE 3

ENGINEERING FEATURES OF THE MADISON SYMMETRIC TORUS*

R. N. Dexter, D. W. Kerst, T. W. Lovell, S. C. Prager, and J. C. Sprott

Physics Department
The University of Wisconsin-Madison
1150 University Avenue, Madison, WI 53706

DESIGN CONCEPT AND PARAMETERS

We describe the design parameters, unconventional features, and status of the Madison Symmetric Torus, MST, an RFP now approaching completion. A desire to minimize field errors dominated the design, leading to flanged gaps and inclusion of a pumping duct with small pump ports into the shell. No liner was to be used in the initial configuration, the versatile aluminum shell being the vacuum containment vessel (VCV). Simplified access to the inside of the vacuum vessel was accomplished by using the tank itself as single-turn poloidal as well as single-turn toroidal field coil. Thus none of the familiar toroidal or poloidal field coil sets surround the tank. A girder structure has been installed to permit removing the core-keeper and top-half of the vacuum vessel for insertion of internal shells or liners. More routinely, we intend to lift core-keeper and top half of the VCV together for entry of personnel into the VCV for changes of internal diagnostics or limiting surfaces, or for installation of movable limiters, etc. All structural features were designed to ease disassembly. Figures 1-3 showing south and east elevations, and a plan view illustrate many of these MST features.

The plasma (R=1.5 m, a=0.52 m) will be driven by a 2 volt-second iron core. Since the size is larger than other modern RFP devices we extrapolate from empirical scaling laws, and anticipate that the plasma parameters, once optimized, will be in the range of I_p~800 kA, T_e~800 eV, n~3 x 10^{13} cm^{-3}, τ_e~2 msec, and pulselength~ 40 msec, with a toroidal loop voltage of ~20 V.

Most critical or unconventional features were tested through construction-phase experiments on the Wisconsin Levitated Octupole tank, operated for two years in a non-circular or in a poloidal divertor RFP configuration. For example, we were successful in forming a sustained RFP with plasma allowed to contact the high-voltage gap without using a liner. We also showed that full and movable, but electrically discontinuous, toroidal rail limiters did not prevent formation of a sustained RFP discharge; this observation supported our plans to incorporate movable limiters in MST for studies of shell proximity effects on the RFP state.

Versatile diagnostic access was included, making use of many small portholes. Many diagnostic features, such as Thomson scattering were tested in the construction phase experiments, and we totally converted our data acquisition system to the M.I.T.-developed Model Data System (MDS). We have used MDS for several months with excellent success. In contrast, the existing control system from the construction-phase experiments will be used essentially intact for the initial phase of MST operation.

MAGNETICS

The toroidal magnetic field is produced by driving current through the vacuum tank. This system produces good diagnostic access (no windings), decreases field ripple, and provides easier demountability of the vacuum tank. The current is carried from discrete transmission lines to the cut in the vacuum tank through a large flange section. This system produces negligible field error since the flange smooths the ripple due to transmission line discreteness, and the conducting vacuum tank provides a boundary condition of zero radial field. A section view in Fig. 4 indicates the geometry.

The plasma current and poloidal magnetic field are driven by a capacitor bank through an iron core transformer with primary windings wound around the core. The conducting vacuum tank carries an image current of the plasma. The axisymmetry of the tank currents is achieved by an additional system of windings (called continuity windings) which connect from one side of the poloidal gap in the vacuum tank to the other side. The continuity windings surround, but do not link the core. Their purpose is to allow the toroidal tank current to continue across the gap without distortion. An additional novel feature of the system is that the continuity winding is connected to the vacuum tank through a flange (which extends in the radial direction). The flange significantly reduces the field error that results from mismatches between the spatial distributions of primary windings and that ideally required by the plasma.

Finally, since the core will be driven towards saturation, leakage flux from the core is a possible cause of additional field error. To eliminate this source of field error, a second primary winding will be wound around the core with the sole function of carrying the magnetizing current for the iron core. It is spatially distributed so that no flux escapes from the core. A third set of windings around the core will be used for reverse biasing. It is anticipated that despite these efforts to minimize field errors, significant errors will remain. We have therefore included some adjustability for primary winding position, and also space for saddle (correction) coils, as illustrated in Fig. 5. Space was also reserved for vertical field windings which may be required for equilibrium position control. All systems are capacitor driven.

GAP PROTECTION, PUMPING, AND PORTHOLES

The vacuum tank is constructed of 6061-T6 aluminum 5 cm thick. It is split at the midplane so that it may be expeditiously disassembled without alteration of the vacuum system. To eliminate the field error that results from large tank holes, vacuum pumping occurs through an array of 193, 3.8 cm diameter holes which are separated by about 15 cm and extend 270° in the toroidal direction, pumping taking place through a large pumping duct within which shielded getters can also be placed (see Figs. 1 and 4). Dummy holes, which don't quite penetrate, cover the remaining 90°, and preserve the toroidal axisymmetry. Three stand-alone turbomolecular pump modules provide removal pumping. A fourth turbo-pump chamber is configured for convenient regeneration of the cryopanel which it also contains.

The tank has 83 portholes for diagnostics and other uses; several apertures are reserved for movable limiter actuators . Most of the portholes are of 3.8 cm diameter. Two pairs of tangential line-of-sight ports and four sets of intersecting arrays, or "boxports" provide 66 additional 3.8 cm diagnostic ports and 26 apertures of 5 cm diameter (see Fig. 3). In addition, of course, the pumpout holes will be useful for diagnostics and feedthroughs. Seventeen holes of 17 cm diameter are provided into the pumping duct, and are used for pumping, electrical access, fueling lines, and mechanical linkages.

The toroidal voltage gap is surrounded by plasma yet must hold-off a startup gap voltage of several hundred volts. After a number of unsuccessful versions in construction phase experiments, we found a solution which has operated for 15 months and thousands of shots of high-voltage startup and RFP discharges without arcing. Briefly, gap insulation (and vacuum sealing) is provided by a 0.63 cm Viton gasket which is shielded from the plasma by tightly fitting machinable ceramic covers. Stainless steel limiters protect the sides of the ceramic forms. Similar gap protectors will be provided at the midplane toroidal gap. Several prototype versions are being constructed; all extend at least 0.8 cm into the plasma away from the aluminum shell.

STATUS REPORT

The vacuum containment vessel is to be ready for shipment to the U.S. from Italy in July 1987; finish machining is virtually complete. On arrival in Wisconsin, finish welding of continuity windings and B_t transmission lines will be performed. First plasma is expected in fall 1987, but budgetary cut-backs will delay installation of primary number 2 and current transformers; neither feature is essential for our initial RFP studies.

* Supported by the U.S.D.O.E.

CAPTIONS

Figure 1. Scaled south elevation of the Madison Symmetric Torus. Delivery of the 5-cm thick vacuum (R=1.5m, a=0.52m) tank is expected in August 1987. The figure shows the iron core and the B_t transformer symmetrically placed below the center leg of the 2.2 Volt-sec core. Pumping modules connect to the 270° pumping duct. The core-keeper and top half of the vacuum vessel are raised by screw-jacks attached to a girder system.

Figure 2. East elevation of MST giving another view of the continuity windings and the box ports.

Figure 3. Plan view of MST. No poloidal or toroidal windings obscure diagnostic access, but planned vertical field windings will probably have to be removed when the core keeper and top half of the VCV are raised for entry into the vacuum vessel.

Figure 4. Section of MST illustrating the B_t feed cylinders, 4-fold transmission lines to the transformer, and the small hole array from pumping duct into the VCV.

Figure 5. Lower half of the poloidal flange of MST indicating planned primary number two, holes for field-error sensing coils, and holes for saddle coils. The large poloidal flanges are expected to reduce field errors. The continuity windings are welded to the poloidal flange and circle the core, but do not link it.

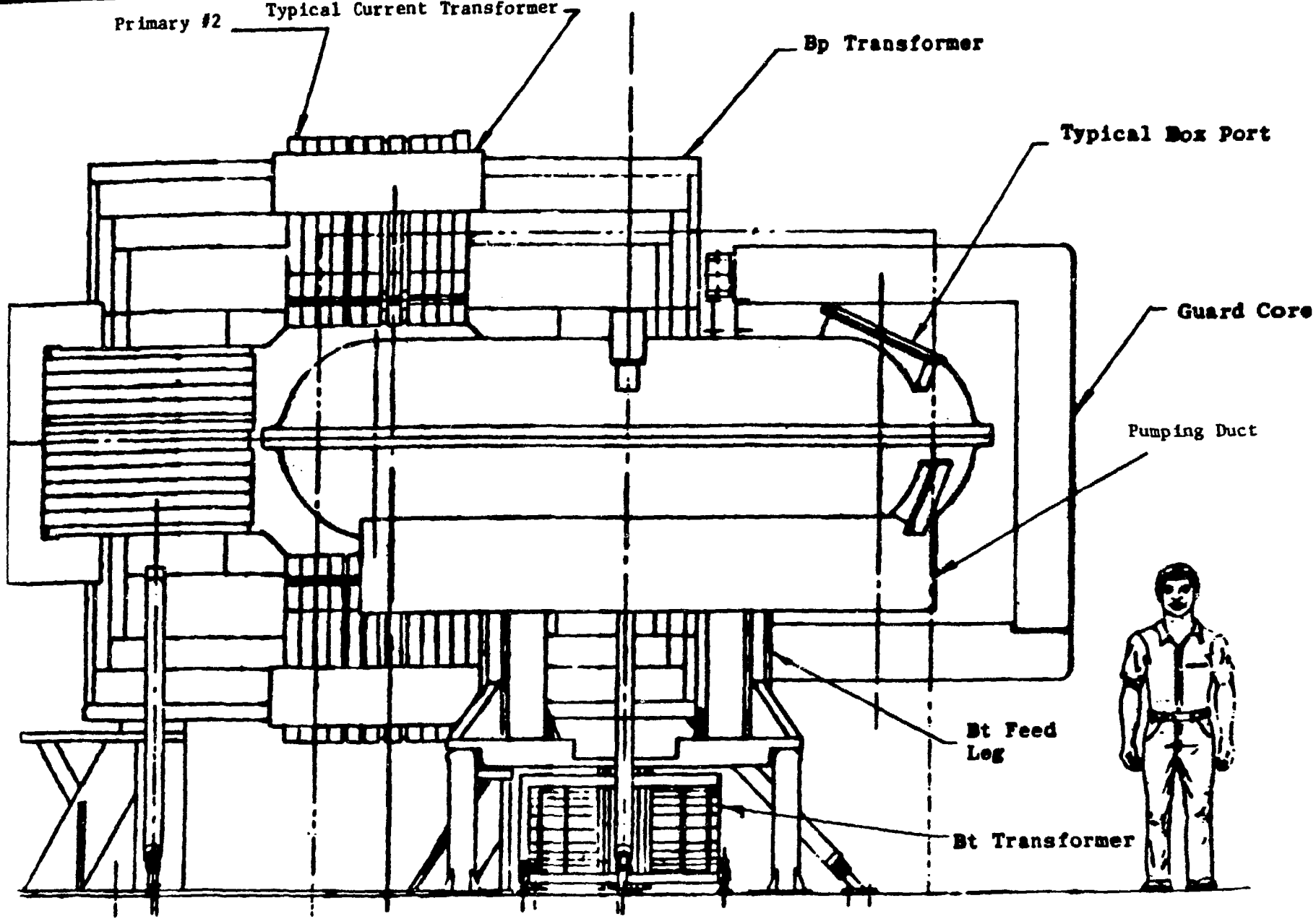

Figure 1 Madison Symmetric Torus

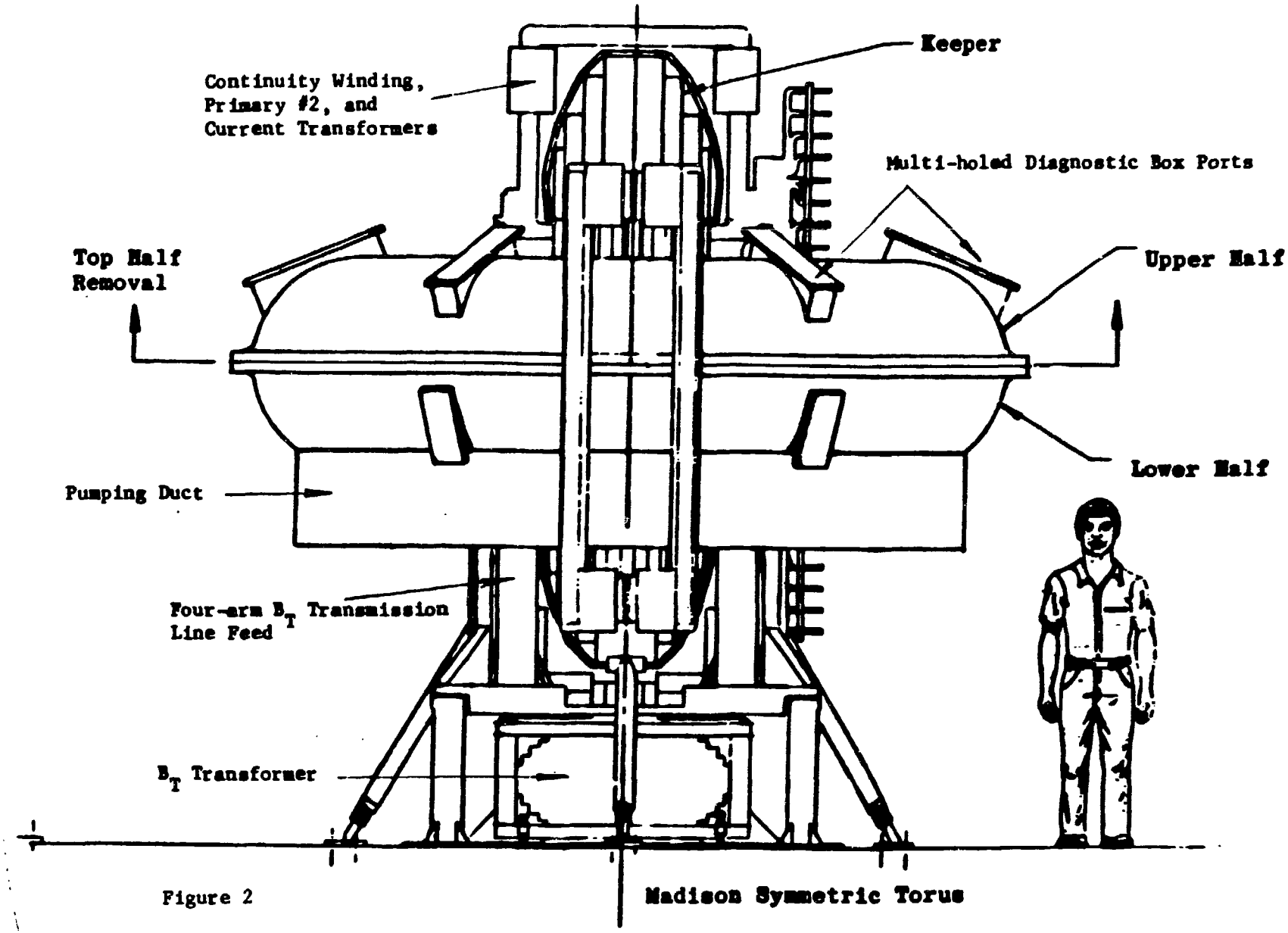

Figure 2

Madison Symmetric Torus

East Elevation

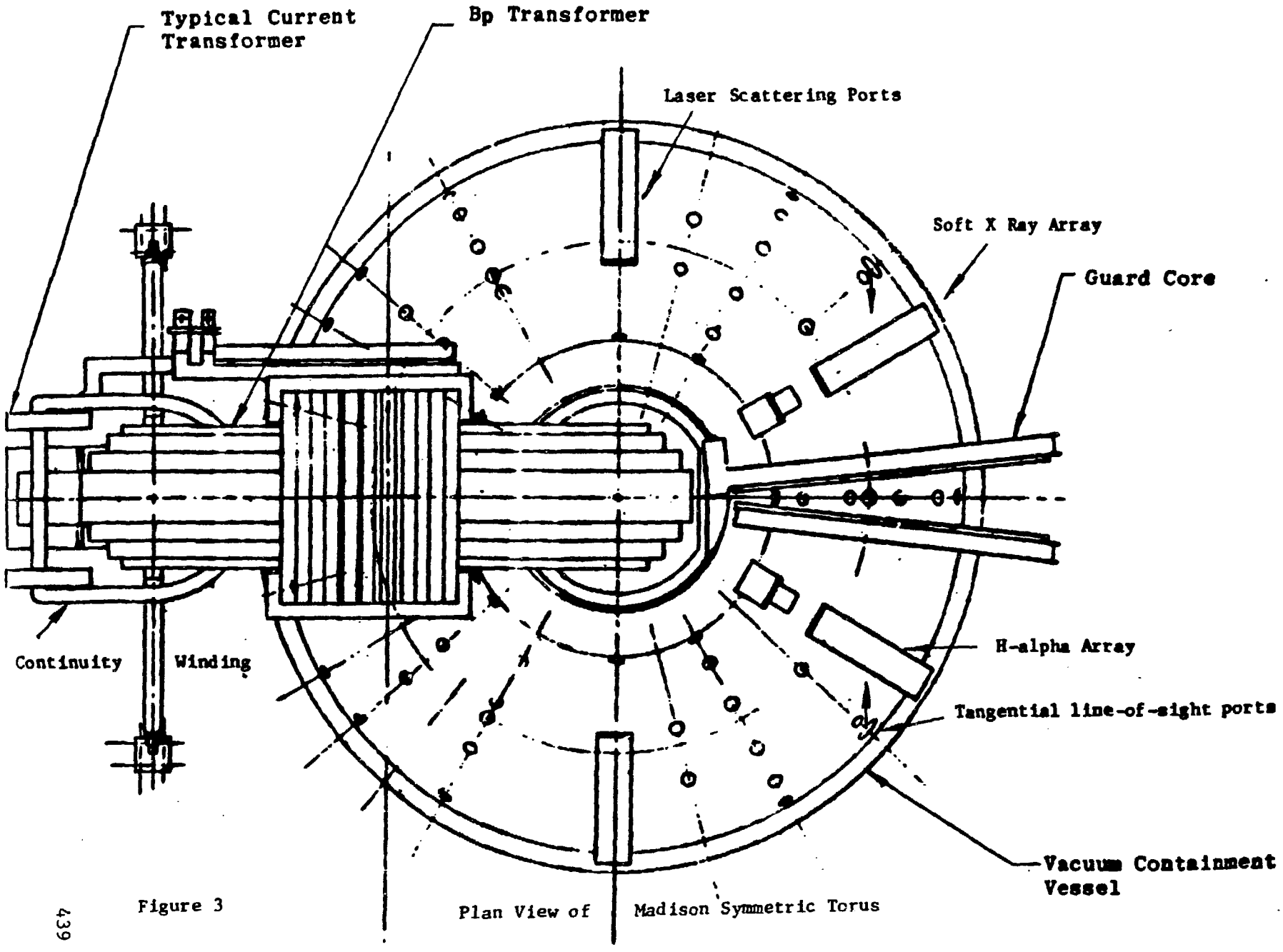

Figure 3 Plan View of Madison Symmetric Torus

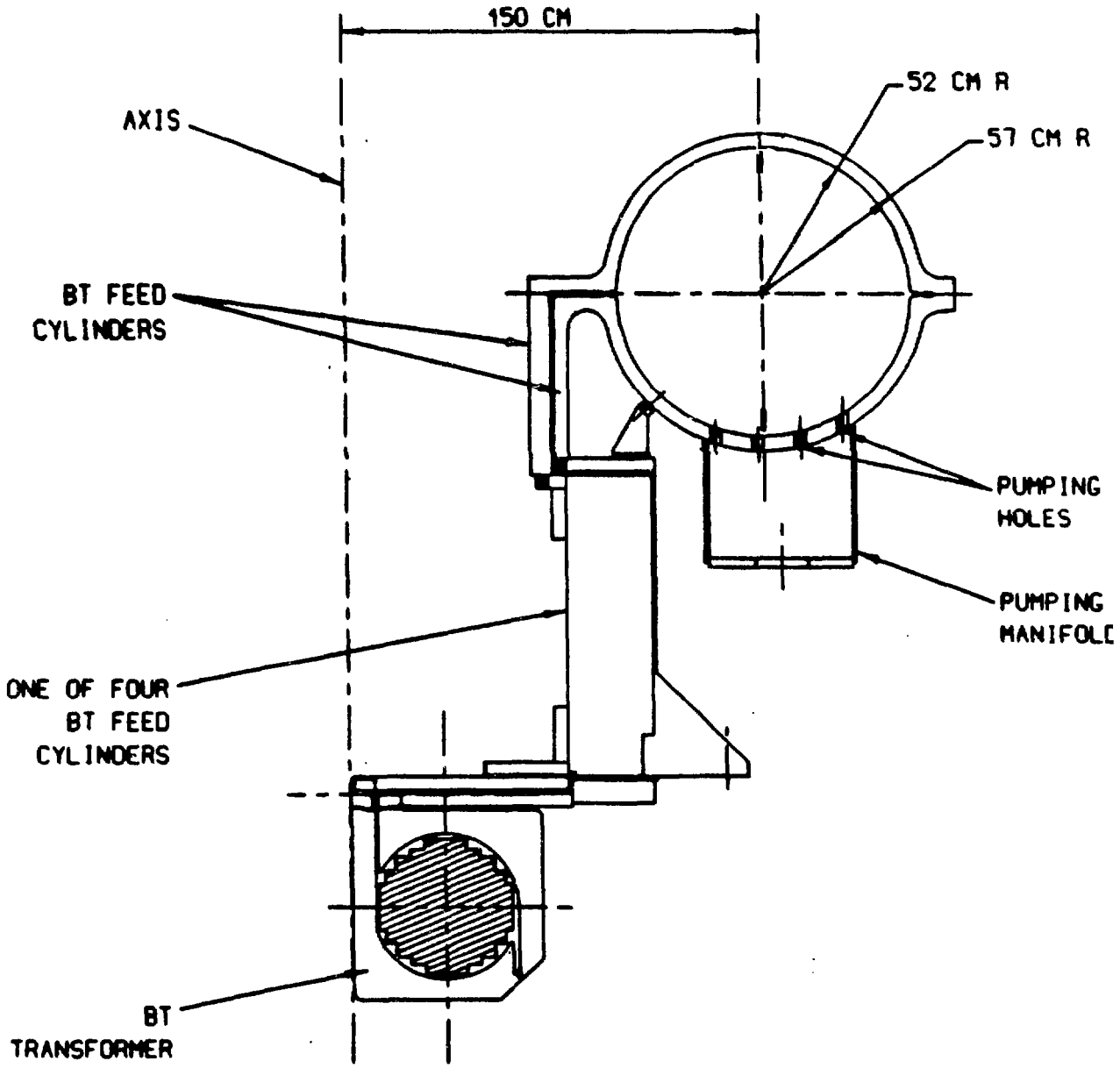

Section of Madison Symmetric Torus

Figure 4

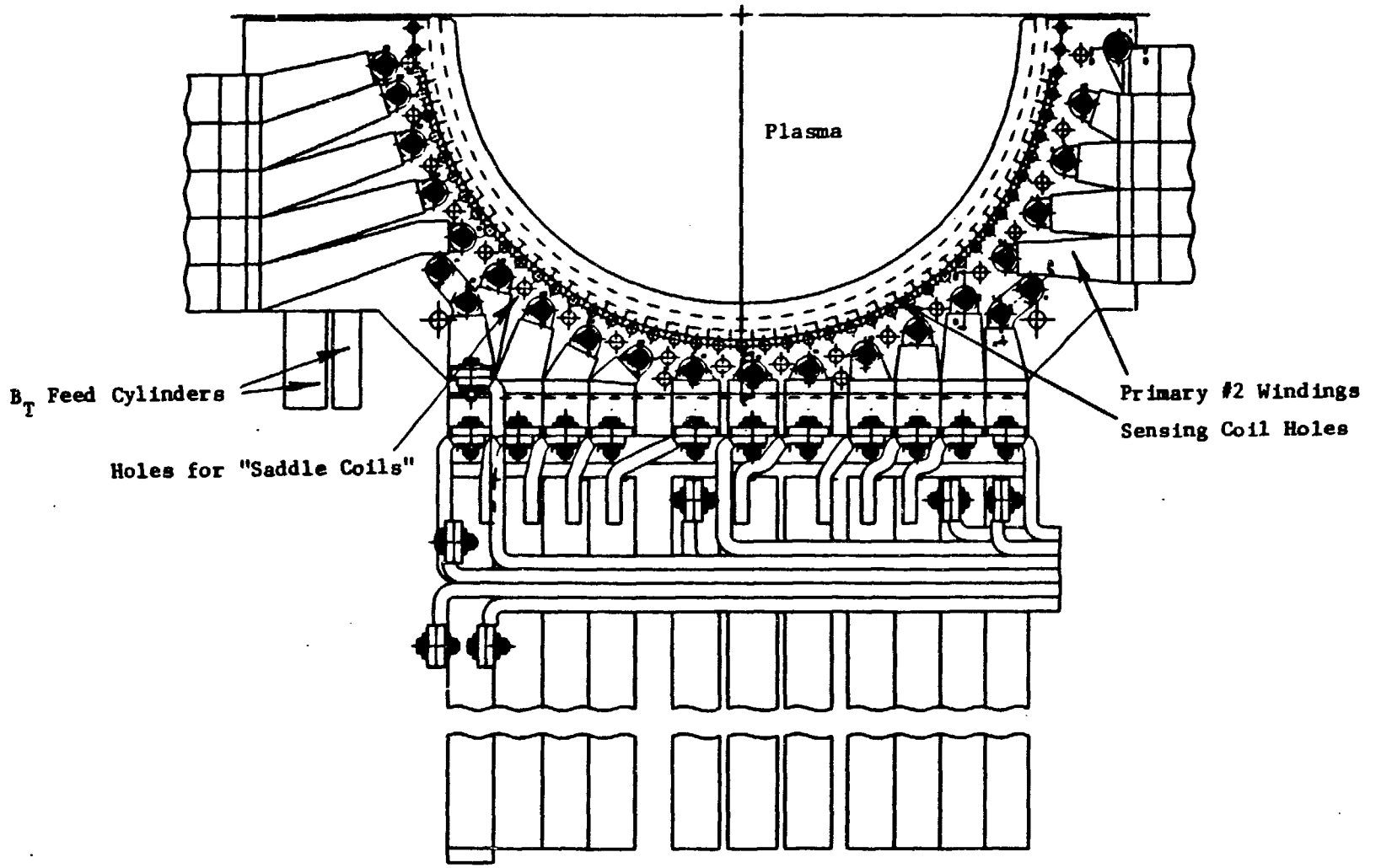

Figure 5 Primary #2 Drive at Poloidal Flange

LAMINATED BEAM ANALYSIS

JEFF HILL

Los Alamos National Laboratory
P.O. Box 1663
Los Alamos, New Mexico 87545

ABSTRACT

Finite element analysis is used to determine the response of two beams which are identical in every respect except internal construction. One beam is a laminated beam with discrete materials. The other is modeled as a single material beam with material properties chosen to mimic the response of the laminated beam. The results of the two analyses are compared directly and indirectly by using the single material beam to predict the stress state of the laminated beam. The technique of using a single material to represent several materials is shown to be useful when the analyst uses care in interpreting the results.

LAMINATED BEAM ANALYSIS

A common method of analysis of objects containing many discrete materials is to use the technique of "smearing" the material properties. Smeared material properties make a single material behave by itself as the discrete materials behave together. This makes it much easier to determine the response of an object; in a finite element analysis, the technique could be used to allow a coarser mesh. The smeared material properties must be chosen to suit the problem. Because the smeared properties do not represent any of the discrete materials exactly, the response of the object containing smeared material may not be exactly like the response of the real object. This report is a brief discussion of one analysis technique which could be used to determine the response of an object externally and internally. The external viewpoint is determined by gross measurements which are made externally, such as load and deflected shape, and could be called the macroscopic viewpoint; whereas the internal viewpoint would be determined by measurements of such things as local stress and strain, and could be called the microscopic viewpoint. A laminated beam bending problem demonstrates a smearing technique and its effects on the macroscopic and microscopic response of the beam.

Large magnetic coils made of copper conductors separated by epoxy are proposed for use in the CPRF/ZT-H machine. The coils are being analyzed using finite element analysis techniques to determine the stresses in the coil materials. The method of analysis used by Steve Girrens and Joel Bennett, LANL Group MEE-13, consists of the following technique (Fig. 1):

1. A small three dimensional section of one of the CPRF coils was modeled with painstaking detail using discrete materials. A set of orthotropic, smeared material properties were determined by loading the model in different ways.

2. A section of the coil was modeled using a coarse mesh, in which the materials could not be discretized, for a three dimensional analysis. Using the material properties determined in step 1, above, the response of the coil to the operating load was determined.

3. The displacements were determined at two cross sections of the smeared material coil in step 2. These displacements were applied to a finely meshed model of the region between the cross sections with discretized materials. Displacements from step 2 were interpolated between known points to all nodes in the descretized material model beam section. The microscopic response of the coil was determined from the response of this section.

The first two steps are frequently used throughout the field of structural mechanics. There are also many variations which can be used.

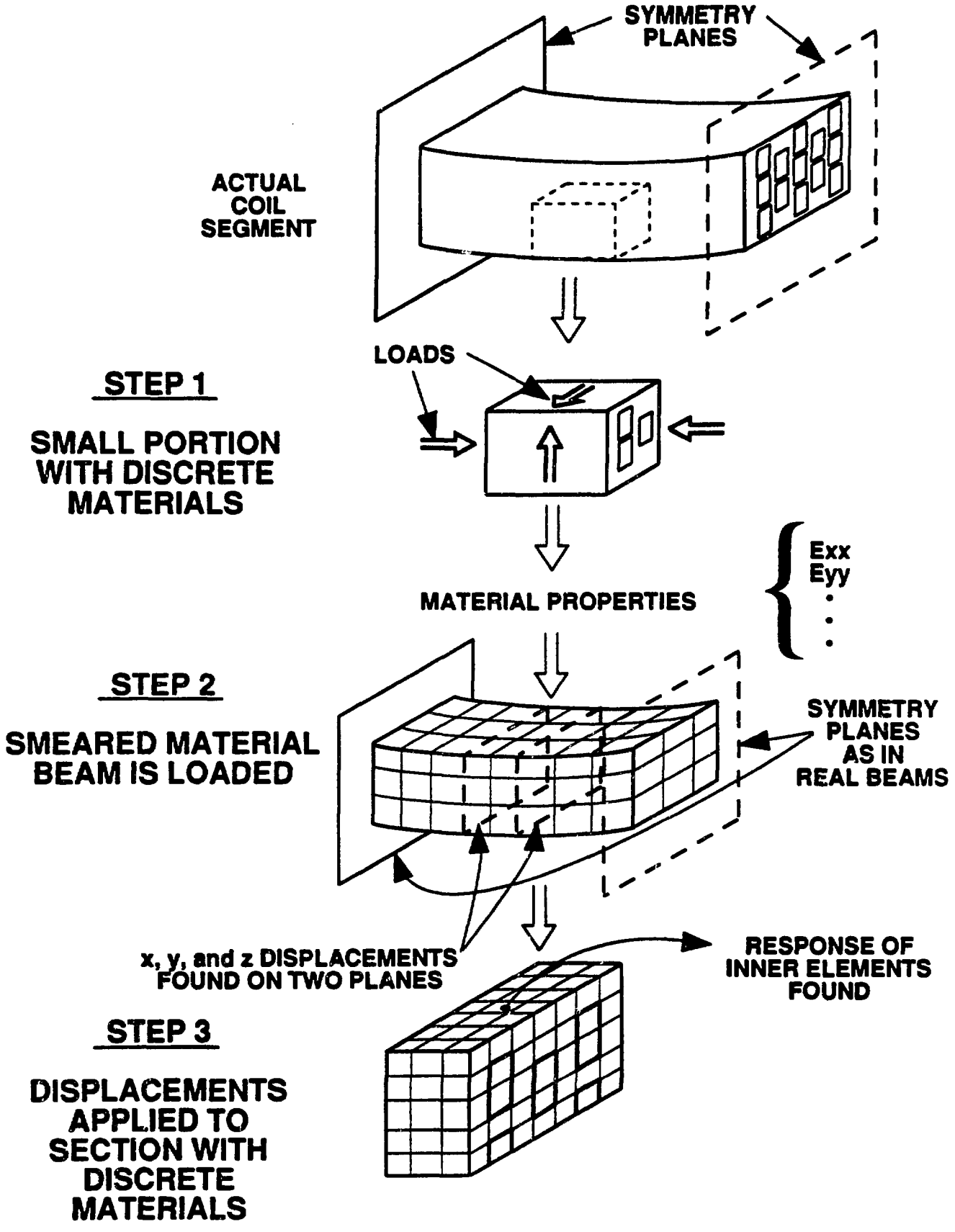

FIG. 1 Technique used for determing response of CPRF coils

METHOD

The primary response of the coils is in bending, so it was natural to apply the technique to two dimensional, laminated beam bending. Also, since much is known about beam bending, the results of many of the analysis steps could be checked analytically using text book formulae. The beam chosen for analysis is shown in Fig. 2. It is a thin beam, having a 10:1 length to height ratio, and it is subjected to a load at the midpoint which causes a 'small' displacement of about .001 times the length of the beam. The beam is considered to be made of three laminations, two outer layers having a high modulus, and an inner layer having a modulus which is 20 times less than that of the outer layers.

The finite element model of the beam consists of the region between the two axes of symmetry; the fixed end condition, and the midsection where the load is applied (Fig. 3). Half the actual load is distributed evenly among the nodes at the midsection. The mesh consists of 24 elements through the thickness and 40 elements along the length. This allows 8 elements through the thickness of each material. The smeared material beam used the same mesh, with each layer having identical material properties. In both beams no slippage was allowed between layers. The first step in the analysis technique is changed slightly by using the results from the finite element analysis of the entire beam, rather than a small piece, to determine the smeared material properties. Also, note that the smeared properties are determined for an isotropic material. The modified technique consists of three steps:

1. The laminated beam model is loaded and the displacement of the midpoint of the beam is noted. A smeared material modulus is determined to give the smeared beam the same displacement at the midpoint as the laminated beam.

2. A smeared beam model using the smeared material modulus is loaded with the same load as in step 1.

3. A cross section taken from the laminated beam is deformed with the displacements found at a cross section in the smeared beam (Fig. 4). Then stresses in the cross section are determined.

The small cross section of the laminated beam, to which displacements from the smeared beam were applied, had 24 elements through the thickness, and used three elements along the length to represent two elements along the length of the full beam model. The middle row of elements were used to compare with the results from the full beam model.

To complete the analysis, the laminated beam results from step 1 are compared with the the results of step three. This provides a direct comparison between an analysis of the entire laminated beam with discrete materials and an analysis using the smeared material technique.

All analyses discussed here were performed using the static finite element code, JAC. All analyses were done using a plane strain element formulation.

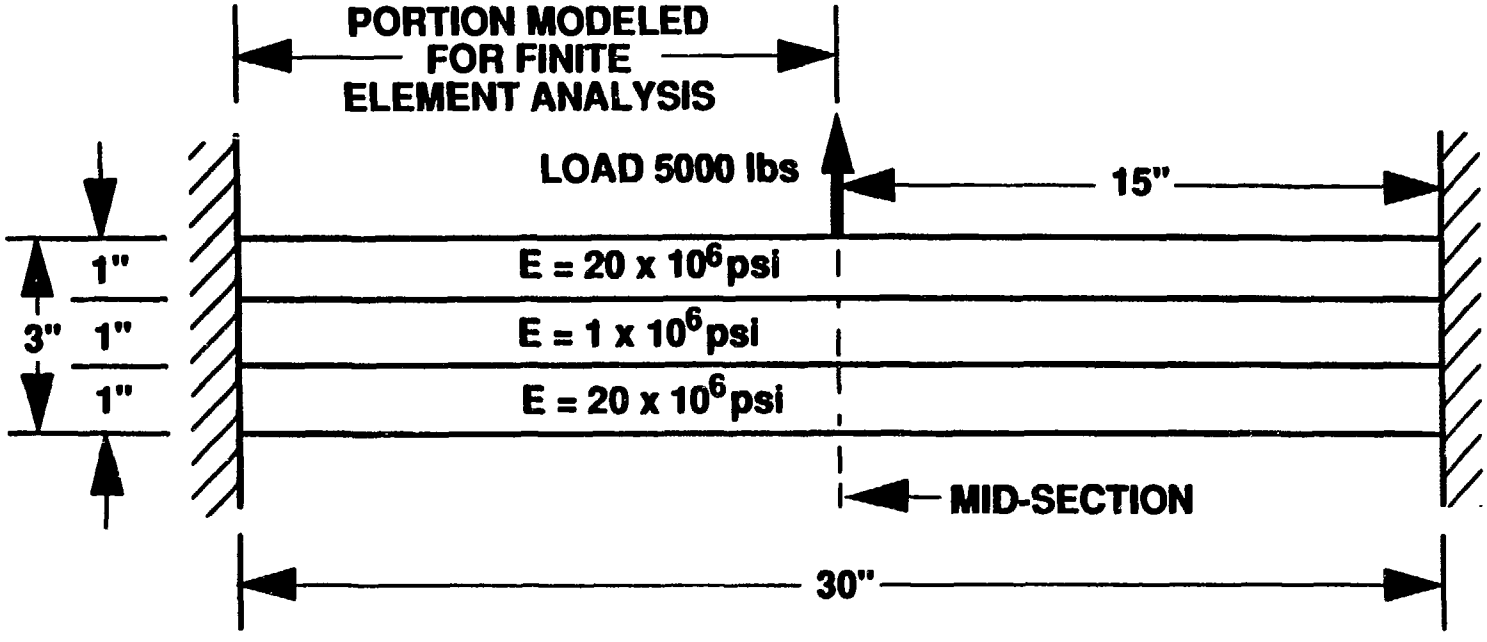

POISSON'S RATIO = 0.30 FOR ALL MATERIALS

Fig. 2 Three layer laminated beam used in example problem

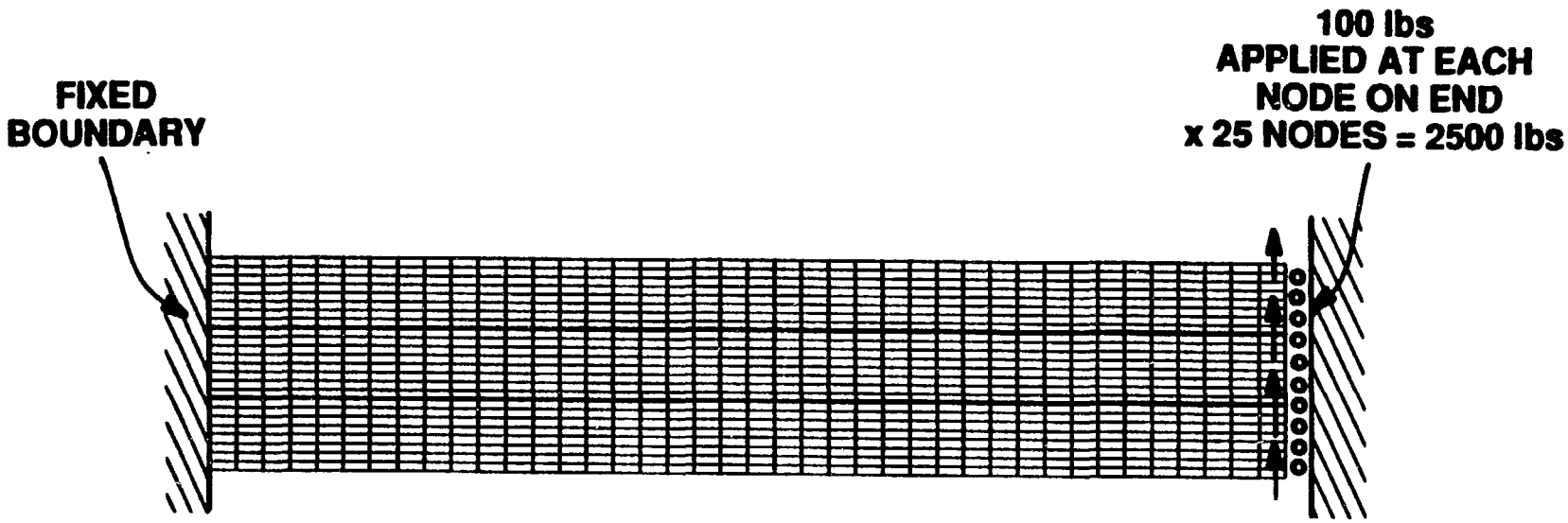

Fig 3 Finite element mesh and boundary conditions

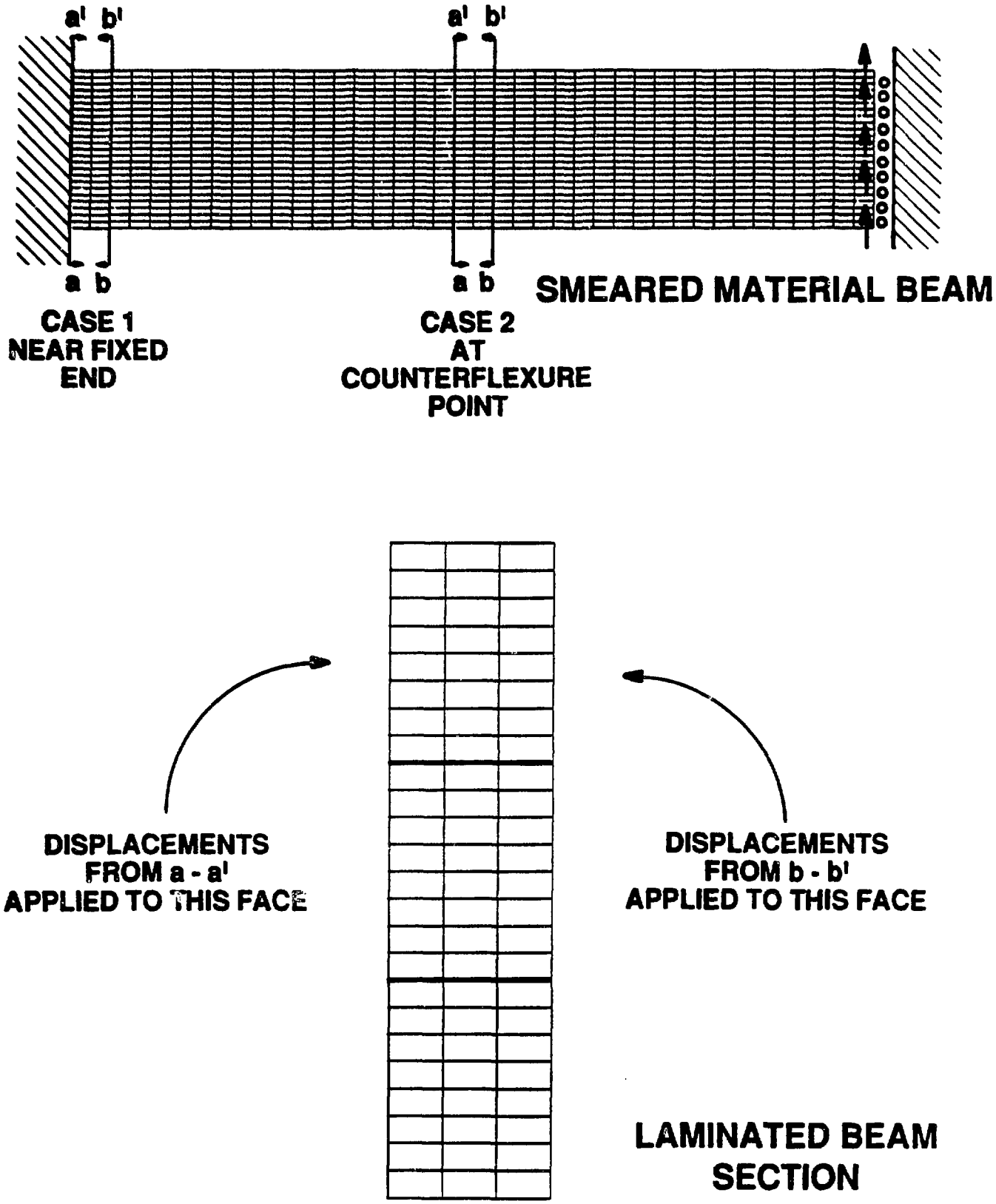

Fig. 4 Applying displacements from smeared beam to laminated section

RESULTS

A comparison of the deformed shapes of the laminated beam and the smeared material beam shows very little difference. The maximum displacement of the two beams is identical to within 0.1 percent, as would be expected given the problem definition. A very close inspection of the displaced shape reveals that the smeared beam has a slightly larger radius of curvature for each of the two curves making up the S shape, when both are magnified 100 times. So, from a macroscopic viewpoint, the beams deform similarly for the same load.

Examination of the deformed mesh from the laminated and smeared material beams reveals that internally the two beams are not alike at all. Figure 5 shows that the deformed shape of a planar section, in the smeared material beam is still planar, but the laminated beam section has a pronounced Z shape. The net result is that the smeared beam outer fibers must displace more in the horizontal direction than those of the laminated beam, the analysis results confirm this observation, the displacements of the outer fibers of the smeared beam are roughly double those of the laminated beam. The laminated beam also has three neutral axes, one in each layer of lamination, compared to one neutral axis for the smeared beam.

After applying the displacements from the smeared beam analysis to a section of the laminated beam (step 3), the results are compared with the results from the laminated beam analysis. The results were compared in two places to show differences in the stress states of the real, laminated beam and the laminated beam section with boundary displacements from the smeared material beam. The results were from a row of elements with centers located about 0.5 inch from the fixed boundary, and from a row of elements at the point of counterflexure. These points represent areas of interest in classic beam theory, and have direct analogues with other types of boundary conditions when selective portions of the beam are considered.

The von Mises stress was selected to exemplify the stress state of the beam. The plots used in the following comparison show the von Mises stress at every element center along a planar section at the point of interest. Comparing the results from the area near the fixed boundary shows that the character of the von Mises stress curve is essentially the same for the laminated beam and the laminated beam section (Fig. 6). The biggest difference between the two curves is that the magnitude of the stress predicted by applying the smeared beam displacements to the laminated beam section is about 60% greater. The areas having the highest stress at this location in the beam are the outer elements farthest from the neutral axis. In this area, the longitudinal or X direction stress dominates the second stress invariant.

At the point of counterflexure of the beam, the shear in the beam is at its highest. The von Mises stress in the laminated beam at this section is compared with the stress state predicted by applying the displacements from the smeared beam to the laminated section (Fig. 7), which reveals a stress state with an entirely different character. As at the section near the fixed boundary, the highest stress in the section is over predicted by 60%, and these stresses occur in the same area of the

beam. However, the stresses in the low modulus material at the center layer of the beam are under predicted by a factor of 10. Overall, the stress state in this area is about six times lower than that at the end.

CONCLUSION

The comparisons made above show that the smeared beam distributes shear through the section more uniformly than the laminated beam. The laminated beam takes advantage of the lower modulus material at the center and causes more shearing in the center material.

The analyses presented in this report demonstrate that the technique of using smeared materials to calculate laminated beam deflections can be used successfully, but should be examined carefully with each application. The test problem showed that the smeared material technique, as it was implemented in the test problem, will be conservative in predicting the response of the beam. That is, it will predict peak stresses which are higher than those actually seen in the real, laminated beam. However, the smearing technique failed to predict the nature of the stress state in the beam in a region of lower overall stress. If the stresses at this point were critical to the design of the beam, the technique would have failed to provide the information necessary. Consequently, the smearing technique should be carefully examined as it is applied to each problem.

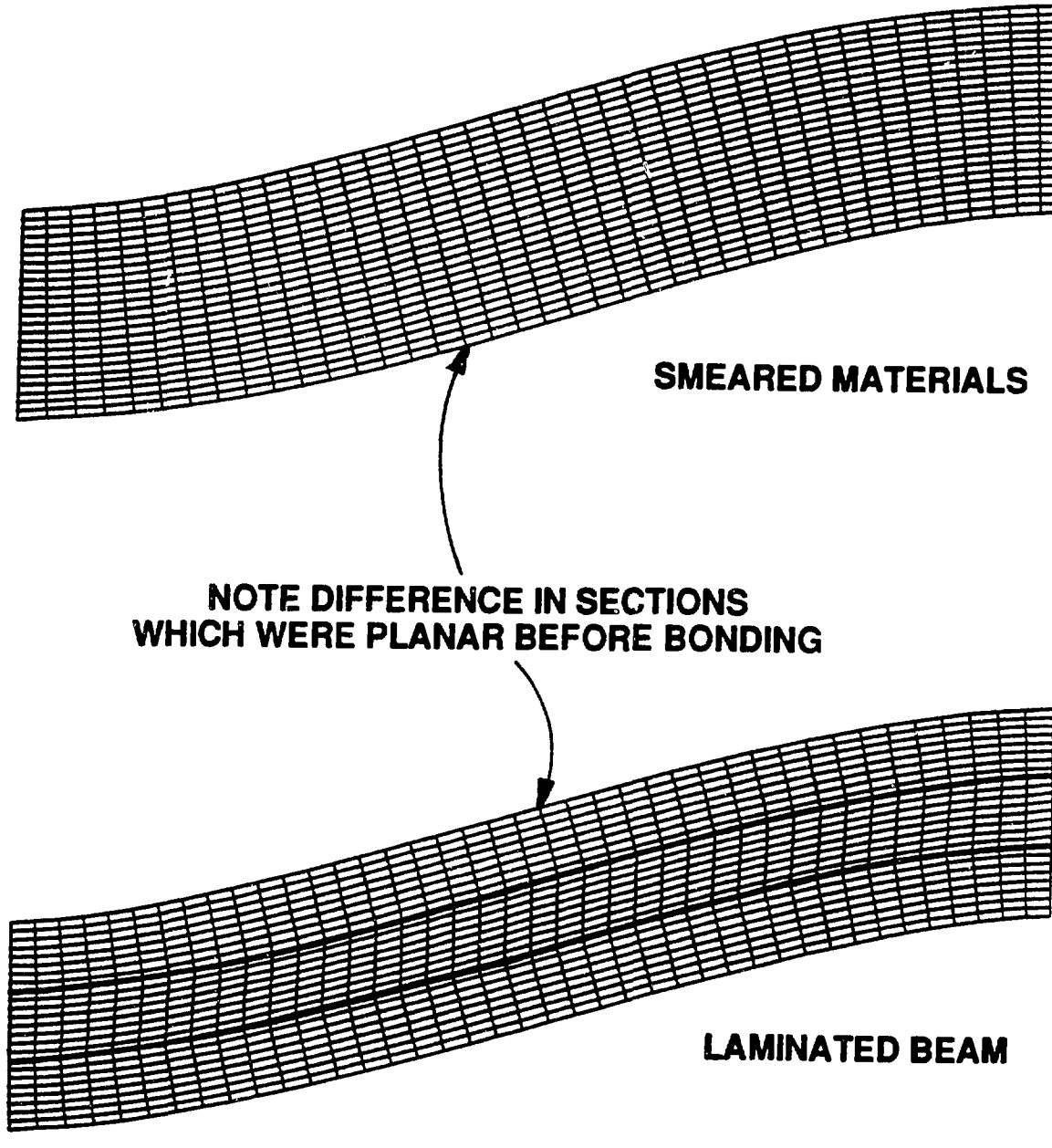

Fig. 5 Deformed mesh for smeared material and laminated beams

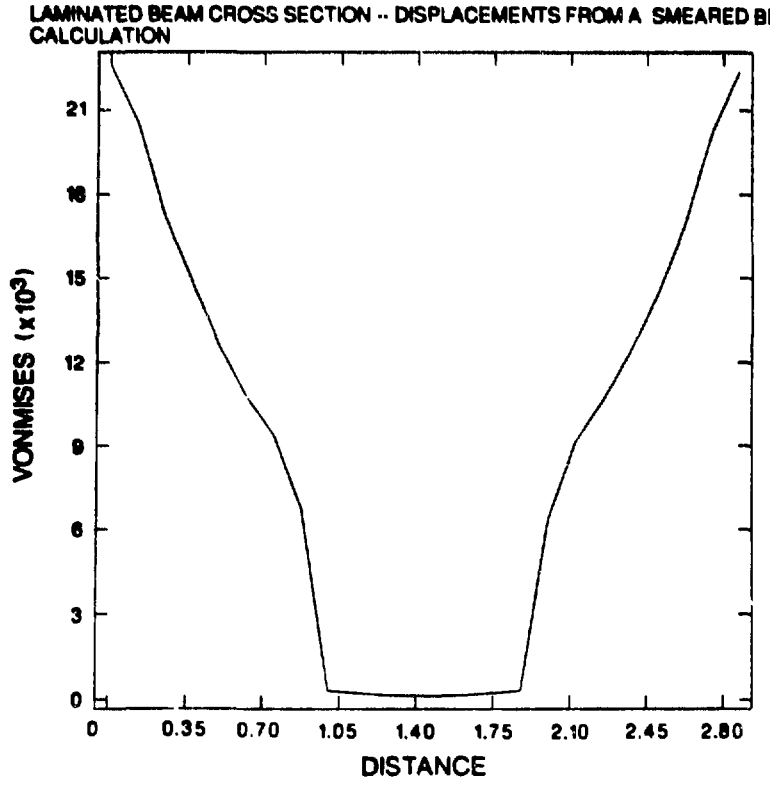

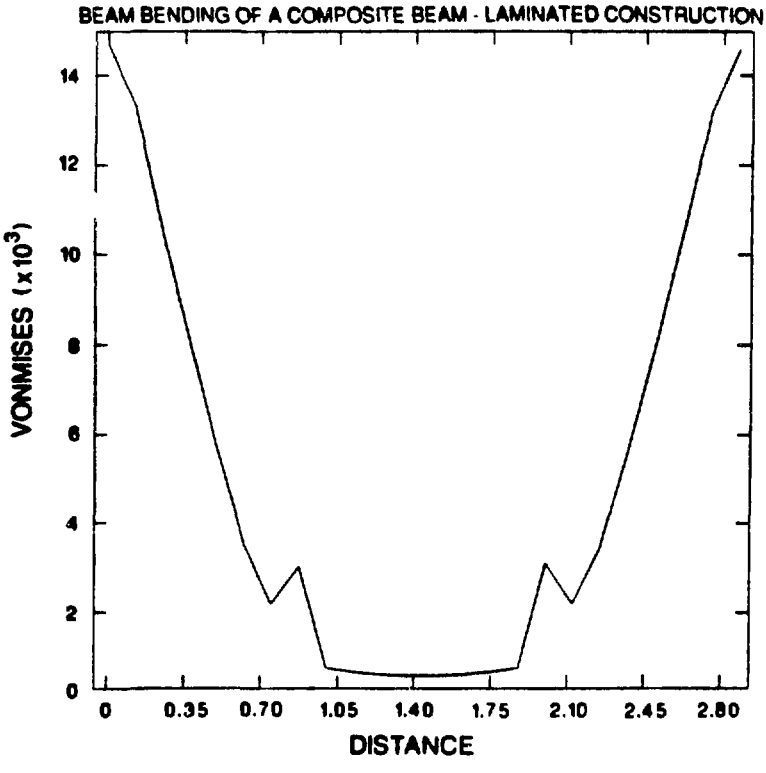

Fig. 6 Vonmises stress near fixed boundary

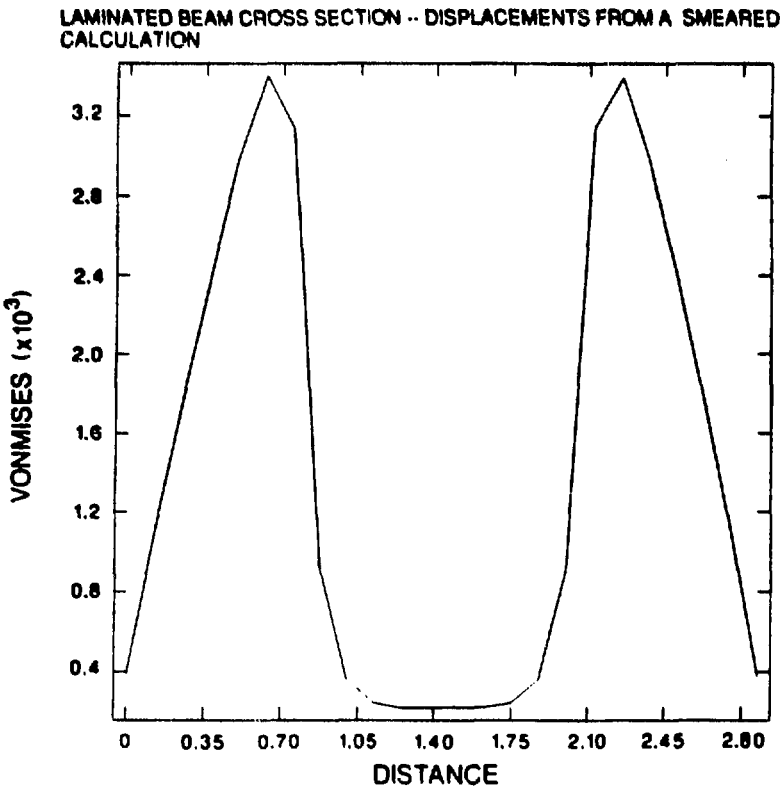

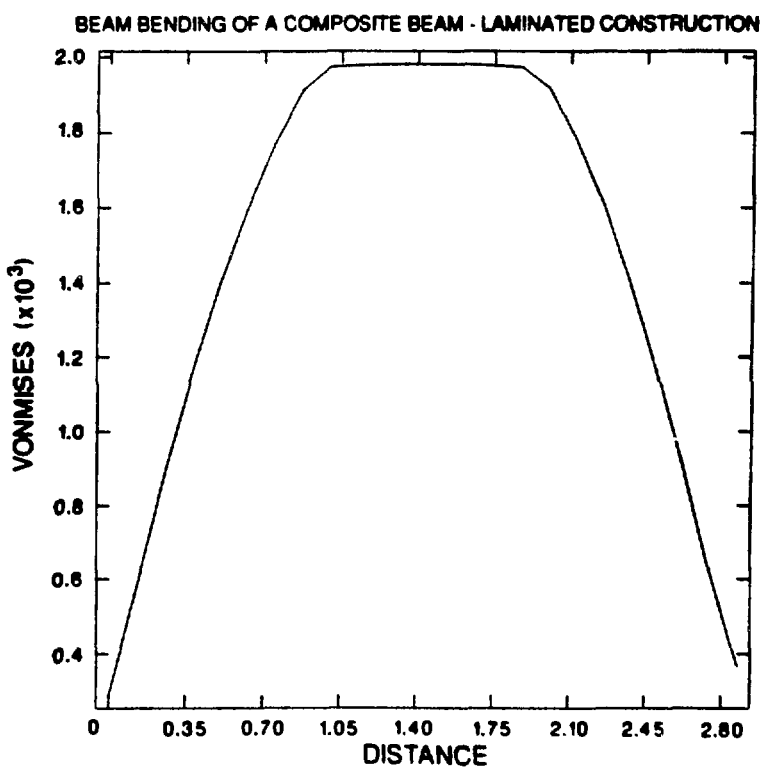

Fig. 7 Stress near point of counterflexure

NUMERICAL ANALYSES OF EDDY CURRENT AND ERROR FIELD FOR RFP BY 'INCANET'

N.Suzuki, M.Uesaka, K.Saitoh*, Z.Yoshida*, and N.Inoue*

Ishikawajima-Harima Heavy Industries Co.,Ltd. (IHI)

*Nuclear Engineering Department, Faculty of Engineering, University of Tokyo

Numerical analyses of eddy current and resulted error field for RFP chamber are presented. The computer code named 'INCANET' uses a network mesh method. It was confirmed that the eddy current induced in a vacuum chamber tends to flow inner part of the torus chamber. The component of eddy current flows around vertical port holes genarates about two times stronger error field than that at no-hole location.

1. Introduction

Recently, eddy current behavior in RFP experimental devices is thought to be an important issue. Especially, error field generated by the eddy current is the most interesting topic. It is reported in some experimental reports that reduction of eddy current effect gives improved RFP plasma discharges. Therefore, configuration of error field and flow pattern of eddy current are to be analyzed in design of chamber(liner) and shell.

In this paper, analyses of eddy current and error field in REPUTE-1 are presented. The eddy current analysis is carried out in case of setting-up phase of plasma. Only a vacuum chamber is considered. The chamber consists of thin bellows parts and straight cylinder parts. In REPUTE-1, the chamber has many big port holes(54 holes). So it is anticipated that a flow pattern of the eddy current becomes rather winding complicatedly.

According to the results of the eddy current in chamber, generated error field is calculated.

Those analyses were carried out by the computer code 'INCANET'(IHI Induced Current Analysys Code by Network Mesh Method) and CAE(Computer Aided Engineering) system installed on VAX 11/780.

2. Outline of Analyzed System

Vacuum chamber of REPUTE-1 is made of INCONEL 625 and consists of bellows and straight short cylinders. Every cykinder has three port holes shaped almost rectangularly.(see Fig.1) Thicknesses of this chamber are 2mm(cylinder part) and 1mm(bellows part). REPUTE-1 has an iron core transformer as a OH-coil. In this paper, a setting-up phase with a characteristic time of 1ms(exponential) is analyzed. Namely, flux change at the torus center(not linked with the chamber) is taken into consideration as an external source of eddy current. Simulated system is 10°-sector of the chamber(5°:bellows, 5°:cylinder) and 112 meshes are set on this sector.

3. Results and Discussions

Fig.2,3 and 4 show flow patterns of eddy current induced in the chamber at t=0.1ms,0.3ms and 1.0ms, respectively. Fig.5 shows the time evolution of the iron core flux and eddy currents. The total eddy current I_1 is separated into two currents I_2 and I_3. I_2 and I_3 are the current flows in inner part of the chamber and the current flows in outer part of it, respectively. From the results shown in Fig.5, it is understood that almost eddy current tends to flow in inner part of the vacuum chamber. The result that flow of outer eddy current I_3 winds sharply around the vertical port hole is a remarkable fact. By this somewhat unexpected flow pattern, dipole-type error field appears so distinctly. Fig.6 and 7 show the error field generated by the eddy current shown in Fig.3 at locations indicated in Fig.2(A-A, B-B). It is confirmed that the error field just under the port holes(A-A) is about two times stronger than in the location with no port hole(B-B).

Fig. 8 and 9 show the contour lines of strength of error field(scalar) in the locations A-A and B-B, respectively.

4. Conclusion

Analyses of eddy current and resulted error field in a vacuum chamber of REPUTE-1 were cariied out.
These analyses give some new information on a behavior of eddy current.

Further analyses of eddy current are under planning. (e.g : behavior of eddy current in the case that the holes are covered by some conducting materials)

Address :

IHI ... Tokyo-Chuo Bldg. 6-2, Marunouchi 1-Chome, Chiyoda-Ku, Tokyo 100 Japan

Univ. of Tokyo

... 3-1, Hongo 7-Chome,Bunkyo-Ku, Tokyo 113 Japan

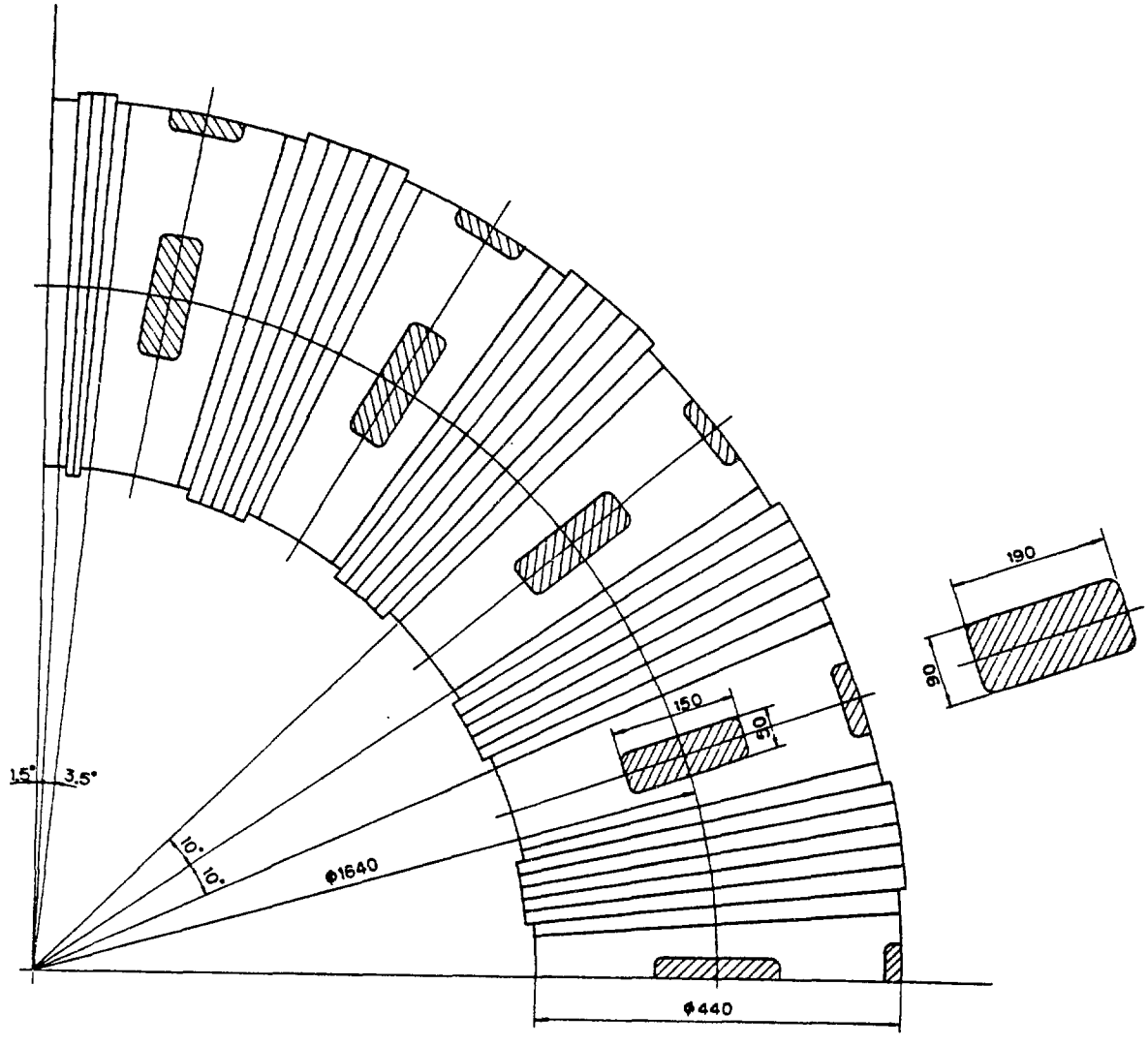

Fig. 1 VACUUM VESSEL

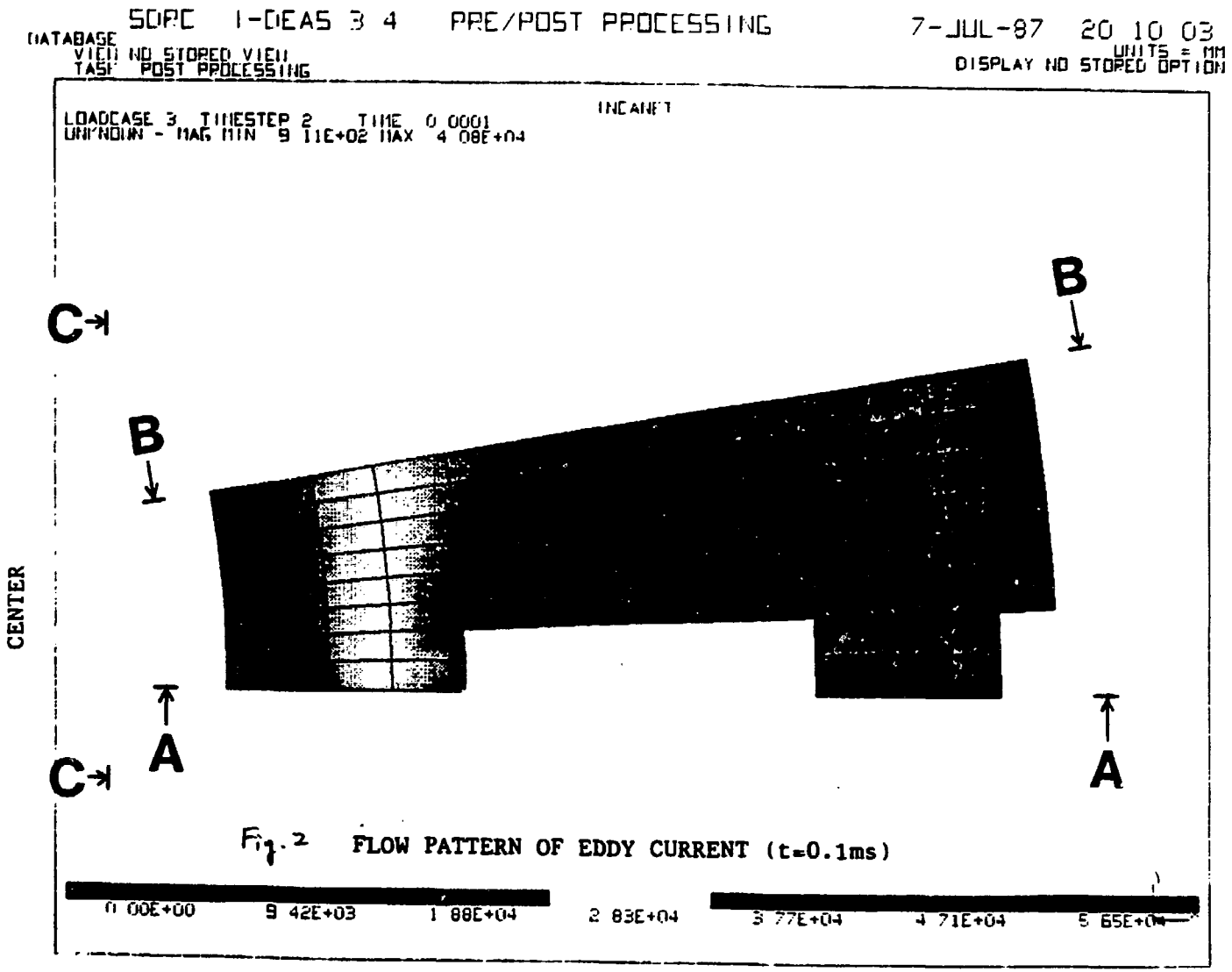

Fig. 2 FLOW PATTERN OF EDDY CURRENT (t=0.1ms)

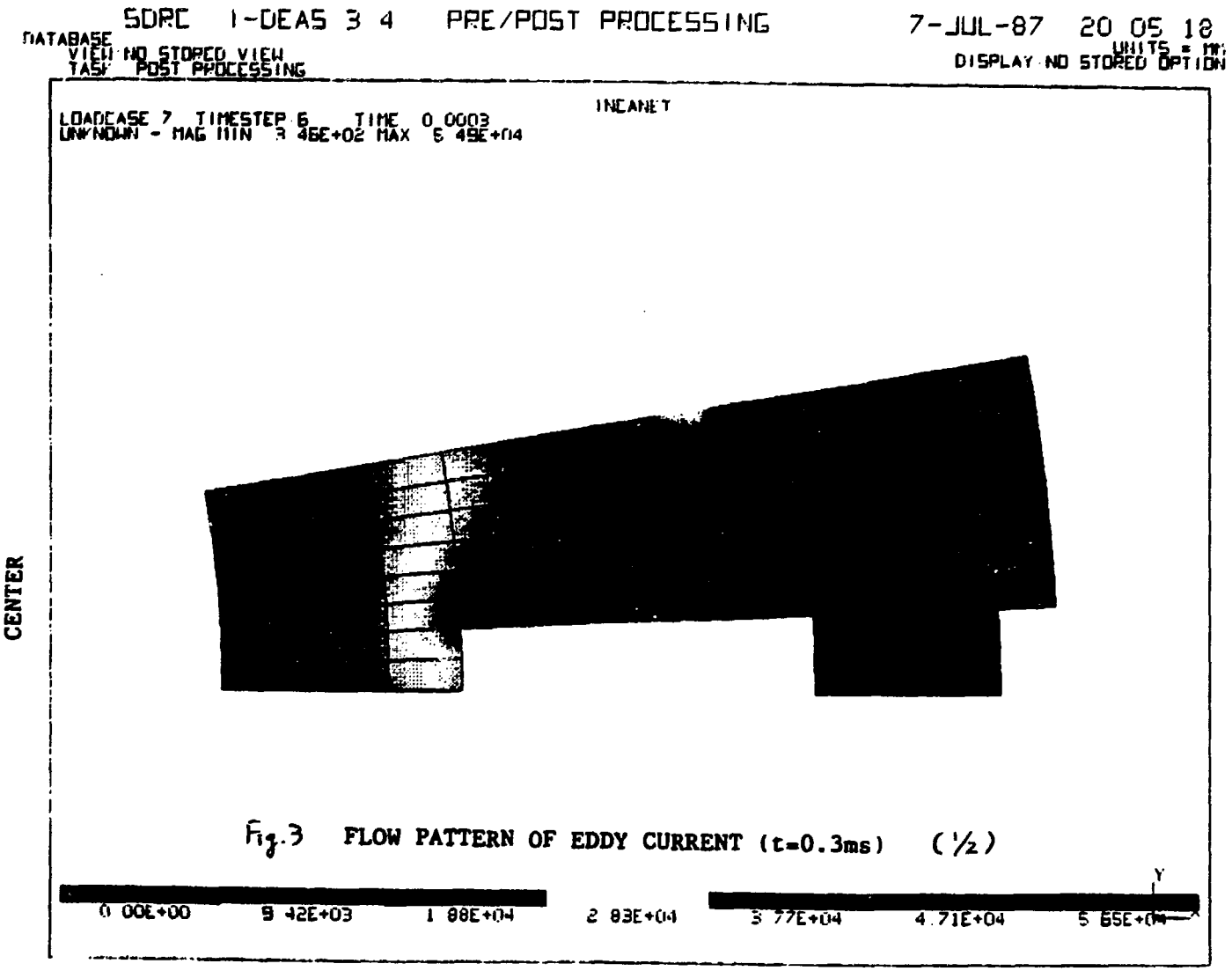

Fig.3 FLOW PATTERN OF EDDY CURRENT (t=0.3ms) (½)

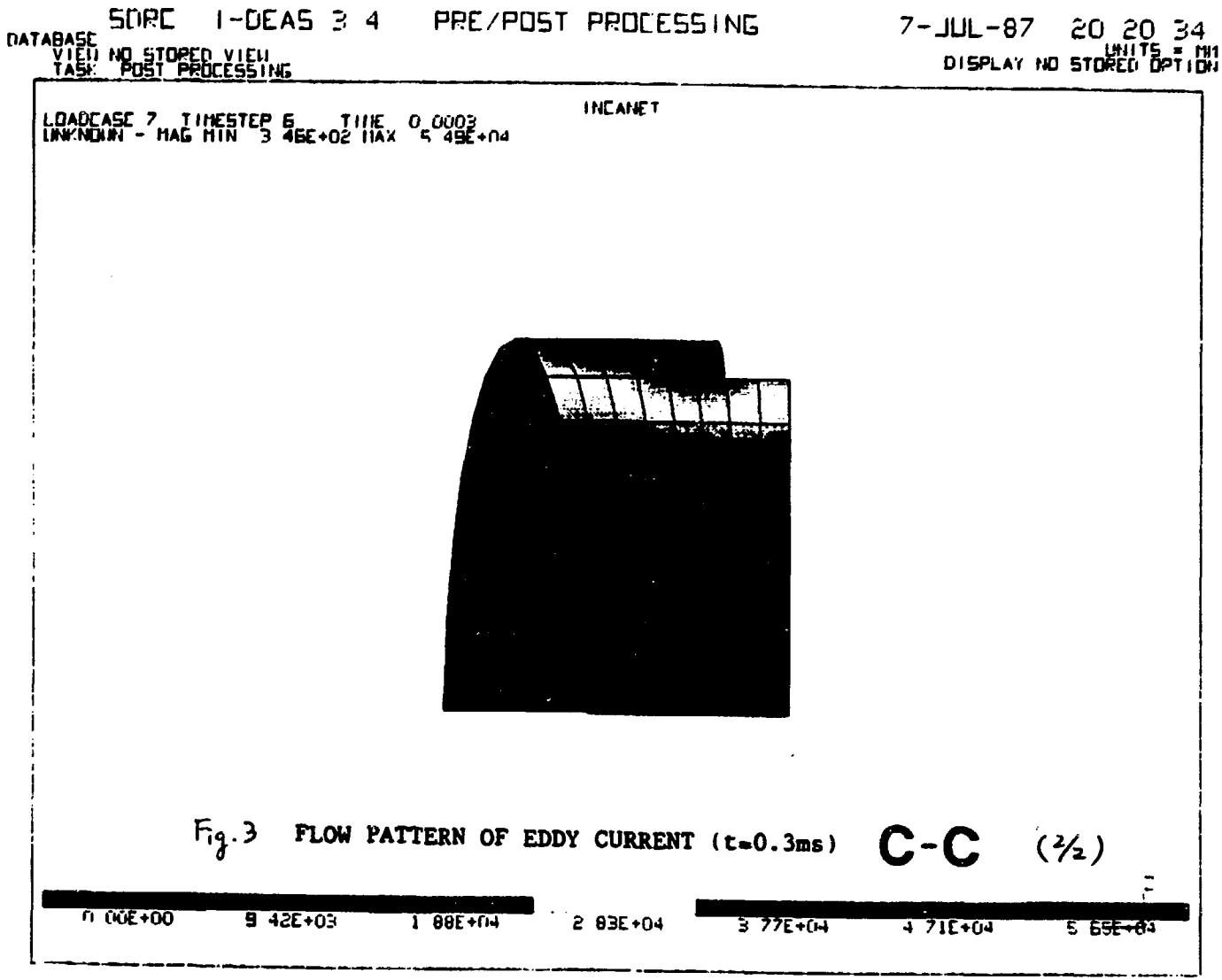

Fig.3 FLOW PATTERN OF EDDY CURRENT (t=0.3ms) **C-C** (2/2)

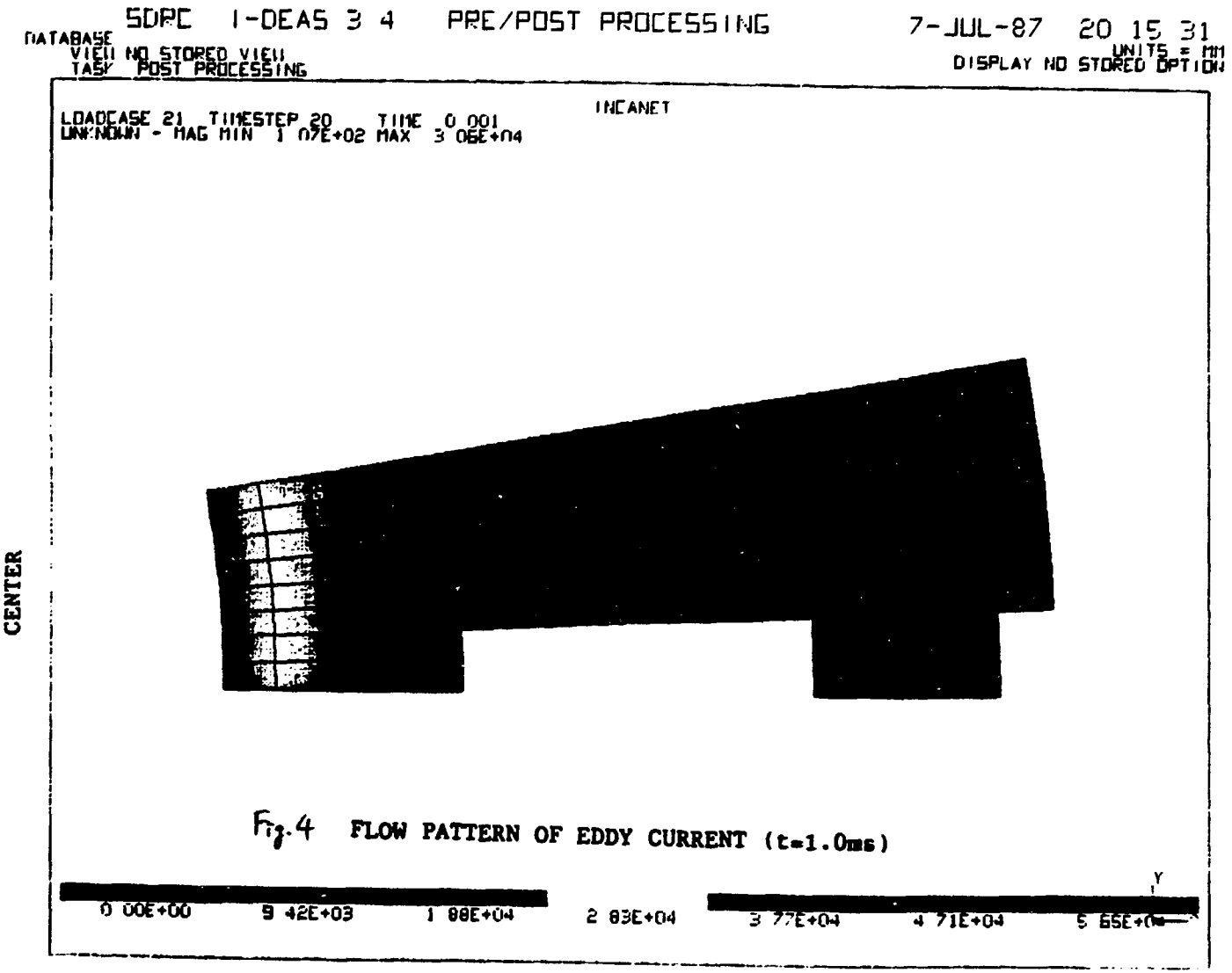

Fig.4 FLOW PATTERN OF EDDY CURRENT (t=1.0ms)

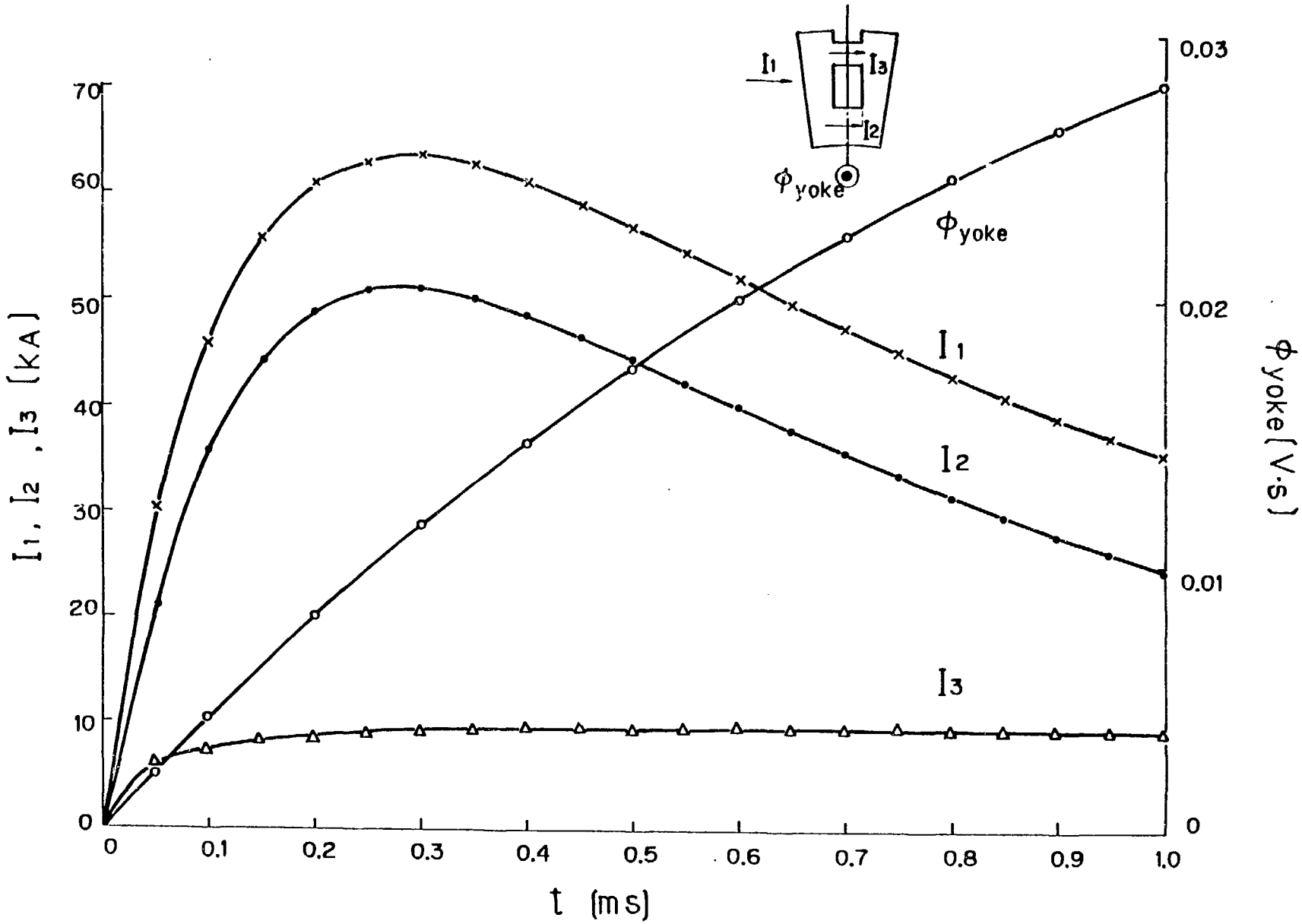

Fig. 5 TIME EVOLUTION OF CORE FLUX AND EDDY CURRENT

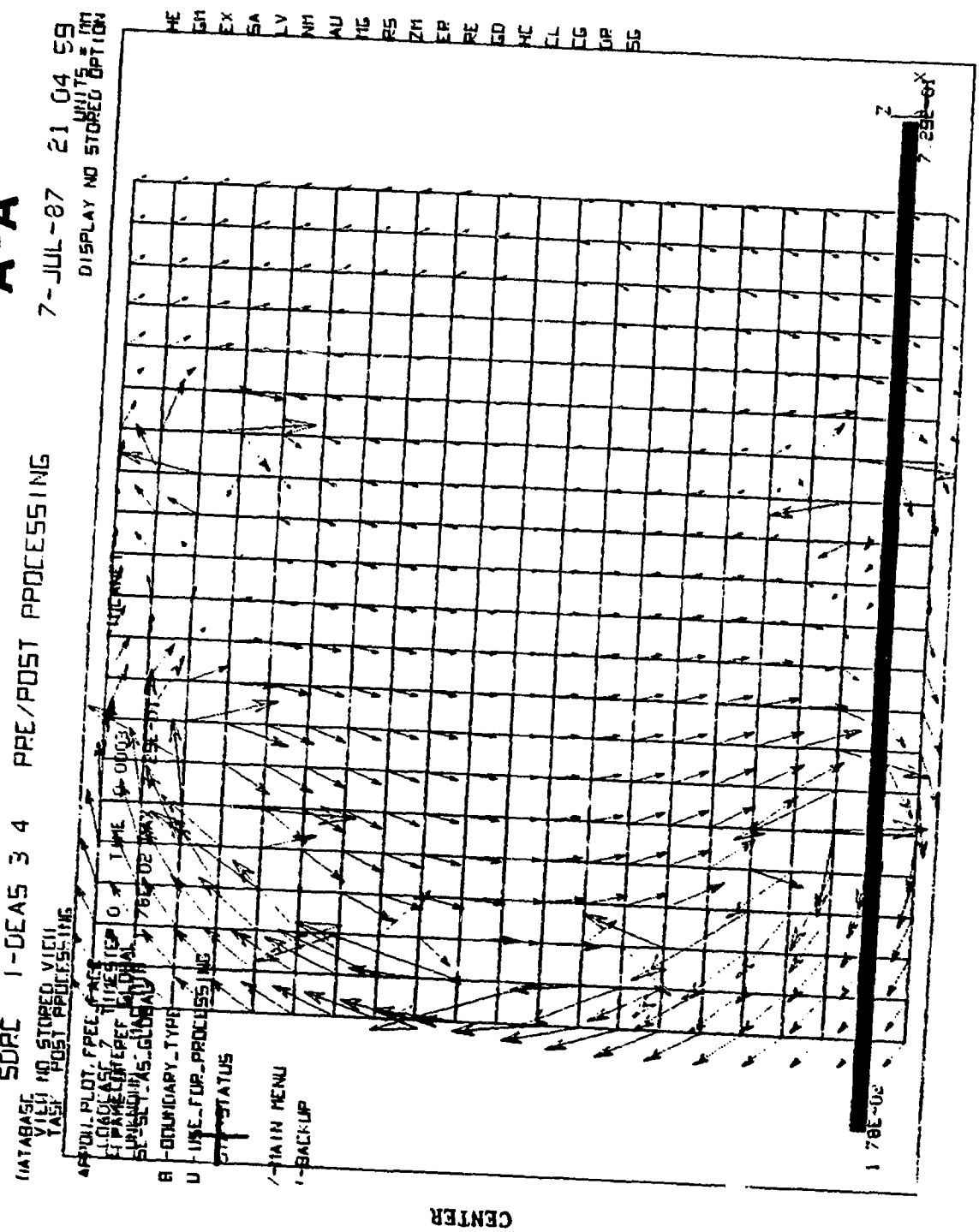
Fig. 6 ERROR FIELD DUE TO EDDY CURRENT (t=0.3ms)
A-A
SDRC I-DEAS 3 4 PRE/POST PROCESSING
7-JUL-87 21 04 59
DISPLAY NO STORED OPTION
UNITS = IN
VIEW NO STORED VIEW
TASK POST PROCESSING
DATABASE
MAIN MENU
BACKUP
CENTER

Fig.7 ERROR FIELD DUE TO EDDY CURRENT (t=0.3ms)

B-B

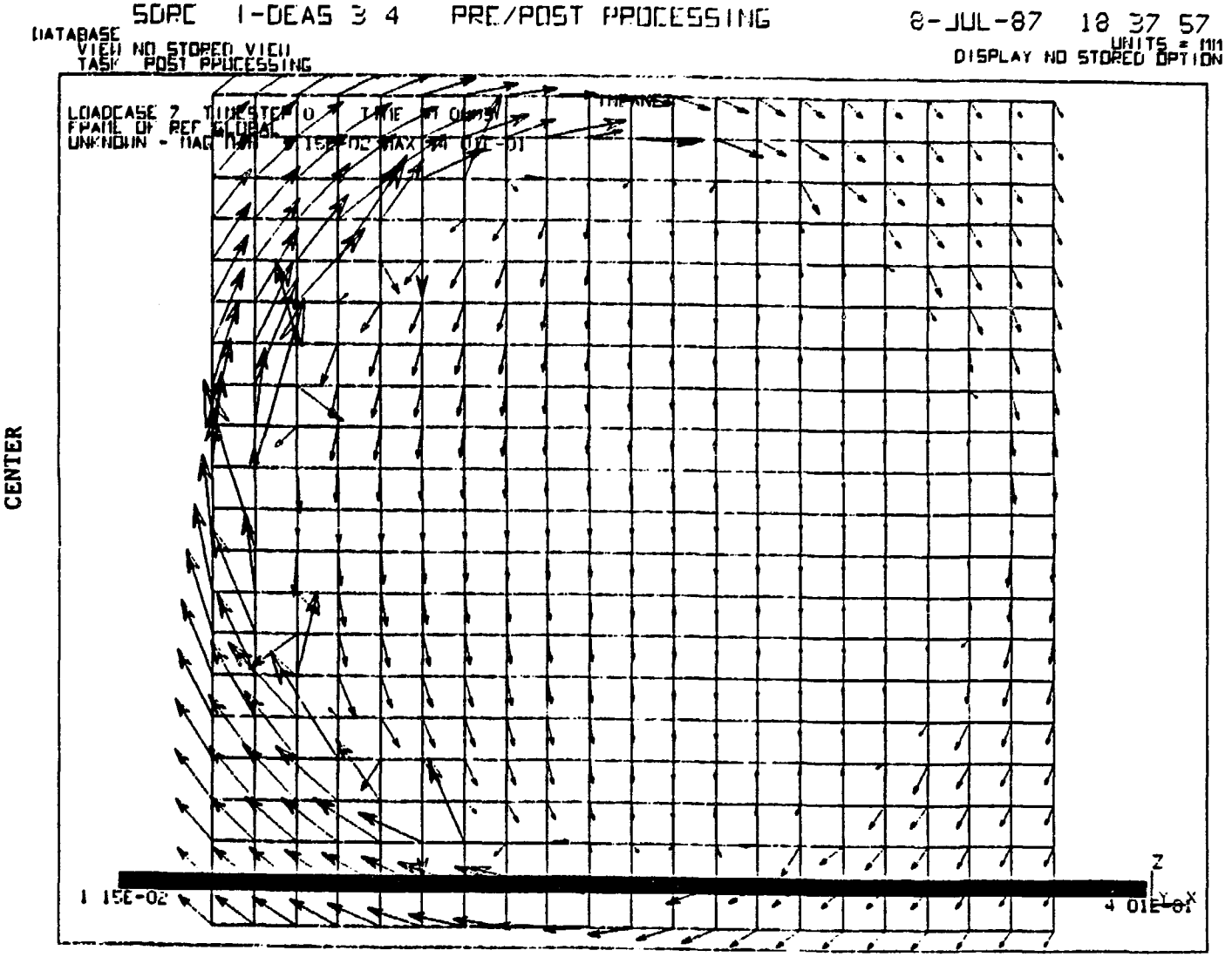

Fig. 8 CONTOUR LINES OF ERROR FIELD STRENGTH (t=0.3ms) A-A
SDPC I-DEAS 3 4 PRE/POST PROCESSING
8-JUL-87 19 05 04
DISPLAY NO STORED OPTION
CENTER
Z

Fig.9 CONTOUR LINES OF ERROR FIELD STRENGTH (t=0.3ms) **B-B**

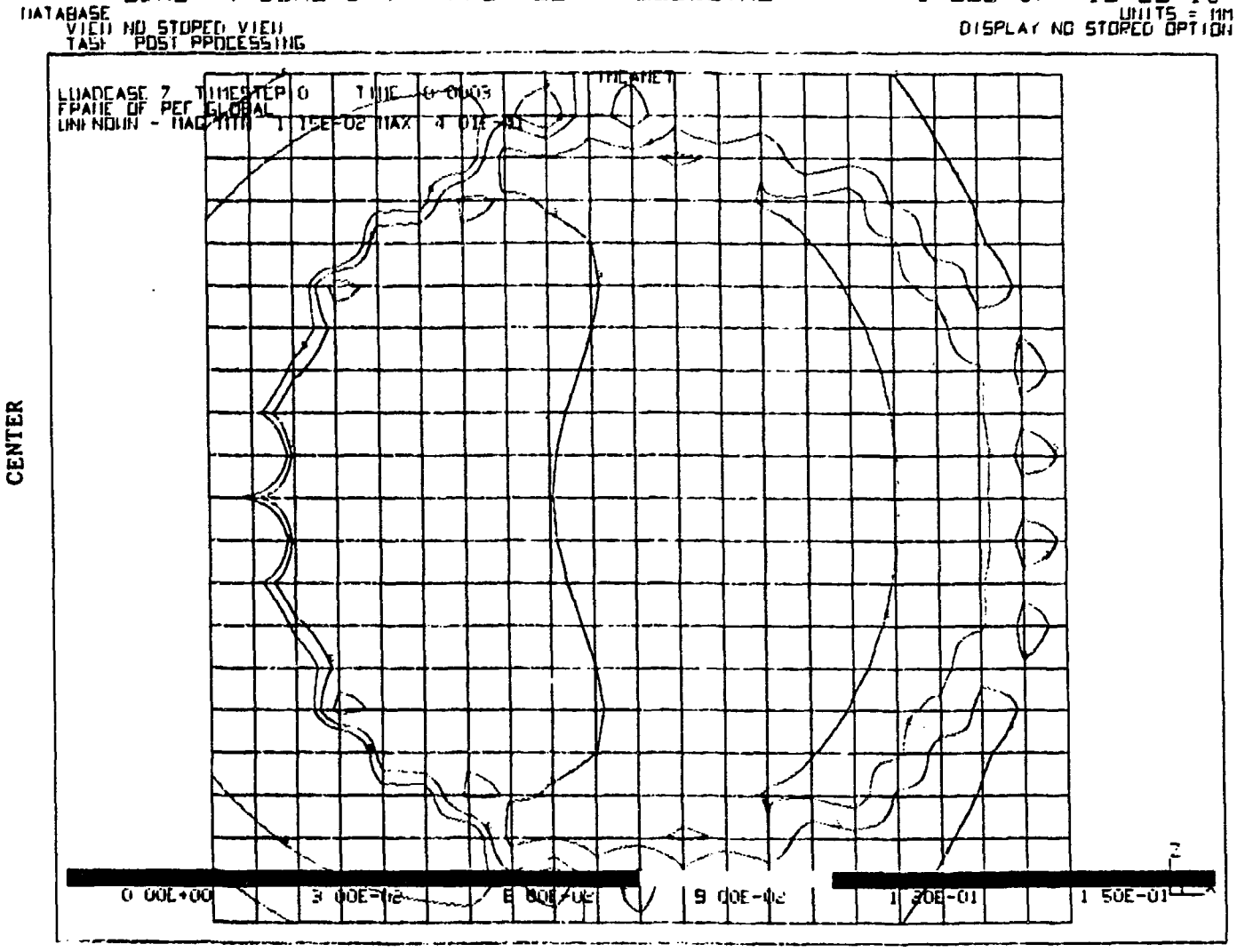

467/HV8

STRESS ANALYSIS OF POLOIDAL FIELD COILS FOR ZTH MACHINE

Steven P. Girrens and Joel G. Bennett
Los Alamos National Laboratory, Los Alamos, New Mexico 87545

INTRODUCTION

Three-dimensional finite element analysis of representative poloidal field (PF) coils for the Los Alamos CPRF/ZTH air core machine is being performed to determine static stress levels developed within the coil structure due to Lorentz-force loading. Magnetic fields for ZTH are produced, in part, by 18 PF coils (10 ohmic heating and 8 equilibrium field). The PF coils are made with copper conductors separated by epoxy insulation. The PF coils are supported by 16, equally spaced, 4.0-in. thick, radial G-10 bulkheads. This paper summarizes the computational procedures used in the analysis and presents coil stress results obtained to date.

COMPUTATIONAL METHOD

Because of the complex coil configuration and degree of detail required to obtain significant results, the computational study is performed in three distinct steps as illustrated in Fig. 1. In step one, a portion of the coil cross section and circumference including the copper conducting coils inside the insulating epoxy matrix is modeled. The step-one model is independently loaded in all three normal directions, plus torsionally, to compute orthotropic material properties representing a bulk or smeared coil material. Step two of the analysis utilizes symmetry to evaluate a bulk material coil section of actual dimension suspended between supporting bulkheads and undergoing axial and radial Lorentz-body-force gradients. During step two, various bulkhead support boundary conditions may be investigated and the step-two analysis results indicate the circumferential coil location of maximum stress. During step three, a detailed coil cross section, including the copper conductors in

the insulation matrix, is again considered. The step-three model circumferential thickness ranges from one-sixth to one-twelfth of the step-two model section. The nodal displacements computed in step two are used to interpolate displacement boundary conditions on all faces of the step-three configuration. Detailed stress results in both conductors and insulation are produced from the step three analysis.

ANALYSIS RESULTS

The analysis procedure described in the previous section has been applied to equilibrium field (EQ) coil 9 and is currently being used to study ohmic heating (OH) coil 5. For EQ9, the step-two analysis indicates that the maximum coil stresses occur in the region located at the center of the bulkhead as shown in Fig. 2. Displacement results from this region were used in the step-three analysis to obtain detailed stress levels in the copper and insulation. The step-two results provide useful information in addition to input for the step-three analysis. Figure 3 is a plot of axial bearing pressure transferred from EQ9 to the bulkhead for various widths of bulkhead support. Figure 4 illustrates maximum vertical displacement versus location along the coil circumference for EQ9 from bulkhead centerline to coil midspan between bulkheads. Table I summarizes stress results obtained from the step-three analysis of EQ9.

TABLE I

MAXIMUM STRESSES IN PSI FOR EQ COIL 9 (12-IN. BULKHEAD)

Stress Type	Copper	Insulation
Von Mises	16 636	1751
Maximum Principal	17 565	1890
Maximum Shear	8 783	945

As seen from Table I, stress levels in the conductors were found to approach values 10 times greater than those computed in the insulation. The maximum stress levels in the copper were found to be in agreement with stresses computed independently at Los Alamos with a modified Princeton coil analysis code for the PF coil specifications.

SUMMARY

As a result of this study, the locations and levels of maximum stresses in both the copper conductors and insulating matrix are being quantified. Stress levels developed in EQ9 were found to be below yield and bond strength limits for the Lorentz-loading applied. In addition, the computational procedures developed provide a method to obtain detailed stress-displacement results for complex field coils.

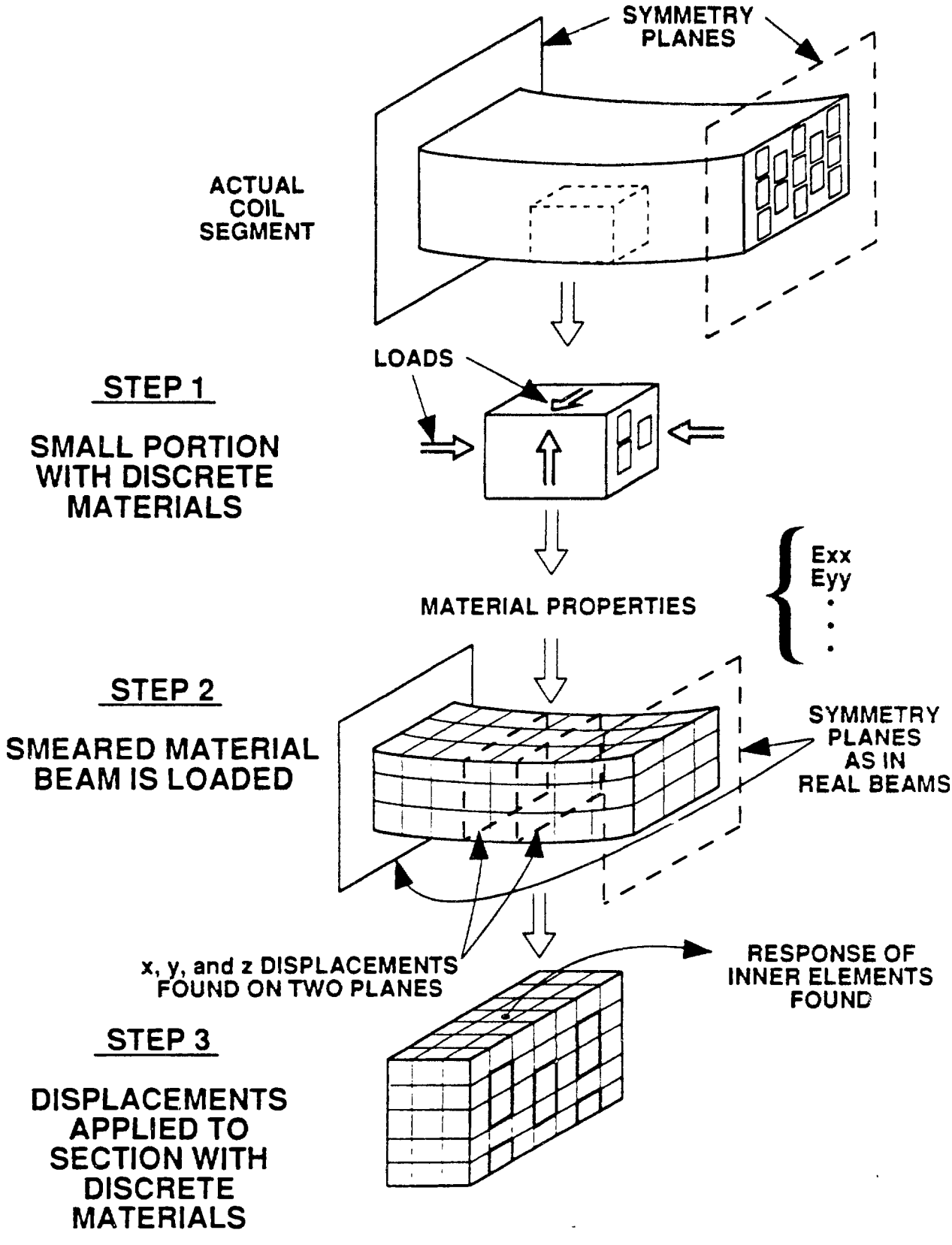

Fig. 1. Computational method outline for coil analysis.

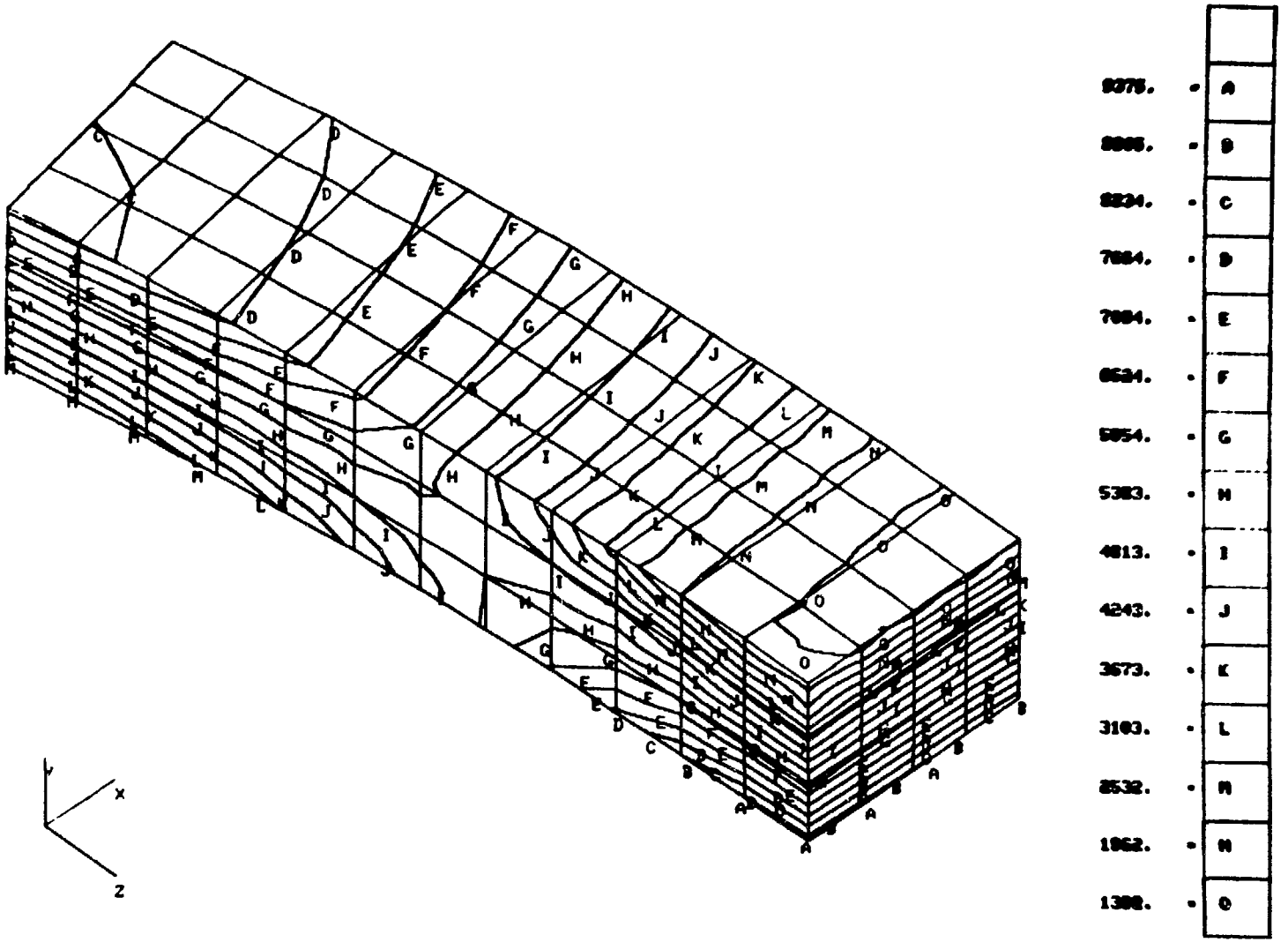

Fig. 2. Von Mises stress contours, for EQ9 bulk coil model.

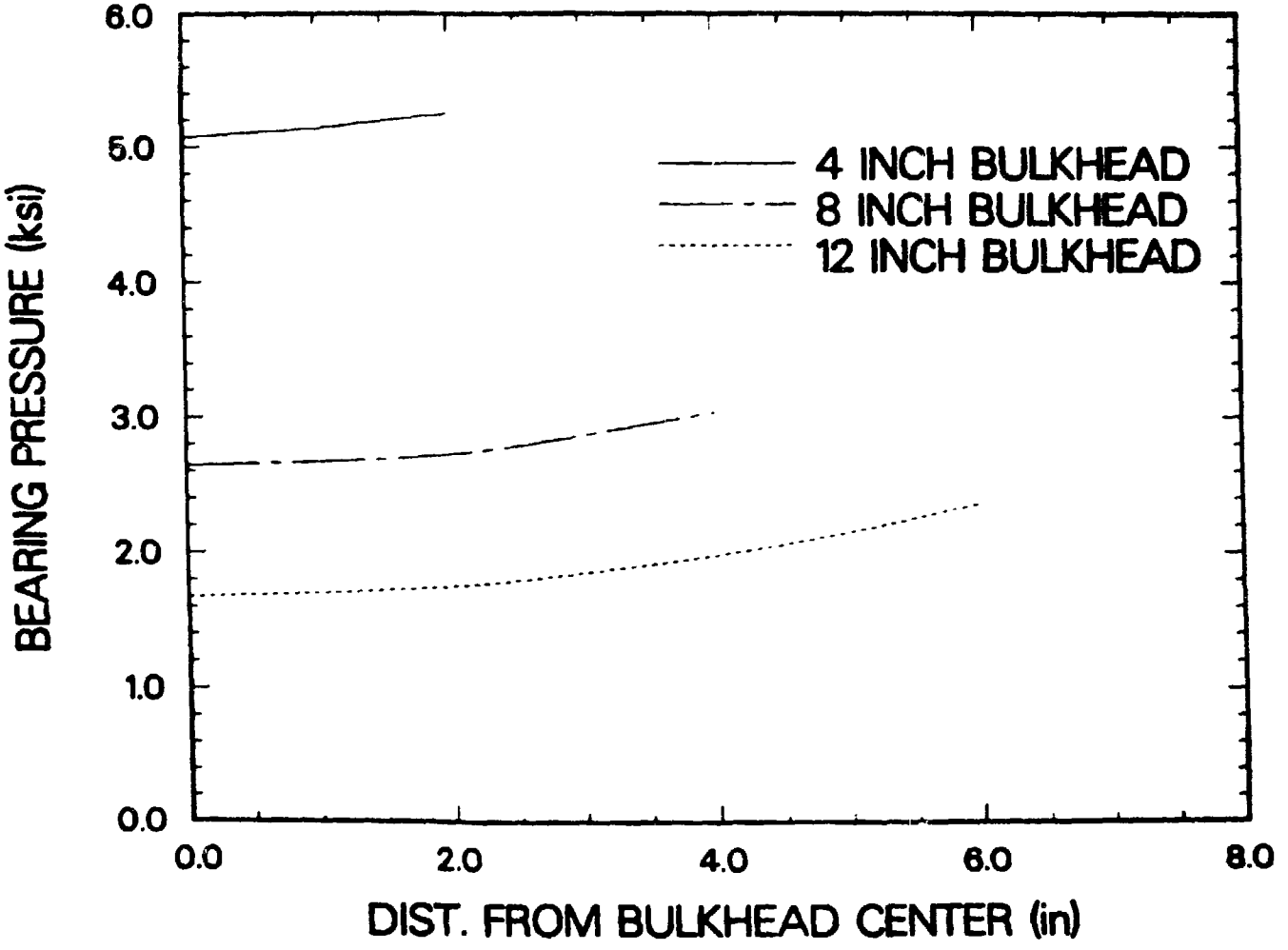

Fig. 3. Bearing pressure on bulkhead to support EQ9.

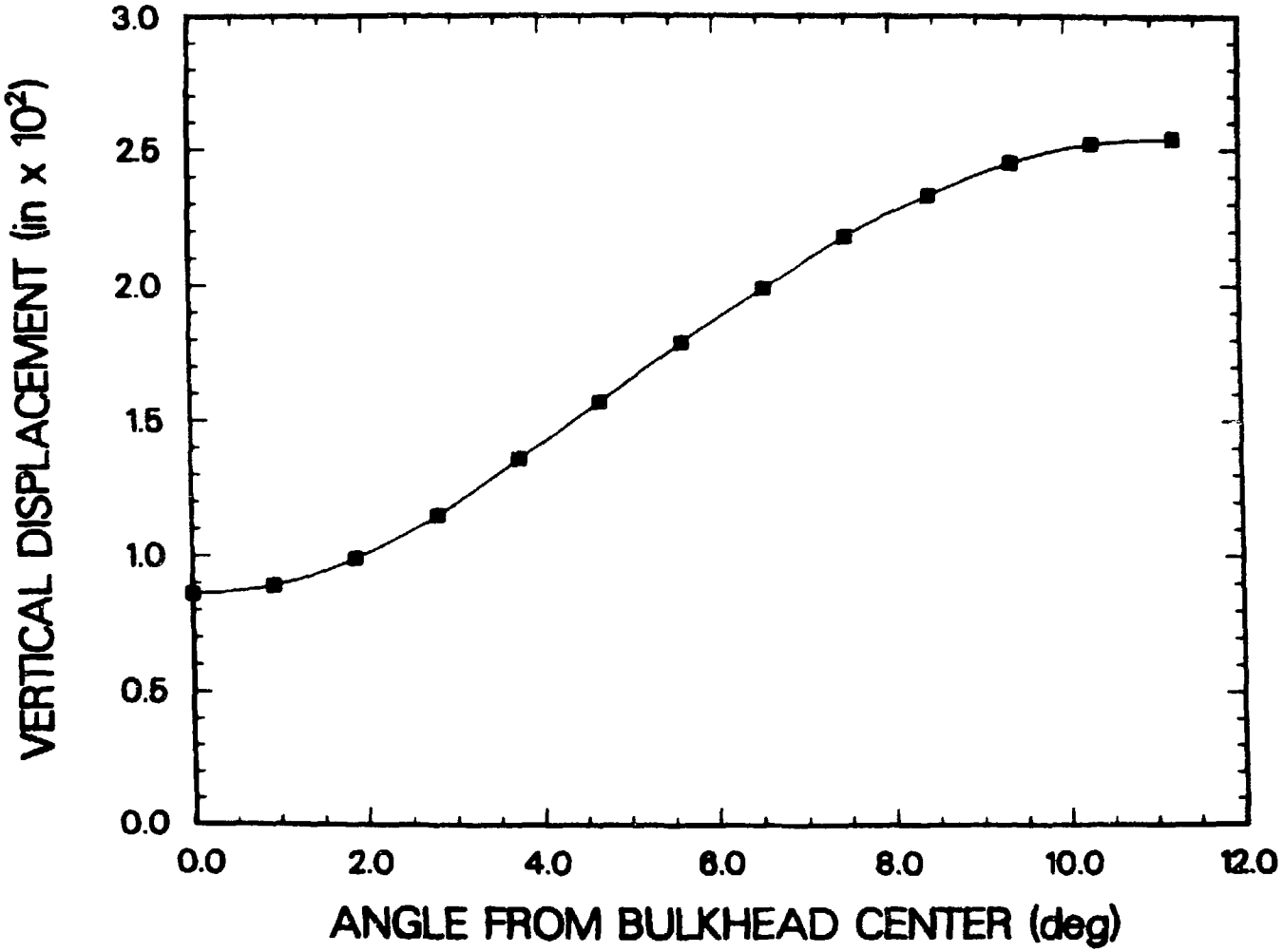

Fig. 4. Maximum vertical displacement versus circumferential location for EQ9.

High Power Closing Switch

K. Ogawa, T. Shimada, Y. Hirano, Y. Yagi,
I. Oyabu*, S. Yamaguchi* and Y. Yamane*

Electrotechnical Lab.
*) Mitsubishi Electric Corp.

1. Introduction

The high power closing switch system has been developed for the power supply system in the TPE-1RM15. This switch has the metal contacts, therefore, the number of coulomb, which passes through the switch, is very large as compared with the arc switch like the ignitron. The contact should be moved fast to use as the start switch, so there are two types of the problems. One is related to the jitter and another is arc problems generated between the contacts caused by the chattering. The arc damage reduces the life time of the switch. The characteristics of this switch is introduced in this memo.

2. Characteristics of the High Power Closing Switch

Fig. 1 shows the high power closing switch system which is used in the OH/coil power supply of the TPE-1RM15. The center white tank is the switch and it is connected to the saturable reactor(SR). This suppresses the switch current during the chattering of the contacts. So no arc is expected between the contacts and the life time is able to be extended. The start timing of the discharge is set by three ignitron switches, which is connected to the resistors. They are used for the balance of the ignitron currents, and the circuit current is translated from the ignitron bank to the high power closing switch bank. In order to reduce the current translation time, the switch bank uses low inductance and resistance cables.

The schematic structure of the switch is shown in the Fig. 2. The switch current flows from the terminal to the terminal(1),(2), and the movable contact(5) and the fixed contacts(3) are in the high pressured Nitrogen gas tank(6). This high pressured gas drives the movable contact's piston(8) and is also useful for the insulation. The external trigger opens the electric control valve(11) and the mechanical control valve(12) loses the high pressured gas from the main cylinder(7). Finally, the movable contacts move to the fixed contact and the switch is closed.

The specification of the high power closing switch is summarized in Table-1. The closing time means the time interval from the trigger in to the first ON of the switch. The jitter is the standard deviation of the closing time, and it is gauranteed values and usually it is almost one third of this values.

The power supply circuit of the OH/coil in the TPE-1RM15 is shown in the Fig. 3. The experiment started at the end of Dec. 1985, and until now the number of the operation is exceeded up to be 4000 times, and we find no defects.

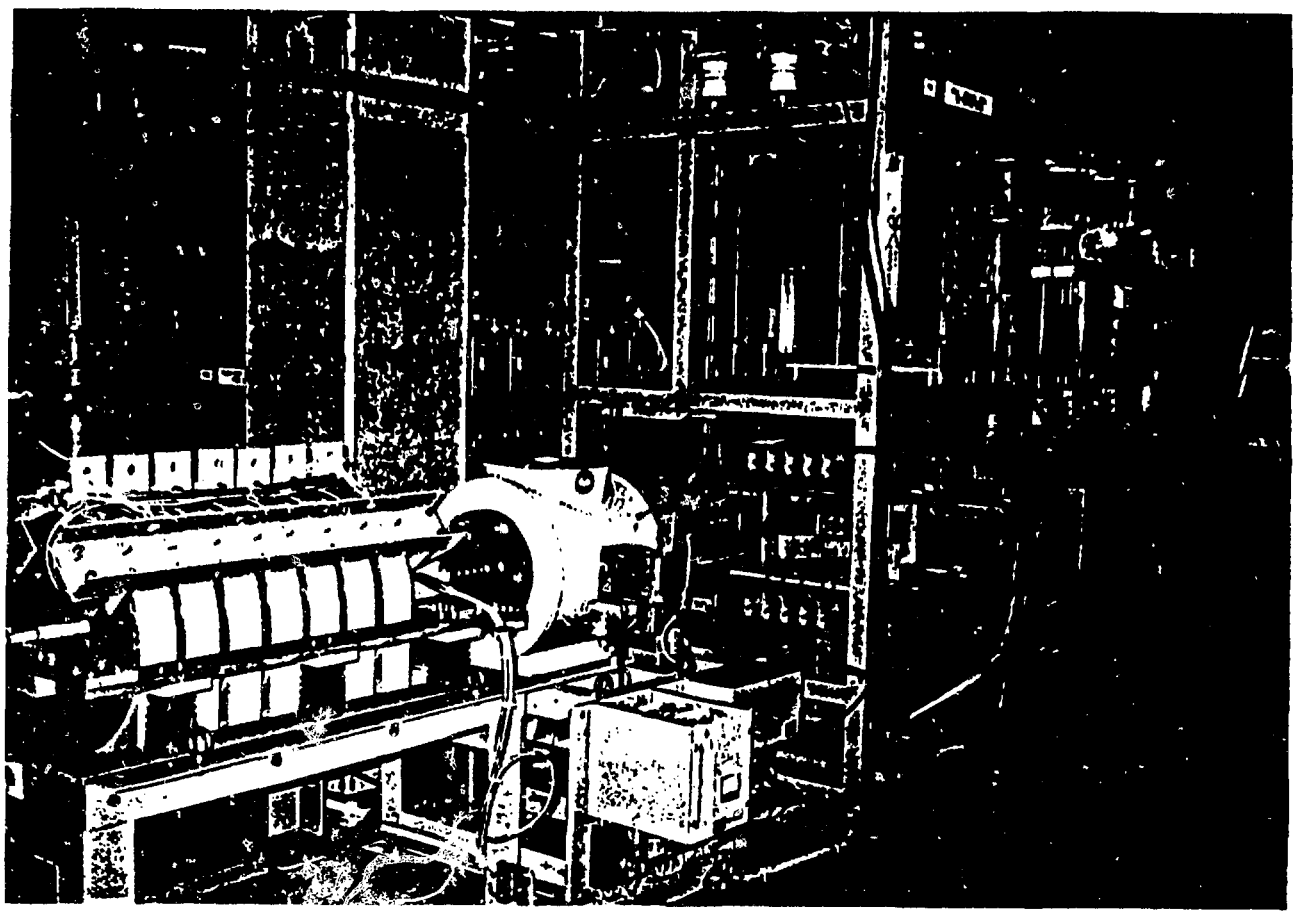

Fig.1 High Power Closing Switch System

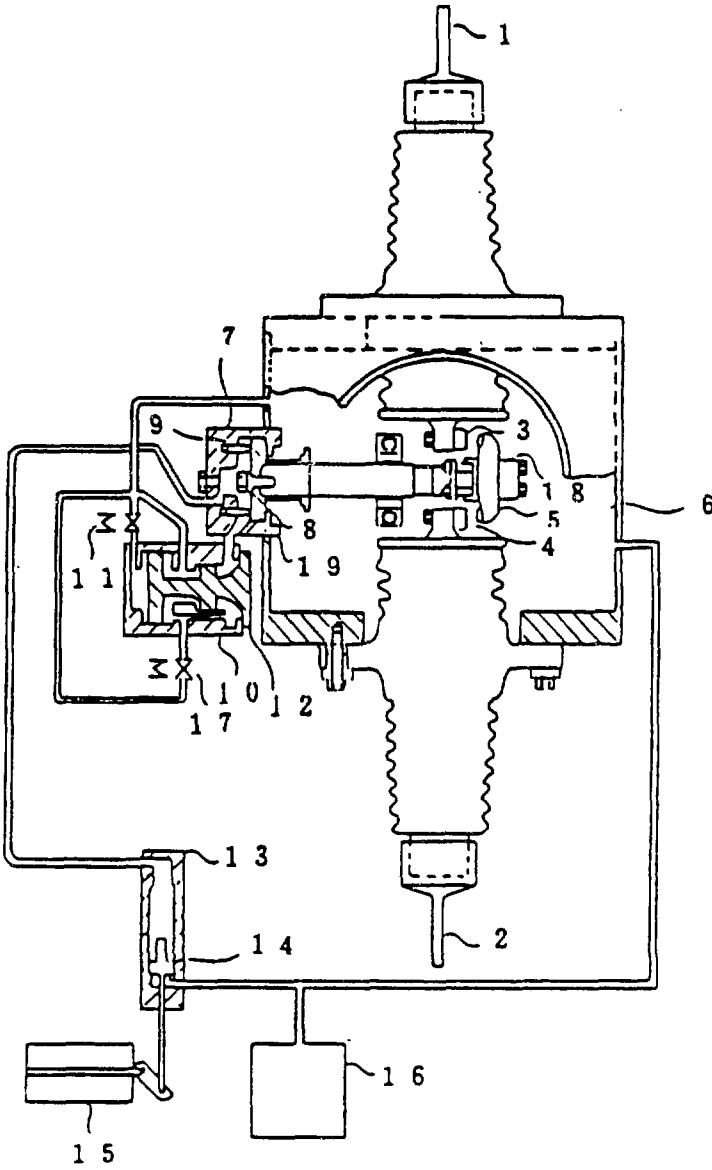

1. 2: Terminal
3. 4: Fixed Contact
5: Movable Contact
6: Tank
7: Cylinder
8: Piston
9: Spring
10: Control Valve
11: Closing Magnet Valve
12: Piston
13: Cylinder
14: Piston
15: Auxiliary Switch
16: Pressure Air Source
17: Magnetic Control Val
18: Rubbur Spring
19: Operation Valve

Fig.2 Schematic Structure of Closing Switch

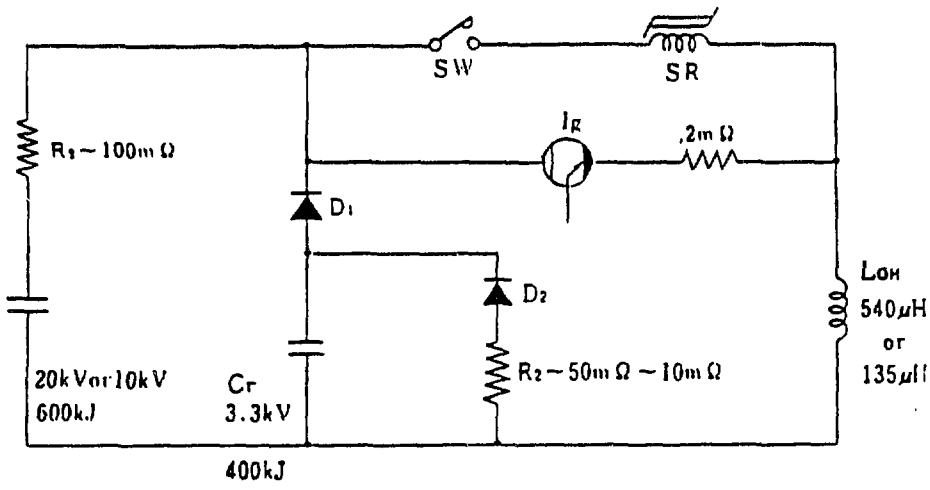

Fig.3 OH/Coil Circuit of the TPE-1RM15

Table-1 Specification of High Power Closing Switch

Rated Voltage	DC 25 kV, 1 min
Rated Current	DC 150 kA 1 sec or DC 60 kA 3 sec
Insulation Voltage	AC 50kV
Closing Time	20ms
Jitter	± 0.35 ms
Operaing Pressure	10kg/cm^2 Air or Nitrogen
Weight	400kg

WORKSHOP SUMMARIES

INTRODUCTION

Topical workshop sessions were held on each of the four topics (1) RFP Physics, (2) Front-End, (3) Magnetics, and (4) Electrical Design. These sessions were conducted in a relatively informal environment to encourage discussion. There was a chairman and technical secretary for each session. Participants were invited to submit papers used at these sessions for the Proceedings and these have been included.

The chairmen of each of the topical workshop sessions gave an oral summary during the final overall summary session. Written summaries of the topical workshop sessions were subsequently submitted for the Proceedings, and are included here.

RFP PHYSICS WORKSHOP
(Summary by Kurt Schoenberg and Paul Weber)

INTRODUCTION

The purpose of the physics workshop was to focus on plasma physics issues that drive RFP engineering design in both present and future experiments. Thirteen total papers (Appendix 1) were given at the formal and workshop sessions. The material presented was categorized into three major subjects: field errors, shell effects, and required plasma environment to insure performance. A summary of these subjects, and how they relate to RFP engineering design, follows.

FIELD ERRORS

The importance of field errors lies in reducing their effect to a level where they do not dominate, or significantly affect the plasma confinement. Ideally, one strives to design RFPs with zero errors. However, the realities of tolerances, diagnostic access, pumping, etc., force one to live with finite field errors. This session focused on two major issues: the importance of field errors to RFP performance in an absolute and relative sense, and whether field error concerns were adequately addressed by the present RFX and ZTH designs. In particular, the session included talks on externally driven field errors due to coil discreteness, coil positions, current feeds, shell imperfections, etc., internally driven field errors due to plasma intrusions such as armor and limiters, and finally equilibrium related errors due to plasma position tolerance and the shell poloidal flux gap.

Ken Sidikman (LANL) presented results from 3-D modeling of the ZTH design with rather realistic boundary conditions. The coils were included at their design position, and the shell penetrations (holes) were also included with their actual sizes and locations. The shell penetrations were treated as independent entities in that they were not assumed to couple to each other. Also the shell gap was not included.

There were two cases studied by the 3-D modeling. The first was a worst case estimate for ZTH, assuming the shell provides the complete plasma equilibrium. For that case, no island structures were discerned. In fact, it required errors 100 times larger than the worst case estimate before island structures were apparent between the reversal surface and the liner.

At 1000 times the present field errors, one might find significant magnetic stochaticity. Of course, caveats include the non-coupling assumption on the shell penetrations (which may be important), the omission of the gap (being evaluated), and the omission of errors in coil positions (which can be included).

General field error estimates for present and future devices were shown by Newton (Culham). He estimates the field errors and computes a figure of merit, that is the flux intersecting the wall normalized to the total wall area. According to these estimates, the larger presently operating devices (HBTX-1B, ZT-40M and OHTE) have rather similar figures of merit. The HBTX-1C experiment is expected to be significantly better, while RFX with a thick shell is likely to be worse. There is evidence, especially from the HBTX series of devices and from ZT-40M, that improving field errors has beneficial effects on confinement. Similarly, centering the plasma equilibrium position is beneficial, as is reducing the magnetic flux at the shell gap. It is, however, difficult to quantify the linkage between field errors and plasma performance, since many details of the plasma properties are poorly documented, and probably change with the magnetic boundary conditions.

The subject of the shell gap was discussed by Moses (LANL). He computes the image currents in the vicinity of gaps of various geometries in the absence of plasma. The "poloidal flux gap" (the gap across the minor cross-section) presents the largest challenge. For a simple butt gap, the estimate of the resulting field error is 20 to 40 times worse than that attributed to the largest vacuum pumping ports on ZTH. Hence, a superior gap is required, and is included in the ZTH design. This tapered gap design is based on a cylindrical model (toroidal corrections are likely to be small) in which the induced currents at the gap, responsible for driving large field errors, are made to cancel. The shell, therefore, maintains a good m=1, n=0 response to plasma equilibrium requirements.

An experiment on the effectiveness of tapered gaps was described by Grey (Culham). He used a series of cylinders and helmholtz coil generated fields, and measured the resultant fields inside the shell mock-ups. The effectiveness of the tapered gap was beyond doubt - there was no measurable change in the field along the length of such a gap.

In conclusion, there is a general consensus regarding the strong dependence of global plasma performance on field errors. However, the physical mechanisms responsible for this phenomenology are presently unclear. Along these lines, both ZTH and RFX designs are cognizant of and address externally driven field errors due to coil discreteness and coil position. Both designs also incorporate adequate voltage reserves to cover reasonable departures from their base design points.

Proper equilibrium control is also extremely important. In the ZTH design, this constraint drives the thin shell and compensated gap design. In RFX, it is anticipated that it will drive the alternate thin shell design.

SHELL EFFECTS

The major focus of this session was the stability requirements for the shell, and the limitations on shell design imposed by other design constraints.

Tamano (GA) described operation of the OHTE device with a 0.8 mm thick brass shell, that has a time constant for vertical magnetic field penetration of 1.5 ms (compared to 30 ms for the previous 14 mm aluminum shell. Operation with the resistive shell was said to be as good as, or perhaps even better than that with the conducting shell in terms of global plasma parameters. A local mode, dubbed "slinky", is occasionally observed with the resistive shell. However, the existence of the "slinky" mode with the old shell is undocumented. Fluctuations in the magnetic fields are independent of the shell type. The plasma resistivity may be a little higher with the resistive shell, perhaps due to machine conditioning, or perhaps attributable to the penetration of the l=6 field from the OHTE helical windings.

The resistive shell permits operation with some radial equilibrium control, which leads to longer discharges than were observed with the old shell. Control of the radial position to better than ± 7 mm may be a necessary condition for avoiding terminations in OHTE, though there is no physics interpretation for this observation.

Concern was expressed by Nebel (LANL) that at the high magnetic Reynolds numbers expected in RFX and ZTH, coherent MHD activity may become dominant, and result in degraded confinement. In this case, the shell time constant would have to be sufficiently long to suppress such modes, perhaps setting a lower time constant limit.

Further experimental evidence on the need for and required properties of a shell were provided by Robertson (U. Colorado). The Reversatron experiment has been operated with a good conducting shell, without a shell, and, presently, with a series of modular shells. The no shell data is reported in detail in Nucl. Fusion 30, 884 (1987), and shows an increased resistance in the plasma, with much shorter plasma duration and with 100 Gauss perturbation fields (compared to a 500 Gauss poloidal field). A global mode with m=1 and low values of n=1,2,3 was documented.

More recent experiments have utilized pieces of 0.25 mm aluminum sheet placed on the machine to form a modular shell, resulting in a time constant for vertical field penetration which is roughly 40 microseconds per layer. With one such layer, and many resultant gaps, the plasma resistance was intermediate between the full shell and no shell cases. Multilayer shells with overlapping gaps (as proposed for HBTX-1C) and with aligned gaps are planned, with some equilibrium control.

On Reversatron, the vertical field value is not critical. Variations of ± 20% in the vertical field from the optimal value make no significant difference to the discharge quality. The intrinsic field errors due to liner currents, finite coil windings, etc., have not been documented. The experimental data points to the desirability of some shell material, but the relationships between plasma quality and shell time constant need to be further explored.

Theoretical work (Marklin, LANL) has been done to examine the effects of shell resistivity on the growth of ideal MHD modes. The computations are preliminary. However the model points to the existence of operating points, characterized by a range of theta values, for which the growth times of the modes are many times larger than the shell time constant.

In conclusion, it appears from both experiment and theory, that the RFP can be operated with a shell whose time constant is smaller than the discharge duration so long as a proper equilibrium is maintained, and the time constant is large enough to suppress the growth of dangerous modes. The shell operation permits desirable aspects of operation, such as plasma position control by active feedback. Further theoretical investigations and planned experiments on HBTX-1C, OHTE, ZT-P and Reversatron, should be able to better address the tradeoff between shell thickness and plasma stability in the near future.

REQUIRED PLASMA ENVIRONMENT AND PERFORMANCE

The successful operation of next generation devices depends critically on the ability to exercise control over plasma parameters. Items such as equilibrium control have been addressed above, and wall protection and impurity control have been discussed at some length elsewhere in these proceedings. Density control by both gas puffing and pellet injection have been demonstrated on several operating devices. The subjects of volt-second consumption, termination control, and treatment of the data base for extrapolation to the design of future devices are discussed here.

The V-s consumption of a device is a strong function of both the start-up scenario employed, and the ultimate plasma quality. A wide variety of methods for establishing the RFP have been examined in ZT-40M by Phillips, et al. (LANL). By chosing the most efficient field programming, savings of 30% in resistive V-s consumption can be realized, in tandem with reductions in the peak voltages needed to increase the plasma current. Specifically, ramping the current while keeping theta at a low value is efficacious. It is also apparent that the dynamo mechanism is sufficiently robust to generate the required toroidal magnetic flux as the current is ramped. These data are quite encouraging in that they point to a reasonably wide operating regime for RFP formation.

Extrapolation to future devices is a strong function of the quality of the present database, and of physics understanding. Statistical methodologies can be applied to the problem, as discussed by Yoshida (U. Tokyo). Factor analysis was used to determine the relationship between

plasma performance and the control parameters. Regression analysis capability will be added in due course. (Such capability exists presently in the LANL LOCUS based data system and has been used in generating parameters expected for ZTH.)

An alternate methodology was used to describe the anticipated performance of the planned REPUTE-2 experiment, and an ultra-low q device to be used as a neutron source (Inoue). It would clearly be of great benefit to the community to have a data base system which is sufficiently comprehensive, and has proper statistical capability for predictions in designing new devices. Efforts toward such a system are being discussed by a number of individuals in the RFP community.

In conclusion, experiments on HBTX-1B and ZT-40M have demonstrated the feasibility of termination control, and both RFX and ZTH will have this capability. Both machine designs will employ graphite armor, which is our present best guess for adequate RFP wall protection and impurity control. In addition, both designs should yield good control of F and Θ, and have adequate volt-second reserves to meet the design operating point. With respect to the front end, the ZTH design and the alternate RFX thin shell design should have adequate equilibrium control capability. A summary of ZTH and RFX specifications is listed in Appendix 2.

APPENDIX 1

Workshop Session Papers (Grouped by Topic)

1. "3-D MHD Simulation of Field Errors in ZTH and ZT-40M," (K. Sidikman, et al.).

2. "Loop Voltages, Field Errors, Field Control, Manipulators, and Other Experience From HBTX-1B Relevant to Next Step RFP," (A. Newton).

3. "A Tapered Poloidal Gap For the Reduction of Field Errors," (R. Moses).

4. "RFP Operations With a Resistive Shell in OHTE," (T. Tamano, et al.).

5. "Operation of an RFP With a Modular Shell," (P. Schmid and S. Robertson).

6. "Instabilities of an RFP With a Resistive Shell," (G. Marklin).

7. "Reversed-Field Pinch and Ultra-Low q Discharges in Repute-2," (N. Inoue, et al.).

8. "RFP Start-Up and ZTH Predictions," (J. Phillips, et al.).

9. "Plasma Data Analysis Using Statistical Analysis System," (Z. Yoshida, et al.).

Formal Papers - Physics Overview Session, 3 papers

Informal Presentations

"Soft Termination Techniques," (C. Munson).

APPENDIX 2

Summary of Specifications

	ZTH	RFX
Poloidal Field System		
Peak plasma current (MA)	4	2
Range of peak plasma current (MA)	0.5-4	0.25-2
Risetime (90%) of I_ϕ (ms)	50 (2 MA)	15-50
	25 (1 MA)	
	12.5 (0.5 MA)	
Maximum toroidal voltage (kV)	1	0.7
Flat-top time for peak current (ms)	250	250
Maximum unipolar flux in magnetizing coil (V-s)	29.3	15
Ramping time (s)	0.4 (2 to 4 MA)	
Toroidal Field System		
Maximum initial toroidal field at R_o(T)		
Phase I (2 MA)	0.3	0.7
Phase II (4 MA)	1.0*	
Reversed field at liner (max. design)(T)		
Phase I	-0.7	-0.55
Phase II	-1.0*	
Reversed field at liner(typical,F=-0.2)(T)	-0.3(@4MA&Θ=1.5)	
Programming mode	Reversal time	
	0.5 to 20 ms	
Liner		
Minor inside radius (m)	0.4	0.475
Major radius (m)	2.400	2
Material	Inconel 625	Inc. 625
Liner resistance R_ϕ, R_Θ (mΩ)	≥ 8; ≥ 0.045	1.1
Wall protection or limiters	Graphite armor	Graphite armor

*To be achieved by the addition of power supplies

	ZTH	RFX
Shell		
Minor inside radius (m)	0.460	0.535
Major radius (m)	2.388	2.0
Type of construction	Single shell	Single shell
	Shielded gap	Butt joint
Time constant, shell wall (ms)	~1.5	20
Time constant, vertical field (ms)	~50	300
Material	Metallic/ Composite	Aluminum
Vacuum System		
Type of pumps	TMP	TMP/Cryo
Characteristic pumping time (s)	$\leq$ 14	2
Base pressure in liner at 22°C (torr)	$\lesssim 2\times10^{-7}$	
Gas fill (deuterium) pressure range (mtorr)	0.24 to 100	
Graphite temp. operate/bake (°C)	200/300	300/350
Power Supply Ratings		
Alternator (MVA)	1430	
Extractable energy (MJ)	600	
OH charging supply (MW)	Same Supply	70
I_ϕ, ramping and flat-top (MW)	200*	70
Equilibrium (MW)	70	70
I_θ, ramping and flat-top (MW)	16	70

*For 2 MA operation; for 4 MA operation will require 800 MW.

	ZTH	RFX
Plasma Parameters		
Design I/N ($\times 10^{-14}$ A-m)	3.4	2-4
Design electron density at 4 MA ($\times 10^{20}$ m^{-3})	2.3	≤ 1
Range of electron density ($\times 10^{20}$ m^{-3})	0.3-5.0	0.3-2.0
Design electron temperature (keV)	T = 1.0×I(MA)	1
Range of electron temperature (keV)	0.5-5.0	0.5-2.0
Design beta theta	0.10	0.1
Range of beta theta	0.05-0.2	0.05-0.15
Design internal inductance l_i	1.4	Similar
Range of l_i	0.5-2.0	Similar
Design Λ	-0.20	Similar
Range of Λ	-0.7 to 0.2	Similar
Design Θ	1.5	Similar
Range of Θ	0.0-1.9	Similar
MBFM μ cut off (design value)	0.72	α=4, Θ_o=1.4
Range of cut off	0.7-0.9	α=2-6, Θ_o=1.4
Design F	-0.2	-0.3
Range of F, Phase I (2 MA)	-1-0	-0.8-0
Phase II (4 MA)	-0.7-0	
Life Cycles		
1 MA discharges	50,000	100,000
2 MA discharges	20,000	10,000
4 MA discharges	10,000	

FRONT-END WORKSHOP
(Summary by David M. Weldon)

Papers were presented describing aspects of three new machines in various stages of design or construction: The Madison Symmetric Torus at the University of Wisconsin, TPE-RX at Tanashi, and ZTH at Los Alamos. Workshop discussions touched on many features of RFX also.

MADISON SYMMETRIC TORUS (MST)

The Madison Symmetric Torus is now under construction. Like the present RFP at the University of Wisconsin, MST uses the magnetic core and electrical system of the Wisconsin Levitated Octupole. However, it will have a new vacuum vessel with smaller field errors and better diagnostic access. Currents are driven in the vacuum vessel itself which serves simultaneously as vacuum liner, shell, and coil system. The new vessel is ready for shipping so the machine is close to final assembly. Some parameters of the machine are: major radius 1.5 m, minor radius 0.52 m, liner thickness 5 cm (aluminum), core volt-seconds 2.2 V-s, current 800 kA.

Three aspects of the machine were of special interest:

1. The plasma can rest directly on the shell which will allow investigations of the effect of the shell-plasma separation and the effect of field errors on plasma resistance.

2. The vacuum chamber can be opened in two hours, and a complete cycle of opening and reassembly can be done in a day. The unique vacuum sealing and gap shielding technology was developed at the University of Wisconsin.

3. An electrical break in the poloidal direction has been developed which will hold the startup voltage in the presence of plasma.

TPE-RX

The area of the TPE-RX design discussed was the mechanical assembly and support philosophy. TPE-RX is designed to use a large number of small structural elements rather than large castings or single piece assemblies seen in RFX or ZTH. Some of the smaller elements can be bolted together for ease of assembly, but the basic units are small. The idea is similar to building a bridge out of standard channel and I-beams.

VACUUM SYSTEMS

The ZTH vacuum stations will be self-contained, each with its own roughing and protection system. If something goes wrong with a station, it will valve itself off and shut down. No redundancy of major components (fore-pumps, roots pumps, etc.) is considered within a vacuum station because of the cost of extra equipment which must be maintained in a standby condition. No manifolding of major components will be done such as was done in the ZT-40 fore-pump and roots system. This modular approach should result in greater overall system reliability.

DISCHARGE CLEANING

Jim Downing introduced a new figure of merit for discharge cleaning effectiveness based on the probability of impurity atoms being pumped away. RFX plans no discharge cleaning between shots, while ZTH plans to use PDC between shots to heat and condition the armor. RFX will maintain the liner at constant temperature by using electric heaters and forced air liner cooling. The RFX PDC will operate at 0.5 Hz; ZTH PDC will operate at 60 Hz between shots, but with an overall duty cycle less than 1. RFX discharge cleaning parameters are loop voltage 150 V, toroidal field 500 Gauss, and duration 2 ms.

MAGNETIC FIELD PROBLEMS FOR TURBO PUMPS

There was agreement that operating turbo pumps in a magnetic field was a potential problem because of overheating of the rotor. In both RFX and ZTH the magnetic field is on for 3 to 5 seconds. Stray field is somewhat greater for ZTH as might be expected. Los Alamos found only one brand of turbo pump which would survive at the desired location for the pump. One possible solution to the problems is to move the turbo pumps farther away, but this also reduces pumping speed and machine access. There were also some cautions about using gate valves if the liner is ever pressurized. The problem is caused by the valve being forced slightly open, tripping the vacuum system off. The use of a "right-angle" valve is suggested.

REFUELING SYSTEMS

ZTH and RFX refueling specifications differ by a factor of 3 to 5. RFX is 7000 mbar-liter/sec, while ZTH is lower. This is not a problem because of the ease with which the number of refueling stations can be increased or the gas pressure increased.

RESIDUAL GAS ANALYZERS

Continuous RGA monitoring of torus and vacuum stations was discussed. The philosophy of data archiving is affected because many present systems are geared to accept and log data only after a shot.

ARMOR SUPPORT AND EROSION

There was general agreement that eddy current torques and forces on armor tiles were small. Forces from diversion of current from the liner into the support structure was considered by the RFX designers because the armor lies against the liner wall. ZTH designers considered the forces caused by breakdown between armor tiles during a plasma termination. This is not a consideration for RFX because of the lower liner resistance. The magnitude of the tile forces depends in both cases on the assumed scenario for plasma termination. A termination time of 0.1 ms was chosen for RFX because it is pessimistic and short times do not give insurmountable problems. Calculations have been done for ZTH to predict the allowed loop voltage at any plasma current with force on the tiles as the parameter for each family of curves. ZTH tile supports are designed to withstand 900 N inward force.

A scrape-off length model of energy transport to the armor has been developed which incorporates the unique features of the RFP. There is a problem of erosion of armor at ports, but guidelines have been developed to design tile shapes which minimize the problem.

ZTH POLOIDAL GAP AND SHELL

During the formal sessions, it was noted that Culham had done calculations on overlapped gaps and performed experiments to verify the calculations. The advantage of the overlap is real, but the construction is intimidating.

A finite element analysis of the ZTH shell is under way. Complete results are not available yet because forces are being added systematically so results can be checked at each step.

THERMAL ANALYSIS OF THE ZTH FRONT-END SYSTEM

An analytic model of the liner cooling has been studied as a preliminary to a finite element calculation. The finite element calculation will investigate the transient solution. Heat flow to shell is 21 kW at 300^{o}C on the liner. (This gives a 20-minute cool down time at 4 MA.) The thermal insulation blanket is perhaps too thick. Temperature of the electric insulation is 120^{o}C at worst.

Workshop Session Papers

1. CPRF/ZTH Shell Poloidal Gap Design and Fabrication (E.J. Yavornik, et al.)

2. CPRF/ZTH Toroidal Conducting Shell Finite Element Analysis (C.L. Baker, et al.)

3. Vacuum/Gas Handling Systems for ZTH (J.N. Downing)

4. Armor Heat Flux Design for ZTH (J.N. Downing)

5. On Procedure of Assembly and Disassembly of RFP Apparatus (N. Suzuki, et al.)

6. CPRF/ZTH System Thermal Analysis (M.T. Gamble)

7. Engineering Features of the Madison Symmetric Torus (R.N. Dexter, et al.)

Formal Papers - Front-End Session, 9 papers

Informal Presentations

MAGNETICS WORKSHOP
(Summary by Andrea Stella)

FIELD ANALYSIS

Stray fields seem to be of paramount importance for the plasma behavior so that a deep analysis of all the possible stray field sources should represent a major concern for the engineering design of the next step RFP devices.

POLOIDAL FIELD SYSTEM

Compared with RFX, ZTH shows background stray field (i.e., with all the coils in their ideal position) which is one order of magnitude larger (1 mT compared with 10 mT).

Other possible sources of stray field from the PF coils have not been examined in a systematic way in ZTH. However, the tolerances specified on the OH coil radii (6.35 mm) appear unnecessarily large, especially having in mind that it is currently normal practice in coil manufacturing to prescribe much tighter tolerances (around 1 mm) for coils of similar size.

It has been stressed that the relatively high loop voltage requirements in large RFPs of the next generation have a strong impact on the overall machine design and represent an engineering drawback, mainly as far as field errors are concerned.

High loop voltage specifications have mainly two implications:

1. Need of subdividing the magnetizing field coils into sections (typically four for RFX and ZTH), with a lot of coil terminals and possibly current imbalance among branches.

2. Substantial induced current into structural conducting elements and vacuum vessel, and current diffusion phenomena within the coil conductors.

Both the items above represent major contributions to the overall stray field so that it can be concluded that high loop voltage and low level of stray fields are, to some extent, conflicting requirements.

TOROIDAL FIELD SYSTEM

All the machinery described during the workshop presented 48 coils, which is supposed to represent the maximum number that was possible to accommodate, having in mind engineering constraints and accessibility requirements; however, since toroidal field ripple is supposed to represent

an extremely negative item, the solution chosen by other machines than RFX, consists in moving the coils as far away from the plasma as necessary.

STRESS ANALYSIS

One of the major question marks about stress analysis is related to the model to be used for finite element calculations. There is a great deal of concern on that issue; also because different models, applied to the same problem, sometimes give different results, as far as stress level is concerned, failing to accurately predict the actual stress, possibly in critical regions. In particular, stresses in the lower modulus materials of a composite structure, as coils are, may be largely underpredicted. It is concluded that the technique of using smeared materials can be successfully used, but should be examined carefully with each application.

A stress analysis, performed on ZTH EF9 coil (which is supposed to be the most critical), shows results remarkably in agreement with the results obtained in RFX for similar coils (E7 and E8). In both machines the coils, clamped on discrete supports, have been analyzed with a similar approach but different models and codes. The similarity of the results gives confidence in the correctness of the method.

Workshop Session Papers

1. Laminated Beam Analysis (J. Hill)

2. Finite Element Analysis of Coils (S. Girrens)

3. Numerical Analysis of Eddy Currents and Error Field for RFP by "INCANET" (N. Suzuki, et al.)

Formal Papers - Magnetics Session, 5 papers

Informal Presentations

The present summary includes major items discussed during the workshop session as well as a number of topics raised at the formal sessions.

ELECTRICAL DESIGN WORKSHOP
(Summary by A. Maschio)

A review of the problems related to the design of the different components of the power supply systems for the RFP machines has been carried out. In the toroidal field circuit it has been observed that the use of modular capacitor banks, though possibly more expensive than the inductive storage devices, leaves a higher degree of flexibility in the programming modes of the toroidal field; moreover, due to recent technical advancements, the energy density of the capacitor is increased, allowing for the design of larger modular banks. Some questions remain as far as the protection of such units is concerned. Finally, there is a risk, due to the uncertainties of the physics, of building capacitor banks much larger than really required.

As for the power supply of the poloidal field circuit, it has been recognized that in very complicated circuits, like in RFX and ZTH, a careful evaluation of the possible fault conditions is essential in the design of the different components. The analysis of the fault conditions requires, in some cases, taking into account the overall system, due to the many interactions among the different parts of the circuit. No defined criteria can be worked out for this activity, which is supposed to take a significant part of the design time. Finally, some detailed aspects of various components such as transfer resistors, converters and their transformers, vacuum circuit breakers, fast making switches and ZnO varistors, have been discussed and recent experimental results have been presented.

Workshop Session Papers

1. TPE-RX-1/1RM15 High Power Closing System (T. Oyabu)

Formal Papers - Electrical Design Session, 9 papers

Informal Presentations